ABSTRACT

Title of dissertation: CHARACTERIZATION OF JOSEPHSON DEVICES FOR USE IN QUANTUM COMPUTATION

Sudeep K. Dutta, Doctor of Philosophy, 2006

Dissertation directed by: Professor Frederick C. Wellstood
Department of Physics

This thesis examines Josephson tunnel junctions as candidate qubits for quantum computation. A large area current-biased junction, known as a phase qubit, uses the two lowest energy levels in a tilted washboard potential as the qubit states $|0\rangle$ and $|1\rangle$. I performed experiments with 10×10 μm^2 Nb/AlOx/Nb qubit junctions, with critical currents of roughly 30 μA. The state of a device was initialized by cooling below 50 mK in a dilution refrigerator. In order for quantum mechanical superpositions to be long-lived, it is necessary to isolate the junction from noisy bias leads that originate at room temperature. I studied two types of isolation: an LC filter, and a broadband scheme that used an auxiliary junction, resulting in a dc SQUID.

One of the main goals of this work was to determine how well a simple Hamiltonian, derived assuming just a few lumped elements, describes the observed behavior of a macroscopic Josephson device, including coherent dynamics such as Rabi oscillations. I did this by comparing results to the expected behavior of ideal two-level systems and with more detailed master equation and density matrix simulations.

I performed state manipulation by applying dc bias currents and resonant microwave currents, and through temperature control. The tunneling escape rate of the junction from the states $|0\rangle$ and $|1\rangle$ (zero voltage) to the running state (finite voltage) depends on the occupation probability of the energy levels and served as state readout.

Experiments to measure the relaxation time T_1 between $|1\rangle$ and $|0\rangle$ were performed by examining the dependence of the escape rate with temperature, yielding a maximum $T_1 \approx 15$ ns. Measuring the decay to the ground state after applying a microwave pulse revealed at least two time constants, one of about 10 ns and another as long as 50 ns. The spectroscopic coherence time T_2^* was estimated to be roughly 5 ns by measuring resonance widths and the decay envelope of coherent Rabi oscillations was found to have a time constant $T' \approx 10$ ns over a wide range of conditions.

CHARACTERIZATION OF JOSEPHSON DEVICES FOR USE IN QUANTUM COMPUTATION

by

Sudeep K. Dutta

Dissertation submitted to the Faculty of the Graduate School of the
University of Maryland, College Park in partial fulfillment
of the requirements for the degree of
Doctor of Philosophy
2006

Advisory Committee:

Professor Frederick C. Wellstood, Advisor / Chair
Professor J. Robert Anderson, Advisor
Professor Christopher J. Lobb, Advisor
Professor Steven M. Anlage
Professor Donald R. Perlis

Preface

While the Acknowledgements recognizes the people that helped me throughout grad school, I wanted to reserve this page for resources I used specifically in preparing this document.

The previous theses from my group are outstanding [1–3]. In the interest of saving trees, I could have replaced about half of my thesis with references to those works. Especially in recent months, Fred Strauch has been an invaluable resource. It would have been easier on both of us if he had just written a few sections of Chapter 3 himself. Intriguing points that he has made over the years appear in several other places.

Naturally, many of the explanations I have provided come straight from the professors. While I was writing this thesis, Dr. Lobb foolishly agreed to play Twenty Questions with me every Wednesday and many of his answers (occasionally more than "yes" or "no") appear throughout the thesis. He and John Matthews are responsible for big chunks of Chapter 2. Over the past few years, Dr. Wellstood has produced a sizeable stack of notes and chalkboards full of diagrams and derivations. These covered topics ranging from dilution refrigerator techniques to quantum mechanical simulations. I have taken quite a bit from these and chosen to lump all of the documents under Ref. [4], as I am unable to read his handwriting and decipher the titles he gave them.

I had the great pleasure of sitting in on PHYS 711: Atomic Physics in the Fall 2005 semester, taught by Drs. Bill Phillips and Trey Porto. Seeing two-level systems presented from a different point of view was enormously beneficial. They cleared up many concepts and I hope they don't mind that I have reproduced some

of their arguments in Chapter 3 [5].

I don't think I've ever typed anything longer than about 12 pages, so I was terrified when I started writing. I started with the LaTeX template created by Dorothea Brosius of the University's Institute for Research in Electronics and Applied Physics and only had to make minor changes. The document was compiled with the open-source MiKTeX 2.4 packages and I used Aleksander Simonic's wonderful shareware editor WinEdt v5.4. Essentially all of the data analysis was performed with MATLAB R12 and R14. I drew graphs with OriginPro 7.5 and layout for the figures was done in Adobe Illustrator CS2.

In loving memory of my father,
who taught me by example,
"If you have to do something, do it right."

Acknowledgements

I've always been amused at how sappy this section of the average thesis is. Now that I've made it through grad school, I have a better idea of where all the emotion comes from. I hope my effort, below, doesn't disappoint future generations.

I will never be able to repay the debt I owe to my advisors, Profs. Fred Wellstood, Chris Lobb, and Bob Anderson, who restored my faith is physics, mankind, and myself in just a few years. If and when I grow up, I want to be like Dr. Anderson, who has an irrepressible wit and is always able to ask the surprisingly penetrating question. Dr. Chris, a fellow New Jerseyan, has uncommonly clear vision on a range of matters, which I relied on to get out of many sticky situations.

As for Dr. Wellstood, I just can't imagine enduring the terrors of grad school under anyone else's direction. In times of relative peace, he often let me call the experimental shots, all the while offering a critical eye, encouragement, and endless notes and derivations. Even though all of my hot leads ended up as incoherent goose chases, I think he understood that the process was enormously satisfying. As deadlines approached, I saw how he made sound decisions (on matters of "politics" and science), and I consider that an invaluable part of my education.

In case my colleagues are reading this and can distinctly picture me screaming, I don't mean to suggest that things were always rosy. At all. In fact, I probably had a violent disagreement with one of the bosses every 17 hours. What sets these gentlemen apart is that when they told me I was wrong, they usually told me *why* I was wrong. By actually bothering to *gasp* advise me, my advisors made me a better scientist and lowered my blood pressure to record lows.

Allow me to sum up. The profs gave me an interesting and timely project, a

lab full of equipment, great people to work with, and good advice whether I asked for it or not. In the end, though, the success of a chunk of the experiments was left to me. Now that's upper management at its finest. I hope they're satisfied with what I chose to do with the pieces of the puzzle.

I should also thank the rest of my thesis committee, Profs. Don Perlis and Steve Anlage, who put up with (nearly) endless delays. In addition, Dr. Anlage somehow tolerated me for two years, when I worked for him as an unruly undergrad; it's fair to say that a day doesn't go by in lab that I don't use something I learned in his group.

I must also acknowledge the members of the experimental nuclear physics group. Prof. Phil Roos was my undergrad research and academic advisor and is occasionally pressed into service to this day. Prof. Betsy Beise taught me about electronics and how to solder well; as far as I can tell, this remains my only marketable skill. I learned just about all of the LabVIEW I know from Fraser Duncan. Prof. Jim Kelly taught me FORTRAN and Mathematica and, perhaps more importantly, the benefits of attacking a problem with all you've got.

A famous biophysicist once compared grad school unfavorably to a deep, dark tunnel. Given the location of our lab, I'll not disagree with that, but I'm sure it's much worse if you're down there alone. It is not possible to overstate the contribution that Huizhong Xu, Roberto Ramos, Andrew Berkley, Mark Gubrud, and a slew of undergrads (including Sam Reed, Bill Parsons, and Joe Foley) made to this thesis. They had the experiment and refrigerator running smoothly when I joined the project, leaving me in the incredibly enviable position of just having to concentrate on taking data. I was particularly fortunate to overlap with the first two guys for 18 months, every day of which I learned something new. Although Huizhong left the project over two years ago, his fingerprints can still be clearly seen on the detection electronics, acquisition and simulation code, and my insatiable

cookie jones. Roberto, who often let me in on specials at ramos.com, taught me a great deal about low temperature physics and the philosophy of doing effective experiments.

I owe a tremendous amount to everyone currently working on the project as well. I was very lucky to witness Tauno Palomaki's seminally fiducial year. I cleverly wrote this thesis very slowly, so that he could do the experiments that explained many of my results. Rupert Lewis was somehow able to herd a sub-basement full of students, while still managing to teach me about microwave and low temperature techniques. I mimicked several experiments that Hanhee Paik first performed; she also taught me half of the Korean I know. It was great fun to watch as Ben "Coop" Cooper and Tony "Tony" Przybysz brought energy and fresh ideas to the project. I'm most impressed with Hyeokshin Kwon for withstanding my Korean. John Wyrwas and Bjorn Van Bael accomplished more than I thought possible in the chaos of our lab. I don't know where to put Ben Palmer, but he was a dependable source of information and insights.

Perhaps the most pleasant surprise about working on this project was our close collaboration with Prof. Alex Dragt and his group, including Phil Johnson, Fred Strauch, Kaushik Mitra, Momahed Abutaleb, and Bill Parsons. These are no ordinary theorists. Not only were they able to turn our confusing experimental data into publishable results, but they also often made staggeringly reasonable proposals for new experiments to try.

I am grateful to the rest of the research group for creating such a pleasant place to work and putting up with all of my quirks. I've known Gus Vlahacos longer than I care to mention; I wonder if either of us will be able to work above sea level. John Matthews was my one-stop-shop for questions about SQUIDs and LabVIEW. Crazy David Tobias was always willing to lend a hand or engage in a little high stakes wagering. The corner of the lab was never quite as friendly after Su-Young

Lee left; she taught me the other half of the Korean I know. Matt Sullivan and Monica Lilly defy description; I'll just say that lab would've been far duller without them. Hua Xu and Zhengli Li were as helpful as they could be, even as we slowly pushed them out of lab. Satheesh Angaiah was my faithful basketball buddy.

The Center for Superconductivity Research has been a terrific place to work. I'll start at the top with Admiral Rick Greene, who runs a tight ship. I'd never admit this to him, but I learned a great deal (about physics and giving talks) in his seminar. Doug Bensen and Brian Straughn not only are capable of solving any of the random problems constantly thrown at them, but can also make you laugh an unhealthy amount while doing so. I'm glad that I don't know how much bureaucratic red tape Belta Pollard, Cleopatra White, Grace Sewlall, and Brian Barnaby cut through so we could get our work done.

I was often suspicious of how friendly and eager to help the students and post-docs in the Center were. I had a number of microwave emergencies that Mike Ricci, Dragos Mircea, Sameer Hemmady, and Nate Orloff handled cooly; they, for instance, helped me do the network analyzer measurements in Chapter 5. I could always go to Yuanzhen Chen and Samir Garzon to ask about low temperature methods or to "borrow" liquid helium. I eased the misery of writing this thesis by commiserating with Josh Higgins. I'm proud to say that, by finishing three months after him, I won our race. Incredibly, Clippity always seemed to know just when I wanted to make a list. You'd be hard pressed to find anyone more enthusiastic or with a better name than Diane Elizabeth Pugel. Maria Aronova has the amazing ability of raising the spirits of any room she walks into; she also was quick to point out how little Korean I actually knew. My memory is failing me (due to a lack of oxygen in lab), so I can only give a partial list of the people that I either stole equipment from or who entertained me in the darker times: Pengcheng Li, Enrique Cobas, Gokhan Esen, Tarek Ghanem, Dan Lenski (my nemesis), Adrian Southard, Todd

Brintlinger, Yung-Fu Chen, Jim Ayari, and Tobias Dürkop.

Next up is the rest of Department of Physics. Prof. Nick Chant couldn't have made it easier for me to meet the program's requirements, for which he has my profound gratitude. Jane Hessing's ability to remember every form that I needed to fill out was truly remarkable. I'm sure I would have ended up in the wrong building on the day of my defense if it wasn't for her. Bernie Kozlowski, Linda O'Hara, and Tom Gleason never turned me away, whether I came to beg for help or just to chat. Jesse Anderson and Bob Dahms dealt with all of my purchasing requests with freakish efficiency. Pauline Rirksopa, Russ Wood, Bob Woodworth, Al Godinez, and George Butler always went out of their way to make my life a little bit easier.

Finally, I wish to thank my family: my cousins, Sompa, Chino, Munu, and Ashim, who did more to make this thesis possible than I could have ever asked; Subrata, my big brother and first physics professor; and Kabita, who has defined nearly every aspect of her son.

I am well aware that second chances of the quality that Maryland has given me don't come along often in life. I could try to describe what this school means to me, but I've already gone on far too long. I'll instead end with a cheer. Go Terps!

Table of Contents

List of Tables

List of Figures

List of Abbreviations

Symbols that are used through the thesis are listed below. Several symbols that are only used in a few sections within the same chapter have been omitted.

Fundamental constants

h	Planck's constant, 6.626×10^{-34} J $\cdot$ s
$\hbar$	$h/2\pi$, 1.054×10^{-34} J $\cdot$ s
e	absolute value of the electron charge, 1.602×10^{-19} C
Φ_0	superconducting flux quantum, $h/2e = 2.068 \times 10^{-15}$ T $\cdot$ m^2
k_B	Boltzmann's constant, 1.381×10^{-23} J/K

Notation

$\boldsymbol{v}$	vector
$\underline{M}$	matrix
$\dot{a}$	derivative of a with respect to time

Junction parameters and controls

γ	phase difference across junction
V_J	voltage across junction
V_b	measured junction voltage on bias line, due to V_J and stray series resistance
I_b	current bias
I_0	critical current
I_r	reduced current bias, I_b/I_0
C_J	shunting capacitance
R_J	shunting resistance
m_J	effective mass of "phase particle," $C_J\,(\Phi_0/2\pi)^2$
L_J	Josephson inductance, $\Phi_0/2\pi I_0 \cos\gamma$
E_J	Josephson coupling energy, $\Phi_0 I_0/2\pi$
E_C	charging energy, $e^2/2C_J$
ω_p	plasma frequency, $1/\sqrt{L_J C_J}$
ω_{p0}	zero-bias plasma frequency, $\sqrt{8E_C E_J}/\hbar$
β_C	Stewart-McCumber hysteresis parameter, $(\omega_{p0}\,R_J C_J)^2$

Q	quality factor, $\omega_p R_J C_J$
$B_\parallel$	in-plane suppression field
$I_{\mu w}$	microwave activation current
P_S	nominal power of $I_{\mu w}$, as set at the source
ω_{rf}	angular frequency of $I_{\mu w}$
$C_{\mu w}$	capacitance that couples $I_{\mu w}$ to qubit

SQUID parameters: In addition to the quantities listed below, each of the SQUID junctions is described by the parameters above. A subscript '1' indicates the qubit junction; '2' indicates the isolation junction. For example, I_{01} is the qubit junction's critical current.

I_b	total current bias
I_1	current through qubit branch
I_2	current through isolation branch
M_b	mutual inductance between the bias line and SQUID loop
I_f	flux current
M_f	mutual inductance between the flux line and SQUID loop
J	circulating current
Φ_A	applied flux due to flux current, $M_f I_f$
Φ_T	total flux due to I_b, I_f, any applied magnetic field, and circulating current
L_1	geometrical inductance of qubit branch of the SQUID loop
L_2	geometrical inductance of isolation branch of the SQUID loop
β	modulation parameter, $L\left(I_{01}+I_{02}\right)/\Phi_0$
N_Φ	flux state label

Coupled qubits

C_C	coupling capacitor
L_C	stray inductance from coupling lines
ζ_0	purely capacitive coupling constant, $C_C/\left(C_J+C_C\right)$
ξ	LC coupling constant, $\sqrt{C_C/\left(C_J+2C_C\right)}$
ω_C	renormalized LC frequency, $1/\left(\xi\sqrt{L_C C_J}\right)$
$\zeta\left(\omega_p\right)$	effective capacitive coupling constant, $\xi^2/\left(1-\xi^2-\omega_p^2/\omega_C^2\right)$

Device names: For the coupled devices, a superscript 'A' or 'B' indicates the individual device. For example, I_{01}^{B} is the qubit junction's critical current for DS_2B.

- LC_2 two capacitively-coupled LC-isolated phase qubits, LC_2A and LC_2B; see §4.2.1
- DS_1 single dc SQUID phase qubit; see §4.3.1
- DS_2 two capacitively-coupled dc SQUID phase qubits, DS_2A and DS_2B; see §4.3.2

Dissipation

- Y shunting admittance
- R_{eff} effective parallel resistance, $1/\mathrm{Re}\,(Y)$
- X_{eff} effective parallel reactance, $-1/\mathrm{Im}\,(Y)$
- L_{eff} effective parallel inductance, X_{eff}/ω
- C_{eff} effective parallel capacitance, $-1/\omega X_{\mathit{eff}}$
- R_{bn} resistance that characterizes noise on the current bias line
- R_{fn} resistance that characterizes noise on the flux bias line

Quantum properties and simulation

- $|n\rangle$ n-th metastable eigenstate of the system; $|0\rangle$ is the ground state
- E_n energy of state $|n\rangle$
- ω_{nm} angular frequency spacing between $|n\rangle$ and $|m\rangle$, $|E_m - E_n|/\hbar$
- ρ density matrix
- ρ_{nm} element of the density matrix
- ρ_n diagonal element of the density matrix, ρ_{nn}
- ρ_{tot} probability of being in the zero-voltage state, $\sum \rho_n$
- P_n normalized occupation probability, ρ_n/ρ_{tot}
- Γ_n tunneling escape rate from state $|n\rangle$
- Γ total escape rate, $\sum P_n\Gamma_n$
- W_{nm} inter-level transition rate from $|m\rangle$ to $|n\rangle$
- W_{nm}^{t} thermal transition rate from $|m\rangle$ to $|n\rangle$
- $\gamma_{n,m}$ matrix element of the phase operator $\hat{\gamma}$ that characterizes transitions
- $\hat{x}$ modified phase operator, $\sqrt{m_J\omega_p/\hbar}\left(\hat{\gamma} - \sin^{-1} I_r\right)$
- T_1 dissipation or relaxation time
- T_ϕ dephasing time

T_2	coherence time, $(1/2T_1 + 1/T_\phi)^{-1}$
$\Delta\omega$	full width at half maximum of a resonance, in terms of angular frequency
T_2^*	spectroscopic coherence time, $2/\Delta\omega$ for $0 \rightarrow 1$ transition
Ω_{nm}	bare Rabi angular frequency between $\|n\rangle$ and $\|m\rangle$
$\overline{\Omega}_{nm}$	effective Rabi frequency; includes detuning
$\Omega_{R,nm}$	minimal Rabi oscillation frequency in a multi-level system; defines resonance (ω_{rf} need not equal ω_{nm})
$\overline{\Omega}_{R,nm}$	effective Rabi oscillation frequency with respect to $\Omega_{R,nm}$
T'	decay time constant of Rabi oscillation envelope

Experimental data

$h\,(t_i)$	number of times the junction switched to the voltage state in the histogram bin centered at time t_i
Γ	measured escape rate, calculated from h
Γ_{bg}	escape rate in the absence of a microwave current
$\Delta\Gamma/\Gamma$	escape rate enhancement due to a microwave current, $(\Gamma - \Gamma_{bg})\,/\Gamma_{bg}$

Chapter 1

Introduction

1.1 A Brief Review of Quantum Computation

In the early 1980's, Feynman pointed out the difficulties of exactly simulating, or perhaps imitating, a quantum system using a classical computer, even one that was probabilistic in nature [6]. In particular, he argued that the size of the classical computer will grow exponentially with the size of the system being studied. As an alternative, he offered the possibility of using a computer that took advantage of the quantum mechanical nature of its own elements to perform simulations and faithfully include the unpredictability of quantum physics.

The building block of a quantum computer is the quantum bit, or qubit, which has two states $|0\rangle$ and $|1\rangle$. Unlike a classical bit, which must be definitively in either state, a qubit can be in an arbitrary superposition $a\,|0\rangle + b\,|1\rangle$, where a and b are complex coefficients. For this reason, a quantum computer may simplistically be thought of as a parallel array of classical processors. A limitation is that, at the end of a computation, only classical information can be extracted. A quantum computer would have access to an additional resource with no classical analog, entanglement, where the states of multiple qubits are inextricably linked. More precisely, the collective state cannot be expressed as the direct product of single qubit states.

Figure 1.1 shows a plot of the number of papers per year that had quantum computation terms in their abstracts. It is evident that there was minimal interest in the field at the time of the original proposals, in the 1980's. While the ideas were intriguing, it was not thought possible to physically realize a quantum computer. Also it was known that the potential power of classical analog computing was largely

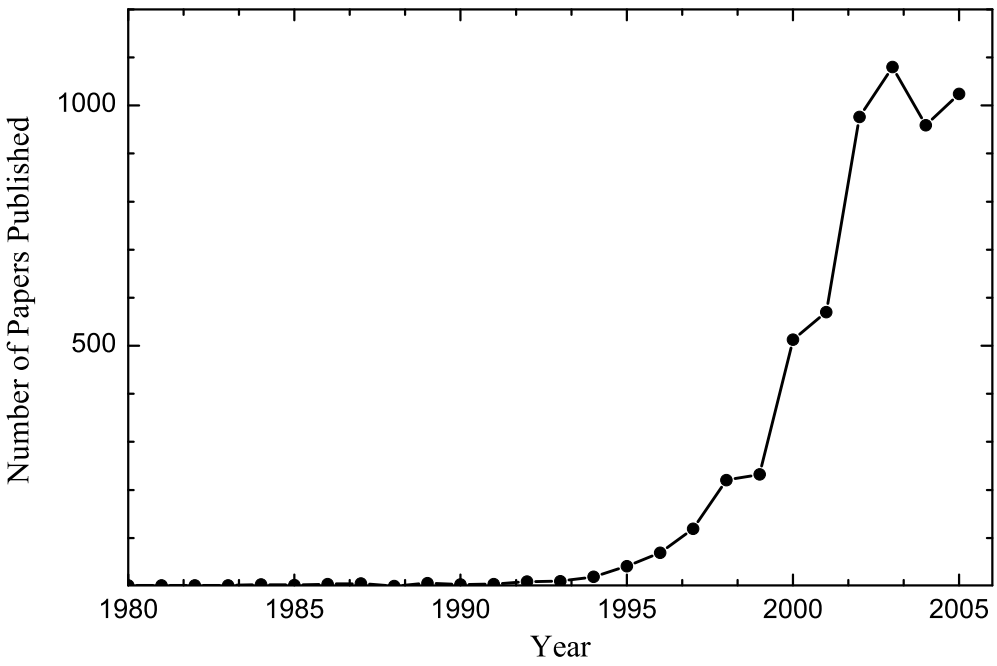

Figure 1.1: Yearly quantum computation publications. The number of papers related to quantum computation was found using INSPEC with the following search string: AB qubit Or AB "quantum comput*" Or AB "quantum information". This by no means gives an accurate total count. For example, the search did not return Feynman's well-known paper, Ref. [6]. Some of the early papers went on to become highly cited, while others have nothing to do with the subject at all.

lost in any physical implementation that was susceptible to noise, and the suspicion was that the same problem would harm a quantum computer.

The explosion of interest in quantum computation in the 1990's can be partly attributed to the development of error correcting algorithms [7–9]. The basic idea is to encode a single "logical" qubit with two orthogonal entangled states of several "physical" qubits. In this way, only a small subset of the possible physical qubit states will be considered valid logical states. During an intentional measurement, no information about the logical state can be gained by only measuring a single physical qubit. In the same way, if a single qubit is disturbed through an interaction with the environment in the form of decoherence, the logical state is not completely destroyed. A specified set of errors induced on the physical qubits can be detected with classical measurements and corrected with a discrete set of quantum gate operations.

Concrete algorithms also emerged around the same time and spurred interest. Shor's algorithm is the most well-known. It provides an efficient way of finding the prime factors of a large number, based on the quantum Fourier transform [10]. Grover's algorithm, developed shortly afterwards, offers a moderately more efficient way of searching an unstructured database [11]. While a classical computer could in principle solve these same problems, it would take an inordinate amount of time to do so as the number or database becomes large.

It may well turn out that the most useful quantum computation application will be quantum simulation, as Feynman originally suggested. Even with the most powerful classical computers, it is only possible to carry out full simulations of Schrödinger's equation for diatomic and triatomic molecules. With a quantum simulator of a few hundred qubits, it would be possible to determine the ground state configuration of a dozen or more atoms [12]. Or perhaps the potential of adiabatic quantum computation will be realized [13]. In this approach, a system is constructed such that the slow evolution of it to its ground state gives a solution of interest. In the related fields of quantum communication and cryptography, products are currently commercially available that allow secure key distribution over distances as large as 100 km [14].

It is perhaps remarkable that experimentalists in several branches of physics were in a position to investigate a wide variety of schemes around the same time the theory gained firmer footing. Approaches that are currently being pursued include using the hyperfine levels of individual ions [15], electronic spin states of a quantum dot [16], and nuclear spin states of individual impurities in semiconductors [17] and of molecules in a more traditional NMR sense [18]. As I will discuss in more detail in the next section, several types of superconducting qubits have been proposed and implemented. One such device, the Josephson phase qubit, is the subject of this thesis. The superconducting approaches are quite different than the previous ones

I listed, as they require quantum information to be stored in macroscopic objects.

Aside from the specific tools and techniques that each scheme requires, David DiVincenzo has proposed a list of generic requirements that any viable qubit must meet [19–21]. They are as follows.

Hilbert space control: The system must be confined to a precisely known set of quantum states and methods should be in place to prevent "leakage" to undesired states. The state space should be expandable with the addition of (typically) particles with a "spin" of 1/2.

State preparation: It should be possible to initialize the system to a well-defined state. As the qubit states are often energy eigenstates, this usually means cooling the system to its ground state. In addition, it may be required to reinitialize auxiliary qubits throughout a computation.

Low decoherence: The system should weakly interact with its environment, so that quantum superpositions are not disturbed. The amount of time needed to perform a gate operation (and perhaps the time needed to perform readout) determines the quality of isolation needed. A reliable error correction algorithm is needed to satisfy this requirement; current theoretical estimates vary widely, but the decoherence time may need to be 10^4 longer than the time to perform a quantum gate operation for error correction to work.

Controlled unitary transformations: A universal set of (typically) one- and two-qubit gates is needed to perform accurate manipulations of the qubit states. The great challenge in quantum computing is balancing this requirement with the previous one. Systems that are easy to control also typically interact with their environments strongly, leading to decoherence.

State-specific quantum measurements: It must be possible to readout a specific subsystem of the Hilbert space, to obtain classical information. The simplest example is a projective measurement of individual qubits, which does not affect the

rest of the system (not possible if all the qubits are entangled).

Quantum communication: "Stationary" qubits (whose properties are given by the previous requirements) must be converted to "flying" qubits, which can be used to faithfully transmit quantum information to a specified location.

1.2 Superconducting Circuits

In the 1980's, there was a tremendous amount of theoretical and experimental work done on the quantum nature of Josephson tunnel junction circuits [22–24]. Experimentally, the quality of tunnel barriers had reached the point where very sensitive experiments could be performed. The fundamental physics of the devices was studied and some understanding of the concepts of coherence and dissipation was established. Twenty years later, there is a variety of superconducting qubits being pursued, based on this early work.

As I will discuss in §2.1, a Josephson junction can be thought of as an inductor, in that the voltage across it is proportional to the time derivative of the current flowing through it. By placing a capacitor in parallel with an ideal junction, a resonator is formed whose two lowest quantum energy levels can be used as the states of a qubit. What makes this a feasible approach is that the value of the Josephson inductance depends on the current flowing through it. This nonlinearity leads to an anharmonic potential that governs the junction dynamics. Because of the resulting unequal energy level spacings, transitions between any two states can be uniquely addressed by applying a properly tuned external high frequency drive to the system.

The potential energy function that describes many junction circuits resembles that of a single atom and in fact much of the terminology is borrowed from NMR and atomic physics. Unlike their natural counterparts, the energy level structure of these artificial atoms can be easily tuned either in the fabrication process or during

operation by adjusting, for example, a bias current or magnetic flux. This tuning can be performed on selected qubits and the interaction between qubits can often be adjusted in the course of an experiment. With this fine control, though, comes the likelihood that the circuits will interact with their environment rather strongly. The challenge with these devices is to retain some level of control, while isolating them sufficiently to preserve quantum mechanical phase coherence of the superconducting state. What makes this feasible is that the relevant energy scales, such as the Josephson coupling energy, can be fairly large so that thermal fluctuations can be made negligible. Another concern is that unlike two rubidium atoms, for example, no two junctions are identical. Some variation in the fabrication may be tolerable, but the solid state approaches to quantum computation will require some strategy for ensuring that the relevant properties are extremely uniform, particularly when scaling to a large number of qubits [25].

Four general classes of superconducting qubits have emerged [26–28]. They are largely distinguished by the ratio of the Josephson energy E_J (which gives the maximum energy stored by the nonlinear inductor) to the charging energy E_C (which gives the energy required to add an electron to the junction). The superconducting phase difference across a junction γ and the number of Cooper pairs N_{CP} form a conjugate pair and thus obey a Heisenberg uncertainty relation, $\Delta N_{CP} \Delta\gamma \geq 1$ (see §2.2 of Ref. [2]). The E_J/E_C ratio determines the term that dominates the relation and also gives a name to each approach. I will briefly describe each of the qubit classes, in increasing order of E_J/E_C.

In the *charge qubit*, $E_C \approx 5\ E_J$ and the number of Cooper pairs on a small superconducting island distinguishes the qubit states; thus ΔN_{CP} is typically small in this case [29, 30]. A gate voltage is used to adjust the electrostatic energy of the states and tunneling of pairs onto the island is controlled by a small Josephson junction. State readout can be performed with a very sensitive electrometer, the single

electron transistor, among several other techniques that have been demonstrated.

With $E_C \approx E_J$, the qubit states of the *charge-flux qubit* are superpositions of several number states. In the *quantronium* configuration [31, 32], two small junctions are placed in a superconducting loop with an additional large junction. The qubit states differ by the circulating current in the loop and state readout can be performed, for example, by measuring the tunneling characteristics of the large junction.

One form of the *flux qubit* uses a large area junction ($E_J > 10\ E_C$) in a superconducting loop [33]. The dynamics of the resulting rf SQUID are governed by a double well potential, where localization in one of the wells corresponds to circulating current in either the clockwise or counter-clockwise direction. The qubit can be readout using a nearby SQUID magnetometer. In the *persistent current* configuration, a superconducting loop is interrupted by three junctions, which allows for a smaller loop inductance and makes the device less susceptible to flux noise [34, 35]. This is an example of how the potential of the Josephson artificial atom can be engineered to improve qubit performance.

Finally, the focus of this work is the *phase qubit*, which in its simplest form is a single current-biased Josephson junction, with $E_J \gg E_C$ [36,37]. The energy level structure of the junction is controlled by a large current, typically on the order of 10 μA. This corresponds to a relatively well-defined phase, with a large ΔN_{CP}.

There are two features of the energy levels of the phase qubit that set it apart from the charge and flux qubits. For one, while all Josephson devices have a second excited state $|2\rangle$, in the phase qubit, the energy difference between $|1\rangle$ and $|2\rangle$ is quite close to the splitting between $|0\rangle$ and $|1\rangle$ for all values of the bias current. For this reason, the phase qubit is more susceptible to leakage out of the qubit space. In addition, in the other qubit types, there is an accessible "sweet spot," where the energy levels are (to first order) independent of the control parameter (for example,

a voltage or flux). By operating at this value, the effects of noise can be minimized. While there is such a point for the phase qubit (at zero current), it is not easy to use the device there. Nevertheless, a single junction is quite insensitive to charge and flux noise, so it only needs to be protected from current noise. In our group, we have attempted to do this either with an LC filter [38] or a broadband inductive current divider [39]. Also, the freedom in choosing an operating point may actually make certain tasks, such as dynamic coupling of multiple qubits, easier to perform [40].

Apart from different configurations and isolation techniques, phase qubits[1] have been made using several different fabrication methods and from a variety of materials, including NbN/AlN/NbN [37], Nb/AlOx/Nb [39, 41, 42], Al/AlOx/Al [38,43,44], epi-Re/epi-Al_2O_3/Al [45], $YBa_2Cu_3O_{7-\delta}$ [46], and $Bi_2Sr_2CaCu_2O_{8+\delta}$ [47] junctions.

1.3 Summary of Thesis

One of the primary goals of this work is to understand the quantum behavior of the phase qubit. Therefore, Chapter 2 contains an overview of Josephson junctions, the derivation of the Hamiltonian for a simple current-biased junction, and an overview of the quantum properties that we tried to experimentally examine. The inductive isolation technique mentioned above uses an auxiliary junction, which results in a dc SQUID, whose properties I will also describe. Chapter 3 contains information about the time evolution of simple quantum systems. I will mostly quote generic analytical results, which predict the type of behavior we should see in the experiments, and outline the numerical techniques used in simulating the actual experiments.

Chapters 4 and 5 contain experimental details. The first focuses on the de-

[1]While current-biased junctions have been studied for decades, the work I have cited was recently done specifically with quantum information processing in mind.

sign and fabrication of the three devices that I studied: two capacitively coupled LC-isolated junctions (referred to as device LC_2), a single dc SQUID (DS_1), and two capacitively-coupled dc SQUIDs (DS_2). The latter chapter mostly concerns the experimental apparatus, including the dilution refrigerator in which all of the experiments were performed. I will also give an overview of the electronics used in the measurements.

Starting with Chapter 6, I will discuss experimental results. This chapter contains details of the measurement of the tunneling escape rate, which is how we obtained nearly all of the information we have about the qubits. I will also describe some of the experimental methods we used to characterize the different devices.

Our approach to investigating the junction Hamiltonian was to turn as many experimental knobs as we had access to and attempt to explain the results. This process begins in Chapter 7, which describes experiments where the temperature, isolation, and bias sweep rates were varied. The second key goal of my work was to evaluate, in as many ways as possible, the potential for using these phase qubits in quantum computation. Therefore, I will also describe how the relaxation time T_1 (which characterizes the speed at which the qubit can dissipate energy to its environment) can be extracted from these experiments.

The final two experimental chapters contain results of microwave activation, which was our primary method of state manipulation. Most of Chapter 8 is devoted to spectroscopy, which demonstrates the quantum nature of the qubit in a dramatic way. I will also describe time domain measurements of T_1, will yielded puzzling results. Coherent Rabi oscillations, which are the prototypical single qubit gate operation for quantum computation, are the subject of Chapter 9. The oscillations serve as a very strong test of our understanding of the coherent dynamics in the junction. Both spectroscopy and Rabi oscillations provide measures of the phase coherence time T_2, an important indicator of the viability of a qubit.

Finally, in Chapter 10, I will summarize the key results from the experiments.

Chapter 2

Josephson Junctions and SQUIDs

In 1962, Brian Josephson proposed a phenomenon that now bears his name [48]. The 22-year-old student of Pippard was interested in finding consequences of the spontaneous symmetry breaking arguments of P. W. Anderson, who was visiting Cambridge at the time, and how the phase of a superconductor might be measured [49]. He suggested that a current of superconducting particles could tunnel through a thin insulating barrier with no voltage drop. Although it seems that even he was not certain of the result (given that the paper is entitled "Possible new effects in superconductive tunnelling"), several experiments quickly confirmed his ideas [50,51]. He was awarded the Nobel prize in 1973 along with Giaever and Esaki, just a year after BCS theory was recognized.

This chapter opens with a discussion of the basic equations that govern the behavior of Josephson junctions. Next, the Hamiltonian of a current-biased junction will be derived and a summary of the classical dynamics presented. In preparation for treating the device as a qubit, I will review some of the techniques for finding quantum mechanical solutions of the Hamiltonian and show results for a typical device. Although all of our qubits act effectively as current-biased junctions, one form of isolation that we use results in a dc SQUID. Therefore, I will also discuss some basics of these devices, largely focusing on the phenomenology of the allowed flux states, because they have a significant experimental impact.

2.1 Josephson Relations

The Josephson effect occurs for any weak link between two superconducting banks. The weak link could be a thin normal metal, a constriction in the super-

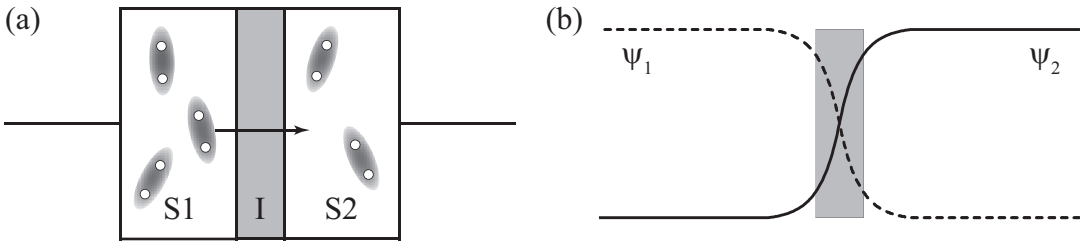

Figure 2.1: Schematic of a Josephson junction. (a) The Josephson effect involves superconducting Cooper pairs from one electrode (S1) tunneling through a thin insulating barrier (I) to another electrode (S2). (b) For this to occur, the barrier must be thin enough for the wavefunctions of each side to overlap.

conductor, or a grain boundary, for example. Our devices resemble the cartoon shown in Fig. 2.1(a), where the weak link is created by an insulating barrier. The Cooper pairs on each side of the junction can be described by an order parameter or wavefunction $\psi = \sqrt{\rho}e^{i\theta}$, where ρ is the number density of pairs and θ is the quantum mechanical phase. Although the wavefunction on one side will exponentially decay within the barrier, it may be non-zero at the other superconducting lead if the barrier is thin enough.

The wavefunctions on the left (ψ_1) and right (ψ_2) sides are connected and can be described by effective Schrödinger equations [52][1]

$$i\hbar\frac{\partial\psi_1}{\partial t} = E_1\psi_1 + T\psi_2 \qquad \text{and} \qquad i\hbar\frac{\partial\psi_2}{\partial t} = E_2\psi_2 + T\psi_1. \tag{2.1}$$

Here, E_1 and E_2 are the energies of the pairs on the left and right sides and T represents the coupling between the superconductors; it will be small for thick barriers. Imagine also that side 1 is held at a potential V_J with respect to side 2 by a battery. In the case of carriers with a positive charge, $E_1 - E_2 = 2eV_J$ for Cooper pairs, where $-e = -1.602 \times 10^{-19}$ C is the charge of a single electron. The symmetry of

[1]This particularly intuitive argument comes from one of Feynman's famous lectures that he gave to a group of sophomores, less than two years after Josephson's original paper. A detailed discussion and several additional references are given in §1.4 of Ref. [53]. See also §II.1 of Ref. [54].

the two equations is preserved by defining the zero of energy to be between E_1 and E_2, yielding

$$i\hbar\frac{\partial\psi_1}{\partial t} = eV_J\psi_1 + T\psi_2 \qquad \text{and} \qquad i\hbar\frac{\partial\psi_2}{\partial t} = -eV_J\psi_2 + T\psi_1. \tag{2.2}$$

Substituting $\psi_1 = \sqrt{\rho_1}e^{i\theta_1}$ and $\psi_2 = \sqrt{\rho_2}e^{i\theta_2}$, and multiplying the first equation through by ψ_1^* and the second by ψ_2^* gives

$$\frac{d\rho_1}{dt} + i2\rho_1\frac{d\theta_1}{dt} = -i\frac{2eV_J}{\hbar}\rho_1 - i\frac{2T}{\hbar}\sqrt{\rho_1\rho_2}\,e^{-i\gamma} \tag{2.3}$$

$$\frac{d\rho_2}{dt} + i2\rho_2\frac{d\theta_2}{dt} = i\frac{2eV_J}{\hbar}\rho_2 - i\frac{2T}{\hbar}\sqrt{\rho_1\rho_2}\,e^{i\gamma}, \tag{2.4}$$

where $\gamma \equiv \theta_1 - \theta_2$ is the phase difference across the junction. In the presence of a magnetic field, this quantity must be gauge invariant and include a term involving the vector potential.

Taking the real part of Eqs. (2.3) and (2.4) gives the time dependence of the pair density as

$$\frac{d\rho_1}{dt} = -\frac{2T}{\hbar}\sqrt{\rho_1\rho_2}\sin\gamma \qquad \text{and} \qquad \frac{d\rho_2}{dt} = \frac{2T}{\hbar}\sqrt{\rho_1\rho_2}\sin\gamma. \tag{2.5}$$

The rate $\dot{\rho}_2$ is equal to $-\dot{\rho}_1$ and is just the current I_J flowing through the junction. Thus we have

$$I_J = I_0\sin\gamma. \tag{2.6}$$

Here, the constant of proportionality $(2T\sqrt{\rho_1\rho_2}/\hbar)$ is known as the critical current I_0, which depends on the junction material and fabrication. Incidentally, although Eq. (2.5) suggests $\dot{\rho}_1 \neq 0$, the presence of the battery ensures that neither side of the junction charges up; Eq. (2.6) gives the value of the current that the battery supplies.

Finally, the imaginary parts of Eqs. (2.3) and (2.4) give

$$\frac{d\theta_1}{dt} = -\frac{eV_J}{\hbar} - \frac{T}{\hbar}\sqrt{\frac{\rho_2}{\rho_1}}\cos\gamma \qquad \text{and} \qquad \frac{d\theta_2}{dt} = \frac{eV_J}{\hbar} - \frac{T}{\hbar}\sqrt{\frac{\rho_1}{\rho_2}}\cos\gamma \tag{2.7}$$

$$\frac{d\gamma}{dt} = \frac{d\theta_1}{dt} - \frac{d\theta_2}{dt} = -\frac{2eV_J}{\hbar} - \frac{T}{\hbar}\sqrt{\frac{\rho_2}{\rho_1}}\left(1 - \frac{\rho_1}{\rho_2}\right)\cos\gamma. \tag{2.8}$$

If both superconductors are the same, then $\rho_1 \approx \rho_2$ and neither will change due to I_J, as mentioned above. Therefore, the magnitude of the voltage across the junction is

$$V_J = \frac{\Phi_0}{2\pi}\frac{d\gamma}{dt}\,, \tag{2.9}$$

where $\Phi_0 = h/2e = 2.07 \times 10^{-15}\ \mathrm{T}\cdot\mathrm{m}^2$ is the superconducting flux quantum.

If no voltage is applied across the junction, then Eq. (2.9) says that the phase difference will not change. What is amazing is that Eq. (2.6), known as the dc Josephson relation, predicts that a steady current of Cooper pairs can flow through the junction. The phase difference will adjust itself to accommodate currents between $-I_0$ and I_0. Typically, we deal with bias currents on the order of 10 μA, so that the value of γ corresponds to the coherent motion of 10^{13} Cooper pairs per second.

If there is a constant voltage across the junction, then Eq. (2.9), known as the ac Josephson relation, predicts that the phase will evolve linearly in time. In this case, the current through the junction will oscillate rapidly according to Eq. (2.6). A dc voltage of 1 μV corresponds to an oscillation frequency of 484 MHz. We will see that this behavior gives a Josephson junction many interesting high frequency properties.

Incidentally, some of the mystery of the quantum mechanical phase difference

can be removed by solving for γ in Eq. (2.9):

$$\gamma(t) = \gamma(0) - \frac{2\pi}{\Phi_0}\int_0^t dt'\, V_J(t')\,. \tag{2.10}$$

The phase difference is just the time integral of the voltage that has appeared across the junction and is thus a perfectly well-defined physical quantity, once the origin of time is chosen.

A useful picture of the junction can be developed by taking a time derivative of Eq. (2.6) and then using Eq. (2.9) to eliminate $d\gamma/dt$. One finds

$$V_J = L_J \frac{dI_J}{dt}, \tag{2.11}$$

where

$$L_J = \frac{\Phi_0}{2\pi}\frac{1}{I_0\cos\gamma} = \frac{\Phi_0}{2\pi}\frac{1}{\sqrt{I_0^2 - I_J^2}}. \tag{2.12}$$

As Eq. (2.11) looks just like the expression for the voltage across an inductor, L_J is known as the "Josephson inductance." As Eq. (2.12) shows that L_J depends on the current, this is a non-linear inductor. The combination of this element with a parallel capacitor forms an anharmonic resonator, whose energy levels we use as states of a qubit. The energy stored in the magnetic field by a solenoid depends on its physical dimensions, leading to the term "geometrical inductance" to describe its properties. Here, energy is being stored in the flow of Cooper pairs (see §6.1 of Ref. [55]) and thus the origin of the Josephson inductance is quite different.

2.2 RCSJ Model

The resistively and capacitively shunted junction (RCSJ) model has been widely used to describe the behavior of current-biased junctions [55–59]. In this model, the parallel combination of three elements is driven by a current bias I_b, as

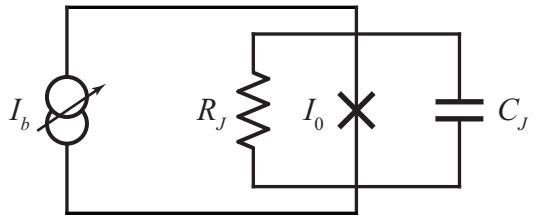

Figure 2.2: RCSJ model circuit diagram. A Josephson junction with critical current I_0 is driven by a current bias I_b. The resistance R_J is responsible for all dissipation in the system and the capacitance C_J is often due mainly to the geometry of the junction.

shown in Fig. 2.2. The cross signifies an ideal junction, *i.e.* an object that exactly obeys the two Josephson relations with critical current I_0. Usually, the parallel plate geometry of the junction itself gives rise to the shunting capacitance C_J. The resistance R_J comes from intrinsic dissipation mechanisms in the junction (such as quasiparticles), normal metal shunts that have been added across the junction, and contributions from the biasing network. As the RCSJ model represents our qubit quite faithfully, I will discuss it in some detail. I will start off with a derivation of the Hamiltonian, using the method outline in Appendix A, and end with a mechanical analog that gives an intuitive picture of its classical dynamics.

2.2.1 RCSJ Hamiltonian

In the RCSJ model, the bias current splits between the three parallel paths formed by the junction, capacitor, and resistor. Current conservation gives

$$I_b = \frac{V_J}{R_J} + C_J \frac{dV_J}{dt} + I_0 \sin\gamma. \tag{2.13}$$

Substitution of the Josephson voltage relation, Eq. (2.9), yields the equation of motion for this circuit,

$$C_J \left(\frac{\Phi_0}{2\pi}\right)^2 \frac{d^2\gamma}{dt^2} = -\frac{d}{d\gamma}\left[-\frac{\Phi_0}{2\pi}\left(I_0\cos\gamma + I_b\gamma\right)\right] - \frac{1}{R_J}\left(\frac{\Phi_0}{2\pi}\right)^2 \frac{d\gamma}{dt}. \tag{2.14}$$

This describes the motion (along coordinate x) of a fictitious particle of mass m_J in a one dimensional potential U with a damping force $-\eta v$, where v is the velocity. Equation (2.14) can be rewritten in the form

$$m\frac{d^2x}{dt^2} = -\frac{dU}{dx} - \eta v, \tag{2.15}$$

with the following identifications

$$x \longleftrightarrow \gamma \tag{2.16}$$

$$v \longleftrightarrow \frac{d\gamma}{dt} \tag{2.17}$$

$$m_J \longleftrightarrow C_J\left(\frac{\Phi_0}{2\pi}\right)^2 \tag{2.18}$$

$$U \longleftrightarrow -\frac{\Phi_0}{2\pi}\left(I_0\cos\gamma + I_b\gamma\right) \tag{2.19}$$

$$\eta \longleftrightarrow \frac{1}{R_J}\left(\frac{\Phi_0}{2\pi}\right)^2. \tag{2.20}$$

The potential U is called the "tilted washboard potential" because of its shape; as shown in Fig. 2.3, the tilt of this potential is set by the current bias and the corrugation is determined by the critical current. U gives the potential energy of the junction as a function of the phase difference γ, which is why the fictitious particle is often referred to as the "phase ball" or "phase particle." I will frequently refer to the motion of this particle in describing the dynamics of junction devices. Equation (2.14) was multiplied through by the flux quantum to give U the correct dimensions; however, the mass of the particle has dimensions of action times time and the force has dimensions of action.

Using the particle analogy, the Lagrangian for the system with no dissipation ($R_J = \infty$) and with γ taken as a generalized coordinate is

$$\mathcal{L}\left(\gamma,\dot{\gamma}\right) = T - U = \frac{1}{2}\left(\frac{\Phi_0}{2\pi}\right)^2 C_J\dot{\gamma}^2 + \frac{\Phi_0}{2\pi}\left(I_0\cos\gamma + I_b\gamma\right). \tag{2.21}$$

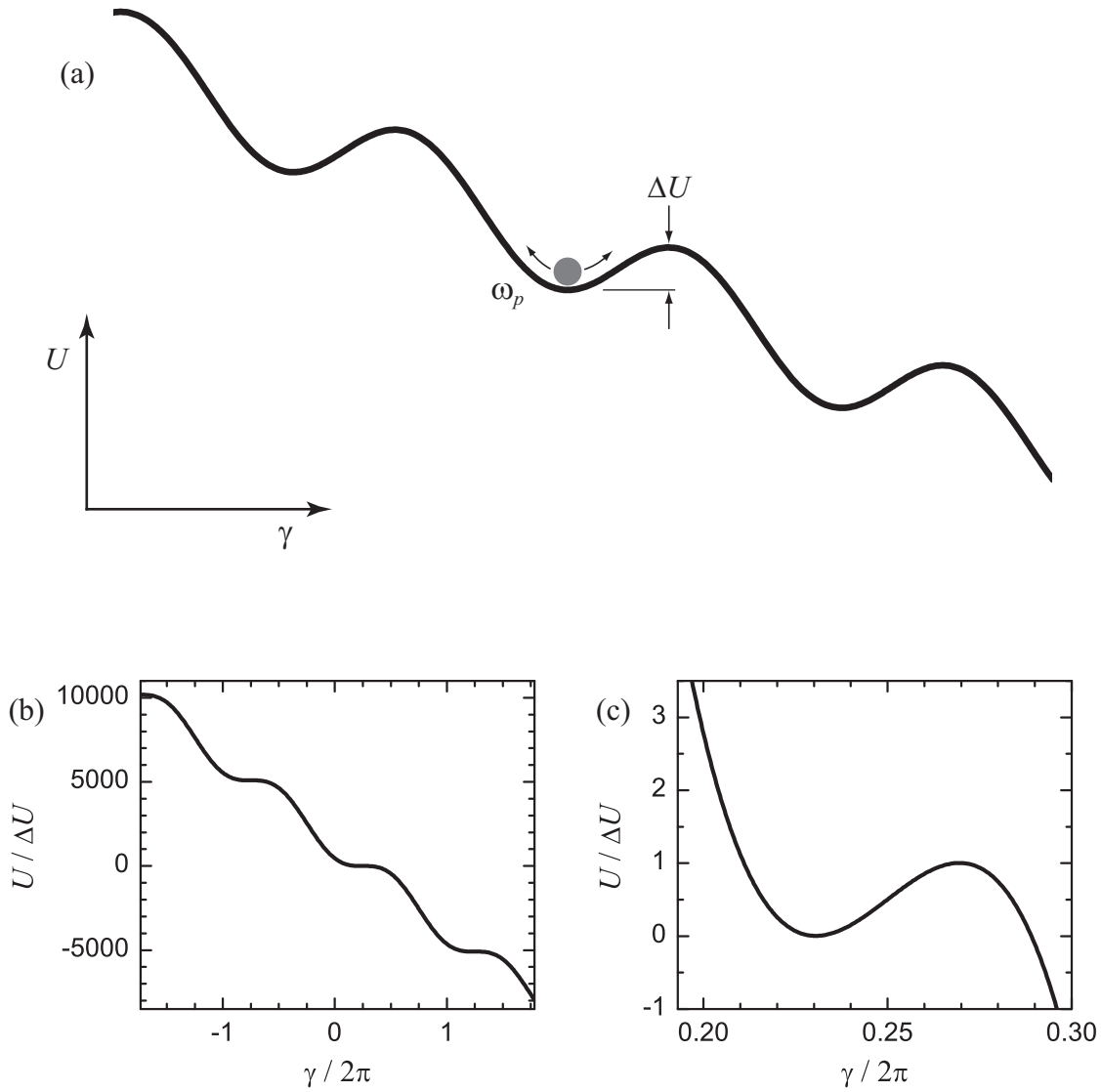

Figure 2.3: The tilted washboard potential. (a) The dynamics of a current biased junction are analogous to a particle moving in a 1-D potential U, where the phase difference γ across the junction is identified with the position of the particle. Classically, when the junction is in the supercurrent state, the particle undergoes oscillations of frequency ω_p in a well with barrier height ΔU. The tilt on the potential is determined by the bias current, which in this case is 0.4 I_0. (b) We perform experiments very close to the critical current, where the well is very shallow compared to the inter-well energy difference; here $I_b = 0.9925\ I_0$, $I_0 = 30\ \mu$A, and $C_J = 5$ pF. (c) The junction dynamics can be approximated by a single one of these wells.

With this Lagrangian, the Euler-Lagrange equation [see Eq. (A.1)] generates the equation of motion, Eq. (2.14). From the Lagrangian, one can also identify the conjugate momentum and generalized velocity:

$$p = m_J\dot{\gamma} = \left(\frac{\Phi_0}{2\pi}\right)^2 C_J\dot{\gamma} = \frac{\hbar}{2e}C_J V_J = -\hbar N_{CP} \quad \Rightarrow \quad \dot{\gamma} = \left(\frac{2\pi}{\Phi_0}\right)^2 \frac{p}{C_J}. \tag{2.22}$$

Thus the momentum is equal to the number of Cooper pairs N_{CP} that have tunneled through the junction, apart from a factor of $-\hbar$ to get the right dimensions and sign. $\mathcal{H}$ can be expressed in terms of the number-phase conjugate pair with $[N_{CP}, \gamma] = i$ (see §2.2 of Ref. [2]).

Finally, the Hamiltonian can be obtained from Eq. (A.3) and expressed in a number of equivalent forms, including

$$\begin{aligned}
\mathcal{H} &= \frac{1}{2}\left(\frac{\Phi_0}{2\pi}\right)^2 C_J\dot{\gamma}^2 - \frac{\Phi_0}{2\pi}\left(I_0\cos\gamma + I_b\gamma\right) && (2.23)\\
&= \frac{1}{2}\left(\frac{2\pi}{\Phi_0}\right)^2 \frac{p^2}{C_J} - \frac{\Phi_0}{2\pi}\left(I_0\cos\gamma + I_b\gamma\right) && (2.24)\\
&= \frac{p^2}{2m_J} - m_J\omega_{p0}^2\cos\gamma - \frac{\Phi_0}{2\pi}I_b\gamma && (2.25)\\
&= \frac{4E_C}{\hbar^2}p^2 - E_J\left(\cos\gamma + I_r\gamma\right) && (2.26)\\
&= 4E_C N_{CP}^2 - E_J\left(\cos\gamma + I_r\gamma\right), && (2.27)
\end{aligned}$$

where $I_r \equiv I_b/I_0$ is the reduced current bias. In Eq. (2.25), $\omega_{p0} \equiv \sqrt{2\pi I_0/C_J\Phi_0}$ is the frequency of small oscillations in a well of the washboard at zero bias, as shown in the next section. In Eq. (2.26), $E_J = \Phi_0 I_0/2\pi$ is known as the Josephson coupling energy and is a measure of the maximum energy that can be stored in the Josephson inductance L_J. It also is analogous to the "spring constant" that describes the harmonic component of the potential at zero bias. $E_C = e^2/2C_J = \hbar^2/8m_J$ is the charging energy, which is the energy required to charge the capacitor with one

electron solely from electrostatic considerations. We perform experiments on large area junctions, where $E_J \gg E_C$, so that the phase difference γ is a relatively well defined quantity compared to N_{CP}, *i.e.* $\Delta\gamma \ll 1$ and $\Delta N_{CP} \gg 1$. Typical parameter values for our qubits are $I_0 = 30\ \mu$A and $C_J = 5$ pF, for which $E_J = 9.9 \times 10^{-21}$ J $= 15$ THz $\cdot\, h = 720$ K $\cdot\, k_B$ and $E_C = 2.6 \times 10^{-27}$ J $= 3.9$ MHz $\cdot\, h = 180\ \mu$K $\cdot\, k_B$.

2.2.2 The Tilted Washboard Potential

In this section, I will discuss some of the basic properties of the tilted washboard potential. Although these are classical results, they will provide considerable intuition about the dynamics of the system.

The potential energy as a function of the phase difference across the junction is

$$U = -\frac{\Phi_0}{2\pi}\left(I_0 \cos\gamma + I_b\gamma\right) = -E_J\left(\cos\gamma + I_r\gamma\right). \tag{2.28}$$

The derivative of the potential disappears when $\sin\gamma = I_r$ (and thus $\cos\gamma = \pm\sqrt{1 - I_r^2}$), so that a local minimum and maximum occur at phases

$$\gamma_{min} = \sin^{-1} I_r \qquad \text{and} \qquad \gamma_{max} = \pi - \sin^{-1} I_r. \tag{2.29}$$

This gives the barrier height as a function of the current as

$$\begin{aligned} \Delta U \equiv U\left(\gamma_{max}\right) - U\left(\gamma_{min}\right) &= 2E_J\left(\sqrt{1 - I_r^2} - I_r \cos^{-1} I_r\right) && (2.30) \\ &\approx \frac{4\sqrt{2}}{3}\, E_J\left(1 - I_r\right)^{3/2}, && (2.31) \end{aligned}$$

where the approximation [60] is valid for $I_r \lesssim 1$.

The second derivative of the potential, evaluated at γ_{min}, is $k = E_J\sqrt{1 - I_r^2}$. Therefore, using the particle mass found in the previous section, the frequency of

small oscillations (known as the plasma frequency) is

$$\omega_p = \sqrt{\frac{k}{m}} = \sqrt{\frac{2\pi I_0}{C_J \Phi_0}} \left(1 - I_r^2\right)^{1/4} = \frac{\sqrt{8 E_C E_J}}{\hbar} \left(1 - I_r^2\right)^{1/4} \tag{2.32}$$

in the absence of dissipation. Notice that ω_p is just $1/\sqrt{L_J C_J}$. For a planar junction, both I_0 and C_J are proportional to the junction area, so the plasma frequency depends only on the critical current density.

Although the capacitor does not appear explicitly in the expression for the potential, it is playing a critical role in motivating its use. Imagine there were no capacitor and we just had an ideal current-biased junction. For any value of $I_b < I_0$, the phase difference would adjust itself in accordance with Eq. (2.6) and γ would stay at a fixed value.

Adding the capacitor (but leaving out the resistor for the moment) gives rise to a finite-mass phase particle. Consider the case of Fig. 2.3(c). Classically, the particle can sit at the minimum of the potential well at $\gamma_0/2\pi = 0.23$ with no kinetic energy, in a situation identical to the one described above. I will refer to this situation as the classical ground state, for lack of a better term. However if the system is given some energy (with a little kick of bias current, for example), then the phase particle will undergo plasma oscillations about the minimum, as sketched in Fig. 2.4.

The current through the junction will then oscillate about the equilibrium value [$I_r = 0.9925$ in the case of Fig. 2.3(c)] in phase with γ. With a time-varying phase difference, a voltage appears across the junction, which drives a current through the capacitor. From Eq. (2.9), this current is 180° out of phase with the γ oscillations. If the phase oscillates with a (small) amplitude $\tilde{\gamma}$, then both currents will have an oscillatory amplitude $I_0 \tilde{\gamma} \cos I_r$, so that the total current is I_b, as required by Eq. (2.13). In other words, it is the redistribution of current through the capacitor that allows γ to explore the tilted washboard and gives rise to the

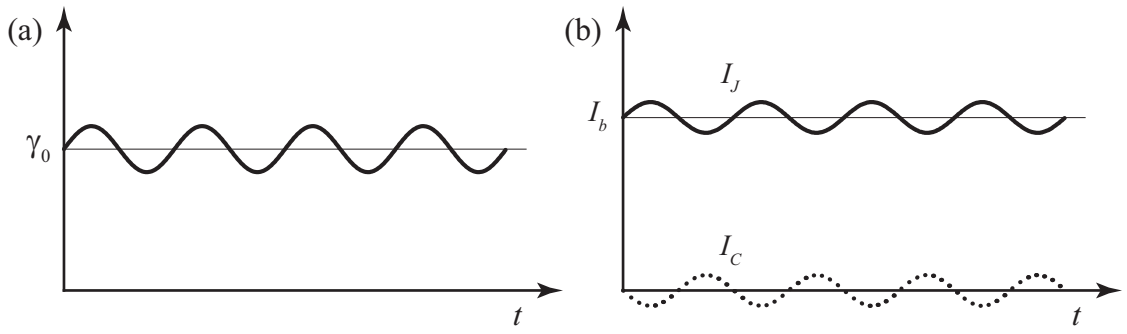

Figure 2.4: Plasma oscillations of a capacitively shunted junction. (a) For fixed I_b, γ oscillates about the equilibrium value γ_0 after the system is kicked. (b) The current through the junction (solid line) and capacitor (dotted) also oscillate, but sum to the value of the dc current bias, I_b.

dynamics that will be discussed throughout this thesis. Alternatively, one can view the oscillation as energy exchange between the junction and charge stored on the capacitor, or between potential and kinetic energy in the mechanical analog.

2.2.3 Junction IV Curve

The nature of the current vs. voltage characteristic (IV) curve for a current-biased junction depends strongly on R_J. The strength of the damping is characterized by the (dimensionless) Stewart-McCumber hysteresis parameter [56, 57]

$$\beta_C = \frac{2\pi}{\Phi_0} I_0 \, R_J^2 \, C_J = \left(\omega_{p0} \, R_J \, C_J\right)^2 = Q\left(0\right)^2 , \tag{2.33}$$

where ω_{p0} is the plasma frequency at zero bias and the quality factor $Q\left(I_b\right) = \omega_p \, R_J C_J$ is identical to that of a traditional parallel RLC oscillator. For our devices, which have large β_C and are therefore "underdamped," the IV curve will resemble the hysteretic one shown in Fig. 2.5 [53].

The different regions of this curve can be understood using the analogy of the particle and tilted washboard potential. Starting at $I_b = V_J = 0$, the potential contains minima for $I_b < I_0$, which can trap the particle (see Fig. 2.3). This is

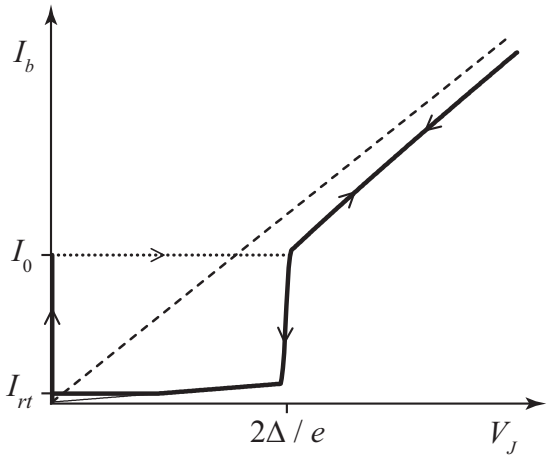

Figure 2.5: IV curve of a current-biased junction. Once the current exceeds the critical current I_0 a voltage develops across the junction. In an underdamped junction the curve is hysteretic, not returning to the supercurrent branch until I_{rt}. The resistance in the sub-gap has been exaggerated for clarity. The dashed line shows the normal state resistance.

known as the trapped, supercurrent, or zero-voltage state and corresponds to the vertical branch of the IV curve at $V_J = 0$. We always operate our qubits in this regime, but the rest of the IV curve is useful in determining junction parameters.

Once $I_b > I_0$, all the well minima disappear and the particle is free to roll down the potential. The result is a continuous evolution of the phase that gives rise to a voltage, which increases rapidly as the particle picks up kinetic energy. When the voltage reaches the value of the full superconducting gap $2\Delta/e$, the system has sufficient energy to break Cooper pairs. Pair-breaking produces a large source of damping that rapidly brings the system to a steady state voltage. In underdamped junctions, the jump to this so-called finite voltage (or running) state is extremely fast (as suggested by the dotted horizontal line in Fig. 2.5), a feature which we will exploit in doing qubit state measurements. Classically, switching out of the zero-voltage state can occur for $I_b < I_0$ if the particle is thermally excited over the barrier [61].

As the bias increases after the junction switches, the additional current is

mainly due to quasiparticle superconductor-insulator-superconductor tunneling, first observed by Giaever [62], and asymptotically approaches the value set by the normal state junction resistance R_n. For an ideal BCS superconductor, the product of I_0 and R_n obeys [63]

$$I_0 R_n = \frac{\pi \Delta(T)}{2e} \tanh\left(\frac{\Delta(T)}{2k_B T}\right), \tag{2.34}$$

which depends on the energy gap Δ and temperature T of the junction, but not its size. In the normal state, $I_b = 4I_0/\pi$ when $V_J = 2\Delta/e$, which relates I_0 to the height of the quasiparticle branch of the IV curve at $T = 0$.

The well minima return once the bias current is lowered beneath I_0. However if the particle is in the running state, its kinetic energy prevents it from immediately "retrapping" into the zero-voltage state, leading to hysteretic behavior. As the bias is lowered, the particle will slow down and the voltage will decrease. Although we always operate our qubits in the supercurrent state, the sub-gap resistance R_{sg} will govern how energy is dissipated when a small ac voltage appears across the junction during plasma oscillations [64–66]. Thus we are particularly interested in this section of the curve. In an unshunted junction, the sub-gap resistance can be quite a bit larger than R_n, as transport may solely be due to quasiparticles thermally excited across the gap. At the retrapping current [55]

$$I_{rt} \approx 4I_0/\pi Q, \tag{2.35}$$

the damping is sufficiently large that the junction jumps back to the zero-voltage state.

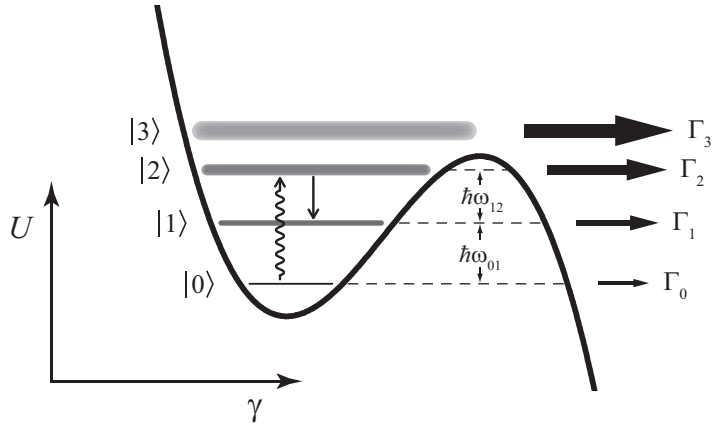

Figure 2.6: Quantum states of the tilted washboard. The RCSJ Hamiltonian gives rise to metastable quantum states $|n\rangle$, which can tunnel to the continuum of voltage states with escape rates Γ_n. The unequal energy level spacings ($\omega_{01} > \omega_{12}$) means that specific transitions can be driven. The potential parameters are the same as in Fig. 2.3.

2.3 Quantum Mechanical Properties of the Josephson Junction

The previous discussion was based on a classical picture of the current-biased junction. However, this system is suitable for studying macroscopic quantum phenomena, which partly motivated the original theoretical work on the device [67]. As sketched in Fig. 2.6, a well of the tilted washboard potential will contain a certain number of reasonably well-localized quantum energy levels $|n\rangle$ (of energy E_n). The exact number depends on I_b, the junction parameters, and what is meant by well-localized. The ground $|0\rangle$ and first excited state $|1\rangle$ serve as the states of our qubit [36], although higher states are always present and can be both beneficial and harmful.

There are two key properties of the potential that determine the nature of these states. First, the nonlinearity of the junction gives rise to an anharmonic well. The energy spacing between $|n\rangle$ and $|m\rangle$, $\Delta E_{nm} = \hbar\omega_{nm}$, decreases higher up in the well. This allows the possibility of selectively driving a transition between specific levels. In practice, we can do this by applying a microwave current drive on the

bias line with a frequency that is resonant with the desired transition. A $0 \rightarrow 2$ transition is drawn in the figure. The influence of such a drive on the other states is a major theme of this thesis. Shown also in the figure is one of the decay processes (in this case, $2 \rightarrow 1$) that are a result of the junction being able to dissipate energy to its environment.

The second important property is that the potential falls off towards minus infinity for increasing γ, creating the barrier ΔU. As a consequence, there are no true bound states of the system (see Chapter 3 of Ref. [2]). While scattering states exist for a continuous spectrum of energies, the density of allowed states will peak at so-called resonances, corresponding to a high probability of being in the well. Normalizable wavefunctions, which I will label $|n\rangle$, can be formed by taking superpositions of the states near these resonance energies. The states $|n\rangle$ are, however, metastable and will eventually leak out of the well, as all the eigenstates extend to $\gamma = +\infty$.

Classically, the phase particle can be thermally driven over the barrier. Quantum mechanically, it can tunnel through a finite barrier (*i.e.* for $I_b < I_0$) even at zero temperature. I will define Γ_n as the tunneling escape rate of the n-th level; the rate can be thought of as the inverse of the lifetime of the metastable state. Experiments distinguishing tunneling from thermal escape were first performed 25 years ago [23] and observation of tunneling from different states followed soon after [24]. Both of these processes leave the junction in the voltage state. In quantum computation, tunneling destroys the information stored by the qubit. While we would want to avoid such an event during a gate operation, studying the tunneling behavior is the easiest way we have of measuring the state of our devices at the moment. As suggested in Fig. 2.6, the states higher in the well have very high tunneling rates, with these short lifetimes corresponding to broad energy levels. In fact, there are resonances above the barrier (see Fig. 3.26 of Ref. [2]), although they may be thought of

as smeared into a continuum. Deep in the well, the resonances can be rather sharp (long-lived) and thus I will refer to these as eigenstates $|n\rangle$ with discrete energies E_n.

To analyze and simulate the junction dynamics, we need to know the energy level spacings $\hbar\omega_{nm}$ and tunneling escape rates Γ_n as a function of I_b. In addition, if we add a microwave signal to the current bias, the inter-level transition rate will depend on $\langle n \,|\, I_b\hat{\gamma} \,|\, m\rangle$, as seen in the Hamiltonian of §2.2.1. Therefore, we also need the matrix elements of the phase operator, $\gamma_{n,m} \equiv \langle n \,|\, \hat{\gamma} \,|\, m\rangle$. Although the Hamiltonian looks simple enough, it is the lack of discrete stationary states that makes the problem difficult. Below, I will only summarize some of the techniques that have been used in the group, as details have been presented by their authors elsewhere.

2.3.1 Harmonic Oscillator Approximation

The lowest-order approach is to ignore the barrier and assume the curvature at the bottom of the well defines a harmonic potential. This results in equally spaced energy levels $E_n = \hbar\omega_p\,(n + 1/2)$, where n is a non-negative integer and the bias-dependent plasma frequency is given by Eq. (2.32). For the potential shown in Fig. 2.6 (typical operating parameters), $\omega_p/2\pi = 7.5$ GHz, or 360 mK in terms of temperature. Therefore, our experiments must be performed at lower temperatures to prevent thermal excitation of the system from one level to the next. I find it remarkable that this quantum mechanical result, simple enough to have been derived essentially from first principles in the previous pages, can be verified in the laboratory with a rather crudely made macroscopic object.

This harmonic model also provides the matrix elements $\gamma_{n,n-1}$ to lowest order:

$$\begin{aligned} \langle n-1\,|\,\hat{\gamma}\,|\,n\rangle &= \langle n\,|\,\hat{\gamma}\,|\,n-1\rangle \approx \left(\frac{\hbar}{2m\omega_p}\right)^{1/2}\sqrt{n} \\ &= \left(\frac{2e^2}{\hbar\omega_p C_J}\right)^{1/2}\sqrt{n} = \left(\frac{2E_C}{E_J}\right)^{1/4}\left(1-I_r^2\right)^{-1/8}\sqrt{n}, \end{aligned} \tag{2.36}$$

where all other elements are zero. In the true anharmonic potential, these other elements (including the diagonal ones) are non-zero and can be quite significant when the well is shallow.

For the full washboard potential, it is useful to measure the barrier height in terms of the harmonic level spacing. This gives an estimate of the number of levels in the well as

$$N_s \equiv \frac{\Delta U}{\hbar\omega_p} = \frac{1}{\sqrt{2}}\left(\frac{E_J}{E_C}\right)^{1/2}\left[\left(1-I_r^2\right)^{1/4} - I_r\left(1-I_r^2\right)^{-1/4}\cos^{-1}I_r\right]. \tag{2.37}$$

At zero bias, $N_s \approx \sqrt{E_J/E_C}$ which is greater than 1000 for our qubits. On the other hand, we typically perform experiments at a value of I_b where $N_s \approx 3$.

2.3.2 Cubic Approximation

Fairly accurate results can be obtained by approximating a well of the washboard with a cubic polynomial (see §2.2 of Ref. [3] and §2.4 of Ref. [1]). As with the tilted washboard, a cubic well supports resonances rather than true bound states and is anharmonic. It can therefore supply all of the quantities we are interested in. Furthermore, a cubic does a fair job of representing the potential even for more general forms of the dc Josephson relation (see Appendix A of [68]). While it has some deficiencies (such as failing at high I_b), this approach has the tremendous advantage of providing analytical solutions which help build intuition over a wide range of device parameters, aiding in the design of qubits.

The strength of the cubic component of the potential is governed by the parameter $\lambda = 1/\sqrt{54 N_s}$. The cubic contribution can be treated as a perturbation to the harmonic oscillator (see §4.3.1 of Ref. [2]). This yields approximate eigenstates inside the well, which can be used to evaluate the needed matrix elements. To second order in λ, some of the matrix elements of $\hat{x}$ for the lowest states are

$$x_{0,1} = \frac{1}{\sqrt{2}}\left(1 + \frac{11}{4}\,\lambda^2\right) \qquad x_{1,2} = 1 + \frac{11}{2}\,\lambda^2 \qquad x_{2,3} = \sqrt{\frac{3}{2}}\left(1 + \frac{33}{4}\,\lambda^2\right) \tag{2.38}$$

$$x_{0,0} = \frac{3}{2}\,\lambda \qquad x_{0,2} = -\frac{\lambda}{\sqrt{2}} \qquad x_{1,1} = \frac{9}{2}\,\lambda \qquad x_{2,2} = \frac{15}{2}\,\lambda, \tag{2.39}$$

where $\hat{x} = \sqrt{m_J \omega_p/\hbar}\,\big(\hat{\gamma} - \sin^{-1} I_r\big)$. As the states are orthogonal, the matrix elements of $\hat{\gamma}$ are proportional to those of $\hat{x}$. The elements given in Eq. (2.39) vanish in the harmonic limit, but grow more rapidly with λ than the "transition" matrix elements of Eq. (2.38).

In order to capture the behavior of the wavefunctions outside of the well and calculate Γ_n, the WKB method can be used (see §4.4 of Ref. [2] and Appendix A of Ref. [1]). The boundary conditions that allow for out-going waves result in a discrete spectrum of complex energies. For an eigenstate with a complex eigenvalue $v = \alpha + i\beta$, the time dependence of the probability density is $\left|e^{-ivt/\hbar}\right|^2 = e^{2\beta t/\hbar}$. We want the tunneling escape rate to be a measure of the decay of this probability, which motivates the definitions

$$E_n \equiv \mathrm{Re}\left(\langle\psi_n \,|\, \mathcal{H} \,|\, \psi_n\rangle\right) \qquad \text{and} \qquad \Gamma_n \equiv -\frac{2}{\hbar}\,\mathrm{Im}\left(\langle\psi_n \,|\, \mathcal{H} \,|\, \psi_n\rangle\right), \tag{2.40}$$

for eigenstates $|\psi_n\rangle$. The tunneling rate in the absence of damping can be found from the probability current density flowing through the barrier as [2]

$$\Gamma_n = \frac{\sqrt{2\pi}\,\left[\,60\,(7.2\,N_s)\,\right]^{n+1/2}}{n!}\;\frac{\omega_p}{2\pi}\;\exp\left(-7.2\,N_s\right). \tag{2.41}$$

Notice that I_b, I_0, and C_J only enter implicity through ω_p and N_s. This sort of universal scaling makes the expression quite useful. The expression also shows that the tunneling increases dramatically for states higher in the well, as $\Gamma_{n+1}/\Gamma_n = 432N_s/\left(n+1\right)$.

Including damping in the problem suppresses the tunneling rate. To first order in $1/Q$, the ground state escape rate for the cubic potential is [22]

$$\Gamma_0 = \sqrt{120\pi\left(7.2\,N_s\right)}\ \frac{\omega_p}{2\pi}\ \exp\left[-7.2\,N_s\left(1+\frac{0.87}{Q}\right)\right]. \tag{2.42}$$

2.3.3 Full Tilted Washboard

Going beyond the cubic approximation, there are several ways to treat the resonances of the full washboard potential. What has been used most often in the group has been to solve Schrödinger's equation with appropriate boundary conditions at the turning points of the well. In the method of complex scaling (see §3.3.2 of Ref. [2]), a transformation is made to complex coordinates: $\gamma \rightarrow \gamma\, e^{i\theta}$ and $p \rightarrow p\, e^{-i\theta}$. While the usual commutation relation is still satisfied, the Hamiltonian becomes non-Hermitian, which allows for complex eigenvalues. Eigenstates are found as a superposition of harmonic oscillator states, with θ adjusted for stability.

Equivalent results are obtained by solving Schrödinger's equation on a grid with simple boundary conditions corresponding to decay to the left of the well and free oscillation to the right; see §2.4 and §3.3.2 of Ref. [1] and Appendix B for the MATLAB code used generate the solutions. Starting from a trial energy and wavefunction (such as a harmonic oscillator state), inverse iteration can be used to numerically relax to a solution (see, for example, §11.7 of Ref. [69]). Equation (2.40) provides the interpretation of the resulting complex eigenvalue. In practice, we run this sort of simulation for a single set of typical parameters and express the escape

rates and energy levels as

$$\Gamma_n = (7.2\,N_s)^{n+1/2}\ \frac{\omega_p}{2\pi}\ \exp\left[-7.2\,N_s + f_\Gamma^n\,(N_s)\right] \tag{2.43}$$

$$\omega_{n,n+1} = \omega_p\ f_\omega^n\,(N_s)\,. \tag{2.44}$$

The idea here is to retain the bias-dependent scaling of the cubic potential solutions, while the functions f_Γ^n and f_ω^n contain corrections. These functions, when expressed as a function of N_s, appear to be universal. As they do not follow any simple functional form, they can be parameterized as a series of cubic splines (in $1/N_s$). In principle the wavefunctions found with this method could be used to calculate the matrix elements, but I found it simpler to use the cubic approximation results, which are sufficient for my purposes.

I will now show a selection of results for a junction with $I_0 = 30\ \mu$A and $C_J = 5$ pF for values of the reduced current bias I_r of interest. Figure 2.7 shows the discrete number of levels within the barrier ΔU (solid line), as determined from Eq. (2.44) (and the value of E_0 from the simulation). There are resonances above the barrier, but they are so short-lived, they probably do not affect the dynamics significantly. This number is well approximated by the continuous function N_s (dashed), given in Eq. (2.37).

The solid line in Fig. 2.8 is the classical plasma frequency ω_p. The anharmonicity of the well leads to smaller transition frequencies ω_{01} (dashed), ω_{12} (dash-dot), and ω_{23} (dotted) between adjacent levels. An upturn in frequency occurs as a level leaves the well. The levels are so wide at these points that we have not experimentally observed such features.

Tunneling escape rates Γ_0 (solid), Γ_1 (dashed), Γ_2 (dash-dot), and Γ_3 (dotted) are shown in Fig. 2.9(a). All of the escape rates increase approximately exponentially with the current bias, as even the simplest theories predict. However, the escape

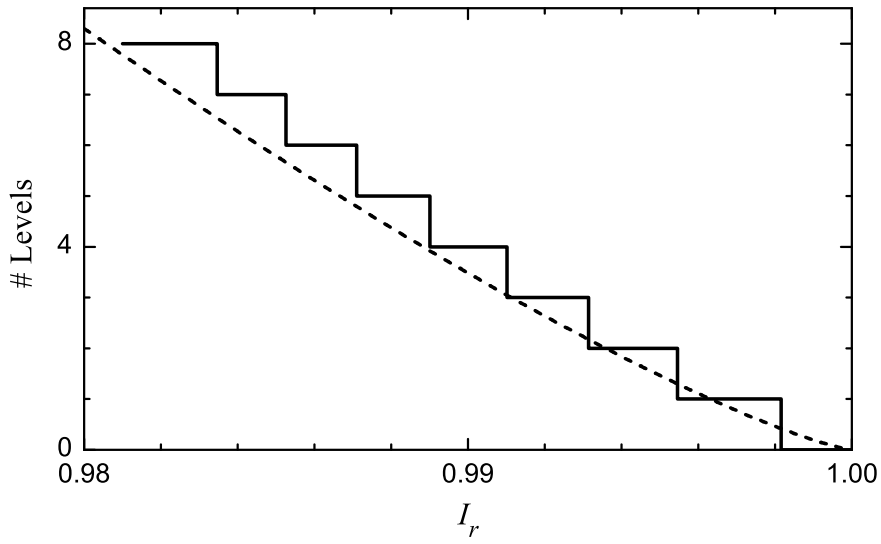

Figure 2.7: Number of levels of the tilted washboard potential. The number of levels (solid) within the barrier ΔU as a function of the reduced current bias I_r as calculated from the quantum simulation of a junction with $I_0 = 30$ μA and $C_J = 5$ pF is discrete. It is reasonably well approximated by the number of harmonic levels in the well N_s (dashed), given by Eq. (2.37).

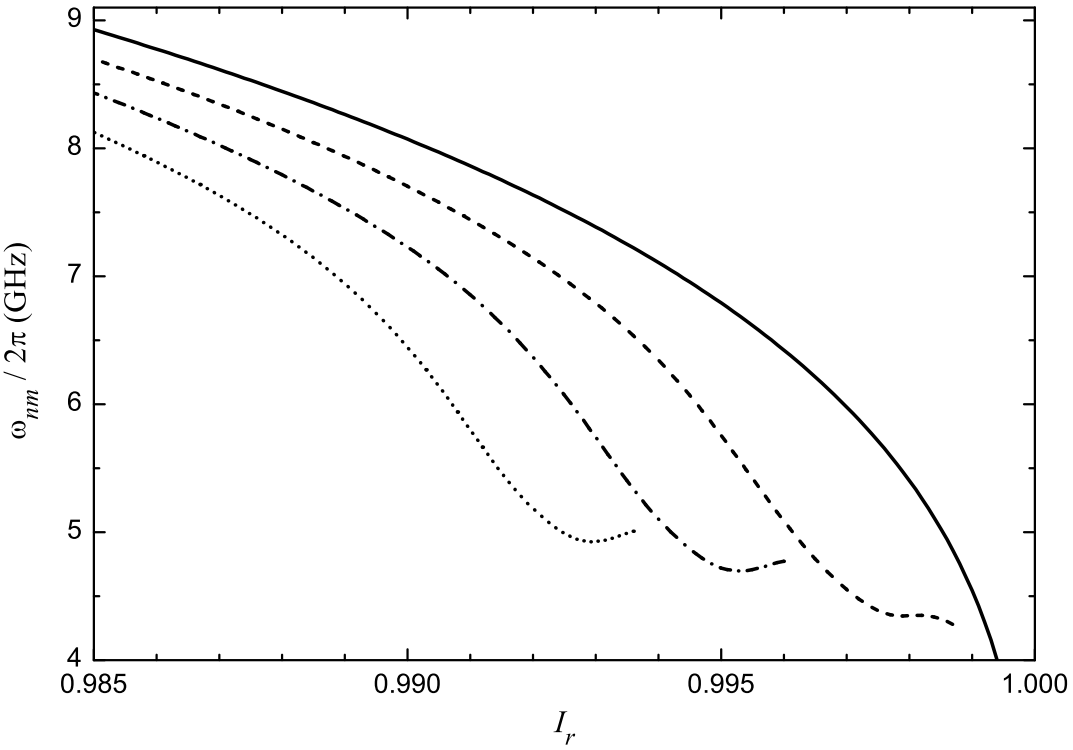

Figure 2.8: Energy level transitions of the tilted washboard potential. The solid line shows the classical plasma frequency ω_p of a junction with $I_0 = 30$ μA and $C_J = 5$ pF. Equation (2.44) gives the transition frequencies ω_{01} (dashed), ω_{12} (dash-dot), and ω_{23} (dotted).

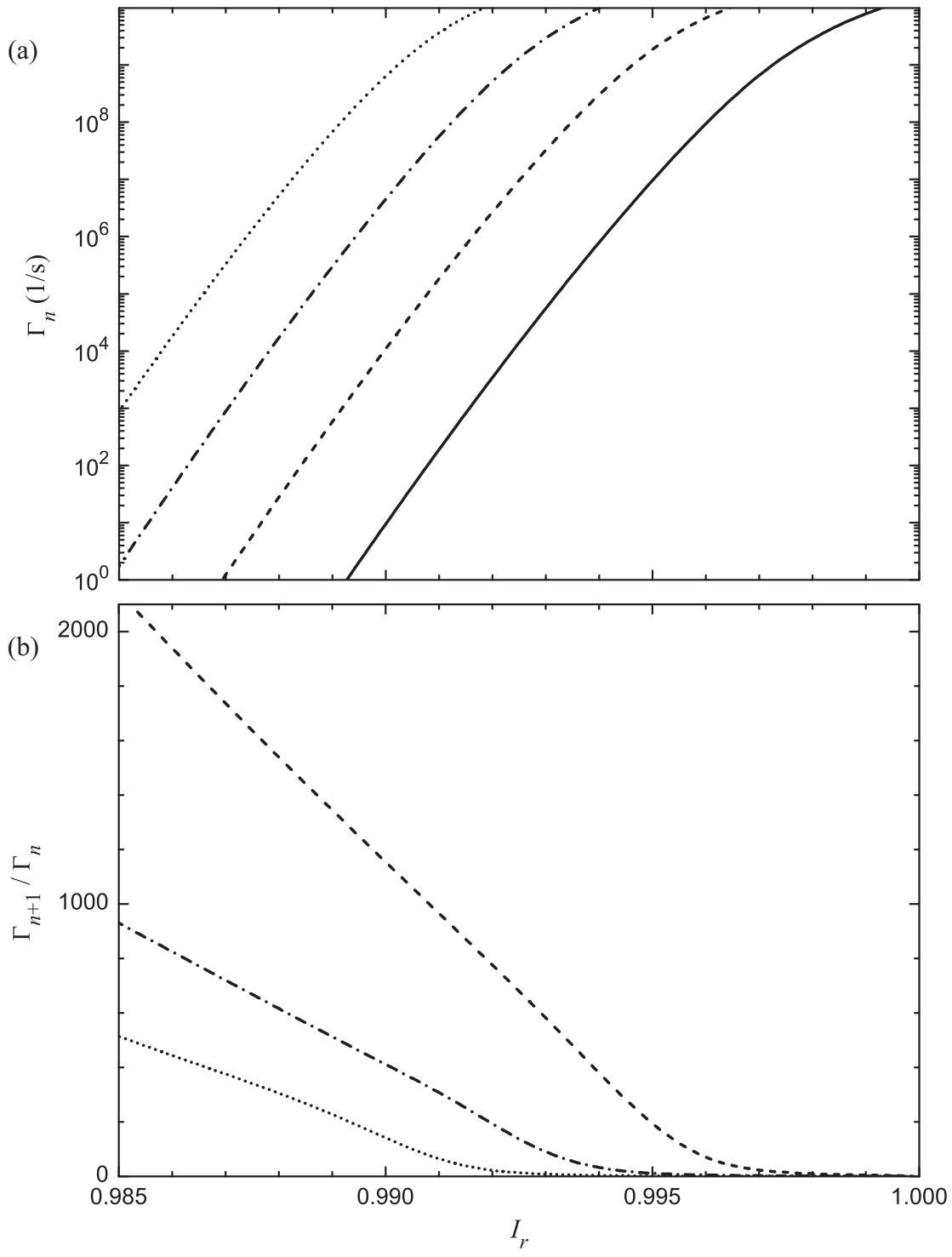

Figure 2.9: Tunneling rates of the tilted washboard potential. (a) Equation (2.43) gives the tunneling escape rates Γ_0 (solid), Γ_1 (dashed), Γ_2 (dash-dot), and Γ_3 (dotted) for a junction with $I_0 = 30$ μA and $C_J = 5$ pF. (b) The ratios Γ_1/Γ_0 (dashed), Γ_2/Γ_1 (dash-dot), and Γ_3/Γ_2 (dotted) are strong functions of the reduced current bias I_r.

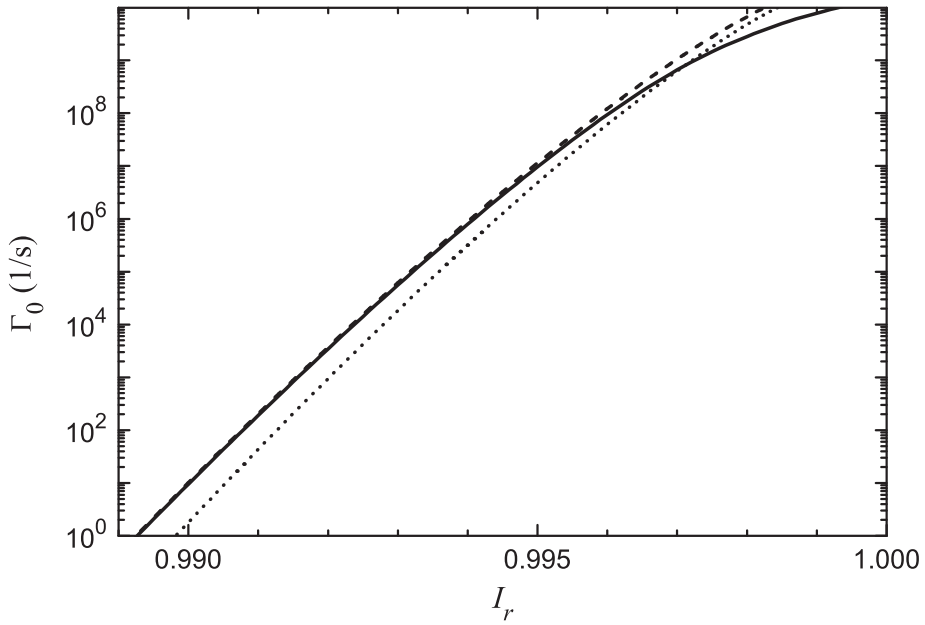

Figure 2.10: Ground state escape rate. Γ_0 is plotted as a function of the reduced current bias for a junction with $I_0 = 30$ μA and $C_J = 5$ pF. The solution of the full potential (solid) agrees with the cubic approximation (dashed) at all but the highest escape rates. With $R_J = 50$ Ω, damping causes a reduction in tunneling (dotted).

rate is roughly bounded by ω_p (which can be thought of as an attempt frequency[2]), although the second method described in this section does not entirely capture this effect. Again, because the lifetimes of states are so short at these high biases, it is difficult to accurately measure the way the rates roll-off. Ratios Γ_1/Γ_0 (dashed), Γ_2/Γ_1 (dash-dot), and Γ_3/Γ_2 (dotted) are plotted in Fig. 2.9(b). The ratios are quite large when the levels are deep in the well, which in principle makes it possible to distinguish tunneling from different states. This becomes much more difficult as levels reach the top of the barrier and the escape rates rapidly saturate.

The solid line of Fig. 2.10 is the same ground state curve as the one shown in Fig. 2.9(a). The dashed line is the tunneling rate for the cubic approximation, from Eq. (2.41). The agreement is quite good below 10^7 1/s. Above this rate, the solution of the full potential rolls off. As the solution of Schrödinger's equation (using the

[2]Simulations suggest that the numerical value of ω_p is the maximum escape rate [2], but the units of the escape rate are, for example, 1/s rather than rad/s.

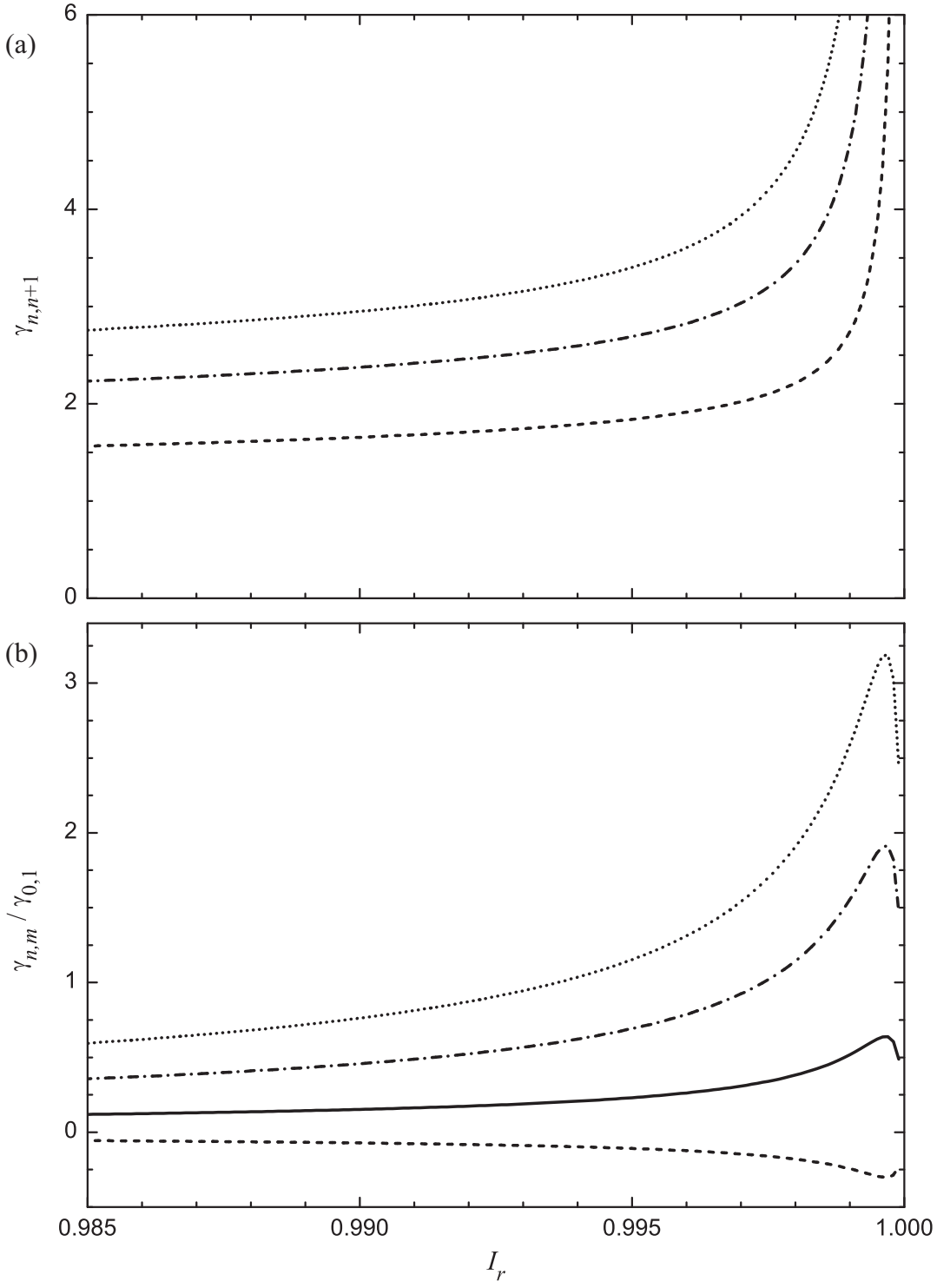

Figure 2.11: Matrix elements of the tilted washboard potential. (a) The matrix elements $\gamma_{0,1}$ (dashed), $\gamma_{1,2}$ (dash-dot), and $\gamma_{2,3}$ (dotted) in the cubic approximation of a junction with $I_0 = 30\ \mu$A and $C_J = 5$ pF are plotted as a function of the reduced current bias I_r, using Eq. (2.38). Each has been multiplied by $(2E_C/E_J)^{-1/4}$. (b) From Eq. (2.39), the ratios of $\gamma_{0,0}$ (solid), $\gamma_{0,2}$ (dashed), $\gamma_{1,1}$ (dash-dot), and $\gamma_{2,2}$ (dotted) to $\gamma_{0,1}$ are finite for the anharmonic potential.

technique described above) breaks down at high bias, the asymptotic value of Γ_0 at $I_r = 1$ was artificially imposed by the choice of $f_\Gamma^0(N_s)$ in Eq. (2.43). The dotted line in Fig. 2.10 is also in the cubic approximation, but with $R_J = 50\ \Omega$. As Eq. (2.42) shows, damping suppresses tunneling. A constant shunting resistance leads to a bias-dependent Q, but a nearly equivalent Γ_0 is obtained for $Q = 12$ (which is the value it takes at $I_r = 0.992$ for the plotted curve). Our qubits appear to have shunting resistance in excess of 1 kΩ. With this value of R_J, damping lowers Γ_0 by ~ 10 % at $I_r = 0.99$; alternatively, this can be viewed as a bias current shift of 1 nA. At $I_r = 0.994$, where many of my experiments were performed, these corrections are ~ 5 % and 0.5 nA. I have ignored the effects of damping on Γ_n in analyzing the data, but it could have had a non-negligible effect for our most poorly isolated qubits.

Finally, several matrix elements of the cubic potential are plotted in Fig. 2.11, calculated with Eqs. (2.38) and (2.39). Figure 2.11(a) shows the transition elements $\gamma_{0,1}$ (dashed), $\gamma_{1,2}$ (dash-dot), and $\gamma_{2,3}$ (dotted), where each has been multiplied by $(2E_C/E_J)^{-1/4}$. From Eq. (2.36), these are 1, $\sqrt{2}$, $\sqrt{3}$, respectively, in the harmonic limit. The anharmonic well causes large deviations, particularly at high bias. Figure 2.11(b) shows $\gamma_{0,0}$ (solid), $\gamma_{0,2}$ (dashed), $\gamma_{1,1}$ (dash-dot), and $\gamma_{2,2}$ (dotted), scaled by $\gamma_{0,1}$. For a harmonic oscillator, all of these would be zero. That they are finite gives rise to some of the rich non-linear behavior that is described in the next chapter.

2.4 Asymmetric dc SQUID Hamiltonian

A single current-biased Josephson junction has many characteristics that make it an attractive candidate for use as a qubit. However, it is typically strongly coupled to the environment through its bias leads, which can be a significant source of dissipation and decoherence. A variety of isolation techniques have been implemented to decrease the effects of decoherence, as discussed later in this thesis. One

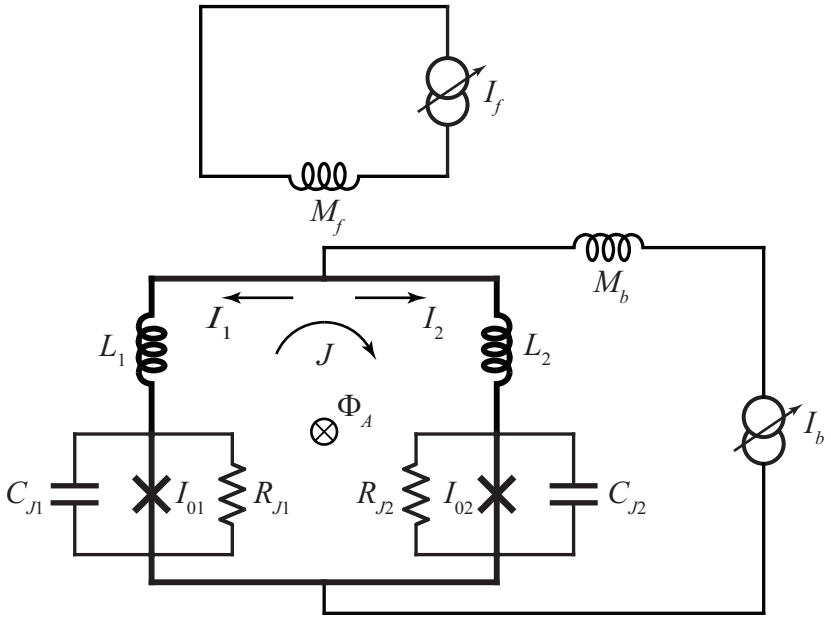

Figure 2.12: dc SQUID circuit diagram. The junction on the left is thought of as the qubit, while the one on right forms an inductive current divider with the geometrical inductance L_1. The branch currents I_1 and I_2 can be independently controlled by simultaneously applying a flux and current bias.

such approach uses an auxiliary inductance and junction in parallel with the main qubit junction [39], as shown in Fig. 2.12. The junction on the left is thought of as the qubit and the one on the right is part of the isolation network.

The motivation for adding these components is to create a broadband inductive current divider that filters noise from the current bias leads. For this approach to work well, L_1 must be much greater than L_2. For the devices that I measured, $I_{01} > I_{02}$, although this is not a strict requirement. A longer discussion of circuit parameters can be found in §4.3. The inclusion of the isolation network results in a dc SQUID that is asymmetric in the loop inductances L_1 and L_2, as well as the junction critical currents and capacitances. However, using the method described in §6.4, the device can be made to behave much like a single current-biased junction. In the derivation of the Hamiltonian that follows [4, 70, 71], I will ignore the resistances R_{J1} and R_{J2}, as their role in dissipation will be discussed separately.

The SQUID is controlled by the usual current bias I_b and an additional current I_f. Each line generates flux in the loop through its own mutual inductance, giving a total of $M_b I_b + M_f I_f$. As the flux line dominates in almost all situations, I will use the symbol Φ_A to represent its contribution. The current bias splits between the two arms of the SQUID; each branch current (I_1 and I_2) further splits between its junction and capacitor as in §2.2.1, so that

$$I_b = I_1 + I_2 \tag{2.45}$$

$$I_1 = C_{J1}\frac{d}{dt}\left(\frac{\Phi_0}{2\pi}\frac{d\gamma_1}{dt}\right) + I_{01}\sin\gamma_1 \tag{2.46}$$

$$I_2 = C_{J2}\frac{d}{dt}\left(\frac{\Phi_0}{2\pi}\frac{d\gamma_2}{dt}\right) + I_{02}\sin\gamma_2. \tag{2.47}$$

It is the coupling of the two junctions by the SQUID loop inductance that makes the dynamics of this device so rich. The naive strength of the coupling is given by $1/\beta$, where β is the modulation parameter

$$\beta = \frac{L\left(I_{01} + I_{02}\right)}{\Phi_0}. \tag{2.48}$$

Here, $L = L_1 + L_2$ is the total loop inductance. An additional constraint on the system comes from flux quantization in the loop. This condition can be found from the general flux-phase relationship for a loop interrupted by N junctions [54],

$$\sum_N \gamma_N = 2\pi\left(n - \frac{\Phi_T}{\Phi_0}\right), \tag{2.49}$$

where n is an integer and γ_N is the phase difference across the N-th junction. The path taken through each of the junctions sets the sign of phase difference to be consistent with the Josephson current relation. The convention used in Eqs. (2.46) and (2.47) is that a clockwise path (which corresponds to negative flux in this case)

around the SQUID loop crosses the qubit with $+\gamma_1$ and the isolation junction with $-\gamma_2$. The total flux in the loop Φ_T is the applied flux plus the flux induced by currents flowing in the loop.[3] Applying Eq. (2.49) to the asymmetric SQUID yields

$$\gamma_1 - \gamma_2 = 2\pi\left(n + \frac{\Phi_T}{\Phi_0}\right) = \frac{2\pi}{\Phi_0}\left(\Phi_A - L_1 I_1 + L_2 I_2 + M_b I_b\right) + 2\pi n. \tag{2.50}$$

With two junctions, there will be two equations of motion. They come from eliminating one of the branch currents in favor of the total current and plugging in Eqs. (2.46) and (2.47):

$$\begin{aligned} I_1 &= C_{J1}\frac{\Phi_0}{2\pi}\ddot{\gamma}_1 + I_{01}\sin\gamma_1 \\ &= -\frac{\Phi_0}{2\pi}\frac{1}{L}\left(\gamma_1 - \gamma_2 - 2\pi n - \frac{2\pi}{\Phi_0}\left(\Phi_A + M_b I_b\right)\right) + \frac{L_2 I_b}{L} \end{aligned} \tag{2.51}$$

$$\begin{aligned} I_2 &= C_{J2}\frac{\Phi_0}{2\pi}\ddot{\gamma}_2 + I_{02}\sin\gamma_2 \\ &= \frac{\Phi_0}{2\pi}\frac{1}{L}\left(\gamma_1 - \gamma_2 - 2\pi n - \frac{2\pi}{\Phi_0}\left(\Phi_A + M_b I_b\right)\right) + \frac{L_1 I_b}{L}. \end{aligned} \tag{2.52}$$

The terms on the far right are the branch currents you would expect from a simple inductance divider. They are modified by a term, equal to $\left(L_2 I_2 - L_1 I_1\right)/L$, that is due to flux quantization in the loop. For a SQUID with inductive symmetry, this term is just equal to the circulating current, $J = \left(I_2 - I_1\right)/2$. Now the force terms can be solved for, after multiplying through by $\Phi_0/2\pi$ [with $m_{J1} \equiv C_{J1}\left(\Phi_0/2\pi\right)^2$ and $m_{J2} \equiv C_{J2}\left(\Phi_0/2\pi\right)^2$]:

$$m_{J1}\ddot{\gamma}_1 = \frac{\Phi_0}{2\pi}\left(-I_{01}\sin\gamma_1 + \frac{L_2 I_b}{L}\right) - \left(\frac{\Phi_0}{2\pi}\right)^2\frac{1}{L}\left(\gamma_1 - \gamma_2 - 2\pi n - \frac{2\pi}{\Phi_0}\left(\Phi_A + M_b I_b\right)\right) \tag{2.53}$$

[3]The Josephson inductance presented in §2.1 does not contribute to the loop inductance in this case, as it does not store magnetic energy.

$$m_{J2}\ddot{\gamma_2} = \frac{\Phi_0}{2\pi}\left(-I_{02}\sin\gamma_2 + \frac{L_1 I_b}{L}\right) + \left(\frac{\Phi_0}{2\pi}\right)^2 \frac{1}{L}\left(\gamma_1 - \gamma_2 - 2\pi n - \frac{2\pi}{\Phi_0}\left(\Phi_A + M_b I_b\right)\right). \tag{2.54}$$

The first terms on the right hand sides would be identical to those for isolated junctions, if it were not for the ratio of inductances multiplying the current bias. Because of the interaction terms, the Langrangian cannot be expressed as a sum of single junctions. Nevertheless, the full Langrangian can be written down directly, by integrating to get the potential:

$$\mathcal{L} = \frac{1}{2} m_{J1} \dot{\gamma_1}^2 + \frac{1}{2} m_{J2} \dot{\gamma_2}^2 - U\left(\gamma_1, \gamma_2, I_b, \Phi_A\right) \tag{2.55}$$

$$\begin{aligned} U\left(\gamma_1, \gamma_2, I_b, \Phi_A\right) &= -\frac{\Phi_0}{2\pi}\left(I_{01}\cos\gamma_1 + I_{02}\cos\gamma_2\right) - \frac{\Phi_0}{2\pi}\frac{I_b}{L}\left(L_2\gamma_1 + L_1\gamma_2\right) \\ &\quad + \left(\frac{\Phi_0}{2\pi}\right)^2 \frac{1}{2L}\left(\gamma_1 - \gamma_2 - 2\pi n - \frac{2\pi}{\Phi_0}\left(\Phi_A + M_b I_b\right)\right)^2. \end{aligned} \tag{2.56}$$

The two-dimensional potential resembles the tilted washboard along the γ_1 and γ_2-axes, but it is also curled up along the $\gamma_1 - \gamma_2$ direction. The last term in the potential is equal to $\left(\Phi_T - \Phi_A - M_b I_b\right)^2 / 2L$ and represents the energy stored in the loop inductance by the bias currents. The large-scale curvature of the potential is inversely proportional to this inductance. The n that was introduced in Eq. (2.50) is discussed in the next section, but setting it equal to 0 is inconsequential for our purposes.

The Lagrangian yields momenta $p_1 = m_{J1}\dot{\gamma_1}$ and $p_2 = m_{J2}\dot{\gamma_2}$, so the Hamiltonian takes on a simple form,

$$\mathcal{H} = \frac{1}{2} m_{J1} \dot{\gamma_1}^2 + \frac{1}{2} m_{J2} \dot{\gamma_2}^2 + U\left(\gamma_1, \gamma_2, I_b, \Phi_A\right) \tag{2.57}$$

$$= \frac{p_1^2}{2m_{J1}} + \frac{p_2^2}{2m_{J2}} + U\left(\gamma_1, \gamma_2, I_b, \Phi_A\right). \tag{2.58}$$

2.5 Classical SQUID Behavior

While the circuit diagram for the dc SQUID is not much more complicated than that of the single junction, the behavior of the device certainly is. In this section, I will give a brief review of some classical properties of the dc SQUID that are relevant to its operation as a qubit.

The sensitivity of the SQUID to magnetic flux leads to complications and is a drawback for quantum computing. Many of the flux characteristics are related to the value of β. With no loop inductance ($\beta = 0$), the device is identical to a single junction with a critical current that is modulated by the applied flux. For very large β, the constraint of Eq. (2.50) can be satisfied in a number of ways, and the two junctions become uncoupled. We have studied devices with β between 20 and 250. I will start out by describing a more strongly coupled device. This simplifies the discussion, but also accentuates low β properties, which only moderately affect our qubits.

Figure 2.13(a) shows the potential energy U of a symmetric SQUID with $\beta = 4.8$, drawn using Eq. (2.56) with I_b, Φ_A, and M_b all zero. The axes are $\gamma_+ = (\gamma_1 + \gamma_2)/\sqrt{2}$ and $\gamma_- = (\gamma_1 - \gamma_2)/\sqrt{2}$, which make the symmetry very clear. Along $\gamma_- = 0$, the potential resembles a simple tilted washboard, even when the device is biased. Wells separated by $2\pi\sqrt{2}$ in the γ_+ direction are equivalent, as both junctions have advanced in the same sense by 2π. The wells in the γ_- direction are physically distinct, as each corresponds to a different circulating current and trapped flux in the loop. The front and back cuts of Fig. 2.13(a) are plotted in Fig. 2.13(b) as a solid and dashed line. Although the modulation due to the Josephson energy is present throughout the potential, there are no local minima for large $|\gamma_-|$. Locations with local minima (stable wells) will lose those minima (becoming unstable) as the current and flux bias change.

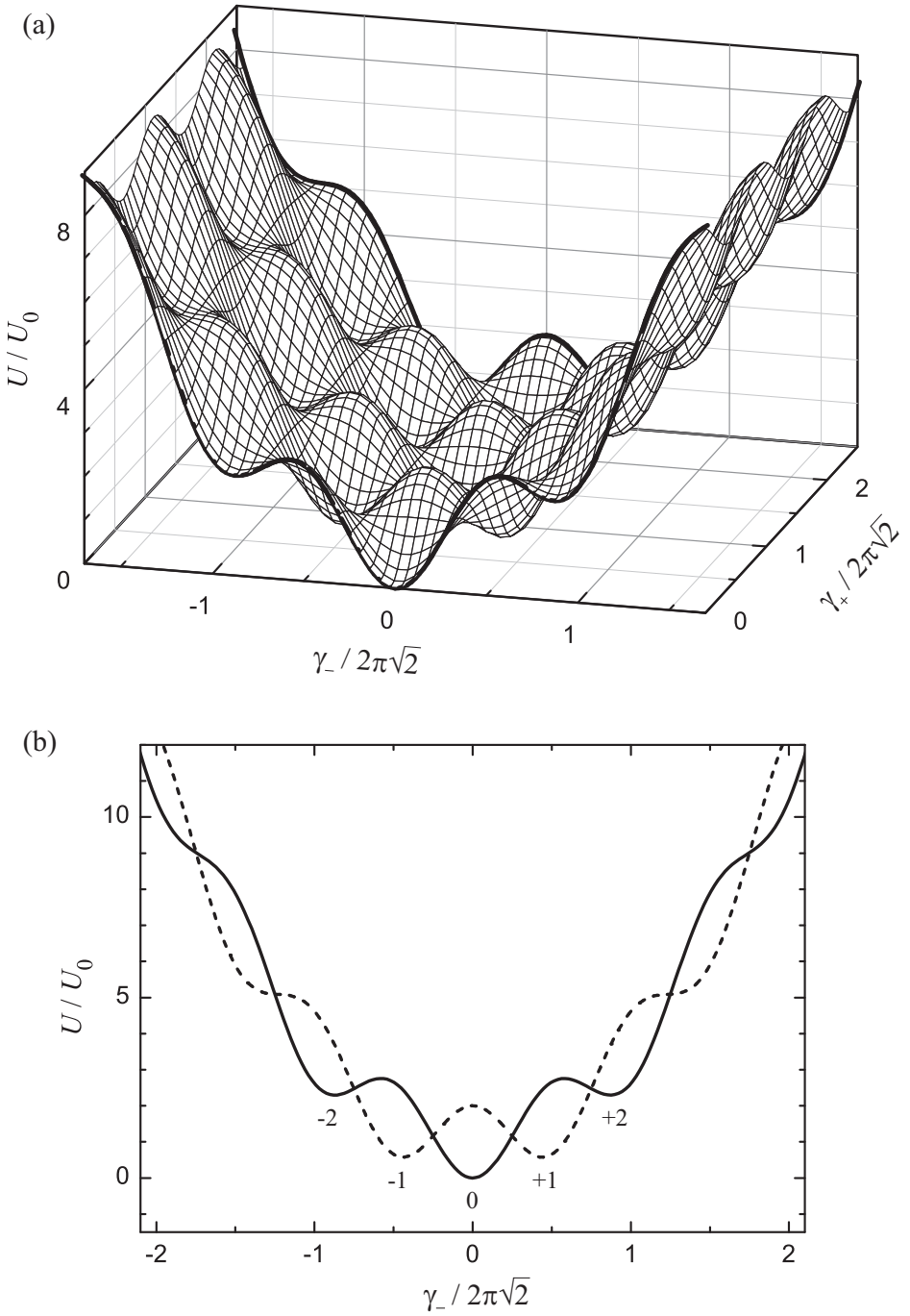

Figure 2.13: Potential of a symmetric dc SQUID with respect to symmetry axes. (a) The potential of a SQUID with $\beta = 4.8$, $L_1 = L_2$, and $I_{01} = I_{02}$ is plotted at $I_b = \Phi_A = 0$ as a function of $\gamma_+ = (\gamma_1 + \gamma_2)/\sqrt{2}$ and $\gamma_- = (\gamma_1 - \gamma_2)/\sqrt{2}$. The potential has been scaled by $U_0 \equiv \Phi_0 (I_{01} + I_{02})/2\pi$ and shifted vertically by the same amount. (b) Cuts at $\gamma_+ = 0$ (solid line) and $\pi\sqrt{2}$ (dashed) can be used to identify the five distinct flux states, which are labeled by N_Φ.

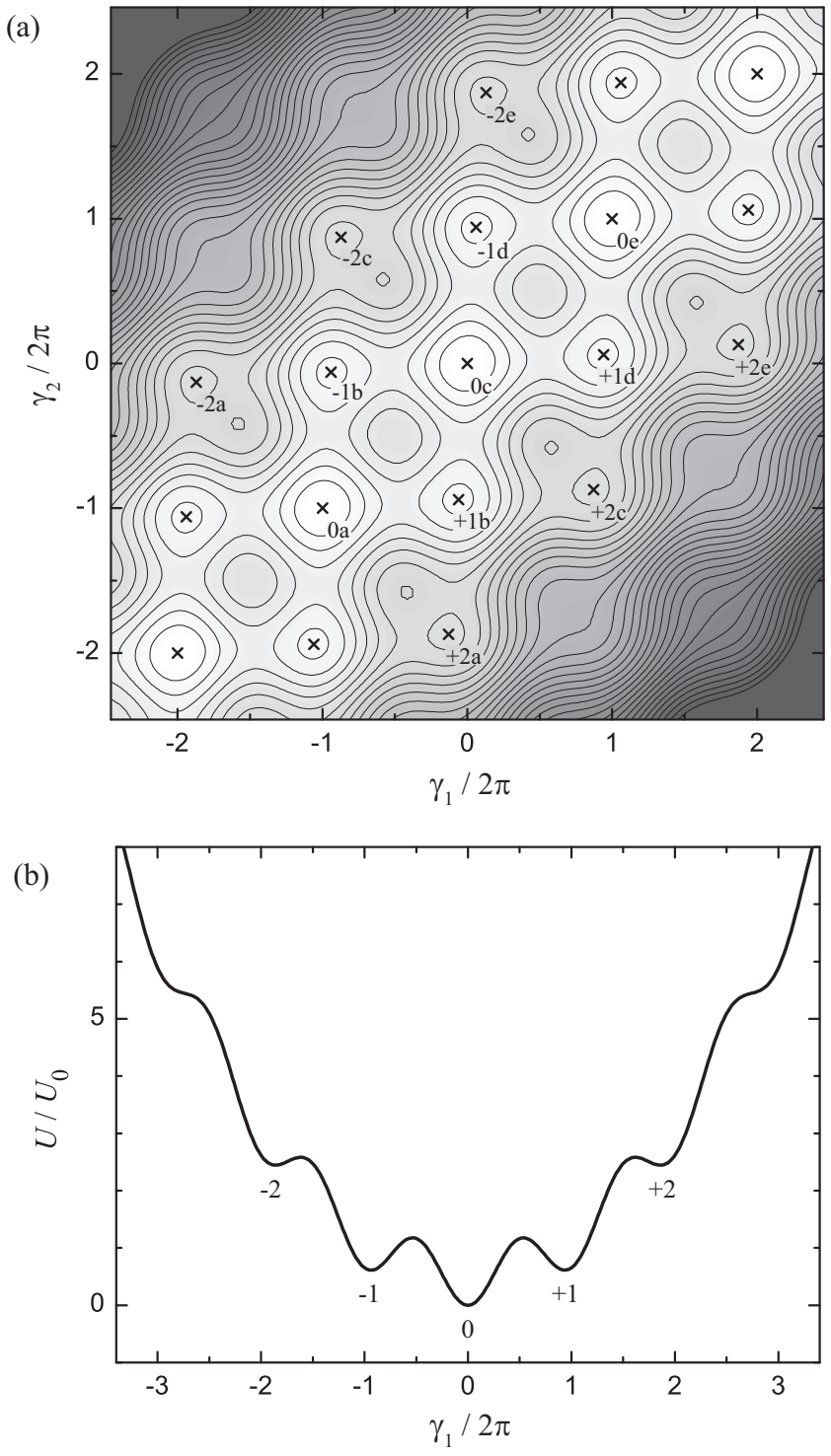

Figure 2.14: Potential of a symmetric dc SQUID with respect to junction axes. (a) The potential for the unbiased SQUID with $\beta = 4.8$ in Fig. 2.13 is plotted as a function of γ_1 and γ_2. The small numbers indicate the flux state N_Φ; indistinguishable wells of the same flux state are labeled with letters, *e.g.* -1b and -1d. (b) In many cases, all of the flux states can be identified on a single cut along $\gamma_2 = 0$.

A contour plot of the same potential is shown in Fig. 2.14(a), plotted as a function of γ_1 and γ_2, with a single line cut in Fig. 2.14(b). Adjacent wells along one of these directions correspond to the phase of one junction advancing by 2π, which gives rise to a change of a flux quantum in the loop.

The location of local minima are marked with crosses on Fig. 2.14(a), with values listed in Table 2.1. These were calculated numerically using Newton-Raphson iteration; see, for example, §9.6 of Ref. [69]. As with the single junction, the system can sit (in the "classical ground state") at the bottom of one these wells with no kinetic energy. In this case, there are no displacement currents through the junction capacitances and $I_b = I_{01} \sin \gamma_1 + I_{02} \sin \gamma_2$. For an unbiased symmetric device, this means that the location of the minima satisfy $\gamma_1 = -\gamma_2$. Thus, the two cuts along γ_- are guaranteed to run through all of the minima of the potential. Each of the letters used to label the wells corresponds to a different value of $\gamma_1 + \gamma_2$. With no inductance, the minima lie at intervals of 2π along γ_1 and γ_2. With finite inductance, the curling of the potential shifts the minima toward the γ_+ axis, so that they are not located along any constant value of γ_1 or γ_2. A single cut of the sort shown in Fig. 2.14(b) can therefore miss shallow wells corresponding to high flux states.

The seventh column of Table 2.1 shows the total flux $\Phi_T = LJ$ due to the circulating current $J = (I_2 - I_1)/2$ for each of the flux states. For finite β, adjacent (distinct) states generate fluxes that differ by $\Delta\Phi < \Phi_0$. The number of these flux units $N_\Phi = \Phi_T/\Delta\Phi$ is used to label the wells in Figs. 2.13 and 2.14.[4] Notice that $\Delta\Phi$ decreases slightly as the total generated flux increases. The sign convention given in Fig. 2.12 sets states with positive N_Φ to have $I_1 < 0$. Incidentally, the number of allowed flux states is set by the maximum circulating current. For large β, $\Delta\Phi \approx \Phi_0$ and the number of states at zero bias is $2(L_1 + L_2) I_{02}/\Phi_0 + 1$, provided $I_{01} > I_{02}$ as in the qubits I studied in this thesis.

[4]In Ref. [72], this quantity is known as n; there, N_Φ is used to denote the total number of allowed flux states.

Table 2.1: Flux state properties of a low β dc SQUID. The second and third columns are the locations of the minima of the potential in Figs. 2.13 and 2.14, with the first column giving the labels used there. The (purely) circulating current generates a non-quantized total flux Φ_T, though the fluxoid is always zero as the sum of the final two columns shows.

N_Φ	$\gamma_1/2\pi$	$\gamma_2/2\pi$	$(\gamma_1+\gamma_2)$	I_1/I_{01}	I_2/I_{02}	Φ_T/Φ_0	$(\gamma_2-\gamma_1)/2\pi$
-2c	-0.871	0.871	0	0.726	-0.726	-1.742	1.742
-1d	0.060	0.940	2π	0.367	-0.367	-0.880	0.880
0c	0	0	0	0	0	0	0
+1d	0.940	0.060	2π	-0.367	0.367	0.880	-0.880
+2c	0.871	-0.871	0	-0.726	0.726	1.742	-1.742
+2a	-0.129	-1.871	-4π	-0.726	0.726	1.742	-1.742
+2e	1.871	0.129	4π	-0.726	0.726	1.742	-1.742

For each flux state, the sum of the final two columns of Table 2.1 is zero, consistent with the fluxoid quantization condition [54], which can be simply taken as an inverted version of the flux-phase relationship of Eq. (2.45). Here, a counter-clockwise path is chosen so that the corresponding flux is positive, yielding $\gamma_2-\gamma_1$. Although the flux in the loop changes for the different states, all of them give a fluxoid equal to the constant n in Eq. (2.56). I should point out that several of the above statements are true only for $\Phi_A=0$. In general, if $\Phi_A=N_\Phi\Phi_0$, then a well labeled N_Φ is at a global minimum. All of the arguments may be repeated with respect to this new minimum.

This example gives me an opportunity to discuss two interpretations of n. So far, I have allowed γ_1 and γ_2 to be unbounded. Knowledge of the fluxoid quantization up to multiples of 2π in Eq. (2.50) can be incorporated into the quadratic term of the potential as shifts in the two coordinates. The remaining terms are periodic in γ_1 and γ_2, so these shifts have no physical consequences. When the system jumps to a new flux state, voltages appear across the junction, which results in the phases

evolving. However, the fluxoid remains constant. Although n is not needed at all, different values could correspond to different histories of these voltages.

Alternatively, γ_1 and γ_2 can be restricted to $[-\pi, \pi]$, with n providing compensation. In that case, Fig. 2.13(a) would look quite different (and confusing!) as blocks of the potential would be shifted back to the origin, not unlike the reduced zone scheme used in band structure diagrams. Switching to different flux states is then encoded in n (which is always the value of the fluxoid). In this case, $N_\Phi = n$. For flux states in the γ_+ direction, n is constant and the states truly are indistinguishable, *i.e.* there is no way to label the path that the system took to get to a state. Although this picture does provide a clear definition of N_Φ, I will otherwise use the "extended zone scheme" (with $n = 0$) which I find easier to visualize.

As an example, consider the first state listed in the Table 2.1. For this state, $\gamma_1/2\pi = -0.871$, $\gamma_2/2\pi = +0.871$, and $n = 0$. The same value of the potential [given in Eq. (2.56)] can be obtained with $\gamma_1/2\pi = +0.129$, $\gamma_2/2\pi = -0.129$, and $n = -2$. As noted in the previous paragraph, with the phases restricted, the entries for the final three flux states in the table would be identical.

So far, I have only discussed the situation at zero bias. As the flux bias is increased, the potential "rolls" in the γ_- direction, resulting in a shift of $2\pi/\sqrt{2}$ for every additional flux quantum of applied flux. Although the shape of the potential is the same at these flux quantum intervals, the N_Φ labels of the wells will change. As the potential rolls, once stable wells become unstable and are replaced by newly stable wells. If the phase particle is in a well that loses its minimum, it will find a new well in a random fashion. We exploit this process in initializing the flux state, as described in §6.5. In practice, we cannot easily check if there is any background flux biasing the loop (from trapped vortices, for example), so Φ_A is measured with respect to $I_f = I_b = 0$.

When the current bias increases, the potential tilts in the γ_+ direction, much as

the 1-D tilted washboard does. At some point, the well barrier will disappear. The conditions for this to happen are described in the next section. This way of making a well unstable is somewhat different than just changing the flux. As before, the system can simply switch to a different flux state. However, if the tilt is sufficiently large, the SQUID will switch to the voltage state. The important difference between the SQUID and the single junction is that the SQUID potential gives the particle two directions to escape in. As described in §6.4, we adjust the biases so that escape always happens in the γ_1 direction when operating the device as a qubit. Although the particle begins to move in this direction, it quickly gains enough energy so that both phases evolve (corresponding to both junctions being in the voltage state).

For quantum computation, we are interested in the quantum properties of the dc SQUID. As with the single junction, there are metastable resonances that we will use as the states of a qubit. Similar techniques as those described in §2.3.3 can be applied to the 2-D potential [73]. A full description of the different solutions could occupy an entire chapter and is beyond the scope of this thesis. However, in the very specific way in which we bias the SQUID, it behaves much like a single junction. This is because the two junctions are generally held well out of resonance with each other and the qubit junction is always made to switch to the voltage state before the isolation junction [39, 72]. Therefore, I will apply the single junction results to the SQUID. While there are important differences between the two [73], the single-junction solution will be sufficient to describe nearly all of the results presented in the experimental chapters that follow.

2.6 Current-Flux Characteristics

Unlike the current-biased junction, a dc SQUID will not necessarily switch to the voltage state at a single value of I_b. There are two reasons for this. As described in the previous section, different flux states correspond to different values

of circulating currents in the loop. In addition, the applied flux serves as a bias for the SQUID, independent of the current bias. Therefore, the IV curve of a single junction is replaced by current-flux characteristics, I_b vs. Φ_A, for the SQUID.

For each value of Φ_A, the critical current can be found by allowing γ_1 and γ_2 to adjust themselves to maximize I_b [given in Eq. (2.45)]. The solution can be found by using the method of Lagrange multipliers, with Eq. (2.50) as the constraint on the phases [74]. This yields the following condition, which will be satisfied at an extremum of I_b:

$$\cos\gamma_2 = -\left(\frac{I_{02}}{I_{01}\cos\gamma_1} + \frac{2\pi}{\Phi_0}\left(L_1 + L_2\right) I_{02}\right)^{-1}. \tag{2.59}$$

Notice that this is independent of M_b.

This equation yields three qualitatively different types of characteristics. However, in high β devices of the sort that we use where

$$\left(L_1 + L_2\right)\frac{I_{01}I_{02}}{I_{01} + I_{02}} \geq \frac{\Phi_0}{2\pi}, \tag{2.60}$$

the relationship between the phases will resemble the one shown in Fig. 2.15(a), which is for the symmetric device of the previous section. This pattern will repeat every 2π in both phases. On both the solid and dashed curves I_b is maximized (for some implicit value of Φ_A), as the second derivatives of Eq. (2.45) confirm. However, for the points on (and within) the dashed loop, the potential of Eq. (2.56) is at a maximum. They are not physically stable solutions and only the loop centered about (0, 0) will be considered below.

In order to convert this loop to the characteristic of Fig. 2.15(b), Eq. (2.45) can be used to calculate I_b and Eq. (2.50) can be inverted to give the necessary

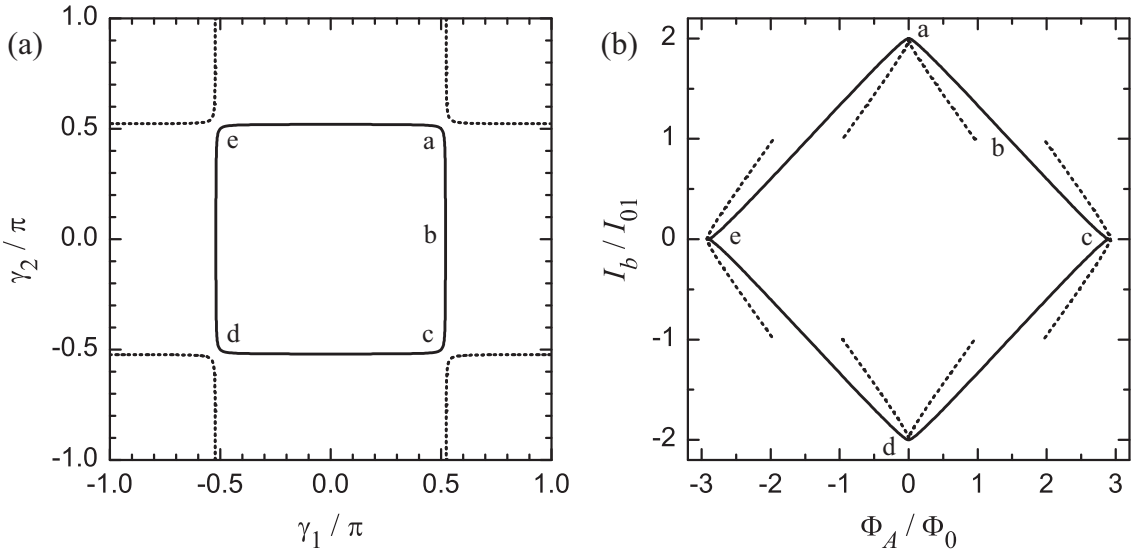

Figure 2.15: Current-flux characteristics of a symmetric SQUID. (a) The total current bias I_b has extrema along physical (solid) and unphysical (dotted) branches for the device introduced in Fig. 2.13. (b) The resulting characteristic shows the closed area where the system can remain in $N_\Phi = 0$. The small letters show the correspondence between the phases in (a) and currents in (b).

applied flux (in the ground state):

$$I_b = I_{01} \sin \gamma_1 + I_{02} \sin \gamma_2 \tag{2.61}$$

$$\Phi_A = \frac{\Phi_0}{2\pi} (\gamma_1 - \gamma_2) + (L_1 - M_b) I_{01} \sin \gamma_1 - (L_2 + M_b) I_{02} \sin \gamma_2. \tag{2.62}$$

Equation (2.59) is always satisfied for $\gamma_1 = \gamma_2 = \pm\pi/2$, so the characteristic will have a maximum at $|I_b| = I_{01} + I_{02}$ and critical points at $\pm (I_{01} - I_{02})$. In fact, these are the only four points on the characteristic where *either* of the junctions is biased at its critical current. A particular flux state ($N_\Phi = 0$ for this figure) is stable if the system stays within the loop. If any of the boundaries are crossed, then the phase particle is forced to find another well. For sufficiently large values of I_b, the system will not be able to re-trap and will go to the running state.

Figure 2.16 shows the characteristics for a SQUID with $I_{02}/I_{01} = 0.4$, $L_1 =$

$5.8\,\Phi_0/I_{01}$, $L_2 = 0.2\,\Phi_0/I_{01}$, and thus $\beta = 8.4$. While the critical current and inductive asymmetries are similar to our qubit devices, I have chosen a relatively low β for clarity. Figure 2.16(a) shows the physical phase loop, repeated at multiples of 2π. The corresponding I_b vs. Φ_A loops are shown in Fig. 2.16(b), for positive I_b. In both panels, only a selection of an infinite family of loops is shown; as before, a line of loops in Fig. 2.16(a) map to the same loop in Fig. 2.16(b) as indicated by the small numbers. The "top" of the loops are indicated with solid lines; the dashed lines are obtained by letting $\gamma_1 \to -\gamma_1$ and $\gamma_2 \to -\gamma_2$, or $I_b \to -I_b$ and $\Phi_A \to -\Phi_A$. Notice that the point $I_b = \Phi_A = 0$ is enclosed by five loops, which is the number of possible flux states and is coincidentally the same number as for the symmetric $\beta = 4.8$ device. There is, however, a small region at finite Φ_A where six states are allowed.

Although Fig. 2.16(a) resembles Fig. 2.14(a), the nature of the information they contain is quite different. The former shows the relationship between γ_1 and γ_2 for all possible flux biases that maximize I_b. The small numbers are used to label the wells and (as mentioned earlier) are the number of applied flux quanta needed to bring the well to the global minimum; these labels extend to infinity in both directions. The latter shows only the stable wells under one particular set of bias conditions. Although they extend to infinity in the γ_+ direction, the γ_- direction distinguishes the allowed flux states. N_Φ not only serves as a label, but also indicates the flux generated by circulating currents in the loop.

In a high β asymmetric device, it is sensible to identify the qubit and isolation junction branches. Comparing Fig. 2.16(a) and (b), each of the steeper solid lines correspond to $\gamma_1 \approx \pi/2 \,(\mathrm{mod}\, 2\pi)$ and therefore represent the qubit switching to the voltage state; they extend from $I_b = I_{01} + I_{02}$ to $I_{01} - I_{02}$. In doing experiments, it is these branches that we will want to cross in order to measure the properties of the qubit junction. On the other hand, the shallow solid lines correspond to

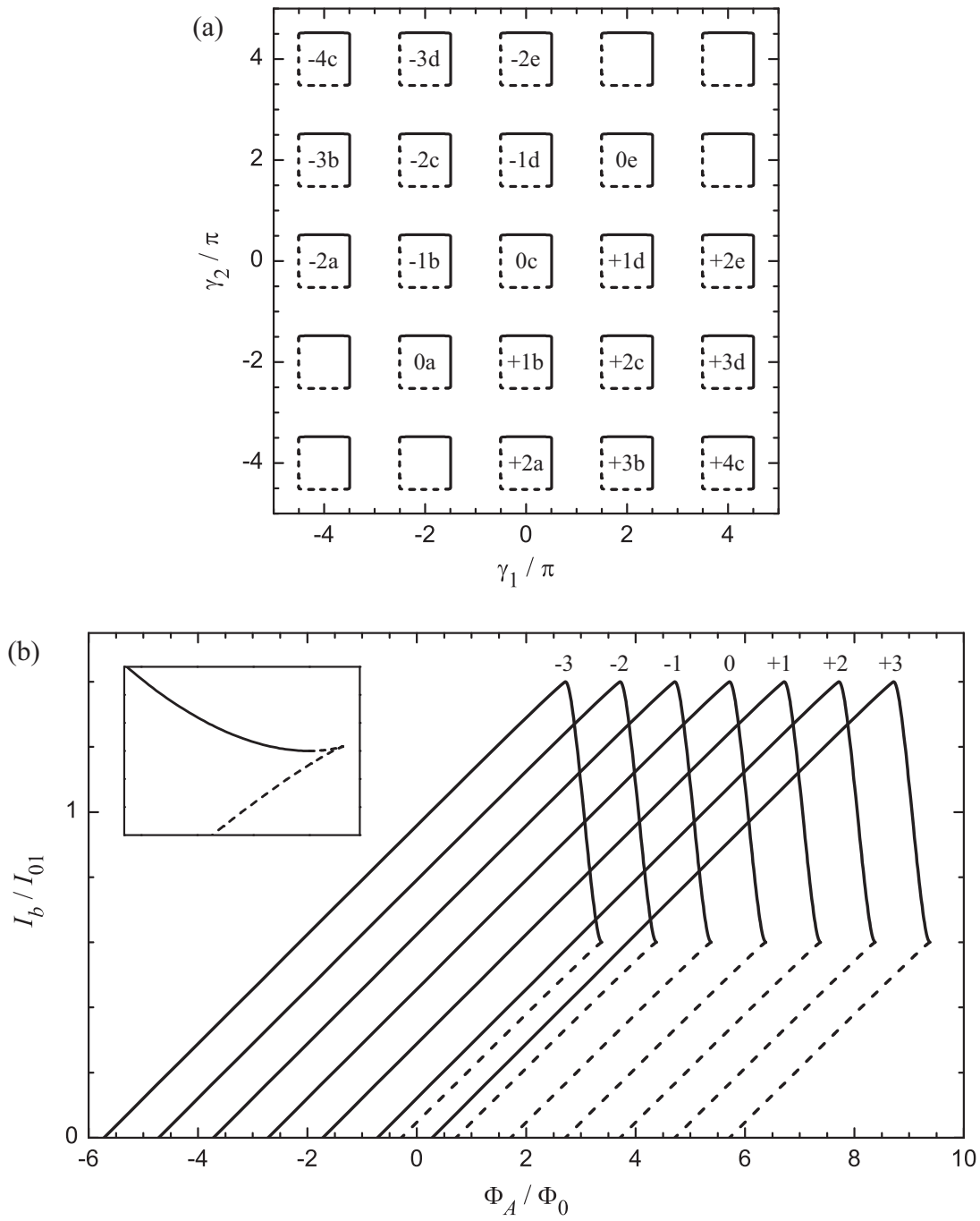

Figure 2.16: Current-flux characteristics of an asymmetric dc SQUID. (a) The critical points for a SQUID with $I_{02}/I_{01} = 0.4$, $L_1 = 5.8\,\Phi_0/I_{01}$, $L_2 = 0.2\,\Phi_0/I_{01}$, and $\beta = 8.4$ repeat at intervals of 2π. The numbers that label each loop specify the flux state N_Φ; loops centered about a common value of γ_- are labeled with the same letter. Panel (b) shows seven of an infinite series of characteristics. The numbers are N_Φ and match the labels on panel (a). Experimentally, the bias trajectories that we use cross the solid lines; the dashed lines may be found by inverting the coordinates and complete the loop of each flux state. The inset shows an expanded view of the intersection of two branches; the box has a width of 0.007 and height of 0.0006.

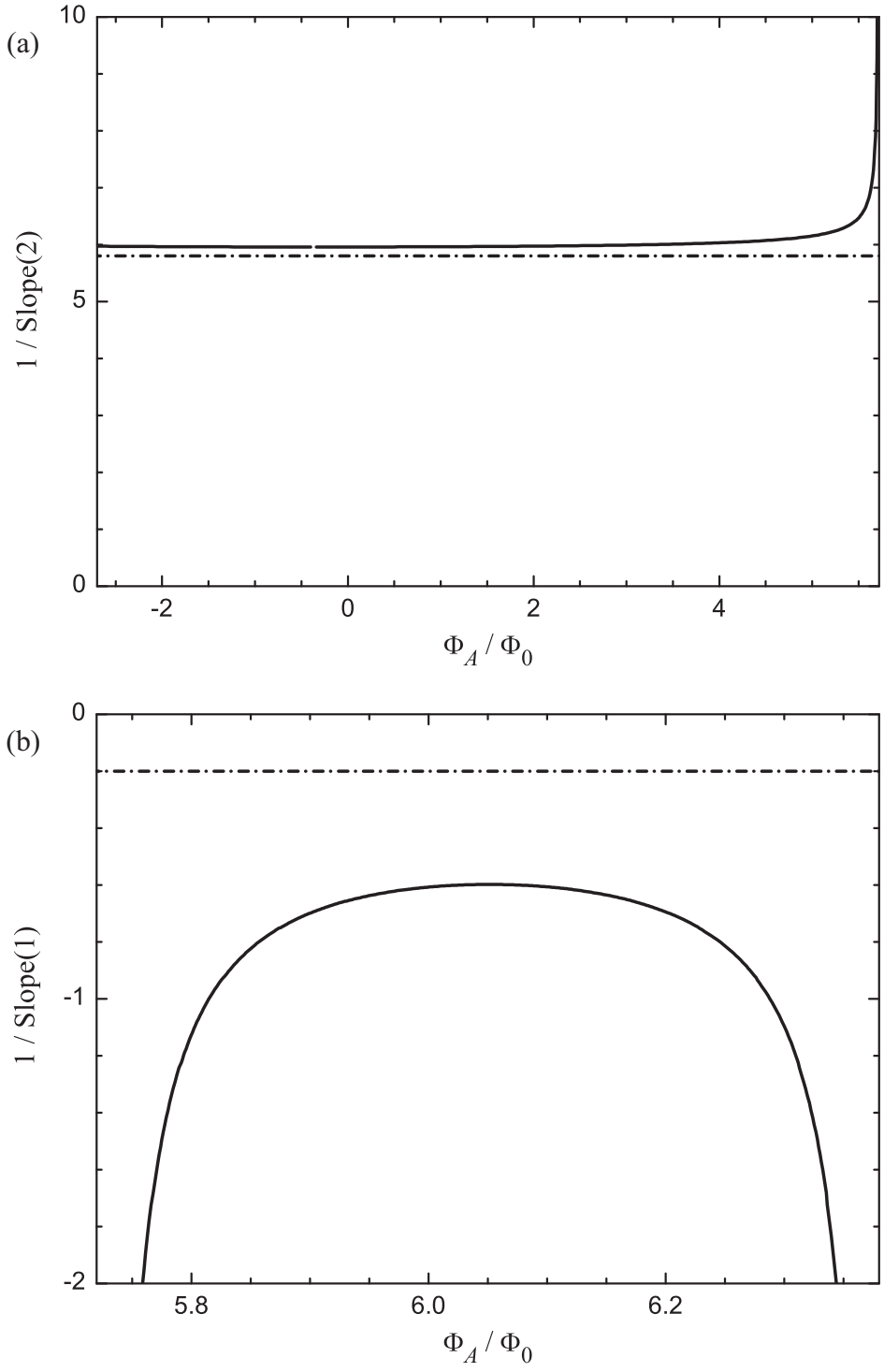

Figure 2.17: Slopes of the current-flux characteristics of an asymmetric dc SQUID. The inverse of the slope of the characteristics shown in Fig. 2.16 for the (a) isolation and (b) qubit branch (in units of Φ_0/I_{01}) have a curvature due to the Josephson inductance of the qubit and isolation junctions, respectively. The horizontal axis shows the full extent of each branch for $N_\Phi = 0$. The dot-dashed lines show the contribution of the geometrical inductances.

$\gamma_2 \approx \pi/2 \,(\mathrm{mod}\, 2\pi)$ and switching of the isolation junction. This branch extends from $I_b = I_{01} + I_{02}$ to $I_{02} - I_{01}$, although we do not experimentally measure its full extent, as discussed in §6.3.

The slope of the characteristic can be understood as follows [4]. Consider a point on the steep (qubit) branch. If Φ_A increases slightly, then the circulating current J (shown in Fig. 2.12) becomes increasingly negative in response. Therefore, a smaller current bias is needed to push the qubit past its critical current, resulting in a negative slope.

An expression for the inverse of this slope can be found by taking a derivative of Eq. (2.62) and substituting in the Josephson inductance of Eq. (2.12):

$$\frac{d\Phi_A}{dI_b} = \frac{\Phi_0}{2\pi}\left(\frac{L_1 + L_{J1} - M_b}{L_{J1}}\right)\frac{d\gamma_1}{dI_b} - \frac{\Phi_0}{2\pi}\left(\frac{L_2 + L_{J2} + M_b}{L_{J2}}\right)\frac{d\gamma_2}{dI_b}. \tag{2.63}$$

One of the phase derivatives may be eliminated using Eq. (2.61) to yield

$$\frac{d\Phi_A}{dI_b} = -\left(L_2 + L_{J2} + M_b\right) + \frac{\Phi_0}{2\pi}\left(\frac{L_1 + L_{J1} + L_2 + L_{J2}}{L_{J1}}\right)\frac{d\gamma_1}{dI_b}. \tag{2.64}$$

Along the qubit branch, the second term on the right can be neglected,[5] so the inverse of the slope is $-\left(L_2 + L_{J2} + M_b\right)$ to a very good approximation. Although the same result is obtained if $d\gamma_1/dI_b = 0$, this limit is not strictly valid, as seen by the slight curvature of the qubit branch in Fig. 2.16(a). For low β devices, both terms of Eq. (2.63) make comparable contributions, but the approximate expression for the slope is nevertheless still valid. Analogous arguments give the inverse of the slope of the isolation branch as $L_1 + L_{J1} - M_b$.

Figure 2.17(a) and (b) show the inverse of the slope of each of the branches of the example device, in units of Φ_0/I_{01}. While these curves were calculated from the numerical solutions of Eq. (2.59), they are indistinguishable on this scale from the

[5]This can be shown numerically for a large range of device parameters.

sum of the geometrical and Josephson inductance for each arm (with the former's contribution indicated by a dot-dashed line). The qubit branch has a much more noticeable curvature because I_{02} and L_2 are small. It is steeper than the isolation branch because I have assumed $L_1 \gg L_2$, as with the devices that I measured.

2.7 Capacitively-Coupled Junction Qubits

A nice feature of phase qubits is that they can be coupled together with a simple capacitor. In this section, I will derive the Hamiltonian for a system of two coupled junctions, which will describe the spectroscopy experiments of §8.6. Detailed derivations and further discussion can be found in Refs. [41, 75–77], §8.1 of Ref. [3], Chapter 8 of Ref. [1], and Chapters 6 and 7 of Ref. [2].

Figure 2.18 shows two current-biased junctions, whose elements are labeled with a superscript A or B, coupled together with a capacitor C_C. The junctions have critical currents I_0^A and I_0^B, which need not be the same, but I will assume that their capacitances are equal ($C_J = C_J^A = C_J^B$). The junctions are biased with independent currents, I_b^A and I_b^B. We found, somewhat accidentally, that the stray inductances L_C^A and L_C^B, together with C_C, form an LC harmonic oscillator mode [78]. The inductances can be ignored, as I will do at first, if the resonant frequency of the mode is above the region of interest. I have also dropped the junction shunting resistances normally included in the RCSJ model.

Each bias current splits between its junction and junction capacitance, as well as the coupling capacitor, giving rise to the equations

$$I_b^A = C_J \frac{d}{dt}\left(\frac{\Phi_0}{2\pi}\frac{d\gamma^A}{dt}\right) + I_0^A \sin\gamma^A + I_C \tag{2.65}$$

$$I_b^B = C_J \frac{d}{dt}\left(\frac{\Phi_0}{2\pi}\frac{d\gamma^B}{dt}\right) + I_0^B \sin\gamma^B - I_C, \tag{2.66}$$

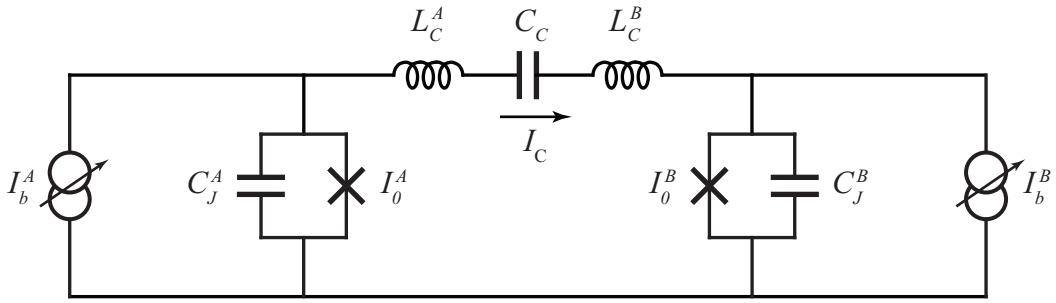

Figure 2.18: Circuit diagram for two LC-coupled junctions. Two current-biased junctions, similar to one shown in Fig. 2.2, are coupled together with a capacitance C_C, through which current I_C flows. Stray inductances L_C^A and L_C^B can have a significant impact.

where the current through the coupling capacitor is

$$I_C = C_C \frac{dV_C}{dt} = C_C \frac{\Phi_0}{2\pi} \frac{d}{dt} \left(\frac{d\gamma^A}{dt} - \frac{d\gamma^B}{dt} \right). \tag{2.67}$$

Thus I_C travels from junction A to B and depends on the rate of change of the voltage V_C across C_C. As the coupling current can be expressed in terms of the two junction phase differences, no additional degrees of freedom have to be introduced. With rearrangements similar to those for the single junction, the equations of motion for the system become

$$m_J \ddot{\gamma}^A = \frac{\Phi_0}{2\pi} \left(-I_0^A \sin\gamma^A + I_b^A \right) - m_C \left(\ddot{\gamma}^A - \ddot{\gamma}^B \right) \tag{2.68}$$

$$m_J \ddot{\gamma}^B = \frac{\Phi_0}{2\pi} \left(-I_0^B \sin\gamma^B + I_b^B \right) + m_C \left(\ddot{\gamma}^A - \ddot{\gamma}^B \right), \tag{2.69}$$

where the effective masses are $m_J \equiv C_J \left(\Phi_0/2\pi\right)^2$ and $m_C \equiv C_C \left(\Phi_0/2\pi\right)^2$.

In each of the equations of motion, the first term on the right is generated by the Lagrangian for a single junction, given by Eq. (2.21). The simplest way to

generate the second term is with the coupling Lagrangian

$$\mathcal{L}_C = \frac{1}{2} m_C \left(\dot{\gamma}^A - \dot{\gamma}^B\right)^2 . \tag{2.70}$$

The conjugate momenta, given by Eq. (A.8), are

$$p^A = (m_J + m_C)\left(\dot{\gamma}^A - \zeta_0 \dot{\gamma}^B\right) \quad \text{and} \quad p^B = (m_J + m_C)\left(\dot{\gamma}^B - \zeta_0 \dot{\gamma}^A\right), \tag{2.71}$$

where the dimensionless coupling constant is

$$\zeta_0 = \frac{C_C}{C_J + C_C}. \tag{2.72}$$

The full Hamiltonian has the simple form $\mathcal{H} = \mathcal{H}^A + \mathcal{H}^B + \mathcal{H}_C$ according to Eq. (A.10), where each term is expressed in terms of the generalized coordinates and velocities. The single junction Hamiltonians $\mathcal{H}^A$ and $\mathcal{H}^B$ are given by Eq. (2.23) and the coupling contribution, obtained from Eq. (A.11), is

$$\mathcal{H}_C = \frac{1}{2} m_C \left(\dot{\gamma}^A - \dot{\gamma}^B\right)^2 . \tag{2.73}$$

To put the Hamiltonian in canonical form, the generalized velocities may be eliminated in favor of p^A and p^B by inverting Eq. (2.71). The system Hamiltonian, expressed in terms of γ^A and γ^B and their conjugate momenta, simplifies to

$$\mathcal{H} = \frac{(p^A)^2}{2m} + \frac{(p^B)^2}{2m} + \frac{\zeta_0}{m} p^A p^B - \frac{\Phi_0}{2\pi}\left(I_0^A \cos\gamma^A + I_b^A \gamma^A\right) - \frac{\Phi_0}{2\pi}\left(I_0^B \cos\gamma^B + I_b^B \gamma^B\right), \tag{2.74}$$

where the effective system mass is defined to be

$$m = m_J \left(1 + \frac{m_C}{m_J + m_C}\right) = \left(\frac{\Phi_0}{2\pi}\right)^2 C_J \left(1 + \zeta_0\right). \tag{2.75}$$

The first three terms in $\mathcal{H}$ represent a kinetic energy contribution, which is the total energy stored by the three capacitors. The mass of the phase particle increases due to the coupling and leads to a downward shift of all of the energy levels. The final two terms give the two-dimensional potential, which resembles an egg crate, in that it is a tilted washboard in each of the junction axes. In the case of the dc SQUID, discussed in §2.4, the coupling of junctions modified the potential, while here the coupling modified the kinetic energy. In particular, C_C has introduced a momentum coupling term.

To represent the states of this two-qubit system, I will use the notation $|A\,B\rangle$ to indicate a direct product of the uncoupled states of junctions A and B. The ground state of the uncoupled system is $|0\,0\rangle$. If the two junctions have the same plasma frequency ω_p, then $|0\,0\rangle$ has energy $\hbar\omega_p$ in the harmonic limit. With no coupling, both $|0\,1\rangle$ and $|1\,0\rangle$ would have energy $2\hbar\omega_p$. The coupling capacitor lifts this degeneracy, leaving the maximally entangled Bell states $\left(|0\,1\rangle \pm |1\,0\rangle\right)/\sqrt{2}$ as the first two excited states, with energies $\left(2 \pm \zeta_0/2\right)\hbar\omega_p$. The momentum coupling term in the Hamiltonian gives the symmetric state (+) the higher of the two energies.

Having discussed the simpler circuit, I will now summarize the results when the coupling inductors in Fig. 2.18 are included [78]. The LC resonator that is created contributes an additional degree of freedom, $\gamma_C = 2\pi L_C I_C/\Phi_0$, which corresponds to the current I_C that flows through the total coupling inductance $L_C = L_C^A + L_C^B$. The renormalized angular frequency of the harmonic LC mode that is created is

$$\omega_C = \left[L_C\left(\frac{C_C C_J}{C_J + 2C_C}\right)\right]^{-1/2}. \tag{2.76}$$

If both junctions are brought into resonance with this frequency, then the three

degenerate levels are split by an amount proportional to the coupling coefficient

$$\frac{\xi}{\sqrt{2}} = \sqrt{\frac{C_C}{2C_J + 4C_C}}. \tag{2.77}$$

If instead, both junctions are in resonance with each other at a frequency ω_p well below ω_C, then the coupling is dominated by the capacitor and can be described by the frequency-dependent coefficient

$$\zeta\left(\omega_p\right) \;=\; \frac{\xi^2}{1 - \xi^2 - \omega_p^2/\omega_C^2} \;=\; \frac{\zeta_0}{1 - \left(1 + \zeta_0\right)\omega_p^2/\omega_C^2}. \tag{2.78}$$

As ω_p/ω_C decreases, the coupling weakens, eventually reducing to the purely capacitive expression given in Eq. (2.72).

Chapter 3

Dynamics of Quantum Systems

In this chapter, I will describe the time evolution of a simple quantum system. The nature of this system is motivated by the solutions of the junction Hamiltonian given in §2.3, but most of the discussion is rather general. In fact, much of the machinery and terminology is borrowed from nuclear magnetic resonance [79] and atomic physics [5].

The system consists of several states $|n\rangle$ of energy E_n, which have a lifetime that depends on energy relaxation (on a time scale T_1) and tunneling (given by the rates Γ_n) which takes the system outside of $|n\rangle$. In addition, phase information is lost on a time scale T_2. We are interested in following the coherent dynamics due to induced transitions and interaction with the environment.

I will start out with an ideal two-level system, for which exact solutions can be found, and then move on to a more realistic three-level system. Once interactions with the environment are included, the density matrix approach must be used. I will give some background on this subject, outline the analytical solutions, and describe how we simulate experiments numerically.

3.1 Bloch Sphere

Often in this chapter, I will limit the discussion to a single isolated two-level system with states $|0\rangle$ and $|1\rangle$. This is exactly what we want for a qubit, although our real system has higher levels that cannot be ignored. A generic wavefunction will be a superposition of the two states,

$$|\psi\rangle = a\,|0\rangle + b\,|1\rangle = \cos\frac{\theta}{2}\,|0\rangle + e^{i\phi}\sin\frac{\theta}{2}\,|1\rangle\,. \tag{3.1}$$

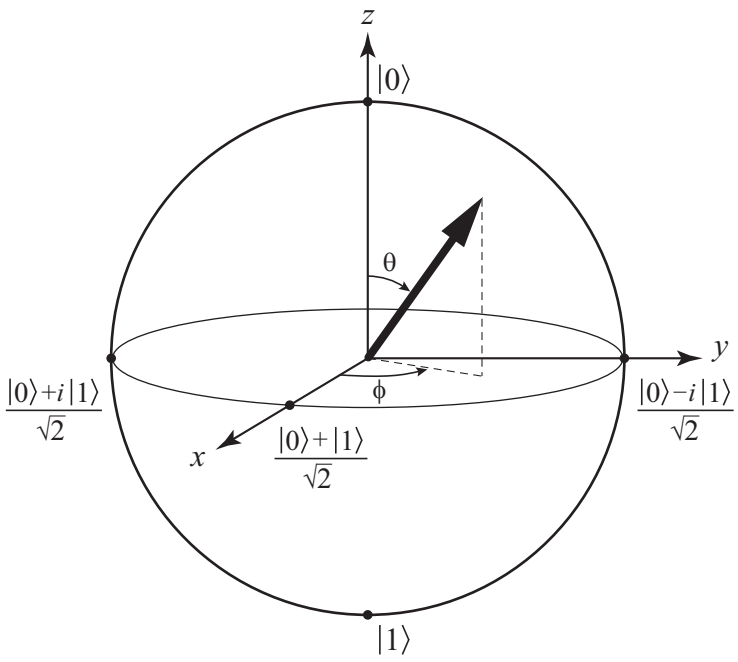

Figure 3.1: Bloch sphere representation of a two-level system. A vector on the unit sphere can be used to represent a normalized superposition of $|0\rangle$ and $|1\rangle$, where the relative phase between the two basis states is complex.

In the middle expression, the complex numbers a and b must satisfy the normalization condition $\sqrt{a^2 + b^2} = 1$. This condition is enforced in the last expression by the real angles $0 < \theta < \pi$ and ϕ. The advantage of this last form is that the state of the system may be graphically represented as a vector on the so-called Bloch sphere, as shown in Fig. 3.1 (see, for example, §1.2 of Ref. [80]). The polar angle gives the relative weight of the two states and the azimuthal gives the relative phase. The state $|0\rangle$ points along the $+z$-axis; $|1\rangle$ is along the $-z$-axis. A 90° rotation in θ of either of these basis states results in an equal superposition of $|0\rangle$ and $|1\rangle$. The location on the equator gives the relative phase: the states $(|0\rangle \pm |1\rangle)/\sqrt{2}$ point along $\pm x$ and $(|0\rangle \pm i\,|1\rangle)/\sqrt{2}$ point along $\pm y$.

Unfortunately, there is no simple graphical analog for a system with more than two states.

3.2 Two-Level Rabi Oscillations

Transitions in a two-level system can be induced by a time-dependent potential. A perturbation with a well-defined frequency will result in a phase coherent manipulation of the system, corresponding to rotating the Bloch vector along a single trajectory [5, 81]. Let the system evolve under the Hamiltonian $\mathcal{H} = \mathcal{H}^0 + \mathcal{H}^i$. $\mathcal{H}^0$ is purely diagonal and accounts for the energies E_0 and E_1 of the orthonormal ground and excited states $|0\rangle$ and $|1\rangle$, with

$$\mathcal{H}^0 |0\rangle = E_0 |0\rangle \qquad \text{and} \qquad \mathcal{H}^0 |1\rangle = E_1 |1\rangle . \tag{3.2}$$

Transitions are due to a potential $\mathcal{H}^i = A\hat{y}\cos(\omega_{rf}t)$, which oscillates at angular frequency ω_{rf}. I will assume that the operator $\hat{y}$ is purely off-diagonal and Hermitian, where the matrix elements of $A\hat{y}$ are

$$\langle 0 \,|\, A\hat{y} \,|\, 1\rangle = \langle 1 \,|\, A\hat{y} \,|\, 0\rangle^* \equiv A_{01}. \tag{3.3}$$

The state of the system at any time is given by

$$|\psi\rangle = a_0(t)\, e^{-iE_0t/\hbar} |0\rangle + a_1(t)\, e^{-iE_1t/\hbar} |1\rangle . \tag{3.4}$$

The time dependence of the weighting coefficients a_0 and a_1 can be found by taking the inner product of $\langle 0|$ and $\langle 1|$ with Schrödinger's equation $|\mathcal{H}\rangle\,|\psi\rangle = i\hbar|\dot{\psi}\rangle$. Some simplification yields

$$\frac{da_0}{dt} = -i\frac{A_{01}}{2\hbar}\left[e^{+i\left(\omega_{rf}-\omega_{01}\right)t} + e^{-i\left(\omega_{rf}+\omega_{01}\right)t}\right] a_1 \tag{3.5}$$

$$\frac{da_1}{dt} = -i\frac{A_{01}^*}{2\hbar}\left[e^{-i\left(\omega_{rf}-\omega_{01}\right)t} + e^{+i\left(\omega_{rf}+\omega_{01}\right)t}\right] a_0, \tag{3.6}$$

where $\hbar\omega_{01} = E_1 - E_0$ is the energy difference between the two states. If the system is driven near resonance, then the first term in brackets for each equation will vary slowly while the second will oscillate rapidly. In what is commonly called the rotating wave approximation, the slow (first) terms are kept and the rapid (second) terms are set to zero [82]. Notice that in Eq. (3.5), the $e^{+i\omega_{rf}t}$ contribution from $\cos(\omega_{rf}t)$ is kept, while $e^{-i\omega_{rf}t}$ is kept in Eq. (3.6).

Taking an additional time derivative and plugging in $\dot{a}_0$ and $\dot{a}_1$ uncouples the two amplitudes, resulting in

$$\frac{d^2a_0}{dt^2} - i\left(\omega_{rf} - \omega_{01}\right)\frac{da_0}{dt} + \frac{|A_{01}|^2}{4\hbar^2}a_0 = 0 \tag{3.7}$$

$$\frac{d^2a_1}{dt^2} + i\left(\omega_{rf} - \omega_{01}\right)\frac{da_1}{dt} + \frac{|A_{01}|^2}{4\hbar^2}a_1 = 0. \tag{3.8}$$

On resonance ($\omega_{rf} = \omega_{01}$), the equations yield $\ddot{a}_0 + (\Omega_{01}^2/4)\,a_0 = \ddot{a}_1 + (\Omega_{01}^2/4)\,a_1 = 0$, where $\Omega_{01} \equiv |A_{01}|/\hbar$ is known as the bare Rabi flopping frequency (between states $|0\rangle$ and $|1\rangle$). Assuming that the system starts out in the ground state at $t = 0$, the solution is $a_1(t) = \sin(\Omega_{01}t/2)$. Thus the occupation probability of the excited state is

$$|a_1(t)|^2 = \sin^2\left(\frac{\Omega_{01}\,t}{2}\right). \tag{3.9}$$

If the perturbation is left on for a time $t = \pi/\Omega_{01}$, then the system will make a transition from the ground state to the first excited state with 100% probability. This is referred to as a π-pulse and can be thought of as a NOT gate for quantum computation. If $\hat{A}$ is left on longer, the system will fully return to the ground state at $t = 2\pi/\Omega_{01}$, repeating the cycle indefinitely in a phenomenon known as a Rabi oscillation.

With an incoherent drive (which does not correspond to a specific path on the Bloch sphere), the analogs of the stimulated emission and absorption rates would

balance each other, resulting in an equal superposition $|a_1|^2 = 1/2$ for all time (if spontaneous emission can be neglected).

With an off-resonant drive, Eqs. (3.7) and (3.8) yield amplitudes

$$a_0(t) = e^{i(\omega_{rf}-\omega_{01})t/2}\left[-\frac{i\,(\omega_{rf}-\omega_{01})}{\overline{\Omega}_{01}}\,\sin\left(\frac{\overline{\Omega}_{01}t}{2}\right)+\cos\left(\frac{\overline{\Omega}_{01}t}{2}\right)\right] \quad (3.10)$$

$$a_1(t) = -i\,e^{-i(\omega_{rf}-\omega_{01})t/2}\,\frac{\Omega_{01}}{\overline{\Omega}_{01}}\,\sin\left(\frac{\overline{\Omega}_{01}t}{2}\right), \quad (3.11)$$

where the effective Rabi frequency is

$$\overline{\Omega}_{01} = \sqrt{\Omega_{01}^2 + (\omega_{rf}-\omega_{01})^2}. \quad (3.12)$$

The occupation probability of the excited state becomes [5]

$$|a_1(t)|^2 = \left(\frac{\Omega_{01}}{\overline{\Omega}_{01}}\right)^2 \sin^2\left(\frac{\overline{\Omega}_{01}\,t}{2}\right). \quad (3.13)$$

Thus with detuning, the oscillation frequency increases (as a function of $|\omega_{rf}-\omega_{01}|$) and the amplitude of the oscillation decreases.

3.3 Three-Level Rabi Oscillations

As I will discuss in Chapter 9, under a strong microwave drive, we have seen clear evidence in our qubits for significant population in the second excited state $|2\rangle$. A strong drive has two effects. For one, additional transitions become relevant to the system dynamics. These are the single photon $1 \rightarrow 2$ and two-photon $0 \rightarrow 2$ transitions. In addition, the third level perturbs the $0 \rightarrow 1$ transition. This is particularly important at high power, where Ω_{01} is close to $\omega_{01} - \omega_{12}$. This regime is of interest for quantum computation, because fast gates require high power. Thus understanding the dynamics of three-level systems is important. The rotating wave

approximation is also useful in describing this system; see Ref. [83] and references therein.

Following the derivation outlined in Appendix C, the Hamiltonian of a three-level system under a time-dependent perturbation $A\hat{y}\cos\omega_{rf}t$ in the rotating wave approximation can be written in matrix form as

$$\mathcal{H} = \hbar \begin{pmatrix} 0 & \Omega_{01}/2 & \Omega_{02}/2 \\ \Omega_{01}/2 & \omega_{01}-\omega_{rf} & \Omega_{12}/2 \\ \Omega_{02}/2 & \Omega_{12}/2 & \omega_{02}-2\omega_{rf} \end{pmatrix}, \tag{3.14}$$

where

$$\Omega_{01} = \frac{Ay_{0,1}}{\hbar}\left[J_0\left(\frac{A\left(y_{0,0}-y_{1,1}\right)}{\hbar\omega_{rf}}\right) + J_2\left(\frac{A\left(y_{0,0}-y_{1,1}\right)}{\hbar\omega_{rf}}\right)\right], \tag{3.15}$$

$$\Omega_{02} = \frac{Ay_{0,2}}{\hbar}\left[J_1\left(\frac{A\left(y_{0,0}-y_{2,2}\right)}{\hbar\omega_{rf}}\right) + J_3\left(\frac{A\left(y_{0,0}-y_{2,2}\right)}{\hbar\omega_{rf}}\right)\right], \tag{3.16}$$

$$\Omega_{12} = \frac{Ay_{1,2}}{\hbar}\left[J_0\left(\frac{A\left(y_{1,1}-y_{2,2}\right)}{\hbar\omega_{rf}}\right) + J_2\left(\frac{A\left(y_{1,1}-y_{2,2}\right)}{\hbar\omega_{rf}}\right)\right]. \tag{3.17}$$

Here, the energy level spacing between states $|n\rangle$ and $|m\rangle$ is $\hbar\omega_{nm}$, J_n is the nth order Bessel function of the first kind, and $y_{n,m} = \langle n\,|\,\hat{y}\,|\,m\rangle$. Despite the notation I have used, in Eq. (3.15) through Eq. (3.17), the terms outside of the square brackets are the bare Rabi frequencies; the Bessel function terms make a frequency-dependent correction.

For the specific case of the current-biased junction, the unperturbed Hamiltonian is given by Eq. (2.23). Assuming that the total bias current is the sum of a dc current I_b and a high frequency current $-I_{\mu w}\cos\omega_{rf}t$, the amplitude of the perturbation is given by

$$A\hat{y} \;=\; \frac{\Phi_0}{2\pi}I_{\mu w}\hat{\gamma} \;\approx\; \frac{I_{\mu w}}{I_0}E_J\sqrt{\frac{8E_C}{\hbar\omega_p}}\;\hat{x}, \tag{3.18}$$

where several matrix elements of $\hat{x}$ in the cubic approximation are given in Eqs. (2.38) and (2.39). Equation (3.16) shows that a direct two-photon transition between $|0\rangle$ and $|2\rangle$, whose strength is given by Ω_{02}, is only possible if the diagonal matrix elements (which I set to zero in the previous section) are finite. In this case, the system need not have a state $|1\rangle$. While all the matrix elements are non-zero for the current-biased junction, $|2\rangle$ can also become populated with off-resonant $0 \rightarrow 1$ and $1 \rightarrow 2$ transitions. It turns out that this mechanism outweighs the direct two-photon process for the power regime we performed experiments in. As the two mechanisms occur at the same frequency $\omega_{rf} \approx (\omega_{01} + \omega_{12})/2$, I will refer to both as two-photon transitions.

In §3.2, the perturbation caused transitions between fixed energy levels. Here, in the case of the current-biased junction, the perturbation adds to the current bias. Thus, the junction's energy levels, which depend on the total bias, will oscillate with time. This effect is accounted for by the non-zero diagonal matrix elements of $\hat{\gamma}$. For the persistent current qubit, the variation of the energy levels due to a strong microwave drive leads to dramatic effects [84].

As usual, the eigenvalues e_i of the Hamiltonian determine the evolution of the system. For example, in Fig. 3.2(a), the three eigenvalues are plotted for a current-biased junction with $I_0 = 30$ μA and $C_J = 5$ pF, at $I_b = 29.8$ μA as a function of frequency ω_{rf}. I have done this for a microwave current of amplitude 5 nA (solid lines) and 15 nA (dashed lines). It appears that there are three avoided level crossing at $\omega_{rf}/2\pi = 6.65$, 6.08, and 5.51 GHz. These are the values of $\omega_{01}/2\pi$, $\omega_{02}/4\pi$, and $\omega_{12}/2\pi$ at $I_b = 29.8$ μA. If a system is in a superposition of eigenstates near an avoided crossing, it will undergo oscillations between the states with a frequency proportional to the magnitude of the splitting. Thus, in this picture, driven Rabi oscillations appear as Larmor oscillations of non-stationary states.

Consider the simple example of a two-level system. The upper left 2×2 block

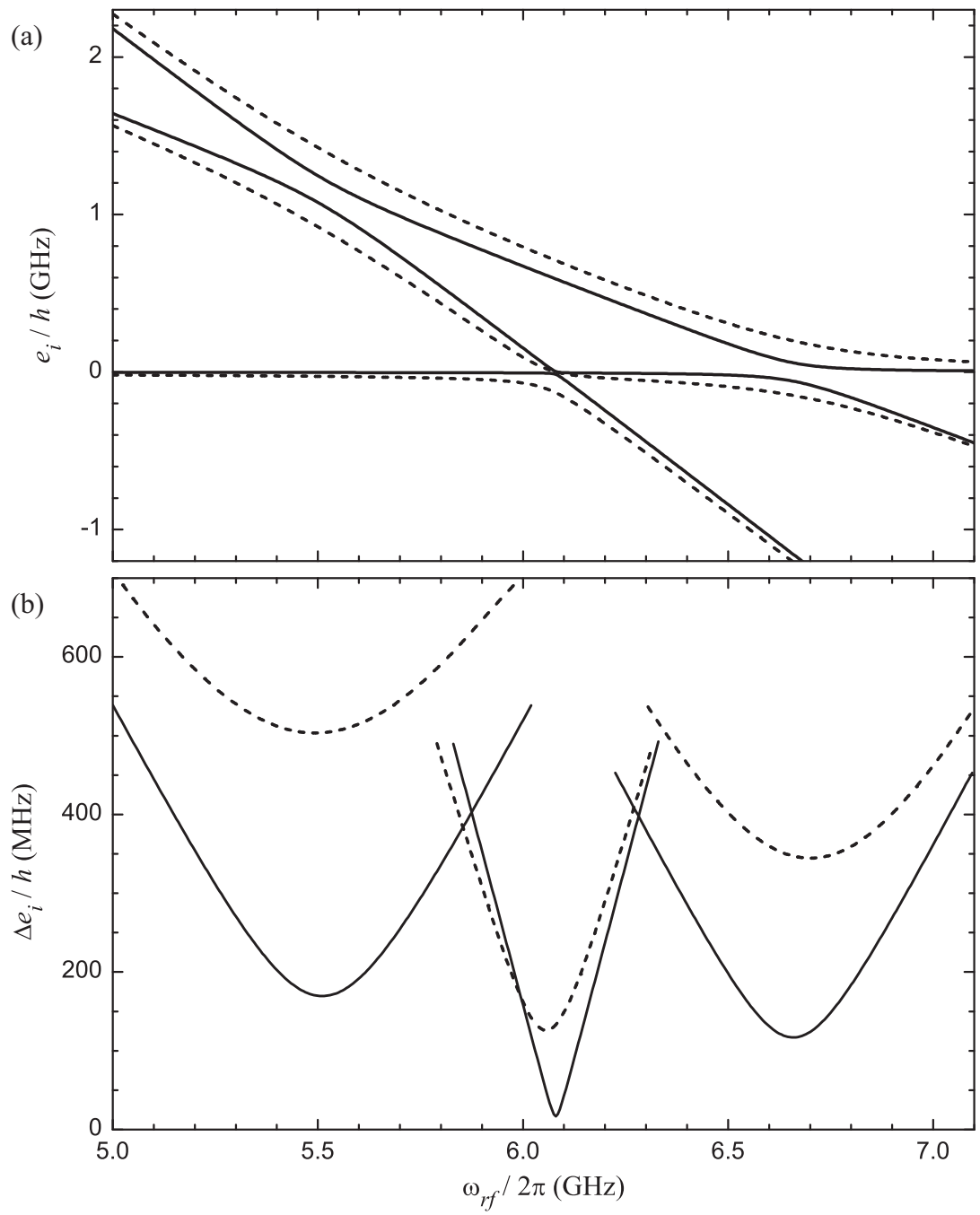

Figure 3.2: Three-level rotating wave approximation. Properties of a current-biased junction with $I_0 = 30$ μA and $C_J = 5$ pF at $I_b = 29.8$ μA are plotted for an applied microwave current of frequency ω_{rf} and magnitude $I_{\mu w} = 5$ nA (solid) and 15 nA (dashed). (a) The eigenvalues e_i of the rotating wave Hamiltonian show avoided crossing at microwave frequencies equal to $\omega_{01}/2\pi = 6.65$ GHz, $\omega_{02}/4\pi = 6.08$ GHz, and $\omega_{12}/2\pi = 5.51$ GHz. (b) The difference of eigenvalues gives the effective Rabi frequency for the three transitions and show that the oscillation frequency increases with detuning.

of Eq. (3.14) gives the Hamiltonian in this case, which has eigenvalues

$$\frac{e_{1,2}}{\hbar} = \frac{\omega_{01} - \omega_{rf} \pm \sqrt{\Omega_{01}^2 + (\omega_{01} - \omega_{rf})^2}}{2}. \tag{3.19}$$

The oscillation frequency between the two states is $\overline{\Omega}_{01} = (e_1 - e_2)/\hbar$, which is equal to $\sqrt{\Omega_{01}^2 + (\omega_{01} - \omega_{rf})^2}$. This is just the expression for the effective Rabi frequency in Eq. (3.12).

For the three-level example, the difference of the eigenvalues is plotted in Fig. 3.2(b). There are three minima (for each value of $I_{\mu w}$), corresponding to on-resonance single photon $0 \rightarrow 1$, two-photon $0 \rightarrow 2$, and single photon $1 \rightarrow 2$ Rabi oscillations, from right to left. The oscillation frequency increases away from resonance, with a stronger detuning dependence for the two-photon process.

Comparing the solid and dashed lines, the oscillation frequency of all of the transition frequencies increases with microwave power, as expected. However a smaller effect appears at high power: the location of the minimum frequency undergoes a shift. For $I_{\mu w} = 15$ nA, the slowest $0 \rightarrow 1$ oscillation occurs at $\omega_{rf}/2\pi = 6.70$ GHz, which is 50 MHz greater than $\omega_{01}/2\pi$. This is due to the presence of the third level and is analogous to the ac Stark shift in atomic physics. The other two transitions in Fig. 3.2(b) move to lower values of ω_{rf} at high power.

I will refer to the minimum oscillation frequency between states $|n\rangle$ and $|m\rangle$ as $\Omega_{R,nm}$. The distinction must be made because, for example, at high power in a multi-level system, $\Omega_{R,01}$ will differ from Ω_{01} (which depends on the matrix elements of the operator connecting the states). And seen above, this new resonance condition need not occur at $\omega_{rf} = \omega_{nm}$. Off resonance, the effective Rabi frequency will be denoted as $\overline{\Omega}_{R,nm}$. In the simple two-level example given in §3.2, $\Omega_{R,01} = \Omega_{01}$ and $\overline{\Omega}_{R,01} = \overline{\Omega}_{01}$ at all drive powers.

In §9.2, I will compare experimental data to the numerical solution of Eq.

(3.14), where the matrix elements are given by Eqs. (2.38) and (2.39) and the energy levels come from Eq. (2.44). However, analytical solutions of the Hamiltonian can be obtained by finding the roots of its cubic characteristic equation. From the point of view of treating the presence of $|2\rangle$ perturbatively, the strength of the coupling of $|2\rangle$ depends on $\omega_{01}-\omega_{12}$. When this quantity is small compared to Ω_{01}, the following approximations hold [83]. In addition, the energy levels and matrix elements have been evaluated in the cubic approximation of the tilted washboard potential.

For fixed ω_{rf}, the minimum Rabi frequency does not occur at $\omega_{01} = \omega_{rf}$, but at $\omega_{01} = \omega_{rf} - \Delta\omega_{R,01}$, where

$$\Delta\omega_{R,01} \approx \frac{\Omega_{01}^2}{2\left(\omega_{01} - \omega_{12}\right)}. \tag{3.20}$$

Conversely, for fixed ω_{01}, the resonance moves to $\omega_{rf} > \omega_{01}$, as seen in Fig. 3.2(b). The minimum oscillation frequency on resonance is

$$\Omega_{R,01} \approx \Omega_{01}\left(1 - \frac{\Omega_{01}^2}{4\left(\omega_{01} - \omega_{12}\right)^2}\right). \tag{3.21}$$

Thus, the third level suppresses the frequency.

Finally, the two-photon $0 \rightarrow 2$ transition has a minimum oscillation frequency

$$\Omega_{R,02} \approx \frac{\sqrt{2}\Omega_{01}^2}{\omega_{01} - \omega_{12}}. \tag{3.22}$$

While the Rabi frequency for a single photon process increases as the square root of the microwave power, it increases linearly for a two-photon process. The oscillation frequency increases with detuning as

$$\overline{\Omega}_{R,02} = \sqrt{\Omega_{R,02}^2 + \left(\omega_{02} - 2\omega_{rf}\right)^2}, \tag{3.23}$$

which is a general result that holds for two-photon processes.

3.4 Dissipation

Inter-level transitions can occur even when we do not apply a microwave signal to a junction. This is because the junction is able to exchange energy with the heat bath that it is in thermal equilibrium with (see §3.2.1 of Ref. [1] and §2.5 of [3]). In the RCSJ model introduced in §2.2, the strength of the coupling between the junction and its environment is characterized by an effective resistance R_J. The situation is analogous to spontaneous and stimulated emission in atomic systems [5,81], with the broadband Johnson-Nyquist current noise of R_J replacing the energy density of Planck blackbody radiation as the source of the transitions.

For large R_J, the thermal noise current I_t can be treated as a perturbation of the junction Hamiltonian of Eq. (2.23), characterized by the term $\mathcal{H}_t = -(\Phi_0/2\pi)\, I_t\, \hat{\gamma}$. The stimulated emission and absorption rate between $|i\rangle$ and $|j\rangle$ (proportional to the Einstein B coefficient of atomic physics) can be found with several techniques (see, for example, Appendix B of Ref. [1][1]) as

$$W_{ij}^{st} = W_{ji}^{st} = \frac{\hbar\omega_{ij}}{2R_J e^2}\, \frac{|\langle i\,|\,\hat{\gamma}\,|\,j\rangle|^2}{\exp\left(\hbar\omega_{ij}/k_B T\right) - 1}\,, \tag{3.24}$$

where ω_{ij} is the angular frequency spacing between the two levels.

In addition to these equivalent rates that are strongly temperature dependent, there is a spontaneous emission rate that persists to $T = 0$ (analogous to the Einstein A coefficient). From the principle of detailed balance, the total emission must exceed the absorption so as to result in a Boltzmann distribution between any two levels (in the absence of additional transition mechanisms). From this, one finds that the

[1] In Ref. [1], W^t is used to represent the stimulated rate. I have chosen to reserve that symbol for the total thermal rates given in Eqs. (3.26) and (3.27).

spontaneous emission rate is

$$\Gamma_{ij} = \frac{\hbar\omega_{ij}}{2R_J e^2} \left|\langle i \left| \hat{\gamma} \right| j \rangle\right|^2 \approx \frac{2}{R_J C_J} \frac{\omega_{ij}}{\omega_p} \left|\langle i \left| \hat{x} \right| j \rangle\right|^2, \tag{3.25}$$

where several matrix elements of $\hat{x}$ in the cubic approximation are given in Eqs. (2.38) and (2.39). The total thermal emission and absorption rates are

$$W_{ij}^t = W_{ij}^{st} + \Gamma_{ij} = \frac{\Gamma_{ij}}{1 - \exp\left(-\hbar\omega_{ij}/k_B T\right)} \tag{3.26}$$

and

$$W_{ji}^t = W_{ij}^t \exp\left(-\hbar\omega_{ij}/k_B T\right) = W_{ji}^{st} = \frac{\Gamma_{ij}}{\exp\left(\hbar\omega_{ij}/k_B T\right) - 1}, \tag{3.27}$$

where $j > i$. While there will be transitions between each pair of states, the spontaneous emission rate between the ground and first excited states serves as a standard characterization of the system. Its inverse

$$T_1 \equiv \frac{1}{\Gamma_{10}} \tag{3.28}$$

is known as the relaxation or dissipation time.

For our junction devices, an estimate for the dissipation can be obtained in the harmonic approximation of the 1-D tilted washboard potential. From Eq. (2.36), $\Gamma_{n,n-1} = n/R_J C_J$ and $T_1 = R_J C_J$, as one would expect classically.

3.5 Tunneling

A current-biased junction will eventually tunnel from a metastable supercurrent state to the finite voltage state, where the occupation probability ρ_i of an energy level $|i\rangle$ decays with a tunneling rate Γ_i. While it is difficult to determine which level the junction was in when it tunneled, it is straight forward to measure the

total escape rate out of all of the metastable states

$$\Gamma = -\frac{1}{\rho_{tot}} \frac{d\rho_{tot}}{dt}, \tag{3.29}$$

where $\rho_{tot} = \sum_i \rho_i$ and the ρ_i do not include the finite voltage state that results after tunneling. If we think of ρ_i as being defined for an ensemble of junctions, then Γ should only depend on those elements of the ensemble that have yet to escape. Therefore, the total escape rate is the weighted sum

$$\Gamma = \sum_i \frac{\rho_i}{\rho_{tot}} \Gamma_i = \sum_i P_i \Gamma_i, \tag{3.30}$$

where

$$P_i = \frac{\rho_i}{\rho_{tot}} \tag{3.31}$$

is the normalized probability of being in state $|i\rangle$. While the total population ρ_{tot} will decay to zero with time due to tunneling, $\sum_i P_i(t) = 1$ for all times.

3.6 The Density Matrix

If we are describing an isolated system interacting with a single mode of radiation, then Schrödinger's equation is sufficient to model the dynamics. However, the state space of our junction qubits is much larger; in practice, the junction interacts strongly with its environment. For example, the energy dissipation described in §3.4 involves losing energy to a huge number of quantum states that constitute a thermal bath at the temperature of the dilution refrigerator mixing chamber. Interaction with these states and those associated with all the bias circuitry leads to dissipation and decoherence. In addition, we depend on tunneling discussed in §3.5 for state readout. The final voltage state lies outside our simple qubit space and may be difficult to describe quantum mechanically [85]. If we are unable to

obtain the Hamiltonian that describes this complicated system, then we must abandon Schrödinger's equation and the hope of describing the system with a single wavefunction.

Although we may not understand every process at a microscopic level, we do know how to describe them in a phenomenological way. For example, dissipation is governed by T_1 and tunneling is characterized by the rates Γ_n. These time constants describe the dynamics for an ensemble of systems, rather the evolution of a single particle. This is particularly applicable to the type of data presented later in this thesis, where we repeat a particular experiment many times to extract statistical information. The standard approach to analyzing this situation is to use the density matrix formalism, which allows us to focus on the quantum evolution of only the subset of the universe that we are interested in, while taking into account interactions with external degrees of freedom.

I will begin by listing a few basic properties of the density matrix [5, 86–88]. The density matrix (or more accurately, density operator) is defined as

$$\rho = \sum_i w_i \left|i\right\rangle \left\langle i\right| , \tag{3.32}$$

where w_i gives the probability of an element of the ensemble to be prepared in the state $|i\rangle$; w_i is non-negative and $\sum w_i = 1$.

In general, this description of the system is quite different than the wavefunction $\psi = \sqrt{w_0}\left|0\right\rangle + \sqrt{w_1}\left|1\right\rangle + ...$, which can only be written down if the phase relationship between the basis vectors is well-defined.

The density operator ρ is Hermitian and can be diagonalized with real eigenvalues. If every element of an ensemble is prepared identically, then w_i is equal to 1 for one value of i and zero for the rest. Then $\rho^2 = \rho$ and $\mathrm{Tr}\left(\rho^2\right) = 1$, which is the definition of a pure state. Here, $\mathrm{Tr}\left(\mathcal{O}\right) = \sum \left\langle i \right| \mathcal{O} \left| i \right\rangle$ is the trace of an operator $\mathcal{O}$.

If more than one of the w_i is non-zero (when ρ is diagonalized), then $\mathrm{Tr}\left(\rho^2\right) < 1$ and the system is said to be in a mixed state or mixed ensemble. The expectation value of an operator $\mathcal{O}$ is given by

$$\langle \mathcal{O} \rangle = \mathrm{Tr}\left(\rho \mathcal{O}\right). \tag{3.33}$$

In order to follow the evolution of an ensemble, the time dependence of the density matrix is needed. The weights in Eq. (3.32) will be constant, so only the state vectors $|i\rangle$ will vary. The time derivative of ρ is

$$\begin{aligned} \frac{\partial \rho}{\partial t} &= \sum_i w_i \left[\left(\frac{\partial}{\partial t} |i\rangle \right) \langle i| + |i\rangle \left(\frac{\partial}{\partial t} \langle i| \right) \right] & (3.34) \\ &= -\frac{i}{\hbar} \left[\mathcal{H}, \rho \right]. & (3.35) \end{aligned}$$

Here, Schrödinger's equation and its adjoint were substituted to simplify the first line. This is known as the Liouville-von Neumann equation, as von Neumann used it to describe quantum evolution, although it resembles Liouville's theorem for classical phase space density.[2]

3.6.1 The Reduced Density Matrix

I will now return to the case of describing our qubit along with the rest of the universe. Let $|i\rangle$ and $|j\rangle$ be orthonormal sets that span the space of the qubit and the rest of the universe, respectively. Assuming that the universe is in a pure state, the wavefunction and density matrix describing it are [5, 86]

$$|\Psi\rangle = \sum_{i,j} c_{ij} |i\rangle |j\rangle. \tag{3.36}$$

[2]This looks like the Heisenberg equation (that gives the evolution of an operator), but differs by more than just a sign; we have been working in the Schrödinger picture, where it is the state vectors that carry the time dependence.

and

$$\rho = |\Psi\rangle \langle\Psi| = \sum_{i,j} \sum_{i',j'} c_{ij} c^*_{i'j'} |i\rangle |j\rangle \langle j'| \langle i'| . \tag{3.37}$$

Imagine we want the expectation value of an operator $\mathcal{O}_i$ that only acts on the qubit (system i). Equation (3.33) gives

$$\langle \mathcal{O}_i \rangle = \mathrm{Tr}\left(\rho \mathcal{O}_i\right) = \sum_i \langle i| \left(\sum_j \langle j \,|\, \rho \,|\, j \rangle \right) \mathcal{O}_i |i\rangle . \tag{3.38}$$

The term in parentheses is the partial trace of ρ over system j and is known as the reduced density matrix for system i,

$$\sigma_i \equiv \mathrm{Tr}_j\left(\rho\right) = \sum_{i,i',j} c_{ij} c^*_{i'j} |i\rangle \langle i'| . \tag{3.39}$$

With σ_i in hand, the expectation value

$$\langle \mathcal{O}_i \rangle = \mathrm{Tr}_i\left(\sigma_i \mathcal{O}_i\right) \tag{3.40}$$

can be found with no direct reference to system j.

If the c_{ij} in Eq. (3.36) represents a product wavefunction between the two systems, then σ_i will still represent a pure state. However, if the two systems are entangled (certainly the case for our experiments), then even a pure ρ will result in a mixed σ_i. In fact, interactions with the environment (that we cannot accurately describe microscopically) will be included as terms in the Hamiltonian that quite clearly create mixed states. This leads to non-unitary evolution, for example, as the junction tunnels to the finite voltage state, which is outside the desired state space. From now on, when I refer to the density matrix ρ of a junction device, I really mean the reduced density matrix σ_i, having traced over the rest of the universe.

3.7 Optical Bloch Equations

In this section, I will revisit the two-level system of §3.2, where Schrödinger's equation gave the time dependence of a particular wavefunction. Now the Liouville-von Neumann equation gives the evolution of an ensemble of systems described by a density matrix [1, 3–5, 88]. This will reproduce the prior results, but also allows the inclusion of the non-unitary transformations that motivated the density matrix approach. Although the two-level model is too simple to describe our devices accurately (particulary for high power microwave drives), it does qualitatively reproduce many of the phenomena that we are interested in. Expressing Eq. (3.35) in a matrix representation in the basis of the eigenstates of $\mathcal{H}^0$ [defined by Eq. (3.2)] yields

$$\begin{pmatrix} \dot{\rho}_{00} & \dot{\rho}_{01} \\ \dot{\rho}_{10} & \dot{\rho}_{11} \end{pmatrix} = -\frac{i}{\hbar}\left[\begin{pmatrix} E_0 & 0 \\ 0 & E_1 \end{pmatrix} + \begin{pmatrix} 0 & \hbar\Omega_{01} \\ \hbar\Omega_{01} & 0 \end{pmatrix}\cos\left(\omega_{rf}t\right), \begin{pmatrix} \rho_{00} & \rho_{01} \\ \rho_{10} & \rho_{11} \end{pmatrix}\right], \tag{3.41}$$

where I have assumed Ω_{01} is real. The diagonal elements of the density matrix, ρ_{00} and ρ_{11}, represent the populations of the ground and excited states, while the so-called off-diagonal coherence terms, ρ_{01} and ρ_{10}, describe correlations between them. In §3.5, I referred to the diagonal element ρ_{ii} as ρ_i.

The matrix equation can be split into four equations that describe the evolution of each of these elements:

$$\dot{\rho}_{00} = -i\Omega_{01}\left(\rho_{10} - \rho_{01}\right)\cos\left(\omega_{rf}t\right) + \frac{\rho_{11}}{T_1} \tag{3.42}$$

$$\dot{\rho}_{01} = -i\Omega_{01}\left(\rho_{11} - \rho_{00}\right)\cos\left(\omega_{rf}t\right) + i\omega_{01}\rho_{01} - \frac{\rho_{01}}{T_2} \tag{3.43}$$

$$\dot{\rho}_{10} = +i\Omega_{01}\left(\rho_{11} - \rho_{00}\right)\cos\left(\omega_{rf}t\right) - i\omega_{01}\rho_{10} - \frac{\rho_{10}}{T_2} \tag{3.44}$$

$$\dot{\rho}_{11} = +i\Omega_{01}\left(\rho_{10} - \rho_{01}\right)\cos\left(\omega_{rf}t\right) - \frac{\rho_{11}}{T_1}. \tag{3.45}$$

On the right hand sides, the terms involving the microwave drive frequency ω_{rf}

and energy level splitting ω_{01} reproduce the unitary evolution of the Schrödinger equation (as those terms came from a valid Hamiltonian).

In addition, I have included the energy dissipation (T_1) and coherence (T_2) times in a phenomenological way. T_1 only affects the state occupancy, increasing the probability that the junction will decay to the ground state. Thermal excitations could have also been included, but for now, I will stay in the limit of zero temperature.

For a single qubit in a superposition of $|0\rangle$ and $|1\rangle$, the relative phase between the basis states becomes ill-defined on a time scale T_2, which only affects the off-diagonal terms of the density matrix $\underline{\rho}$. The decoherence rate is often expressed as the sum

$$\frac{1}{T_2} = \frac{1}{2T_1} + \frac{1}{T_\phi}. \tag{3.46}$$

Here, phase information is lost as the system relaxes to the ground state; in the way that T_2 enters the Bloch equations, the factor of 2 is needed to ensure consistency (see §2.6.1 of Ref. [3] and Refs. [5, 88]). T_ϕ is known as the dephasing time and characterizes processes that do not change the energy of the qubit. Simply defined, T_ϕ is the mean time for a system in the pure quantum state $a|0\rangle + b|1\rangle$ (which has a well-defined phase) to evolve through interactions with the environment to the mixture specified by the density matrix $|a|^2 |0\rangle\langle 0| + |b|^2 |1\rangle\langle 1|$ (which has the same occupation probabilities without any phase information) [21]. In addition, decoherence in a real (multi-state) system may involve a change of the amplitudes a and b and leakage into states outside of the qubit space.

Once again, the system will respond at the drive frequency, so it is convenient to move to a frame rotating with this frequency. The density matrix becomes

$$\underline{\rho} = \begin{pmatrix} \widetilde{\rho}_{00} & \widetilde{\rho}_{01} e^{+i\omega_{rf}t} \\ \widetilde{\rho}_{10} e^{-i\omega_{rf}t} & \widetilde{\rho}_{11} \end{pmatrix}, \tag{3.47}$$

which is Hermitian. To proceed, it is also convenient to express Eqs. (3.42) to (3.45) in matrix form, converting the density matrix to a vector. After some simplification, the resulting matrix equation becomes

$$\begin{pmatrix} \dot{\widetilde{\rho}}_{00} \\ \dot{\widetilde{\rho}}_{01} \\ \dot{\widetilde{\rho}}_{10} \\ \dot{\widetilde{\rho}}_{11} \end{pmatrix} = \begin{pmatrix} 0 & i\Omega_t e^{+i\omega_{rf}t} & -i\Omega_t e^{-i\omega_{rf}t} & \frac{1}{T_1} \\ i\Omega_t e^{-i\omega_{rf}t} & -i\delta - \frac{1}{T_2} & 0 & -i\Omega_t e^{-i\omega_{rf}t} \\ -i\Omega_t e^{+i\omega_{rf}t} & 0 & i\delta - \frac{1}{T_2} & i\Omega_t e^{+i\omega_{rf}t} \\ 0 & -i\Omega_t e^{+i\omega_{rf}t} & i\Omega_t e^{-i\omega_{rf}t} & -\frac{1}{T_1} \end{pmatrix} \begin{pmatrix} \widetilde{\rho}_{00} \\ \widetilde{\rho}_{01} \\ \widetilde{\rho}_{10} \\ \widetilde{\rho}_{11} \end{pmatrix}, \tag{3.48}$$

where $\Omega_t \equiv \Omega_{01}\cos(\omega_{rf}t)$ and $\delta \equiv \omega_{rf} - \omega_{01}$ is the detuning of the microwave drive from resonance. In the matrix, all of the time dependence is contained in terms of the form

$$\cos(\omega_{rf}t)\, e^{\pm i\omega_{rf}t} = \left(\frac{e^{+i\omega_{rf}t} + e^{-i\omega_{rf}t}}{2}\right) e^{\pm i\omega_{rf}t} = \frac{1}{2} + \frac{1 + e^{\pm i2\omega_{rf}t}}{2} \approx \frac{1}{2}, \tag{3.49}$$

where the rotating wave approximation is made by neglecting the term with frequency $2\omega_{rf}$, as it will time average to 0.

With these simplifications, the equations of motion become [4, 5, 88]

$$\dot{\widetilde{\rho}}_{00} = +\frac{i\Omega_{01}}{2}(\widetilde{\rho}_{01} - \widetilde{\rho}_{10}) + \frac{\widetilde{\rho}_{11}}{T_1} \tag{3.50}$$

$$\dot{\widetilde{\rho}}_{01} = -\frac{i\Omega_{01}}{2}(\widetilde{\rho}_{11} - \widetilde{\rho}_{00}) - \frac{\widetilde{\rho}_{01}}{T_2} - i\delta\widetilde{\rho}_{01} \tag{3.51}$$

$$\dot{\widetilde{\rho}}_{10} = +\frac{i\Omega_{01}}{2}(\widetilde{\rho}_{11} - \widetilde{\rho}_{00}) - \frac{\widetilde{\rho}_{10}}{T_2} + i\delta\widetilde{\rho}_{10} \tag{3.52}$$

$$\dot{\widetilde{\rho}}_{11} = -\frac{i\Omega_{01}}{2}(\widetilde{\rho}_{01} - \widetilde{\rho}_{10}) - \frac{\widetilde{\rho}_{11}}{T_1}, \tag{3.53}$$

which are known as the optical Bloch equations. Although there are four elements of the density matrix specified here, there can only be three independent equations,

as ρ is Hermitian. The change of variables

$$u = \frac{1}{2}\left(\widetilde{\rho}_{01} + \widetilde{\rho}_{10}\right) \tag{3.54}$$

$$v = \frac{1}{2i}\left(\widetilde{\rho}_{01} - \widetilde{\rho}_{10}\right) \tag{3.55}$$

$$w = \frac{1}{2}\left(\widetilde{\rho}_{11} - \widetilde{\rho}_{00}\right) \tag{3.56}$$

puts Eqs. (3.50) to (3.53) in a simple form. The time derivatives of Eqs. (3.54) to (3.56) give the equations of motion in the new coordinates,

$$\dot{u} = \delta v - \frac{u}{T_2} \tag{3.57}$$

$$\dot{v} = -\delta u - \Omega_{01} w - \frac{v}{T_2} \tag{3.58}$$

$$\dot{w} = \Omega_{01} v - \frac{1}{T_1}\left(w + \frac{1}{2}\right). \tag{3.59}$$

These are equivalent to the classical Bloch equations that govern the motion of a spin 1/2 system in a magnetic field (NMR). In Eq. (3.59), I have assumed that $\widetilde{\rho}_{00} + \widetilde{\rho}_{11} = 1$ for all time. While dissipation and decoherence are non-unitary processes, they are trace (*i.e.* population) preserving, as seen in Eqs. (3.50) to (3.53).

Several interesting phenomena can be found from the Bloch equations; see, for example, §4.4 of Ref. [1] and Ref. [89]. In steady state (all time derivatives of Eqs. (3.50) to (3.53) or Eqs. (3.57) to (3.59) set to zero), the excited state population is

$$\widetilde{\rho}_{11}^{eq} = \frac{\Omega_{01}^2 T_1 T_2/2}{1 + \left(\omega_{rf} - \omega_{01}\right)^2 T_2^2 + \Omega_{01}^2 T_1 T_2}. \tag{3.60}$$

Equation (3.18) shows that the Rabi frequency Ω_{01} is proportional to the microwave current $I_{\mu w}$; thus, Ω_{01} increases as the square root of the applied microwave power. Using Eq. (3.60), $\widetilde{\rho}_{11}^{eq}$ is a Lorentzian resonance centered at ω_{01} for a fixed power.

The full width at half maximum of the peak is

$$\Delta\omega = \frac{2}{T_2}\sqrt{1 + \Omega_{01}^2 T_1 T_2}. \tag{3.61}$$

This shows that the resonance width will increase with Ω_{01}, an effect known as power broadening.

The solid lines in Fig. 3.3(a)-(c) show the excited state population as a function of detuning, calculated with Eq. (3.60), for increasing microwave power. For low powers, the width of the resonance is $2/T_2$, while the height of the peak increases quadratically with Rabi frequency (linearly with power). The dashed curves of Fig. 3.3(a)-(c) show the resonances for a toy model, where these two trends hold at all powers.

The on-resonance excited state population is plotted in Fig. 3.3(d). The solid line is for the two-level system; it saturates at 0.5. The dashed is for the toy model; in this case, the excited state population can be greater than 1 at high power, which is unphysical.

At large detuning, the solid and dashed curves in Fig. 3.3(a)-(c) are nearly identical. However, close to the resonance, the excited state population is limited to 0.5. This restriction pushes the full width out, as indicted by the horizontal arrows. In Fig. 3.3(b), notice that both curves have nearly the same width at the excited state population of 0.125. However, the toy system does not reach half maximum until 0.25, where its width is still $2/T_2$. Thus, power broadening can be viewed as a consequence of two-level saturation [5].

The time-dependent solution of the Bloch equations gives the form of a Rabi oscillation. In the absence of dissipation and decoherence, the expressions for the amplitude and frequency are the same as in Eqs. (3.13) and (3.12). With T_1 and T_2, the oscillations decay in amplitude, eventually reaching steady state. On resonance,

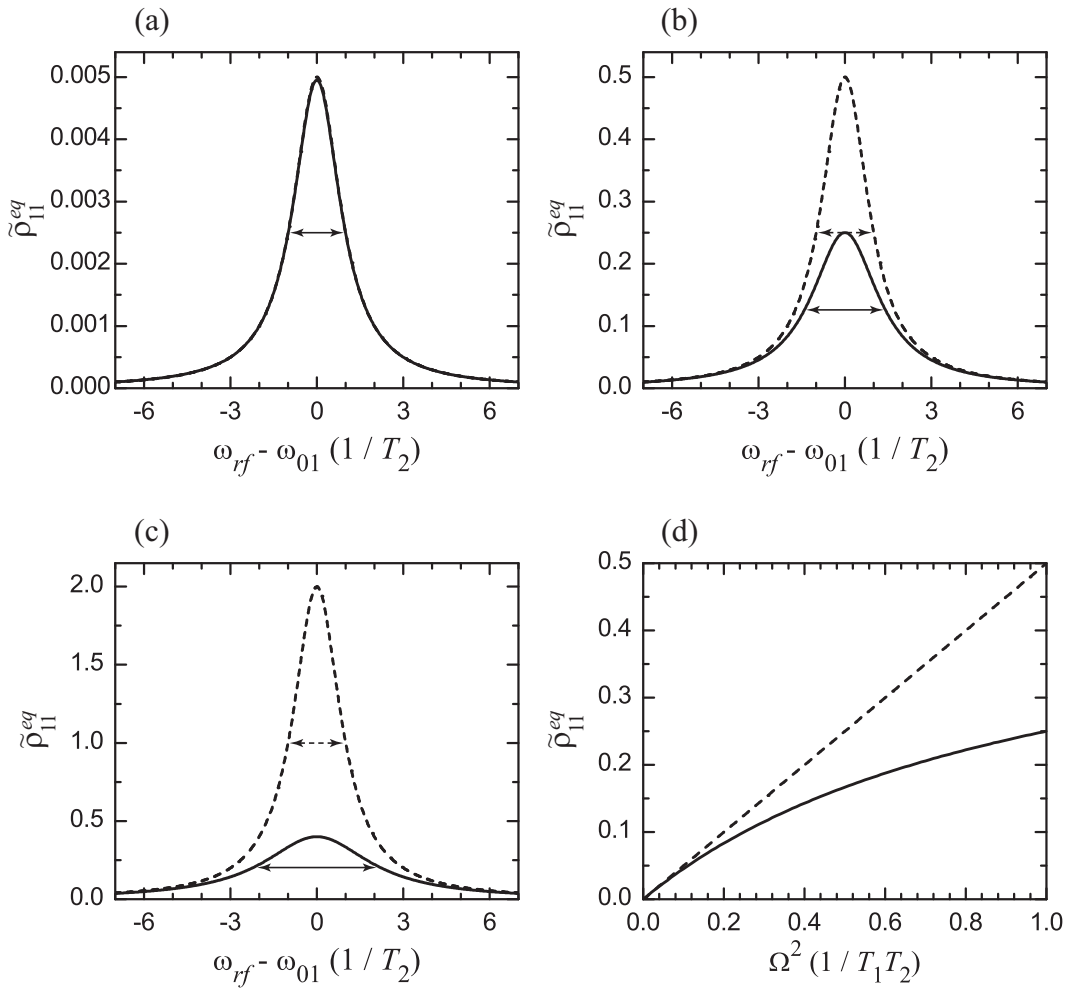

Figure 3.3: Power broadening in a two-level system. The excited state population $\widetilde{\rho}_{11}^{eq}$ is plotted against the angular frequency detuning $\omega_{rf} - \omega_{01}$ (in units of $1/T_2$) for $\Omega_{01}^2 T_1 T_2$ equal to (a) 0.01, (b) 1, and (c) 4. The solid lines are for a two-level system, while the dashed are for a toy system that does not saturate; the horizontal arrows indicate the full width $\Delta\omega$ for each of the resonances. Panel (d) shows the excited state population on resonance for the two-level (solid) and toy (dashed) systems as a function of Ω_{01}^2 (in units of $1/T_1T_2$).

the excited state population is

$$\widetilde{\rho}_{11}(t) = \widetilde{\rho}_{11}^{eq} - \widetilde{\rho}_{11}^{eq}\, e^{-t/T'} \left[\cos\left(\overline{\Omega}_{01} t\right) + \frac{\sin\left(\overline{\Omega}_{01} t\right)}{T'\,\overline{\Omega}_{01}} \right], \tag{3.62}$$

where the equilibrium level $\widetilde{\rho}_{11}^{eq}$ is given by Eq. (3.60) (evaluated at $\omega_{rf} = \omega_{01}$), the time constant of the decay envelope is

$$\frac{1}{T'} = \frac{1}{2T_1} + \frac{1}{2T_2}, \tag{3.63}$$

and the effective on-resonance Rabi frequency with dissipation is

$$\overline{\Omega}_{01} = \sqrt{\Omega_{01}^2 - \left(\frac{1}{2T_1} - \frac{1}{2T_2}\right)^2}. \tag{3.64}$$

Tunneling can also be included in the optical Bloch equations in a simple way. We have chosen to add a term $-\left(\Gamma_i + \Gamma_j\right)/2$ to the right hand sides of $\dot{\rho}_{ij}$ in Eqs. (3.42) to (3.45). For the diagonal element ρ_{ii}, this corresponds to a decay rate of Γ_i, which (at least for Γ_0) we can observe directly in experiments. In addition, tunneling leads to a loss of phase coherence.

The Bloch equations can be solved in a similar way, resulting in a resonance full width of [4]

$$\Delta\omega = \frac{2}{T_2'}\sqrt{1 + \Omega_{01}^2\, T_1'\, T_2'}, \tag{3.65}$$

where the effective relaxation and coherence times are defined by $1/T_1' \equiv 1/T_1 + \Gamma_1$ and $1/T_2' \equiv 1/T_2 + \left(\Gamma_0 + \Gamma_1\right)/2$.

In the limit of low power ($\Omega_{01} \ll \sqrt{T_1' T_2'}$) and dissipation-limited decoherence ($T_2 = 2T_1$), Eq. (3.65) reduces to $\Delta\omega = 1/T_1 + \Gamma_0 + \Gamma_1$. Thus, the full width is the sum of the rates of all of the transitions that depopulate either of the levels. In other words, the resonance width (in terms of angular frequency) is the inverse of

the lifetime, as one might expect. This can be generalized for the resonance between levels $|n\rangle$ and $|m\rangle$, which has a full width

$$\Delta\omega = \sum_j W^t_{jn} + \sum_j W^t_{jm} + \Gamma_n + \Gamma_m + 2\sigma_I \frac{\partial \omega_{nm}}{\partial I_b}, \tag{3.66}$$

where W^t_{nm} are the thermal rates given in §3.4 and Γ_n is the escape rate from $|n\rangle$; see §3.2 and §7.2 of Ref. [3] and Refs. [38,90–92]. The final term in the sum gives the approximate contribution from low frequency current noise with an rms value σ_I. If there is a slow fluctuation in I_b, then the junction will be biased at a different value on each trial, which leads to a smearing of all of the escape rate features (calculated for an ensemble of systems). The assumption in Eq. (3.66) is that the noise enters as a simple sum with the other broadening mechanisms. A more careful treatment that takes the frequency dependence of the current noise into account involves modeling the system with the stochastic Bloch equations [93].

The width of a resonance is often characterized by the spectroscopic coherence time,

$$T_2^* \equiv \frac{2}{\Delta\omega}. \tag{3.67}$$

As T_2^* is bounded below by $2T_1$, it is a simple way to characterize the impact of dephasing, tunneling, and inhomogeneous broadening.

These analytical solutions will be useful when attempting to extract T_1 and T_2 from experimental data.

3.8 Multi-Level Density Matrix

In the regime that we usually operate in, our junction qubits must be described by a model with at least three levels. In this case, analytic solutions of the Liouville-von Neumann equation with dissipation and decoherence can be difficult to obtain.

However, it fairly straight forward to write the equation in the form

$$\frac{d\boldsymbol{\rho}}{dt} = \underline{P}\boldsymbol{\rho}, \tag{3.68}$$

where, for a system with N levels, $\boldsymbol{\rho}$ is a vector of N^2 elements and $\underline{P}$ is an $N^2 \times N^2$ matrix that describes its evolution. $\boldsymbol{\rho}$ can propagated forward a small time Δt as

$$\begin{aligned} \boldsymbol{\rho}(t+\Delta t) &\approx \boldsymbol{\rho}(t) + \frac{d\boldsymbol{\rho}(t)}{dt}\Delta t & (3.69)\\ &\approx (\underline{I} + \underline{P}\Delta t)\,\boldsymbol{\rho} & (3.70)\\ &\approx e^{\underline{P}\Delta t}\boldsymbol{\rho}, & (3.71) \end{aligned}$$

which can be iterated numerically to find $\boldsymbol{\rho}(t)$. Typically, Eq. (3.71) is stable while Eq. (3.70) is not, so an efficient algorithm for matrix exponentiation is required. To perform simulations, I used the MATLAB function `expm`, which uses Padé approximation with scaling and squaring (see Ref. [94], method 3). The structure of $\underline{P}$ for the simulations I performed is given in §D.1.

Incidentally, this integration naturally gives rise to the two-photon transitions described in §3.3. This can be seen by taking the time derivative of Eq. (3.35), which gives

$$\frac{\partial^2\rho}{\partial t^2} = -\frac{i}{\hbar}\left[\frac{\partial\mathcal{H}}{\partial t}, \rho\right] - \frac{1}{\hbar^2}\left[\mathcal{H}, [\mathcal{H}, \rho]\right], \tag{3.72}$$

which contains terms quadratic in $\mathcal{H}$. Of course, the Hamiltonian itself must allow these transitions, but no special provisions need to be made for them to appear in the numerical solution.

Chapter 4

Qubit Design and Fabrication

This chapter contains basic information about the qubits I measured for this thesis. I will begin with an overview of the fabrication process that was used to make the chips, so it will be clear how various structures were made when I discuss specific devices. I studied two types of qubit isolation, one using a simple LC filter and another using an inductive current divider that showed more complex behavior. I will summarize the physics of each technique and give details about how they were actually implemented. I will also give a brief outline of the experimental set-up while each device was studied. A complete review of the equipment used will be presented in the next chapter.

4.1 Hypres Fabrication Process

The three devices that I studied were fabricated by Hypres, Inc., in Elmsford, New York [95]. Their multi-layer process made it easy to design a variety of structures. The process has a Nb/AlOx/Nb trilayer (with a critical current density of either 30 or 100 A/cm^2) and three superconducting wiring layers with two additional metal layers. Our devices were made on oxidized silicon substrates.

Figure 4.1 shows a schematic of a chip cross-section and the circuit it forms. Mask layers M0,[1] M1, M2, and M3 are niobium. They are separated by sputtered SiO_2 insulation layers and can be connected by vias I0, I1B, and I2. The vias have to be larger than a minimum size, but small enough that the wet etch process that forms the opening stops where it was intended to. Mask layer I1A specifies

[1]Structures located on layer M0 actually specify where the ground plane is etched away. I will, however, refer to M0 as the ground plane for convenience.

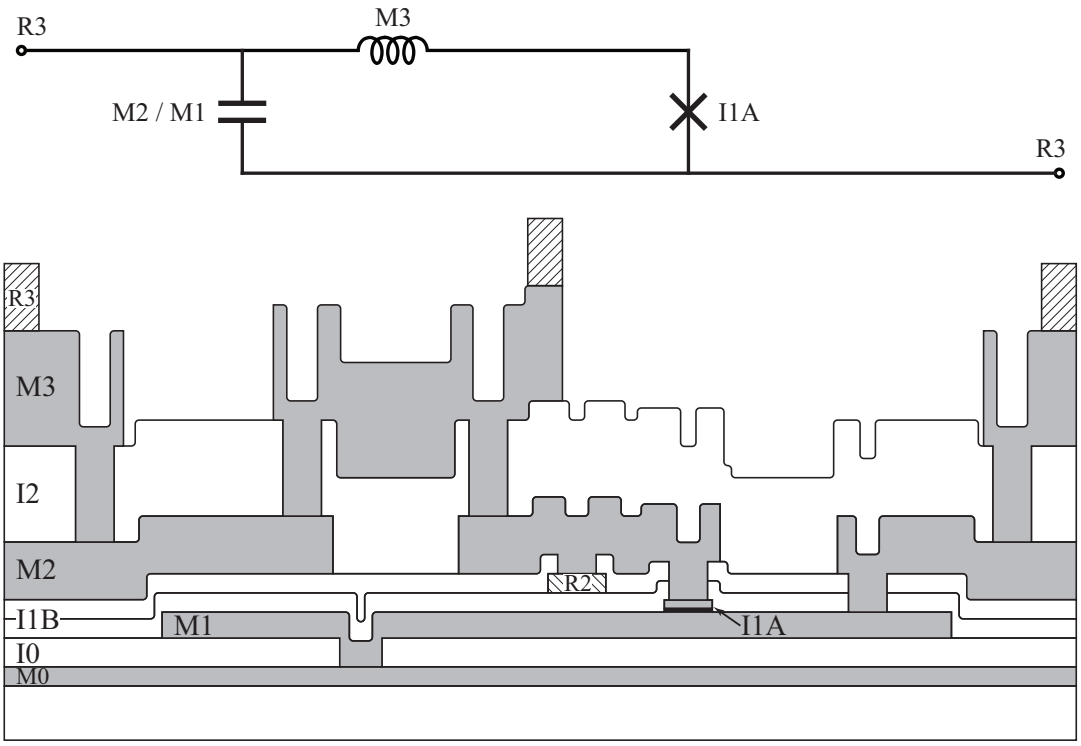

Figure 4.1: Hypres fabrication process. The LC-isolated circuit diagram at the top could be implemented with a chip whose cross-section is shown (although the third dimension is not shown). Gray and hatched areas represent metal; each layer is labeled by its mask name. Open areas are SiO_2 insulation layers labeled by the via that can pass through them. The anodization layer that is currently part of the Hypres process was not used when the devices I have studied were made.

where not to remove the counter electrode of the trilayer, thus leaving a junction behind. R2 is molybdenum (used for resistive shunts in other applications) and R3 is a thick Ti/PdAu layer for contacts. While the thicknesses in the figure are to scale, the widths are highly compressed, which exaggerates the layout of the vias. Nonetheless, it is important to keep in mind thickness variations as layers are added. For example, R2 should not be deposited on top of any edges, as it is thin enough to be become disconnected.

Figure 4.1 also shows how we implement some common structures. Some of the devices used the lowest ground plane (M0), which provided some shielding and reduced the number of wire bonds needed. Most capacitor plates were

formed by M1/M2 (0.208 fF/μm^2), although M2/M3 (0.080 fF/μm^2) and M1/M3 (0.058 fF/μm^2) are also useable. Most wiring is located on M1 (which starts out as the junction base electrode) and M2. Although we did have some lines defined on M3 (which has the highest critical current density), it is inadvisable to put important structures on this layer, as it comes so late in the fabrication process.[2] Wire bonding pads were made on R3.

We used R2 or R3 to form quasiparticle traps [96]. When a niobium junction switches to the voltage state, it is able to break Cooper pairs. The resulting quasiparticles will be at an energy at least Δ_{Nb} above the Fermi surface. The idea of the traps is to place a material in contact with a junction electrode that has available density states at energies less than Δ_{Nb}. Once the quasiparticles "drop" into this area, they do not have enough energy to come back to the junction, where they are a source of dissipation. The hope is that by using molybdenum (which superconducts at about 1 K and has $\Delta_{\mathrm{Mo}} \sim \Delta_{\mathrm{Nb}}/10$), the quasiparticles not only get trapped, but also recombine quickly. We did not performed separate tests to determine how well the traps worked in practice.

4.2 *LC*-Isolated Phase Qubit

A major concern for quantum computing with superconducting devices is the difficulty of excluding all noise in the microwave frequency range from the bias lines. Even a small amount of noise power at the plasma frequency ω_p of the junction could alter its quantum state. Figure 4.2(a) shows one technique we used to reduce the bias noise. In the schematic, a junction with critical current I_0, capacitance C_J, and intrinsic resistance R_J is biased by current source I_b, which has a noise component characterized by resistance R_{bn}. The LC circuit formed by inductor L_i and capacitor C_i protects the junction at high frequencies using non-dissipative

[2] We received many useful tips such as this from Anna Kidiyarova-Shevchenko.

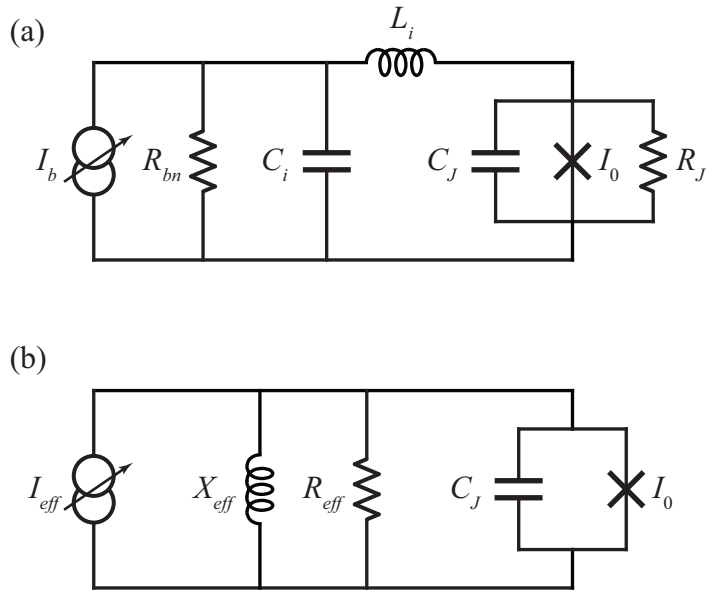

Figure 4.2: LC isolation of a current-biased junction. (a) A junction with critical current I_0, capacitance C_J, and intrinsic resistance R_J is biased by current source I_b. The filter formed by L_i and C_i isolates the junction from the dissipative element R_{bn} at high frequencies. (b) The circuit can be viewed in an equivalent way, where the junction is driven by an effective current source I_{eff} and shunted by R_{eff} and X_{eff}, which are purely resistive and reactive. I have chosen to represent X_{eff} with an inductor, but its value can be of either sign.

elements. A complete discussion of this approach with more realistic models can be found in Ref. [97], Chapter 7 of Ref. [3], and §5.2 of Ref. [1].

One point of view is to treat the LC circuit as a current divider, as a high frequency signal from the current source will get shunted to ground before reaching the junction, which is thought of as the load. For this to work, the cut-off frequency of the filter $1/\sqrt{L_i C_i}$ must be set well below ω_p.

An alternate way to characterize the isolation of a junction circuit is shown in Fig. 4.2(b). Here the biasing circuitry and junction resistance have been replaced by the parallel combination of an effective shunting resistance $R_{\mathit{eff}}(\omega)$ and shunting reactance $X_{\mathit{eff}}(\omega)$. In addition, I_b has been replaced by an effective source I_{eff}. These effective quantities are, in general, functions of frequency ω. In this picture, the junction is treated as a source that drives R_{eff} and X_{eff}. The ability of the junction

to dissipate energy is due to the resistance and quantified by the relaxation time of the system (introduced in §3.4), which is roughly $T_1 = R_{\mathit{eff}} C_J$. The expression suggests that a large C_J is desirable, which is one reason that our qubit junctions have relatively large 100 μm^2 areas. Recently, concerns about the quality of oxide barriers have brought this approach into question [98]. In particular, if R_{eff} is dominated by intrinsic dissipation in the junction caused by dielectric loss, then $R_{\mathit{eff}} \approx R_J$ will increase with the junction area; in this case $T_1 = R_{\mathit{eff}} C_J$ would be independent of the area.

If a complex admittance $Y(\omega)$ appears across the junction, then $R_{\mathit{eff}} = 1/\mathrm{Re}(Y)$ and $X_{\mathit{eff}} = -1/\mathrm{Im}(Y)$.[3] If $X_{\mathit{eff}} > 0$, then the effective reactance is most simply thought of as an inductor with a value of $L_{\mathit{eff}} = X_{\mathit{eff}}/\omega$. This element appears in parallel with the Josephson inductance of the junction. L_{eff} has a small effect on the junction resonance if L_i is chosen to be large (see §6.2 of Ref. [3]). If $X_{\mathit{eff}} < 0$, then it can be thought of a capacitor with $C_{\mathit{eff}} = -1/\omega X_{\mathit{eff}}$. In this case, the relaxation time becomes $T_1 = R_{\mathit{eff}}(C_J + C_{\mathit{eff}})$.

Without the LC network, $1/R_{\mathit{eff}} = 1/R_{bn} + 1/R_J$. Determining R_{eff} in a real device is not straightforward. We expect $R_{bn} \approx 50\ \Omega$ at high frequencies, due to coaxial lines and the output impedance of the function generator that is responsible for I_b. It could however be quite different, as the network of filters close to the junction is somewhat complicated. Nonetheless, assuming $R_{bn} = 50\ \Omega$ and taking $C_J = 5$ pF, T_1 is predicted to be 250 ps in the absence of any isolation. The relevant time scale for quantum computation is the inverse of the plasma frequency, which is roughly 200 ps for our usual operating conditions. Thus, some form of filtering is required to make the qubit useable.

The function of the LC isolation network is to boost the impedance. The

[3] If the total shunting impedance is Z, then according to Fig. 4.2(b), $\mathrm{Re}(Z) = X_{\mathit{eff}}^2 R_{\mathit{eff}} / \left(X_{\mathit{eff}}^2 + R_{\mathit{eff}}^2\right) \neq R_{\mathit{eff}}$. $\mathrm{Re}(Z)$ would be the correct quantity to consider if R_{eff} and X_{eff} appeared in series in the dissipation model.

shunting admittance across I_0 and C_J in Fig. 4.2(a) is

$$Y(\omega) = \left[i\omega L_i + \frac{1}{1/R_{bn} + i\omega C_i} \right]^{-1} + \frac{1}{R_J}. \tag{4.1}$$

Neglecting R_J, which is probably not a good approximation, the effective parallel resistance and reactance are

$$R_{\mathit{eff}}(\omega) = \frac{\omega^2 L_i^2}{R_{bn}} + R_{bn}\left(1 - \omega^2 L_i C_i\right)^2 \tag{4.2}$$

$$X_{\mathit{eff}}(\omega) = \frac{\omega^2 L_i^2 + R_{bn}^2\left(1 - \omega^2 L_i C_i\right)^2}{\omega L_i - \omega R_{bn}^2 C_i\left(1 - \omega^2 L_i C_i\right)}. \tag{4.3}$$

Figure 4.3 shows R_{eff} and C_{eff} for the LC isolation circuit used with device LC_2 (described in the next section). With $L_i = 8.2$ nH and $C_i = 84$ pF, the resonance frequency (in the absence of any other resistance) is 190 MHz. In Fig. 4.3(a), the effective resistances for $R_{bn} = 50\ \Omega$ (solid) and 15 Ω (dashed) are plotted as a function of frequency. Typically, our qubits are biased such that $\omega_p/2\pi \approx 5$ GHz. In this frequency range, $R_{\mathit{eff}} > 1\ \mathrm{M}\Omega$, which should result in $T_1 > 5\ \mu$s for $C_J = 5$ pF, again assuming $R_J \to \infty$. As Fig. 4.3(b) shows, the impedance transformation factor R_{eff}/R_{bn} is dependent on R_{bn} only near the LC resonance. This quantity may also be regarded as the factor by which noise power on the bias line is attenuated. From this point of view (where I_b is the source), the loading of the filter network by the junction itself is ignored.

Below the filter resonance, X_{eff} looks capacitive. These values are plotted against the left axis of Fig. 4.3(c). For the larger value of R_{bn}, $C_{\mathit{eff}} \approx C_i$ at low frequency. The value is greatly reduced as R_{bn} decreases; when $R_{bn} < \sqrt{L_i/C_i} \approx 10\ \Omega$, the reactance does not look capacitive at any frequency. Above resonance, the effective inductance is plotted (right axis). In both cases $L_{\mathit{eff}} \approx L_i$ at high frequency.

Figure 4.3 implies that the LC filter should adequately protect the junction

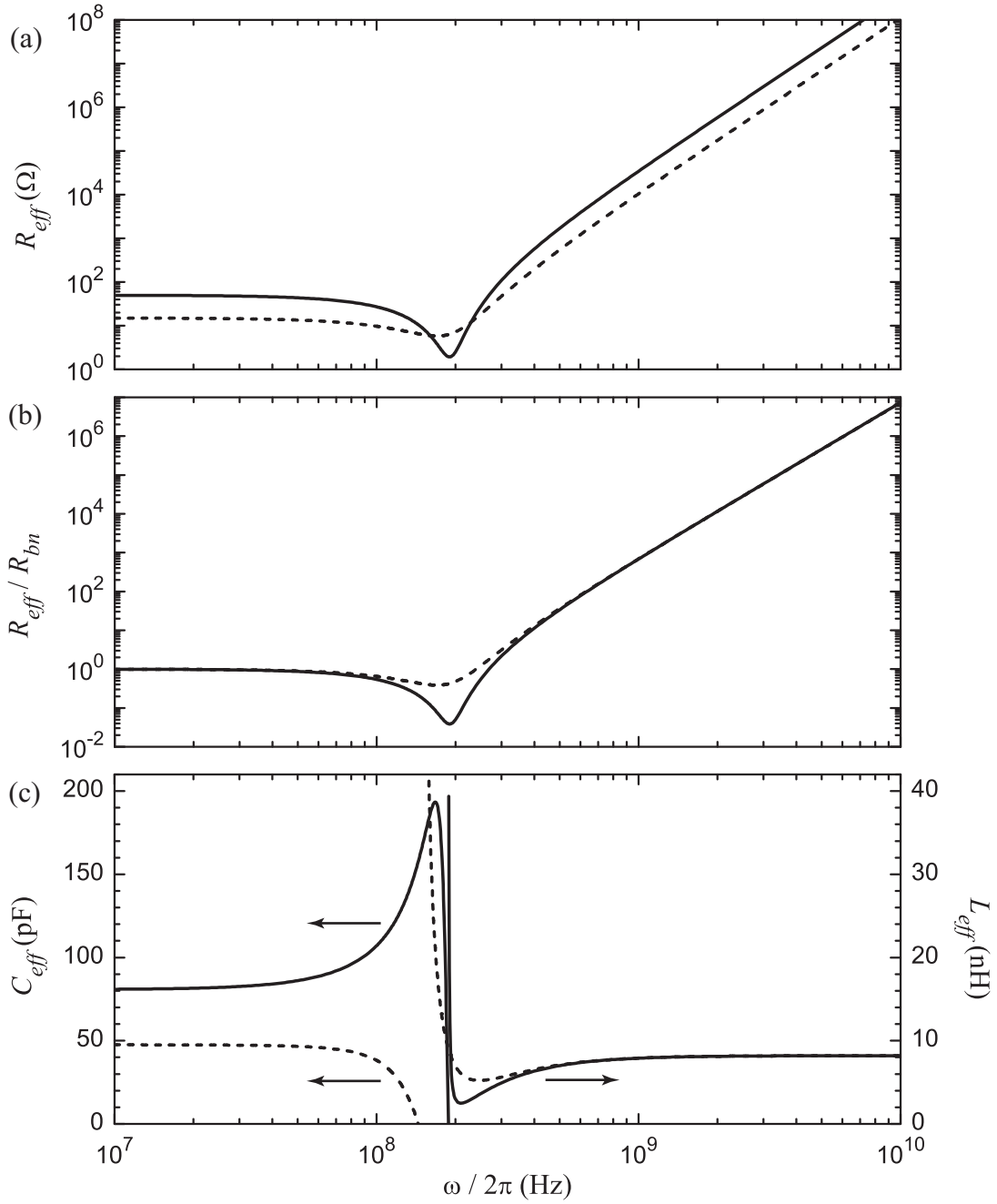

Figure 4.3: Effective impedances of an LC isolation network. The theoretical properties of a filter with $L_i = 8.2$ nH and $C_i = 84$ pF are plotted as a function of frequency, for $R_{bn} = 50\ \Omega$ (solid) and 15 Ω (dashed). (a) The effective resistance R_{eff} is greater than 1 MΩ for $\omega/2\pi > 2$ GHz. (b) The normalized resistance R_{eff}/R_{bn} is the same for both cases, except for frequencies near the LC resonance. (c) For frequencies less (greater) than the filter resonance, the capacitance C_{eff} (inductance L_{eff}) is plotted with respect to the left (right) axis. For all plots, the intrinsic resistance of the qubit junction was ignored.

at its plasma frequency of a few GHz. However, serious problems occur at lower frequencies. In particular, the network has no effect on R_{eff} at dc, allowing any low frequency noise to reach the junction without attenuation. This frequency range must be addressed with another filtering scheme. Also, at the LC resonance, the isolation fails dramatically and $R_{eff} \lesssim R_{bn}$. It is possible that current noise in this frequency range causes inhomogeneous broadening in qubits using LC isolation (see §6.1 of Ref. [3] and §5.2.3 of Ref. [1]).

4.2.1 Device LC_2

Figure 4.4 shows a photograph of two capacitively coupled LC-isolated phase qubits, a device which I will refer to as LC_2.[4] The chip was made using design "ajblc13" and was taken from Hypres Mask 297, Lot 43112, Wafer KL556, which was fabricated with their 100 A/cm^2 process. The two qubits, denoted LC_2A and LC_2B, are (nearly) mirror images of each other. I will use a superscript A and B to label the various quantities for each qubit, as in Fig. 2.18. For example, the qubits were controlled with two independent current biases I_b^A and I_b^B.

Table 4.1 lists important parameters for each qubit of LC_2. The top plate of the isolation capacitor C_i was formed by molybdenum layer R2 to increase the capacitance per unit area (and not because we wanted a quasiparticle trap). Taking advantage of the multi-layer process, the isolation inductor is formed by a 122 μm $\times$ 122 μm square spiral of 7.25 turns. The lines are 2 μm wide and separated by 2 μm.[5] I estimated the inductance L_i as 8.2 nH using Ref. [100]. The spiral is expected to self-resonate at a relatively high frequency. A large fraction of the capacitance that shunts L_i comes from the return path from inside the spiral; see §6.5 of Ref. [3] and

[4]The same device is called LCJJ-Nb2 in Ref. [1] and hypres2 in Ref. [3]. Results from this device are given in Refs. [41, 77, 78, 99].

[5]I believe that the current minimum allowed spacing on layer M1 of 2.5 μm was established after this device was fabricated.

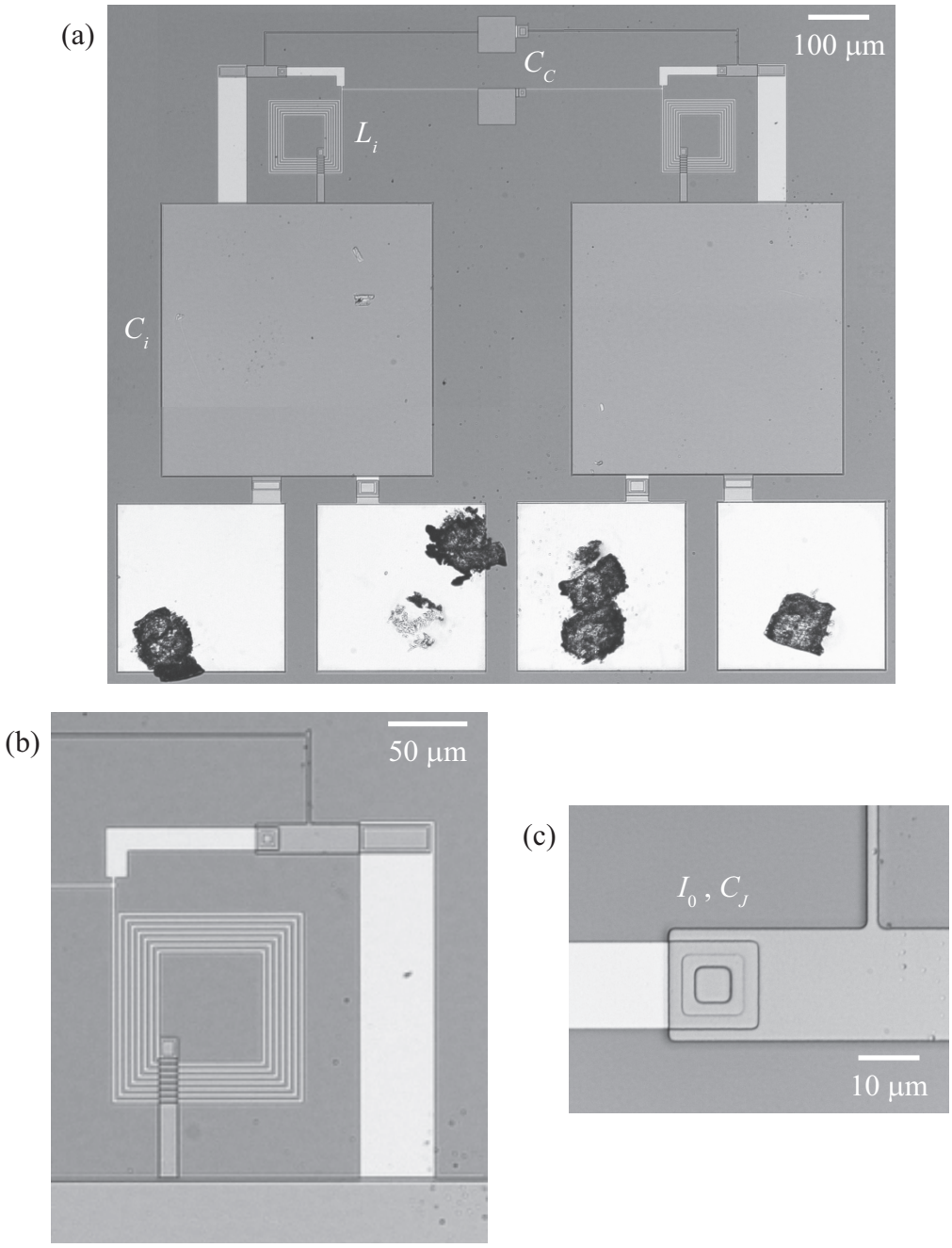

Figure 4.4: Photographs of device LC_2. (a) Two LC-isolated junctions are coupled together with two capacitors. The series combination of the two capacitors give the coupling capacitance C_C. The ground plane has been removed from the entire chip. Remnants of wire bonds are seen on the four pads at the bottom. Close-up views of (b) the right qubit and (c) its junction show more details. The scale bars are based on the CAD drawings.

Table 4.1: Parameters of device LC_2. The two coupled qubits of this device have nominally identical properties. The isolation of the qubit is provided by C_i and L_i. The qubit junction has capacitance and critical current C_J and I_0. Coupling of the qubits is achieved by L_C and C_C (the final row refers to each of the capacitors). The third column specifies the layers used in fabrication; commas separate layers that are in electrical contact (or vias between metal layers), while a slash indicates a capacitance. Values in the second and fourth columns are based on drawings; the fifth shows extracted values from experimental results at 20 mK, as described in the text.

Element	Size (μm $\times$ μm)	Layers	Design Value	Expt. Value
Bond Pad	280×280	R3, M3		
C_i	450×450	M2, I1B, R2 / M1	84 pF	
L_i	122×122	M1	8.2 nH	
C_J	10×10	M2, I1B, I1A / M1	4.15 pF	4.85 pF
I_0	10×10	I1A / M1	97 μA	130 μA
L_C	780×90	M1 and M2	2.6 nH	1.7 nH
$2C_C$	60×62	M2 / M1	770 fF	660 fF

§5.2.2 of Ref. [1]. I estimate an overlap area of 170 μm^2, which gives a capacitance of 35 fF and a self-resonance frequency near 10 GHz. I did not have a simple way of experimentally measuring either C_i or L_i.

The qubit junction is 10 μm $\times$ 10 μm, which is the size used for all of the qubits I studied. By including the "missing area" estimated by Hypres, the design value of the critical current is 97 μA at 4.2 K. In contrast, the measured diffraction patterns of Fig. 6.3 show that both I_0^A and I_0^B are 130 μA at 20 mK in the absence of a suppression field.

The design value of the junction capacitance C_J is 4.15 pF; most of this comes from the junction area itself, but the overlap area of layers M1 and M2 does make a small contribution. The coupling of the qubits is due to two capacitors, each of which is designed to be 770 fF. The total coupling capacitance C_C is half of this value,

because the two capacitors are in series. As the qubits are nearly 1 mm apart, the inductance due to the lines attaching the capacitors is significant. The inductance of a 2 μm trace, located well above the grounded sample box, is roughly 1.5 pH/μm;[6] the coupling lines form a 780 μm $\times$ 90 μm loop, resulting in $L_C \approx 2.6$ nH.

From Eq. (2.76), the frequency of the LC mode created by the coupling elements is $\omega_C/2\pi = 5.5$ GHz. Using Eqs. (2.77) and (2.78), we expect that the coupling strength varies from $\xi/\sqrt{2} = 0.20$ at the triple degeneracy to $\zeta_0 = 0.085$ when the plasma frequency of the junctions is well below ω_C. Experimental values for C_J, C_C, and L_C were extracted by fitting spectra when the qubits were brought in resonance with each other [78]. Using these values, $\omega_C/2\pi = 7.2$ GHz, $\xi/\sqrt{2} = 0.17$, and $\zeta_0 = 0.064$.

We studied the same device during three runs of the refrigerator, designated 40 (January to November 2003), 41 (November to December 2003), and 42 (December 2003 to April 2004).

During Run 40, a single line went from the junction to the top of the refrigerator, which was used to supply I_b and measure the junction voltage. This two-wire measurement made detecting the running state a bit challenging, as the voltage drop across the lossy manganin line was significant [as seen in the IV curve of Fig. 6.2(a)]. Detection was performed by high pass filtering the voltage and looking for a step. Starting with Run 41, a separate voltage line was added, as described in the next chapter. Although not essential, we high pass filtered the signal on this new line for detection.

In addition, beginning with Run 41, two changes were made to greatly improve the timing resolution of the escape rate measurement (see §6.2). The capacitance of the discrete LC filter at the mixing chamber was reduced to decrease the charging time of the voltage line. Also, the voltage amplifiers and their power supplies were

[6] I used the calculator available at http://www.emclab.umr.edu/pcbtlc/microstrip.html to estimate this value.

upgraded to the ones described in §5.4.

When I refer to a measurement on junction LC_2A, the I_b^B lead was generally shorted to the refrigerator common after its bias resistor (at the top of the refrigerator). With no current through LC_2B, its plasma frequency was usually greater than 20 GHz (depending on its critical current), well out of resonance with LC_2A.[7] With this arrangement, it is possible that LC_2B could escape to the voltage state at some time and sit in the sub-gap region (see §4.1.2 of Ref. [3]). We did a few tests where LC_2B was reset on every trial and never saw an effect.

4.3 dc SQUID Phase Qubit

Viewed as a current divider, the LC circuit described in the previous section is a simple way to isolate a junction with non-dissipative elements. The performance could be improved significantly by replacing the capacitor with a small superconducting inductor, which would remove the offending resonance and provide broadband isolation down to zero frequency. However, our usual measurement technique involves monitoring the bias line to determine when the junction tunnels to the voltage state. During a switch, most of this voltage would appear across L_i; at dc, the bias line would be shorted out by the new inductor. Nonetheless, the resulting structure resembles an rf SQUID, which has been used in a variety of qubit designs [33].

In the circuit shown in Fig. 4.5, the qubit junction (JJ1) has critical current I_{01}, capacitance C_{J1}, and resistance R_{J1}. Compared to the LC isolation technique, here C_i has been replaced with an auxiliary Josephson junction (JJ2) with parameters I_{02}, C_{J2}, and R_{J2}, as first proposed in Ref. [39]. When this isolation junction is in the zero-voltage state, its Josephson inductance L_{J2} (see §2.1) acts with L_1 to

[7] The presence of the coupling capacitor still had a significant impact, particulary with the spectrum of excitations; see Ref. [78] and §8.1.

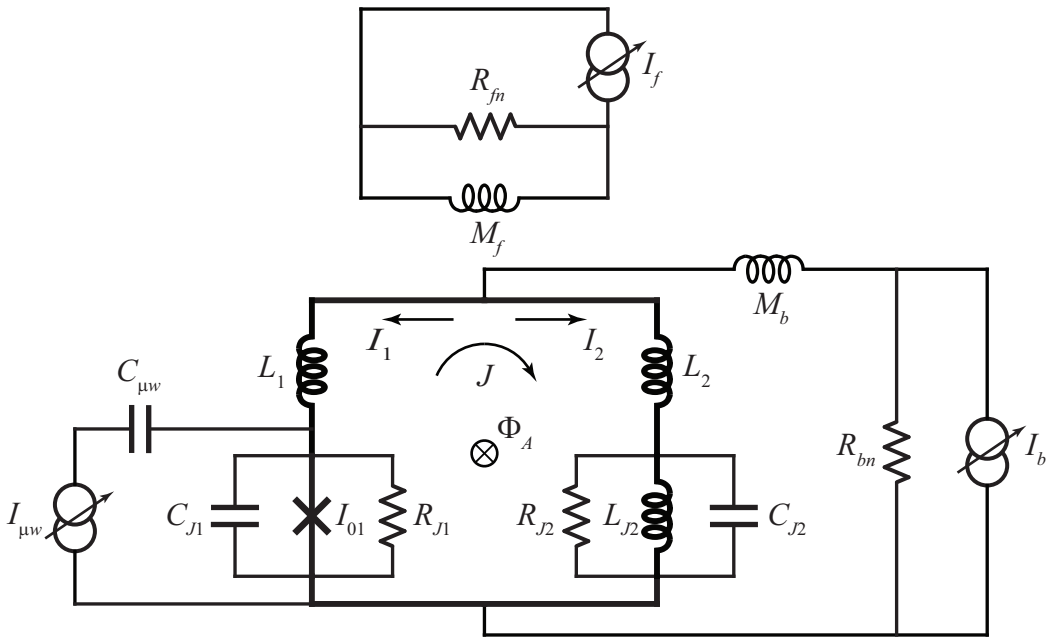

Figure 4.5: dc SQUID phase qubit. The junction on the left (JJ1) with critical current I_{01}, capacitance C_{J1}, and resistance R_{J1} is thought of as a phase qubit. The junction on the right (JJ2) with parameters I_{02}, C_{J2}, and R_{J2} forms an isolation network with inductances L_1 and L_2. To emphasize this role, I have replaced the ideal junction with its Josephson inductance L_{J2}. The qubit can be biased with current I_b and flux $\Phi_A = I_f M_f$ (and a smaller contribution $I_b M_b$). The total currents on each of the SQUID arms are I_1 and I_2; the circulating current is J. The isolation protects the device from noise characterized by resistances R_{bn} and R_{fn}. Energy level transitions are driven with the microwave current $I_{\mu w}$, which couples to the qubit through $C_{\mu w}$.

form a frequency-independent current divider. I replaced the usual junction symbol by an inductor to suggest this function. When the qubit junction tunnels to the finite-voltage state, the finite impedance on its arm causes current to flow through the isolation junction, making it switch as well if we choose $I_{02} < I_{01}$. Therefore, after the qubit junction switches the current bias line will be held at the gap voltage of the superconductor,[8] which can be measured as usual.

There are a few complications to this approach. When the current bias I_b increases, most of the current will get shunted to ground (just as we want for any

[8]In Ref. [39], a 50 Ω shunting resistor forced the junction to stay in the sub-gap region, to minimize quasiparticle generation.

current noise), causing the isolation junction to switch first. However, if all of the connections are superconducting, then the resulting structure is just an asymmetric dc SQUID, which was described in §2.4. It can be controlled with an independent flux bias $\Phi_A = M_f I_f$, where the current I_f generates a flux through mutual inductance M_f. If both I_b and I_f are ramped in the proper proportion (see §6.4), then only the qubit is biased, resulting in a device that behaves in many ways as a single isolated current-biased junction. Details of this approach can be found in Refs. [39, 72, 101, 102] and §5.4 of Ref. [1].

The effect of the dissipative element R_{bn} can be found with the model in Fig. 4.2(b). In fact, the circuits shown in Figs. 4.2(a) and 4.5 have nearly the same structure [1]. In the SQUID circuit, L_i is replaced by L_1. The other branch of the divider consists of L_2 and the parallel combination of L_{J2} and C_{J2}. The total impedance is purely reactive and may be thought of as a capacitance (although it could be negative). This leads to the substitution

$$\frac{1}{C_i} \;\rightarrow\; -\omega^2 \left(L_2 + \frac{L_{J2}}{1 - \omega^2 L_{J2} C_{J2}} \right) \approx -\omega^2 \left(L_2 + L_{J2} \right), \tag{4.4}$$

where the approximation holds for ω well below the plasma frequency of the isolation junction, $1/\sqrt{L_{J2} C_{J2}}$. In Eq. (4.4), I have ignored R_{J2} and the mutual inductance M_b from the bias line to the SQUID, for simplicity. In the low frequency limit, the effective shunting resistance is given by Eq. (4.2) as

$$R_{\mathit{eff}} = \frac{\omega^2 L_1^2}{R_{bn}} + R_{bn} \left(\frac{L_1 + L_2 + L_{J2}}{L_2 + L_{J2}} \right)^2 \approx r R_{bn}, \tag{4.5}$$

where I have ignored R_{J1} and $r = \left[\left(L_1 + L_2 + L_{J2} \right) / \left(L_2 + L_{J2} \right) \right]^2$ is known as the isolation factor [101]. The first term in the middle expression is typically small enough to ignore.

From Eq. (4.5), we see that to provide good isolation, $L_1 / \left(L_2 + L_{J2} \right)$ should be

large. This will lead to a large modulation parameter β [defined in Eq. (2.48)] and many possible flux states, as described in §2.5. This complication can be addressed with the flux shaking procedure to be discussed in §6.5. The distinct benefit of a large inductance is that the coupling between the junctions becomes small [72]. For this reason, we can think of one SQUID junction as the qubit and the other as simply providing isolation. To further weaken the coupling, we bias the SQUID with I_b and I_f in such a way that the current I_2 on the isolation branch is small. In this case, L_{J2} is held near its minimum value of $\Phi_0/2\pi I_{02}$. Thus, a large I_{02} is also desirable, but to use our standard measurement technique, we typically require $I_{02} < I_{01}$. However, switching may not always occur even with this choice of parameters. In the devices I studied, $I_{01} > 2I_{02}$, so that the qubit branch of the current-flux characteristic (see §2.6) extends over a relatively large range of I_b. On the other hand, for large I_{02}, it can happen that when the flux state corresponding to zero trapped flux ($N_\Phi = 0$) becomes unstable, the current bias will not be large enough to force the entire system to the finite voltage state. In this case, our simple detection scheme would not work and an alternate method would need to be used [4].

Equation (4.5) shows that it is possible to change the level of isolation from the bias leads provided by JJ2 by varying the Josephson inductance L_{J2} [101, 102]. This can be accomplished by adjusting the isolation junction current I_2. The ability to vary the isolation turns out to be quite useful in investigating the source of decoherence in these devices and placing bounds on R_{bn}. I will show some results of experiments on varying r in §7.2.2.

Figure 4.6 shows the real and imaginary components of the effective parallel shunting impedances of a dc SQUID phase qubit. For these plots, I used Eqs. (4.2), (4.3), and (4.4), with $R_{bn} = 50\ \Omega$ (solid lines) and 15 Ω (dashed). The chosen parameters ($L_1 = 3.52$ nH, $L_2 = 25$ pH, $C_{J2} = 2.09$ pF, $I_{02} = 4.4\ \mu$A with $I_2 = 0$ so that $L_{J2} = 75$ pH) describe SQUID DS_1 under suppression field

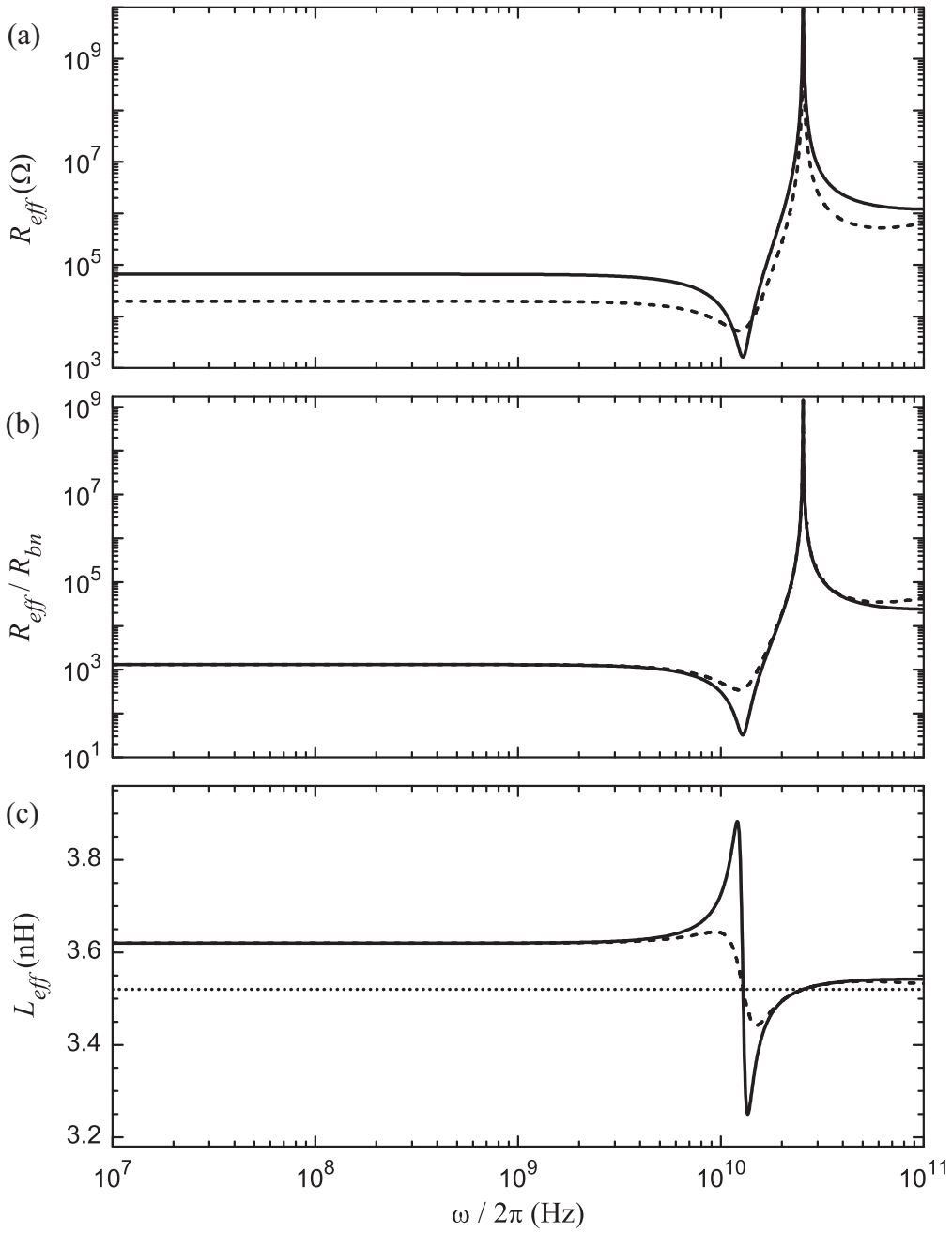

Figure 4.6: Isolation of a dc SQUID phase qubit from its bias line. The properties of a filter created by inductors $L_1 = 3.52$ nH and $L_2 = 25$ pH and an unbiased junction (with $I_{02} = 4.4$ μA, $C_{J2} = 2.09$ pF) are plotted as a function of frequency, for $R_{bn} =$ 50 Ω (solid) and 15 Ω (dashed). (a) The effective resistance R_{eff} is uniformly large below typical values of the qubit plasma frequency. (b) The normalized resistance R_{eff}/R_{bn} is the same for both cases, except near LC resonance frequencies. (c) The effective shunting reactance is always inductive; L_{eff} is dominated by L_1 (dotted line). For all plots, the intrinsic resistance of the qubit junction was ignored.

#2 (see Table 6.1), which are the conditions under which most of the data on this device were taken. R_{eff} is nearly constant below 10 GHz, which protects the qubit at its plasma frequency and attenuates low frequency noise. For $R_{bn} = 50\ \Omega$ and 15 Ω, $R_{eff} = 65$ kΩ and 20 kΩ, leading to predictions for T_1 of 270 ns and 80 ns, respectively, for $C_{J1} = 4.17$ pF. These values of T_1 are quite sensitive to L_2, which is difficult to measure accurately. While relaxation times of this order would make a wide variety of experiments possible (on the assumption that the decoherence time is not significantly shorter), considerably longer times will ultimately be required for quantum computation.

Examination of Fig. 4.6(a) shows that R_{eff} has strong resonant features, just as with the LC isolation network. However, these can be designed to occur at very high frequencies. In this case, there is a dip at the plasma frequency of the isolation junction $1/2\pi\sqrt{L_{J2}C_{J2}} = 13$ GHz and a spike at $1/2\pi\sqrt{L'C_{J2}} = 22$ GHz, where L' is the parallel combination of L_{J2} and L_2. The dip in the isolation could cause a problem, if this frequency is resonant with a higher order transition, such as $0 \rightarrow 2$. The value of R_{eff} at its minimum and the slight upturn at high frequencies is due to the first term in Eq. (4.2).

The effective inductance L_{eff}, shown in Fig. 4.6(c), is mostly due to L_1 (drawn as a dotted line). Below its plasma frequency, the isolation junction makes an inductance contribution, while it looks capacitive at higher frequencies. Ironically, the isolation is most effective at these higher frequencies, where the isolation network resembles an LC filter.

The qubit can also dissipate energy through the resistance R_{fn}, associated with the flux line [1, 39]. The shunting impedance due to R_{fn} can be found using the equivalent circuit shown in Fig. 4.7, where the junction has been replaced by a voltage source V_1 (and the effective impedance R_{bn} on the current bias line is taken to be infinite). The circulating current J in the SQUID loop induces a current J_f

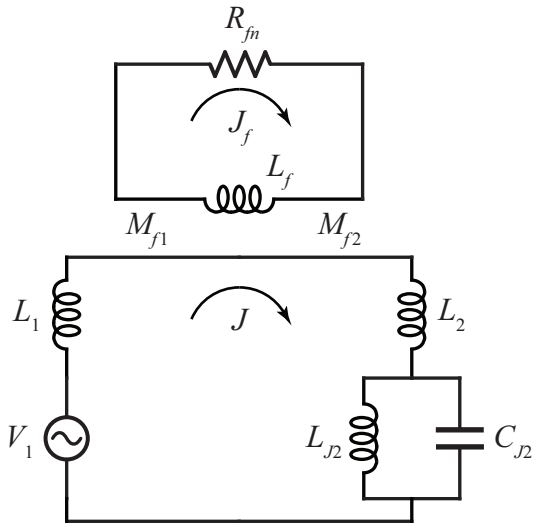

Figure 4.7: Flux line coupling to SQUID. The shunting impedance from the flux noise resistance R_{fn} can be found by considering the circulating current J due a voltage source V_1 that replaces the qubit junction. J induces a current J_f that flows through R_{fn} and the flux line inductance L_f. M_{f1} and M_{f2} are the mutual inductances between L_f and the SQUID geometrical inductances L_1 and L_2.

in the loop formed by the flux line inductance L_f and R_{fn}. Kirchhoff's voltage law at frequency ω for the two loops gives (see, for example, §11.5 of Ref. [103])

$$V_1 = \left(L_1 \frac{dJ}{dt} + M_{f1} \frac{dJ_f}{dt}\right) + \left(L_2 \frac{dJ}{dt} + M_{f2} \frac{dJ_f}{dt}\right) + \frac{i\omega L_{J2}}{1 - \omega^2 L_{J2} C_{J2}} J \tag{4.6}$$

$$0 = \left(L_f \frac{dJ_f}{dt} + M_{f1} \frac{dJ}{dt} + M_{f2} \frac{dJ}{dt}\right) + J_f R_{fn}, \tag{4.7}$$

where M_{f1} (M_{f2}) is the mutual inductance between L_f and L_1 (L_2). The Josephson inductance of the isolation junction does not store magnetic energy and only enters as a simple impedance assuming all signals are small. Assuming that the currents have a time dependence $e^{i\omega t}$ and that $M_f = M_{f1} + M_{f2}$, the junction shunting admittance is [1]

$$Y(\omega) = \frac{J}{V_1} = \left[i\omega L_{tot} + \frac{\omega^2 M_f^2}{R_{fn} + i\omega L_f}\right]^{-1}, \tag{4.8}$$

where

$$L_{tot} = L_1 + L_2 + \frac{L_{J2}}{1 - \omega^2 L_{J2} C_{J2}}. \tag{4.9}$$

From Eq. (4.8), the effective parallel shunting resistance and reactance due to the flux line are

$$R_{\mathit{eff}}^M \;=\; \frac{1}{\mathrm{Re}\,(Y)} \;=\; R_{fn}\left(\frac{L_{tot}}{M_f}\right)^2 + \frac{\omega^2\left(M_f^2 - L_{tot}L_f\right)^2}{M_f^2 R_{fn}} \;\approx\; R_{fn}\left(\frac{L_{tot}}{M_f}\right)^2 \tag{4.10}$$

$$X_{\mathit{eff}}^M \;=\; -\frac{1}{\mathrm{Im}\,(Y)} \;=\; \frac{\omega\, L_{tot}^2\, R_{fn}^2 + \omega^3\left(M_f^2 - L_{tot}L_f\right)^2}{L_{tot}\, R_{fn}^2 - \omega^2 L_f\left(M_f^2 - L_{tot}L_f\right)} \;\approx\; \omega L_{tot}, \tag{4.11}$$

where the approximations hold for perfect coupling between the inductors, when $M_f = \sqrt{L_{tot}L_f}$.

For good isolation, then, M_f should be chosen to be much smaller than L_{tot}. However, if it is too small, then the required value of I_f could be so large as to cause heating at the mixing chamber of the dilution refrigerator. With the simultaneous bias trajectory shown in Fig. 6.7(d) and discussed in §6.4, the maximum flux current we need to apply is roughly $(L_1/M_f)\,(I_{01} + I_{02})$.

The effective impedances for SQUID DS_1, calculated with Eq. (4.9) and the approximations in Eqs. (4.10) and (4.11), are plotted in Fig. 4.8. I have assumed the inductors are perfectly coupled for simplicity, but this is clearly untrue. From experimental measurements, L_{tot} is larger than 3.5 nH. If this were perfectly coupled to L_f with a resulting mutual inductance $M_f = 51$ pH (also from measurements), then L_f would be less than 1 pH. Given the length of the flux line (shown in Fig. 4.9), this prediction is far too small. Nonetheless, the approximation in Eq. (4.10) is a lower bound to the full expression, so the simplification is a useful one.

Near $\omega/2\pi = 5$ GHz, the effective shunting resistance due to the flux line is $R_{\mathit{eff}}^M = 250$ kΩ and 75 kΩ for $R_{fn} = 50$ Ω and 15 Ω, respectively. With a qubit junction capacitance of $C_{J1} = 4.17$ pF, T_1 is roughly 1000 and 310 ns for the two

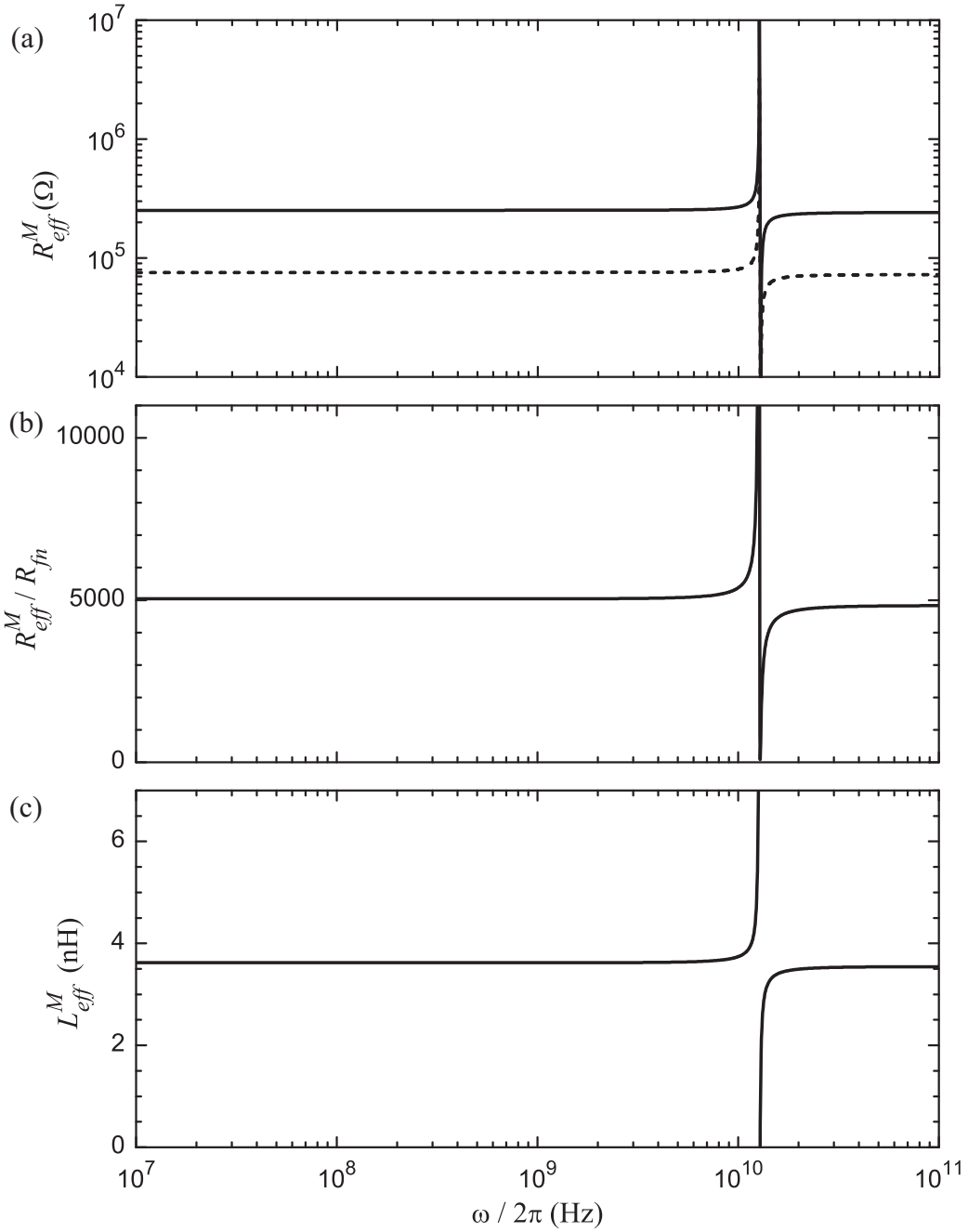

Figure 4.8: Isolation of a dc SQUID phase qubit from it flux line. The properties of the coupling between a SQUID (with $L_1 = 3.52$ nH, $L_2 = 25$ pH, $I_{02} = 4.4$ μA, $I_2 = 0$, $C_{J2} = 2.09$ pF) and noise resistances $R_{fn} = 50$ Ω (solid) and 15 Ω (dashed) by $M_f = 51$ pH are plotted as a function of frequency. (a) The effective resistance R^M_{eff} is constant, except near the plasma frequency of the isolation junction. (b) The normalized resistance R^M_{eff}/R_{fn} is the same for both cases and is exactly zero at a single frequency. (c) The effective shunting reactance is dominated by L_1. For all plots, the intrinsic resistance of the qubit junction was ignored.

cases, if the flux line is the only source of dissipation. As discussed earlier, the effective shunting resistance due to the current bias line is $R_{eff} = 65$ kΩ and 20 kΩ for $R_{bn} = 50$ Ω and 15 Ω. The total shunting resistance is given roughly by the parallel combination of R_{eff} and R_{eff}^{M}, which is dominated by the current bias line in this case (assuming comparable R_{bn} and R_{fn}). For both the current and flux lines, the isolation fails at the plasma frequency of the isolation junction. This is potentially more serious for the flux line, because (in the simplified model I have used) R_{eff}^{M} goes to zero near this frequency.

4.3.1 Device DS_1

A single dc SQUID phase qubit, which I will refer to as device DS_1,[9] is shown in Fig. 4.9. This device is located on chip design "ajblc13" and was fabricated at Hypres during the same run as device LC_2, although it was on a physically different chip.

The two control currents, I_b and I_f, were returned on the ground plane M0, which is the light area in the middle of the photograph of Fig. 4.9(a). The bonding pad connected to M0 was then connected to the sample box, which was electrically connected to the main body of the refrigerator.

The applied currents I_f and I_b were used to flux-bias the SQUID loop through the mutual inductances M_f and M_b. I estimated these values by assuming that the lines were one dimensional and neglecting the effect of the ground plane. The mutual inductance M is given by the Neumann formula (see, for example, §11.4 of Ref. [103]) as

$$M = \frac{\mu_0}{4\pi} \oint \oint \frac{d\boldsymbol{l_1} \cdot d\boldsymbol{l_2}}{r}, \tag{4.12}$$

where a line integral is taken around each of the structures being considered and r

[9] The same device is called LJJJ-Nb in Ref. [1]. Results from this device are given in Refs. [72, 101, 102].

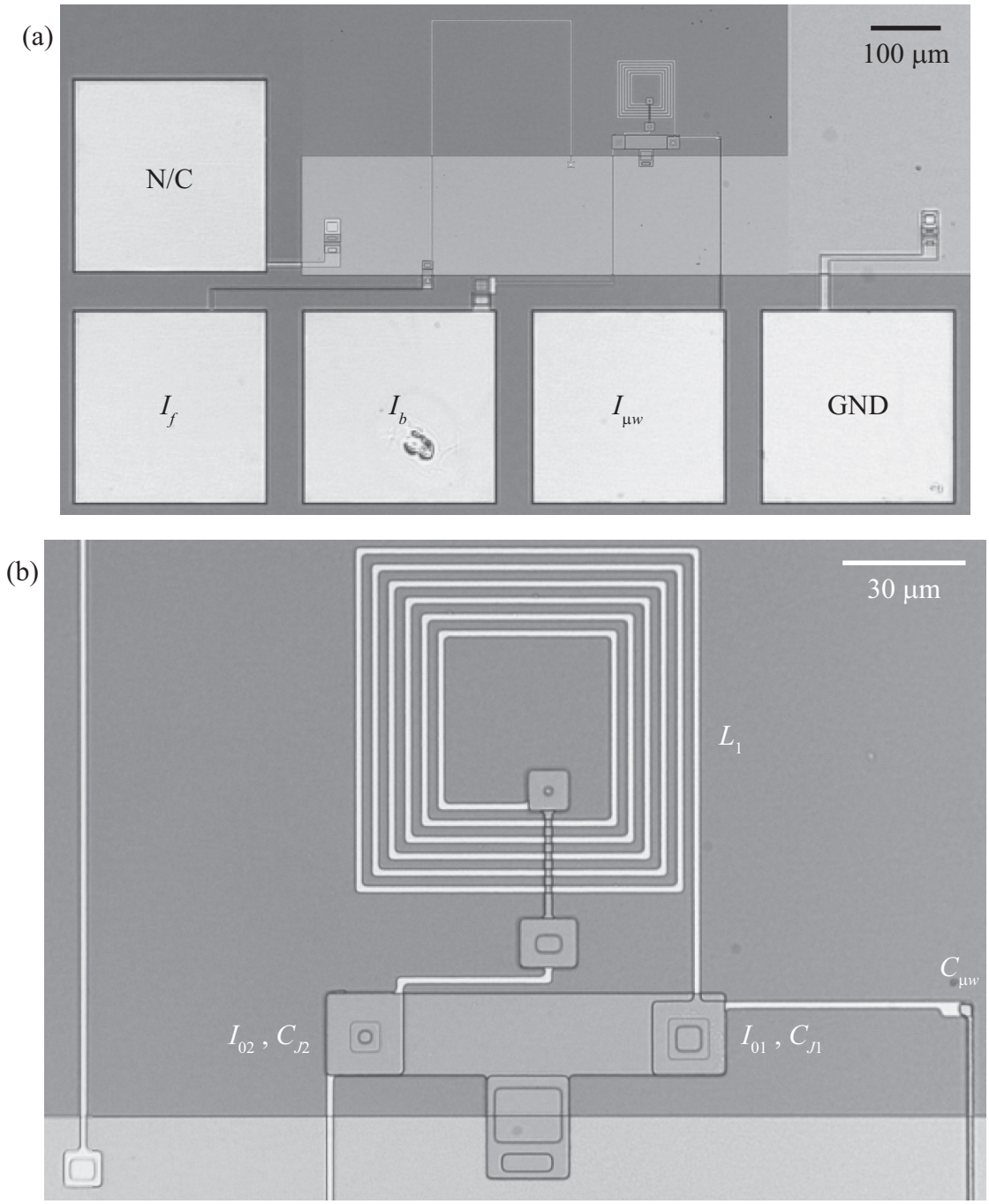

Figure 4.9: Photographs of SQUID DS_1. (a) The dc SQUID phase qubit is controlled by three current lines, each of which is returned on a common ground plane, which appears as a light area. Four bonding pads are labeled with the signal line that they were wired to. (b) A close-up view shows the qubit junction (10 μm $\times$ 10 μm, with critical current I_{01}), the isolation junction (7 μm $\times$ 7 μm, I_{02}), the 6-turn loop forming L_1, the flux line which carries I_f, and the microwave coupling capacitor $C_{\mu w}$. These photographs show a device nominally identical to the one actually studied.

Table 4.2: Device parameters of SQUID DS_1. The capacitance and critical current of the isolation junction are C_{J2} and I_{02}, while those for the qubit are C_{J1} and I_{01}. The geometrical inductances of the SQUID arms are L_2 and L_1. Microwaves are coupled to the qubit through $C_{\mu w}$. The experimentally measured quantities come from Table 6.1 and microwave spectroscopy.

Element	Size (μm $\times$ μm)	Layers	Design Value	Expt. Value
Bond Pad	280×280	R3, M3		
L_2	40 μm	M1 and M2	< 40 pF	< 30 pF
C_{J2}	7×7	M2, I1B, I1A / M1	2.09 pF	
I_{02}	7×7	I1A / M1	46 μA	51.7 μA
L_1	84×84	M1	3.3 nH	3.5 nH
C_{J1}	10×10	M2, I1B, I1A / M1	4.17 pF	4.43 pF
I_{01}	10×10	I1A / M1	97 μA	107.9 μA
$C_{\mu w}$	4×4	M3 / M1	0.9 fF	

is the distance between the two differential elements. In practice, I evaluated the integral numerically with the MATLAB function `dblquad` along paths that started and ended at bonding pads or that traced around the SQUID loop.

The return path of I_f through the ground plane has a significant impact on the value of M_f. Under the assumption that current flows from the via of the flux line [shown in the lower left corner of Fig. 4.9(b)] in a straight line to the via of the ground connection [shown in the lower right of Fig. 4.9(a)], Eq. (4.12) returns $M_f = 53.8$ pH. Less than half of this comes from the intended path on layer M1. We measured a value of 51 pH from current-flux characteristics (see Table 6.1), so the simple ground path appears to be a good approximation. With reference to the photograph, a positive I_f (one that flows from bonding pad 'I_f' to 'GND') generates a flux out of the plane of the page at L_1. The SQUID responds with a circulating current that spirals outwards and adds to the current through the qubit. This is just what a positive applied flux Φ_A does, based on the sign conventions shown in the

circuit diagrams of Figs. 2.12 and 4.5. That M_f is positive conveys that a positive I_f generates a positive Φ_A.

The current bias I_b also applies a small amount of flux to the SQUID. The current flows on a line on layer M1 that leads to the SQUID and returns on the ground plane. By assuming a direct via to via return path, M_b is about 16 pH, although the chosen boundary between the bias line and the SQUID loop (which are electrically continuous) affects this value.

Table 4.2 lists key parameters for this device. The qubit junction (10 μm $\times$ 10 μm) is the same size as in device LC_2. The isolation junction was chosen to be roughly half its area. However, we almost always operated this device in a suppression field $B_\parallel$ (and the two junctions present a different cross-sectional area to the field), so this ratio was not maintained for the bulk of the measurements I will discuss. The experimental values for the critical currents are from Table 6.1. I estimated the qubit junction capacitance C_{J2} from microwave spectroscopy. It is difficult to do the same for the isolation junction, because it has a lower quality factor Q.

We designed DS_1 to have a large inductance L_1 on the qubit arm of the dc SQUID. This was accomplished with a 6-turn spiral with 2 μm line width and spacing. Using Ref. [100], the prediction is $L_1 = 3.3$ nH, in good agreement with the value of 3.5 nH obtained experimentally by fitting the current-flux characteristics. Actually, only $L_1 - M_b$ can be measured with this technique, but L_1 dominates this difference. In this device, the crossover capacitance is much smaller than it is for the spirals of LC_2. With an area of 20 μm^2, the shunting capacitance is roughly 4 pF for a self-resonance above 40 GHz. In this case, the resonance may be determined by other factors, such as the total length of the coil.

The inductance L_2 is due to the stray inductance on the isolation arm and is difficult to predict and measure. Given that the I_b feed and return lines are separated

by 40 μm, L_2 is likely to be of order 40 pH. From Table 6.1, the experimental value of $L_2 + M_b$ varies from -5.2 to 32.6 pH for different values of $B_\parallel$. In this case, M_b could be making a significant contribution, particularly if the value is negative. In many of the devices studied in the group at present, I_b and its return are located near each other on parallel paths to minimize both L_2 and M_b.

In order to resonantly excite the junction, we applied a microwave current $I_{\mu w}$ to the qubit junction through a small capacitor $C_{\mu w}$ [see the circuit diagram of Fig. 4.5 and the lower right of the photograph of Fig. 4.9(b)], designed to be about 1 fF. We were not careful in providing an impedance matched and shielded path for the microwaves, so it is very likely that the capacitor was not solely responsible for the coupling strength of $I_{\mu w}$ to the junction.

We studied device DS_1 during Run 43 of the refrigerator (April 2004 to December 2004).[10] As the flux line was required to carry up to 15 mA, we installed a new superconducting line for I_f. In addition, the previous copper sample box was replaced with an aluminum one, to provide magnetic shielding to the device. More details on these topics are given in the next chapter.

4.3.2 Device DS_2

The final device I will discuss, DS_2, consists of two dc SQUID phase qubits coupled by a capacitor.[11] It is located on chip design "umdqc04," taken from Hypres Mask 308, Wafer KL700, which was fabricated with their 30 A/cm^2 process. Photographs of a nominally identical device made during the same run are shown in Fig. 4.10. As with LC_2, I will label properties of the individual SQUIDs (DS_2A and DS_2B) with a superscript A or B.

As comparison of Figs. 4.9 and 4.10 shows, each SQUID in DS_2 is geometrically

[10] Two resonantly isolated devices (see §9.2 of Ref. [3] and §5.3 of Ref. [1]) were wired for study at the same time.

[11] Results from this device are given in Refs. [83, 104]

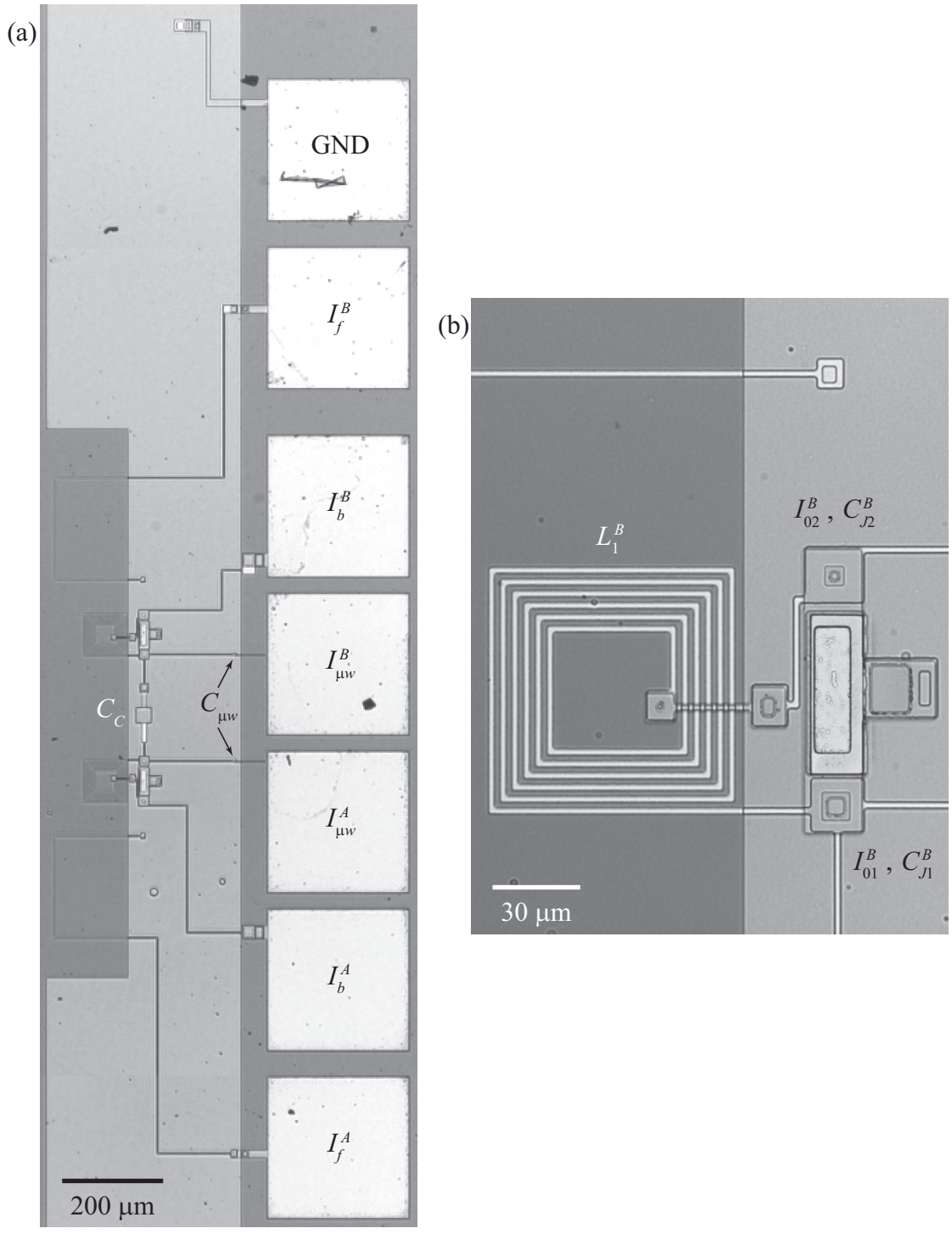

Figure 4.10: Photographs of coupled SQUIDs DS_2. (a) Two dc SQUIDs are coupled by a single capacitor and share a common ground plane. (b) Each SQUID is similar to DS_1, with the exception of a quasiparticle trap located between the junctions. These photographs are of a device nominally identical to the one actually studied.

Table 4.3: Parameters of device DS_2. Each of the two coupled qubits has the same design values, as listed below. The size of all of structure are the same as DS_1, however the junction properties are different because of the lower 30 A/cm^2 process used in the fabrication. For the critical currents I_{01} and I_{02}, the two experimental values listed are for DS_2A and DS_2B. Coupling of the devices is achieved by the single capacitor C_C and stray inductance L_C.

Element	Size (μm $\times$ μm)	Layers	Design Value	Expt. Value
Bond Pad	280×280	R3, M3		
L_2	40 μm	M1 and M2	< 40 pF	< 30 pF
C_{J2}	7×7	M2, I1B, I1A / M1	1.92 pF	
I_{02}	7×7	I1A / M1	13.8 μA	3, 6 μA
L_1	84×84	M1	3.3 nH	3.4 nH
C_{J1}	10×10	M2, I1B, I1A / M1	3.82 pF	4.4 pF
I_{01}	10×10	I1A / M1	29.1 μA	24, 20 μA
$C_{\mu w}$	4×4	M3 / M1	0.9 fF	
L_C	280 μm	M0, M1, and M2	~ 200 pH	
C_C	30×30	M2 / M1	190 fF	130 fF
QP Trap	56×20	R3, M3, I2, M2		

identical to device DS_1 (although DS_2B is its mirror image). However, because of the lower critical current density, I_{01} and I_{02} are much smaller. The capacitances of the junctions are also slightly smaller in DS_2. Because the plasma frequency of the junctions, when biased so that tunneling to the voltage state was measurable, was roughly 6 GHz, we never applied a suppression field when studying this device. For the experimental values of the critical currents, the two values listed are for DS_2A and DS_2B, based on IV curves and current-flux characteristics. It is odd that they differ from the design values by such a large amount, particularly in the case of the isolation junctions. In addition, these values changed several times over the course of data taking, by as much as 2 μA in the case of DS_2B. Some of these events were operator-induced, but the critical currents often appeared to change slowly over

time or after helium transfers. One possibility is that there was a vortex trapped in the films near the junction. However, as all the critical currents were low, this is unlikely.

The base electrode of each of the qubits is coupled by a 190 fF capacitor C_C. The counter electrodes are connected by the ground plane. As the lines leading to capacitor are directly above the ground plane, their self-inductance is likely to be small. The coupling inductance L_C is probably dominated by the ground plane connection. The grounding vias for the two SQUIDs are separated by 280 μm. As the current path between SQUIDs could be quite wide, the total L_C is probably of order 200-300 pH. The frequency of the LC coupling mode is $\omega_C/2\pi = 27$ GHz, using Eq. (2.76) with the design values. This is higher than the zero-bias plasma frequency of the qubits. If the qubit could be brought into resonance with this mode, Eq. (2.77) gives a coupling strength of $\xi/\sqrt{2} = 0.15$. If (as usual) the qubits are in resonance well below ω_C, the coupling is reduced to $\zeta_0 = 0.047$, calculated with Eq. (2.78). The experimental values of C_J and C_C come from a fit to the spectrum of the coupled system, shown in §8.6.

The ground plane was extended to run underneath the junctions, in the hope of providing some extra isolation. A quasiparticle trap was also added, by connecting the wide (low inductance) lead that forms half of the SQUID loop to an island on layer R3 (Ti/PdAu). I also have not considered the capacitance of the wiring lines to the ground plane. Hopefully, any resonant modes created are at sufficiently high frequency to ignore.

The flux biasing of this device was somewhat complicated, due to the large cross mutual inductance between the SQUIDs. The total flux[12] in each SQUID due to the two current (I_b^A and I_b^B) and two flux (I_f^A and I_f^B) bias lines can be expressed

[12]With the convention I have chosen, the applied flux Φ_A does not contain a contribution from a SQUID's own bias line. The total flux Φ_T is due to all four control currents and the circulating current.

in terms of the matrix equation $\boldsymbol{\Phi_T} = \underline{M}\boldsymbol{I}$ or

$$\begin{pmatrix} \Phi_T^A \\ \Phi_T^B \end{pmatrix} = \begin{pmatrix} M_f^{AA} & M_b^{AA} & M_f^{BA} & M_b^{BA} \\ M_f^{AB} & M_b^{AB} & M_f^{BB} & M_b^{BB} \end{pmatrix} \begin{pmatrix} I_f^A \\ I_b^A \\ I_f^B \\ I_b^B \end{pmatrix}. \tag{4.13}$$

For example, M_f^{BA} is the mutual inductance between flux line B and SQUID A. Using Eq. (4.12) (with the assumptions about return currents discussed in the previous section), I estimated the mutual inductance matrix as

$$\underline{M} = \begin{pmatrix} +90.7 & +28.3 & -0.18 & +2.7 \\ -62.5 & -45.7 & +13.4 & -27.5 \end{pmatrix} \text{pH}. \tag{4.14}$$

The large asymmetry between DS_2A and DS_2B is due to the ground path which runs very close to the loop of B. Unfortunately $\left|M_f^{AB}\right| > \left|M_f^{BB}\right|$, so biasing DS_2A without significantly affecting DS_2B was difficult. One approach to the problem is the subject of §5.2.2. Finally, there is a mutual inductance between the two SQUID loops, which is predicted to be 3.0 pH. This can be an issue if the flux state of one device (randomly) changes, which then affects biasing of the other.

We measured the mutual inductance matrix using data from the current-flux characteristics as described at the end of §6.3 and found

$$\underline{M} = \begin{pmatrix} +71.92 & - & +0.44 & -1.10 \\ -52.82 & -54.94 & +17.73 & - \end{pmatrix} \text{pH}. \tag{4.15}$$

The quantitative disagreement between experiment and theory is not terribly surprising. For one, the mutual inductance of a bias line to its own SQUID cannot be measured with the experimental method we used. Secondly, the presumed return

current path may be an oversimplification, as it does run very close to the SQUIDs. In addition, the presence of the ground plane and its proximity to the SQUIDs alters the flux coupling in a way that is not taken into account by Eq. (4.12).

It is worth noting that if more than a few of these devices are to be coupled together, the issue of cross mutual inductance needs to be seriously addressed. This not only applies to I_f and I_b, but also to the microwave current $I_{\mu w}$. In both LC_2 and DS_2, when we intended to excite one device with a microwave drive, the other also responded (but to a smaller extent). Some of this was undoubtedly due to the connection provided by the coupling capacitors, but the paths leading from the wire bonds were not properly shielded. While providing individual current returns should provide a great improvement to these problems, even small levels of cross talk will still be rather difficult to deal with using the present design. A possible solution is to encase each qubit in an on-chip superconducting shield.[13]

We studied device DS_2 during Run 44 (March 2005 to June 2006) of the refrigerator. Before this run, the wiring for DS_1 was duplicated to accommodate the additional SQUID. Two new discrete LC filters and four new copper powder filters (which are highly attenuating) were mounted in new housings. We kept the same sample box, but anchored the copper plate on which the chip was mounted directly to the mixing chamber with a copper wire.

As with LC_2, almost all of the experiments on DS_2 that I will discuss involved just one of the qubits. Often, we grounded all of the lines of the other at the top of the refrigerator. However, we noticed that this seemed to affect the biasing somewhat, presumably due to changes in the mutual inductance matrix from different ground paths. Therefore, we usually kept all of the lines connected, but held the unused bias and flux current lines at zero voltage (at the function generators) and placed a large resistor to ground on the voltage readout line.

[13] A device of this sort designed by Anna Kidiyarova-Shevchenko will be tested in the group soon.

4.4 Summary

A simple current-biased junction would make a poor qubit because it could dissipate energy through the effective shunting resistance R_{eff} due to its bias leads. Therefore, an isolation scheme must be used to boost this resistance, so quantum superpositions can be maintained. The quality of the isolation can be characterized by the relaxation time $T_1 = R_{\mathit{eff}} C_J$, where C_J is the junction capacitance.

An LC filter, with a resonance near 200 MHz, will protect a qubit at its plasma frequency $\omega_p/2\pi \approx 5$ GHz. For device LC_2, consisting of two coupled LC-isolated phase qubits, the prediction for T_1 is roughly 5 μs. However, this time may not be realized because the filter fails at its resonance frequency and below.

In the dc SQUID phase qubit, one junction serves as the qubit, while the other forms an arm of a inductive current divider. While this does provide broadband isolation, our implementation does not boost R_{eff} to the levels of the LC isolation. For the single qubit DS_1 and the coupled device DS_2, the prediction for T_1 is 250 ns due to the stepped up lead impedance.

Both T_1 predictions were made by assuming that the bare bias line resistance was 50 Ω. However, it is difficult to determine this value accurately, particularly over the wide frequency range that could be important. Also significant is that the dissipation could be dominated by intrinsic processes in the junction, which the isolation techniques cannot prevent.

Chapter 5
Instrumentation and Experimental Apparatus

This chapter contains a description of the electronics and other equipment I used in the experiment. In terms of electronics, I will mainly focus on the measurement of the tunneling escape rate of a junction to the voltage state, where the vast majority of the data in the rest of the thesis comes from. Other experiments only called for minor changes. I will also discuss some of the special precautions that had be taken when assembling the wiring and filtering, as the devices operated at 20 mK on a dilution refrigerator. Throughout this chapter, I will refer to various runs of the refrigerator when different components were used. The devices studied during these runs are described in §4.2.1, §4.3.1, and §4.3.2.

Figure 5.1 shows a block diagram overview of the electronics used in the escape rate experiments. The device (a dc SQUID in this case) was mounted on the mixing chamber of a dilution refrigerator, located inside an rf shielded room, which attenuates electromagnetic fields above a few kHz.[1] The device was biased by two currents, I_b and I_f, created by dropping the voltage from arbitrary waveform generators (AWGs) across resistors R_b and R_f. Each of the bias lines was filtered at the shielded room wall by a pi filter and passed through a unity gain buffer to avoid ground loops. Additional protection was provided by an LC filter and a copper powder filter at the mixing chamber of the refrigerator (on both bias lines) and the on-chip isolation techniques described in Chapter 4. Resonant transitions were driven with a microwave current $I_{\mu w}$. If pulses were required, the microwave source was gated by a pulse generator.

The I_b and I_f AWGs were triggered by a square wave from an additional function generator (labeled 'Master Clock' in Fig. 5.1). The trigger line was optoisolated,

[1] Testing of the shielded room was performed by Musaddiq Awan.

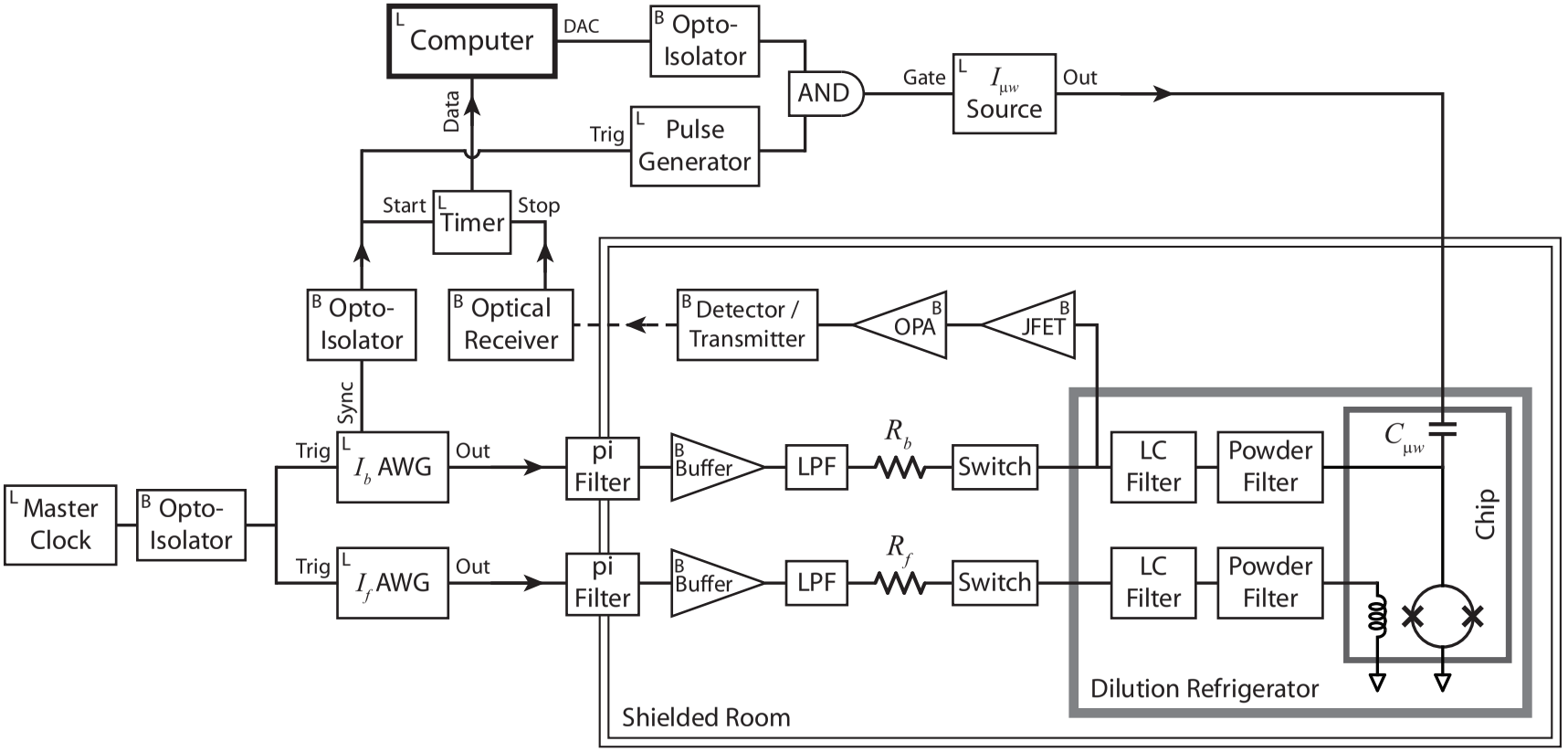

Figure 5.1: Overview of experimental set-up. The block diagram shows the typical arrangement of electronics for measuring the escape rate of a device to the voltage state. Two synchronized arbitrary waveform generators (AWGs) biased a SQUID through a series of filters, including a single-pole low pass filter (LPF). By monitoring the amplified junction voltage and sending an optical pulse over a fiber (dashed line), the time (with respect to the sync of the AWG) that the device switched was recorded. A microwave pulse could be sent to the junction to, for example, induce Rabi oscillations. Active components are labeled with an 'L' or 'B' to indicate whether they were line or battery powered. When measuring single LC-isolated junctions, the flux bias circuitry was removed. When measuring coupled qubits, the biasing circuitry (and detection circuitry, at times) was duplicated.

Table 5.1: Commercial electronics used in the escape rate measurement. The table lists the most common instruments I used. "SRS" is Stanford Research Systems.

Function	Instrument
I_f, I_b	Agilent 33120A Arbitrary Waveform Generator, Opt. 001
Master Clock	Dynatech Nevada Exact 628 Function Generator
Timer	SRS SR620 Universal Time Interval Counter, Opt. 01
Pulse Gen.	SRS DG535 Digital Delay Generator, Opt. 01
$I_{\mu w}$	Hewlett-Packard 83731B Synthesized Signal Generator
	Hewlett-Packard 83732B, Opt. 1E1, 1E2, 1E5, 1E8, 1E9, 800
GPIB	National Instruments PCI-GPIB
DAC / ADC	National Instruments PCI-6110 Data Acquisition Card
	& BNC-2110 BNC Connector Block

in an attempt to keep the AWG as noise-free as possible. When studying device DS_2, the bias circuitry was duplicated for the second SQUID. In this case, all four AWGs were synchronized. When studying the LC-isolated devices, the flux bias circuitry was absent, but the rest of the set-up was the same.

All commercial line-powered instruments (indicated with an 'L' in Fig. 5.1) were located outside of the shielded room and (with the exception of the microwave source and computer) were powered through an isolation transformer that broke the ground connection from the wall. A list of the equipment in given in Table 5.1. The active circuits built in-house[2] were powered by sealed lead acid batteries (indicated with a 'B'), which had to be recharged after roughly 50 hours of operation.

Our basic experiment involved measuring the time at which a junction switched to the voltage state, with respect to the start of a particular trial. The various signals that are involved in the measurement for a single cycle are sketched in Fig.

[2]The majority of the electronics that I used were designed and assembled by Huizhong Xu and Andrew Berkley, although several other people contributed as well.

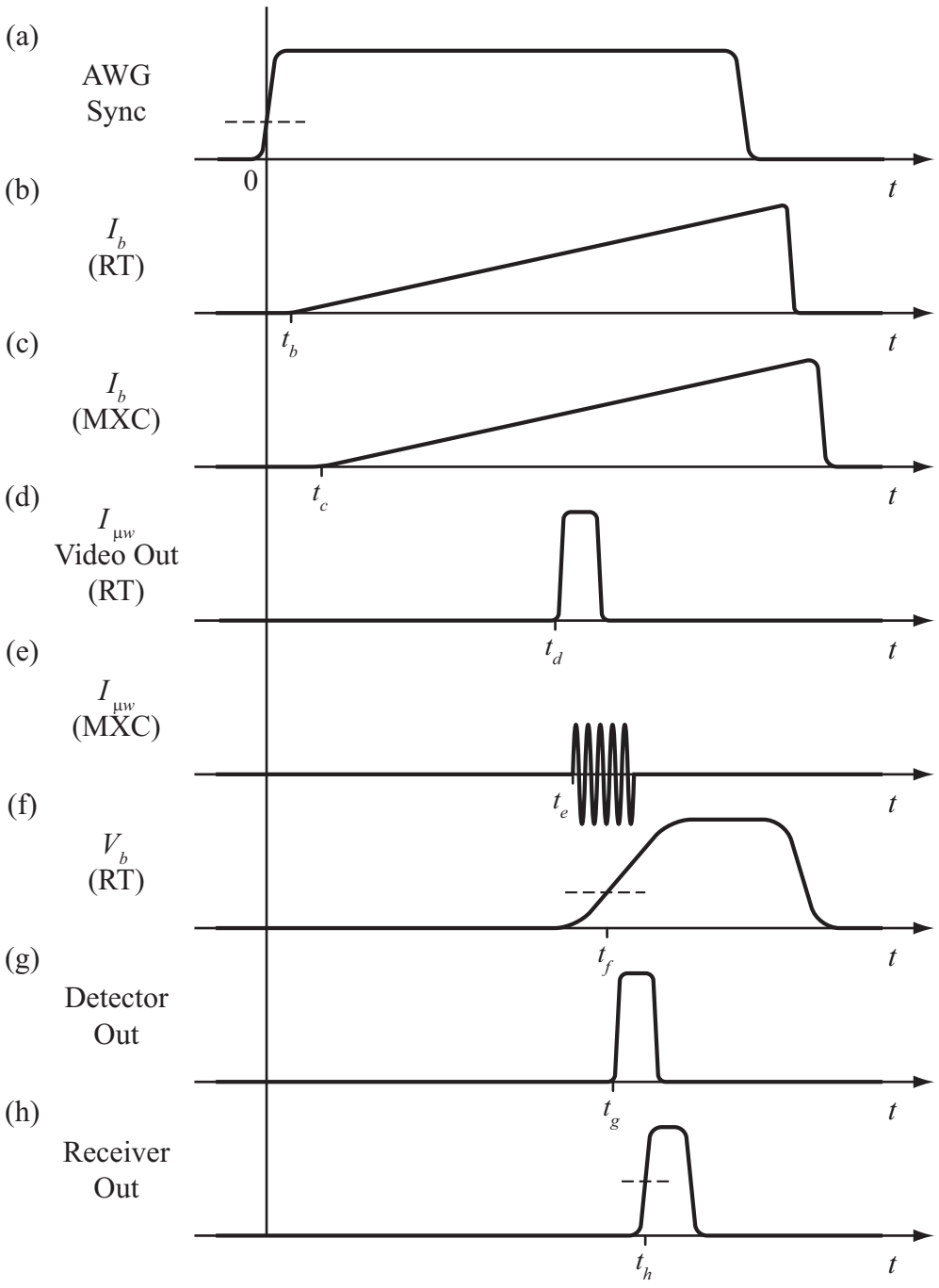

Figure 5.2: Timing diagram for escape rate measurement. The cartoons show the time dependence of several signals at points where they are measurable at room temperature (RT) and at the device, near the refrigerator's mixing chamber (MXC). (a) The reference time $t = 0$ is determined by the timer, when the AWG sync exceeds a threshold. The combination of a (b), (c) bias current and (d), (e) microwave current pulse force the junction to switch to the voltage state. When the (f) junction voltage exceeds a set value, the (g) detector sends a pulse that is relayed to the (h) receiver, whose output triggers the timer to stop. See §5.5 for a full discussion.

5.2. Some of the signals are shown both at room temperature (RT) where they can be measured and at the device (MXC). Delays and distortion between the two points need to be considered when performing current calibrations.

An interval counter ('Timer' in Fig. 5.1) was triggered by the isolated sync from the bias AWG. I_b began to increase at this time, defined to be $t = 0$. Typically, the ramp was linear, reaching the junction critical current in about 1 ms. The voltage on the bias line V_b was continuously monitored by a two-stage amplifier. At some point, the junction would switch to the voltage state. Because of the relatively large capacitance on the bias line, V_b increased somewhat slowly after the device switched, which was a major factor in determining the timing resolution of the experiment. When V_b surpassed a preset trigger threshold (roughly 200 μV), a light pulse was sent over a fiber optic cable to a receiver located outside of the shielded room. The output of the receiver then stopped the timer.

The timer sent the single time interval to a computer, which was equipped with a National Instruments PCI-GPIB card. A program written with National Instruments LabVIEW 6.1 was used to collect, display, and record data from a large number of trials (anywhere from several thousand to several million). The master clock signal (not the computer) controlled the repetition frequency, which was on the order of 200 Hz. The method used to convert a histogram of switching times to escape rate is discussed in §6.2.

If the experiment required a microwave drive, we also wanted data taken without microwaves, so that the escape rate enhancement could be calculated. The computer coordinated this by sending an isolated TTL signal to the gate of the microwave source. Generally, 10000 cycles with microwaves were followed by the same number without. If we wanted a microwave pulse, then the output of a logical AND between the computer's signal and a pulse generator (which outputs a "dc pulse") was sent to the gate of the microwave source. The computer was also used

to automatically update the waveforms of the AWGs, change the frequency and power of the microwaves, and control the parameters of the pulse generator. The GPIB connections that allowed this communication are not shown in Fig. 5.1.

5.1 Cryogenics

We used an Oxford Instruments model 200 dilution refrigerator, shown in Fig. 5.3, to cool the devices to as low as 20 mK. The refrigerator has several distinct vacuum sub-systems. The dilution unit, shown in Fig. 5.3(a), is enclosed in a vacuum can (which attaches to the 4 K flange) and the entire refrigerator is immersed in a dewar filled with liquid ^{4}He. The dewar is surrounded by a cylinder of mu metal, to help shield magnetic fields. The vacuum in the can (initially created with a diffusion pump, but greatly improved by contact to the ^{4}He bath) thermally isolates the various stages of the refrigerator during operation.

Cooling of these stages is provided by the closed circulation of a ^{3}He/^{4}He mixture [105]. When the mixture first enters the refrigerator, it is cooled by contact with the 1 K pot, which is an isolated volume of ^{4}He that fills from the bath and is pumped by a dedicated rotary pump (Leybold S40B or Alcatel 2063A). The mixture liquifies at the pot and cools as it passes through two stages of heat exchangers before reaching the mixing chamber. Below 870 mK, the mixture undergoes a phase transition and separates into ^{3}He-rich and ^{3}He-dilute phases. The dilute phase extends from the mixing chamber to the still, where it cools incoming mixture and is pumped by the combination of a roots blower (Leybold RUVAC WSU 501) and a sealed rotary pump. For the rotary pump, we used either a Leybold S65B (specially retrofitted for Oxford) or an Alcatel 2063H. The evaporative cooling of ^{3}He atoms crossing the phase boundary to keep the dilute phase in equilibrium is what provides the cooling power.

The ^{3}He gas that is pumped out of the still passes through nitrogen and helium

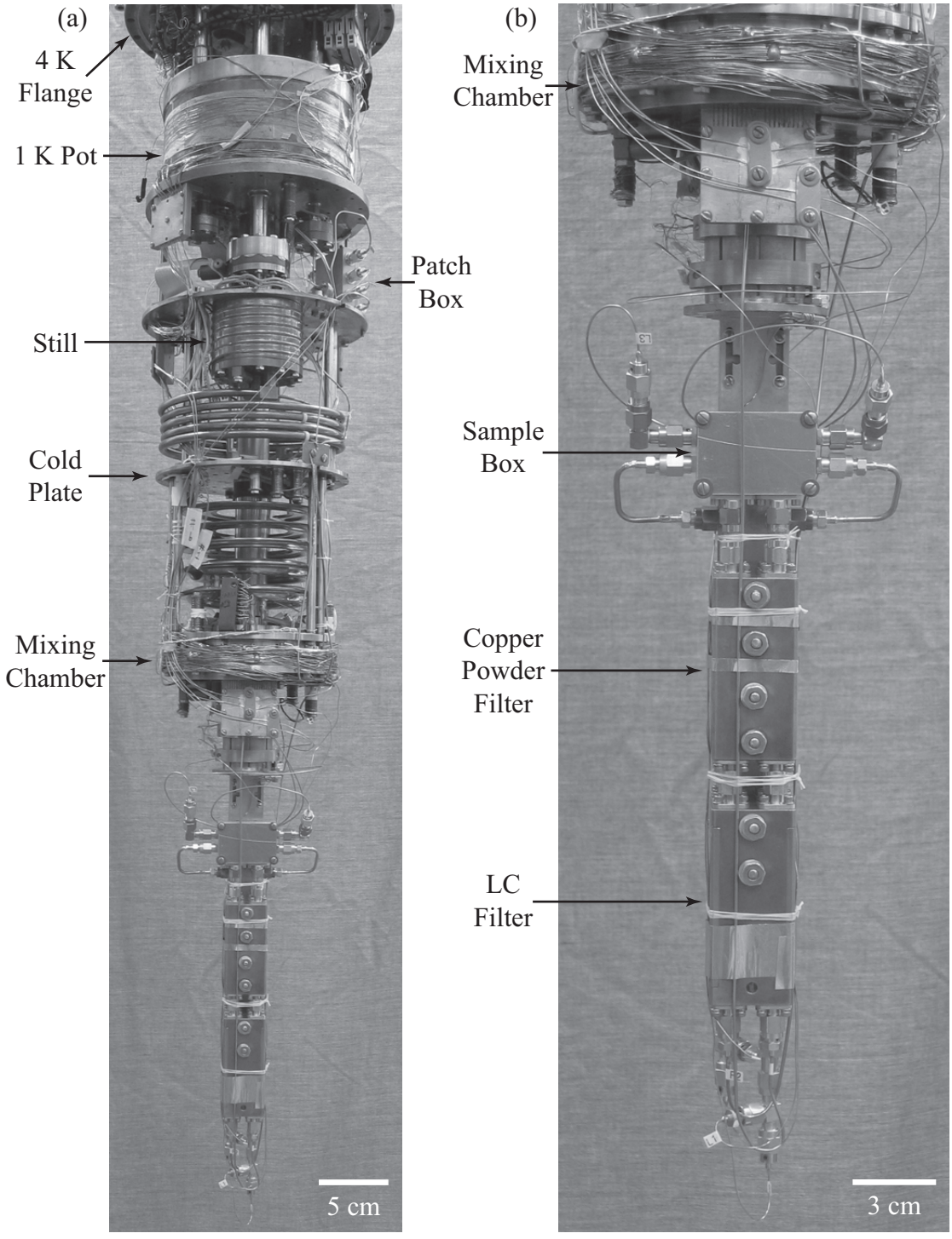

Figure 5.3: Refrigerator photographs. (a) The labeled stages reach progressively colder temperatures, ending with the mixing chamber at 20 mK. (b) The discrete LC filters, copper powder filters, and sample box are attached directly to the mixing chamber. These pictures were taken before run 44, when device DS_2 was studied.

traps before returning to the refrigerator, allowing the system to operate indefinitely, as long as the main ^{4}He bath is replenished every 60 hours. We have been able to stay at base temperature for months at a time, interrupted only by having to clean the traps or service vacuum pumps. There is a small leak into the vacuum can (due to ports for the microwave lines at room temperature and other unidentified sources), so we placed a small amount of absorbing charcoal at the bottom of the can. We have run the refrigerator for well over a year without saturating the charcoal.

As seen in Fig. 5.3(b), the sample box, copper powder filters, and discrete LC filters were each housed in separate metal boxes, to provide some modularity. They were mated with SMA connectors and mounted to the base plate of the mixing chamber with additional copper plates (not seen in the photograph) for mechanical support and thermal contact. The sample box was mounted closest to the mixing chamber, to provide it with the strongest thermal link. This meant that the current and flux lines had to be carefully bent to make connections at the bottom of the LC filters.

We used the system's original vacuum can and thermal shield (bolted to the still plate) that fit inside the small bore of a high field magnet, even though that magnet was removed from the system. For this reason, the filters had to fit within a 2 inch diameter and the lines had to be carefully arranged so as not to cause any thermal shorting.

A superconducting NbTi magnet was mounted on the outside of the vacuum can. The magnet produces 11.13 mT/A, up to a maximum of 50 mT, along the central axis of the refrigerator. It was centered about the sample box, which is described next. The devices were mounted vertically, so that the field was in the plane of the junctions. This magnet was only used for devices LC_2 and DS_1, when we generally applied a field to suppress the critical currents of the junctions. Once adjusted, the magnet was persisted, although the current lines were permanently

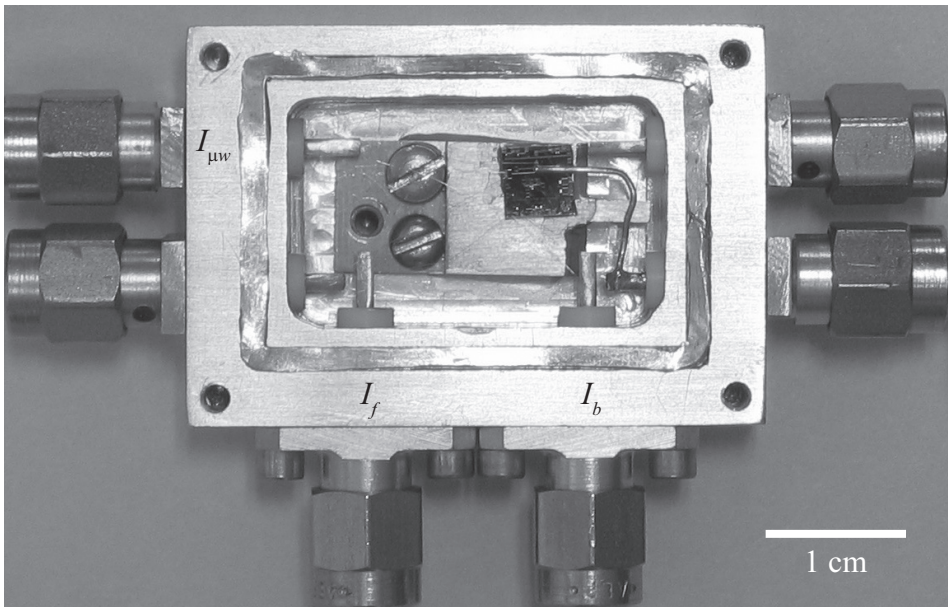

Figure 5.4: Sample box photograph. The dc SQUID phase qubits were mounted in an aluminum box to provide a superconducting magnetic shield at milliKelvin temperatures. Wire bonds connected the center conductor of each SMA connector to the Hypres chip. The chip was mounted to a copper slab to provide thermal anchoring. This picture was taken after run 43, when DS_1 (whose spiral inductor is barely visible in the lower left of the chip) was studied. The bent wire on the right side is an antenna used to couple microwaves to two devices that were wired at the same time.

attached. We never saw any evidence for field drift, but did not check carefully.

A picture of the sample box used for DS_1 and DS_2 is shown in Fig. 5.4. It is an aluminum box, which shields devices from external magnetic fields once it becomes superconducting. Visible in the photograph is an indium O-ring used to complete the shielding when the cover is screwed on. With the refrigerator at 20 mK, we saw no effect on the switching histograms while changing the field of the NbTi magnet. This was somewhat of a surprise, as there are holes in the box where the SMA connectors are mounted, and the switching experiment is extremely sensitive to junction critical currents. The refrigerator had to be heated above 500 mK for the field to penetrate, even though the critical temperature of aluminum is 1.1 K. Upon cooling back down, the critical currents often changed, suggesting that the

field lines in the box moved once the box became superconducting.

A thin layer of GE varnish on the bottom of the sample chip was used to attach it to a small copper plate. In addition, a small amount of silver paint was applied around the edges of the chip to provide a stronger mechanical and thermal connection. The copper plate was screwed into the aluminum box with two brass screws (see Fig. 5.4). For run 44, this plate was thermally anchored to the mixing chamber with a copper wire that passed through a small hole in the box. Al/Si wire bonds connected the SMA center conductors to pads on the chip. The pad(s) for the current return was bonded to the copper plate. A concern for this arrangement is that the presence of the normal metal copper plate under the SQUID could have coupled in magnetic noise, adversely affecting the qubit.

The sample box used for LC_2 was similar in design, but made from copper. It only had two SMA connectors, which was sufficient, because microwaves were coupled to the bias lines through the copper powder filters. As the box was made of copper, it provided less magnetic shielding. This was not a serious issue since the current-biased junctions of LC_2 were not SQUIDs.

5.1.1 Thermometry

Standard resistance thermometers were located on every stage of the dilution refrigerator. Their values were measured using a Picowatt AVS-47 resistance bridge. The data taking computer could communicate using GPIB with an AVS47-IB, which in turn was optically connected to the bridge.[3] This ensured that no digital noise from the computer reached the thermometry lines, which could potentially cause heating in addition to noisy signals.

Originally, a calibrated RuO_2 resistor (denoted $R6$) from Scientific Instruments

[3]We used a LabVIEW program written by Sam Reed to display and log thermometry data. This was particularly useful while initially cooling the refrigerator down.

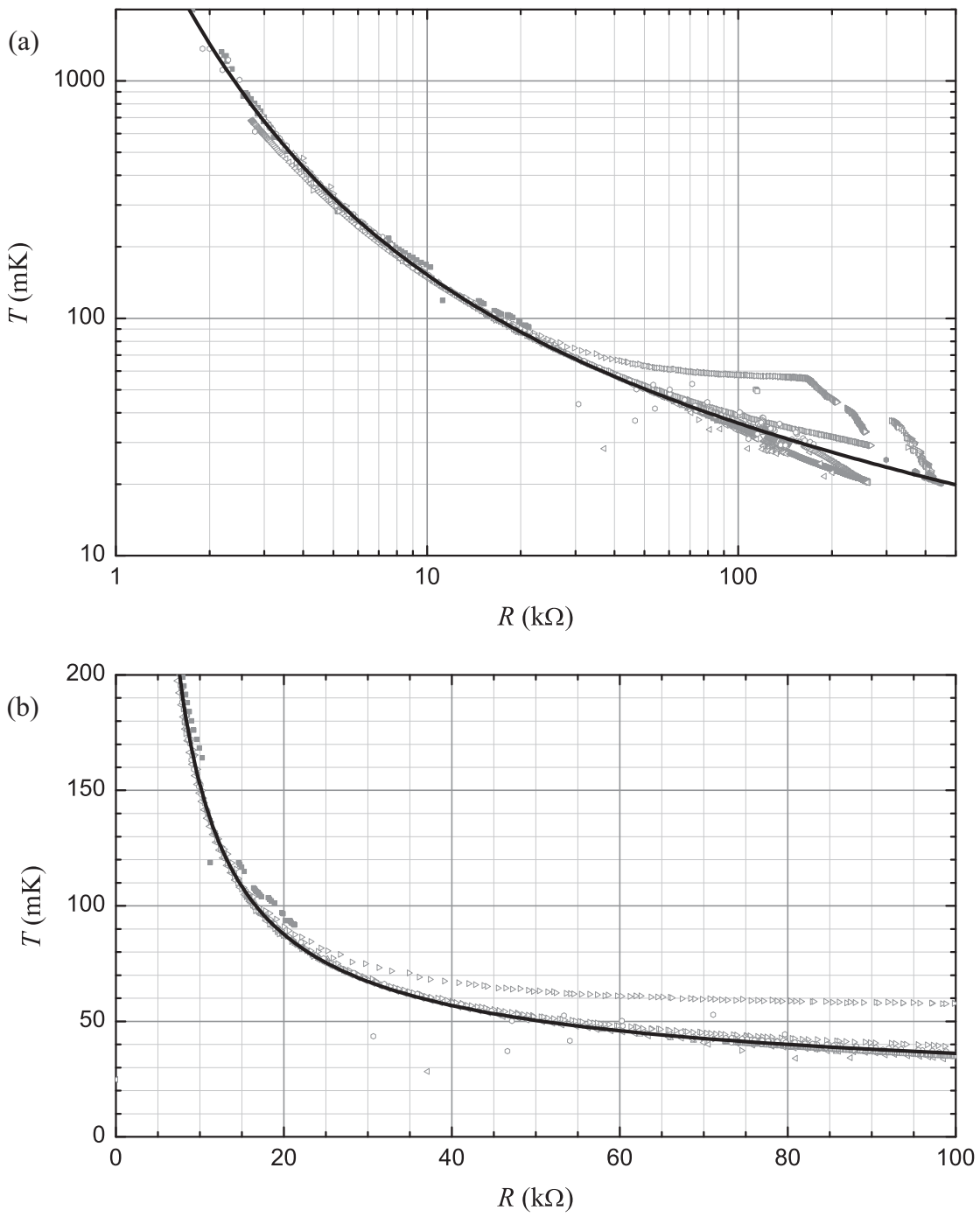

Figure 5.5: Mixing chamber thermometer calibration. The temperature dependence of the resistance of the mixing chamber RuO_2 thermometer, as obtained from a cross-calibration with a commercially calibrated resistor, is plotted on a (a) log and (b) linear scale. Each symbol represents data taken on a different day and potentially different excitation voltage. The spread in the points is indicative of the uncertainty of the fit (solid line) given in Eq. (5.1).

was mounted along side an uncalibrated resistor ($R7$) of the same type on the mixing chamber of the refrigerator. After $R6$ was removed for repair, our main thermometer became $R7$. To determine the temperature, I used a cross-calibration with $R6$, the results of which are shown in Fig. 5.5. The functional form of the fit (provided by the manufacturer) is

$$\ln T = a + \frac{b}{\ln R} + \frac{c \ln R}{R}, \tag{5.1}$$

with a = -7.98, b = 53.2, c = 354, where R is the resistance in ohms and T is the temperature in kelvin.

The spread in the data points is due to incomplete thermalization of the thermometers and varying bridge excitations. However, the majority of the experiments we performed required being well below the energy level spacing of the junction, so knowledge of the exact temperature was not critical. A few experiments did require elevated temperature to create excited state population, so the thermometer calibration was a source of error.

5.2 Current and Flux Bias

The current bias (and the flux bias for the dc SQUIDs) was generated by dropping a voltage across a room temperature resistor, R_b (and R_f); see Fig. 5.1. The voltage came from an Agilent 33120A Arbitrary Waveform Generator (AWG), whose digital-to-analog converter can produce waveforms of 16000 points with a 12-bit vertical resolution.[4] For historical reasons having to do with the design of the voltage detector, I usually used a negative voltage waveform. With the exception of Fig. 5.13, which shows an example of waveforms, I will invert the actual sign of the current and flux bias, which seems more natural. In order to maximize the

[4]The instrument has a serious "phase creep" bug that causes arbitrary waveforms to drift with respect to the sync over the course of hours. It can fixed by sending the command "DIAG:POKE 16,0,1".

signal-to-noise ratio, our goal was to set the voltage of the waveform to about 5 V. Thus, for a typical critical current of 30 μA, R_b was chosen to be about 200 kΩ. Because the required current for the flux line was much higher, $R_f \approx 1$ kΩ.

The bias voltage generally entered the shielded room through a pi-section filter (Spectrum Control 9001-100-1010), with a roll-off frequency near 20 kHz. This filter attenuated high frequency noise that might have been present on the biasing lines and also smoothed out steps in the AWG output. If a higher bandwidth was required (for example, for high frequency flux shaking; see §6.5), the signal entered directly into the shield room, although we could have used a filter with a higher roll-off. For device DS_2, the steps in the waveform did cause a problem, which is addressed below.

A battery-powered buffer amplifier was used inside the room, so that the bias voltage was referenced to the refrigerator (and not the shielded room) to eliminate ground loops.[5] For most of my experiments, an AMP03 differential amplifier with unity gain served as the buffer; see §6.3.1 of Ref. [1] and §4.1.2 of Ref. [3] for circuit diagrams. A single-pole low-pass RC filter was used to remove high frequency components from the buffer output. The roll-off frequency for this was anywhere from 20 to 100 kHz, depending on the situation.

Just before entering the refrigerator, each line was connected to a switch. With the switch closed, the line was connected to the refrigerator wiring. With it open, both sides saw the refrigerator ground. The switches were opened whenever powering up or reconfiguring the room temperature electronics to protect the junction. I forgot to do this several times, with no adverse effects; either I was lucky or the large-area niobium junctions are quite robust.

[5]The efficacy of this can be checked by measuring switching histograms with a very fast repetition rate of an LC-isolated junction and looking for a 60 Hz signal in the time series. However, due to multiple flux states, this is difficult to do with a high β SQUID.

5.2.1 Refrigerator Wiring

The current bias lines entered the refrigerator on coated manganin wires, chosen to minimize the heat load (see Fig. 5.6). The wiring was done in twisted pairs, but we only used one member of each pair, as there were no dedicated returns for each line either "above" or "below" this point. Instead, all currents were returned on the refrigerator itself. The wires were inserted into Teflon tubing and then a Cu/Ni tube, which was placed in a wiring port that ran to the vacuum can; *i.e.* all of bias lines for the devices were in vacuum below the room temperature plate of the refrigerator and were never in direct contact with the helium bath space.

Upon entering the vacuum can, each wire was patched to a length of Thermocoax 1 Nc Ac 05, which was thermally anchored at each stage (1 K pot, still, cold plate) until reaching the mixing chamber of the refrigerator. This coaxial cable has a stainless steel outer conductor, MgO dielectric, and NiCr center conductor.[6] It was designed to be used as a heating element, but has gained popularity in low temperature physics in situations where lines that have high attenuation at microwave frequencies are required [106]. At room temperature, the combination of the manganin and Thermocoax had a dc resistance of 90 Ω.

As we were most concerned with high frequency performance of the Thermocoax, we characterized a section of cable with an Agilent 8722D network analyzer. Figure 5.7(a) shows the transmission coefficient $|S_{21}|$, which gives the attenuation of a signal on the bias line. Above 5 GHz, the transmission is below the noise floor of the analyzer. Thus, Thermocoax provides a simple way to prevent high frequency noise at the top of the refrigerator from reaching the junction.

The network analyzer can also measure the impedance of an element. If a load impedance Z_L terminates a transmission line with characteristic impedance Z_0, the

[6] Over time, several sections of our cable developed shorts on the order of 10 MΩ. It is possible that the dielectric absorbed water; this problem can be avoided by sealing the ends of the cable when putting connectors on it and storing it.

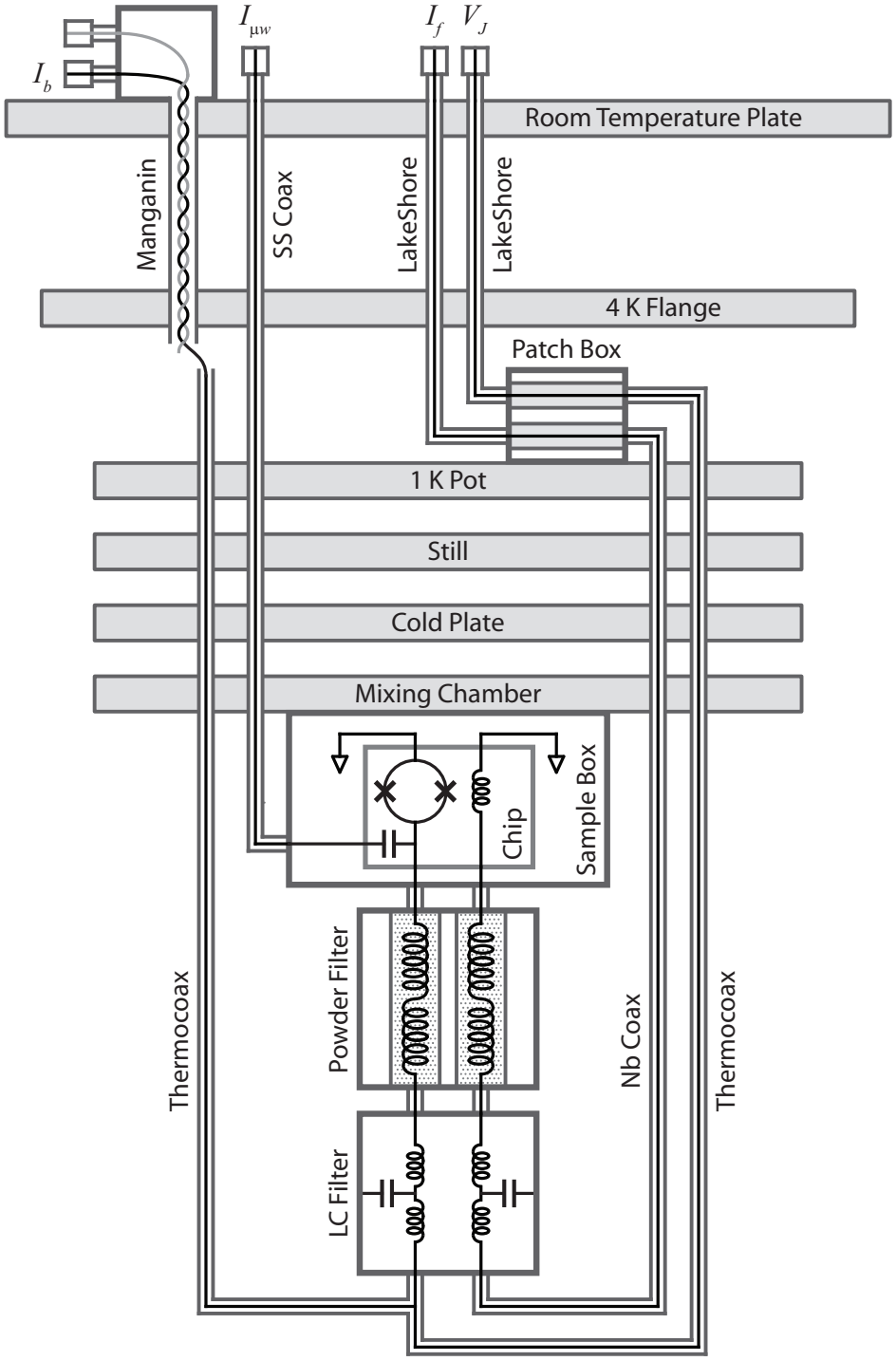

Figure 5.6: Schematic of refrigerator wiring. Lines for the current bias I_b, junction voltage V_J, flux bias I_f, and microwave current $I_{\mu w}$ begin at room temperature at SMA connectors. As they proceed down the refrigerator, they are mechanically clamped to each refrigerator stage, before reaching the SQUID at the mixing chamber. All lines are either commercial coaxial cable or a wire inside of a metal tube. The flux line was not in place for LC_2; all needed lines were duplicated for the coupled devices, LC_2 and DS_2.

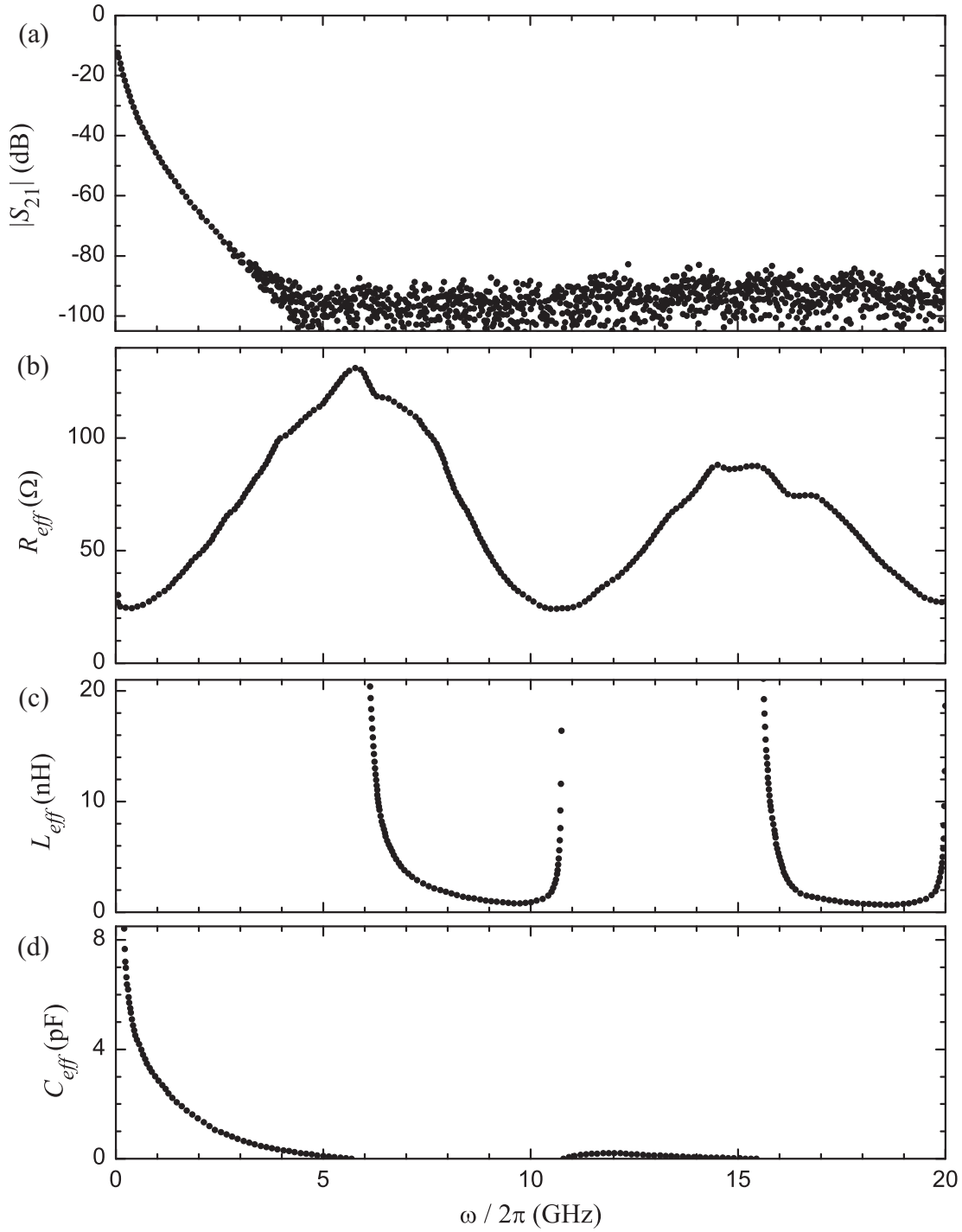

Figure 5.7: High frequency properties of Thermocoax. (a) The measured transmission coefficient $|S_{21}|$ reaches the noise floor of the network analyzer above 5 GHz for an 80 cm length of cable at room temperature. As the analyzer measures voltages, $|S_{21}|$ expressed in dB is given by $20\log_{10}\sqrt{[\mathrm{Re}\,(S_{21})]^2 + [\mathrm{Im}\,(S_{21})]^2}$. The effective parallel (b) resistance R_{eff}, (c) inductance L_{eff}, and (d) capacitance C_{eff} were calculated from S_{11}, using Eqs. (5.3) and (5.4).

complex reflection coefficient is [107]

$$S_{11} = \frac{Z_L - Z_0}{Z_L + Z_0}. \tag{5.2}$$

Here, Z_0 represents the measurement lines of the analyzer and is equal to 50 Ω. By inverting this equation, the resistive and reactive parts of the load are given by

$$R_L = \frac{1 - [\mathrm{Re}\,(S_{11})]^2 - [\mathrm{Im}\,(S_{11})]^2}{[1 - \mathrm{Re}\,(S_{11})]^2 + [\mathrm{Im}\,(S_{11})]^2} \tag{5.3}$$

$$X_L = \frac{2\ \mathrm{Im}\,(S_{11})}{[1 - \mathrm{Re}\,(S_{11})]^2 + [\mathrm{Im}\,(S_{11})]^2}, \tag{5.4}$$

where $Z_L = R_L + iX_L$. For a two-port device (like a section of cable), the value of the one-port impedance Z_L will depend on how the other port is terminated, equaling Z_{sc} if it is short-circuited and Z_{oc} if it is left open. The characteristic impedance of the device is $\sqrt{Z_{sc}Z_{oc}}$ [107]. In the case of the Thermocoax, the attenuation was high enough that the termination had little effect on S_{11}.

The discussion in §4.2 of the impedance that shunts the junction and Fig. 4.2(b) apply here as well. When the analyzer measures S_{11}, port 2 is terminated with 50 Ω, so using S_{11} to calculate Z_L is perhaps a good approximation to the arrangement that the junction sees. The effective parallel resistance and reactance are $R_{\mathit{eff}} = 1/\mathrm{Re}\,(Y)$ and $X_{\mathit{eff}} = -1/\mathrm{Im}\,(Y)$, where $Y = 1/Z_L$. R_{eff} never dips below 20 Ω, as shown in Fig. 5.7(b), and will contribute to the shunting resistance that determines the relaxation time T_1 of the junction. The effective inductance and capacitance are shown in Fig. 5.7(c) and (d). This particular section of Thermocoax has a few resonances and looks inductive near typical junction plasma frequencies.

We avoided using highly resistive manganin and Thermocoax for the flux bias lines of the SQUIDs, in order to avoid excess heating from the large currents required on these lines. For the flux lines, a first section of LakeShore CC-SR-10 coax went

from room temperature to a patch box on the still plate, as sketched in Fig. 5.6. The conductors are made of steel, which is a poor thermal conductor and provided some attenuation to high frequency noise. Inside of the copper patch box, each line entered a small cavity. This design allows for the insertion of a filter. However, we instead just used the box to heat sink each line to the refrigerator's still, which has a large cooling power. This was done by attaching a coated wire to a wall of the cavity with GE varnish.

The rest of the flux bias path was formed using homemade coax.[7] A niobium wire served as the center conductor, which was threaded through Teflon tubing. This combination was inserted into stainless steel tubing that formed the outer conductor. It was difficult to precisely control the geometry with this arrangement, but this line only carried relatively slow signals, so impedance mismatches were not a major concern.

To provide additional protection against high frequency noise, each current and flux bias line passed through an LC filter and a copper powder filter at the mixing chamber of the refrigerator; see §4.2.2 of Ref. [3] and §6.2.2 of Ref. [1] for additional details. The LC filter, shown in Fig. 5.8, is made of discrete components and is designed to have a cut-off frequency near 10 MHz. It was originally designed for use with the LC-isolated qubits and protects the junction over the region where the on-chip isolation fails (see Fig. 4.3). We did, however, use a filter of this sort on each of the current and flux bias lines for the dc SQUID phase qubits, as shown in Fig. 5.6.

Network analyzer measurements of an LC filter are shown in Fig. 5.9. The isolation, as measured by $|S_{21}|$ is not particularly good above 500 MHz. Different filters, made with nominally identical components, had characteristics that were quite different. Of more concern is that R_{eff} drops below 10 Ω at several points,

[7] The coax was designed and assembled by Roberto Ramos.

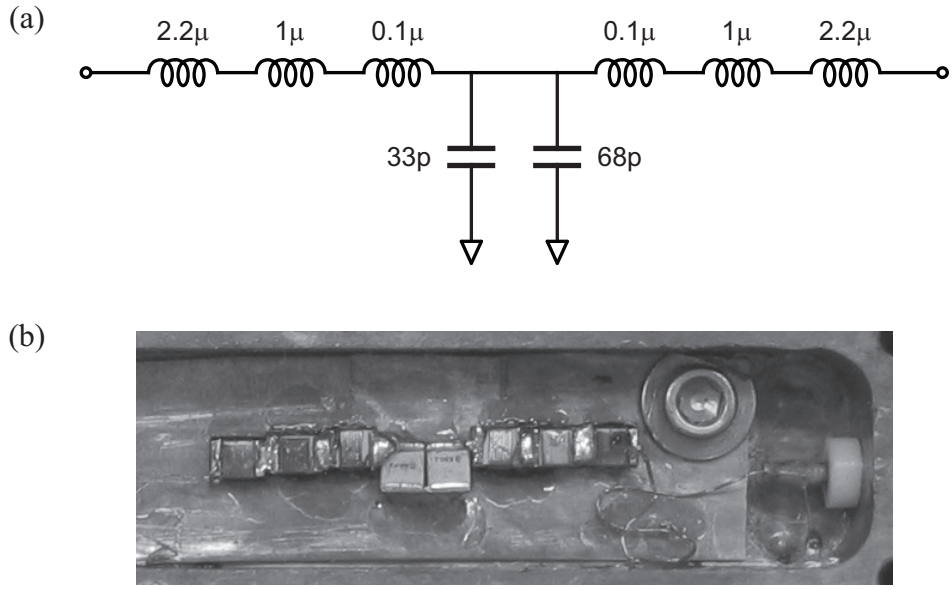

Figure 5.8: Discrete LC bias filter. (a) Each T-filter was composed of six inductors and two capacitors, as shown in the circuit diagram. (b) The photograph shows one of the filters that was used during runs 43 and 44. The components were assembled on a piece of copper foil, which was mounted on a copper housing. This arrangement provides good thermal anchoring for the bias lines.

even though it surpasses 1 kΩ at others. Needless to say, measuring S_{11} of the entire bias line (at operating temperature, rather than in sections at room temperature) would give the most accurate picture of the environment that the qubit and its on-chip isolation see, as each stage of filtering may load others in non-trivial ways.

At very high frequencies, stray capacitance and inductance lead to a failure of the discrete components. To make up for this, we followed the LC filters with copper powder filters (see Refs. [108–110] and §6.2.2 of Ref. [1]). These work by passing a signal wire near small grains of metallic powder. At high enough frequencies, the skin depth becomes comparable to the grain size and the large surface area of the powder leads to strong damping. We used two types of filters. The first, which I will refer to as the "short filter," was used during runs 40 to 43. For run 44, when DS_2 was studied, we were concerned that the filtering of the bias lines was insufficient and switched to the "long filter."

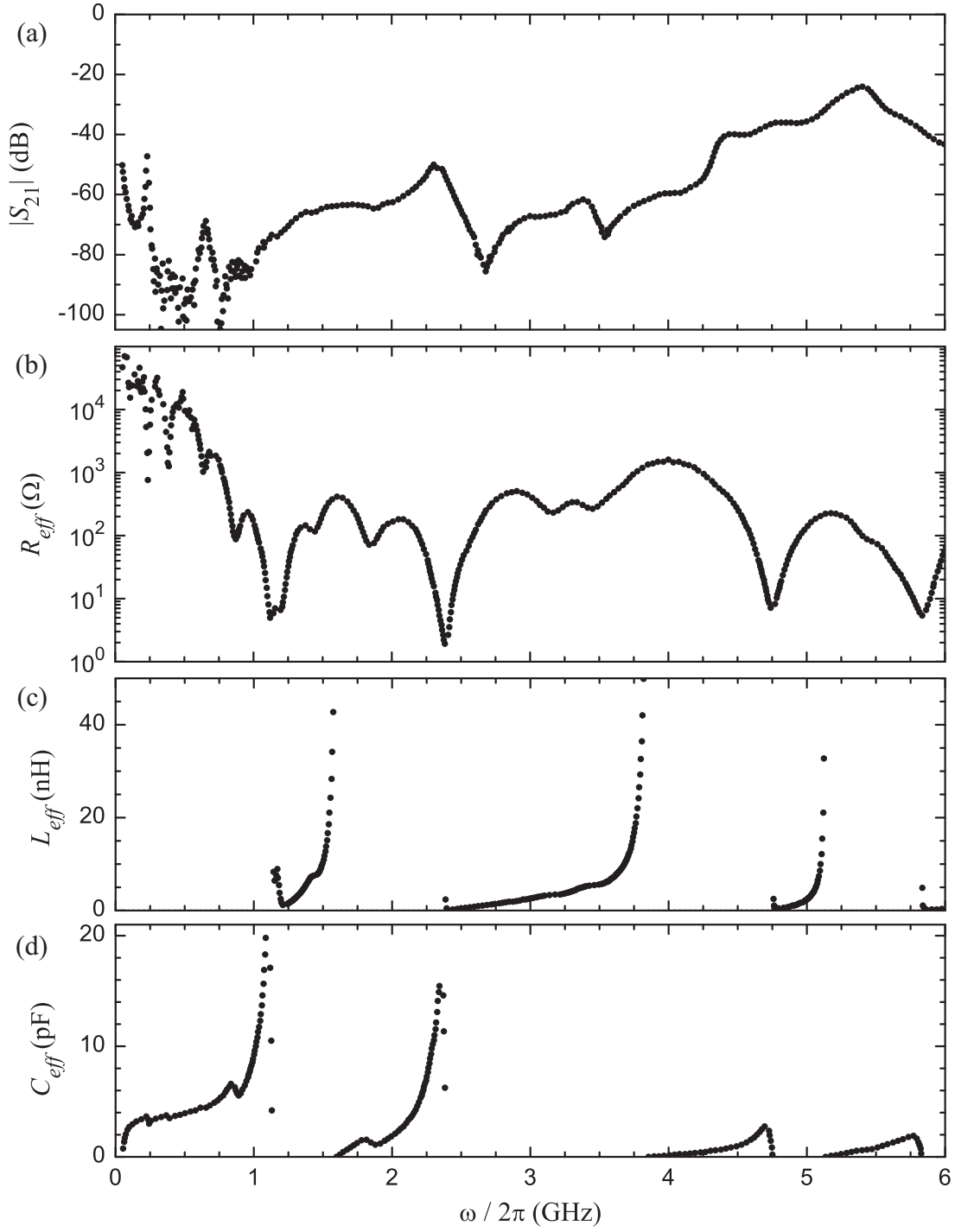

Figure 5.9: High frequency properties of an LC filter. (a) The transmission coefficient $|S_{21}|$, measured by a network analyzer, is small below 1 GHz, but increases as the discrete components fail. The effective parallel (b) resistance R_{eff}, (c) inductance L_{eff}, and (d) capacitance C_{eff} were calculated from S_{11}.

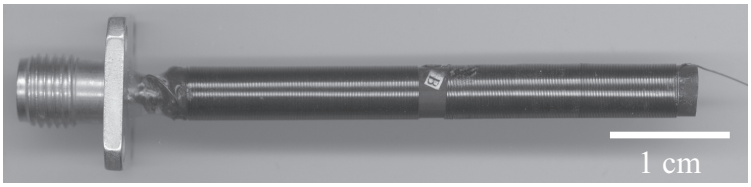

Figure 5.10: Photograph of a long copper powder filter. Niobium wire was wrapped around a core, with a 4.3 mm diameter, formed by Stycast 2850FT and copper powder. The turns reverse direction half-way down the filter to try to minimize pick-up from stray magnetic fields. This piece was inserted into a copper housing and potted with epoxy. Another SMA connector was attached to finish the filter. There are roughly 300 turns, for a total wire length of about 400 cm.

The short powder filter resembled the one described in Ref. [108]. The signal wire passed through a cavity that was filled with a mixture of Stycast 2850FT epoxy and copper powder. For the LC-isolated junctions, microwaves were coupled to the bias line by inserting an antenna into the cavity.

The long powder filter was based on the design presented in Ref. [110].[8] First, a 50-50 mixture (by mass) of Stycast and 200 mesh copper powder was cast into a cylindrical core with a diameter of 4.3 mm. The signal wire (3 mil niobium wire, with a copper cladding) was wound around the core, with the direction of the turns reversed at the midpoint, as shown in the photograph of Fig. 5.10. The assembly was then placed in a hole in a copper housing and filled with more epoxy to provide mechanical stability and thermal anchoring.

Once again, we used the 8722D network analyzer to characterize the filters at room temperature. Results are shown for a short (solid circles) and long (open) filter in Fig. 5.11. It is unclear how the performance of the long filter changes when it becomes superconducting. The extra length of wire increases the attenuation of the long filter over the short one, particularly at low frequencies. Nonetheless, neither filter performs as well as the Thermocoax at 10 GHz. The effective parallel

[8]The procedure was refined with extensive testing, including varying the powder size and density, in our lab by Patrick Detzner, Tristan Guha-Gilford, and Tara McCarron.

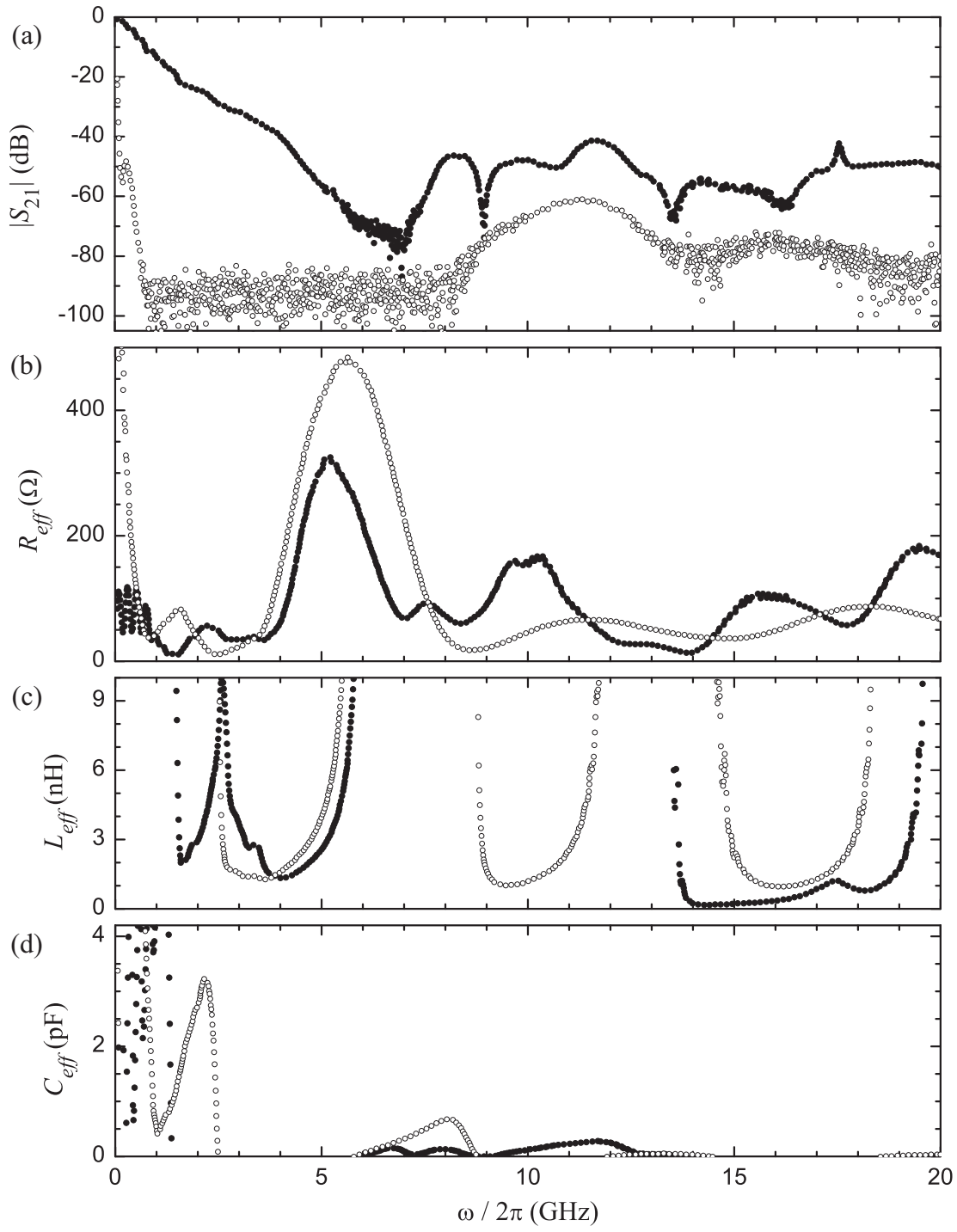

Figure 5.11: High frequency properties of copper powder filters. A network analyzer was used to measure a short (solid circles) and long (open) filter at room temperature. (a) The transmission coefficient $|S_{21}|$ is smaller for the long filter over the entire frequency range. The effective parallel (b) resistance R_{eff}, (c) inductance L_{eff}, and (d) capacitance C_{eff} were calculated from S_{11}.

impedances are plotted in Fig. 5.11(b)-(d). As the sample box was directly attached to the copper powder filters, it is possible that R_{eff} for this filter set the bare noise resistance R_{bn} in Fig. 4.2(a). Unfortunately, R_{eff} varies from an acceptable 400 Ω to less than 20 Ω at several frequencies, which could result in a high level of dissipation.

At a typical plasma frequency of 5 GHz, the filtering on the bias lines appears to provide a total of at least 200 dB of attenuation. I tested this by using a bias tee at the top of the refrigerator to couple a microwave current onto the current bias line during run 44.[9] Even with a source power of 1 μW at 5 GHz, no change was observed in the switching histograms. A signal of this strength on the dedicated microwave line would have produced a Rabi oscillation in excess of 500 MHz. To test the efficacy of the shielded room, we performed several experiments with its door open. This never had an observable impact on Rabi oscillations, which are the most sensitive measurement that we performed. The high level of attenuation on the bias lines may be sufficient at the present time. (The shielded room did provide acoustic isolation, which lead to greater stability for the refrigerator.) It is puzzling, then, why we saw clear evidence for high frequency noise at frequencies above ω_p on the bias lines, as discussed in §7.2. This suggest that the noise was not coming from room temperature, but from a source within the refrigerator that still needs to be investigated.

The behavior of the filters at lower frequencies is also of interest. Figure 5.12 shows the voltage-biased transfer function of the long copper powder filter (dashed), LC filter (dotted), and both filters in series (solid), measured with the circuits drawn as insets. The usual AWG was used to provide an oscillating voltage $V_s \cos(\omega t)$, where $\omega/2\pi$ was limited to 15 MHz. A Tektronix TDS 3054B oscilloscope measured the input voltage $V_i \cos(\omega t + \theta_i)$, output voltage $V_o \cos(\omega t + \theta_o)$, and phase shift

[9] I recommend saving this test for the end of a run. When I lowered the drive frequency to roughly 1 GHz, the critical currents of the junctions suddenly changed during one of events obliquely referred to in §4.3.2.

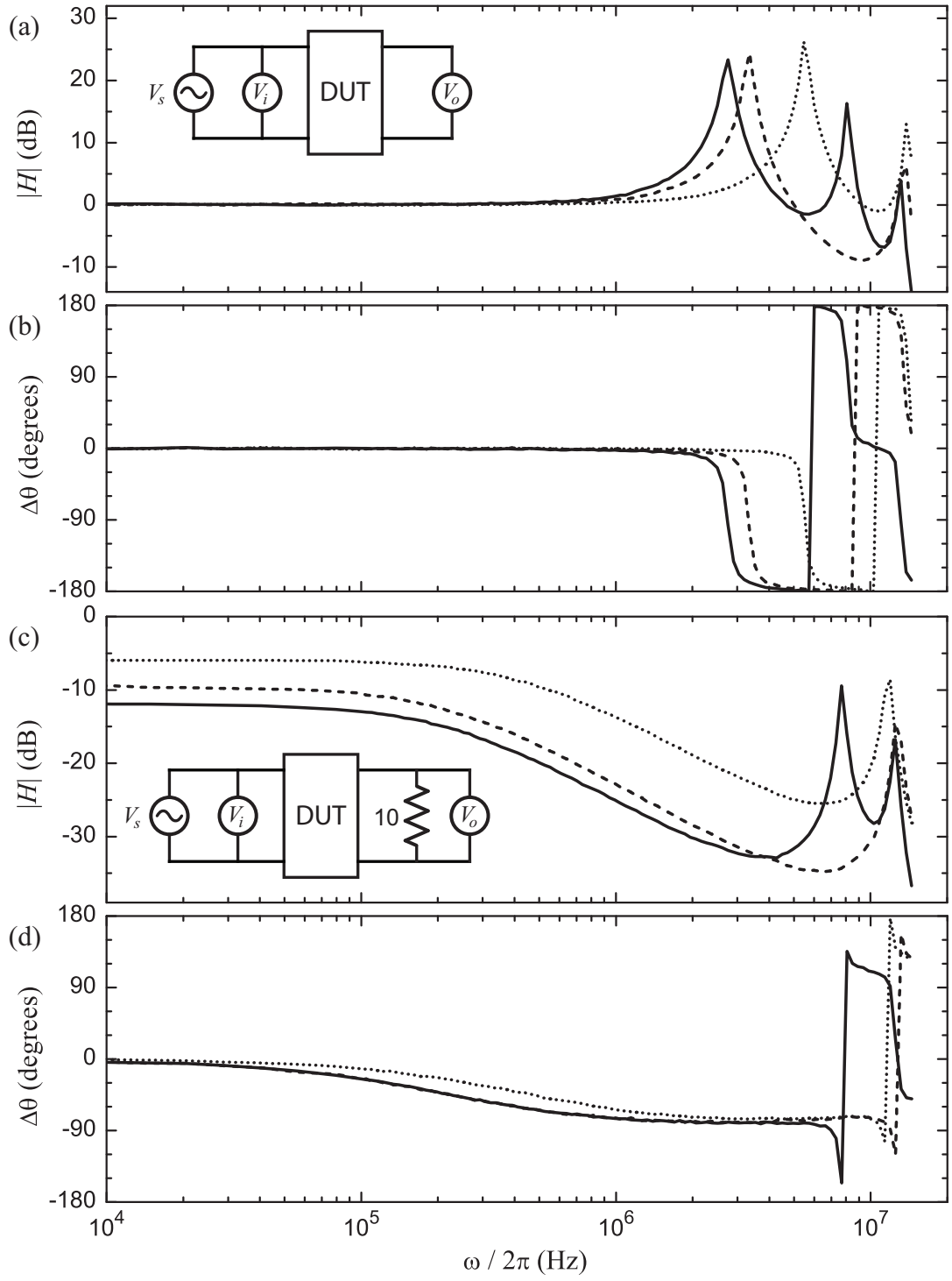

Figure 5.12: Low frequency properties of the bias filters. The measured (a) magnitude and (b) phase of the transfer function $H = V_o/V_i$ for the long powder filter (dashed), LC filter (dotted), and combination of the two (solid) is plotted as a function of frequency. (c), (d) The attenuation of the filters is visible when a load of 10 Ω is placed on their outputs.

$\Delta\theta = \theta_o - \theta_i$. I used this simple configuration to measure several of the components in the experiment. To accurately determine their behavior, however, the input and output impedances would have to be set the values actually seen in operation.

The magnitude of the transfer function $H\,(\mathrm{dBm}) = 20\log_{10}(V_o/V_i)$ is plotted for (a) an open circuit and (c) with a 10 Ω load to simulate the junction. The attenuation below 1 MHz in the latter case is nearly the same for both filters, suggesting that this was due to the measurement set-up. A current-biased measurement might have given more accurate results. The most prominent features in all cases are the sharp resonances near 10 MHz. In the case of the powder filter, I believe these are due to the inductance and stray capacitance between the large number of closely spaced windings in the filter. Further testing is needed to determine the positive and negative effects of the various forms of filtering.

5.2.2 Biasing of DS_2

Three additional factors affected the biasing of DS_2, which had two coupled SQUIDs. The first had nothing to do with the device itself, but the filtering used when it was studied. The long copper powder filters installed before run 44 introduced an LC resonance that could be excited by the steps in the discretized output of the AWG for the flux current. The resulting switching histograms [calculated with the technique discussed in §6.2] had numerous spikes, rendering them useless. To overcome this, we low-pass filtered I_f^A and I_f^B (where the superscript distinguishes the two SQUIDs, DS_2A and DS_2B) with the pi filters at the shielded room wall and, at times, with additional RC filters.

Although the current bias lines were filtered with the same sort of copper powder filters, current steps on these lines did not appear to have easily detectable adverse effects. Nonetheless, as we almost always wanted $I_b \propto I_f$ (for reasons discussed in §6.4), it was convenient to filter I_b the same way as I_f.

The second problem was that this device showed very strong heating effects when a junction was left in the voltage state. This could be remedied with a slow repetition rate (50 Hz or so), which made data taking quite inconvenient. Alternatively, the rate could be increased to over 200 Hz if the junction was forced to retrap within a few microseconds of tunneling. While this could have been accomplished with additional circuitry [111], we chose to include the quick shut-off in the I_b waveform, so that the device saw identical biasing on every cycle. For example, when DS_2B was left in the voltage state for about 300 μs (corresponding to a dissipation of 22 pJ) with a repetition rate of 230 Hz at 20 mK, the escape rate was nearly identical to what was measured at 95 mK when the junction was forced to quickly retrap. I do not know why this effect in SQUID DS_1 was far less pronounced.

It was impossible to force a quick retrap when the bandwidth of the current bias lines was reduced by the pi filter. Therefore, we used pi filters on the flux lines[10] and left the bias lines unfiltered at room temperature. As the current and flux lines then had different bandwidths, the waveforms for the AWGs had to be modified to give $I_b \propto I_f$ after the filters.

Finally, the cross mutual inductances between the two devices were large enough to cause problems. Ideally, when performing an experiment with coupled qubits, we would have liked to determine the biasing of each device independently. The current return line and proximity of the devices of DS_2, as discussed in §4.3.2, made this impossible.

To address the second problem, I first measured the complex transfer function $H(\omega)$ of each of the four bias lines between the AWG and the bias resistor R.[11] Imagine that the goal was to have $I_f = mI_b$. I first chose a voltage time series $W_b(t)$ that the AWG for the current bias would output, which was generally some

[10]Because of the reduced bandwidth, I_f decayed to zero relatively slowly at the end of each cycle. However, as it is only I_b that controls retrapping, this had no effect on heating.

[11]In making these measurements, it was quite important to consider the phase shift across the output impedance of the AWG, as well as the filters and bias resistor.

sort of ramp. A prediction for the current that this generates comes from taking a fast Fourier transform, applying the transfer function, and transforming back:

$$I_b(t) = \frac{\mathrm{FFT}^{-1}\left(H_b(\omega)\,\mathrm{FFT}\left(W_b(t)\right)\right)}{R_b}. \tag{5.5}$$

I used LabVIEW's Complex FFT.vi and Inverse Complex FFT.vi to do this calculation, but kept only the positive frequency components to force the answer to be real-valued. The voltage time series for the flux bias AWG was then set to

$$W_f(t) = \mathrm{FFT}^{-1}\left(\frac{\mathrm{FFT}\left(I_f(t)\,R_f\right)}{H_f(\omega)}\right), \tag{5.6}$$

where $I_f(t) = mI_b(t)$ in this case.

As the bandwidth of the current bias line was higher than than of the flux bias, I tried to "round" $W_b(t)$ to remove high frequency components. I did not use any sophisticated algorithm to do this, so if all of the Fourier components were kept in Eq. (5.6) (the Nyquist frequency of the time series was generally about 2 MHz), the resulting $W_f(t)$ oscillated quite a bit. Therefore, I usually cut the transforms off above 100 kHz. This procedure worked reasonably well (in that a high repetition rate yielded nearly smooth histograms with none of the signatures of heating) and was used for much of the data that will be presented on DS_2.

Biasing both of the devices at the same time proved to be more of a challenge. Again, I first selected voltage waveforms for the current biases and calculated $I_b^A(t)$ and $I_b^B(t)$ using Eq. (5.5). If the goal had been to bias either of the devices individually, then the necessary flux currents would have been $I_{f0}^A(t) = m^A I_b^A(t)$ and $I_{f0}^B(t) = m^B I_b^B(t)$. In order to produce the corresponding fluxes in both devices simultaneously, Eq. (4.13) yields

$$I_f^A(t) = \frac{M_f^{BA}\left(M_b^{AB}\ I_b^A - M_f^{BB}\ I_{f0}^B\right) - M_f^{BB}\left(M_b^{BA}\ I_b^B - M_f^{AA}\ I_{f0}^A\right)}{M_f^{AA}\ M_f^{BB} - M_f^{AB}\ M_f^{BA}} \tag{5.7}$$

$$I_f^B(t) = \frac{-M_f^{AA}\left(M_b^{AB}\ I_b^A - M_f^{BB}\ I_{f0}^B\right) + M_f^{AB}\left(M_b^{BA}\ I_b^B - M_f^{AA}\ I_{f0}^A\right)}{M_f^{AA}\ M_f^{BB} - M_f^{AB}\ M_f^{BA}}, \qquad (5.8)$$

where each of the currents is a time series. As the same current biases are used for both the independent and coupled situations, M_b^{AA} and M_b^{BB} do not enter these expressions. The voltage waveforms for both of the flux AWGs were then found by using Eq. (5.6).

The coupled spectra of §8.6 were produced with flux waveforms generated with this procedure (see Fig. 5.13). In this experiment, device DS_2A was first quickly ramped and then slowly ramped starting at 500 μs. DS_2B was linearly ramped so that the qubits were degenerate at 780 μs. After the bias was reset to allow the junctions to retrap, flux shaking (see §6.5) was used to simultaneously initialize the flux state of each device.

Figure 5.13(a) shows the waveforms output by the flux AWGs. The inverse Fourier transforms used to calculate them yielded many high frequency components, particularly in producing the nearly flat section for DS_2A. When I measured the currents at the bias resistors [see Fig. 5.13(b)], these components had been filtered out and the waveforms matched those for the current bias. That the flux shaking oscillations do not begin with a constant amplitude shows that the procedure has flaws. The flux applied to each SQUID predicted by Eq. (4.13) (using measured values of I_b^A, I_b^B, I_f^A, and I_f^B) is plotted in Fig. 5.13(c). Notice that because I_f^A has a large effect on DS_2B, a bi-linear I_f^B must be used to get a linear Φ_T^B. Also, because M_f^{BB} was rather small, I_f^B was somewhat large to be sending to the mixing chamber of a dilution refrigerator. The superconducting coax used for this line worked quite well; although the sample thermometer did register a small increase, there were minimal signs of heating in the data. Incidentally, the little jump in Φ_T^B near 780 μs is due to both current biases being shut-off, as this is the time that the junctions tunneled to the voltage state.

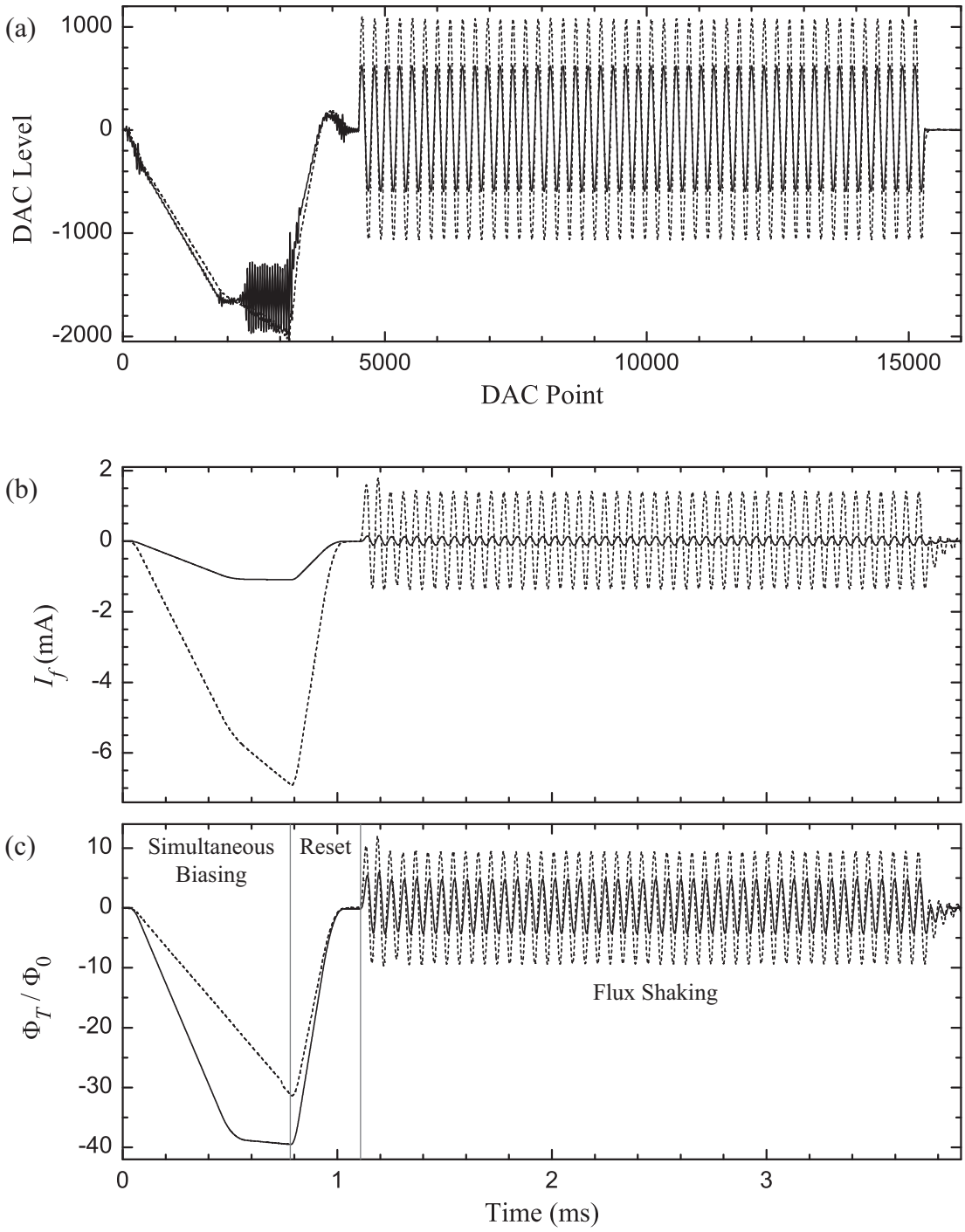

Figure 5.13: Avoided crossing biasing of device DS_2. (a) The waveforms used by the AWGs for the flux bias of DS_2A (solid) and DS_2B (dashed) have many high frequency components. (b) These components are filtered out at the shielded room wall and are not seen in I_f^A and I_f^B, as measured at the top of the refrigerator. (c) The predicted flux biasing, which takes into account cross mutual inductances, roughly stabilizes DS_2A, while DS_2B is linearly ramped.

The idea behind this process was to be able to set the biasing of each device independently and then combine them so that both SQUIDs would switch to the voltage state at the same time. In practice, they would miss by as much as 100 μs for the sort of waveforms shown in Fig. 5.13. Because of the shallow slope used for DS_2A, a small error in the flux level would lead to a large shift in the switching time. Therefore, a fair bit of trial and error was used to arrive at waveforms that produced a good degeneracy. A large source of error is that I was only able to measure the transfer functions of the lines and the currents at the top of the refrigerator. The hope was that the cold filtering did not greatly affect the relatively low frequency waveforms. The origin of the significant error in the coupled biasing remains somewhat of a mystery.

5.3 Microwaves

The microwave current $I_{\mu w}$ was generated by Hewlett-Packard 83731B and 83732B synthesized sources. The 1 Hz resolution and 1.5×10^{-9} fractional drift per day of the 83732B were far better than we required. The one feature that we did take advantage of was a TTL gate that could produce a pulse of under 10 ns, for frequencies above 1 GHz. While this gate was convenient to use, more sophisticated pulse shaping will ultimately be required for quantum operations [112, 113].

The pulses that gated the microwaves were created by a Stanford Research Systems DG535. The instrument has the unique combination of a long total time range of 1000 s with a remarkable 5 ps precision. The rise time of the pulse is a rather slow 3 ns, but this did not cause any noticeable effects. As described in the beginning of this chapter, we used a logical AND between the pulse and a dc level from the computer (from the digital output of a National Instruments PCI-6110 data acquisition card) to interleave data with and without microwaves. A CD74HCT132E chip was used to do this and a faster chip might have improved the

timing resolution.

Inside the refrigerator, we used coaxial cable for the microwave lines. Initially, there were multiple segments of coax with filters inserted along the way, to protect the junction from noise and to thermalize the center conductor. However this introduced impedance mismatches along the path, which gave the lines a strong frequency dependence. Starting with run 41, a single length of UT-34-SS-SS coax went from the room temperature plate to the mixing chamber, as shown in Fig. 5.6. The stainless steel outer and center conductors offered some attenuation. The outer jacket of the cable was clamped to the refrigerator at multiple stages, allowing some cooling of the center conductor through the Teflon dielectric. At room temperature, each line had a dc resistance of 50 Ω.

5.4 Voltage Detection

The success of the escape rate measurement hinged on the ability to precisely detect when a junction switched to the voltage state. During run 40, the voltage of the junctions was measured on the same line that provided the current bias. In this two-wire configuration, there was a significant contribution to the total voltage from the drop along the bias line, due its relatively resistive manganin section. Nonetheless, it was still possible to detect the switch by looking for the fast edge that it produced. In addition, the Johnson noise due to the manganin section was large enough to limit the timing resolution of the experiment.

Starting with run 41, a dedicated line was used to measure the voltage across the device (see Fig. 5.6). The upper section of this line was LakeShore CC-SR-10 coax, which went to the patch box on the still plate, just as with the flux bias lines. Its stainless steel center conductor was less resistive than the manganin wire, but still not too thermally conductive. From the box, roughly 1 m of Thermocoax was used to go to the mixing chamber, where the current bias line was tapped. At room

temperature, the dc resistance of the LakeShore and Thermocoax sections were 8 and 60 Ω, respectively. The resistance on the current bias line from the voltage tap to the junction was under 1 Ω when the refrigerator was cold. At the mixing chamber, noise on both the current bias and voltage lines was attenuated by a length of Thermocoax, a discrete LC filter, a powder filter, and on-chip isolation.

As the gap $2\Delta/e$ in Hypres-deposited niobium is only 2.8 mV, it was necessary to amplify the voltage across the device at room temperature before it could be used to trigger the timer to stop. At different times, we used a combination of commercial (usually a Stanford Research Systems SR560) and homemade amplifiers. For the data that I will present, the most common choice was two stages of homemade circuits. Although they had fixed gain and bandwidth, their voltage noise was lower than any commercially available instrument we could obtain. See §4.1.4 of Ref. [3] and §6.3 of Ref. [1] for detailed descriptions and circuit diagrams.

A common-source JFET inverting amplifier was used as the first stage. The voltage noise of the amplifier was reduced to less than 0.3 nV/$\sqrt{\text{Hz}}$ by using sixteen 2SK117 transistors wired in parallel. The transfer function, measured with the same procedure that produced Fig. 5.12(a), is shown in Fig. 5.14(a). The bandwidth is about 5 MHz.

The first stage's gain of 40 is not quite sufficient to produce a voltage that is easy to monitor. Therefore, we followed the JFET amplifier with a second stage that used an AD829 op-amp inverting amplifier. The transfer function of this stage alone is shown in Fig. 5.14(b). The gain is about 50 above 10 kHz and rolls off above 1 MHz, due to the open-loop gain of the op-amp. The input of the amplifier has a 10 kHz high pass filter, created with an additional AD829, that serves two purposes. For one, it removes the roughly 5 V offset created by the dc biasing of the JFET amplifier. In addition, it minimizes the contribution to the voltage measured at the top of the refrigerator due to the drop along the bias lines.

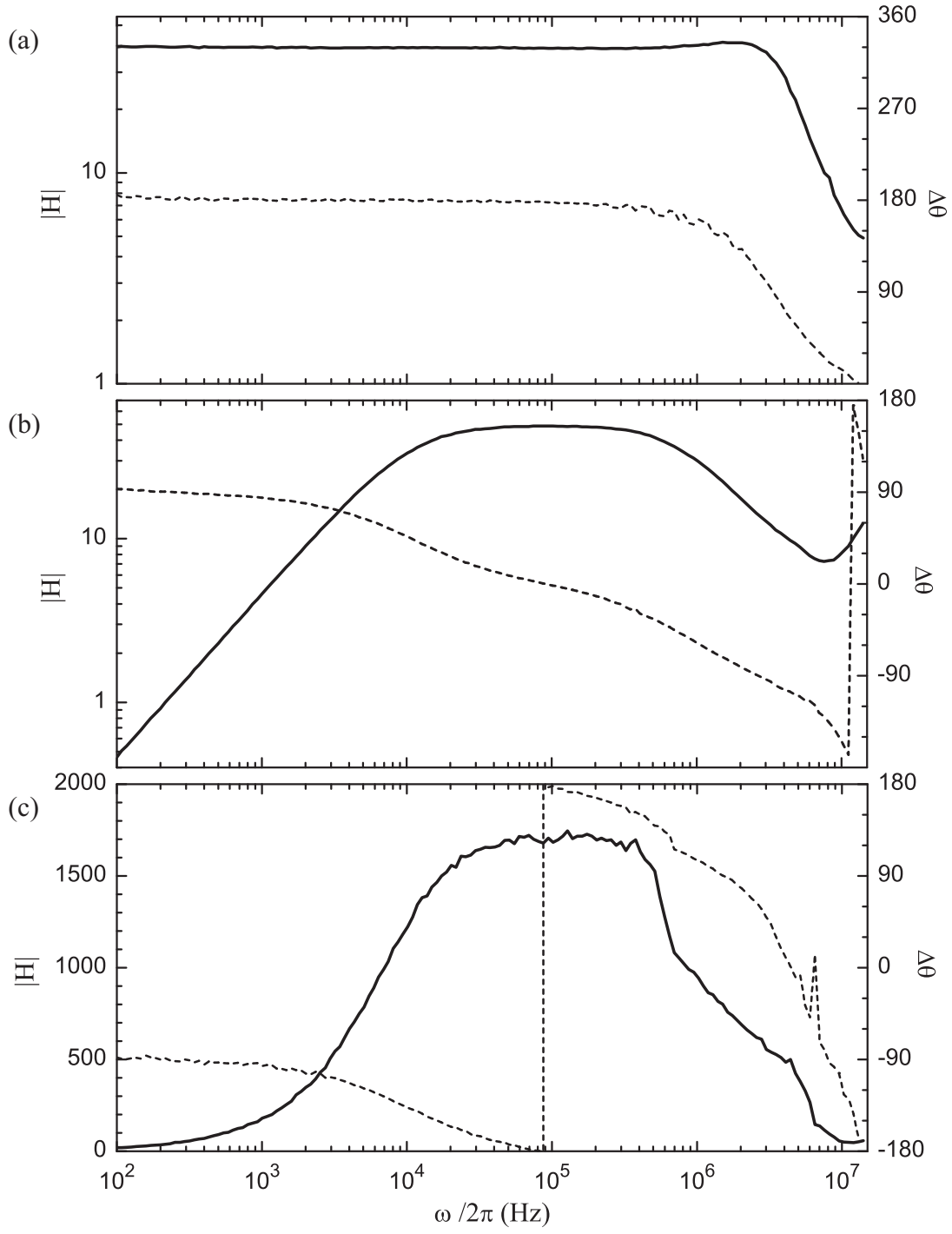

Figure 5.14: Gain and phase shift of the homemade voltage amplifiers. Measurements are shown for the (a) first stage amplifier, (b) the second stage amplifier, and (c) the two in series, where in each plot the left axis corresponds to the gain $|H|$ (solid line) and the right to the phase shift $\Delta\theta$ (dashed line).

The gain of both amplifiers in series is shown in Fig. 5.14(c). The maximum value of 1700 amplified the junction voltage to nearly 5 V, which was convenient to work with. To further improve the amplifier performance, both stages used battery-operated low noise power supplies that were regulated with active feedback.

The amplifiers produced a large voltage step when the junction switched to the running state. The final step was to get this signal from the amplifiers at the top of the refrigerator to the timer located outside of the shielded room. If we had done this by sending the amplified junction voltage directly to the timer, we would have had to filter the signal at the shielded room wall to prevent noise and grounding problems. Unlike the biasing lines, which carry relatively low frequency signals, we wanted a very high bandwidth on the voltage detection line. Therefore, we converted the output of the amplifiers to a digital signal by sending their output to a Schmitt trigger (*i.e.* a comparator with hysteresis), made from a high speed CLC420 op-amp. When the trigger's input decreased below an adjustable negative value, it produced a pulse that drove an LED, which in turn was coupled to an optical fiber. The fiber left the shielded room through a narrow waveguide and coupled to an optical receiver. The signal was finally converted to a TTL-compatible pulse with another CLC420.

5.5 Timing

The escape rate measurement required currents and voltages from a variety of instruments (see Fig. 5.1) that were physically separated by non-negligible distances. Precisely determining the temporal relationship between the different signals is somewhat involved. Figure 5.2 shows what the signals qualitatively look like for one cycle of the experiment where a microwave pulse excites the junction, forcing it to escape to the voltage state. The profiles are not drawn to scale and I have changed some of their polarities for clarity.

A cycle started when the bias AWG (Agilent 33120A) received a positive TTL edge from the master clock, a Dynatech Nevada Exact 628 function generator. To protect the AWG from noise, the clock was first sent to a 6N137 inverting optoisolator. The master clock's square wave output had a period that varied noticeably at times. In addition, the AWG had a 25 ns jitter on its trigger input. The origin of time, however, was set by the sync output of the AWG (not the master clock), so any delays or jitter in triggering the AWG are unimportant. The trigger jitter does limit the synchronization of multiple AWGs.

The sync output signal from the AWG was sent to the start input of a Stanford Research Systems SR620 universal time interval counter ('Timer' in Fig. 5.1). This instrument can measure the time between two voltage edges with a resolution of 4 ps. Again, to protect the AWG, its sync was optoisolated. This both delayed the edge (not important) and increased its risetime from 2 ns to about 40 ns, depending on what the output was connected to. As indicated by a dashed line in Fig. 5.2(a), the start trigger of the timer was set to the voltage where the sync output was rising most rapidly, in order to minimize the effect of the slow risetime. In addition, we usually ac coupled this input, to minimize trigger waveforms from slow fluctuations due to the instrument being line powered.

It was critical that the output of the AWG was synchronized with its sync; I measured the jitter to be better than 100 ps (by using the timer in a simple experiment). The bias current was (usually) filtered at the shielded room wall, buffered, and filtered again. This lead to a distortion of the waveform. For a particular value of the current, this can be thought of as a time delay t_b for the current bias just before it entered the refrigerator, as shown in Fig. 5.2(b). The signal was further distorted by the wiring and filters in the refrigerator; as these were designed to cut off much higher frequencies, the effective delay t_c at the device was not expected to be too different from t_b.

For Rabi oscillation experiments, I also needed to switch on the microwaves at a specified time. The process started when the pulse generator was triggered by the AWG sync (see Fig. 5.1). In conjunction with a dc level from the computer and a logical AND gate, the generator created a dc pulse that gated the microwave source. The source outputted a microwave pulse as well as a TTL 'video out' signal that was held high for the duration of the pulse. The video out, drawn in Fig. 5.2(d), was a 5 V signal we could easily measure. There was a delay and jitter on the pulse generator's trigger, its output, the inputs and outputs of the AND gate, the gate of the microwave source, and its video out. These can all be taken into account by measuring the video out and defining the pulse to start at t_d. The jitter on t_d, due to the full chain of instruments, is less than 200 ps (and much of this could be due to the timer, which was used to measure the value).

There is a delay ($<$ 100 ns, according to the manufacturer's specifications) and jitter between the microwave source's video out and its rf output, propagation delay along roughly 5 m of room temperature SMA cable, delay and distortion on the stainless coax in the refrigerator, and an impedance mismatch at the sample. All of this leads to the pulse appearing at the junction at a time t_e that is delayed with respect to the original trigger signal from the AWG sync.

I will make the assumption that I_b and $I_{\mu w}$ are sufficiently high to force the junction to switch to the running state immediately at t_e. I will also ignore the very short time that it takes for an unshunted junction to reach the gap voltage (of order $C_J\left(2\Delta/e\right)/I_0 \approx 1$ ns). In order for our amplifiers to detect the switch, however, the discrete LC filter and about 2 m of cable in the refrigerator had to be charged to the gap voltage. This lead to a relatively slow rise in the voltage V_b at the top of refrigerator, as indicated by Fig. 5.2(f).

Figure 5.15(a) shows measurements of V_b as a function of time when junction LC_2A switched to the voltage state, taken with a Tektronix TDS 1002 oscilloscope

during run 41, at 20 mK. For this plot, I averaged the data to remove bit noise in the traces. With the oscilloscope (set to a 1 MΩ input impedance) connected directly to the voltage line (dashed line), the signal reaches a maximum in 300 ns. The initial slope of the voltage and the noise on the line set the resolution for determining the switching time. The scope averaged 128 traces and the sharp feature at the maximum voltage is an artifact of the triggering. The 1.5 MHz ringing that follows is due to the excitation of a resonance, although I was not able to identify the components that were producing it.

With an SR560 amplifying the voltage [solid line in Fig. 5.15(a)], the charging time is longer. In making this plot, I divided the trace by the gain of the amplifier (100), so the slope of the output signal in V/s is actually quite a bit higher than the direct measurement. However, the bandwidth and input capacitance of the amplifier do slow the output signal.

The open circles in Fig. 5.15(a) show the (ac coupled) output of the first stage FET amplifier, again scaled by its gain. With its 1 MHz bandwidth, this amplifier further slows the signal. While the charging time is perhaps a bit shorter than for the SR560, the maximum scaled slope is definitely smaller. The high frequency ringing has also been attenuated. Finally, the solid circles show the scaled output of the two-stage homemade amplifier. The charging time has been increased even further and the signal decays due to the high pass filter on the second stage.

The voltage noise at the amplifier output and the switching slope set the resolution for determining the switching time. By measuring the voltage line directly with an oscilloscope, the noise was under 150 μVrms[12] and the maximum slope was about 20 mV/μs, corresponding to a timing resolution of less than 7.5 ns. The output of the SR560 with a gain of 100 (and the input hooked to the voltage line)

[12]The dashed line in Fig. 5.15(a) was taken with averaging on the oscilloscope, which is why it looks very quiet. I made some of the voltage noise measurements well after the curves in that figure were taken. As the instrumentation was nearly identical, the values should be fairly accurate.

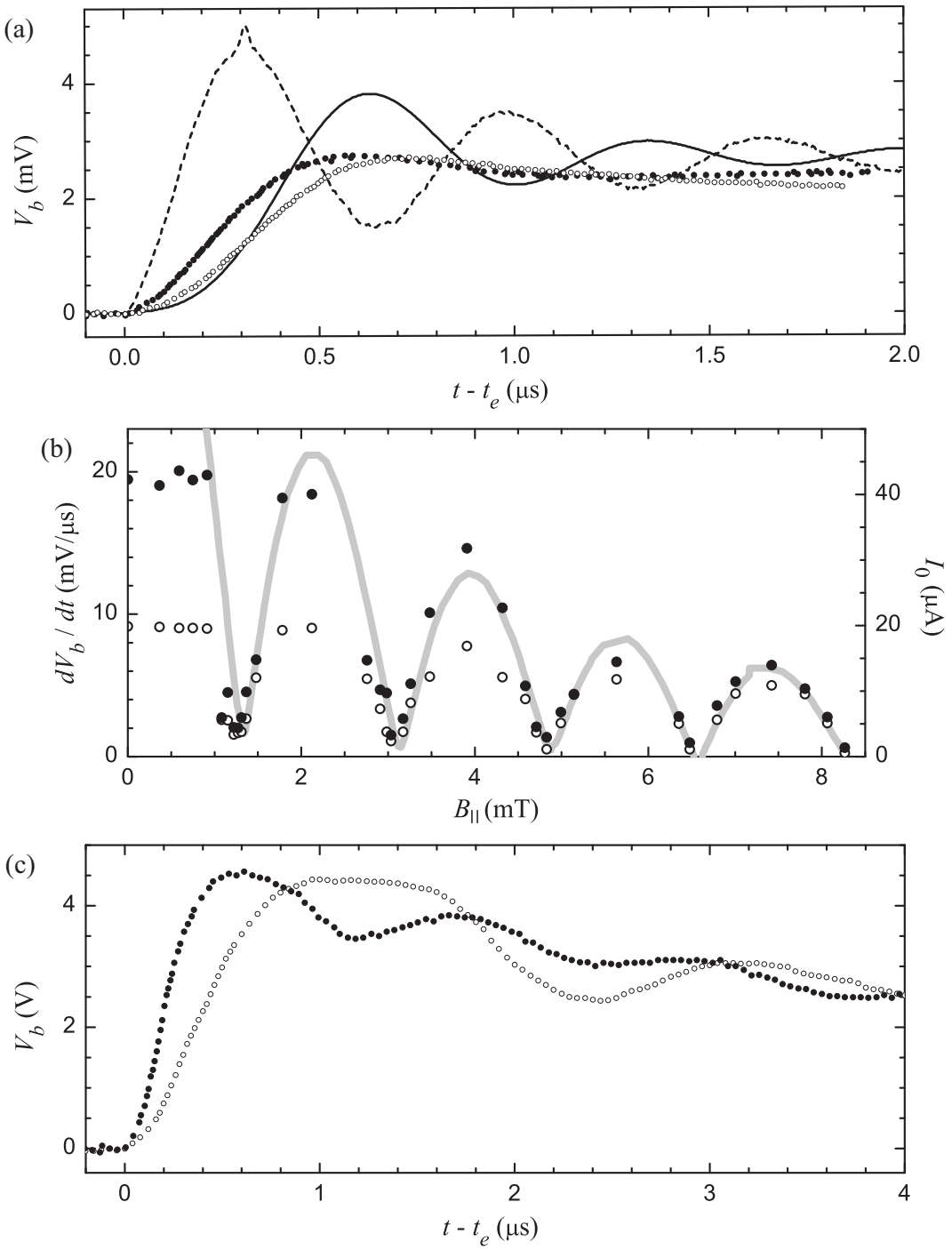

Figure 5.15: Charging of the voltage line. (a) For junction LC_2A during run 41, the voltage on the bias line was measured with an oscilloscope directly (dashed line), an SR560 amplifier (solid line), the JFET amplifier (solid circles), and the two homemade amplifiers connected in series (open circles). (b) The initial slope of the voltage, as measured with the scope directly (solid) and an SR560 amplifier (open), varies with the junction critical current I_0 (indicated by the gray line, with the right axis). (c) The voltage versus time for SQUIDs DS_1 (solid) and DS_2B (open) shows different ringing frequencies.

had a noise of 900 μVrms. Even though there was more noise on the SR560, the slope of its output during a switch was 900 mV/μs, so the resolution was a much improved 1 ns. The output of the first stage amplifier had a noise of 170 μVrms; with a switching slope of 300 mV/μs, the resolution was about 600 ps. The gain of the first stage amplifier was smaller than that of the SR560, but the low noise of the homemade amplifier lead to a better timing resolution. Finally, with both homemade stages hooked to the voltage line, the output had a signal of 720 μVrms. The switching slope was 10 V/μs, for a resolution of under 100 ps, which was the best of the four scenarios shown in Fig. 5.15(a). This value could be improved by increasing the bandwidth of the homemade amplifiers or by using cold amplifiers inside the refrigerator.

The (maximum) slope of the signal on the voltage line is set by the combination of three factors (see §6.2.3 of Ref. [1]). The fastest rise time possible is determined by the inductance and capacitance on the voltage line that must be charged to the gap voltage. However, this time might not be realized if the bias current which is available to charge the line is not sufficiently high. Finally, as Fig. 5.15(a) showed, the bandwidth of the detection amplifiers may also limit the slope.

We attempted to observe the different effects by varying the critical current I_0 of junction LC_2A with an in-plane suppression field $B_\parallel$, which results in a diffraction pattern (see §6.1). The traces in Fig. 5.15(a) were taken in the absence of a field, where $I_0 = 130$ μA. The wide gray curve in Fig. 5.15(b) shows the critical current variation as a function of $B_\parallel$, with the right axis. Plotted with the left axis is the maximum slope of the junction voltage, as measured directly with the scope (solid circles) and with an SR560 amplifier (open circles).

The slope has a clear dependence on the critical current, but it is not a linear one over the full range. At low values of I_0, the charging is limited by the critical current and the capacitance it has to charge. Here, the slope is linear in I_0 and both

measurements of the slope agree. As the critical current increases, the bandwidth required to measure the slope also increases. At some point the slope saturates, as the measuring instruments are no longer fast enough to follow the charging. As the SR560 has a lower bandwidth than the scope, the SR560 clips at lower value of I_0 (about 10 mV/μs) than the scope (about 20 mV/μs).

It is possible that the saturation seen with the scope is not due to its bandwidth, but to the components inside the refrigerator that must be charged. When these data were taken (Run 41), the component value for the discrete LC filter at the mixing chamber were 1.1 μH-100 pH-1.1 μH; *c.f.* Fig. 5.8(a). Assuming the filter is responsible for most of the inductance and that the total capacitance of the filter and coaxial lines is about 0.5 nF, the analysis presented in §6.2.3 of Ref. [1] predicts a voltage slope of roughly 25 mV/μs. This agrees well with the solid circles in Fig. 5.15(b), so it is plausible that scope was not the limiting factor in this case.

To sum up, for low critical currents, it is important to keep the capacitance on the voltage line low, while still providing sufficient filtering for the junction. At high critical currents, fast amplifiers are needed to take advantage of the faster charging times.

Figure 5.15(c) shows the junction switching voltage versus time from SQUIDs DS_1 (solid circles) and DS_2B (open). The output of the two-stage amplifier was recorded with a TDS 3054B oscilloscope and the traces have not been scaled by the amplifier gain. The charging time is comparable to that seen for junction LC_2A, although it is shorter for DS_2B, because of its smaller critical current. The frequency of the ringing is different for the two devices, perhaps due to the different powder filters used while measuring each.

When the amplified junction voltage surpassed a set threshold at time t_f, the Schmitt trigger outputted a pulse (with some jitter and a small delay) at time t_g, as sketched in Fig. 5.2. It was then converted to an optical pulse, traveled through

about 4 meters of fiber optic cable, reconverted to an electrical signal, and finally input to the receiver's comparator to create a fast edge. The output from the receiver, sketched in Fig. 5.2(h), was sent to the stop trigger on the timer. When the voltage crossed an adjustable threshold, the timer stopped (with some jitter). The output from the timer was read by the computer, which ended the cycle.

I measured some of the delays and estimated the others. The current calibration technique, described in the next section, measures the bias current at the top of the refrigerator. While this accounts for the delay t_a, t_b can only be inferred by looking at the switching data. The delay on the detector side can be measured with a microwave pulse. We usually applied a short 10 ns off-resonant microwave pulse, adjusting its time to coincide with a large number of counts in the switching histogram. The start of pulse at t_d (and its width) can be measured at the microwave source's video out using an additional SR620 timer. With a sufficient number of repetitions, the detected time t_h can be read from the switching histogram. The detector delay $t_h - t_e$, plus the small propagation delay $t_e - t_d$, was usually about 500 ns.

Figure 5.15 reveals a potential weakness of our detection scheme. We just used a single threshold value to determine the switching time, treating $V_b(t)$ as if it had a sharp edge. The time resolution could be substantially improved by using the full time-dependent waveform provided by an oscilloscope. What made this impractical was the slow repetition rate (under 10 Hz) needed in order to digitize and record each trace. With both a Tektronix TDS 3054B and TDS 7254B, a limiting factor was the time needed to arm the scope trigger on each cycle. Nevertheless, even with a small amount of data, the full trace information can be valuable for diagnostic purposes. On a few occasions, we noticed that the voltage profile was not consistent from cycle to cycle. By recording each trace, it was possible to determine if specific features in the calculated escape rate were due to switches of a certain form.

Short of digitizing the entire waveform, some improvement in the resolution can be obtained by using two Schmitt triggers (and two receivers and SR620 timers) set at different threshold values. Assuming a roughly linear voltage, a line fit through the two points can be extrapolated to find the switching time. As shown in Fig. 5.15(b), the slope of V_b depends on the value of I_b at the time of the switch. By calculating the slope based on the two points, we could see the variation of slope across a single histogram peak that was 150 nA wide, suggesting that the relative time resolution was quite good. Even with this technique, we saw no change (from using using a single detector) in the escape rate during Rabi oscillations. While there are several places where we could improve the time resolution in the experiment, the overall resolution appeared to be shorter than 1 ns (based on being able to see sharp features in the measured escape rate on this time scale) and did not appear to limit any of the experiments I will present.

The issues of timing could be avoided by using a scheme that more closely resembles the usual notions of measurement (as discussed in §6.6) together with a readout that could be performed after an arbitrarily long delay [114]. We are currently pursuing both objectives in the group.

5.6 Current Calibration

When performing experiments such as Rabi oscillations, we only needed the switching time information. In measuring a spectrum, though, knowledge of the current that the junction switched at was also important.

We most often used a simple measurement to calibrate I_b and I_f as a function of time. Even if this method suffered from systematic errors, the energy levels and escape rates could still be parameterized with slightly modified values for the critical current and capacitance of the junction. For this calibration technique, we simply recorded the voltage drop across the room-temperature bias resistances

R_b and R_f as a function of time; we used the analog-to-digital converter (ADC) on the computer's PCI-6110 data acquisition board, which has a 12-bit vertical resolution and a full range set to $\pm 5\ V$. Simultaneously, the optoisolated sync from the bias AWG was digitized to provide the origin of time. Sampling the voltages at a rate of 4 MS/s generally provided an adequate profile for the waveforms. For these measurements, the junction grounding switches at top of the refrigerator were closed (junctions connected), to try to measure the currents just as they would be during data taking. The resistance of the wires inside of the refrigerator (above the point where they are thermally clamped to a stage) changed by a few Ohms with the level of the helium bath. Therefore, the accuracy of the current calibration was limited by these fluctuations. For this reason, we saw no reason to use anything more stable than ordinary 1% metal foil resistors for R_b and R_f.

The voltage across the resistors was amplified with a Stanford Research Systems SR560 in differential mode, without filtering. As the output line was attached to the shielded room wall, the presence of the amplifier perhaps provided some protection to the devices (although breaking the ground connection between the input and output of the amplifier would have been preferable). The input to the SR560 is limited to 1 V, so for the bias resistance R_b we used the series combination of a large resistor and roughly 1 kΩ, across which the voltage was measured. With a careful choice of the R_f resistors, the SR560 could be kept on the same gain setting (roughly 20) during the calibration of I_b and I_f. There was no concern when this was not possible, because we experimentally found that the dc gain of the amplifier varied by less than 0.5% from nominal values.

This electronics configuration was also used to measure IV curves, such as the ones shown in §6.1. Typically, the voltage was measured directly with another SR560 (with a gain of 500 and no filters), whose output was sent to the computer's ADC. The usual homemade amplifiers could not be used, because the first stage

produced a large voltage offset and the second stage had an ac coupled input.

Returning to the current calibration, the various instruments in the experiment lead to significant timing delays (defined in Fig. 5.2), as described in the previous section. When the data collection computer registered a count at time t_h, the switch actually occurred at an earlier time t_e. This has to be taken into account when the current calibration is used to convert the computer's switching times to I_b and I_f. This was particularly important for high speed ramps.

We also used an alternative approach to create a refined current calibration, which took advantage of the junction being an extremely sensitive detector. The assumption that we commonly make is that the $0 \rightarrow 1$ resonance occurs at a fixed value of I_b and is independent of the bias ramp rate (and temperature and the trapped flux in a SQUID, in other circumstances). Thus the slope of a linear I_b ramp can be found by varying its dc offset and tracking the location of the resonance at a particular microwave frequency. In doing this, none of the delays in Fig. 5.2 have to be considered, as all measurements are made with respect to the time axis of the computer. To finish the calibration, the "offset" of the bias ramp needs to be found. This can be done by stabilizing the bias at a large value where the escape rate is measurable. For a steady bias current, the current through R_b should be very close to the actual current flowing through the device. The value of I_b at other escape rates can then be found with the slope previously measured.

As an example, Figs. 7.1 and 7.12 show escape rate data of junction LC_2B taken with ramp rates of 0.07 and 0.93 A/s, respectively. While the switching times differed by an order of magnitude, the escape rates plotted as a function of I_b should coincide. However, using the simple calibration method, the curves differed by nearly 1 μA. With the refined escape rate calibration just described, the disagreement was only 15 nA. The results for the measurement of the slope were fairly good, but determining the value of I_b with the stabilized ramp turned out to be quite tricky.

The escape rate method mostly improved the calibration for the faster ramp rate, which is more sensitive to the frequency response of the lines and electronics delays. Aside from Fig. 7.12, all of the data that I will present were taken at relatively slow rates, so I ordinarily just used the simple current calibration.

Chapter 6

Device Characterization and Measurement Techniques

This chapter is the first devoted to experimental results. I will begin by describing the current-voltage (IV) characteristic curves of the devices and discuss the various parameters that can be extracted from them. Almost all of the data in the chapters that follow come from measurements of the rate at which a junction tunnels to the finite voltage state. Therefore, I will describe the technique in some detail, although it is well established in the field. The escape rate, which was first introduced in Chapter 2, is useful because it is a measure of the population in the excited states of the qubit. By measuring the escape rate while varying system parameters (such as the bias current, temperature, or microwave power), a remarkable amount of information about the device can be extracted.

The IV curves and tunneling measurement technique are covered in the first two sections of the chapter and apply to both the LC-isolated junctions and dc SQUID phase qubits described in Chapter 4. The three sections that follow are specific to the dc SQUIDs. In particular, I will describe how the current-flux (I_b vs. Φ_A) characteristics can be found from escape rate measurements. From these, we can determine many of the device parameters. The I_b vs. Φ_A curves are also essential in determining how the SQUID should be biased so that it behaves much like a single junction. Finally, I will describe the technique used to initialize the SQUID to a particular flux state.

The last section contains a general discussion of quantum state readout methods for current-biased junctions. While most of the data that will follow come from escape rates, we have also used two pulsed techniques that provide valuable

information and conform to more traditional ideas of quantum measurement.

6.1 IV Curves

As described in §2.2.3, even a simple IV curve contains useful information about a junction. As an example, Fig. 6.1(a) shows data from device LC_2A, taken during Run 42 (see §4.2.1 for a description of this device and the runs during which it was studied). The IV curve for LC_2B was quite similar. The measured voltage V_b is across the junction and a small series resistance ($\sim 0.1\ \Omega$) that is on the line. For this measurement, the current bias I_b is sinusoidally swept with a frequency of 20 Hz (see §5.6 for a description of the instrumentation used for these measurements). The junction stays in the supercurrent state up to the critical current $I_0 \approx 124\ \mu$A, when it switches to the voltage state where $V_b = 2\Delta/e \approx 2.8$ mV. The IV curve then traces out the quasiparticle branch, not retrapping until a very low current bias. The current rise, here up to 210 μA, and its hysteresis are visible in all of our devices and is independent of the current sweep frequency. Whenever there is a sharp jump in the voltage, the "overshoot" is due to ringing on the voltage line.

Based on the slope of the IV curve in Fig. 6.1(a) at high voltage, the normal state resistance R_n is roughly 14 Ω. From this value and Eq. (2.34), the expected low temperature critical current is 160 μA (much higher than the design value of 97 μA given in Table 4.1). That the measured value is 20% smaller could be an indication of the junction quality. However,it could be a result of the size of the junction. The assumption I have made so far has been that the phase difference γ is constant across the face of the junction. This breaks down for large junctions, where the field generated by the supercurrents gives rise to a current screening analogous to the Meissner effect in bulk superconductors [115]. The length scale for this screening is

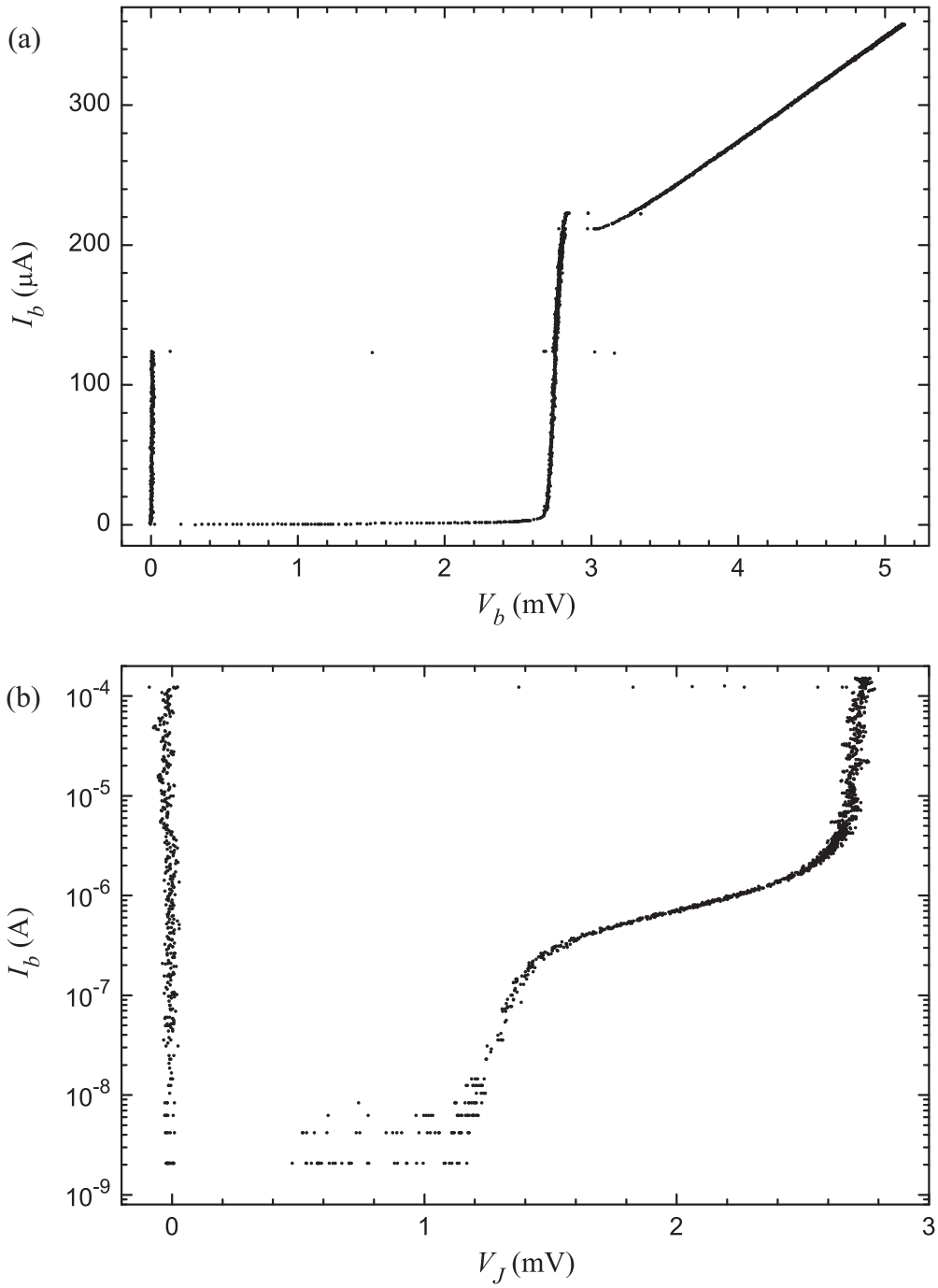

Figure 6.1: *IV* curves of device LC_2. (a) The *IV* curve of junction LC_2A, taken with a 20 Hz sinusoidal current sweep at 20 mK, shows the quasiparticle branch from which the normal state junction resistance can be calculated. (b) The subgap region, shown for junction LC_2B with a 3.5 mHz excitation, is important in preliminary evaluations of the device for use as a qubit.

given by the Josephson penetration depth

$$\lambda_J = \sqrt{\frac{\hbar}{2e\mu_0 J_0 (2\lambda + d)}}, \tag{6.1}$$

where J_0 is the critical current density of the junction, the junction barrier has an effective thickness of $2\lambda + d$ to an applied field, λ is the usual superconducting penetration depth, and d is the thickness of the oxide (generally thin enough to ignore). The idea is that the supercurrent will be confined to a distance λ_J from the edge of the junction. For small junctions, the fields, currents, and phase difference will be uniform over the area of the junction. On the other hand, if the junction is larger than $2\lambda_J$ in either dimension, the current will be significantly screened from the center of the junction and the maximum critical current will be smaller than expected from the critical current density and area. For device LC_2, Hypres quotes a nominal J_0 of 100 A/cm^2 and $\lambda \approx 100$ nm for their niobium films, yielding $\lambda_J \approx 36$ μm. Thus, for a 10 μm $\times$ 10 μm junction, the size should not be an issue, leaving the smaller than expected I_0 as a possible concern.

Figure 6.1(b) shows the sub-gap region of the IV curve for LC_2B, taken during Run 40, when the voltage was measured on the current bias line. The contribution from a series resistance of 140.7 Ω has been subtracted in calculating the junction voltage V_J. A careful measurement of the sub-gap characteristic can be performed by voltage-biasing the junction with its critical current suppressed [64]. However, the only change we made in taking this data was to use Wavetek model 20 analog function generator to avoid a discretized current bias.

Accurately identifying $I_b = 0$ is difficult given the offsets of the measuring instruments, but it appears that $I_b \approx 1$ nA when $V_J = 1$ mV. Assuming that the curve is roughly linear for small voltages, the sub-gap resistance R_{sg} should be well above 100 kΩ. This is comparable to values reported for similar junctions used for

quantum computation [64, 66, 96, 116].

Although the junction appears to retrap at $V_J = 0.5$ mV, I can only say that the retrapping current is smaller than about 1 nA. Using Eq. (2.35), the quality factor Q is greater than 1.5×10^4. Both from the design of the device and spectroscopy measurements, we know the junction capacitance is $C_J \approx 5$ pF. Equation (2.33) gives $R_J > 100$ kΩ (obtained from the retrapping current and the RCSJ model), consistent with the sub-gap resistance (measured directly). It will be interesting to keep this value in mind as we use other techniques to measure the dissipation of our qubits. However, we should expect R_J to depend on frequency, and the mV scale at which we have obtained R_J corresponds to roughly 500 GHz, well above the operating frequency of the qubit.

By applying a field in the plane of a junction (denoted $B_\parallel$), its critical current can be suppressed [117]. This effect occurs because of interference which is analogous to single-slit diffraction in optics. The critical current follows the Fraunhofer pattern [118],

$$I_0\left(\Phi_\parallel\right) = I_0\left(0\right)\left|\frac{\sin\left(\pi\Phi_\parallel/\Phi_0\right)}{\pi\Phi_\parallel/\Phi_0}\right|, \tag{6.2}$$

where $\Phi_\parallel$ is the applied flux in the junction barrier due to $B_\parallel$ and I have assumed the junction has a uniform critical current density.

Figure 6.2 shows IV curves at three different fields, taken on LC_2B during Run 40. Figure 6.2(a) shows the voltage on the bias line at zero field, while in Fig. 6.2(b) the contribution from the series resistance has been subtracted off. The combination of this correction, bit noise from the function generator supplying I_b, and the discrete values from the ADC measuring V_b lead to the noticeable scatter in the data. With no applied field, the junction switches to the full gap value, just as in Fig. 6.1. Panels (c) and (d) show curves for two different values of $B_\parallel$. As expected, the critical current (indicated by an arrow) decreases. However, the first jump in

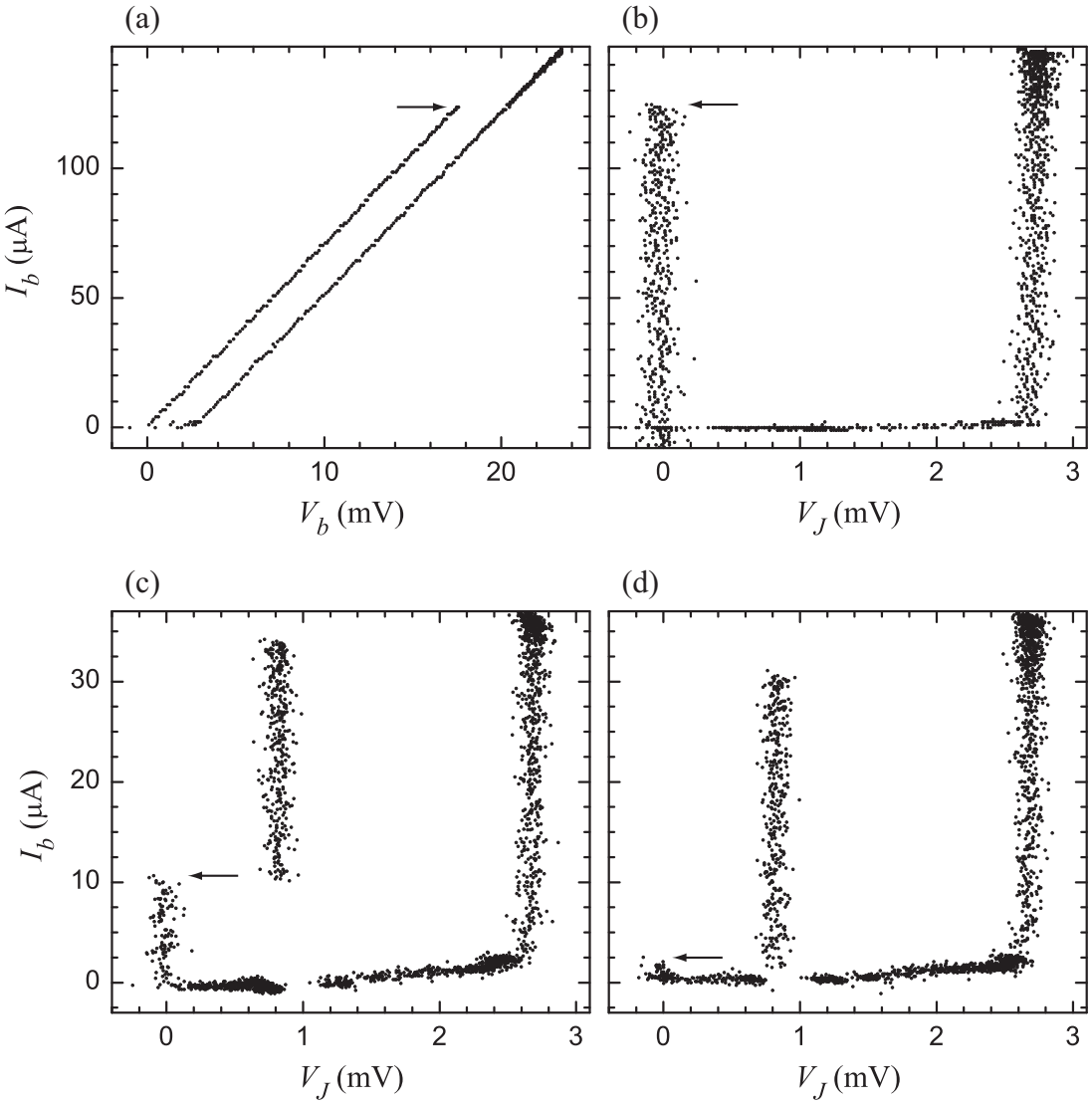

Figure 6.2: IV curves of junction LC_2B as a function of field. The IV curves were taken by applying a 1 Hz sinusoidal current drive at 25 mK, while measuring the voltage on the bias line. An arrow indicates the critical current. (a) The slope of the zero-voltage branch is due to a series resistance of 142 Ω on the bias line. In all other panels, its contribution has been subtracted away. (b) At $B_\parallel = 0$, there is a single switch to the full gap voltage. By increasing $B_\parallel$ to (c) 1.32 mT and (d) 1.41 mT, the critical current decreases, as the system moves down the main diffraction peak. For low I_0, the junction goes to the gap in two steps. Although the currents for the two jumps depend on the field, the voltage of the first switch is 800 mV in both cases. The location of this feature is also evident on the quasiparticle branch.

junction voltage is only to 800 mV, with the jump to the gap voltage occurring at a higher current. The origin of these sub-gap features is unknown, although similar things have been seen before in our group (see §2.4 of Ref. [3]).

By taking IV curves over a range of $B_{\|}$, the critical currents can be assembled into a diffraction pattern. Figure 6.3(a) shows two such patterns taken on Device LC_2B. The open points show an asymmetric curve that never exhibits full suppression. At the same time, the device was not switching in a reproducible way to the voltage state while we were measuring the escape rate (described in the next section). This is typical behavior when trapped flux is present in the junctions. After cycling the sample to 20 K, the solid data points were taken and the switching became much cleaner. Suppression of I_0 to less than 1% of its maximum value is indicative of a junction with a uniform barrier. From these results, one can see that the diffraction pattern is a valuable diagnostic tool for evaluating the fabrication quality and condition of a Josephson junction.

Because the maximum critical current shown here corresponds to a large plasma frequency, we generally operated device LC_2 with a suppression field. In general, we tried to leave the device at one of the diffraction peak maxima, where it was least sensitive to field fluctuations. However, this was not always possible as the switching characteristics were not necessarily stable at these points.

The dashed line on panel Fig. 6.3(b) is a fit of Eq. (6.2) to the main peak. This peak is reproduced nicely, but the fit underestimates the height and period of the higher order peaks. Although there is uncertainty in the value of the field $B_{\|}$ (because the sample is not exactly on the axis of the solenoid, for example), it is almost certainly off by a simple multiplicative constant, so the discrepancy in the widths of the different peaks is puzzling. As the junction is small compared to λ_J, it is unlikely that this is due to non-uniform field penetration. However, the base electrode of the junctions is comparable in thickness to λ, so the effective barrier

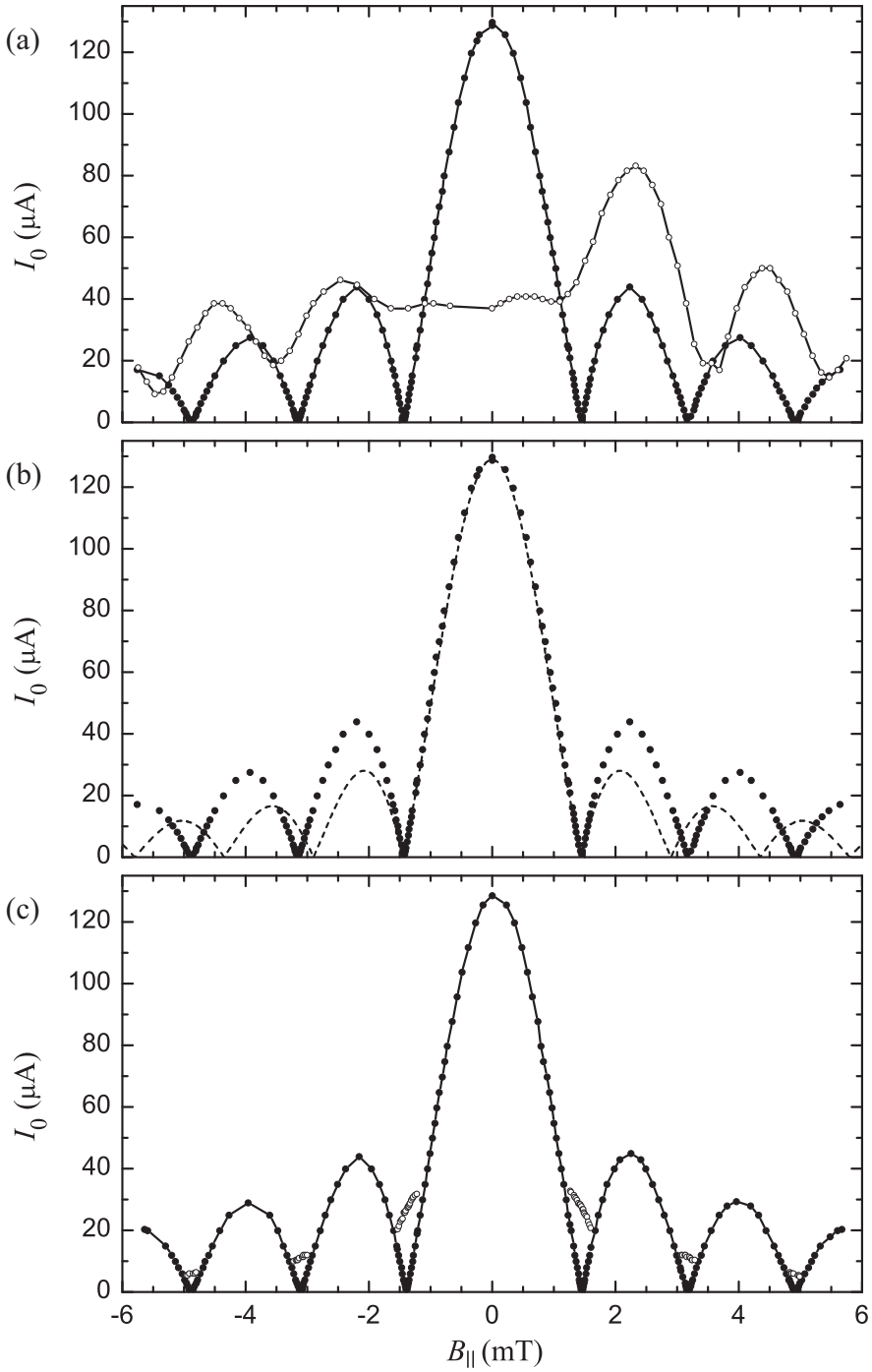

Figure 6.3: Diffraction patterns of device LC_2. (a) The current at which a voltage first appeared is plotted as a function of the in-plane suppression field $B_{\|}$. For junction LC_2B, an initially odd pattern (open circles) was restored (closed) by thermally cycling the device above T_c. (b) A fit to the simple theory (dashed line) shows qualitative differences with the data (circles). (c) For low I_0, there were two switches, where the first one (solid circles) marked the departure from the supercurrent state and the second (open) ended at the full gap voltage. This occurred in both devices, but data from junction LC_2A is shown. The data were taken at roughly 30 mK.

thickness could depend on the value of $B_{\|}$. In addition, Eq. (6.2) applies to an exactly rectangular junction; the rounded corners of our junctions could cause some deviations [53]. Nevertheless, the fit gives $\Phi_{\|} = (\Phi_0/1.45\ \mathrm{mT})\, B_{\|}$ or a cross-sectional area for the junction of 1.4 μm^2. For a 10 μm wide junction, this gives an effective barrier thickness of 140 nm. As we expect the thickness to be $2\lambda \approx 200$ nm, this value is not unreasonable.

For LC_2A, the corresponding patterns before and after thermal cycling were nearly identical to the one shown in Fig. 6.3(b), even though the measurements were separated by five months. This curve matches the one for LC_2B (after it was cycled), suggesting that both junctions on the coupled device are nearly identical. In Fig. 6.3(c), I_0 is indicated with solid circles, while the secondary switches [of the sort shown in Fig. 6.2(c) and (d)] and are shown with open circles. Although the sub-gap state occurred at roughly a single voltage, the current at which the system jumped to the gap voltage varied with $B_{\|}$.

For the dc SQUID phase qubits, IV curves are more difficult to interpret because the two junctions have different critical currents. Data taken on device DS_2 are shown in Fig. 6.4, with $I_f = 0$. Because of the different allowed flux states, there is a wide range of I_b at which the device switched to the voltage state. The full range of these "critical currents" is indicated by the gray rectangles. Although the maximum value (expected to be the sum of the critical currents of the two junctions, $I_{01} + I_{02}$) is similar in the two devices, the minima (which can be no small than $I_{01} - I_{02}$) are quite different, which is an odd combination. One possibility is that the devices were exposed to different levels of noise either during switching or retrapping. After thermally cycling the devices, the critical current ranges changed slightly, but were still unequal, suggesting that these nominally identical devices differed in a significant way. Despite the difference in the critical current modulation, both of the SQUIDs have essentially the same quasiparticle branch, with a normal

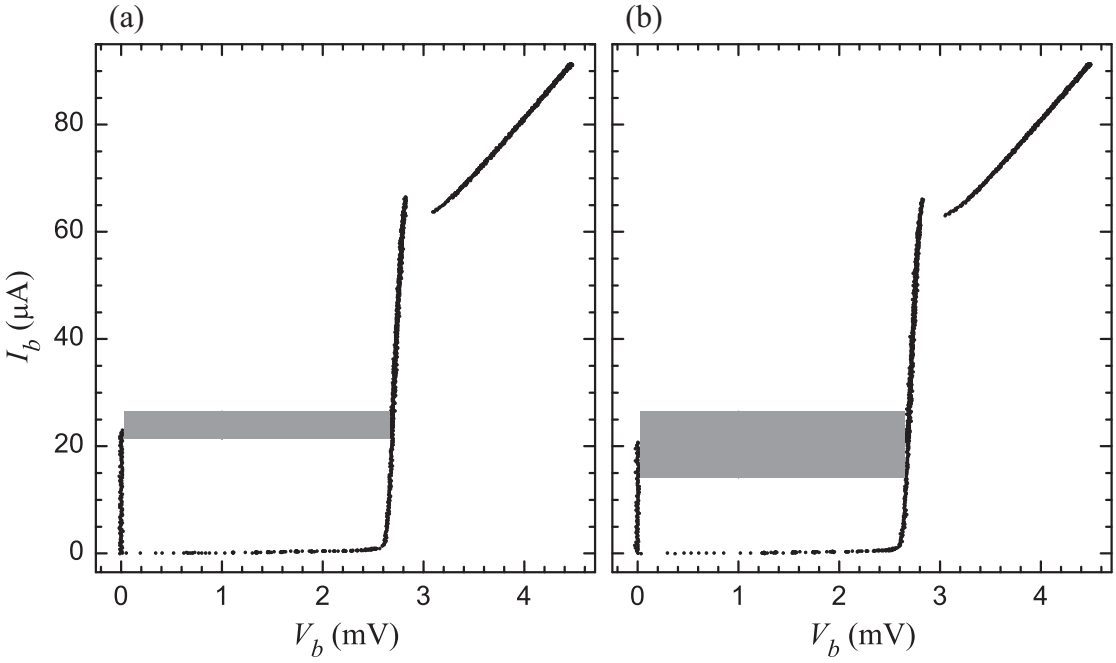

Figure 6.4: IV curves of device DS_2. The quasiparticle branches for SQUIDs (a) DS_2A and (b) DS_2B are nearly identical, for curves taken with a 1 Hz sinusoidal current drive at 20 mK. However, the ranges of critical currents are quite different, as indicated by the gray rectangles. If many IV curves were plotted on top of each other, the gray rectangles would contain several well defined lines, corresponding to switching from the different allowed flux states.

state resistance $R_n \approx 48\ \Omega$.

Because the SQUIDs were mounted in an aluminum box, it was difficult to controllably vary the magnetic field and measure a diffraction pattern. In addition, although $B_\parallel$ was nominally in the plane of the SQUID loop, it undoubtedly was biasing the SQUID as well as suppressing the junction critical currents. In retrospect, it might have been useful to add single junctions to the Hypres chips so that the fabrication quality of a particular foundry run could be evaluated with the measurements described in this section.

6.2 Escape Rate Measurement

To measure the escape rate, our standard measurement sequence proceeds in the following way, which is nearly identical to the method developed more than 30 years ago [60]. Each repetition starts with the junction unbiased, in the zero-voltage state. At time defined to be $t = 0$, I_b is increased. Usually, this is done in a linear fashion, although some of my experiments required a slightly more complicated waveform. For the SQUIDs, the flux-bias current I_f is ramped simultaneously with the current bias I_b, as described in §6.4. At some point during this process, the device escapes to the finite voltage state and stays there. The time (with respect to $t = 0$) at which this switch occurs is recorded to a precision better than 1 ns. The bias current is then reset to a slightly negative value to ensure retrapping to the supercurrent state. The reset occurs at a predetermined time and is independent of the switching time.

This process is then repeated anywhere from a few thousand to a few million times, depending on the desired precision in the escape rate. Depending on the situation, we varied the repetition frequency from 1 Hz to 1 kHz, typically using about 200 Hz. For rates above 1 kHz, heating effects from the junction being in the voltage state were evident. Each repetition may be regarded as a phase particle evolving in the tilted washboard potential. It is convenient to think of N serial experiments as an ensemble of N identically prepared phase particles. For this reason, I will use the terms "state occupation probability" and "population" interchangeably. Tunneling causes the population in the supercurrent state to decrease exponentially with time. The escape rate of the device is thus comparable to the inverse of the mean lifetime of a radioactive sample, where switching to the voltage state is analogous to decay. The distinction is that in the case of the Josephson junction, the decay time is dependent on I_b and therefore time t, if the current through the junction is being

ramped. This time-dependent total escape rate Γ is defined through the relationship

$$\frac{dN(t)}{dt} = -\Gamma(t)\, N(t)\,, \tag{6.3}$$

which integrates to

$$\int_{t_1}^{t_2} \Gamma(t)\, dt = \ln\left[\frac{N(t_1)}{N(t_2)}\right], \tag{6.4}$$

where $N(t)$ is the number of elements of the initial ensemble of $N(0)$ trials that remain in the zero-voltage state at time t.

To calculate Γ numerically, a histogram h of the $N(0)$ switching times is first made with bin size Δt, where $h\,(t_i)$ is the number of counts in the bin centered at time t_i. An example of such a plot with $\Delta t = 2$ ns is shown in Fig. 6.5(a), in the absence (open circles) and presence (solid) of an applied continuous microwave drive. The histograms show a small number of counts at short switching times because the escape rate is small at these bias currents. The number of counts increases as the escape rate increases exponentially with time. Eventually, the number of counts decreases again, as all members of the ensemble have already tunneled out. A microwave signal can induce transitions from the ground state $|0\rangle$ to the first excited state $|1\rangle$. The open circles show that in this case a well-defined bump appears at a definite current in the histogram, when the microwaves are resonant with the junction.

Under the assumption that Γ is constant during Δt, the second expression of Eq. (6.4) can be discretized to yield (see Ref. [60], §4.4 of Ref. [3], and §2.5 of Ref. [1])

$$\Gamma\,(t_i) = \frac{1}{\Delta t} \ln\left[\frac{N\,(t_i)}{N\,(t_{i+1})}\right] = \frac{1}{\Delta t} \ln\left[\frac{\sum_{j\geq i} h\,(t_j)}{\sum_{j\geq i+1} h\,(t_j)}\right]. \tag{6.5}$$

Notice that $\Gamma\,(t)$ is independent of the distribution of counts before time t. In the limit of small time bins, when $h\,(t_i) \ll N\,(t_{i+1})$, the logarithm reduces to the ratio of

counts in a particular bin to the total number left in the zero-voltage state. If $h(t_i)$ and $N(t_{i+1})$ are regarded as uncorrelated variables governed by Poisson statistics, the uncertainty in the escape rate is

$$\sigma_\Gamma(t_i) = \frac{1}{\Delta t}\sqrt{\left[\frac{1}{N(t_i)}\right]^2 h(t_i) + \left[\frac{1}{N(t_{i+1})} - \frac{1}{N(t_i)}\right]^2 N(t_{i+1})}\,. \tag{6.6}$$

Equation (6.5) was used to generate the escape rate curves shown in Fig. 6.5(b) from the histogram. Here, the x-axis has been converted into bias current using the escape rate calibration method described in §5.6; the full axis corresponds to the same time interval shown in Fig. 6.5(a). In Fig. 6.5(a), there are more counts at 43.18 μs in the absence of microwaves than with microwaves. This is because some fraction of the ensemble has already escaped to the voltage state in the region of the microwave resonance, while the total number of counts in both experiments is the same. However, in Fig. 6.5(b), both escape rates at the corresponding current 33.48 μA are the same, which indicates that the microwaves are far detuned from resonance at this point. In this way, Γ is a particularly convenient way of comparing data sets taken under different conditions or with different numbers of total counts.

It is also useful to define the escape rate enhancement as

$$\frac{\Delta\Gamma}{\Gamma} \equiv \frac{\Gamma - \Gamma_{bg}}{\Gamma_{bg}}, \tag{6.7}$$

where Γ_{bg} and Γ are the escape rates without and with applied microwaves. Figure 6.5(c) shows $\Delta\Gamma/\Gamma$ for the data in Fig. 6.5(b). The microwave resonance at $I_b = 33.43$ μA is nearly Lorentzian. The scatter at low bias currents is due to poor counting statistics from the low escape rates there. In Chapter 8, I will show how a spectrum of transitions can be measured by mapping out the resonance as the microwave frequency is varied. The application of the escape rate measurement to state readout is discussed in §6.6.

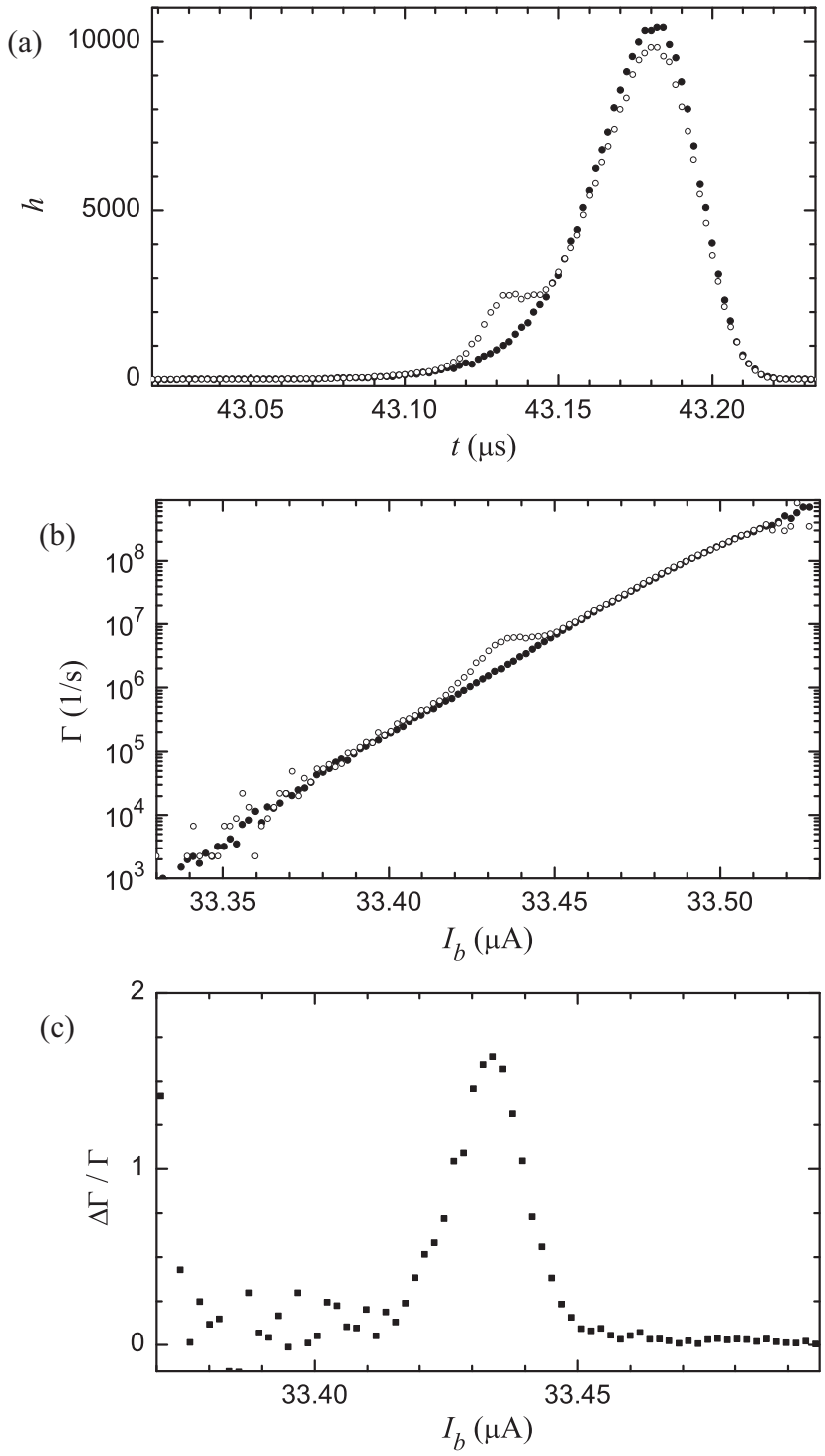

Figure 6.5: Switching experiment. (a) The histograms h of the time when the junction switched to the voltage state during a linear current ramp with (open circles) and without (solid circles) microwave activation have the same number of total counts. (b) From these data, the escape rate Γ of the device can be calculated as a function of current bias. (c) The escape rate enhancement $\Delta\Gamma/\Gamma$ due to microwaves shows the resonance at this one frequency. This data set was taken with a microwave frequency of 5.9 GHz at 20 mK on junction LC_2B.

6.3 Current-Flux Characteristics

The SQUID I_b vs. Φ_A curves discussed in §2.6 are useful in identifying flux states and bias trajectories. In this section, I will show that there are several ways to measure these characteristics and that each provides information about the device.

Figure 6.6 shows an I_b vs. Φ_A characteristic for SQUID DS_1. Switching histograms were taken by sweeping I_b at 280 fixed values of I_f. Rather than the single peak shown in Fig. 6.5(a), SQUID histograms contain several peaks corresponding to different flux states. In Fig. 6.6, each of the histograms forms a vertical line of the grayscale map. Because of the inductive asymmetry, most of the current bias gets shunted to the isolation junction, so the shallow branches corresponding to it switching to the voltage state are clearly visible. Although there is a very rich structure in these lines, I will focus on the flux states and the extraction of parameters that determine the efficacy of the isolation.

The data look similar to Fig. 2.16(b), but no counts occur for $I_b < 30.7$ μA, whereas the isolation junction branch should continue to $I_b = 0$. This happens because the potential must be tilted at least a certain amount before the phase particle will switch to a continuously running voltage state when its well becomes unstable (in the sense described in §2.5).

The situation is sketched in Fig. 6.7(a), which shows simulated characteristics of the $\beta = 8.4$ SQUID introduced in Fig. 2.16. The solid vertical line indicates a path when the current bias is swept, with the flux bias held constant. A particular flux state becomes unstable if the path begins inside of a characteristic loop and crosses a critical line. A switch to the voltage state will occur (thus forming a histogram peak) if the flux state is occupied and I_b is above the horizontal gray line. This outcome is indicated by open circles. If the isolation branch is crossed below the gray line (indicated by a square), the well does become unstable, but the system

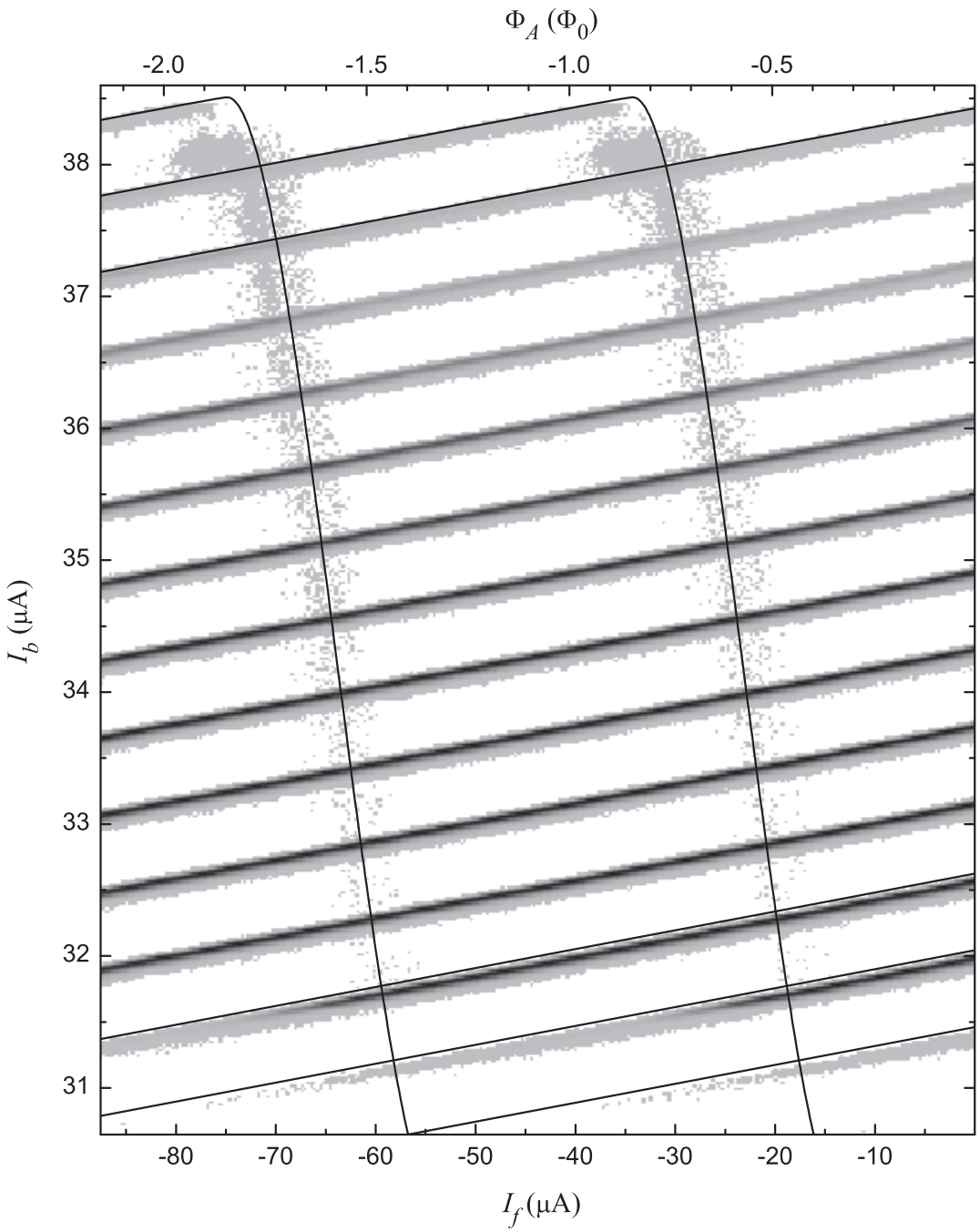

Figure 6.6: I_b vs. Φ_A characteristic of SQUID DS_1. Histograms, measured with fixed flux at 20 mK, are stacked next to each other to form the map, where black represents a large number of counts. The shallow lines represent the isolation junction switching from different flux states. The steeper qubit junction branches are not defined as clearly. The solid lines are drawn for $I_{01} = 34.23\ \mu$A, $I_{02} = 4.28\ \mu$A, $L_1 = 3.535$ nH, $L_2 = 10$ pH, $M_b = 0$, for $N_\Phi = -60, -59, -58$ (top three curves) and $N_\Phi = -48, -47, -46$ (bottom three curves) with an offset of $-0.34\ \Phi_0$.

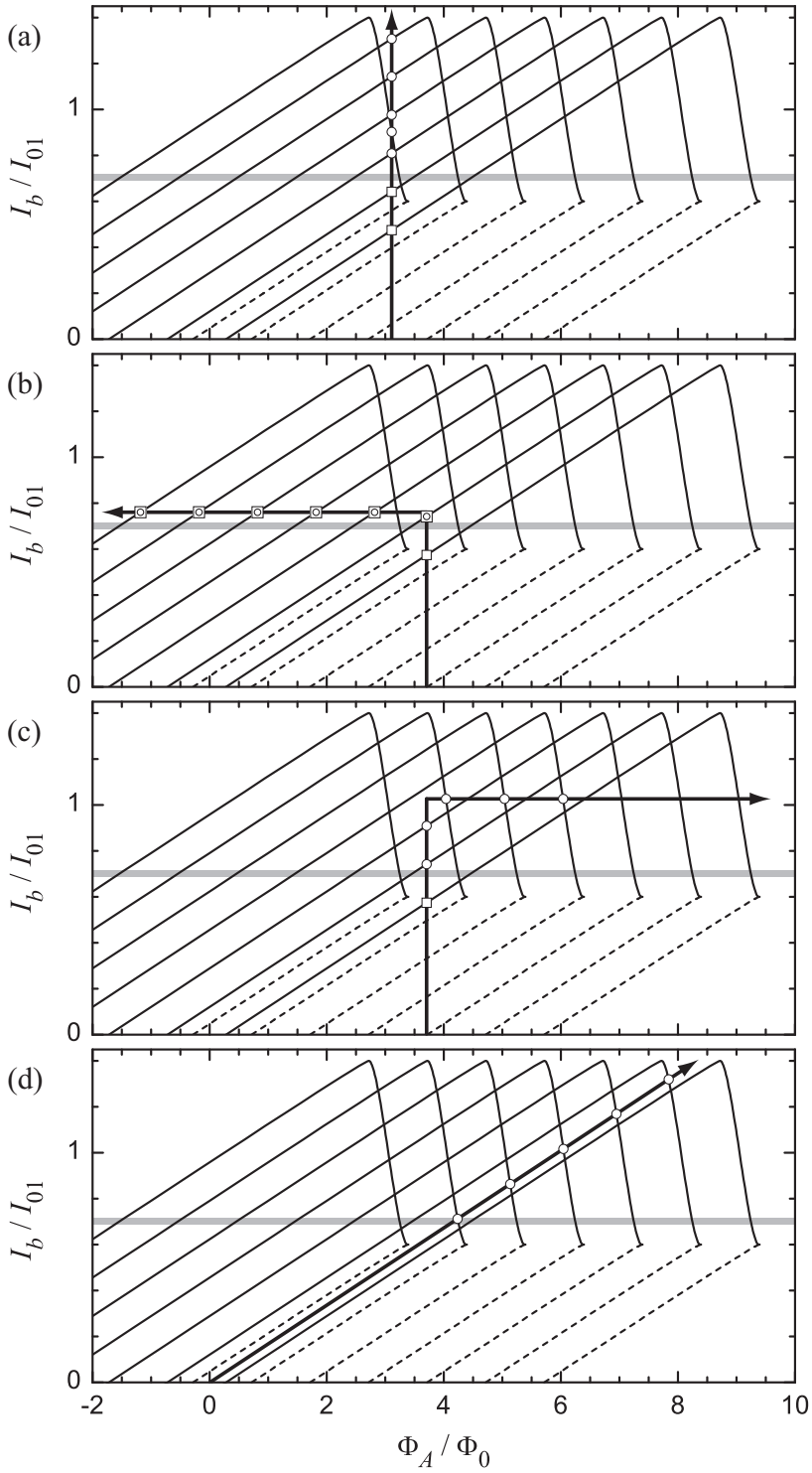

Figure 6.7: Bias trajectories for a dc SQUID. The heavy black lines indicate paths where (a) I_b is swept, (b) I_f is swept negatively, (c) I_f is swept positively, and (d) I_b and I_f are swept simultaneously. When a critical line is crossed, the system either must find a new flux state (squares) or switch to the voltage state (circles). The isolation junction will switch to the voltage state if I_b is above the gray bar, with the possible exception of biasing very close to the gray critical bar, as in (b).

quickly retraps in one of the stable flux wells. The minimum value of I_b required to produce switching depends on the damping in the device, but I have not performed modeling of the retrapping process. In the example shown in the Fig. 6.7(a), the histogram will contain five peaks, with one corresponding to the qubit switching to the voltage state first. Notice that the highest four flux states that switch were not stable at the beginning of the ramp at $I_b = 0$. They only have the possibility of becoming occupied during the retrapping indicated by the two squares.

The value of measuring the characteristic by sweeping I_b is that the maximum switching current is very close to $I_{01} + I_{02}$. I say close, because a junction will tunnel through its potential barrier for $I_b < I_0$; there is no direct way to measure I_0. In addition, the slope of the isolation branch gives the value of L_1 and the periodicity of the branches gives M_f. Calibration of I_f is straightforward in this case.

Similar information can be obtained with the bias path shown in Fig. 6.7(b). In this case, I_b is ramped up and stabilized at some level, after which I_f is ramped negatively. The full characteristic is mapped out by varying the I_b level. However, during the I_f ramp, only the isolation junction can switch, as the qubit branches are crossed in the unstable-to-stable direction. Typically, once I_b crosses the gray line, no retrapping can occur and a maximum of five histogram peaks (in this case) will be seen, even though more isolation branches are crossed. If I_b is stabilized close to the gray line, though, either switching or retrapping can occur, depending on the level of noise and dissipation in the system. In Fig. 6.7(b), I have indicated the uncertainty of the outcome with a square and a circle for the isolation branches crossed near the gray bar. For example, the flux state that switches at $\Phi_A = -1.25\ \Phi_0$ can only become occupied if a retrapping event occurred earlier on the bias path. The result of many sweeps is a histogram with more than five peaks.

Figure 6.8(a) shows a characteristic for DS_1, measured by sweeping the flux negatively. To the right of the dashed line, I_b is being stabilized, so the x-axis should

be thought of as time in this region. Once the flux ramp begins, only the isolation junction switches, with the total number of branches decreasing as I_b increases. Switching disappears completely below $I_b = 31$ μA and many peaks are seen for 31 μA $\lesssim I_b \lesssim$ 32 μA, which is the bias range where both switching and retrapping can occur.

To obtain information about the qubit junction, the bias path shown in Fig. 6.7(c) can be used. First I_b is stabilized and then I_f is ramped positively. During the first part of the ramp, crossing of the isolation branches leads to retrapping and switching to the voltage state. Once I_b crosses the gray line, the total number of histogram peaks is fixed. During the I_f ramp, the qubit is guaranteed to switch. If I_b is stabilized at a low value, it is possible to observe all of the stable flux states switch on their qubit branches with repeated sweeps. This is only true if there is nothing analogous to the gray line for the qubit; *i.e.* the SQUID always goes to voltage state when a qubit branch is crossed.

An I_b vs. Φ_A characteristic, obtained experimentally by sweeping I_f positively, is shown in Fig. 6.8(b). Again, the dashed line separates the I_b and I_f ramps. In these data, the steep qubit branches are well defined and their slopes and periodicity give L_2 and M_f. The lack of counts in the lower left corner may be due to retrapping. The complex structure at the bottom of each branch, which is barely visible in the figure, may be related to the part of the characteristic drawn with dashed lines in Fig. 6.7.

As with junction LC_2, we generally operated SQUID DS_1 with a suppression field $B_\parallel$ to reduce the plasma frequency of the qubit. The data of Figs. 6.6 and 6.8 were taken at what I will refer to as field #2. While the magnet was set to $B_\parallel = -2.9$ mT with the aluminum sample box at elevated temperature, the critical current definitely changed as the box became superconducting (see §5.1). Unless otherwise noted, all data in the thesis on DS_1 were taken at this field value. However,

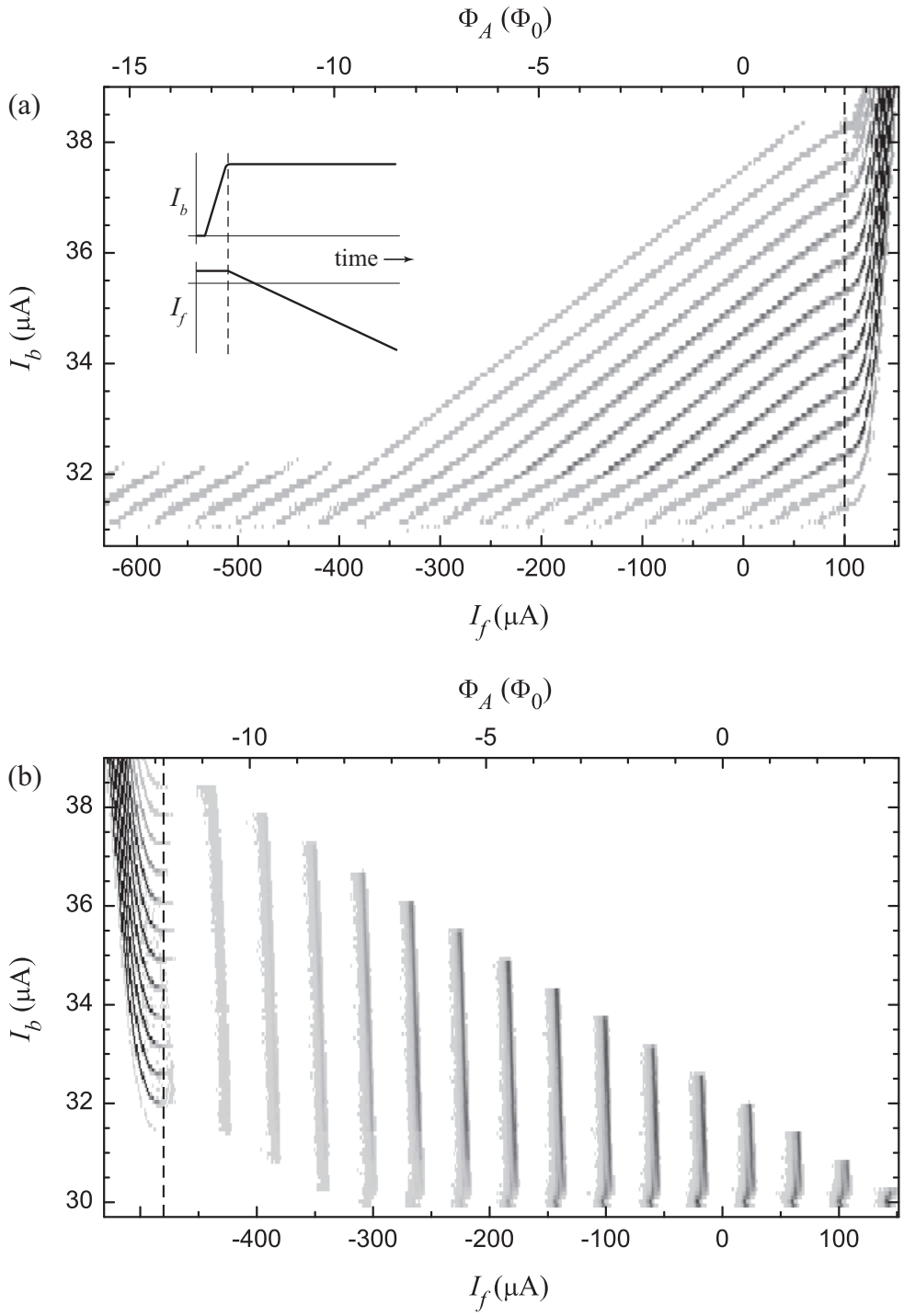

Figure 6.8: Swept-flux I_b vs. Φ_A characteristic of SQUID DS_1. (a) By first stabilizing I_b and then ramping I_f negatively, only the isolation branch is crossed. The diagram shows a cartoon of the bias waveforms; the dashed line marks the division between the bias and flux ramps. (b) Similarly, by sweeping I_f positively, only the qubit branch is seen.

we did look at the three types of current-flux characteristics with no suppression field and two other values of $B_\parallel$. For fields #1 and #3, $B_\parallel$ was set to 2.5 and 0.5 mT, respectively. Information gleaned from linear fits to the junction branches of the characteristics is summarized in Table 6.1. For the characteristics where I_b is swept, the values refer to the isolation branch.

The periodicity in I_f gives M_f for all trajectories. M_f should be independent of the field. The average of the twelve measurements is 50.90 ± 0.08 pH, where the variation is due to uncertainty in the I_f current calibration.

As mentioned, the maximum possible switching current is $I_{01}+I_{02}$. If the entire qubit branch is visible (as I am assuming), then it ends at $I_{01} - I_{02}$. Therefore, the range of I_b for which switches were observed is indicated in rows labeled "Max I_b" and "Min I_b." For each field, the overall maximum and minimum were used to calculate I_{01} and I_{02} and the zero-bias Josephson inductances L^0_{J1} and L^0_{J2}. The uncertainty in I_b is under 1%.

As discussed at the end of §2.6, the inverse of the slope of the isolation branch is $L_1^{tot} \equiv L_1 + L^0_{J1} - M_b$ and the negative of slope of the qubit branch is $L_2^{tot} \equiv L_2 + L^0_{J2} + M_b$. I have assumed that the dependence of the Josephson inductances on I_1 and I_2 is only important at the ends of the branches. Due to the dependence of L^0_J on the junction critical current, L_1^{tot} and L_2^{tot} are functions of $B_\parallel$, although L_1^{tot} is only weakly so.

One way to find the slope is to measure the spacing of the branches along I_b, assuming a periodicity of Φ_0 and that the branches are nearly straight lines; values obtained from this method are denoted $L^{tot}\,(\Delta I_b)$. Alternatively, the slope can be measured directly and M_f can be used to convert the dimensionless ratio to an inductance; the result of this method is denoted $L^{tot}\,(\text{slope})$. The statistical uncertainty in L^{tot} from fitting all of the branches of a particular set is generally less than 10 pH, though it is quite a bit smaller for a few. Some of the variation

Table 6.1: Current-flux characteristic properties of SQUID DS_1. The properties of the primary branch for three bias trajectories are listed for four suppression magnetic fields. Unless otherwise noted, data in this thesis were taken at field #2. Entries marked with an asterisk are anomalous; see text.

	Zero Field	Field #1	Field #2	Field #3
		I_b swept		
M_f (pH)	51.30	50.30	50.61	50.72
$L_1^{tot}(\Delta I_b)$ (nH)	+3.506	+3.517	+3.530	+3.501
L_1^{tot} (slope) (nH)	+3.506	+3.517	+3.531	+3.504
Max I_b (μA)	159.6	48.0	38.7	136.3
Min I_b (μA)	70.0	22.4	30.7	51.0
		I_f swept negatively		
M_f (pH)	50.89	51.15	51.07	51.01
$L^{tot}(\Delta I_b)$ (nH)	-1.150*	+3.509	+3.530	-0.0254*
L^{tot} (slope) (nH)	-1.176*	+3.522	+3.535	-0.0256*
Max I_b (μA)	154.2	47.6	38.4	135.8
Min I_b (μA)	69.4	22.9	31.1	52.0
Jumps* (μA)	106.7*	31.4, 39.0*		82.2*
		I_f swept positively		
M_f (pH)	51.04	50.87	50.95	50.92
$L_2^{tot}(\Delta I_b)$ (pH)	-37.4	-42.5	-70.9	-35.3
L_2^{tot} (slope) (pH)	-39.6	-42.2	-69.5	-37.3
Max I_b (μA)	156.9	47.8	38.4	135.4
Min I_b (μA)	56.1	23.1	29.9	38.4
# peaks	177	43	15	167
		Extracted parameters		
I_{01} (μA)	107.9	35.6	34.3	87.4
I_{02} (μA)	51.7	12.5	4.4	49.0
L_{J1}^0 (pH)	3.0	9.2	9.6	3.8
L_{J2}^0 (pH)	6.4	26.4	75.2	6.7
$L_1 - M_b$ (nH)	3.503	3.508	3.520	3.499
$L_2 + M_b$ (pH)	32.6	15.6	-5.2	30.3
# states	177	43	15	167

for the swept-flux characteristics is due to I_b not quite stabilizing when the I_f ramp started (largely due to the finite bandwidth of the lines).

With the total inductances and critical currents (and thus L_J^0) in hand, $L_1 - M_b$ and $L_2 + M_b$ may be calculated. These values should be independent of the critical currents and thus the suppression field. For the qubit side, the average value is $L_1 - M_b = 3.508 \pm 0.004$ nH. On the isolation side, the average value is $L_2 + M_b = 18.3 \pm 8.7$ pH. The large uncertainty in $L_2 + M_b$ is disappointing, as this value (in conjunction with L_{J2} and L_1) determines the level of isolation; see 4.3. That the value appears to scale with the critical currents suggests that the discussion in §2.6 needs a small correction or that there is a systematic error in the measurement of the characteristics. On the experimental side, calibration of I_f is the most likely culprit, although no similar pattern is seen in M_f. Incidentally, using this method, it is not possible to extract a value for M_b (aside from its sign), but that is not an important issue because M_b only appears as $L_1 - M_b$ or $L_2 + M_b$.

For the trajectory where I_f is swept positively, the total number of peaks is an indication of the number of allowed states (and thus β), so this value is listed in the table as "# peaks." The theoretical number is calculated by counting the number of stable wells of the potential for the extracted device parameters at zero bias, and is listed as "# states." Although the two numbers agree, I essentially enforced this by assuming that we could see the entire qubit branch.

Finally, there was an odd feature in some of the characteristics of DS_1 where I_f was swept negatively. For fields #1 and #2, the isolation branch was seen as expected. For field #1, the branches were not completely straight, with two small jumps at the I_b values listed in the table. It is possible that they were artifacts of the measurement. For zero field and field #3, not only did the slope of the observed branch not match the isolation branch, the sign of the slope was wrong. In addition, there were fairly noticeable jumps near I_{01}. In the case of field #3, the

unphysical solution mentioned in §2.6 happens to have a slope of -23.3 pH and a discontinuity at I_{01}. It is unclear how crossing this branch could result in a switch to the voltage state. The ~ 1.2 nH slope of the zero field data remains a complete mystery. However, the 'sweep flux +' characteristics always appeared as expected, so there is no reason to believe that the high β devices cannot be used as qubits.

In Fig. 6.6, I have drawn solid lines for six branches using the parameters extracted from the characteristics for field #2. However, a few small adjustments had to made to the device parameters (given in the figure caption), as this data set was not the one used to calculate the values listed in Table 6.1. With the modified parameters, there is good agreement for the isolation branch and there is a high density of qubit switches that fall under the characteristic. However, there are quite a few qubit switches above the critical line, which should never happen, so the fit (or our understanding of the switching dynamics) is not perfect.

We performed similar measurements on DS_2 to extract parameters for both SQUIDs. The isolation branch had an inverse slope of 3.35 and 3.39 nH for DS_2A and DS_2B, respectively, so the spiral inductors are nearly identical. As discussed in §4.3.2 and §5.2.2, the cross mutual inductances were significant for these devices. A matrix equation relating the four control currents (I_b^A, I_b^B, I_f^A, and I_f^B) to the flux in each SQUID loop is given by Eq. (4.13).

For example, one of the matrix elements is M_f^{BA}, which is the mutual inductance between flux line B and SQUID A. We measured switching histograms of device A by ramping I_b^A at fixed values of I_f^B (and $I_f^A = 0$). These were stacked together to form a I_b vs. Φ_A characteristic, whose periodicity gave $M_f^{BA} = -0.18$ pH. Similar characteristics were constructed to measure five other elements, the results of which are given in Eq. (4.15). With this method, the mutual inductance of a bias line to its own SQUID (M_b^{AA} and M_b^{BB}) cannot be measured. Although these elements can be large, the flux generated by the small current biases is not very

large. More importantly, these elements are not needed in the procedure I used to bias both devices simultaneously, as shown in Eqs. (5.7) and (5.8).

6.4 Simultaneous Biasing

It greatly simplifies the operation of a dc SQUID phase qubit if it can be treated as a simple current-biased junction, leaving the auxiliary junction to provide broadband isolation, well out of resonance. However, if we were to just ramp I_b as in §6.2, then almost all of the current would go through the isolation junction, causing it to switch to the voltage state first. Instead, in order to measure the escape rate of the qubit junction, we simultaneously ramp both I_b and Φ_A in an attempt keep γ_2 fixed at some initial value. Usually, we choose the initial I_b and I_f to be zero, so $I_1 \approx I_b$ and $I_2 \approx 0$.

As we are interested in the classical ground state of the SQUID (no displacement currents), Eqs. (2.61) and (2.63) can be used to find the relationship between small changes in current bias (ΔI_b) and flux bias (ΔI_f) needed to ensure $d\gamma_2/dI_b = 0$. The corresponding change in the applied flux is

$$\Delta\Phi_A = M_f \Delta I_f = (L_1 + L_{J1} - M_b)\,\Delta I_b. \tag{6.8}$$

The implication of this result is that keeping γ_2 fixed corresponds to following a trajectory parallel to the isolation branch of the current-flux characteristic.

What makes this difficult to do experimentally is that the Josephson inductance L_{J1} is a function of I_b. Although L_{J1} only changes appreciably when I_1 is very close to I_{01}, this is exactly the region where we want to measure the escape rate.

In practice, we simply ramp both I_b and I_f linearly with a ratio experimentally determined from the middle of the shallow branch of the current-flux characteristic. This corresponds to Eq. (6.8) evaluated roughly at the zero-bias value of the qubit's

Josephson inductance L_{J1}^0. At first, all of the bias current will go through the qubit as desired, but as the ramp proceeds and L_{J1} increases, a small amount of I_b will get shunted through the isolation junction. The trajectory on the current-flux characteristic is shown in Fig. 6.7(d). As none of the isolation branches are crossed, there are never any retrapping events and each flux state is guaranteed to switch to the voltage state when occupied.

No matter what the bias trajectory is, we would like to be able to calculate the current through each of the junctions. The current division for an incremental increase in the biases will depend on the instantaneous value of the Josephson inductances. An integral can be taken along the bias path to follow the branch currents [4]. Alternatively, as the final state is independent of the path taken, the SQUID potential at the I_b and Φ_A of interest will provide the same answer. The location of the local minimum for the well of the flux state N_Φ gives the classical ground state values of γ_1 and γ_2. Thus, the branch currents can be found without explicitly invoking the Josephson inductance, as in Table 2.1 (which was computed for zero bias).

Calculations for a typical device are shown in Fig. 6.9, under the simple simultaneous ramp [*i.e.* Eq. (6.8) evaluated at L_{J1}^0]. The simulation parameters are $I_{01} = 30$ μA, $I_{02} = 5$ μA, $L_1 = 3.5$ nH, $L_2 = 50$ pH, $M_b = 0$, and the qubit capacitance is $C_J = 5$ pF. Figure 6.9(a) shows the current through the isolation junction. Ideally, this would always be zero, but it reaches about 50 nA or 0.1% of I_b by the end of the ramp. As this is a very small fraction of I_{02}, the isolation junction should hardly be affected.

In Fig. 6.9(b), the calculated ground state escape rate Γ_0 of the qubit junction is plotted with a solid line. I have assumed that this value depends only on γ_1 and not γ_2, so that Eq. (2.43) may be used. The dashed line shows what Γ_0 would be for a perfect simultaneous ramp where $I_1 = I_b$. The two lines would coincide if they

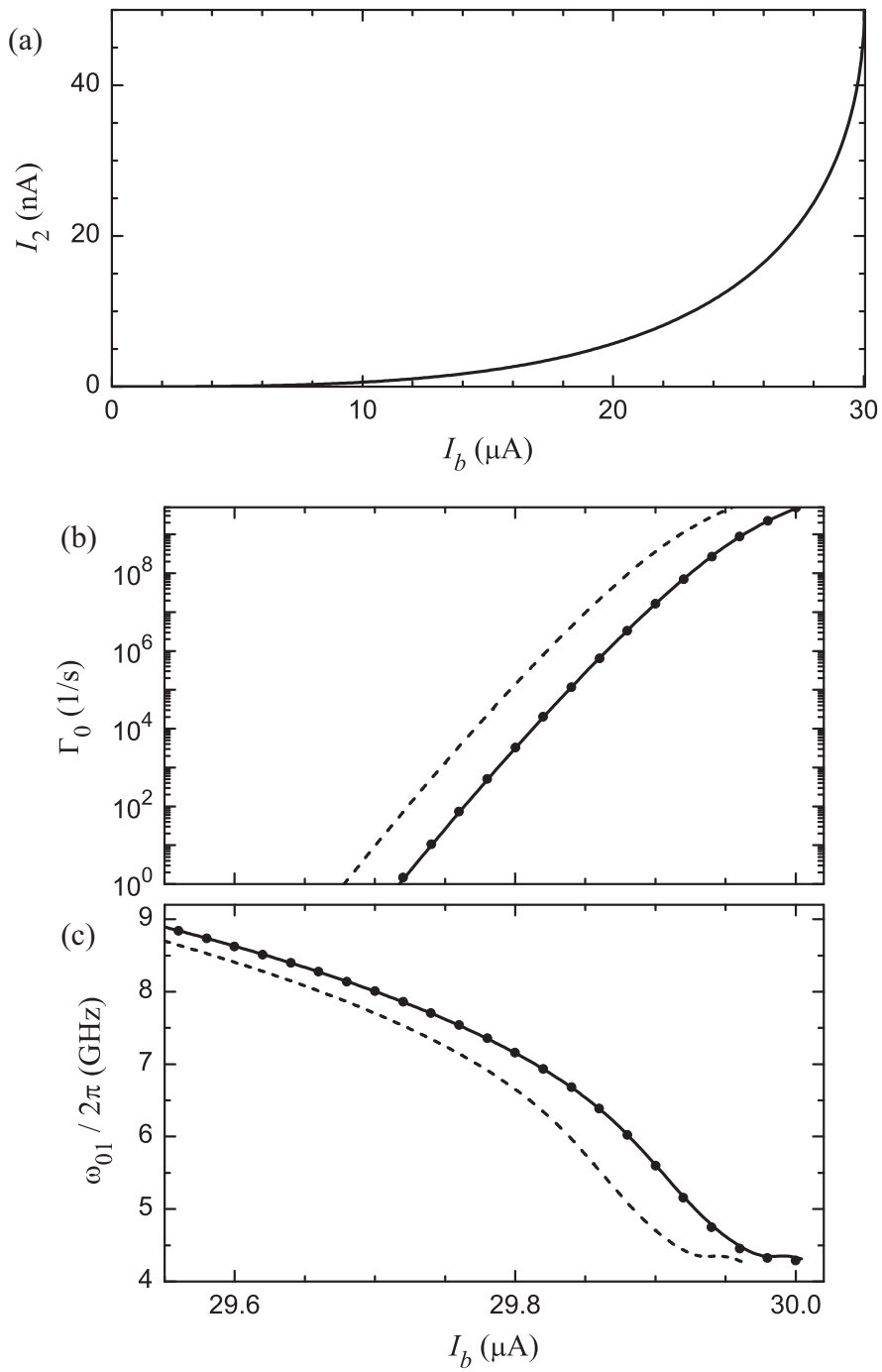

Figure 6.9: Simultaneous biasing of a dc SQUID phase qubit. Simulations are shown for a SQUID with $I_{01} = 30$ μA, $I_{02} = 5$ μA, $L_1 = 3.5$ nH, $L_2 = 50$ pH, and $M_b = 0$, biased with a simple simultaneous ramp. (a) The current I_2 through the isolation junction starts at zero, but increases as the Josephson inductance of the qubit increases. (b) This results in a shift of the ground state escape rate (solid line) with respect to what it would be if $I_1 = I_b$ (dashed) (calculated for $C_J = 5$ pF). Values for a SQUID under the simple ramp are reproduced by a single junction with effective parameters (circles). (c) A shift also occurs between the two biasing conditions for the level spacing between the ground and first excited states, ω_{01}.

were plotted as a function of I_1 instead of I_b. Figure 6.9(c) shows similar curves for the lowest energy level spacing ω_{01}, calculated with Eq. (2.44).

It is generally difficult to calculate I_1 accurately from experimental data, because precise values of all the inductances and the background flux must be known. For the simple simultaneous ramping, the current shunted through the isolation junction results not only in a shift in the current axis, but also a small change in the slope of Γ_0 and ω_{01} with respect to I_b. Therefore, it might seem that plots made as function of I_b (which is relatively easy to measure) could not be compared to single junction theoretical results. However, Γ_0 for the SQUID under the simple ramp is nearly identical to Γ_0 for a single current-biased junction with $I_0 = 30.048$ μA (instead of 30 μA) and $C_J = 4.662$ pF (instead of 5 pF), which is plotted with solid circles in Fig. 6.9(b). For ω_{01}, agreement is found for $I_0 = 30.044$ μA and $C_J = 5.045$ pF [see solid circles in Fig. 6.9(c)]. These effective junction parameters also do a good job of describing the escape rates and energy levels of the higher states $|n\rangle$ and different flux states.

To summarize, if we use a simple simultaneous biasing designed to make the qubit junction switch, $I_1 < I_b$ during the ramp. Nonetheless, we expect the qubit properties to resemble those of a single junction when plotted as a function of I_b. However, the critical current and capacitance of the model junction will differ slightly from the actual qubit values and no single model will describe both the escape rates and energy levels. The discrepancies, however, are fairly small in our devices, which makes the independent junction approximation useful.

In practice, I often fit the experimental base temperature escape rate as a function of I_b to extract I_0^Γ and C_J^Γ and independently fit the $0 \rightarrow 1$ transition frequencies to extract I_0^ω and C_J^ω. These parameters could then be used to predict Γ_n and ω_{nm} for higher levels over a range of I_b.

A potentially serious flaw in the previous discussion is that I used classical

arguments (based on properties of the 2-D potential) to determine the branch currents I_1 and I_2. I then assumed that I_1 determined the energy levels and escape rates. Quantum mechanically, the expectation value $\langle\gamma_1\rangle$ of the phase difference across the qubit junction determines I_1. Because the potential wells are anharmonic and the metastable states $|n\rangle$ have a significant weight outside of the well, $\langle\gamma_1\rangle$ is closer to the potential barrier than the well minimum. Thus, the redistribution of I_b will differ for classical and quantum treatments. In fact, full quantum simulations show that the magnitude of the branch currents depends on the state of the qubit junction [73]. Therefore, even if the single junction model with certain values of I_0 and C_J describe Γ_0 for the SQUID's qubit junction, they may not describe Γ_1 correctly. Since the difference in $\langle I_1\rangle$ for $|0\rangle$ and $|1\rangle$ is predicted to be a few nA for our devices [73], I have ignored this effect. Nonetheless, it is small source of error for the simulations in the chapters that follow.

6.5 Flux Shaking

As I discussed in §6.3, our SQUIDs can retrap in different flux states. When performing the simultaneous ramp, each of these states sits in a slightly different potential and will switch to the voltage state at a different current (due to the circulating current from the trapped flux). Of course, I_{01} and I_{02} are independent of the flux state, but I will refer to the flux states as having different critical currents for simplicity. For the phase qubit, satisfying the DiVincenzo criterion concerning qubit initialization [20, 21] usually refers to occupation of the ground state $|0\rangle$ of a tilted washboard well. However, for our SQUIDs, there are multiple wells that are distinguishable and each has its own $|0\rangle$. In this case, the "classical" initialization to one particular well is also required.

To set the SQUID in a specific flux state, we use a procedure similar to one developed for a symmetric low β dc SQUID [119]. In those experiments, a "shaker"

circuit was used to oscillate the current bias with an amplitude slightly less than the maximum critical current. If the device was in the maximum critical current state, it would remain there throughout the oscillations. However, if it was not, then it would switch to the voltage state and eventually retrap when the bias was reset. This switching and retrapping would continue until the device happened to retrap in the highest critical current state.

For reasons discussed below, we chose to oscillate the flux bias to perform the initialization [72], using the process sketched in Fig. 6.10. The applied flux has the form $\Phi_A(t) = \Delta\Phi_A + \widetilde{\Phi}_A \sin(\omega_A t + \phi)/2$, where $\Delta\Phi_A$ is a static flux offset and $\widetilde{\Phi}_A$ is the peak-to-peak amplitude of a sine wave of angular frequency ω_A. The value of ϕ is chosen so that $\Phi_A(0) = 0$; the oscillations run for a total time T, where $\omega_A T/2\pi$ is an integer. To explain the process, I will use the picture of the SQUID developed in §2.5. Consider the simple case of a symmetric dc SQUID with $\beta = 4.8$ at $I_b = 0$. The left column of Fig. 6.10 shows cuts in the γ_1 direction for different values of the flux. Notice that in each case, the potential can support five flux states, although this range is centered about a value dependent on Φ_A.

In the sequence shown, the flux oscillates about an offset of $\Delta\Phi_A = 1\ \Phi_0$, with a peak-to-peak amplitude of $\widetilde{\Phi}_A = 4\ \Phi_0$ (although three snapshots at integral values of Φ_A/Φ_0 are not drawn). With this choice, the well marked by a vertical arrow is stable at all times and is therefore the one that the shaking will tend to occupy.

The solid circles show an example of what the phase particle might do during an oscillation. In this example, the device starts out in the $N_\Phi = -2$ state after retrapping from the voltage state. When $\Phi_A(t) = \Phi_0$, this flux state becomes unstable and the particle must settle in one of the states that are then allowed ($N_\Phi = -1$ to 3). I will assume that the retrapping is random and that in principle the particle could end in any allowed well. Say it goes to 0. At $\Phi_A(t) = 2\ \Phi_0$, this state is still stable and nothing happens. At $3\ \Phi_0$, the well is unstable and

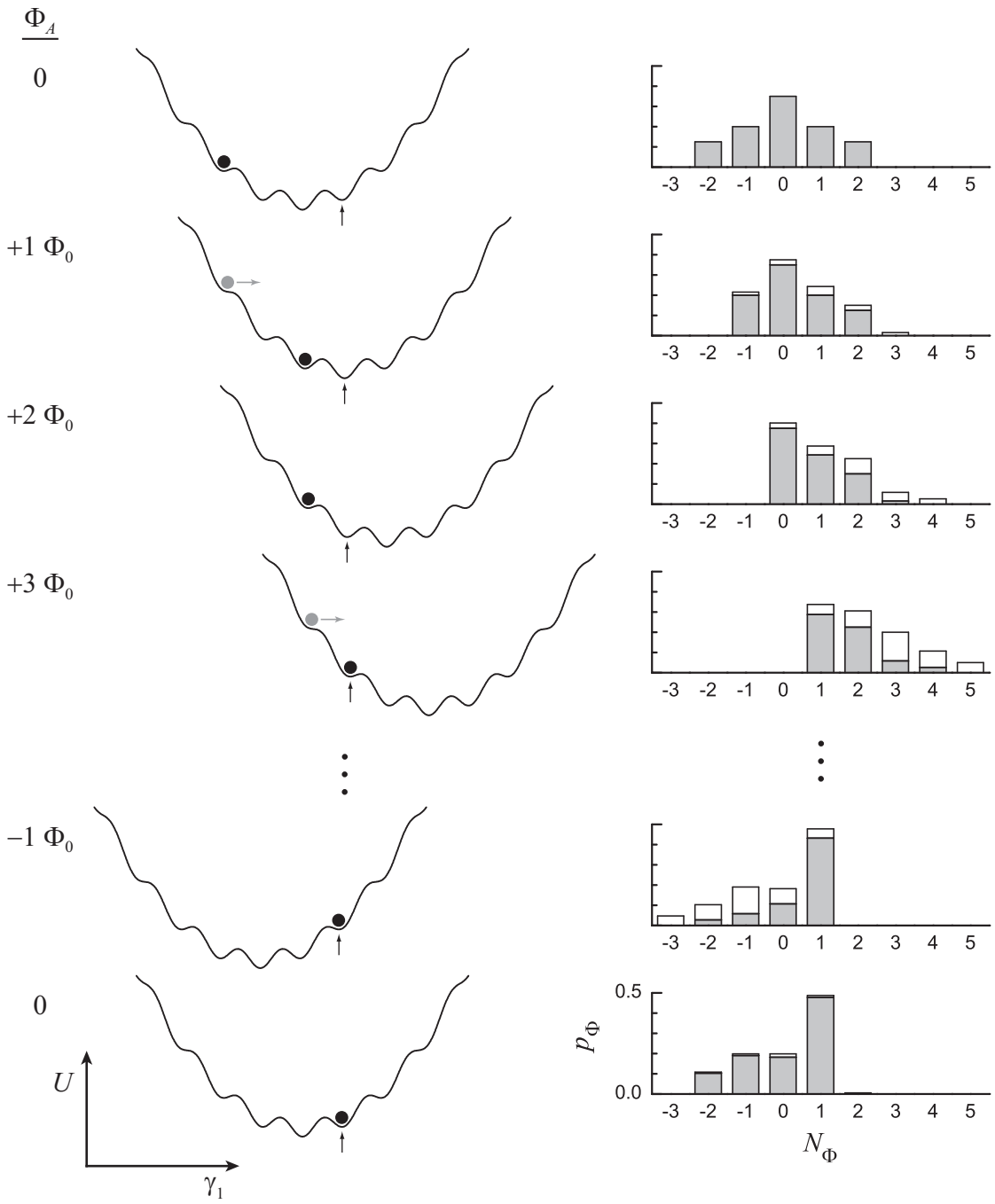

Figure 6.10: Schematic of the flux shaking procedure. The left column shows a cut through the potential of a symmetric SQUID with $\beta = 4.8$ as the applied flux is oscillated to force occupancy of the $N_\Phi = 1$ state (vertical arrows). The solid circles represent what the flux state might do for any one trial. The right column shows the probability of occupying the different flux states for an ensemble of measurements, starting from the simple (fictitious) distribution at the top. This distribution also governs how the occupation probability of a well that becomes unstable is redistributed, as the shaking proceeds. The solid part of each bar represent population carried over from the previous step; the open part is due to redistribution.

the particle must switch again. If, as in the figure, the device settles in $N_\Phi = 1$, then it will stay there for the remainder of the oscillation (and any shaking that follows). If it retraps in any other well, it would be forced out within one cycle and the whole process would repeat. Each time the system switches flux states, it enters the running state for a brief amount of time (on the order $T_1 \approx 50$ ns). On the other hand, if we had used current shaking [119], the system would remain in the voltage state longer and cause heating and possibly decoherence due to quasiparticle generation or other effects.

The right column of Fig. 6.10 shows the probability $p_\Phi(N_\Phi)$ for occupying flux state N_Φ, from a simple model of the shaking dynamics [4]. The first histogram shows an example of what p_Φ could be upon retrapping from the finite voltage state. These initial vales are given by the discrete probability distribution ρ^0_Φ. In the example, I have taken $\rho^0_\Phi(N_\Phi) = 0.125, 0.2, 0.35, 0.2, 0.125$ for $N_\Phi = -2, -1, 0, 1, 2$, respectively (with all other values equal to zero). As the $N_\Phi = 0$ well is at the lowest energy, it has the highest probability of being occupied. The desired $N_\Phi = 1$ state starts out at $p_\Phi(1) = 0.2$.

For simplicity, I will assume that wells become unstable when the applied flux is equal to an integral number of flux quanta. At $\Phi_A(t) = \Phi_0$, $N_\Phi = -1$ through 2 remain stable. Thus p_Φ for these states are carried over from $\Phi_A = 0$, represented by the solid bars in the second histogram. However, $N_\Phi = -2$ has become unstable and any system in that state must settle in one of the newly allowed states. The redistribution is governed by the discrete probability distribution $\rho_\Phi(N_\Phi - \Phi_A/\Phi_0)$. A key assumption in the model is that $\rho_\Phi = \rho^0_\Phi$. Thus at $\Phi_A(t) = \Phi_0$, the probabilities $p_\Phi(-2)\,\rho_\Phi(N_\Phi - 1)$ are added to $p_\Phi(N_\Phi)$, which are indicated by open bars in the second histogram. Here, $p_\Phi(-2) = 0.125$ is the occupation probability of $N_\Phi = -2$, before it became unstable.

This process continues, with a different set of five flux states having a non-zero

occupation probability every time Φ_A increases by a flux quantum. For example, at $\Phi_A(t) = 3\ \Phi_0$ the $N_\Phi = 2$ state inherits a probability of 0.225 from the previous step. In that previous step, $p_\Phi(0) = 0.402$, 20% of which now goes to $N_\Phi = 2$, bringing its total to $p_\Phi(2) = 0.306$.

For the one oscillation shown in the figure, $p_\Phi(1)$ increases from 0.2 to 0.488. Notice that the "lower" states end with finite probability, while the "higher" are completely empty. This situation would be reversed with a flux oscillation of the opposite polarity. In either case, the occupation probability of the desired well increases quite dramatically with further shaking. A different well could have been selected simply by changing the offset $\Delta\Phi_A$ of the oscillations, whereas when shaking the current bias, the system can be initialized to only the highest critical current state.

Before continuing, I should point out that Fig. 6.10 is slightly misleading. A cut along the γ_1-axis was chosen in an attempt to show all of the flux states using a single graph. However, as indicated in §2.5, this cut could miss flux states that have shallow wells. More importantly, the figure suggests than when the system jumps to a new flux state, it is only γ_1 (or γ_2, if the perpendicular cut is chosen) that changes value. In reality, when a flux well becomes unstable, it leaves the phase particle with sufficient energy to explore a large region of the 2-D phase space (which, incidentally, is one reason why we assume the redistribution probabilities ρ_Φ are close to the retrapping ones ρ_Φ^0). However, as the measurement is only sensitive to the final flux state and not the chaotic trajectory that was taken to get there, the simplified cartoon conveys the essence of the technique.

Our SQUIDs are highly asymmetric (in critical currents and inductances) and can have many flux states. Nonetheless, the flux shaking procedure still works. As we do not know the device parameters exactly, the peak-to-peak amplitude $\widetilde{\Phi}_A$ and offset $\Delta\Phi_A$ of the oscillations need to be found experimentally.

Figure 6.11 shows an example of data for SQUID DS_1, measured at 20 mK. We measured switching histograms with the usual simultaneous current and flux bias ramps. However, before starting the ramps, ten sinusoidal flux oscillations were applied to the device at $I_b = 0$. Cartoons of the waveforms used for I_f are shown in the figure. The left and right side panels of Fig. 6.11(a) show the resulting histograms for $\widetilde{\Phi}_A = 0$ and 14.4 Φ_0. Each vertical line of the central panel of Fig. 6.11(a) is a histogram of this sort, where dark colors represent a large number of counts. As the simultaneous ramp is designed not to change the initial flux state of the SQUID, the number of counts in a histogram peak is a good measure of the occupation of the corresponding flux state.

In Fig. 6.11(a), $\widetilde{\Phi}_A$ (indicated by the vertical arrow on the sample waveform) was varied in order to find the optimal value. In addition, $\Delta\Phi_A$ was set to $\widetilde{\Phi}_A/2$ in each case, so that the flux was always positive. I have labeled the x-axis in both current and flux, where $M_f\widetilde{I}_f = \widetilde{\Phi}_A$ (and $M_f = 51.2$pH). The histogram with no flux oscillations is centered about $I_b = 33.5$ μA, as shown in the left panel. As the oscillation amplitude and offset increase, the critical current of the maximally occupied state increases. In fact, every time $\widetilde{\Phi}_A$ increases by a flux quantum, the range of occupation shifts up by one state. This trend continues until the highest critical current state is occupied with a probability of 0.473 at $\widetilde{\Phi}_A = 14.4$ Φ_0. The histogram at this oscillation amplitude, for which only one allowed state is always stable, is shown in the right panel of Fig. 6.11(a). This state had zero counts in the initial distribution. Once $\widetilde{\Phi}_A > 15$ Φ_0, no single potential well is stable throughout a full cycle of an oscillation, so the flux shaking does not isolate any state.

To find the best offset for selecting a single state, we next varied $\Delta\Phi_A$ with fixed $\widetilde{\Phi}_A = 14.5$ Φ_0 [see Fig. 6.11(b)]. In this figure, $M_f\Delta I_f = \Delta\Phi_A$. As the offset increases, the critical current of the selected state increases, as expected. The SQUID could be initialized to any of the sixteen observed flux states, if the offset

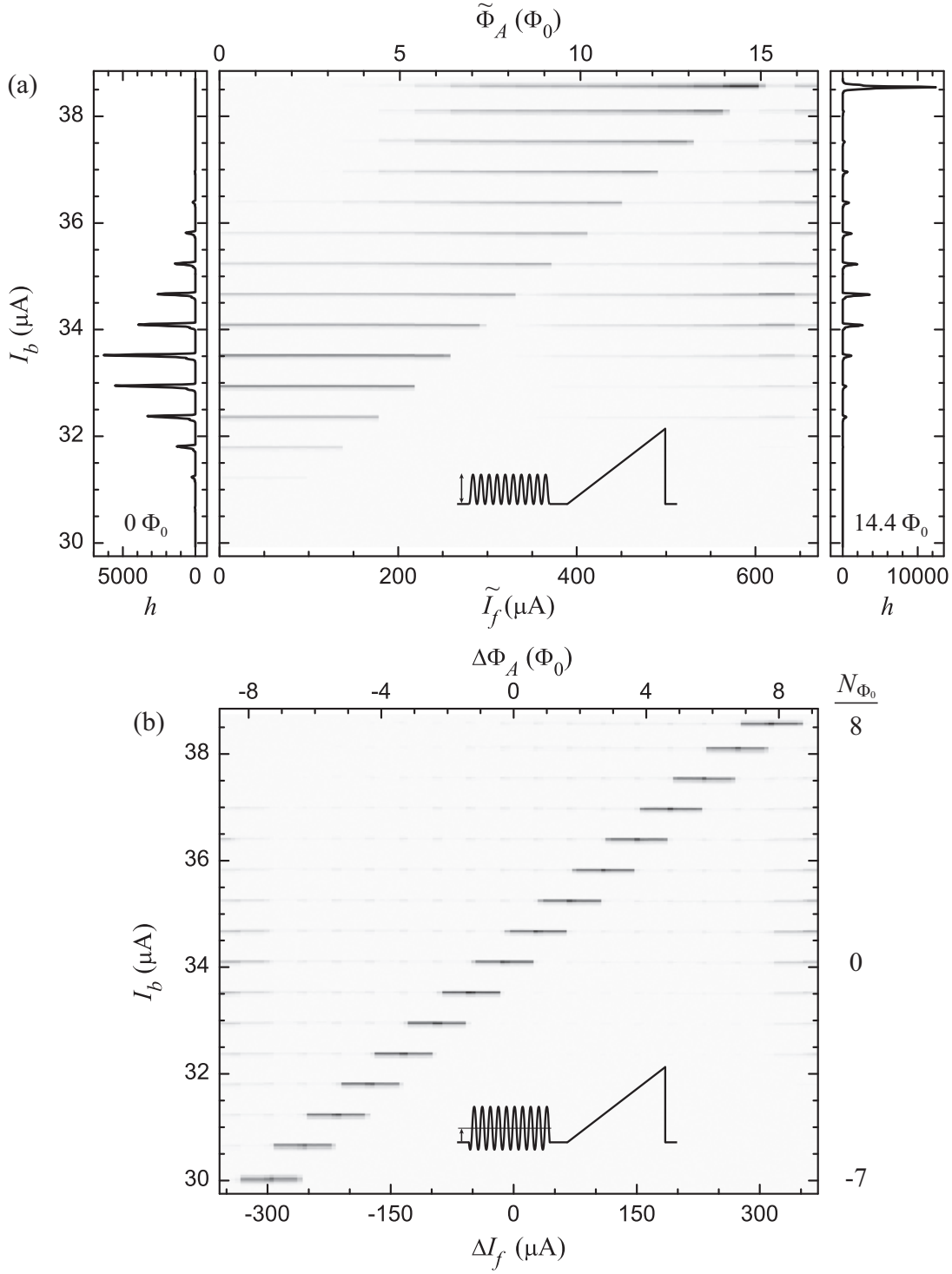

Figure 6.11: Experimental determination of shaking amplitude and offset. The grayscale maps show switching distributions. (a) Ten oscillations at 44 kHz that are entirely positive (inset) occupy the flux state of SQUID DS_1 with the highest critical current with increasing probability as the oscillation amplitude ($\widetilde{I}_f$ or $\widetilde{\Phi}_A$) increases. (b) By changing the offset (ΔI_f or $\Delta\Phi_A$) of the oscillations (with $\widetilde{\Phi}_A = 14.5\ \Phi_0$), the SQUID can be initialized in any of the sixteen visible flux states.

was chosen carefully. At $\Delta\Phi_A = 7.2\ \Phi_0$, the fifteenth and sixteenth states are nearly equally occupied, as are the fourteenth and fifteenth at $6.2\ \Phi_0$. Only near $\Delta\Phi_A = 6.7\ \Phi_0$ is the shaking effective in isolating the fifteenth state. Naively, one would expect the best performance to occur at an integral number of flux quanta. There is an apparent $0.3\ \Phi_0$ shift on the $\Delta\Phi_A$-axis. This could be due to the fact that the flux waveform resets slightly negatively to match the current waveform. Also, it could simply be due to a calibration error or to an additional source of flux near the device, such as trapped vortices. This offset tended to vary with time and particularly after helium transfers, so the parameters for the flux shaking often had to be fine tuned.

An unbiased SQUID made from conventional s-wave superconductors is always able to support an odd number of flux states, so this device ought to have at least seventeen states. If we identify the flux state that is isolated with an offset of $\Delta\Phi_A = -0.3\ \Phi_0$ as $N_\Phi = 0$, the highest critical state is $N_\Phi = 8$, consistent with this number. In addition, the $N_\Phi = 0$ state would have a critical current consistent with the value of I_{01} listed in Table 6.1, as required. It is possible that $N_\Phi = -8$ is "invisible" because the system does not escape to the voltage state when that state's critical current is exceeded during the simultaneous ramp. It is, however, curious that the initialization worked for a peak-to-peak amplitude of $14.5\ \Phi_0$. For seventeen states, the minimum of $\widetilde{\Phi}_A = 15\ \Phi_0$ would occur only for a fortuitous value of β.[1] The inconsistency between the experimentally measured value and the prediction based on the number of states is perhaps due to a calibration error with the former. That the amplitude is so close to the critical value explains why the offset had to be adjusted so carefully to pick out a single state. I suspect that if we had used a slightly larger $\widetilde{\Phi}_A$ in Fig. 6.11(b), each flux state would have been

[1]This is true when the "end" flux state is being isolated and there is no flux offset. For any other state, it is possible that a peak-to-peak amplitude of $14\ \Phi_0$ would isolate one of seventeen states.

isolated for a wider range of $\Delta\Phi_A$.

The data shown in Fig. 6.11 for DS_1 were taken under suppression field #2. The values listed in Table 6.1 might not be exactly right, as they imply fifteen flux states at zero bias. The discrepancy could be due to an error in the current calibration, misidentification of $I_{01} - I_{02}$ on Fig. 6.8(b), or a drift in critical currents during the five months separating measurement of the current-flux characteristics and flux shaking. As I_{02} only needs to be larger by 200 nA to result in seventeen states, any of the possibilities is plausible.

An alternate explanation is that there was some background flux biasing the SQUID when $I_f = 0$, which is also entirely likely. In this case, the SQUID could support an even number of states, as mentioned in the discussion of Fig. 2.16. As an example, consider the simultaneous bias path shown in Fig. 6.7(d). It crosses the qubit branch of five flux states, which is the maximum number of peaks that will be seen in a histogram, independent of flux shaking. Assume instead that the "slope" of the trajectory is the same, but that it starts at $\Phi_A = -0.5\ \Phi_0$. In this case the path crosses six branches, all of which can be seen in a switching histogram, as long as the flux shaking is performed in the presence of the overall flux offset; *i.e.* this offset is independent of the applied offset $\Delta\Phi_A$.

Figure 6.12(a) shows the expected number of flux states for the parameters listed in Table 6.1 as a function of the applied flux. Figure 6.12(b) contains the same information for a SQUID with a slightly larger I_{02}. In both cases, the number of states is odd when Φ_A is near an integral number of flux quanta and even when it is near a half-integral number of flux quanta. Thus if the simultaneous ramp used to measure the histograms actually began at finite Φ_A (which we know it does), it would be possible to see sixteen peaks and the experimental value of the flux shaking amplitude in Fig. 6.11 would make sense. In fact, for a SQUID with the parameters of Fig. 6.12(b), the bias trajectory would have to be carefully set in order to see an

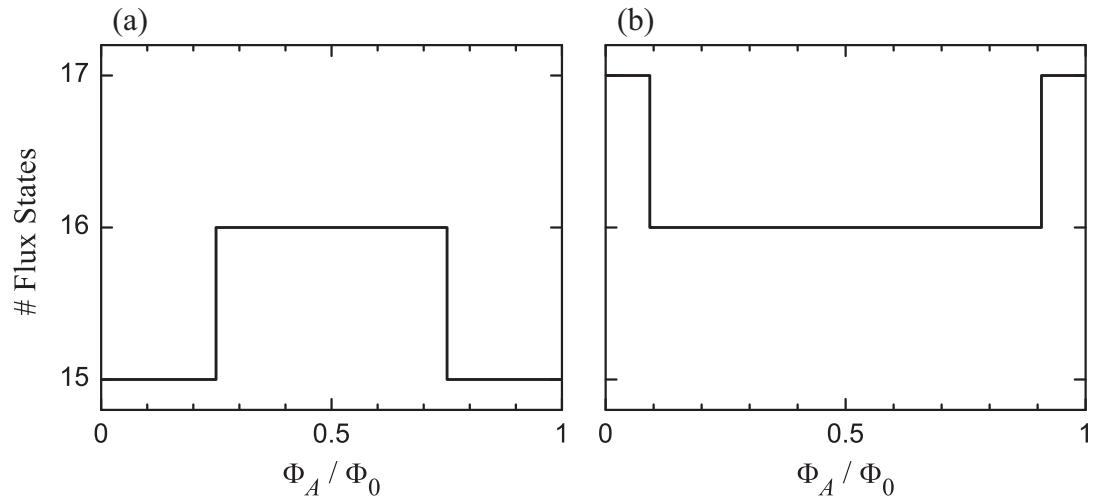

Figure 6.12: Flux dependence of the number of allowed states. The number of flux states for a dc SQUID is plotted as a function of the applied flux at $I_b = 0$. The device parameters are $I_{01} = 34.3$ μA, $L_1 = 3.520$ nH, $L_2 = -5.2$ pH, and $M_b = 0$, with I_{02} equal to (a) 4.4 μA and (b) 4.6 μA.

odd number of states; a small offset during the simultaneous biasing would lead to an even number of histogram peaks. This explanation is not inconsistent with the fifteen peaks seen in Fig. 6.8(b), as the bias path used to generate that data set was quite different.

We can test the model of flux shaking sketched in Fig. 6.10, by assuming that the initial multi-peak histogram obtained without any shaking gives the redistribution probabilities ρ_Φ. I will assume that there are seventeen states. In Fig. 6.13(a-c), oscillations with $\widetilde{\Phi}_A = 14.8$ Φ_0 and $\Delta\Phi_A = -0.4$ Φ_0 were used to initialize the system to $N_\Phi = 0$; in Fig. 6.13(d-f), $N_\Phi = 8$ was occupied with the same amplitude and $\Delta\Phi_A = 7.7$ Φ_0. The bars give the occupation probability of each of the states after one, five, and ten oscillations and the dots indicate the levels predicted by the redistribution model. The agreement is reasonable in all cases with discrepancies likely due to the simplification of the redistribution process.

In the model, I assumed that flux states only become unstable when Φ_A is equal to an integral number of flux quanta. At this point, the potential is the same

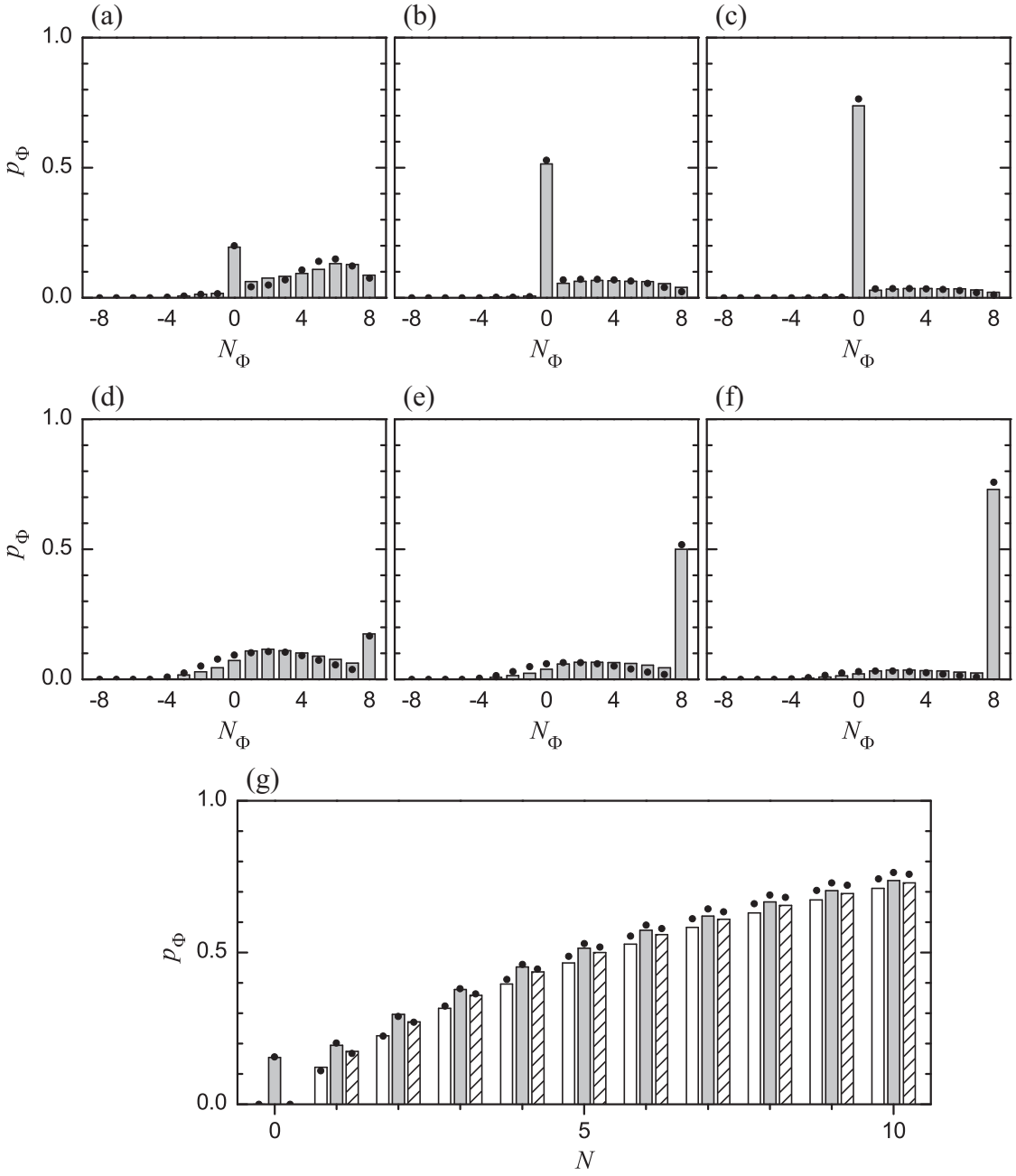

Figure 6.13: Flux shaking with a variable number of oscillations. The occupation probability p_Φ of each of the flux states for SQUID DS_1 is plotted for shaking that occupies $N_\Phi = 0$ after (a) one, (b) five, and (c) ten oscillations. (d-f) Comparable results are plotted for occupancy of $N_\Phi = 8$. The solid circles show the result of the simple redistribution model. (g) The occupation probability of $N_\Phi = -7$ (open bars), $N_\Phi = 0$ (gray), and $N_\Phi = 8$ (hatched) are nearly the same after $N = 10$ oscillations that occupy those states, even though their initial values are quite different.

as at $\Phi_A = 0$ (apart from a shift in the coordinates), which motivated the assumption $\rho_\Phi = \rho_\Phi^0$. However, as seen in Fig. 6.12, a flux state will generally become unstable at some fraction of a flux quantum during the oscillations. For an increasing flux, this happens at $\Phi_A = 0.751\ \Phi_0$ and $0.092\ \Phi_0$ in Fig. 6.12(a) and (b). When the system is forced to find a new well, the potential can be quite different than at zero bias. Thus, it is not surprising that the model does not reproduce the data perfectly.

Figure 6.13(g) shows the occupation probability of $N_\Phi = -7$, 0, and 8 after N oscillations whose offsets isolate those states; for example, for $N_\Phi = -7$, $\Delta\Phi_A = -7.3\ \Phi_0$. Although the high flux states start off with probabilities under 10^{-4}, all three states reach comparable levels within just a few oscillations. It is also clear that flux shaking has its largest impact in the first few oscillations. Again, the agreement between the data and model (circles) is good, although the model seems to overestimate the occupancy.

We also studied flux shaking in device DS_1 with suppression field #3, where there were many more flux states. Figure 6.14(a) shows the initial experimental probability distribution after retrapping. Note in particular that $p_\Phi(0) = 0.03$. After just five oscillations with no offset [see Fig. 6.14(b)], the distribution changes quite dramatically; $p_\Phi(0)$ increases to 0.09. As Fig. 6.14(c) shows, after 45 oscillations $p_\Phi(0)$ reaches 0.5. The small dots indicate the results of the simple model, which are in reasonable agreement with the data. One issue is that ρ_Φ^0 was not determined with a great deal of precision. The insets to Fig. 6.14 shows the same data (with experimental values shown with solid lines) plotted on a log scale.

For the data in Fig. 6.14, the flux oscillations had a frequency of 19.2 kHz with a peak-to-peak amplitude of $166.4\ \Phi_0$. This implies anywhere from 167 to 169 flux states. Interestingly, we were able to see 167 histogram peaks by varying $\Delta\Phi_A$. That the oscillation amplitude is consistent with the number of peaks seen with the current-flux characteristic obtained by sweeping the flux positively (for suppression

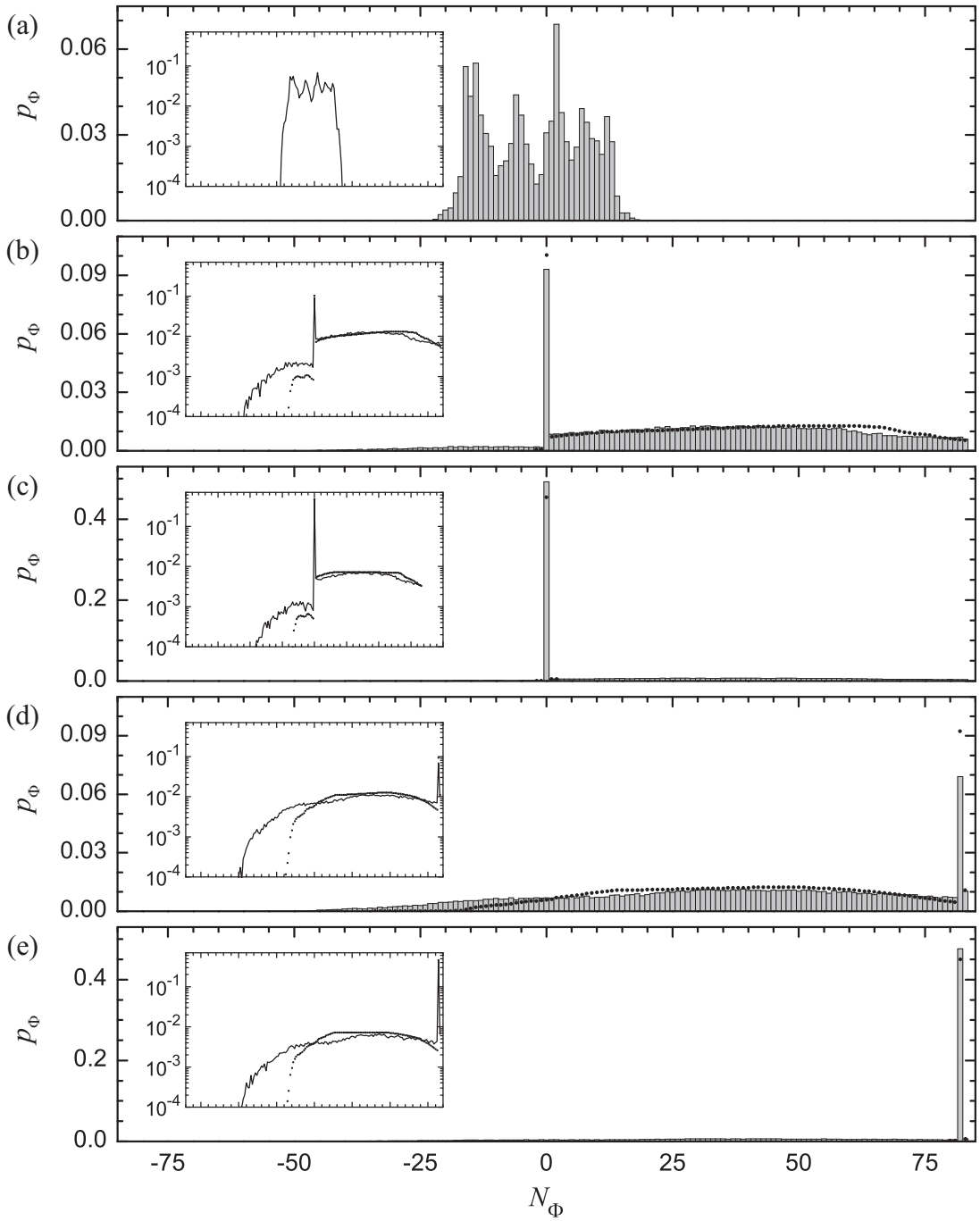

Figure 6.14: Flux shaking with a large number of states. The bars indicate the occupation probability of each of 167 allowed flux states of SQUID DS_1, measured at 20 mK. The dots show the results of the simple model, although some have been omitted for clarity. The insets have the same information on a log scale, with experimental data indicated with solid lines. (a) Only a quarter of the states are occupied with no shaking. The system can be effectively initialized to the $N_\Phi = 0$ state with (b) 5 or (c) 45 oscillations or to the $N_\Phi = 82$ state with (d) 5 or (e) 45 oscillations.

fields #2 and #3) is what lead me to assert that the entire qubit branch could be seen with that bias trajectory.

A flux offset $\Delta\Phi_A = 83.7\ \Phi_0$ was used for the data in Fig. 6.14(c) and (d), which isolated $N_\Phi = 82$. The implication is that the calibration must have had significant error, as the offset is about a flux quantum larger than expected. After 45 oscillations, $p_\Phi(82) = 0.48$, although it was not seen at all in the initial distribution. Thus even large β devices can be initialized effectively and are viable qubits, insofar as initialization is concerned. A similar technique has been applied to high β rf SQUIDs to provide an on-chip precision flux bias [120].

Although flux shaking appears to work well with single devices, we were concerned that there could be problems with the coupled qubits that are ultimately needed. When one device is forced to switch flux states, it briefly enters the voltage state before retrapping. While we were unable to measure any voltages with the detection electronics, this process still could affect neighboring qubits. For example, a current pulse could reach a neighbor through a coupling capacitor, causing it to switch out of the desired well.

We did some preliminary testing on DS_2. First, with DS_2B grounded, 45 oscillations (with no offset) were applied to DS_2A at 17 kHz, initializing it to $N_\Phi = 0$ with a probability greater than $p_\Phi(0) = 0.999$. Next, DS_2A was grounded and 45 flux oscillations were applied to DS_2B, thereby initializing it with a probability of $p_\Phi(0) = 0.986$. Finally, oscillating currents were applied to both flux bias lines simultaneously. It was difficult to determine the occupation probabilities of both devices using the simultaneous biasing, because the switching of one device to the voltage state could trigger the other, even if both were not initialized to $N_\Phi = 0$. While it was clear that the probability of DS_2A fell by a small amount, the joint initialization probability was greater than 0.98. From this we conclude that there is no reason to believe that simultaneous shaking of multiple SQUIDs will not work,

but that further tests are needed to optimize the process.

An unexpected benefit of the different flux states is that they correspond to different amounts of current through the isolation junction and thus different levels of isolation from the bias leads (see §4.3). In the rest of the thesis, unless otherwise noted, the SQUID was initialized with at most one trapped flux quantum, where the isolation from the current bias leads works best.

6.6 State Readout

If junctions or SQUIDs are to be used in performing quantum gate operations, a reliable method of determining the state occupation needs to be developed. Even with a more modest goal of understanding the dynamics of these devices, this knowledge is useful. We have used three schemes, sketched in Fig. 6.15, each of which has advantages and disadvantages. Unfortunately, what they have in common is that the qubit junction ends in the voltage state on each measurement cycle. The resulting large electric field across the junction may lead to charge motion effects in the barrier in addition to heating. In terms of quantum computation, these are then destructive measurements and are quite different from continuous state measurements, where the system is projected to an eigenstate of interest. As the voltage state is outside of the qubit basis, error correction cannot be implemented on the qubit. These techniques could be used with auxiliary measurement qubits, which are needed for error correction.

In principle, it should be easy to "calibrate" any of these techniques. By driving the $0 \rightarrow 1$ transition with sufficient power, it should be possible to saturate the $|1\rangle$ population at very close to 0.5, which is the value a measurement should return. Unfortunately, with the short coherence times of our devices, it was difficult to produce a precisely known saturation without also exciting a non-negligible occupation of $|2\rangle$. As a result, evaluating the performance of the measurements was a bit more

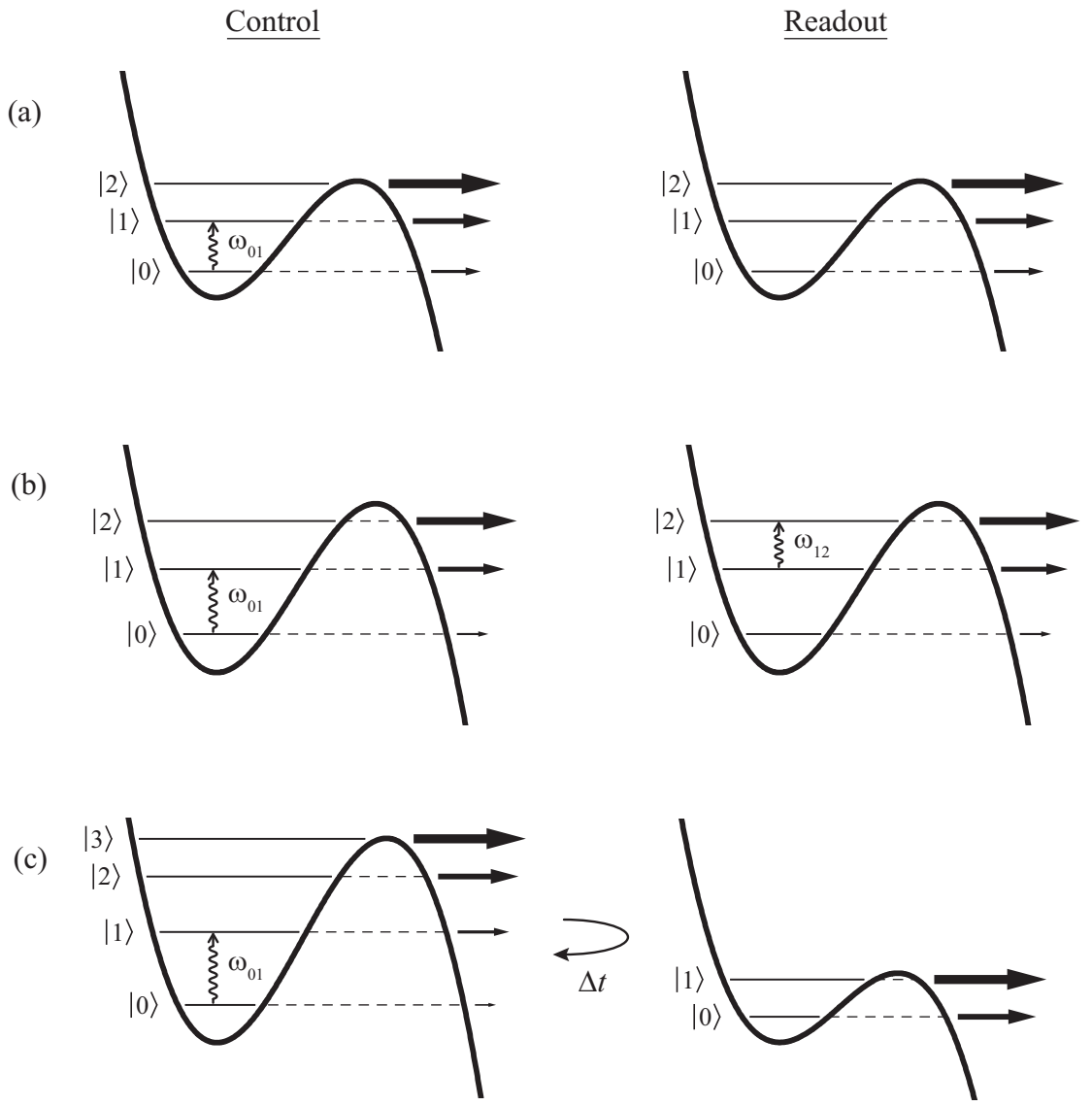

Figure 6.15: Schemes for state readout. The left column shows the potential, energy levels, and tunneling rates during state manipulation (microwave activation at ω_{01} in this case). The right shows the conditions for readout. (a) For the direct tunneling measurement, the bias current is set so Γ_0 and Γ_1 are both measurable. (b) With a microwave pulse readout, the anharmonic nature of the potential is exploited by exciting only the $1 \rightarrow 2$ transition to perform readout. (c) Lower bias currents can be used with the bias pulse readout, where the bias is held high for a short time Δt, long enough for $|1\rangle$ (but not $|0\rangle$) to escape. While the potentials have been drawn for realistic values of I_b, the anharmonic level spacing has been exaggerated for clarity.

involved.

6.6.1 Direct Tunneling

Unless otherwise noted, the method I used for state readout was to measure the escape rate to the voltage state. The total escape rate, which is experimentally accessible, is the sum of the individual state populations weighted by the corresponding escape rates. As the ratio of escape rates between adjacent energy levels is generally quite large, this is a particularly sensitive way of detecting excited state population.

For example, assuming that only the two lowest states are occupied, Eq. (3.30) gives the total escape rate as $\Gamma = P_0\Gamma_0 + P_1\Gamma_1$, where P_i is the normalized probability of being in state $|i\rangle$ [see Eq. (3.31)]. Using $P_0 + P_1 = 1$, we can write the excited state population due to a microwave current as

$$P_1 = \frac{\Gamma - \Gamma_0}{\Gamma_1 - \Gamma_0} \approx \frac{\Gamma_0}{\Gamma_1}\frac{\Delta\Gamma}{\Gamma}, \tag{6.9}$$

where the approximation holds for $\Gamma_1 \gg \Gamma_0$ and under the assumption that the escape rate Γ_{bg} measured without microwaves is equal to Γ_0. Thus the escape rate enhancement $\Delta\Gamma/\Gamma$ defined in Eq. (6.7) is proportional to P_1, and P_1 can be extracted once Γ_0/Γ_1 is estimated from theory. A major source of error is that even a small population in $|2\rangle$ can have a dramatic effect on Γ, due to the size of Γ_2.

At times, the sensitivity to upper levels makes the technique quite useful. For example, consider a junction at fixed bias in dynamic equilibrium. In this case, the normalized probabilities P_i will be constant. Thus, Γ will also be constant even as the occupation probabilities ρ_i decay to zero due to tunneling. However, if interlevel transitions or tunneling move the system away from equilibrium, then P_i and Γ will change and the total escape rate will give an accurate picture of the dynamical

processes of the junction.

The power of this technique lies in its simplicity and its well-understood characteristics. It only requires that a particular experiment be repeated many times to build up a histogram of switching time with good statistics. No extra timing or calibration is required. In some sense, it is a passive measurement, where no potentially disruptive action is taken on the junction, other than the switching itself. As one histogram will give information over a range of bias currents (if a current ramp is being used), it is easy to collect a fair amount of data quickly.

The technique also has several drawbacks, particularly with respect to quantum computation. For one, we do not initiate the measurement. The junction can escape before, during, or after the manipulation that is being performed. Also, tunneling can shorten the lifetime of an excited state in a very direct way and thus itself is a source of decoherence. These decohering effects are strongest at high escape rates, where it is easiest to take data.

Perhaps the most serious issue for the work presented here is that it can be difficult to extract the populations from the total escape rate, because the individual rates are not necessarily known beforehand. While Γ_0 can often be measured precisely, the higher escape rates are easier to predict than to measure. Work is still ongoing in the group to obtain accurate experimental data of Γ_1 and Γ_2, using the technique described in §6.6.3 [104].

Lastly, it is only easy to measure escape rates between 10^2 and 10^8 1/s, which restricts the range of bias currents that can be studied. For slower rates, each repetition will take a long time. To reach faster rates, the bias current has to be swept quickly so that the junction will not escape prematurely. As Γ increases exponentially, the accessible escape rate range corresponds to a bias current range of less than one percent of the critical current for the types of devices we study.

6.6.2 Microwave Pulse

Some of the shortcomings of the previous technique can be addressed by using a microwave pulse to perform state readout [39,44]. This approach takes advantages of the anharmonic potential, which leads to unequal energy level spacings. The general idea is that the junction is biased where both Γ_0 and Γ_1 are so low that the system is unlikely to tunnel during the course of a particular experiment. Manipulations can then be performed between $|0\rangle$ and $|1\rangle$ without fear of tunneling. When it comes times to perform a measurement, a microwave pulse of frequency $\omega_{12} < \omega_{01}$ is applied. If the junction is in $|1\rangle$ at this time, it will be excited into $|2\rangle$. It will then quickly tunnel to the voltage state, if Γ_2 is large enough. If the junction is in $|0\rangle$ at the time of the pulse, the pulse ideally has no effect and the junction stays in the zero-voltage state.

Knowledge of individual escape rates is not needed and measurements can be performed at even lower bias currents by using a pulse of frequency ω_{13}. In principle, by adjusting the length and power of the pulse, this technique can be a "single-shot" measurement. For each trial, one only has to know if the junction tunneled to the voltage to know whether it was in $|0\rangle$ or $|1\rangle$. In addition, the measurement is performed at the same current bias as the manipulation, which is an advantage that the technique discussed in the next section does not have.

In practice, we found that the excitation process was too inefficient to realize a single-shot measurement. At low microwave power, the excitation rate may not be sufficiently faster than the relaxation rate from $|2\rangle$ to promote all of the population in $|1\rangle$. The slow rates may also lead to a long measurement time, making it difficult to resolve fast dynamics (for example, during a Rabi oscillation). At high power, the resonances broaden and the system will tunnel even if it is in $|0\rangle$. Also, it can be somewhat difficult to determine the resonance condition accurately, especially for energy levels deep in the potential well. For these reasons, this technique has a

limited "measurement fidelity" associated with it that the direct escape rate does not suffer from. The initial results were not very promising, so I never quantitatively determined the efficiency of this technique at optimal conditions or tried a $1 \rightarrow 3$ transition. A measurement of the relaxation time determined with this technique is described in §8.7.

6.6.3 dc Bias Pulse

The central idea of the microwave pulse measurement, as previously discussed, is to selectively force the population in $|1\rangle$ to tunnel to the voltage state on demand by promoting it to a state with large escape rate. In the dc bias pulse technique, this is accomplished instead by freezing the populations, but quickly increasing all of the escape rates by applying a quick pulse of current (or flux) bias. If the height and width of this pulse are chosen carefully, the system will only escape if it started in $|1\rangle$. This process is somewhat reminiscent of the standard way of manipulating charge qubits and has been applied to charge-phase [31], flux [121], and phase qubits [43, 114] successfully.

As with the microwave pulse, the dc bias pulse can be a single-shot measurement. It is, however, easier to implement, faster, more efficient, and can give information about the population in $|2\rangle$ in a natural way.

Care has to be taken that the pulse itself does not excite population into higher states. In practice, a line normally used for microwaves was used to supply the pulse. The small capacitive coupling from this line to the junction and the limitations of the pulsing electronics probably kept the Fourier components of the pulse well below the plasma frequency of the junction.

Another issue with this technique is that it involves sweeping the junction through a potentially large range of current. If there are, for example, spurious resonances that couple to the junction (see §8.5), the system will decohere while

passing through. This effect has been claimed to cause a reduction in measurement fidelity [98]. However, for our devices the pulses are very fast (roughly 2 ns) and the splittings are very small (less than 5 MHz), so that this effect should be small [104].

6.7 Summary

I began this chapter by showing IV curves of the junctions. These provide a fairly straight-forward method of determining the junction quality, including the barrier uniformity and leakage. It was difficult to measure the sub-gap resistance, but it appears to be greater than 100 kΩ at dc. This sets the minimum intrinsic dissipation of any of our qubits.

The escape rate measurement which I described in §6.2 is our primary method of determining the behavior of our junctions. Our basic experiment involves measuring the time at which a junction switches to the finite voltage, with respect to, for example, the start of a current bias ramp. By repeating the experiment many times, we can calculate the rate of tunneling Γ from the ensemble statistics. Γ is very sensitive to excited state population and is one way to readout the state of a qubit. However, the pulsing techniques in §6.6 are more powerful, although they still need to be optimized.

We would like to operate our SQUIDs so that one junction serves as a qubit and the other provides isolation, where the qubit acts as a single current-biased junction. This can be accomplished by initializing the flux state to a particular value (§6.5) and applying a current and flux bias in such a way that adds no current through the isolation junction (§6.4). The bias trajectory to follow can be determined experimentally by measuring the current-flux characteristics (§6.3).

Chapter 7
Tunneling Escape Rate Measurements

We can learn a great deal of information about phase qubits by studying tunneling from the zero-voltage state. All of the measurements described in this chapter involve simply measuring the rate of tunneling (which is a very sensitive gauge of excited state occupation probability) as a function of the current bias, as described in §6.2. There are three main goals for these experiments. First of all, the more experimental results we can explain, the more confidence we have that our model of the device is accurate. Secondly, we can use the tunneling data to determine some key device parameters, such as critical currents. Finally, for quantum computation, measurements of the dissipation time T_1 are very important, as T_1 sets an upper bound on the time during which quantum gate operations can be performed. Estimates for the dissipation can be found by considering the interplay of the unknown decay rate with other processes that we understand. For example, changing the temperature of the junction results in thermal transitions governed by the Boltzmann factor and the bias ramp rate has a dynamical effect that is fairly easy to characterize.

Figure 7.1 shows the total escape rate Γ of junction LC_2B measured at six temperatures T (as determined by the thermometer at the refrigerator's mixing chamber). At 25 mK, Γ is roughly exponential in the current bias I_b, as one would expect for tunneling from the ground state alone (see §2.3.3). As the temperature increases, higher states become thermally populated. These states have higher tunneling rates, leading to an enhanced Γ. Because the escape rate measurement works over a particular range of Γ, it was possible to obtain data over a different range of I_b for each temperature. The scatter at both ends of each curve is due to poor counting statistics. At high I_b, several of the curves appear to approach each other.

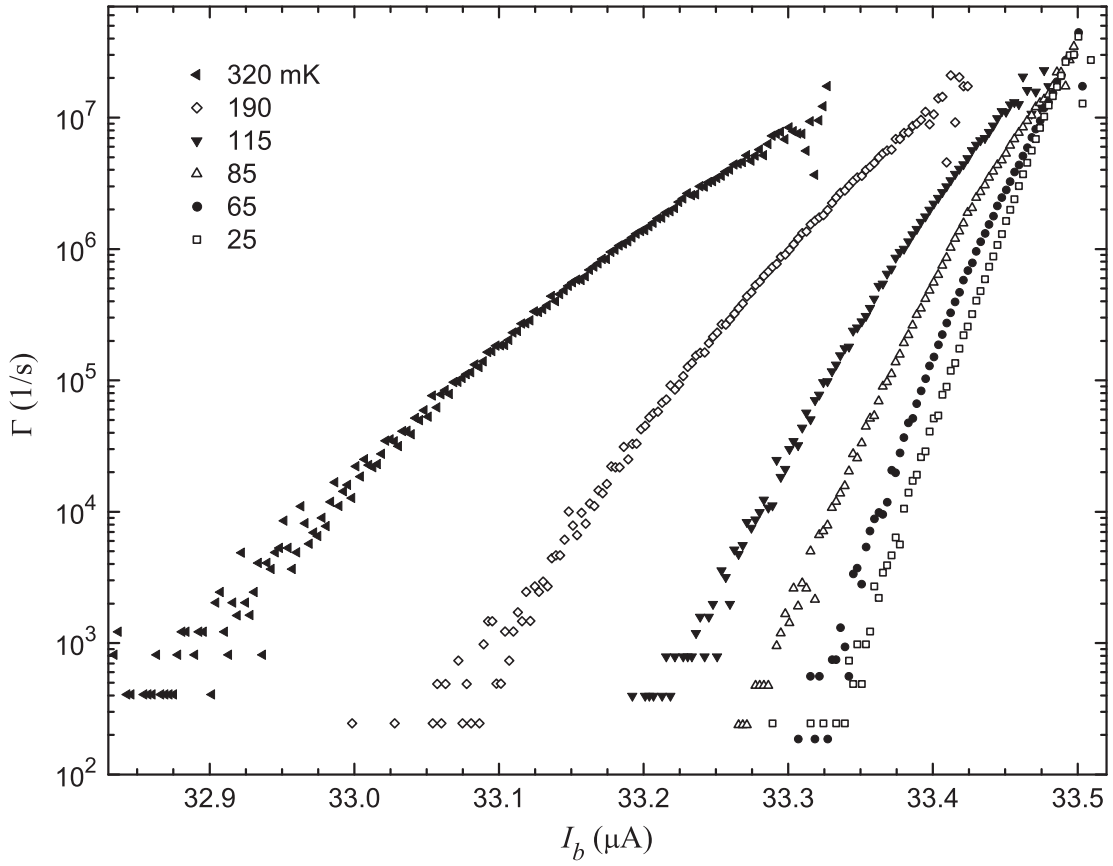

Figure 7.1: Temperature-dependent escape rates of junction LC_2B. For a given current bias I_b, the total measured escape rate Γ increases quite dramatically with the temperature of the mixing chamber as higher energy levels are thermally occupied. The data was taken at a ramp rate of 0.07 A/s with the suppression field $B_\parallel$ set to 2.7 mT, by Huizhong Xu.

The goal of much of this chapter is to describe the various features of data sets of this kind. I will first show that a classical model of the junction reproduces the high temperature data. However, to describe the lowest temperatures, the quantum results of §2.3 must be employed. With the two extremes covered, I will then summarize the master equation formalism that can be used to describe experiments in which the dynamics occur on a time scale much longer than the coherence time T_2. Finally, I will describe how both slow and fast bias ramps can be used to measure the dissipation time T_1.

7.1 Thermal Activation and Macroscopic Quantum Tunneling

One approach to understanding the temperature series shown in Fig. 7.1 is to treat the junction classically, as was first done over 30 years ago [60]. Deviations from classical behavior formed some of the first evidence for macroscopic quantum tunneling in these systems [23, 122, 123]. This approach can provide a confirmation of the description of the circuit and a simple method for determining the dissipation in the system [111, 124].

The classical analysis begins with the assumption that the Josephson relations and the properties of the tilted washboard given in §2.2.2 are valid. The assumptions will be justified if the resulting model describes the data faithfully. The classical rate at which thermal activation allows the phase particle to escape the potential well is [61, 125]

$$\Gamma = a_t \frac{\omega_p}{2\pi} \exp\left(-\frac{\Delta U}{k_B T_{esc}}\right), \tag{7.1}$$

where ω_p is the plasma frequency [given by Eq. (2.32)], ΔU is the barrier height of the well [given by Eq. (2.30)], and a_t is a classical thermal prefactor that parameterizes damping. T_{esc} can be thought of as an effective escape temperature that characterizes the lifetime of the supercurrent state. In a classical system, T_{esc} will be equal to the refrigerator temperature T and will be independent of I_b.[1] In describing experimental data with this model, neither may be true.

T_{esc} can be calculated for each value of Γ, by inverting Eq. (7.1) [68, 123]. The difficulty of this method is that the junction critical current I_0 must be independently measured in order to evaluate ω_p and ΔU. Alternatively, Eq. (7.1) may be rewritten,

[1] Alternatively, T_{esc} can be defined by Eq. (7.1) with $a_t = 1$ [123]. In this case, $T_{esc} \neq T$ in the presence of damping and it could be a function of I_b.

using the approximation for the barrier in Eq. (2.31), as

$$\left[\ln\left(\frac{a_t\,\omega_p}{2\pi\,\Gamma}\right)\right]^{2/3} = \left(\frac{4\sqrt{2}}{3}\frac{E_J}{k_B T_{esc}}\right)^{2/3}\frac{I_0 - I_b}{I_0}. \tag{7.2}$$

If $T_{esc} = T_{esc}\,(T)$ is taken to be a constant with respect to I_b, then the expression on the right side is linear in I_b and the equation can be written as $\omega_\Gamma = c_1 I_b + c_0$, where $\omega_\Gamma \equiv [\ln(a_t\,\omega_p\,/2\pi\Gamma)]^{2/3}$. Using an initial guess for I_0, the data can be fit to a line,[2] with the fitting parameters giving the critical current and escape temperature as

$$I_0 = -\frac{c_0}{c_1} \qquad \text{and} \qquad T_{esc} = -\frac{4\sqrt{2}}{3}\,\frac{\Phi_0}{2\pi}\,\frac{1}{k_B}\,\frac{1}{c_1\sqrt{c_0}}\,. \tag{7.3}$$

This extracted value of I_0 can then be used to recalculate ω_Γ and another fit performed. This process converges in just a few iterations to self-consistent values of I_0 and T_{esc} [111, 124]. A value for the junction capacitance C_J is still needed to calculate ω_p, but I have found that T_{esc} generally changes negligibly when C_J is varied by as much as 50%.

7.1.1 *LC*-Isolated Phase Qubits

I performed the T_{esc} fitting procedure on the data shown in Fig. 7.1. ω_Γ and the best fit line (whose parameters were used to calculate ω_Γ) are plotted in Fig. 7.2(a). The open points in Fig. 7.3(a) and (b) show the extracted values of T_{esc} and I_0 from the fits, as a function of temperature (for more values than shown in Fig. 7.1). Based on the quality of the fits, the uncertainties in T_{esc} and I_0 are roughly 3% and 4%, respectively. In doing the analysis for Fig. 7.1(a) and the open circles in Fig.

[2] I used the Levenberg-Marquardt method for these fits (with uncertainties determined from counting statistics of the histograms); see §15.5 of Ref. [69]. The algorithm generates a covariance matrix; the uncertainties in the fitting parameters are given by the square root of the main diagonal of this matrix. Unless otherwise noted, this is always the algorithm I used for nonlinear fitting or, as in this case, for linear fitting with unequal weighting.

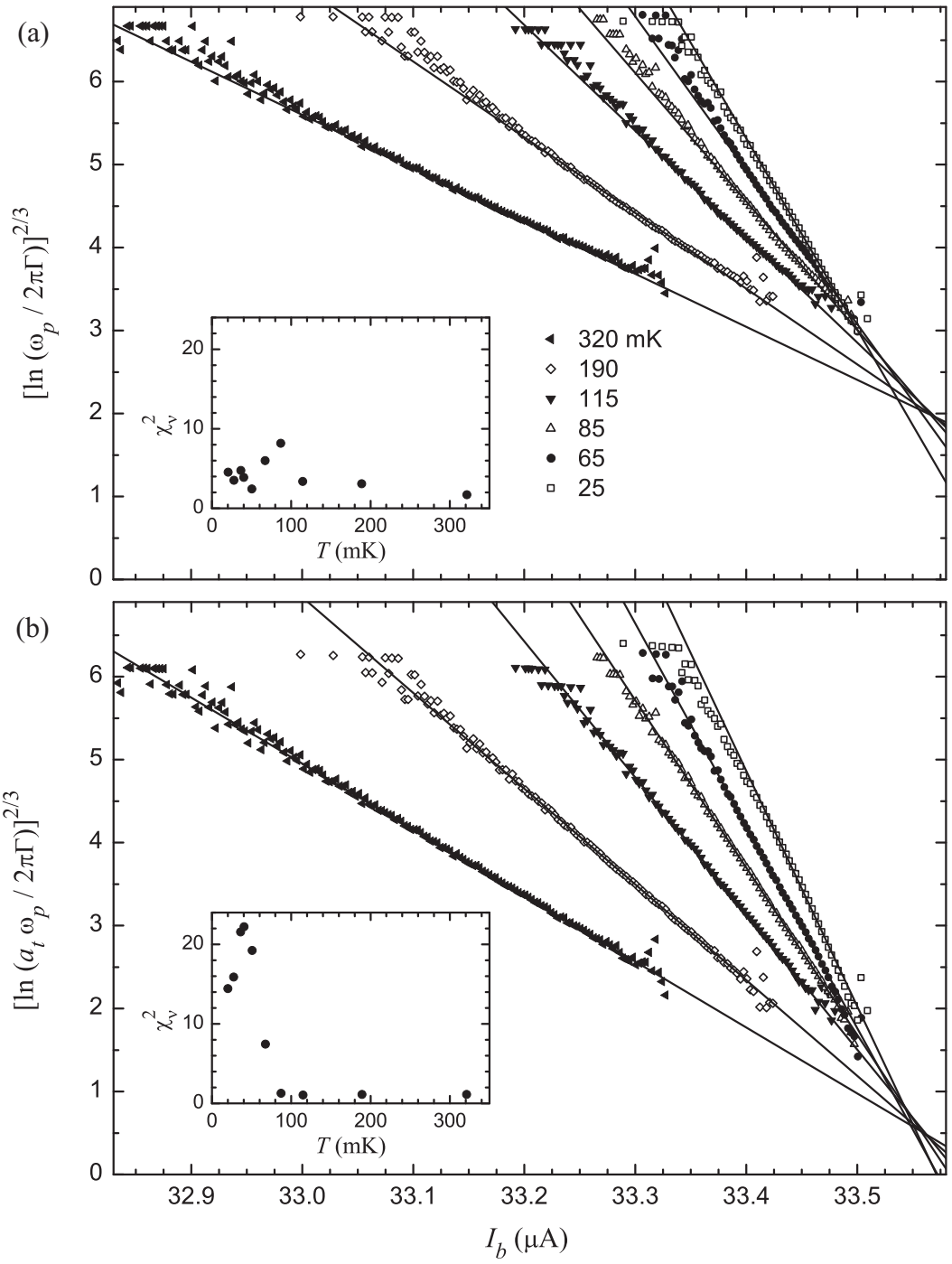

Figure 7.2: Thermal activation in junction LC_2B. Each of the curves of Fig. 7.1 is roughly linear when plotted as ω_Γ, as predicted by Eq. (7.2). The solid lines show the end results of an iterative fitting procedure, with the reduced χ^2 shown in the insets (for more temperatures than shown in the main figure). The quality of the fits at high temperature is worse (a) assuming no damping ($a_t = 0$) than for (b) $R_J = 2$ kΩ. The reverse is true at low temperature.

7.3(a) and (b), I have assumed that $a_t = 1$. In addition, I have taken $C_J = 4.2$ pF, consistent with the design value and the spectroscopic measurements discussed in the following chapter.

I will first discuss the results for $T > 50$ mK (with $a_t = 1$). Figure 7.1(a) shows that ω_Γ is roughly linear in I_b, suggesting that the junction is displaying classical behavior. However, the data do show some curvature and other features, as reflected in the large reduced chi-square (or χ^2 per degree freedom) χ^2_ν, shown in the inset to Fig. 7.2(a), particularly at low temperature. In addition, Eq. (7.2) predicts that the linear fits will coincide at the point ($\omega_\Gamma = 0$, $I_b = I_0$), but they do not. The lowest temperature curves appear to disagree the most. In fact, the best fit value of I_0 [open circles in Fig. 7.3(b)] varies quite strongly with T. Although T_{esc} does increase in proportion to T, it does not agree as well as one might expect if the theory were complete.

Some of the deficiencies of the classical theory can be addressed by including the effects of damping. In the limit of low damping, the thermal prefactor is [61]

$$a_t = \frac{4}{\left[\sqrt{1 + (Qk_BT/1.8\Delta U)} + 1\right]^2}\,, \tag{7.4}$$

where $Q = \omega_p R_J C_J$ is the bias-dependent quality factor of the junction, determined by the effective shunting resistance R_J of the RCSJ model (see §2.2). Notice that $a_t = 1$ if $Q = 0$, and this is what I used for the fits discussed in the previous paragraphs.

I repeated the iterative fitting procedure with $R_J = 2$ kΩ. A selection of the fits are shown in Fig. 7.2(b) and self-consistent values of T_{esc} and I_0 are plotted as solid circles in Fig. 7.3(a) and (b). Figure 7.3(c) shows the calculated values of $a_t\,(I_b)$ for the lowest (solid) and highest (dashed) temperatures.

Although the fits at low temperature are somewhat worse with the inclusion

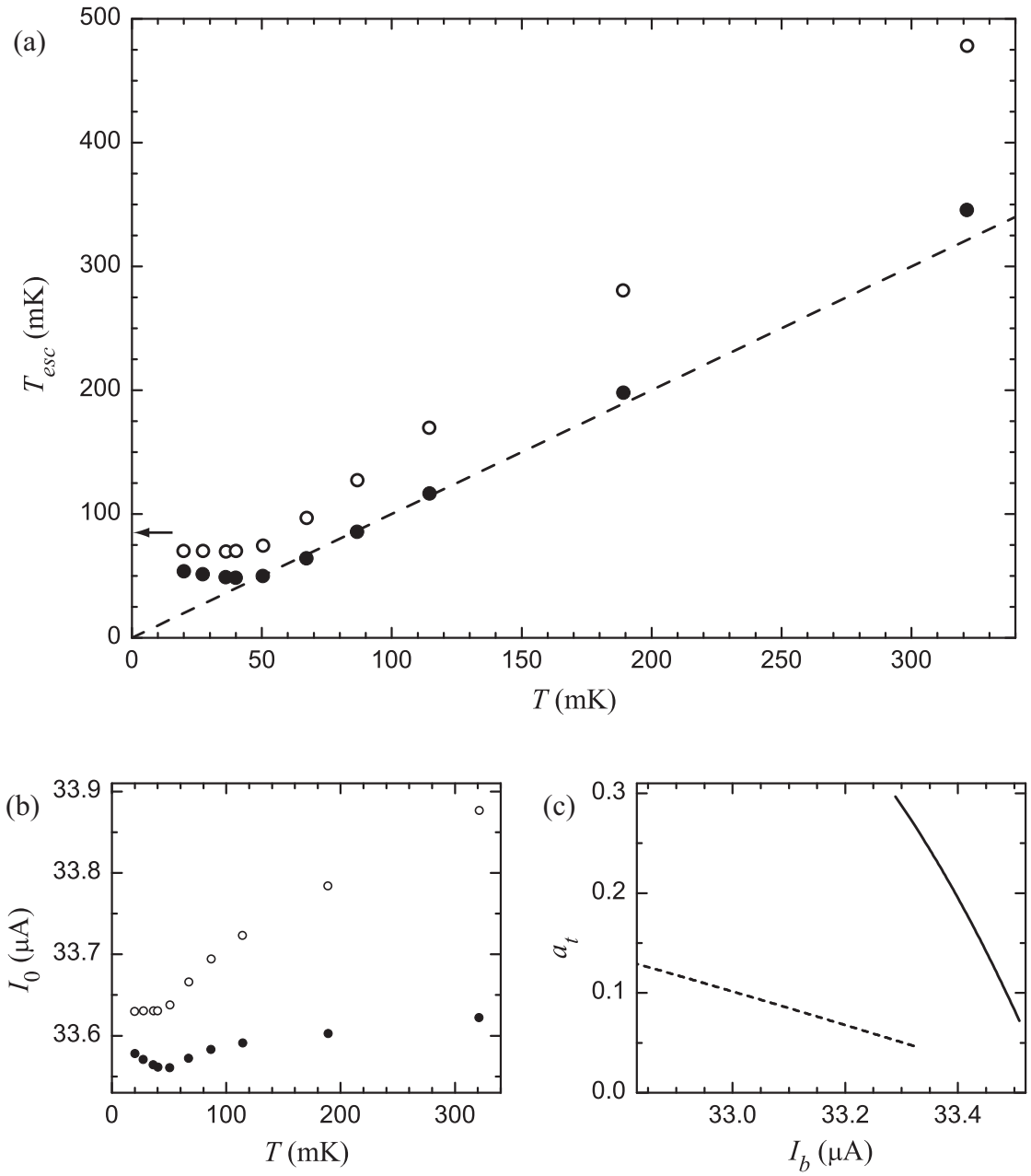

Figure 7.3: Effective escape temperature for junction LC_2B. The best fit (a) effective escape temperature T_{esc} and (b) critical critical current I_0 are plotted as a function of the refrigerator temperature T, with $C_J = 4.2$ pF. Several of the escape rate curves that were analyzed to generate these points are plotted in Fig. 7.1. The open points correspond to $a_t = 1$, while the solid are for $R_J = 2$ kΩ. An arrow marks the prediction for the zero-temperature escape temperature T^0_{esc} from Eq. (7.5). (c) The calculated values of a_t for $R_J = 2$ kΩ at $T = 25$ mK (solid) and 320 mK (dashed) are strongly bias-dependent and show that dissipation has a significant effect on activation.

of damping, χ^2_ν for the four highest values of T are nearly equal to 1 [see Fig. 7.2(b)]. For these values, the extrapolation of the fits do nearly coincide at $\omega_\Gamma = 0.5$. Furthermore, the solid circles of Fig. 7.3(a) show that the values of T_{esc} now lie very close to T, which is how I selected the value of R_J to use. Finally, the variation in the extracted values of I_0 has been reduced to about $\pm 0.1\%$. All of this suggests that the classical theory with damping is accurately describing the switching of the junction to the voltage state at high temperatures.

Nevertheless, there are several sources of error in this experiment that need to be considered. First of all, there are the usual concerns with the current calibration. As all of the data were taken with the same nominal bias ramp, this is unlikely to be a serious problem and likely just results in an overall shift of I_0. However, we often saw shifts in the switching histograms as a function of T that were clearly unrelated to junction dynamics. Although I was not able to find their origin, it is possible that these shifts were due to the current supplied to the mixing chamber heater or a temperature-dependent resistance on the current bias line. Fortunately, even if I shifted I_b by 2% in doing the analysis, the extracted value of I_0 would shift by a comparable amount, but T_{esc} changed negligibly. As the experimental I_b shifts were generally less than 20 nA, they should not affect the analysis significantly. The other problem is the calibration of the mixing chamber thermometer, as discussed in §5.1.1. It is quite possible that the values of T could be incorrect by 10% or more at high temperatures. In addition, the temperature of the sample could be different than that of the thermometer. Hopefully, this error is somewhat smaller than the corrections introduced by damping. Finally, the junction capacitance is required in the analysis. Fortunately, as I noted earlier, T_{esc} has a particularly weak dependence on C_J. Herein lies the power of this technique. With a simple experiment and an analysis method that makes only a few assumptions and is relatively insensitive to experimental parameters, an estimate for the shunting resistance (and thus the

relaxation time $T_1 = R_J C_J$) can be easily found; in this case, $T_1 \approx 8$ ns.

Turning now to the low temperature data, T_{esc} saturates at $T \approx 50$ mK (both with and without the inclusion of damping), meaning that even when the thermodynamic temperature was 20 mK, the junction behaved as a classical system would at 50 mK. If the junction were truly classical, then T_{esc} would continue to decrease, as required by Eq. (7.1). At $T = 0$, there would be no thermally activated switching and the junction would go to the finite voltage state only when $I_b \geq I_0$ (in the absence of electrical noise). The saturation behavior is consistent with quantum tunneling; even at absolute zero with the system in the ground state $|0\rangle$, it will tunnel out at a rate Γ_0.

The theoretical ground state escape rate of a junction was described in §2.3. By comparing Eqs. (7.1) and (2.42), the effective escape temperature at $T = 0$ (where $a_t = 0$) for the cubic approximation to the washboard potential is

$$T_{esc}^0 = \frac{\hbar \omega_p}{k_B} \frac{1}{7.2\,(1 + 0.87/Q)} \left[1 - \frac{\ln \sqrt{120\pi\,(7.2\,N_s)}}{7.2\,N_s\,(1 + 0.87/Q)} \right]^{-1}, \tag{7.5}$$

where N_s is the harmonic approximation to the number of levels in the well, defined in Eq. (2.37). This expression provides an interesting way to predict the low temperature value of T_{esc} in the quantum limit, as the input parameters (I_0 and R_J) can come from fitting high temperature data to a classical theory. The transition between quantum and classical character occurs at the crossover temperature T_{cr}. In the case of low damping, a simple estimate for this temperature is [126, 127]

$$T_{cr} \approx \frac{\hbar \omega_p}{2\pi k_B}. \tag{7.6}$$

For the devices that I have studied, the base temperature of the dilution refrigerator was always well below T_{cr}. With regards to quantum computation, the expression shows that as the critical current density decreases, the temperature required to

initialize a junction to its ground state also decreases.

As tunneling has a different functional form than thermal activation, T_{esc}^0 is a function of I_b. I will choose to evaluate it where Γ can be measured precisely. The "middle" of the base temperature Γ curve in Fig. 7.1 is at about 10^5 1/s, where $I_b \approx 33.41$ μA. Near this value of I_b (with $I_0 = 33.6$ μA and $C_J = 4.2$ pF), $\omega_p/2\pi \approx 8$ GHz and T_{esc}^0 is roughly 85 mK, with an uncertainty of about 10 mK. With $R_J = 2$ kΩ, dissipation gives a correction of less than 1 mK; this is consistent with Fig. 2.10, which suggests that damping does not greatly affect Γ_0 in our devices. An arrow marks T_{esc}^0 on Fig. 7.3(a), as in all of the T_{esc} plots in this section. Given the uncertainty in I_0 and C_J, there is perhaps reasonable agreement with the open circles, which were also calculated with $a_t = 1$.[3] The estimate for the crossover temperature is 60 mK at the chosen value of I_b, which is roughly the value of T where saturation begins.

A useful feature of the LC-isolated devices is that a suppression magnetic field $B_\parallel$ could be used to adjust the junction critical current (see §6.1). At $B_\parallel = 4.4$ mT, I_0 for junction LC_2A was reduced to 21.5 μA. Even at the base temperature of the refrigerator, the measured escape rate was exponential in I_b only to a certain value. Above 5×10^7 1/s, Γ rolled off noticeably. It is possible that this was an artifact of the detection scheme. If the voltage that develops across the junction when it switches to the running state does not have the same time dependence on each trial, then a smearing will be introduced in the switching histogram.[4] The same effect can occur if there is a loss of timing resolution from sources external to the junction. For example, this data set was taken with a high ramp rate of 0.52 A/s, leading to short switching times. The highest escape rates correspond to a small number of counts, so they can be easily distorted. In this particular case, the switching

[3]The solid circles were calculated using a classical theory of dissipation. Thus, the disagreement of these points with T_{esc}^0 and the increasing T_{esc} with decreasing T at low temperature only suggest that the theory does not apply in this temperature range, as expected.

[4]Plots of this voltage, as measured at the top of the refrigerator, are shown in Fig. 5.15(a).

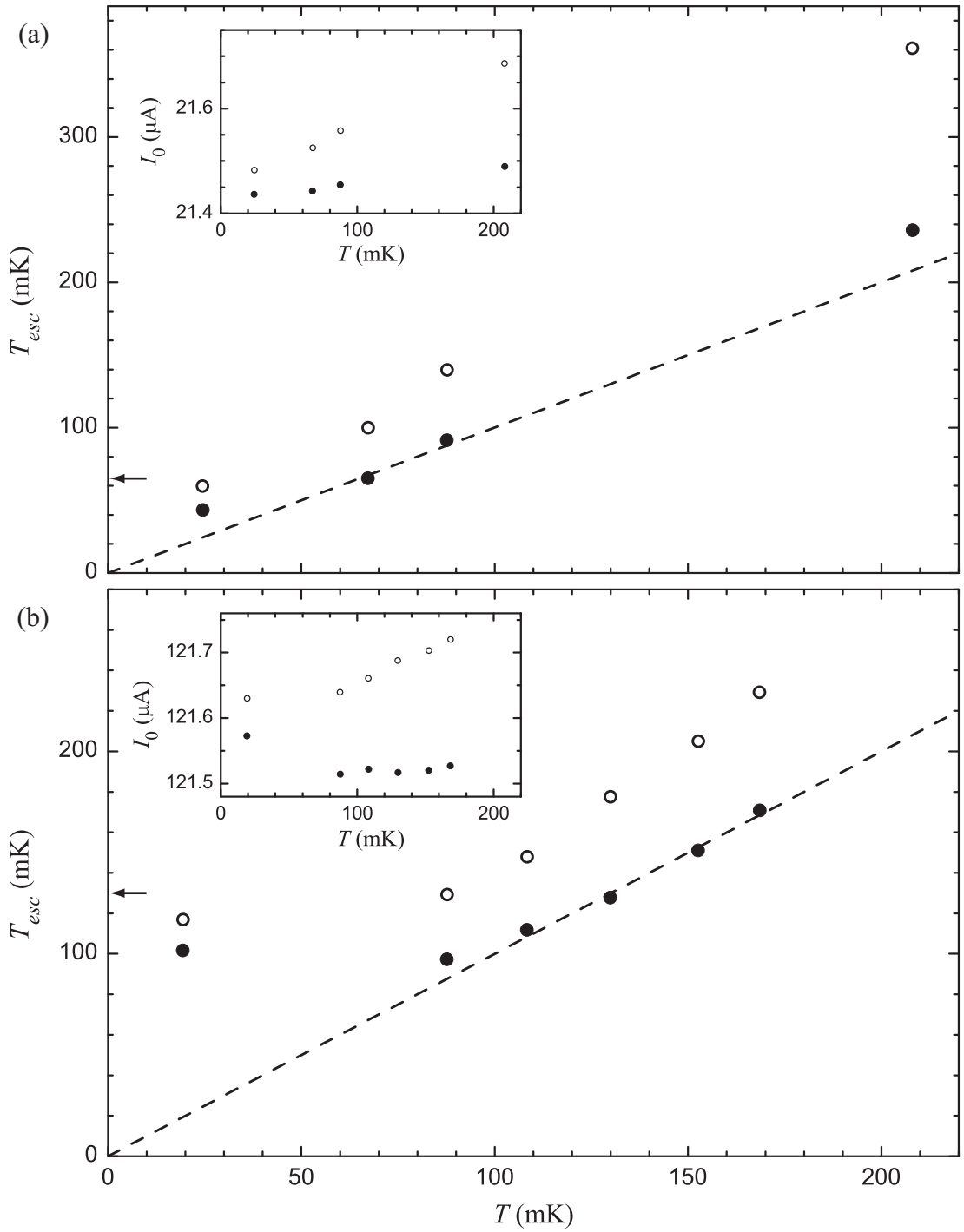

Figure 7.4: Effective escape temperature for junction LC_2A. The best fit value of the escape temperature T_{esc} is plotted against the refrigerator temperature T, for analysis with (solid) and without (open) damping. (a) When $\omega_p/2\pi \approx 6.5$ GHz ($B_\parallel = 4.4$ mT), near agreement is found between the two temperatures for $R_J = 2$ kΩ, although the fits were performed for $\Gamma < 10^7$ 1/s. (b) At the unsuppressed critical current, where $\omega_p/2\pi \approx 13$ GHz, a smaller value of 500 Ω is needed. The insets show the self-consistent values of I_0 from the iterative fitting procedure.

waveforms did not look out of the ordinary, but the distortion of the escape rates was quite pronounced. As the lower Γ data behaved as expected, I kept $\Gamma < 10^7$ 1/s in the analysis that follows.

Figure 7.4(a) shows T_{esc} and I_0 obtained for LC_2A from the iterative fitting procedure under these conditions. The open circles were calculated with $a_t = 1$ and show a hint of saturation at low T. I used $C_J = 4.8$ pF in this case, which was the value derived from the spectroscopic method described in the next chapter, but T_{esc} is relatively insensitive to small changes in the capacitance.[5] At high temperatures, T_{esc} agrees with T for $R_J = 2$ kΩ. With this value of R_J, the fits of ω_Γ vs. I_b are of higher quality than those with $a_t = 1$, but χ^2_ν does not improve as dramatically as it does in Fig. 7.2. Not shown is that ω_Γ for the different temperatures do coincide near $\omega_\Gamma = 0$ with the inclusion of damping, as expected. At $T = 24$ mK, $\Gamma = 10^5$ 1/s at $I_b = 21.32$ μA. Taking $I_0 = 21.45$ μA, Eq. (7.5) predicts $T^0_{esc} \approx 65$ mK, consistent with the data (open circles). At this point $\omega_p/2\pi \approx 6.5$ GHz, corresponding to a crossover temperature of 50 mK.

The data used to generate Fig. 7.4(b) were taken in the absence of a suppression field, so the critical current was at a maximum. The escape rates again were not featureless (although not rounded off), but restricting the fitting range had little effect on T_{esc}, so I kept all of the data. The solid dots were calculated for $C_J = 5$ pF (again, from spectroscopy) and $R_J = 500$ Ω. Although the fits were not perfect, the classical model clearly does not work for the value of 2 kΩ used for the previous data sets. As before, the coincidence of ω_Γ provides a good measure for the quality of the R_J determination (not shown). At $I_b = 121.15$ μA, the base temperature escape rate is 10^5 1/s. At this point with $I_0 = 121.54$ μA, $T^0_{esc} \approx 130$ mK, $\omega_p/2\pi \approx 13$ GHz, and $T_{cr} \approx 100$ mK.

[5]The capacitance of the junction should not be a function of $B_\parallel$, but the coupling between the junction and the LC mode created by the coupling capacitor depends on ω_p and leads to a renormalized capacitance. It is not entirely clear how this affects the classical theory.

It is perhaps telling that the shunting resistance is smaller at the highest critical current. The two data sets of Fig. 7.4 were taken within two weeks of each other (Fig. 7.1 was taken seven months earlier on a different junction) and there were no concerns with the device at this time. In fact, the unsuppressed data were taken three weeks after thermally cycling the refrigerator above 20 K, after which the field had never been turned on. However, the base temperature escape rate was not exactly exponential, so it is possible that there were problems. Of course, a possible explanation for the discrepancy is that the classical activation model is breaking down in some subtle way. Alternatively, it could be that R_J varies with frequency. It is not clear whether this is due to the design of the isolation network itself or, for example, resonances in the sample box or electrical components.

7.1.2 dc SQUID Phase Qubits

The same fitting procedure can be applied to the escape of the dc SQUID phase qubits. With the simultaneous biasing described in §6.4, the qubit junction first escapes to the voltage state, while the isolation junction remains near zero bias. In this case, the thermal theory for escape from a 1-D potential should approximate the behavior of the SQUID. I will give further details of the measurement of Γ for SQUIDs in §7.2.2.

Escape rates for DS_1 are shown in Fig. 7.5(a) for a range of temperatures. The current I_1 through the qubit was calculated from the calibrations of the current and flux biases, I_b and I_f, and the device parameters in Table 6.1 for field #2. I assumed that there was no flux offset (at $I_f = 0$), which could result in a small shift in I_1. At the lowest temperatures, a noticeable bump appears at $I_1 = 33.89\ \mu$A. The feature persists to higher temperatures, but gets washed out as higher states become thermally occupied. There will be a brief discussion of this and other features in the next section.

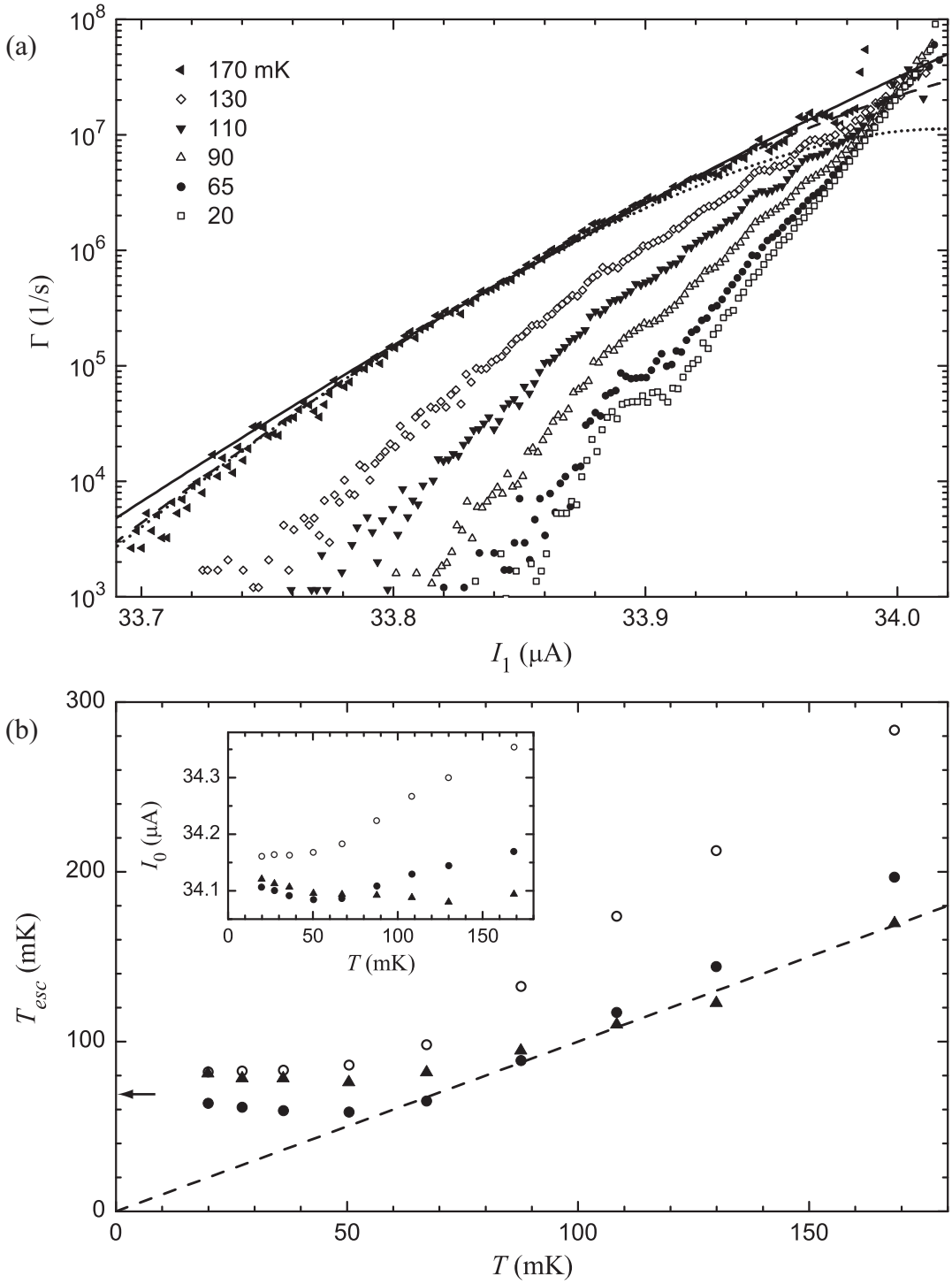

Figure 7.5: Effective escape temperature for SQUID DS_1. (a) As in Fig. 7.1, high temperatures show an enhancement in the total escape rate Γ. However, in the dc SQUID devices, additional features are seen at the lowest temperatures. The lines show fits of the thermal activation theory to the $T = 170$ mK data, with $R_J = 0$ (solid), 2 kΩ (dashed), and 8 kΩ (dotted). (b) Fits of this sort also yield the effective escape temperature T_{esc} and the self-consistent critical current I_0, for $a_t = 1$ (open circles), $R_J = 2$ kΩ (solid circles), and $R_J = 8$ kΩ (triangles).

The extracted values of T_{esc} and I_0 for DS_1 are shown in Fig. 7.5(b), for $a_t = 1$ (open circles) and $R_J = 2$ kΩ (solid circles), with $C_J = 4.4$ pF. The presence of the bump does call the results of the fits into question. However, when I restricted the fits to $10^5 < \Gamma < 10^7$, T_{esc} only changed by a few percent at all but the highest temperature. The agreement between T and T_{esc} with damping is not as good as it was for the junction LC_2. Also, the SQUIDs were expected to provide better isolation, corresponding to a larger R_J. Increasing R_J further would bring the higher temperatures into line, but would send the intermediate temperatures below the $T = T_{esc}$ line.

Figure 7.5(b) shows that good agreement is found by restricting the fits to $\Gamma < 10^6$ and setting $R_J = 8$ kΩ (plotted as triangles). The predicted values of Γ at $T = 170$ mK from Eq. (7.1) are plotted in Fig. 7.5(a) for $a_t = 0$ (solid line), $R_J = 2$ kΩ (dashed), and $R_J = 8$ kΩ (dotted). The last two match the data well at low bias, but the $R_J = 8$ kΩ curve clearly underestimates Γ at high I_1. In addition, the convergence of ω_Γ is not nearly as good as it is for $R_J = 2$ kΩ (not shown). Thus I can only restrict the shunting resistance to the range 2 kΩ $< R_J <$ 8 kΩ, which corresponds roughly to 10 ns $< T_1 <$ 30 ns.

At $T = 20$ mK, the escape rate is equal to 10^5 1/s at $I_1 = 33.92$ μA. At this current with $I_{01} = 34.1$ μA, $T_{esc}^0 \approx 80$ mK, $\omega_p/2\pi \approx 8$ GHz, and $T_{cr} \approx 60$ mK.

Aside from the usual concerns about the temperature calibration and detection errors, there could be several flaws in the theory. As I will discuss in §7.4, even at high temperatures, the quantum nature of the junction asserts itself quite clearly at high current bias, which could explain some of the discrepancies there (and perhaps why this was not as serious a problem for LC_2, where the damping was stronger).

It could also be that R_J is a function of temperature [65,66], but the relatively small range of temperatures measured should correspond to a negligible variation. However, the $T = 170$ mK curve covers a current range corresponding to almost 3

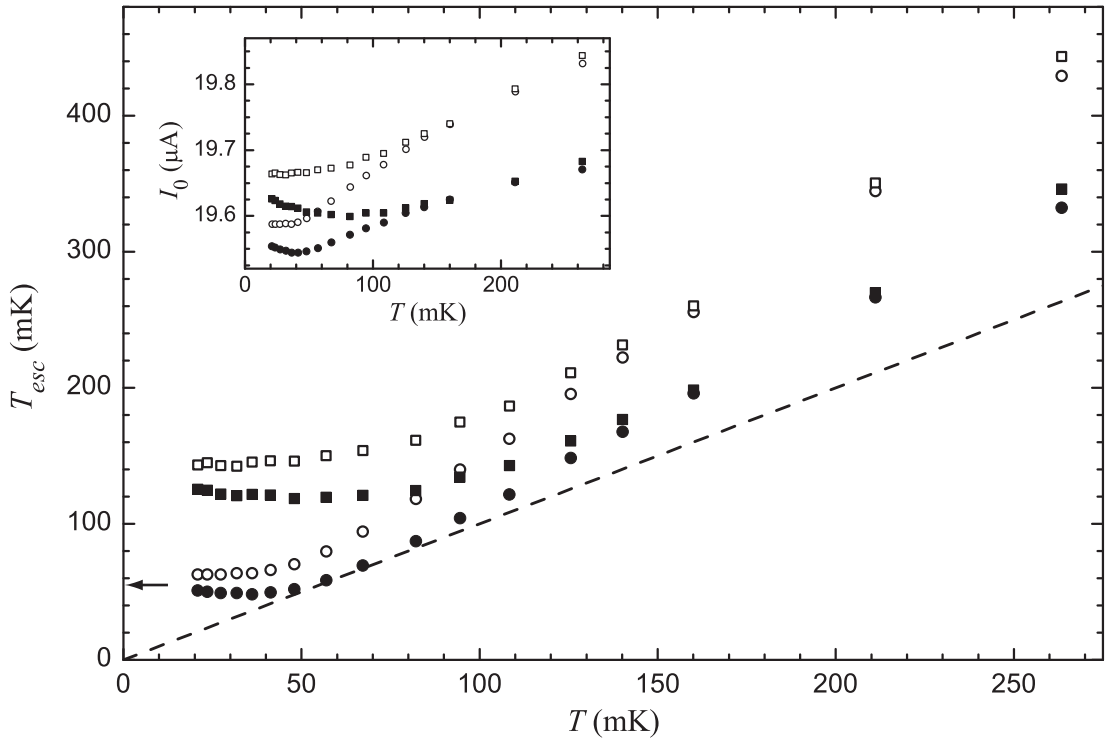

Figure 7.6: Effective escape temperature for SQUID DS_2B. The best fit value of the escape temperature T_{esc} is plotted against the refrigerator temperature T, for $a_t = 1$ (open) and $R_J = 1.5$ kΩ (solid). Significant heating was observed when then junction was left in voltage state for 400 μs (squares), as compared to when it was forced to retrap quickly (circles). The inset shows the self-consistent values of I_0 from the iterative fitting procedure.

GHz in $\omega_p/2\pi$. Therefore, if R_J were a rather strong function of frequency, it could result in apparent temperature dependence, as each curve covers a different range of I_1 (because the escape rate measurement is sensitive to a fixed range of Γ). Finally, although we bias the device so that it will act as a single junction, the potential that determines its dynamics is two-dimensional. Particularly at high temperature, the phase particle could explore a wider range of escape trajectories, as previous experiments have reported both in the classical [119] and quantum [128] regimes.

The open circles in Fig. 7.6 show T_{esc} and I_0 for SQUID DS_2B, for $C_J = 4.5$ pF and $a_t = 1$. ω_Γ was calculated with Γ as a function of the current bias I_b, rather than the qubit current I_1, because I did not know all of the device parameters well enough to extract I_1. Based on the previous data set, I found this introduces very

little error in T_{esc}. The solid circles in Fig. 7.6 were calculated with $R_J = 1500\ \Omega$ (corresponding to about 7 ns) and show a smaller, but still prominent disagreement between T_{esc} and T. The disagreement is similar to what I saw in DS_1 in Fig. 7.5(b). If these devices are to be used for quantum computation, it is critical to determine whether the low values of R_J accurately describe the junction's isolation or if they are due to flaws in the theory (or its application). Nonetheless, the agreement is qualitatively correct and many quantitative aspects also agree well. For example, I will predict the characteristic temperatures at the bias current where $\Gamma = 10^5$ 1/s. At $I_b = 19.42\ \mu$A, $T_{esc}^0 \approx 60$ mK, $\omega_p/2\pi \approx 7$ GHz, and $T_{cr} \approx 55$ mK, in good agreement with the open circles of Fig. 7.6.

One concern in claiming that the low temperature saturation of T_{esc} is due to quantum tunneling is that the junctions may not be getting as cold as the mixing chamber thermometer indicates. That the minimum escape temperature of a particular device varies with critical current, as in Fig. 7.4, is a good indication that this is not the case. Applying heat in an alternate way serves as another check, which I will discuss next.

As described in §4.3.2 and §5.2.2, DS_2 showed fairly strong heating effects if the junctions were left in the finite voltage state. In Fig. 7.6, I forced the junctions to retrap within 2 μs of the end of the histogram peak, for the values plotted with open and closed circles. For the squares, I allowed the junctions to stay in the voltage state for 400 μs, with I_b linearly decreasing to zero 200 μs after a switch. T_{esc} with $a_t = 1$ (open squares) and with $R_J = 1500\ \Omega$ (solid squares) look qualitatively similar to their unheated counterparts and are nearly equal to them for $T > 150$ mK. Below 150 mK, the curves diverge as heating becomes evident. In doing the fits of ω_Γ vs. I_b to extract T_{esc} (not shown), the expected intersection of the curves at high bias (of the sort shown in Fig. 7.2) is not as good as for the unheated data. This by itself might not be a serious cause for concern. However, additional problems are

apparent. Based only on the heated data, $I_b = 19.37\ \mu$A when $\Gamma = 10^5$ 1/s, where T^0_{esc} should still roughly be 60 mK, for $I_{01} = 19.62\ \mu$A. At the smaller current bias, the plasma frequency increases by 500 MHz at most, corresponding to $T_{cr} \approx 60$ mK. Both of the characteristic temperature predictions are well below the values seen in the plots of the heated data. The lack of consistency between T^0_{esc} and the observed saturation of T_{esc} is one piece of evidence that we are not observing macroscopic quantum tunneling in the heated data set. For this device, the saturation level is slightly above T^0_{esc}, even when the junctions retrap quickly, so more careful tests are needed in order to check if smaller heating effects are present. The slow retrapping data in Fig. 7.6 also suggest that leaving the junction in the running state has the same effect as increasing the refrigerator's temperature.

As I discussed in Chapter 2, the retrapping current I_{rt} also depends on the junction shunting resistance [see Eq. (2.35)]. Therefore, it is possible to estimate R_J by measuring a retrapping histogram [129,130]. This becomes easier at high temperatures where thermally excited quasiparticles decrease R_J by the factor $\exp(\Delta/k_BT)$, where 2Δ is the superconducting energy gap. For niobium, $\Delta/k_B \approx 16$ K, so experiments would have to be done at relatively high temperatures to obtain an easily measurable retrapping current. It would be interesting to compare effective resistance values obtained from both switching and retrapping, but I did not obtain sufficiently precise measurements of the IV curves to allow this to be done in a meaningful way.

7.2 Low Temperature Escape Rate

In the previous section, I compared the low temperature (saturated) value of T_{esc} to the quantum prediction, in order to judge whether the junction was escaping due to quantum tunneling from the ground state at Γ_0. Rather than characterize the full curve with a single number, I will now examine the bias dependence of Γ

measured at the base temperature of the refrigerator. Unfortunately, simply lowering the thermodynamic temperature of a junction does not guarantee the absence of excited state population.

7.2.1 *LC*-Isolated Qubits

Figure 7.7(a) shows the total measured escape rate Γ versus bias current I_b of the *LC*-isolated junction LC_2B at $T = 25$ mK. The data plotted as open squares were taken at a bias ramp rate of 0.07 A/s (identical to the data in Fig. 7.1), while the solid circles were taken at 0.93 A/s. Because the junction is given less time to escape at lower Γ, a faster ramp rate allows a measurement of higher escape rates. In order to convert switching time to I_b for this plot, we performed a calibration using the escape rate method described in §5.6, for both the 0.93 and 0.07 A/s rates. This gives a reliable value for the slope of the ramp, but the "offset" is more difficult to measure. As a result, the escape rates for the two sweeps were close but did not lie on top of each other, although we have every reason to believe they should. The calibration was more accurate for the slower rate, so I added an offset of 15 nA to the 0.93 A/s data so that the two data sets were coincident.

For comparison, the solid line in Fig. 7.7(a) is the theoretical Γ_0 for a single junction with $I_0 = 33.648$ μA and $C_J = 4.24$ pF, calculated with Eq. (2.43). At first glance, the good agreement over nearly seven orders of magnitude is quite encouraging and confirms our description of the device. However, the iterative fitting procedure for the thermal theory with damping returned a critical current closer to 33.6 μA [see solid circles in Fig. 7.3(b)]. A 50 nA difference over such a small range is somewhat troubling. A bigger concern comes from comparison to the I_0 and C_J parameters found by fitting the spectrum of excitations to theory (see Fig. 8.1(b) in §8.1). For that measurement, the extracted parameters are $I_0 = 33.663$ μA and $C_J = 7.32$ pF. Γ_0 for these spectroscopically derived values is plotted as a dashed

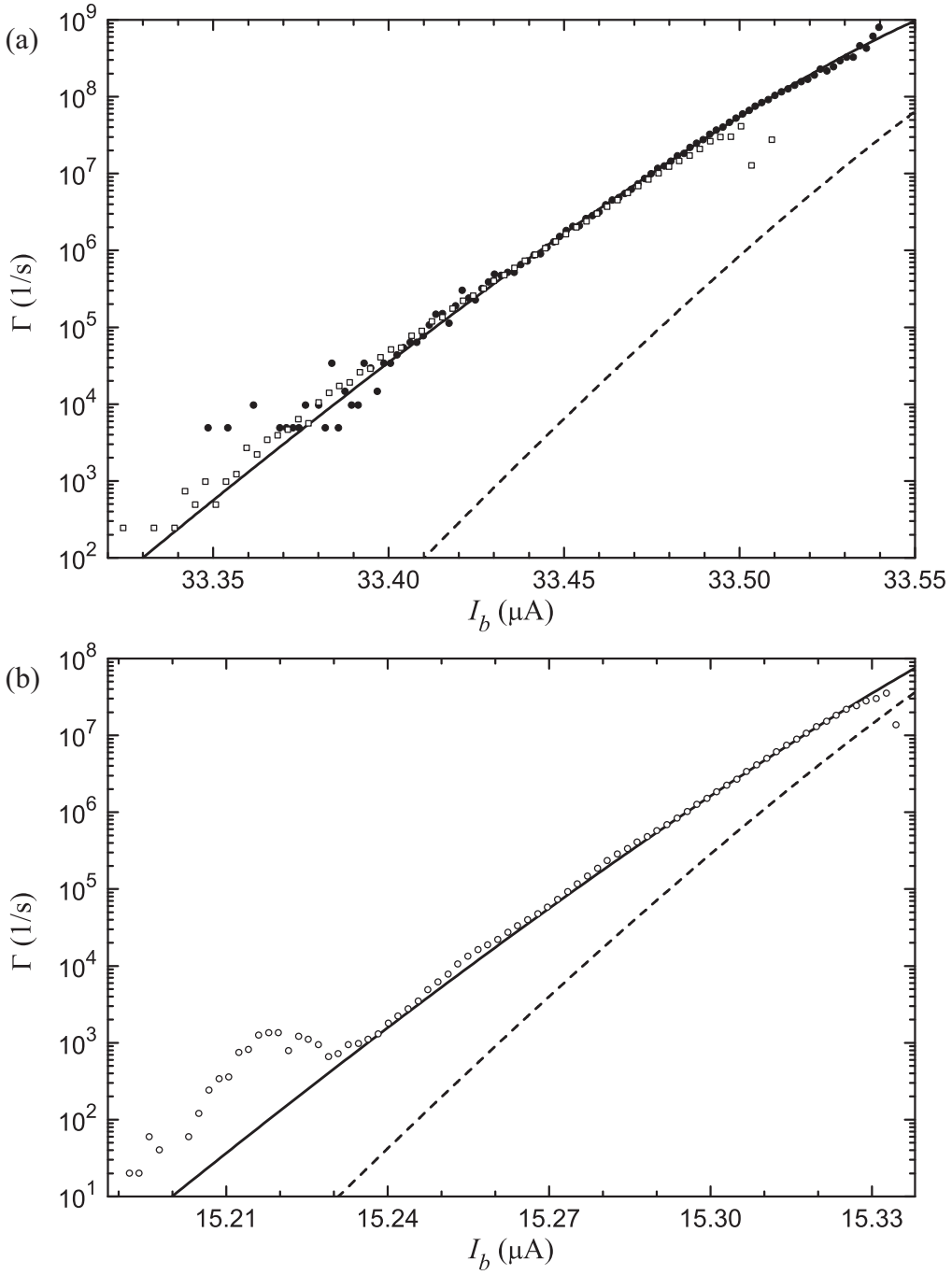

Figure 7.7: Low temperature escape rate of junction LC_2B. (a) With $I_0 \approx 33.6$ μA, the measured escape rate at $T = 25$ mK agrees for a 0.07 A/s (squares) and 0.93 A/s (circles) bias ramp rate. A fit to the data (solid line) yields $I_0 = 33.648$ μA and $C_J = 4.24$ pF. Spectroscopic measurements (see §8.1) give $I_0 = 33.663$ μA and $C_J = 7.32$ pF, corresponding to a lower Γ (dashed). (b) When the critical current is further suppressed to $I_0 \approx 15.4$ μA, the escape rate follows that of a junction with $I_0 = 15.434$ μA and $C_J = 3.4$ pF (solid), except near a noise induced feature at 15.22 μA. Spectroscopy gives $I_0 = 15.420$ μA and $C_J = 5.65$ pF, parameters which again underestimate the measured Γ.

line in Fig. 7.7(a). It is likely that some of the disagreement is due to the device (LC_2A) coupling to its neighbor, qubit LC_2B, through the coupling capacitor C_C and inductor L_C.

The effect of the LC mode created by the coupling network could be reduced by lowering the critical current of LC_2B. The circles in Fig. 7.7(b) show the measured values of Γ at $T = 20$ mK when $I_0^B \approx 15.4$ μA.[6] The solid line shows the fit to Γ_0 using $I_0 = 15.434$ μA and $C_J = 3.4$ pF, which agrees well with the data. The dashed line is drawn for the junction parameters obtained from spectroscopy [see Fig. 8.1(a)]. The disagreement between the curve derived from spectroscopy and the data is not as bad as it is in Fig. 7.7(a), but still significant. While this is suggestive that the LC resonance is causing the discrepancy, a full quantum simulation would have to be done to determine if the coupling capacitor is causing deviations from single junction behavior and if the escape rates and energy levels can both be described by a junction with the same "renormalized" parameters.

The escape rate in Fig. 7.7(b) has a very prominent feature at $I_b = 15.218$ μA and a weak oscillation at higher currents. These unexpected features are of particular interest if they are due to a failure of the isolation network at the high frequencies where they occur. As these data were taken below T_{cr}, it is unlikely that the features are due to a thermal noise current at frequency ω_{01} from an object in equilibrium with the refrigerator and device. There are a number of other suspects. I cannot discount the possibility that the smaller oscillation is an artifact of the biasing (as I_b was generated by a digital voltage source) or detection. For example, if voltage developed across the junction when it switched to the running state in a particularly pathological way, it could lead to false features in Γ. It is noteworthy that no oscillations are seen in Fig. 7.7(a), although features with a variety of forms have been seen for other values of I_0. It could be that Γ_0 for the device is not

[6] These are conditions under which the spectra of Ref. [41] were taken.

the simple exponential that one would expect for a single junction. For example, resonant coupling [131, 132] between the junction and the LC coupling mode or the other junction might lead to such oscillations. If neither of these are the problem, then the features are indicative of excited state population created by an external noise source. As Γ_1 and Γ_2 are so much larger than Γ_0 [see Fig. 2.9(b)], only a tiny population in the quantum states $|1\rangle$ or $|2\rangle$ would be necessary to explain the features.

7.2.2 dc SQUID Qubits

For the dc SQUID phase qubits, measurement of the escape rate was somewhat more involved. While this lead to some experimental complications, it also allowed us to better pin down the source of deviations in these devices. For one, the bias trajectory had to be selected. By ramping the current bias I_b with flux bias $I_f = 0$, the isolation junction generally switches first [see Fig. 6.7(a)]. Because the device can re-trap in a number of flux states, the histogram shown in the inset to Fig. 7.8(a) consists of several peaks. Each corresponds to a different qubit current I_1 when the isolation junction switches. By drawing the current-flux characteristics with the device parameters for field #2 in Table 6.1, I found that the peaks marked with symbols correspond to flux states N_Φ = -47 (circle) and -53 (square). The escape rate for each state can then be plotted as a function of the isolation junction current I_2, which was calculated using the method described in §6.4. In order for I_2 not to exceed the input value of I_{02}, I had to assume that there was background flux of 0.35 Φ_0 when $I_f = 0$.

The escape rate of the isolation junction looks quite different than the previous ones in that it appears to be a double exponential, governed by two rather different constants. Although the I_b ramp was linear, it is possible that I_2 varied in some complicated way. However, with the device parameters that I assumed, one expects

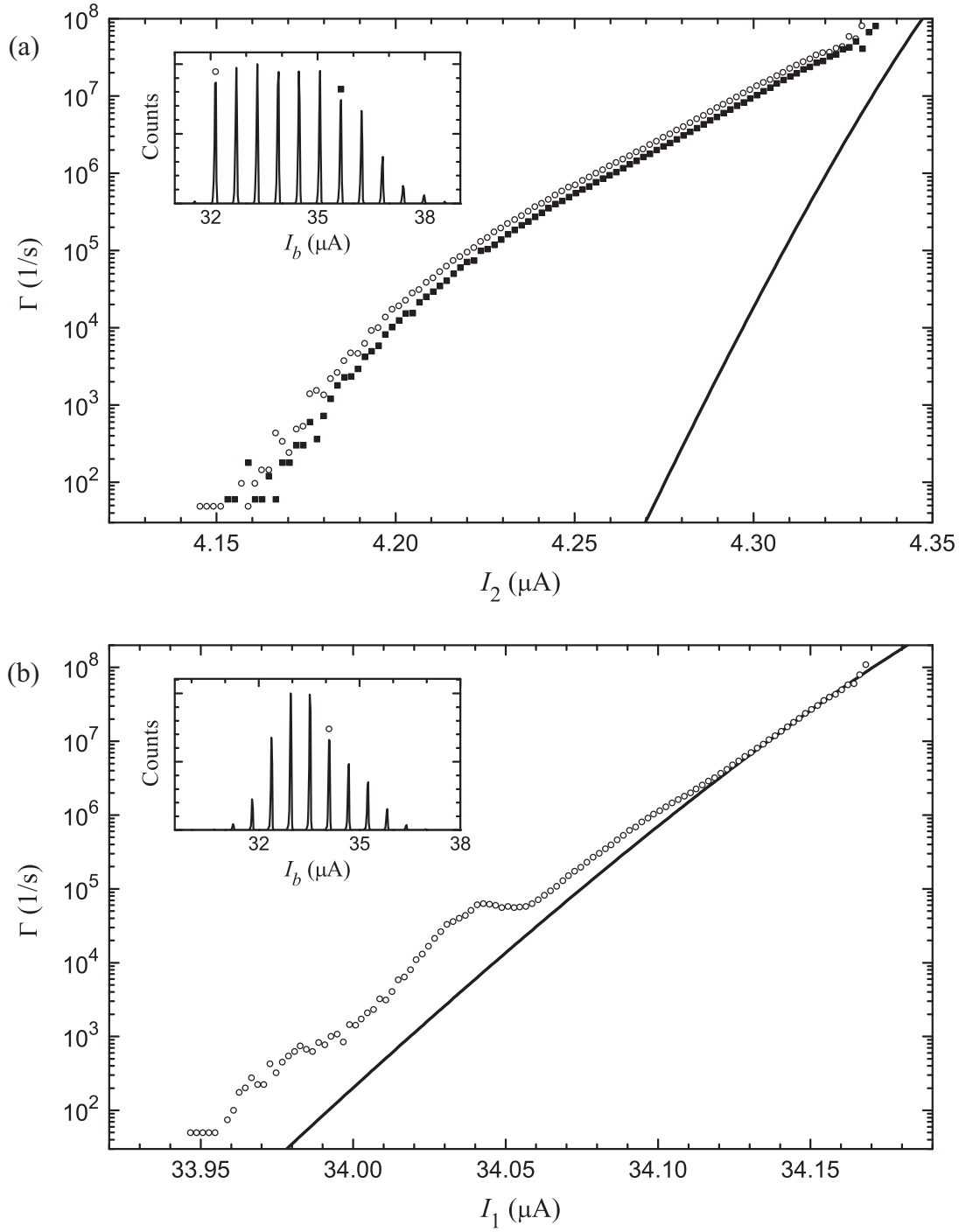

Figure 7.8: Low temperature escape rate of SQUID DS_1. (a) The escape rate of the isolation junction is not exponential in the current I_2. Data are shown for two flux states, N_Φ = -47 (circles) and -53 (squares), with the full histogram in the inset. The line is drawn for $I_0 = 4.4$ μA and $C_J = 2$ pF. (b) The escape rate of the qubit junction in the flux state $N_\Phi = 0$ behaves as expected at high bias, but shows an excess tunneling rate at lower bias. The line is drawn for $I_0 = 34.308$ μA and $C_J = 4.43$ pF, parameters which come from the spectrum shown in Fig. 8.2(a) (except for a +8 nA offset). Histograms of multiple flux states are shown as insets.

that I_2 is quite linear over the range plotted. In addition, if the current division depended strongly on the Josephson inductance of the qubit, then Γ would vary for the two flux states. Instead, they are essentially identical aside from a current shift. If L_1 is taken as 3.515 nH instead of 3.520 nH, then the two measured curves (and those for other flux states) are indistinguishable on the scale shown. In principle, this type of analysis could be used to determine the device parameters with higher accuracy in high β devices where the junctions may be regarded as being independent.

The solid line in Fig. 7.8(a) shows the expected ground state escape rate of a single junction with $I_0 = 4.4\ \mu$A (from Table 6.1) and $C_J = 2$ pF (roughly the design value for the isolation junction), calculated using Eq. (2.43). As there is no on-chip isolation for this junction, it is expected that the observed Γ is due to excited state population created by noise on the bias line. The data is somewhat reminiscent of that shown in Figs. 7.1 and 7.12, where population was excited thermally. As I will discuss in §7.4, the value of the relaxation time T_1 determines the value of Γ_0 where depopulation of all of the excited states occurs. For the short T_1 expected for this junction, the collapse to Γ_0 should occur at a relatively high current; following the curve to higher Γ (using a faster I_b ramp rate) could elucidate the situation.

By simultaneously ramping I_b and I_f with the proper ratio, we can guarantee that the qubit junction switches first [see §6.4 and Fig. 6.7(d)]. This is the path that I used for the thermal activation measurements of §7.1.2. The measured escape rate using this bias trajectory is shown in Fig. 7.8(b), when the device was initialized in the flux state $N_\Phi = 0$.[7] This state is marked with a circle in the inset, which shows the multi-peak histogram. As with the isolation junction, I calculated the current through the qubit I_1 using the device parameters in Table 6.1. For reasons discussed

[7]Flux shaking was not used in acquiring this data set. The unshaken retrapping probability of $N_\Phi = 0$ was sufficiently high.

in §8.2, I assumed a background flux of $-0.263\ \Phi_0$.[8]

From a spectrum taken at the same time as Γ [see Fig. 8.2(a)], I extracted the qubit junction parameters $I_0 = 34.300\ \mu$A and $C_J = 4.43$ pF. The solid line in Fig. 7.8(b) is the prediction of Γ_0 for a junction with this capacitance, but with a critical current of 34.308 μA. The small offset brings data and theory into very close agreement at high bias. As discussed in §6.4, a single value of C_J will describe both the energy levels and escape rates of the qubit, when these quantities are plotted as a function I_1 (and not I_b). The 8 nA offset could be needed due to errors in the calculation of I_1 or because the qubit junction of the dc SQUID device does not quite behave as an independent junction.

Figure 7.8(b) shows that there is an enhancement above the presumed ground state escape rate that is even larger than it was for LC_2B. Some insight into the origin of these features can be gained by examining their variation with flux state. As long as the same simultaneous bias path is used, the biasing of the qubit should remain almost unchanged. What does vary with flux state is I_2.[9] When $|I_2|$ increases, so does the Josephson inductance of the isolation junction; thus, the isolation factor introduced in §4.3 decreases and the isolation degrades with an increasing amount of trapped flux [101].

The escape rates of fifteen flux states of DS_1, obtained by initializing the device with flux shaking (see §6.5), are shown in Fig. 7.9(a). I have shifted the curves along the current axis for clarity; the x-axis is I_b for $N_\Phi = 0$. I took some spectroscopic measurements at the same time as these background curves. The arrows indicate the position of the $0 \rightarrow 1$ resonance at 7.4 GHz, which we expect to occur at the same value of I_1 if the junctions are sufficiently decoupled.

[8]The data in Fig. 7.8(a), which required a positive flux offset, was taken just a few days before the data in Fig. 7.8, which required a negative offset. This points to an error in identifying N_Φ or in the determination of device parameters.

[9]This can also be accomplished by remaining in the same flux state and adding a dc offset to the applied flux [101].

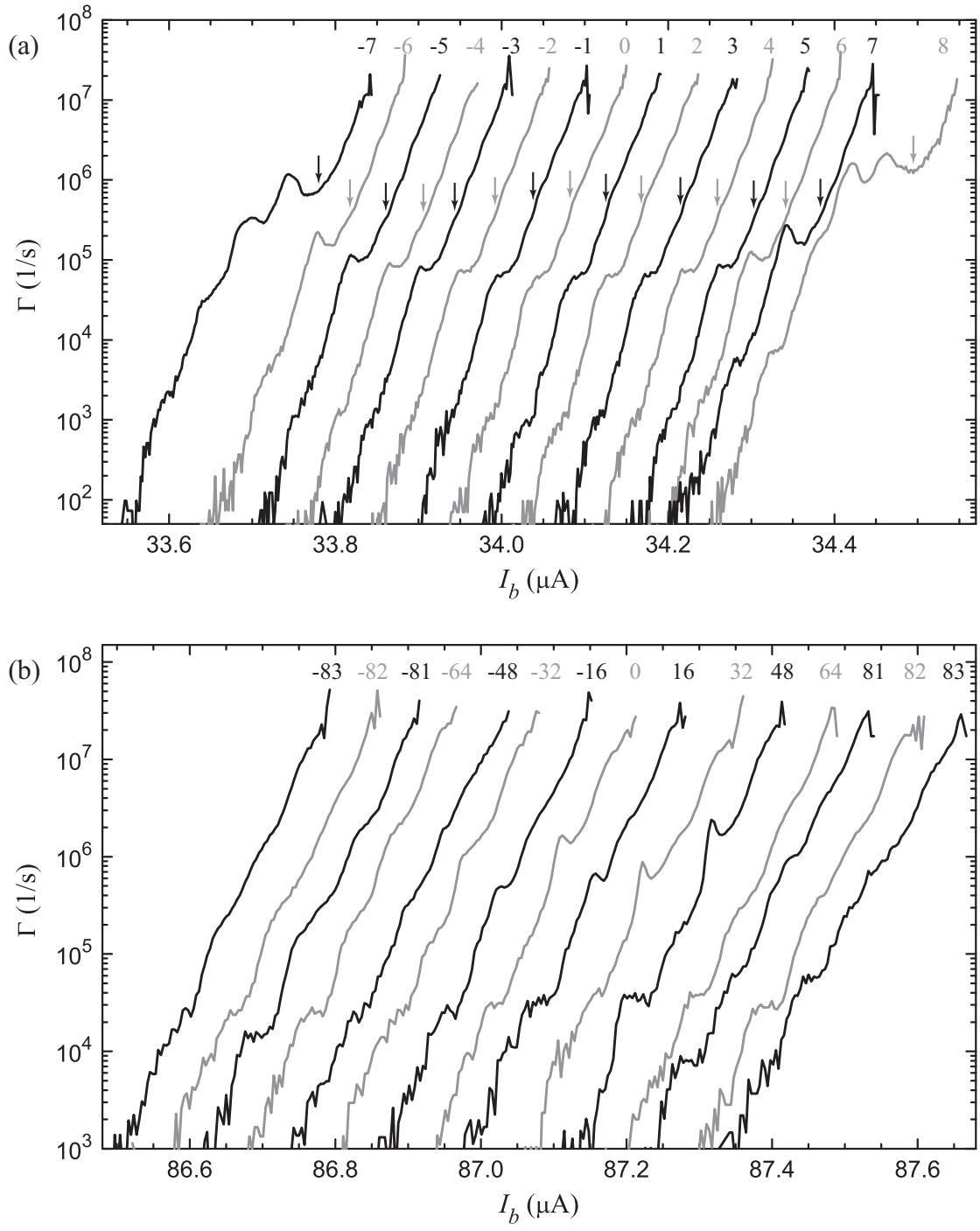

Figure 7.9: Flux state dependence of Γ for SQUID DS_1. The measured escape rate Γ varies quite strongly with the flux state N_Φ (indicated by the small numbers). Large values of $|N_\Phi|$ correspond to poor isolation and lead to additional excited state population and features in Γ. The different curves for (a) suppression field #2 and (b) field #3 (see Table 6.1) are shifted for clarity; the x-axis is labeled for $N_\Phi = 0$. The arrows in panel (a) indicate the bias value where $\omega_{01}/2\pi = 7.4$ GHz.

In each curve, which I should emphasize was taken at $T = 20$ mK without a microwave drive, there is one or more prominent bumps. There are at least two distinct phenomena seen in the different curves. First of all, the large bump that is seen for $N_\Phi = 0$ grows in height with increasing $|N_\Phi|$. With reference to the arrows, the location of the bump (in terms of I_1 or ω_{01}) is fixed. The fact that the size of the bump decreases as the isolation improves suggests that the bump is due to current noise on the bias line that is being filtered by the isolation junction. A convincing argument for this theory can be made by scaling the escape rate enhancement by the estimated isolation factor. The resulting curves all lie on top of one another and are a measure of full noise power on the bias line [101]. It is still unclear to me what determines the profile of the enhancement, but presumably it is a combination of the noise spectra and the isolation junction filtering.

Secondly, for $N_\Phi = -7$ and 8, a new peak appears to the left of the old one. That scaled down versions of it are not obvious for the other flux states suggests that a new noise source has been introduced. As $|I_2|$ increases (by changing flux states), L_{J2} also increases, which degrades the broadband isolation of the qubit. However, it is important to remember that one arm of the inductive divider is a junction and the isolation will fail at its plasma frequency. In an aluminum SQUID studied in our group (device AL1 in Ref. [101]), it was deduced that noise at the plasma frequency of the isolation junction was exciting the $0 \rightarrow 2$ transition of the qubit [102]. In the case of SQUID DS_1 under field #2, $\omega_{01}/2\pi$ for the isolation junction at zero bias is roughly 12.5 GHz. From spectroscopic measurements, $\omega_{02}/2\pi$ for the qubit junction is equal to 12.5 GHz when $I_1 \approx 34.1$ μA [see Fig. 7.8(b)], where no distinct feature is seen. Either there was an error in the calculation of the plasma frequency of the isolation junction or something else is causing the most prominent feature in Fig. 7.9(a). Also, it could be that the new features that appear at high flux states are due to first excited state population.

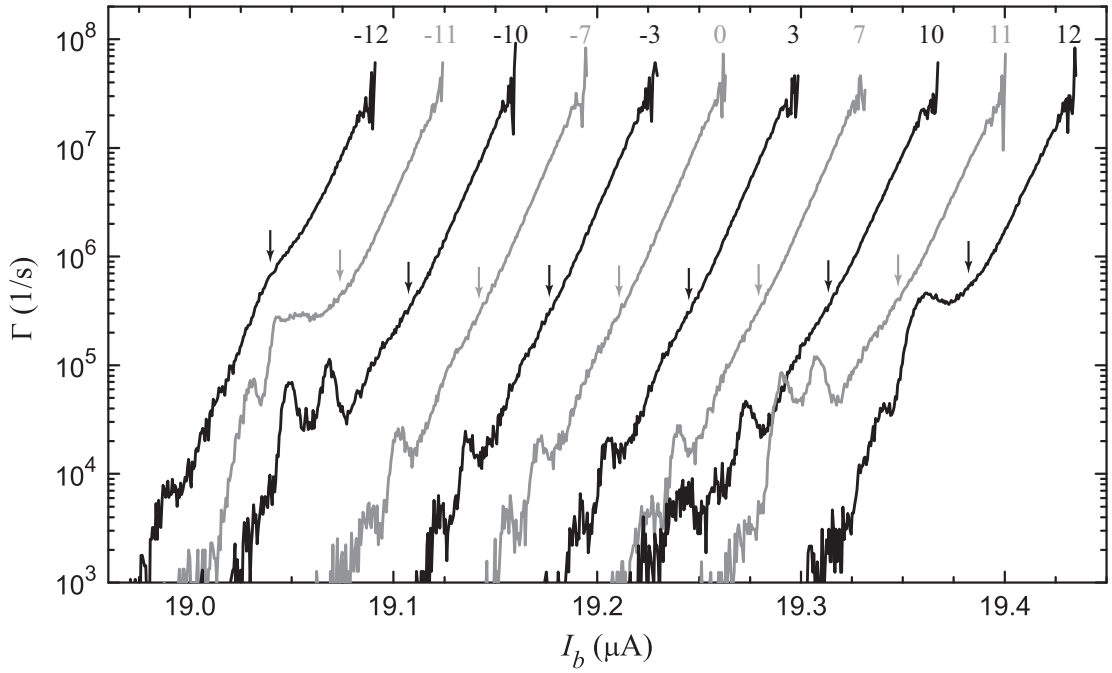

Figure 7.10: Flux state dependence of Γ for SQUID DS_2B. The (shifted) escape rate is plotted for different flux states. The arrows indicate the location of $\omega_{01}/2\pi = 5.9$ GHz.

Figure 7.9(b) shows Γ for a selection of flux states taken for suppression field #3, when the critical currents of both SQUID junctions were larger. There are several prominent features, suggesting that the isolation is poor. In this case, where the Josephson inductance of the isolation junction is small, the isolation factor should be large. In device LC_2A, the isolation appeared to degrade at high frequencies as well, as shown in Fig. 7.4(b), although it is not clear if there is a connection. There is, however, no obvious trend in the size of the enhancement as the flux state changes, as one would expect if the broadband isolation were failing. In this case, the zero-bias plasma frequency of the qubit is closer to 40 GHz. It seems unlikely that the sharp peak seen for $N_\Phi = 0$ is due to thermal noise at this frequency, so more careful measurements are needed to determine the origin of the various features.

Finally, Fig. 7.10 shows the low temperature escape rate for several flux states of SQUID DS_2B. Once again, there are features that grow in size but remain fixed in location and others that move in frequency as $|I_2|$ increases. During this run of

the refrigerator, we installed new copper powder filters with a high attenuation on all of the lines. There are features even at the best isolation, suggesting that the excitations are not due to high frequency noise from room temperature. By using a pulse technique to place an upper bound on the total excited state population (see §6.6.3 and Ref. [104]), it seems that the features could only be due to population in $|2\rangle$ or perhaps higher states [133]. For this device, where I_{02} is relatively large, it could be that that the plasma frequency of the isolation junction corresponds to ω_{02} of the qubit. Interestingly, Γ for $N_\Phi = -12$ is relatively featureless. This is likely due to the fact that when I_2 is sufficiently large, the filtering action of the isolation junction fails at a frequency that the qubit is not sensitive to [102].

In order to make a high quality qubit, it will be essential to eliminate the source of these excitations. This may require stronger filtering or a more careful engineering of the frequency response of the filters. On the other hand, from spectroscopy and Rabi oscillation measurements, the relaxation and coherence times are independent of the level of isolation from the bias line [101], so other noise sources need to be addressed first.

7.3 Master Equations

I have now addressed the low temperature escape rate with the quantum prediction for Γ_0 and the high temperature ($T > T_{cr}$) data with a classical model, both with a certain amount of success. As seen from the values of χ^2_ν in Fig. 7.2, the escape rates near the crossover region cannot be described with either simple approach. One solution is to define a tunneling prefactor similar to the one of Eq. (7.4), but that applies to intermediate temperatures [68]. Instead, I will use a formalism that explicitly takes into account the quantum nature of the junction. The idea is follow the evolution of a system of quantum states $|i\rangle$ subject to a number of transitions.

The density matrix approach introduced in Chapter 3 should accurately describe the dynamics of the escape rate experiments at any temperature. However, as the time scales being considered are much longer than the coherence time T_2, the off-diagonal terms of the density matrix ρ are negligible throughout the bias sweep.[10] As a result, the equations simplify and are equivalent to what are known as the master equations; see Refs. [91] and [92], §3.1 of Ref. [1], and §2.5 and §2.6.2 of Ref. [3]. This generic approach to describing the dynamics of a quantum system is quite intuitive, in that the population of each level can be found by solving a coupled set of rate equations. When analytical expressions can be derived, the master equations provide more transparent expressions than the density matrix formalism. In addition, it is often faster to numerically integrate the master equations than to time step the density matrix equations, particularly at low I_b where escape rates are small (so that the time step may be large).

As in Chapter 3, I will use the simplified notation ρ_i to denote the diagonal elements of the density matrix ρ_{ii}. From the references given above, the time rate of change of the occupation probability of $|i\rangle$ is

$$\frac{d\rho_i(t)}{dt} = \sum_{j \neq i} \left[-W_{ji}\, \rho_i(t) + W_{ij}\, \rho_j(t) \right] - \Gamma_i\, \rho_i(t)\,, \tag{7.7}$$

where Γ_i is the tunneling escape rate from $|i\rangle$ (discussed in §2.3.3 for the tilted washboard potential) and W_{ij} is the total inter-level transition rate from $|j\rangle$ to $|i\rangle$. I will only consider the thermal transitions described in §3.4, but the effects of a microwave drive could also be included in W_{ij} (see §3.2.2 of Ref. [1]). In Eq. (7.7), the first and last terms on the right account for depopulation of $|i\rangle$, while repopulation from other levels is given by the second.

In order to investigate the behavior of the master equations, first assume that

[10] Measurements of T_2 for our devices, which will be described in the next two chapters, yield values under 20 ns.

tunneling can be turned off and the junction is held at a fixed bias current. Then, using detailed balance, the thermal rates will balance each other (given enough time) resulting in a Boltzmann distribution amongst the states. The resulting equilibrium populations will therefore only depend on the energy level spacing and temperature.

Now suppose that tunneling is turned back on. The probabilities ρ_i will exponentially decay to zero, the only possible equilibrium solution. However, at some point during this decay, the *ratio* of the probabilities will hit steady state. This is also true for the normalized probabilities $P_i = \rho_i/\rho_{tot}$ (where $\rho_{tot} = \sum \rho_j$) of Eq. (3.31) and thus the total escape rate $\Gamma = \sum P_i \Gamma_i$ of Eq. (3.30). As the tunneling and thermal rates must balance each other out, the new equilibrium state will not be a Boltzmann distribution. If the current bias changes slowly enough, the system can stay in this dynamic equilibrium, the so-called stationary condition, until the junction switches to the voltage state (see §3.4.1 of Ref. [1]).

One way to find the stationary solution of the master equations is to re-feed the population that escapes back into the ground state (see §2.5 of Ref. [3] and Ref. [92]) and to set $\dot{\rho}_i = 0$ (where the dot indicates a time derivative). This is not physical, but provides sufficiently accurate results as long as the excited state population is small.

Instead I will use the fact that when the normalized probabilities reach steady state, their time derivatives vanish in the stationary limit, yielding

$$\frac{dP_i}{dt} = \frac{d}{dt}\left(\frac{\rho_i}{\rho_{tot}}\right) = \frac{1}{\rho_{tot}}\frac{d\rho_i}{dt} + \frac{\rho_i}{\rho_{tot}}\left(-\frac{1}{\rho_{tot}}\frac{d\rho_{tot}}{dt}\right) = \frac{1}{\rho_{tot}}\frac{d\rho_i}{dt} + \Gamma P_i = 0, \qquad (7.8)$$

where $\dot{\rho}_i$ is given by Eq. (7.7). I will discuss the solution for a two-level system in detail in the next section. For more than two levels, analytical solutions can be difficult to obtain. Numerical solutions are easy to find, as the system of equations of Eq. (7.8) can be solved iteratively using the Newton-Raphson method (see, for

example, §9.6 of Ref. [69]). While this method only converges if the initial guess is fairly close to the final answer, a Boltzmann distribution is sufficient in most cases. In practice, starting from low bias, where the system will be very nearly in thermal equilibrium, and bootstrapping up a current ramp is often quicker.

When considering a large (non-stationary) ramp rate, corresponding to continuously evolving P_i, I usually just solved Eq. (7.7) for the populations numerically. As with the Liouville-von Neumann equation in §3.8, Eq. (7.7) is easily cast into the matrix form

$$\frac{d\boldsymbol{\rho^d}}{dt} = \underline{p}\,\boldsymbol{\rho^d}. \tag{7.9}$$

For a system with N levels, $\boldsymbol{\rho^d}$ is the main diagonal of the full density matrix (and is therefore a vector of N elements) and $\underline{p}$ is an $N \times N$ matrix that describes its evolution. The structure of $\underline{p}$ is given §D.2. The evolution of the system can then be found efficiently with matrix exponentiation, as shown in Eq. (3.71), with a potentially time-dependent $\underline{p}$.

7.4 Determination of T_1 With a Slow Bias Sweep

The relaxation time T_1 is one of the key indicators of the quality of isolation of a qubit. Many experiments to measure T_1 have been performed on a variety of qubits. Perhaps the most common is to create an excited state population with a microwave pulse and then monitor the decay time back to the ground state [39]. I will show results of this technique in §8.7, but this technique is not without problems. One concern we had was that the microwave wiring lines must be filtered or weakly coupled to the qubit, which could give these leads a complicated frequency response. If a resonance of this wiring is also excited by the pulse, the observation of the decay could be determined by the lifetime of the resonance and not just the junction. This is particularly an issue when trying to measure times of several nanoseconds, as in

device LC_2. Similarly, the junction can be excited by a "dc pulse" in the bias current [37], but the bandwidth of the bias and detection lines must be high enough so as not to influence the results. Care must also be taken that this extra bandwidth does not introduce additional noise to the qubit.

The dissipation time may also be found by simply ramping the bias current, when there is a thermally created excited state population. The escape rate can be studied classically, as in §7.1, or with the quantum master equations, which predict features dependent on the junction shunting resistance R_J [134]. In general, finding the resistance from such data requires detailed modeling and knowledge of the system [135], especially when the junction temperature is much higher than its characteristic frequency. The problem is that the escape rate can depend strongly on parameters aside from R_J.

The situation is greatly simplified if the junction is held at a slightly elevated temperature (near the crossover temperature T_{cr}), where only the two lowest levels have a non-negligible probability of being occupied [4, 99]. This technique complements the thermal activation analysis nicely, as each approach works in a different temperature range. In addition to a careful choice of temperature, the bias ramping rate must be high enough to highlight the desired feature in the data, but low enough to remain in the stationary limit, so as not to affect the junction dynamics. These will be the assumptions in the analysis that follows. If these requirements are met, an estimate for T_1 can be found in a straightforward way.

The basic idea is as follows. Consider the two-level system shown in Fig. 7.11(a). The states $|0\rangle$ and $|1\rangle$ are separated by $\Delta E \equiv \hbar\omega_{01}$ and tunnel to the voltage state with rates Γ_0 and Γ_1. Thermal emission and absorption occur with rates $W_- \equiv W_{01}^t$ and $W_+ \equiv W_{10}^t$ [defined in Eqs. (3.26) and (3.27)]. The inclusion of tunneling will take the system away from a Boltzmann distribution. We can (presumably) directly measure Γ_0 and from it predict Γ_1. By setting the temperature

T, we also know the ratio of W_+ to W_-. The one true unknown is $T_1 \approx 1/W_-$, which can be estimated by finding the new equilibrium that the four rates create. The current bias I_b provides a simple way to drastically change the escape rates and it turns out that at a particular value of I_b, the equilibrium values can be found with little effort.

The occupation probabilities ρ_0 and ρ_1 can be found with the master equations of Eq. (7.7), of which there are now two:

$$\frac{d\rho_0}{dt} = -\left(W_+ + \Gamma_0\right)\rho_0 + W_-\rho_1 \tag{7.10}$$

$$\frac{d\rho_1}{dt} = W_+\rho_0 - \left(W_- + \Gamma_1\right)\rho_1. \tag{7.11}$$

The two-level master equations describe the system on the long time scales we are interested in. If I_b is varied slowly, then there is the additional constraint that the normalized probabilities P_i are effectively constant at any instant. From Eqs. (7.8) and (7.10), the time derivative of P_0 is

$$\frac{dP_0}{dt} = -\left(W_+ + \Gamma_0\right)P_0 + W_-P_1 + \Gamma P_0. \tag{7.12}$$

As $P_0(t) + P_1(t) = 1$, we also know that $\dot{P}_1 = -\dot{P}_0$. The expression takes on a convenient form if it is expressed in terms of the ratio of probabilities:

$$\left(1 + \frac{P_1}{P_0}\right)^2 \frac{dP_0}{dt} = W_-\left(\frac{P_1}{P_0}\right)^2 + \left(\delta W + \delta\Gamma\right)\frac{P_1}{P_0} - W_+, \tag{7.13}$$

where $\delta W \equiv W_- - W_+$ and $\delta\Gamma \equiv \Gamma_1 - \Gamma_0$ are the differences in the thermal and escape rates, both positive quantities. The stationary condition is imposed by setting the time derivative to zero, resulting in the exact expression for the probability ratio

$$\frac{P_1}{P_0} = \frac{-\left(\delta W + \delta\Gamma\right) + \sqrt{\left(\delta W + \delta\Gamma\right)^2 + 4W_+W_-}}{2W_-}. \tag{7.14}$$

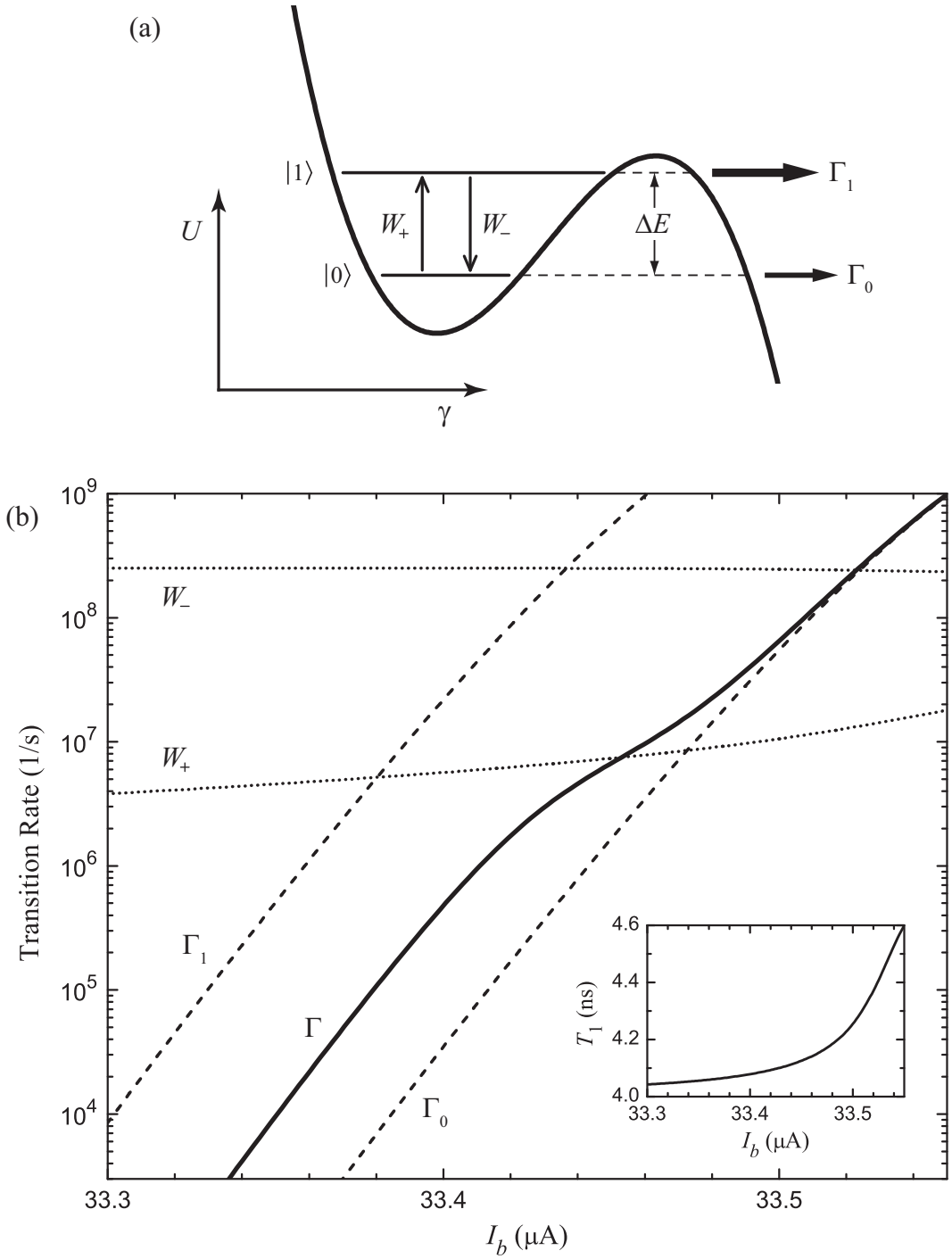

Figure 7.11: Transitions of a two-level system. (a) The two lowest levels of the washboard, $|0\rangle$ and $|1\rangle$, are separated by energy ΔE. Γ_0 and Γ_1 are the tunneling rates from the two levels and the inter-level transitions W_+ and W_- keep the system in thermal equilibrium in the absence of tunneling. (b) The escape rates are plotted as a function of I_b as dashed lines, while the inter-level transitions for $R_J C_J = 4$ ns and $T = 80$ mK are shown with dotted lines. The inset shows the bias dependence of T_1. The total escape rate Γ (solid) collapses to Γ_0 under a stationary sweep when $\Gamma_1 = W_-$, resulting in a feature that can be used to estimate T_1.

I will now examine Eq. (7.14) in a few limits, applicable to data taken under certain conditions, to highlight the simple behavior dictated by this expression (see §3.4.2 of Ref. [1]). At low temperatures, $W_- \gg W_+$, so that $P_0 \approx 1$ for all bias currents, while $P_1 \approx W_+/(W_- + \delta\Gamma)$. This excited state occupation probability is qualitatively different for high and low values of I_b. At low bias currents, where $\delta\Gamma < \Gamma_1 \ll W_-$ and thus $P_1 \approx W_+/W_-$, the system is essentially in thermal equilibrium because tunneling is a small perturbation to the thermal rates. Tunneling is nonetheless important, as it allows us to gauge the state populations through the total escape rate, which is $\Gamma \approx \Gamma_0 + \Gamma_1 e^{-\Delta E/k_B T}$.

In contrast, at high currents, $\Gamma_1 > \delta\Gamma \gg W_- \gg W_+$, so that $P_1 \approx W_+/\delta\Gamma$ vanishes and Γ collapses to Γ_0 (even though the temperature of the junction has not changed). This is due to the depopulation of the excited state as a result of strong tunneling from this state.[11] As shown by the solid line in Fig. 7.11(b) [which was generated with Eqs. (7.14) and (3.30)], the shift between these two limiting behaviors occurs near the bias current (denote it I_b^*) where $\Gamma_1 = W_-$. For the case drawn, $I_b^* = 33.44\,\mu$A, but note that I_b^* is weakly dependent on temperature through W_-. The corresponding total escape rate at the crossing point is $\Gamma \approx \Gamma_0 + W_+/2$, with the (generally valid) assumption that $\Gamma_1 \gg \Gamma_0$.

W_+ varies slowly with bias current (through the energy level spacing), while Γ_0 increases exponentially. This results in a clear shoulder in Γ at a bias current of I_b^*. Therefore, this feature (and thus I_b^* and W_+) can be directly identified on an escape rate curve, as long as the temperature is chosen so that the junction behaves as a two-level system. T_1 is then given by $e^{-\Delta E/k_B T}/W_+$, where microwave spectroscopy can be used to directly measure $\Delta E\,(I_b^*)$. However, the fact that $1/T_1 \approx W_- = \Gamma_1$

[11] This has always struck me as counter-intuitive. A high tunneling rate from the excited level ought to lead to a large Γ. However, Γ depends on the product $\Gamma_1 P_1$. The transition rates (in particular W_+) are unable to *maintain* a significant P_1 which leads to the lower Γ. Thus it is not important that it is tunneling that exceeds W_-. Any process that removes population from $|1\rangle$ at a rate faster than $W_+ e^{\Delta E/k_B T}$ will take the system away from a Boltzmann distribution.

occurs at I_b^* allows a rough estimate for T_1 to be obtained from the escape rate curves alone. At very low temperature, the total escape rate is just $\Gamma_0(I_b)$, as P_1 is negligible. While Γ_1/Γ_0 is a function of I_b, this ratio (evaluated at I_b^*) is on the order of 500 for a large range of T_1 for the tilted washboard potential [see Fig. 2.9(b)]; thus

$$T_1 \approx [500\ \Gamma_0(I_b^*)]^{-1}\,. \tag{7.15}$$

At low bias currents and sufficiently high temperatures, the levels above the first excited state will have non-negligible occupation. Each of the levels will empty out in order, leading to a series of shifts in Γ. At slow sweep rates, these tend not to be as pronounced as the single distinct feature for the two-level case. Nonetheless, such features have been previously reported [134].

7.4.1 *LC*-Isolated Phase Qubits

Figure 7.12(a) shows the total escape rate Γ as a function of bias current I_b for junction LC_2B, at temperatures between 25 and 320 mK. This data was taken at the same time as Fig. 7.1, except at a higher I_b ramp rate of 0.93 A/s. Below 50 mK, the escape rate is roughly exponential in the bias current, as expected for tunneling out of the ground state alone. As the temperature increases, thermally excited population in the higher states gives rise to higher escape rates. As discussed above, each of these levels will empty out as the sweep progresses, once its tunneling rate exceeds the dissipation rate for that state. For large I_b only the ground state retains any population and all the curves collapse onto Γ_0. The escape rate at which this collapse occurs increases with temperature, because W_+ increases as well.

The ramp rate was chosen to be just high enough to follow this trend. At lower rates, the junction is more likely to escape at lower bias currents, so we were unable to follow Γ all the way up to the current where collapse occurs. At higher rates,

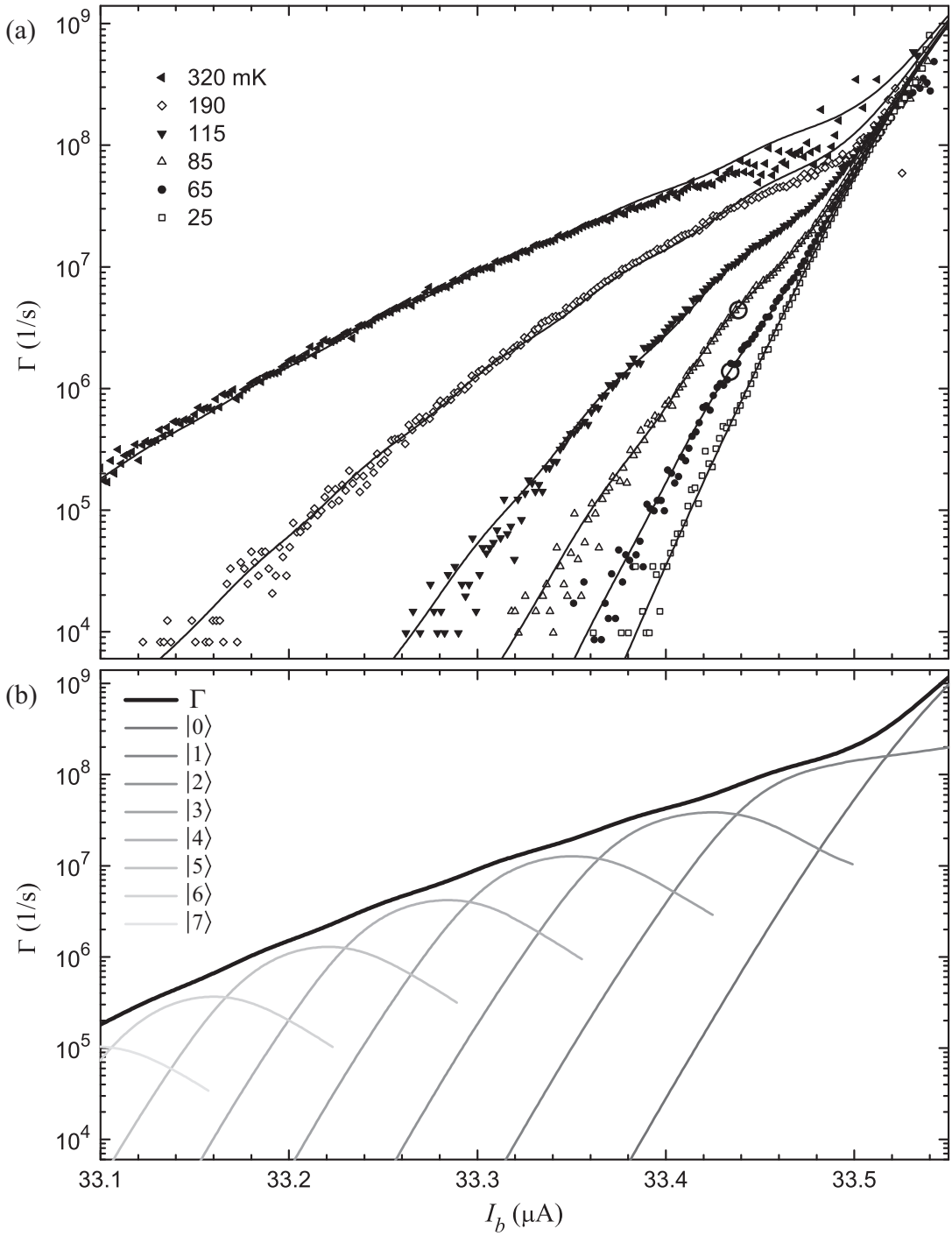

Figure 7.12: Master equation simulation of junction LC_2B. (a) The symbols show the measured escape rate Γ at several temperatures T, under the same conditions as in Fig. 7.1, except that the bias ramp rate was 0.93 A/s. T_1 can be estimated from the shoulder feature (marked with large open circles) at 65 and 85 mK. The solid lines come from a master equation simulation, with $T_1 = 4$ ns, including anharmonic matrix elements (second fitting technique described in text). (b) The simulated contribution to Γ by each of the eight levels and the total Γ are plotted for $T_{fit} = 275$ mK.

the sweep goes further into the non-stationary regime and unnecessarily complicates the dynamics, which we want to avoid for now. Incidentally, the classical thermal pre-factor in Eq. (7.4) predicts the same qualitative suppression of Γ with increasing I_b (see §2.5.1 of Ref. [3]), as seen in Fig. 7.3(c). However, the dotted line in Fig. 7.5(a) clearly shows that the classical theory neglects the fact that total escape rate is bounded below by Γ_0. This is the reason why I chose the low ramp rate data for the thermal activation analysis in §7.1.1.

Even at this modest ramp rate, the calibration of the bias current as a function of time was a serious challenge, as discussed at the beginning of §7.2.1. In addition to the 15 nA offset I mentioned there, I added a small offset to I_b for each temperature (for reasons described in the discussion of Fig. 7.3), to produce the expected convergence at high bias currents. These adjustments, all less than 15 nA, could be needed because of an incomplete knowledge of the calibration (*e.g.*, its temperature dependence), or to small drifts in the detection electronics over the course of the data taking. The small offsets could also be needed because the actual critical current of the junction changed with time. In this case, it is not legitimate to simply shift escape rate curves, but this is unlikely to introduce major errors for such small changes.

Examination of Fig. 7.12(a) shows that at 65 and 85 mK, Γ does not increase much over its 25 mK values. This suggests that the two-level analysis is applicable at these temperatures. That the three escape rates are nearly parallel at low bias currents supports this claim, as does the single well-defined shoulder feature at the elevated temperatures. Using Fig. 7.11(b) as a guide, this features begins at $I_b^* \approx 33.435\ \mu$A for both temperatures (indicated by the large open circles). At this current, $\Gamma_0\left(I_b^*\right) \approx 5 \times 10^5$ 1/s and thus our rough rule Eq. (7.15) gives $T_1 \approx 4$ ns.

The master equation can be used to perform a more quantitative analysis at all temperatures. I did use the fully time dependent form of Eq. (7.7), although

in principle, this data was taken at a low enough ramp rate to use the stationary solution. The escape rate at 25 mK (which should be nearly independent of R_J, T, and sweep rate) was fit to the single junction model to give $I_0 = 33.648$ μA and $C_J = 4.24$ pF. I assumed that the tunneling rates from the higher levels were given by a single tilted washboard with these parameters.

I made a few simplifying assumptions in an initial attempt at modeling the data [99]. I assumed that the energy levels were given by the same junction parameters as the escape rate. In addition, I used the harmonic approximation in calculating the spontaneous emission rates Γ_{ij} [given by Eq. (3.25)], so that thermal transitions only occurred between adjacent levels. Finally, Γ_{ij} was taken to be independent of I_b, although W_{ij}^t were bias-dependent through the Boltzmann factor.

With these assumptions, the results of an eight-level simulation agree well with the data, when R_J is set at 1 kΩ, corresponding to $T_1 = 4.2$ ns.[12] It is encouraging that this more thorough analysis produced a T_1 consistent with the rough estimate above. The values of the temperature I used in the simulation are listed as $T_{fit}^{(1)}$ in Table 7.1. As expected, they are reasonably close to the temperature of the mixing chamber T, given the uncertainty of our thermometry. In doing the fits, I added the values $\Delta I_b^{(1)}$ in Table 7.1 to the current axis for the *data*, so that the escape rates would converge at high bias. The quality of the fits is indicated by $\chi_\nu^{2(1)}$ in the table; here, the number of degrees of freedom ν varied from 100 at the lowest temperature to over 300 at the highest.

We had additional information about junction LC_2B in the form of spectroscopic measurements. From Figs. 7.7(a) and 8.1(b), it seems that the low temperature escape rate and the $0 \rightarrow 1$ transition frequency are not described by a single set of parameters for an ideal current-biased junction. This is most likely due to

[12] I did not use a formal fitting procedure here, because the unknown I_b offset was rather important, but it was not a truly free parameter. Instead I varied parameters by hand in trying to minimize χ_ν^2. For a chosen bias offset, this was fairly easy to do.

Table 7.1: Master equation fit parameters for junction LC_2B. The escape rate data shown in Fig. 7.12(a) were fit with an eight-level master equation simulation, for six values of the refrigerator temperature T. Using a simple model of inter-level transitions, the fit temperatures $T_{fit}^{(1)}$ were extracted. A more accurate treatment yielded $T_{fit}^{(2)}$. The data were shifted by ΔI_b to produce the expected collapse to Γ_0 and the quality of the fits is indicated by χ_ν^2; these two quantities are listed for both fitting attempts.

T (mK)	$T_{fit}^{(1)}$ (mK)	$\Delta I_b^{(1)}$ (nA)	$\chi_\nu^{2(1)}$	$T_{fit}^{(2)}$ (mK)	$\Delta I_b^{(2)}$ (nA)	$\chi_\nu^{2(2)}$
25	25	0	1.5	25	0	1.5
65	73	-3.5	1.9	59	-3.2	2.3
85	98	-4.5	1.9	80	-4.5	2.0
115	134	-10.5	2.5	109	-10.3	2.3
190	215	-13	6.4	174	-13.5	5.7
320	340	-15	4.2	275	-15.5	4.1

the harmonic mode created by the coupling capacitor to LC_2A. Instead of finding the energy levels and escape rates of the entire coupled system, I just let the escape rates be described by $I_0^\Gamma = 33.648$ μA and $C_J^\Gamma = 4.24$ pF, while the energy levels and matrix elements behaved as a single junction with $I_0^\omega = 33.663$ μA and $C_J^\omega = 7.32$ pF. A nice feature of the master equation approach is that these experimentally measured parameters can be input in a phenomenological (yet accurate) way, even if the underlying physics is not entirely understood.

I also tried a second approach to modeling the data. I allowed the spontaneous rate to be bias-dependent, using Eq. (3.25) and the cubic approximation for the matrix elements $\gamma_{n,m} = \langle n \,|\, \hat{\gamma} \,|\, m \rangle$. From that Eq. (3.25), it might seem that T_1 would decrease with increasing I_b because $\gamma_{0,1}$ increases [see Fig. 2.11(a)]. As the inset to Fig. 7.11(b) (which was drawn with the improved set of parameters) shows, T_1 actually increases slightly due to a concurrent decrease of ω_{01}. W_- decreases as well, although the Boltzmann factor overwhelms this at higher T, where W_-

increases with I_b. Using the cubic approximation to evaluate $\gamma_{n,m}$ also leads to inter-level thermal transitions between every pair of states. Some of the matrix elements are given in Eqs. (2.38) and (2.39).

With this improved model of transitions, the best choice for $R_J C_J$ (which is the value of T_1 at low I_b) in the eight-level master equation simulation is 4 ns. The results are plotted as solid lines in Fig. 7.12. In plotting the data in the figure, I added the values $\Delta I_b^{(2)}$ in Table 7.1 to the current axis. It is interesting that both T_1 and the quality of the fits (indicated by $\chi_\nu^{2(2)}$ in the table) do not change appreciably from the simpler first attempt. In fact, the simulated curves are virtually identical for the two attempts, although I have only plotted the results for the second one.

However the simulation temperatures for the improved model, listed as $T_{fit}^{(2)}$ in the table, generally show better agreement with T. The highest temperature is the only exception, but that could be due to an incorrect choice of ΔI_b, as the data does not extend to the Γ_0 collapse. The change in fit temperatures is largely due to the more accurate treatment of energy levels, as I_0^Γ and C_J^Γ overestimate the level spacing; because the device did not behave as a single junction, I_0^ω and C_J^ω do not completely parameterize ω_{01} over the entire range of interest. The more accurate values of $\Gamma_{n,n+1}$ also had a small impact, while the inclusion of more than adjacent-level relaxation had a negligible effect.

The solid lines in Fig. 7.12 do a good job of capturing the features in the data, for a value of R_J that is independent of temperature and frequency. The only major failing is the collapse to Γ_0 at the highest temperatures, which appears to be faster than the simulation predicts. The reason for this is unclear. The simulation does predict some gentle oscillations in Γ, some of which are seen in the data. The origin of these features is made clear in Fig. 7.12(b), which shows Γ for $T_{fit}^{(2)} = 275$ mK as a heavy black line. The contributions from each level $\Gamma_i P_i$ that sum to this value are shown as a series of gray lines. As a level reaches the top of the potential barrier,

its large escape rate leads to depopulation and a decreasing contribution to Γ even as its escape rate continues to increase. This leads to the ripples in Γ. I artificially forced Γ_i to saturate at roughly 5×10^{10} 1/s (because the quantum simulation that generates them eventually breaks down), but the particular way in which they roll-off is unimportant due to this depopulation. It is interesting that at any given I_b, only two or three levels make a substantial contribution to Γ.

Given the assumptions of the model, T_1 is determined with good precision. For example, if $R_J C_J$ is chosen to be 6 ns, then for the data at $T = 65$ mK, the minimum χ^2_ν increases to 3.5 at $T_{fit} = 61$ mK. Comparison of the fit to the data would show that the shoulder feature is not reproduced well.

7.4.2 dc SQUID Phase Qubits

In the order to perform the same type of analysis on SQUID DS_1, I first had to adjust the calculation of I_1. By assuming a background flux offset of 0.26 Φ_0, Γ at 20 mK of Fig. 7.5(a) could be made to overlap the curve of Fig. 7.8(b). With this agreement, I then took $I_0^\Gamma = 34.308$ uA, $I_0^\omega = 34.300$ μA, and $C_J^\Gamma = C_J^\omega = 4.43$ pF, as in the later figure. I used a microwave peak at 7.0 GHz to align the higher temperature curves. This resulted in the expected collapse at high I_b, as seen in Fig. 7.13, without having to explicitly enforce it with an additional offset.

Due to the obvious signs of excited state population at low temperature, it is impossible to apply the rough estimate of Eq. (7.15). Starting at about 100 mK, it seems that thermal excitations overwhelm the effects of the bias noise, so I used the eight-level master equations (with matrix elements calculated in the cubic approximation and a bias-dependent T_1) to describe that data. Unfortunately at these high temperatures, allowing T to vary somewhat results in a fair bit of uncertainty in T_1. The solid lines in Fig. 7.13 are drawn for $R_J C_J = 14$ ns, which corresponds to $R_J \approx 3\,\mathrm{k}\Omega$. Taking the value as 10 or 20 ns results in noticeably worse

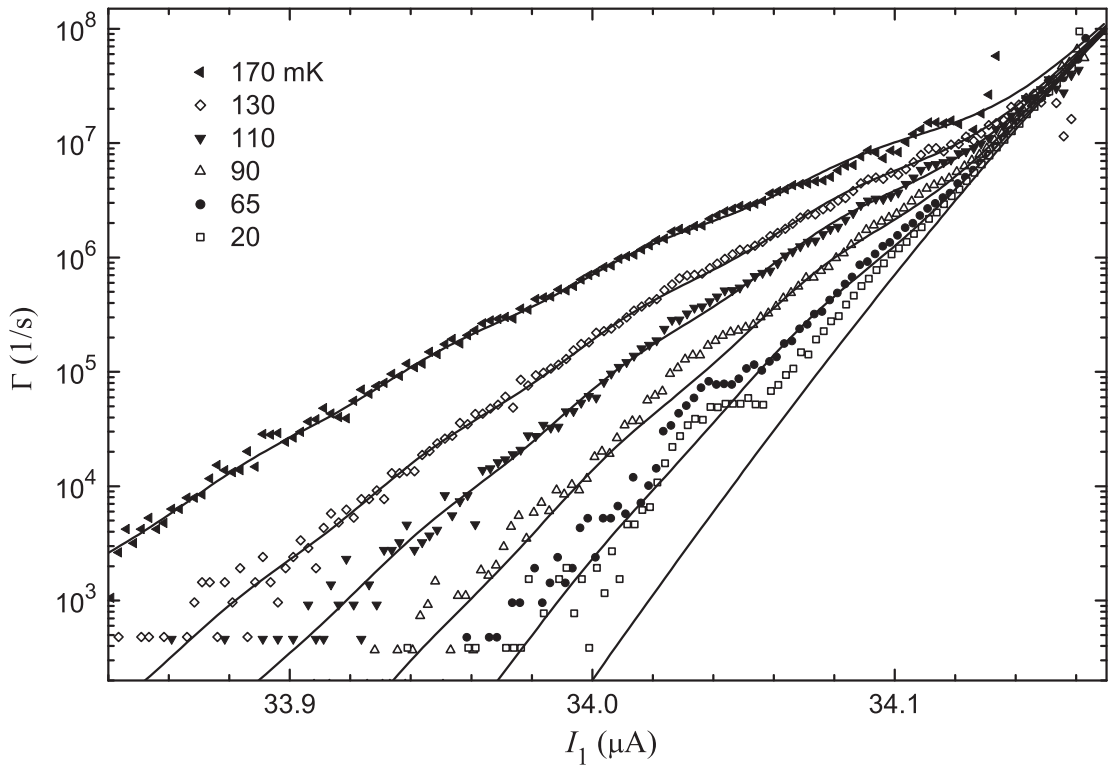

Figure 7.13: Master equation simulation of SQUID DS_1. The symbols show the same data as in Fig. 7.5(a), with the qubit current I_1 adjusted to match Fig. 7.8(b). The ramp rate is 0.1 A/s, slow enough to stay in the stationary limit. The solid lines come from an eight-level master equation simulation, with $T_1 = 14$ ns.

agreement, but without a well defined feature to fit to, it is difficult to pin down the value with much more precision. At low temperatures, the calculated escape rate underestimates the data. This was done intentionally, as the enhancement is not expected to be entirely thermal in this case. For mixing chamber temperatures of 20, 65, 90, 110, 130, and 170 mK, the simulation revealed fit temperatures of 20, 74, 93, 117, 138, and 179 mK.

To summarize, the slow bias sweep escape rate technique is easy to perform and provides an estimate of T_1 with little data analysis. The main assumption is that the device is described by a tilted washboard potential. In the case of the energy levels, this assumption can be checked. However, verifying the tunneling rates of the excited states is more difficult, but it appears that this can be accomplished using

a pulsed measurement technique [104]. Deviations from single junction behavior, absent a better model, will cause problems with the application of Eq. (7.15) and the full master equations.

7.5 Fast Sweep

In the previous section, I asserted that a slow bias sweep would result in negligible $\dot{P}_i$. This begs the question, slow compared to what? The answer comes from recognizing that the escape rates Γ_0 and Γ_1 increase nearly exponentially with bias current. If the bias current is ramped linearly in time,[13] then the escape will be exponential in time as well. It is convenient to assume that the escape rates have the form $\Gamma_i = \Gamma_i^0 e^{\alpha t}$, where α characterizes the speed of the ramp (see §3.4.3 of Ref. [1]).

The escape rate for a typical junction at elevated temperature, as calculated with the two-level master equations, is plotted for several ramp rates in Fig. 7.14. The solid black line is drawn for stationary conditions, where the dynamics are independent of the sweep rate. As discussed in the previous section, Γ begins to collapse towards Γ_0 at the bias current where $\Gamma_1 \approx W_- \approx 1/T_1$.

The escape rate for a ramp rate of 0.1 A/s is shown as a dotted line and deviates slightly from the stationary case. The sweep rate parameter α, numerically calculated as $(1/\Gamma_0)\, d\Gamma_0/dt = d \ln \Gamma_0/dt$, is plotted as a nearly horizontal gray dotted line segment. The same information is plotted for 1 (dashed) and 10 (dot-dashed) A/s. For these faster rates, the shoulder feature moves to higher escape rates. Rather than it beginning when $\Gamma_1 = W_-$, it occurs roughly when $\Gamma_1 = \alpha$. Thus, it seems that Γ deviates from its stationary values roughly when $\alpha > 1/T_1$.

In Fig. 7.12, I_b was ramped at 0.93 A/s, which corresponds to $\alpha = 7 \times 10^7$ 1/s.

[13] In the previous section, when escape rates were measured in the stationary limit, the "waveform" used for I_b was entirely unimportant. At each value of I_b, the system reached dynamic equilibrium, so the path taken to get there had no effect.

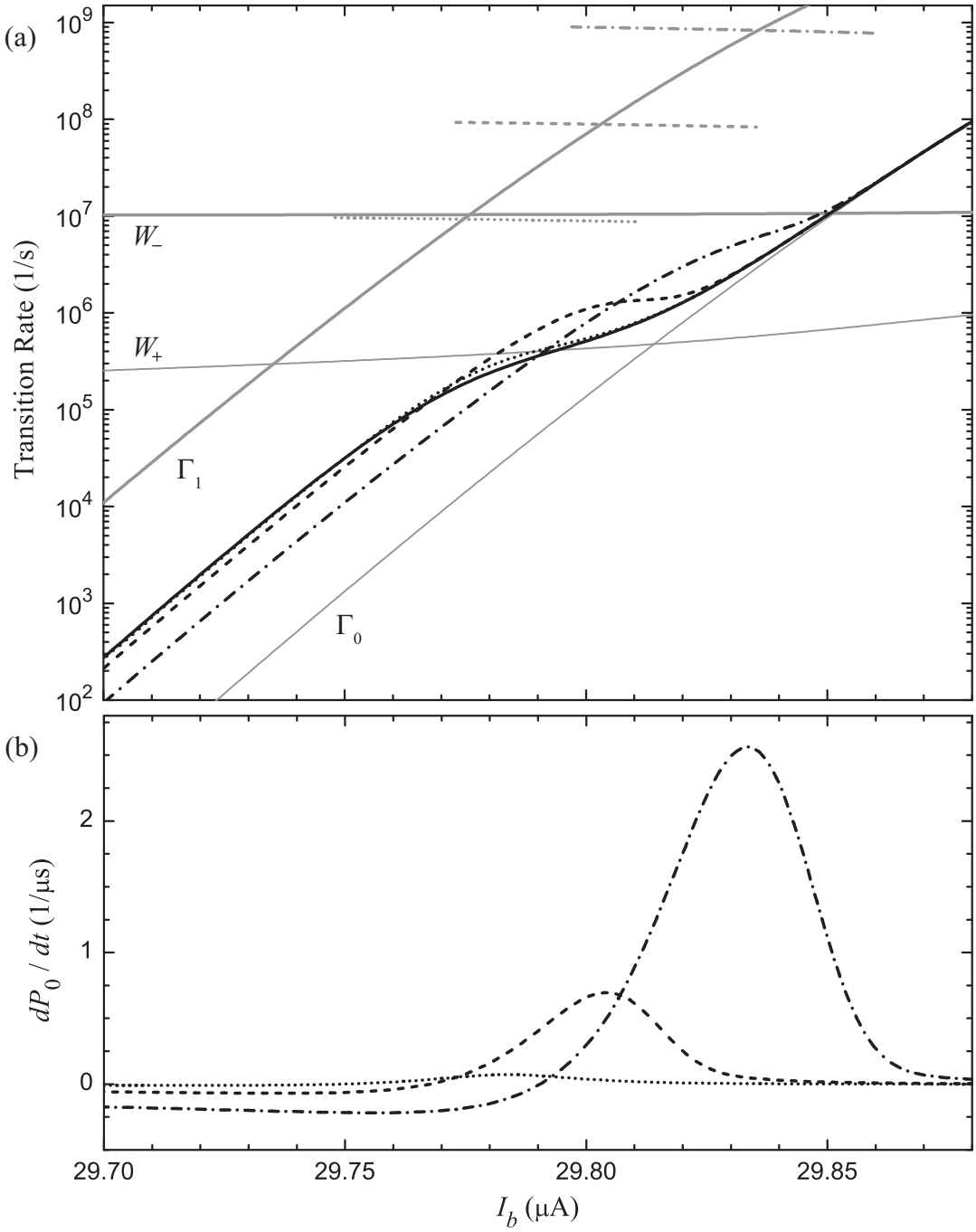

Figure 7.14: The effect of sweep rate on Γ. (a) The solid black line shows the stationary escape rate for a junction with $I_0 = 30$ μA, $C_J = 5$ pF, $T_1 = 100$ ns, at $T = 100$ mK. The dynamics are set by Γ_0, Γ_1, W_+, and W_- (drawn as extended gray lines), and a shoulder is seen at the value of I_b where $\Gamma_1 \approx W_-$. The shoulder in Γ moves for ramp rates of 0.1 (dotted black line), 1 (dashed), and 10 (dot-dashed) A/s to the current where Γ_1 is roughly equal to the sweep rate parameter α (drawn as gray line segments for each of the ramp rates). (b) As the ramp rate increases, the dynamics move further from the stationary limit, as reflected by the time derivative of normalized ground state occupation probability.

Therefore, the stationary condition is met if T_1 is less than 15 ns, which turned out to be the case for the LC_2B. In Fig. 7.13, the 0.1 A/s ramp rate corresponds to $\alpha = 8 \times 10^6$ 1/s. Thus any system with $T_1 < 125$ ns will remain stationary.

Although the method for finding T_1 presented in the previous section no longer applies, the fast sweep provides another technique. Over some "low" range of sweep rates, the total escape rate will be independent of α, as the dynamics stay nearly stationary. At some point, however, Γ will start to deviate; the value of α at this rate is roughly $1/T_1$ [4]. This conclusion can be verified by continuing to increase the ramp rate and following the shoulder. While we have seen small deviations in Γ as a function of the ramp rate, we have never clearly seen this clear shoulder movement behavior with our devices. Thus it seems that $1/T_1$ is faster than the ramp rates that we can experimentally implement, suggesting that T_1 is shorter than 50 ns [133].

The condition for steady state can also be examined using the sweep rate analysis. Fig. 7.14(b) shows $\dot{P}_0$ for the three finite ramp rates in Fig. 7.14(a); it is identically zero for the stationary case. The values are quite large near the shoulder feature for the fastest ramp, indicating that the system is far from stationary when the depopulation of $|1\rangle$ occurs. The excited state population is in effect frozen, as not enough time is allowed for the system to relax to the ground state. At even higher temperatures, a very fast sweep leads to a sequential emptying of levels, providing dramatic evidence of energy level quantization (see Ref. [134], §3.4.3 of Ref. [1], and Ref. [104]).

As the ramp rate increases, not only does the shoulder move, but Γ at lower bias also decreases uniformly. This is due to the fact that as I_b increases, ω_{01} decreases. If the system has time to adjust to a Boltzmann distribution, then the first excited state becomes progressively more heavily populated as the ramp proceeds, leading to the stationary limit. For fast ramp rates, W_+ does not have sufficient

time to populate $|1\rangle$ during the time when the level spacing is small. Thus, even though the thermodynamic temperature is the same for all cases in Fig. 7.14, the fast ramp rate cases appear to be at a lower temperature (at $I_b = 29.70\ \mu$A).

This discussion motivates another way of looking at the effect of the various transitions rates of the system. The occupation probability of the first excited state can be characterized by an effective temperature,

$$T_{\mathit{eff}} = -\frac{\hbar\omega_{01}}{k_B \ln\left(P_1/P_0\right)}. \tag{7.16}$$

T_{eff} is plotted in Fig. 7.15 for the simulations of Fig. 7.14(a). In the stationary case (solid line), $T_{\mathit{eff}} = T = 100$ mK at low bias. In this region, tunneling has a negligible effect, resulting in a Boltzmann distribution. As I_b and Γ_1 increase, the first excited state state becomes depopulated, resulting in what appears to be a colder junction. The situation is quite similar to evaporative cooling, where the hottest particles are selectively removed from a sample, leaving behind a smaller and colder population.

The general behavior of the effective temperature at the higher ramp rates is similar, except that the starting point (on the graph) is lower and the cooling is delayed to higher I_b. The minimum temperature that the junction reaches is independent of α.

This raises an intriguing possibility for initializing a qubit [4]. If the temperature cannot be made low enough, then I_b could be quickly set to a high value. For a particular trial, if the system is in $|1\rangle$, it will be more likely to tunnel to the voltage state, at which point the trial ends. If it does not tunnel, then the bias can be lowered to the point where the manipulation is to done, with a certain amount of confidence that the system is in the ground state. Two issues could make this procedure difficult to implement. First of all, in order obtain a low T_{eff}, Γ must be made quite large. Thus the fraction of the total number of trials that is useable could be

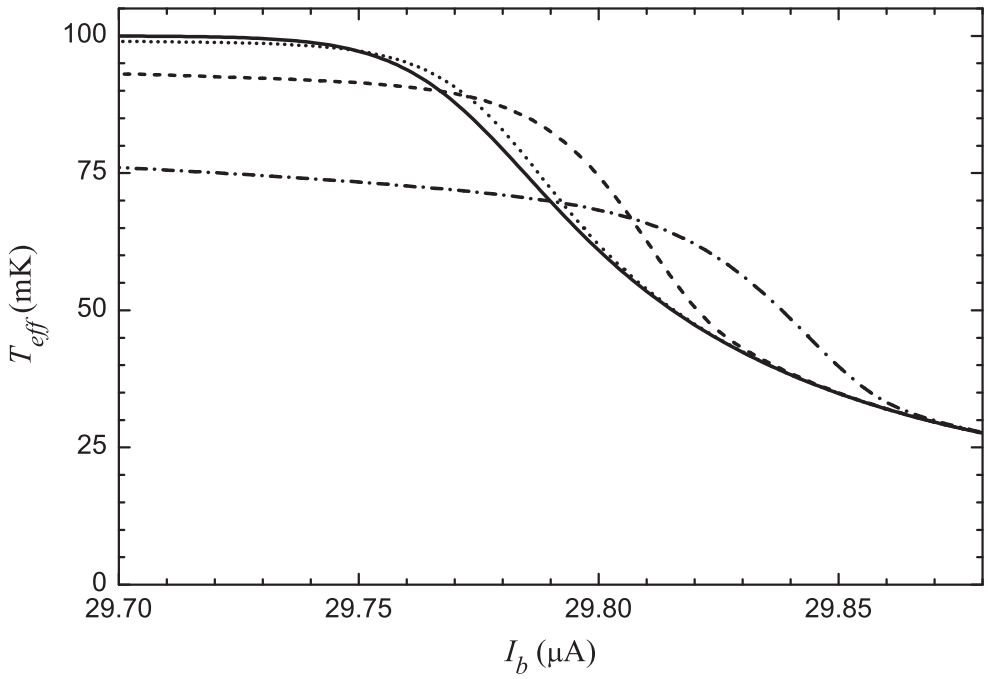

Figure 7.15: "Evaporative cooling" of a Josephson junction. For the escape rates shown in Fig. 7.14(a), depopulation of the first excited state by tunneling leads to a non-Boltzmann distribution. Thus, the effective temperature decreases quite quickly with the current bias.

quite low. More importantly, the source of the heating might still be present. Thus when I_b is lowered, T_{eff} might initially be low, but W_+ could quickly repopulate $|1\rangle$.

However, the technique could be quite useful for diagnostics. For example, in §7.2.2, I showed several unusual low escape rate curves. A major question is whether these odd features are due to complex potentials that determine the dynamics of these systems or whether they are the result of some small, athermal excited state population. If the latter is true, then a pulse of I_b that takes the system to a high escape rate and then back to one of the features, will result in a lower Γ. As mentioned, this will be true as long as the pulse occurs on a time scale shorter than any re-excitation. Variations on this type of measurement suggest that the measured escape rate features seen in our devices are due to excited state population [133].

7.6 Summary

The amount of information that can be gained from the tunneling escape rate alone is amazing, which undoubtedly is the reason that it has been used to study macroscopic quantum phenomena for so long. At very low temperatures, the experimental escape rate can be fit to theoretical predictions that were calculated with straight-forward techniques for a simple junction Hamiltonian. The utility of the escape rate comes from its extreme sensitivity to excited state population. This is what made it possible to extract T_1 from slow sweep experiments in §7.4 at moderate temperatures, where the thermal excitations were minimal. At higher temperatures, Γ follows classical activation theory with damping, as discussed in §7.1.

The experiments in this chapter provide the first evidence (in this thesis) for the quantum behavior of our devices. In addition, I extracted the relaxation time T_1 both in the classical and quantum regimes. For the LC-isolated qubits, the classical thermal theory gave a shunting resistance of $R_J \approx 2$ kΩ when the junction plasma frequency was near $\omega_p/2\pi \approx 5$ GHz (see Fig. 7.3). With a junction capacitance of $C_J \approx 4$ pF, $T_1 \approx 8$ ns. Using a master equation simulation (and a rough rule, derived for a two-level system), I determined the relaxation time of the same junction to be about 4 ns[14] (see Fig. 7.12). It is possible that the discrepancy is due to the effects of the coupling capacitor or to a frequency-dependent R_J, but a factor of two difference with the techniques is hardly a cause for concern at this point. In any case, the value is far below the 5 μs predicted in §4.2, presumably due to a failure of the LC filter or intrinsic junction dissipation. The isolation also appears to degrade for plasma frequencies above 10 GHz (presumably for different reasons) and it may be important to determine on what frequency scale R_J varies.

[14] In the simulation, I assumed that the shunting impedance was independent of frequency (and thus the current bias I_b), leading to a constant value of $R_J C_J$. However, T_1 picks up a bias dependence through the matrix element $\langle 0 \,|\, \hat{\gamma} \,|\, 1 \rangle$.

Using the thermal activation analysis shown in Figs. 7.5 and 7.6 for the SQUID phase qubits, R_J appeared to be between 2 and 8 kΩ, corresponding to T_1 between 10 and 30 ns. The master equation simulations suggest that $T_1 \approx 14$ ns (see Fig. 7.13). It is possible that the spurious features in the intermediate temperature range [see Fig. 7.5(a)] led to an incorrect value of classical T_{esc} there. Placing an upper bound on Γ (which I did in order to get 8 kΩ) could be necessary because the classical theory does not predict the collapse to Γ_0 correctly. The longer T_1 is, the sooner the collapse happens, which is why there might have been more problems with the SQUID data. Nonetheless it does appear that the broadband scheme did improve the qubit performance, but again, the measured T_1 is quite a bit shorter than the prediction of roughly 200 ns in §4.3.

Chapter 8

Spectroscopy and Non-Coherent Dynamics

The chapters begins with a description of how we measured the spectrum of transitions for the LC-isolated qubits. The dc SQUID phase qubit requires additional techniques and analysis, as we were interested in just the properties of one of the two junctions. With the methodology established, I will then describe the wealth of information that can be obtained from spectra. For example, the width of a resonance gives important information about the isolation of the qubit. Spectra also reveal the nature of the coupling of the qubit to other degrees of freedom; I will show evidence for two-level systems that interact with the qubit and spectra of two SQUID phase qubits that are capacitively coupled together. The chapter closes with measurements of the relaxation time T_1, obtained with microwave pulses.

8.1 Spectroscopy of LC-Isolated Phase Qubits

To measure the energy level spectrum of an LC-isolated phase qubit, we find the enhancement $\Delta\Gamma/\Gamma$ in the tunneling escape rate due to a microwave current $I_{\mu w}$, as described in §6.2. The current bias I_b is linearly ramped while a continuous wave microwave signal of fixed angular frequency ω_{rf} is applied to the junction. Whenever the microwave drive is resonant with a transition between qubit energy levels, an excited state population will be generated and this leads to a peak in the escape rate enhancement $\Delta\Gamma/\Gamma$, such as that shown in Fig. 6.5(c). By repeating this measurement at a series of drive frequencies (usually at intervals of 50 or 100 MHz), the transition can be mapped out.

Figure 8.1(a) shows a spectrum of junction LC_2B when the critical current

was quite suppressed.[1] LC_2A was held at zero bias throughout the data taking, so that it was well out of resonance with LC_2B. Each horizontal line of the grayscale map shows the resonant peak at a particular drive frequency, where dark colors represent a large escape rate enhancement. However, I have normalized each line to its maximum enhancement. As this data set was taken at the base temperature of the refrigerator, the excited states of the qubit should not be thermally occupied. The microwave signal can therefore only make the $0 \rightarrow 1$ transition (at frequency ω_{01}) visible, provided the power is not too high.

The circles indicate the current bias at which the enhancement reached a maximum for each setting of ω_{rf}. As expected, ω_{01} decreases with increasing I_b, as the well of the tilted washboard potential becomes more shallow. These points were fit to a simulation of ω_{01} for a single junction generated with Eq. (2.44); the solid line corresponds to a junction with critical current $I_0 = 15.420$ μA and capacitance $C_J = 5.65$ pF. Over the frequency range shown, the fit is rather good. Despite the presence of the measurement electronics and on-chip circuitry, the junction still retains its simple quantum nature.

The fit capacitance of 5.65 pF is larger than the value of 4.85 pF listed in Table 4.1. This is due to the presence of the junction coupling network of LC_2, which created an LC mode at 7.2 GHz [78]. While the zero-frequency coupling constant is $\zeta_0 = 0.064$ [see Eq. (2.72)], the effective frequency-dependent constant is $\zeta\,(4.8\text{ GHz}) = 0.12$ [see Eq. (2.78)] at the average frequency of the spectrum. This leads to an effective capacitance $C_J\,(1 + \zeta\,(\omega)) = 5.4$ pF [see Eq. (2.75)], which is fairly close to the fit value. Here, I have included the effect of the LC mode with an effective frequency-dependent C_C; the number listed in Table 4.1 came from fitting a spectrum to a more accurate model, where the LC mode was treated as a quantum degree of freedom [78].

[1] The escape rate under the same conditions is plotted in Fig. 7.7(b).

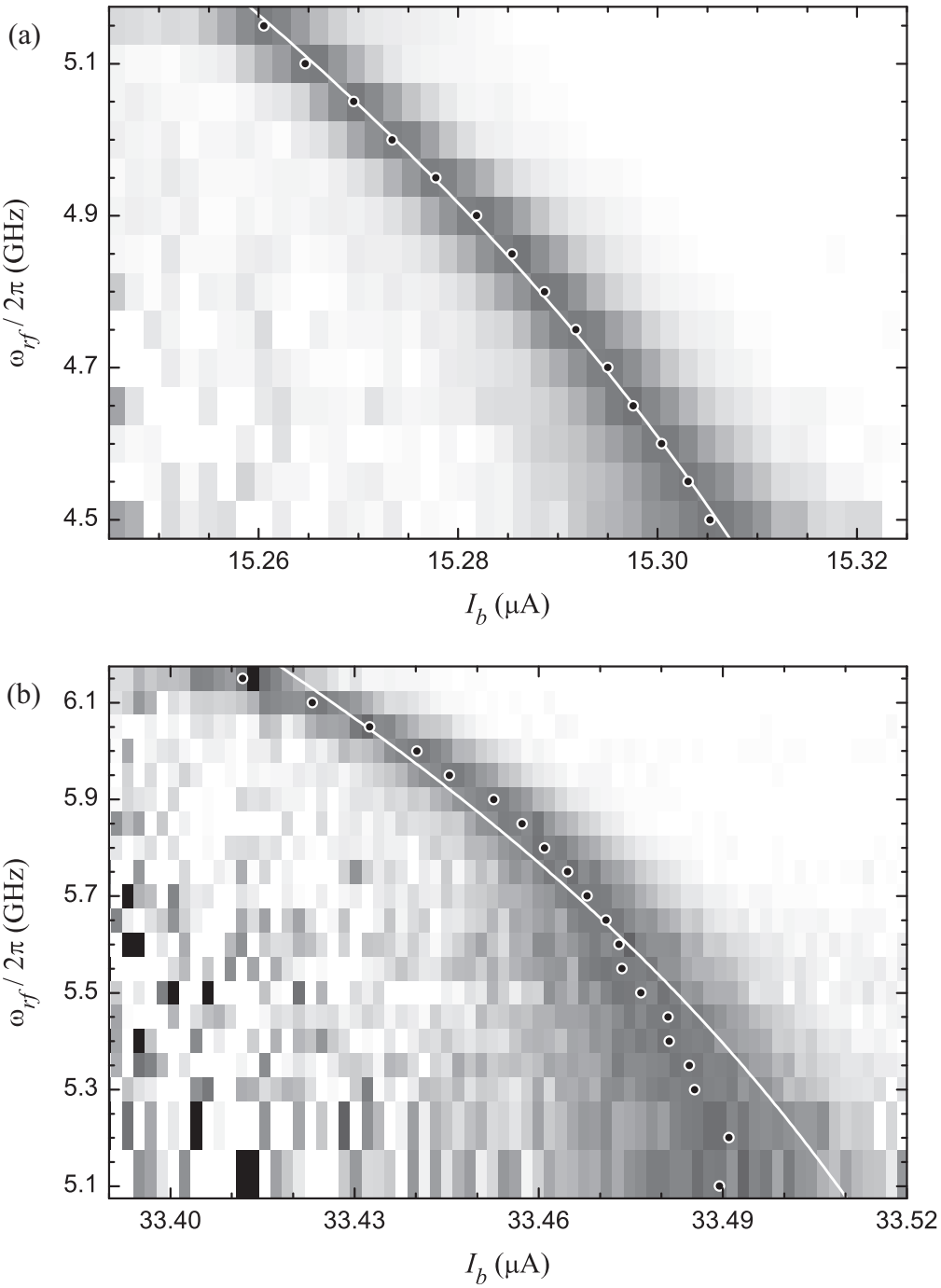

Figure 8.1: Transition spectra of junction LC_2B. (a) The escape rate enhancement due to microwave activation is plotted as a grayscale map, where dark colors represent larger values. The white curve is a fit of ω_{01} to the maximum enhancement at each frequency (plotted as circles), with $I_0 = 15.420$ μA and $C_J = 5.65$ pF. (b) At a different suppression magnetic field, the plasma frequency of the junction is close to the resonant frequency of the LC mode created by the coupling network to LC_2A, causing a deviation from single junction behavior. The line is drawn for $I_0 = 33.663$ μA and $C_J = 7.32$ pF. Both data sets were taken at 25 mK by Huizhong Xu and Andrew Berkley.

When taking a spectrum, we typically set the microwave power such that the escape rate enhancement $\Delta\Gamma/\Gamma$ was between 1 and 5. This is large enough to ensure a clearly visible peak, but not so large as to cause power broadening. In the case of Fig. 8.1(a), the nominal power P_S of the microwaves at the room temperature output port of the source was set to -15 dBm for all frequencies. For other data sets, in order to account for the frequency-dependent attenuation of the microwave lines, we had to adjust P_S for different ω_{rf} to obtain an enhancement in the desired range.

As I noted in §6.2, the escape rate is difficult to measure precisely when it is small. For example, at 5.15 GHz the resonance was located at $I_b = 15.26$ μA, where the background escape rate was $\Gamma_{bg} \approx 2.6 \times 10^4$ 1/s. By applying a relatively strong drive, the escape rate with microwaves $\Gamma_{\mu w}$ was boosted to about 5.5×10^5, which was easily measured. However, the large uncertainty in Γ_{bg} leads to scatter in $\Delta\Gamma/\Gamma$. In an attempt to remedy this problem when plotting a spectrum, I typically used the background data from all of the frequencies to calculate Γ_{bg}. This reduces the noise at low I_b in Fig. 8.1(a) quite dramatically. Experimentally, this also means that more time can be devoted to taking microwave data at each frequency.

What can make this averaging process difficult is that the background switching time essentially always drifts over the 5 to 50 hours during which a spectrum is taken. This can be due to the biasing and detection electronics warming up, the temperature of the lab fluctuating, the level of liquid helium in the refrigerator's dewar decreasing, as well as actual changes in I_0. As a result, simply using all the data to calculate a single Γ_{bg} would lead to smeared out features and incorrect values. To monitor the drift, we always interleave background and microwave data.

I usually attempt to correct for the drift with the following simple procedure. An average switching time $\bar{t}$ is selected. The average of the first N background data points is calculated to be t_{bg}. Then $\Delta t = \bar{t} - t_{bg}$ is added to each of the first N

points of both the background and microwave data. This is repeated for each block of N points. The key is to pick N large enough so that the features of the histogram are not smoothed over, but smaller than the scale of the drift. Typically, there are no obvious variations in the enhancements for values of N between 5000 and 20000. If there are large drifts of I_0, there is no justification for this procedure, as it is not known how various features of a histogram will change. Nonetheless, I did perform the correction for the spectra presented in this chapter [including Fig. 8.1(a)], where the drifts were relatively small.

Figure 8.1(b) shows a spectrum of LC_2B taken at a different suppression field where I_0 was larger. These are the same conditions under which the T_1 measurement in Fig. 7.12 was performed. The fit of the circles to a single junction spectrum, drawn as a solid line for $I_0 = 33.663$ μA and $C_J = 7.32$ pF using Eq. (2.44), shows fairly significant disagreement with the data. This is due to the plasma frequency of the junction approaching the LC coupling mode frequency of 7.2 GHz. In this case, $\zeta\,(6\text{ GHz}) = 0.24$, which gives an effective capacitance $C_J\,(1 + \zeta\,(\omega)) = 6.0$ pF, which is still smaller than the fit value. It may that the coupling strength is changing so quickly that the effective parameter will not faithfully reproduce the energy levels. While the data could have been fit to a system with two degrees of freedom (such as shown in Fig. 2(b) of Ref. [78]), the single junction fit sufficiently characterizes the device for the T_1 measurement simulation. Notice that the fit capacitance for the spectrum is quite large, while the value that describes the ground state escape rate Γ_0 [4.24 pF, from Fig. 7.7(b)] is much closer to the design value of the junction. This suggests that the coupling to the LC mode does not have a strong effect on the escape rates.

The spectroscopy measurements were always performed with a slow bias ramp[2] [0.037 and 0.93 A/s for Figs. 8.1(a) and (b)], so it did not influence the dynamics.

[2]A discussion of what is meant by a slow ramp in given in §7.5.

Therefore, the same results could have been obtained by sweeping ω_{rf} at fixed I_b. We did not sweep ω_{rf} because of two challenges. Given the finite bandwidth of the biasing lines, it takes a certain amount of time for I_b to stabilize to a dc value. If I_b is settling to a value where the escape rate is directly measurable, then many switching counts will occur before ω_{rf} can be swept. The measurements described in §6.6.2 and §6.6.3 could alleviate this problem, because they can be used at lower bias. In addition, the microwave lines have a frequency-dependent attenuation. By sweeping I_b we can find the resonance location for a particular frequency and power of microwaves. If ω_{rf} were swept, then we would have to work at fixed P_S and features in the enhancement could be due to the energy level structure of the qubit or resonances of the microwave lines.

8.2 Spectroscopy of dc SQUID Phase Qubits

The basic procedure for measuring and analyzing a spectrum of a dc SQUID phase qubit is the same as described above. However, the bias trajectory and flux state serve as potentially useful degrees of freedom.

The simplest bias path to take while measuring a spectrum is shown in Fig. 6.7(a), where the current bias I_b is swept at fixed flux bias I_f. In this case, I never saw any clear enhancement peaks. This is because with this trajectory, the isolation junction usually switches to the voltage state. As it is not protected from noise on the current bias line, the resonances will be very broad; apparently they are too broad to be seen.

Instead, the qubit junction can be studied with the simultaneous current and flux ramping scheme sketched in Fig. 6.7(d). Figure 8.2(a) shows a spectrum of SQUID DS_1 for flux state $N_\Phi = 0$ with the simultaneous biasing. The $0 \rightarrow 1$ transition is clearly visible. Although this was taken at the base temperature of the refrigerator, there is a hint of the $1 \rightarrow 2$ transition.

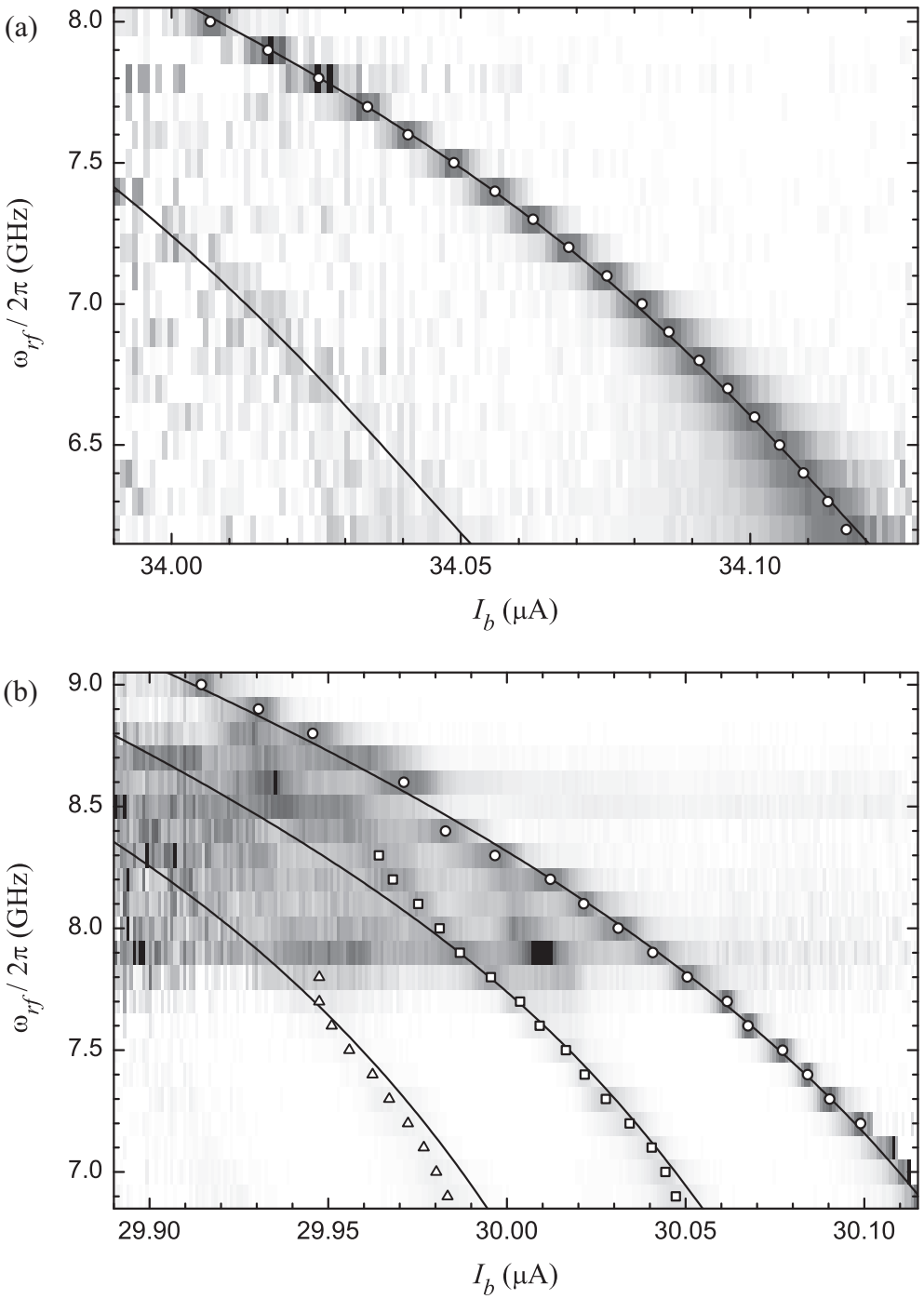

Figure 8.2: Spectra of SQUID DS_1. (a) At 20 mK, the $0 \rightarrow 1$ transition of the qubit is clearly visible, under simultaneous biasing of flux state $N_\Phi = 0$. The circles indicate the peak enhancement and the lines show ω_{01} and ω_{12} for a single junction with $I_0 = 34.275$ μA and $C_J = 4.48$ pF. (b) The spectrum for $N_\Phi = -7$ shows much more structure, including the $0 \rightarrow 1$ (circles), $1 \rightarrow 2$ (squares), and $2 \rightarrow 3$ (triangles) transitions. Lines are drawn for these three frequencies for $I_0 = 30.304$ μA and $C_J = 4.30$ pF.

As the bias path is designed to hold the current I_2 through the isolation junction at nearly zero, the current I_1 through the qubit is roughly I_b. Therefore, the device can be modeled as a single junction biased by I_b, as I discussed in §6.4. The solid lines show the transition frequencies as a function of I_b for $I_0 = 34.275$ μA and $C_J = 4.48$ pF, calculated with Eq. (2.44); the agreement between the data and calculation show that the single junction model provides a good parameterization of the SQUID energy levels.

For Fig. 8.2(b), we initialized the device to $N_\Phi = -7$. The spectrum has quite a few features that were not present at $N_\Phi = 0$. The transition for ω_{01} is visible, although it is not nearly as well defined as in Fig. 8.2(a). In addition, the $1 \rightarrow 2$ and $2 \rightarrow 3$ transitions can be seen in the escape rate enhancement (but not clearly on the grayscale map), even though the refrigerator was at base temperature. As discussed in §4.3, this is due to noise on the bias leads and the degradation of the isolation by the Josephson inductance of the isolation junction. I fit the $0 \rightarrow 1$ transitions peaks (marked by circles) with the single junction model (biased by I_b), which yielded $I_0 = 30.304$ μA and $C_J = 4.30$ pF. These same values were used to draw ω_{12} and ω_{23}, which agree fairly well with the data, even though $I_b < I_1$ for this flux state. The $0 \rightarrow 1$ data deviate significantly from the fit near 8.5 GHz, where there appears to be an avoided crossing. The difference in I_b for $N_\Phi = 0$ and -7 suggests that $I_2 \approx -4$ μA in the latter case. Assuming that $I_{02} = 4.4$ μA (see Table 6.1) and $C_{J2} = 2.09$ pF (see Table 4.2), $\omega_{01}/2\pi$ for the isolation junction is predicted to be 8.1 GHz at this bias current. Thus the two SQUID junctions could be degenerate at this flux state, with the coupling between them leading to an energy level splitting.

The values of I_0 are quite different for the two flux states, because the fits were performed with respect to I_b. As the qubit's critical current is independent of N_Φ, it is the circulating current due to the trapped flux that makes up the difference. Fits with respect to the qubit branch's current I_1 should return the same value of

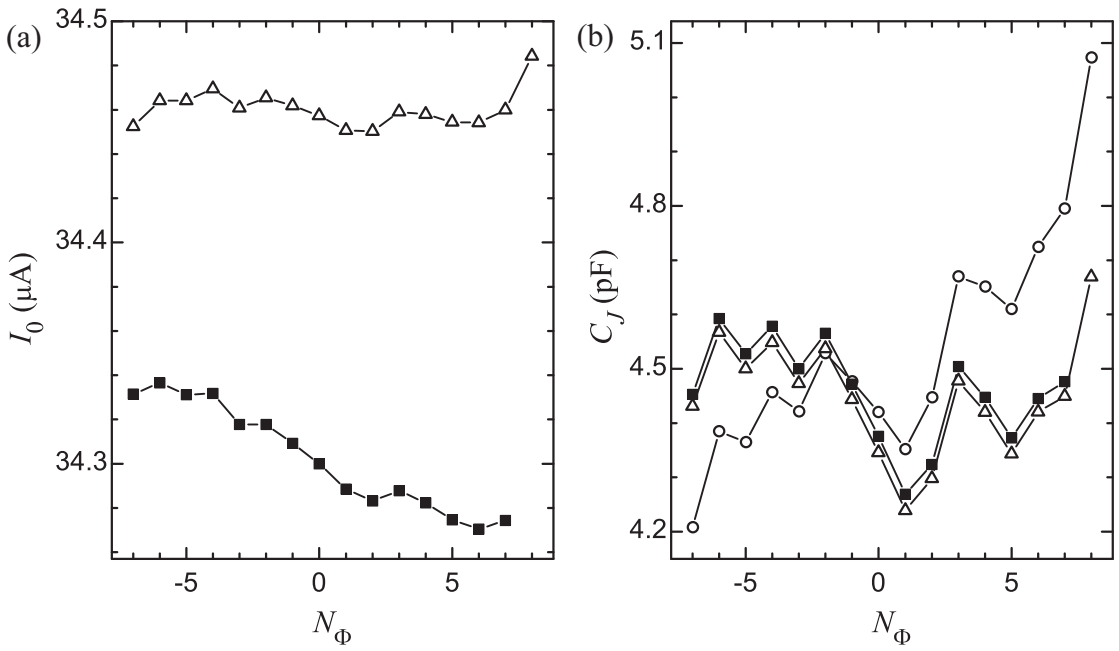

Figure 8.3: Spectral fit parameters for SQUID DS_1. By fitting the measured spectrum of DS_1 to ω_{01} for a single junction, the effective (a) critical current I_0 and (b) capacitance C_J of the qubit can be extracted. The value depends on the flux state N_Φ that the SQUID was initialized to. The open circles are the result of fitting to the current bias I_b. For the solid squares, the qubit current I_1 was calculated with $I_{01} = 34.3$ μA, $I_{02} = 4.4$ μA, $L_1 = 3.520$ nH, $L_2 = -5.2$ pH, $M_b = 0$, $M_f = 51$ pH, and flux offset $\Phi_T^0 = -0.487$ Φ_0. More consistent values of I_0 are found for $L_2 = 25$ pH and $\Phi_T^0 = -0.2$ Φ_0 (triangles).

I_0. I attempted to verify this with the data set shown in Fig. 7.9(a), where DS_1 was initialized to sixteen different flux states with flux shaking. We took microwave data for only four frequencies (7.2, 7.3, 7.4, 7.5 GHz), so there was more uncertainty in the fit parameters than for the data of Fig. 8.2.

I first used the single junction model to fit ω_{01} vs. I_b. In this case, I_0 increases by roughly 570 nA when N_Φ increases by 1 (results not plotted). The fit values of the capacitances are shown in Fig. 8.3(b) as open circles. They vary by almost 20% over all the flux states.

Rather than just fitting to I_b, I_1 can be calculated using the method of finding potential minima described in §6.4, as long as I_f is known throughout the bias ramp. Table 6.1 gives the following device parameters for field #2: $I_{01} = 34.3$ μA,

$I_{02} = 4.4\ \mu$A, $L_1 = 3.520$ nH, $L_2 = -5.2$ pH,[3] $M_b = 0$, $M_f = 51$ pH. The solid squares in Fig. 8.3 show the resulting fit values of I_0 and C_J vs. N_Φ. In order for the fit value of I_0 to equal the input value of $I_{01} = 34.3\ \mu$A for $N_\Phi = 0$, I had to assume that there was a background flux offset of $\Phi_T^0 = -0.487\ \Phi_0$ (which was present when $I_f = I_b = 0$). Ideally, I_0 and C_J would be independent of N_Φ, but there is quite a bit of variation in I_0. Worse still, with these parameters, the bias trajectory does not cross the qubit branch for $N_\Phi = 8$.

I performed the same analysis on the spectrum of Fig. 8.2(a). As this data set was taken five months after the one shown in Fig. 7.9, the device parameters appeared to be slightly different. A fit to the measured spectrum ω_{01} vs. I_1 (for $N_\Phi = 0$) yielded $I_0 = 34.300\ \mu$A and $C_J = 4.43$ pF, for a flux offset $\Phi_T^0 = -0.263\ \Phi_0$. The extracted parameters for other flux states, measured simultaneously, varied to a similar extent as in Fig. 8.3. Nonetheless, these are junction parameters I used in Figs. 7.8(b) and 7.13 as I_0^ω and C_J^ω to describe the energy levels of the qubit.

Returning to Fig. 8.3, I tried to improve the consistency by choosing the modified values $L_2 = 25$ pH and $\Phi_T^0 = -0.2\ \Phi_0$. The results are shown as triangles in Fig. 8.3. The values of I_0 vary over a much smaller range than before. However, they are centered about 34.6 μA, even though I_{01} was set to 34.3 μA to calculate I_1. I could not lower this value while maintaining solutions for all of the states. This inconsistency and the systematic variation of the fit parameters suggest that the device parameters have not been identified correctly, the biasing model has been overly simplified, the independent junction assumption breaks down for large $|N_\Phi|$, or there were errors in taking the data. The analysis in the rest of this chapter and the next will not be significantly affected by these small errors. The main message of Figs. 8.2(b) and 8.3 is that assuming $I_b \approx I_1$ under the simultaneous ramp will

[3]Only the sum $L_2 + M_b$ can be determined from I_b vs. Φ_A characteristics. Here, I have chosen to set $M_b = 0$, which has no effect on the biasing calculation. However, L_2 can be negative as a result, if M_b is sufficiently negative (a result of the sign conventions).

result in an energy level structure that resembles a single current-biased junction, with a corresponding capacitance close to C_{J1}. However, when one takes a close look at the data, some discrepancies with the model become apparent.

As another test, Fig. 8.4 shows a spectrum of DS_1 taken with an intentionally shallow bias trajectory. While the simple simultaneous biasing described in §6.4 corresponds to a ramp ratio of $\Delta I_f/\Delta I_b = 69$, these data were taken at a ratio of 109. In addition, the mixing chamber of the refrigerator was heated to 110 mK. As $|1\rangle$ was thermally occupied, the spectrum shows both ω_{01} (circles) and ω_{12} (squares).

For the asymmetric $\beta = 8.4$ SQUID shown in Fig. 6.7, the bias path results in two types of switches. For low I_b, the path crosses the isolation branch along the dotted lines; this will result in the SQUID retrapping in another flux state. For higher I_b, the qubit will switch to the voltage state in the usual way. As there is retrapping along the way, the full experimentally measured histogram shown in the inset to Fig. 8.4(a) is quite asymmetric, unlike what would result from a proper simultaneous ramp. Interestingly, fifteen peaks are seen in this histogram (although not all are visible on the plot), with the first apparently coming from the isolation junction switching to the voltage state. I made the arbitrary choice to analyze the flux state marked with an arrow.

In Fig. 8.4(a), the transition frequencies are plotted as a function of I_b, which we ordinarily only do for the proper simultaneous ramp (when $I_b \approx I_1$). Nonetheless, the transition frequencies have the usual dependence on the current bias. A fit to ω_{01} (solid lines) gives $I_0 = 31.660$ μA and $C_J = 3.57$ pF, with reasonable agreement. However ω_{12} for the same parameters underestimates the data by 500 MHz. The experimental values of ω_{12} are faithfully reproduced for a single junction with $I_0 = 31.688$ μA and $C_J = 3.52$ pF (dashed lines), but the corresponding ω_{01} is too large.

To get sensible fits in this case, I_f and the trapped flux of this particular state must be considered. By using the current-flux characteristics with values listed in

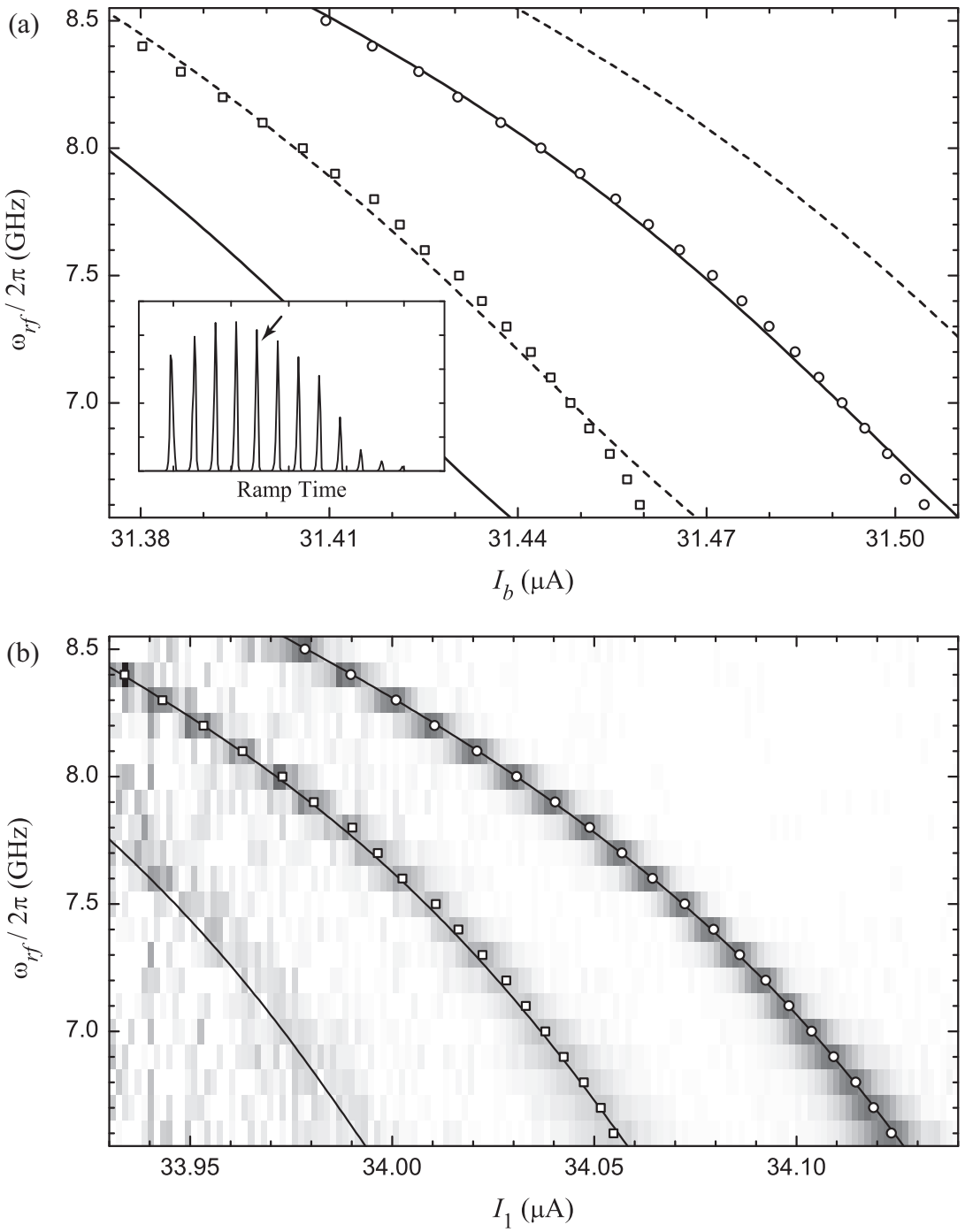

Figure 8.4: Shallow ramp spectrum of SQUID DS_1. At 110 mK, both the $0 \rightarrow 1$ (circles) and $1 \rightarrow 2$ (squares) transitions are clearly seen in the spectrum. (a) When the spectrum is viewed as a function of I_b, both transitions cannot be described by a single junction model. The solid lines are drawn for $I_0 = 31.660$ μA and $C_J = 3.57$ pF, while the dashed are for $I_0 = 31.688$ μA and $C_J = 3.52$ pF. The inset shows the full (unshaken) histogram, with an arrow indicting the peak that was analyzed. (b) A good fit to the transitions is found by plotting the spectrum against I_1, which takes I_f and trapped flux into account. The grayscale map shows the normalized enhancement.

Table 6.1, it appears that this peak is $N_\Phi = 27$. This state can only be occupied by retrapping along the bias path, so flux shaking cannot be used for initialization. The combination of the circulating current due to trapped flux, I_b, and I_f were used to calculate the current through the qubit I_1 as plotted in Fig. 8.4(b). Now a fit to ω_{01} yields $I_0 = 34.300$ μA and $C_J = 4.51$ pF, which also describes the $1 \rightarrow 2$ transition. These fits are of a higher quality than those shown in Fig. 8.4(a). In the grayscale map, which is the normalized escape rate enhancement, the $2 \rightarrow 3$ transition is barely visible. The model junction reproduces this branch as well.

The usual simultaneous biasing does not add any current through the isolation junction. For the range plotted in Fig. 8.4, I_2 is roughly -2.6 μA and changes appreciably. In Fig. 6.7(a), a better fit value of I_0 could have been obtained by shifting the I_b-axis; however this would not have changed the slope and the fit value of C_J would still have been incorrect.

Agreement between the fit value of I_{01} and the value from the current-flux characteristics was enforced by adding a constant offset flux of $\Phi_T^0 = -0.364\Phi_0$ to the bias path. In calculating I_1 in Fig. 8.4(b), I used $L_2 = -5.2$ pH. With $L_2 = 30$ pH, the fit values become $I_0 = 34.275$ μA and $C_J = 4.50$ pF, which essentially corresponds to a small shift. Thus, the difficulty in determining L_2 is not a serious problem for extracting I_{01} and C_{J1}.

In everything that follows for the SQUIDs, I used the simultaneous current and flux biasing as shown in Fig. 6.7(d). This example was given just to show that the picture of the SQUID that we have developed holds together and to suggest a technique to verify that the qubit junction is being biased as expected.

8.3 Spectroscopic Coherence Time

Aside from locating the ω_{01} resonance and providing a measurement of I_0 and C_J (which in turn can be used to predict tunneling rates), spectroscopy also can be

used to measure the spectroscopic coherence time T_2^* of the system; see §3.7. This quantity, which depends on the relaxation time T_1, the coherence time T_2, and low frequency noise sources, is a useful indicator of the quality of the isolation of a qubit from its environment.

The first step in calculating T_2^* is to find the full width at half maximum of a resonant transition. If the level spacing were held constant while ω_{rf} was swept, the system only had two levels, and there was no tunneling or current noise, we would expect to see peaks with Lorentzian linewidths if the excited state population was plotted as function of ω_{rf} [see Eq. (3.60)].

Experimentally, we were only able to gauge the resonance width by measuring the total escape rate due to a microwave current. As shown in Fig. 6.5(c), when the microwaves are resonant with a qubit transition, a peak is seen in the escape rate enhancement $\Delta\Gamma/\Gamma$. As the enhancement is roughly proportional to the excited state population (see §6.6.1), the resonance width can be estimated from $\Delta\Gamma/\Gamma$. A more careful analysis shows how the enhancement is related to the true width (see §3.5.1 of Ref. [1] and §2.6.3 of Ref. [3]).

I usually fit the measured escape rate enhancement as a function of ramp time to extract the full width at half maximum Δt and the peaks were often slightly asymmetric (due to, for example, bias-dependent escape rate ratios) and not described well by Lorentzians or Gaussians. I often just identified the width by eye or fit to another functional form, even if there was no physical justification for doing so. I found that the asymmetric double sigmoidal,[4]

$$y = \frac{A}{1+\exp\left(-\frac{x-x_c+w_1/2}{w_2}\right)}\left[1-\frac{1}{1+\exp\left(-\frac{x-x_c-w_1/2}{w_3}\right)}\right], \tag{8.1}$$

had enough degrees of freedom to provide a high quality fit. Here, A is related to

[4]This function and many others are included in Origin's fitting utility.

the height, x_c controls the center, and w_1, w_2, w_3 set the width and asymmetry. No matter the method, there was typically a 10% uncertainty in determining Δt. It was often larger at low and high currents, where the counting statistics tended to be poor.

Using the calibration of I_b as a function of time, I then converted Δt to the full width at half maximum ΔI_b in terms of current. Figure 8.5(a) shows ΔI_b as a function of ω_{01} (assuming a resonance peak is centered about $\omega_{rf} = \omega_{01}$) for the junction LC_2B spectra in Fig. 8.1(a) (open circles) and Fig. 8.1(b) (open squares), and the SQUID DS_1 spectrum in Fig. 8.2(a) (solid triangles). Each spectrum happened to cover a different frequency range, which was dictated by the range of the measurable escape rates. At the low frequency end of each spectrum (*i.e.* a shallow potential well) the widths increase rapidly, while at high frequencies they appear to saturate.

The spectrum gives ω_{01} as function of I_b, which may be used to convert ΔI_b to a width $\Delta\omega$ in frequency. The assumption is that if we had performed the experiment by holding I_b constant and sweeping ω_{rf}, we would have measured a resonance width $\Delta\omega$. Results of this conversion, which are independent of the current calibration when plotted as a function of ω_{01}, are shown with symbols in Fig. 8.5(b). The qualitative frequency dependence is preserved between Δt and $\Delta\omega$, but there is an interesting effect with the two data sets for LC_2B. Because Fig. 8.1(b) was taken over frequencies close to the LC coupling mode, $|d\omega_{01}/dI_b|$ is relatively small as ω_{01} approaches the bias independent mode.[5] Therefore even though ΔI_b for the squares is larger than for the circles, $\Delta\omega$ for the squares is slightly smaller (at the highest frequencies). It is possible that the circles are limited by current noise, while the squares saturated due to an intrinsic mechanism. In general, even if ΔI_b saturates

[5]The fit of the spectrum was quite poor for this data set, so I converted ΔI_b to $\Delta\omega$ by hand, rather than by using extracted values of I_0 and C_J. At the lowest frequencies, I was unable to do this, which is why there are fewer squares in Fig. 8.5(b) and (c).

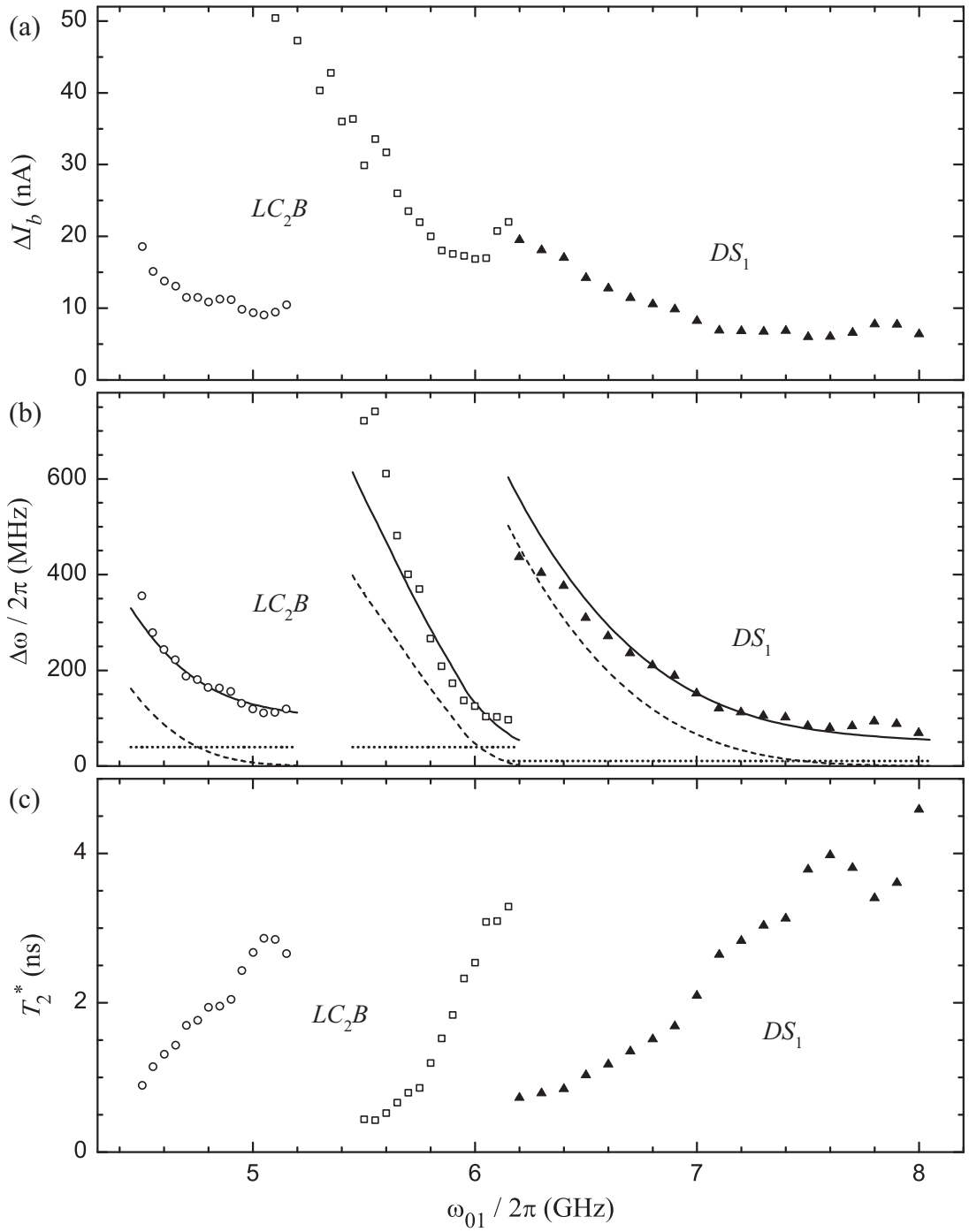

Figure 8.5: Resonance widths of LC_2B and DS_1. Peak statistics are shown for the junction LC_2B spectra in Fig. 8.1(a) (open circles) and Fig. 8.1(b) (open squares), and the SQUID DS_1 spectrum in Fig. 8.2(a) (solid triangles). The (a) full width ΔI_b at half maximum of the resonance in current was converted to a (b) full width $\Delta\omega$ at half maximum in frequency by using the ω_{01} transition frequencies. The lines show estimates for dissipation (dotted), tunneling (dashed), and the sum of both and current noise (solid). (c) The spectroscopic coherence time is $T_2^* = 2/\Delta\omega$.

with increasing frequency, $\Delta\omega$ will continue to decrease due to the decreasing value of $|d\omega_{01}/dI_b|$.

In the case of DS_1, the width at 7.5 GHz is about 75 MHz, for a resonance quality factor of roughly 100. However assuming $T_1 \approx 15$ ns, $Q \approx 700$ using the definition $Q = \omega_p R_J C_J$ given in §2.2.3. This latter value is based only on dissipation. That the observed Q is much smaller suggests that other broadening mechanisms are at work. As shown by Eq. (3.66), $\Delta\omega$ is due to all of the transitions that depopulate either $|0\rangle$ or $|1\rangle$, assuming that pure dephasing and power broadening are negligible. At low temperatures, where $W_{01}^t \approx 1/T_1$ and $W_{10}^t \approx 0$, $\Delta\omega \approx 1/T_1 + \Gamma_1 + 2\sigma_I\, \partial\omega_{01}/\partial I_b$ [38]. Here, the escape rate Γ_1 of the first excited state is much larger than than that of the ground state and σ_I is the rms value of the low frequency current noise.

The dotted lines in Fig. 8.5(b) show the contribution to $\Delta\omega$ by dissipation. Based on the measurements in §7.4, I assumed T_1 was 4 ns for junction LC_2B and 15 ns for SQUID DS_1 (and that it had no frequency dependence). The contribution from tunneling is indicated by the dashed lines. Γ_1 increases quickly with increasing I_b (or decreasing ω_{01}), which accounts for the increase in $\Delta\omega$ at high bias. Finally, $1/T_1 + \Gamma_1 + 2\sigma_I \partial\omega_{01}/\partial I_b$ is plotted with solid lines.[6] For LC_2B, I chose $\sigma_I = 3.2$ nA; this value roughly reproduces $\Delta\omega$ for the circles and squares, although there are significant quantitative discrepancies. For DS_1, I set $\sigma_I = 2$ nA, suggesting that the inductive isolation did reduce the low frequency current noise, as it was designed to do. It is unclear why there are systematic deviations between the data and prediction in all cases, but they may be due to the simplifications in Eq. (3.66) and difficulty of accurately calculating Γ_1. In principle, this method can be used to determine T_1, by choosing parameters that give the best fit; see §7.1 of Ref. [3].

[6]For the circles, I calculated the energy levels with Eq. (2.44) for junction parameters $I_0^\omega = 15.420\ \mu$A and $C_J^\omega = 5.65$ pF; escape rates cames from Eq. (2.43) with $I_0^\Gamma = 15.434\ \mu$A and $C_J^\Gamma = 3.4$ pF. For the squares, the spectrum could not be accurately fit with the single junction model, so I extracted vales directly from the data; tunneling rates were calculated with $I_0^\Gamma = 33.648\ \mu$A and $C_J^\Gamma = 4.24$ pF. For the triangles, $I_0^\omega = 34.308\ \mu$A, $I_0^\Gamma = 34.300\ \mu$A, and $C_J^\omega = C_J^\Gamma = 4.43$ pF.

Finally, values of the spectroscopic coherence time $T_2^* = 2/\Delta\omega$ [see Eq. (3.67)] are plotted in Fig. 8.5(c). The SQUID phase qubit (triangles) is better isolated than the LC-isolated qubit, as seen in the saturation values of $\Delta\omega$ and T_2^*. In both cases, T_2^* is well below estimates for $2T_1$, suggesting that dephasing and inhomogeneous broadening are significant.

It could also be that the saturation of ΔI_b is not due to σ_I or T_1, but instead to the measurement technique. For example, if the timing resolution of the escape rate measurement was sufficiently poor, then no peak could be narrower than a certain value. Also, we measure the resonance peak by sweeping I_b linearly to I_0. The linewidth is only reproduced faithfully if the time scale of the sweeping is much slower than the dynamics of the junction.[7] Of lesser concern is the accuracy of the current calibration, as these errors are largely removed by measuring peak widths in terms of frequency rather than current.

These issues are addressed by Fig. 8.6, which shows the statistics for the resonance peaks of SQUID DS_2B taken at three different ramp rates of I_b.[8] As seen in Fig. 8.6(a), Δt does scale with the ramp rate, increasing by a factor of 4 between 0.0258 A/s (circles) and 0.0041 A/s (triangles). However, when these are expressed in terms of frequency, they are in reasonable agreement [see Fig. 8.6(b)]. I have not shown the intermediate step of ΔI_b, but these values saturate at about 4 nA. Thus this check shows that there is no obvious connection between the saturation of I_b and the experimental technique. The scatter above 5.7 GHz is indicative of the uncertainty of the peak fits. Certain features, such as the large width at 6.4 GHz, appear to be real.

As in Fig. 8.5(b), the dotted line in Fig. 8.6(b) shows the contribution to $\Delta\omega$ by dissipation; here, I assumed $T_1 = 15$ ns. The dashed line comes from tunneling

[7] A similar situation is discussed in §7.5

[8] The goal was to hold the ratio of I_f and I_b constant for the three rates, but this was an additional source of error.

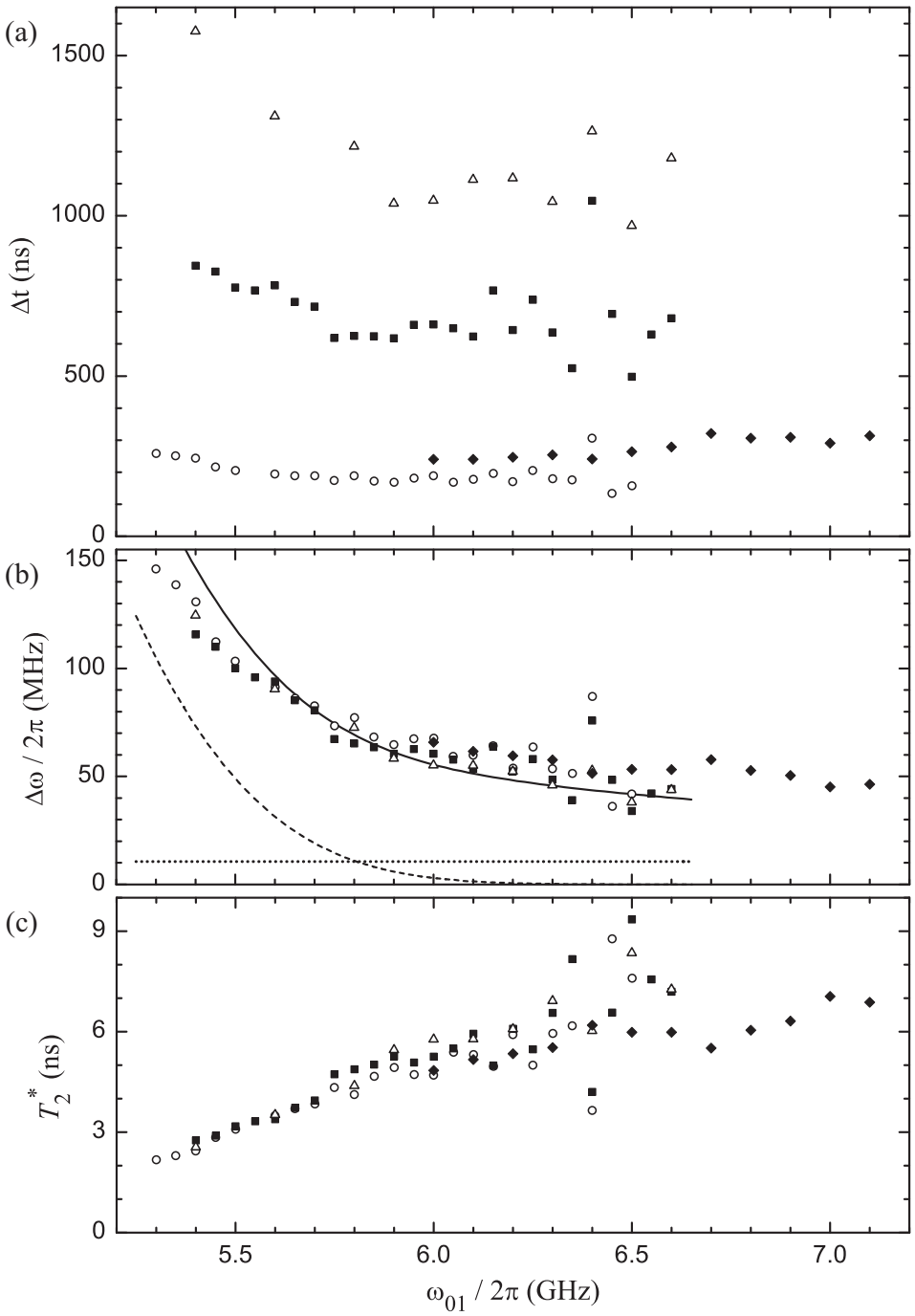

Figure 8.6: Resonance widths of SQUIDs DS_2A and DS_2B with different ramp rates. The peak statistics were calculated from spectra of DS_2B measured at 20 mK, with I_b ramp rates of 0.0258 A/s (open circles), 0.0066 A/s (solid squares), and 0.0041 A/s (open triangles). The solid diamonds come from a spectrum of DS_2A, taken with a 0.018 A/s ramp. While the (a) resonance width in terms of the ramp time depends on the rate, the (b) width in frequency and (c) spectroscopic coherence time do not. The lines in (b) show estimates for dissipation (dotted), tunneling (dashed), and the sum of both and current noise (solid) for DS_2B.

out of the first excited state. The solid line is the sum of both of these contributions plus that of low frequency noise, with $\sigma_I = 1.5$ nA.[9]

The values of T_2^* plotted in Fig. 8.6 for SQUID DS_2B are longer than those for SQUID DS_1 in Fig. 8.5(c) (triangles) and the value of σ_I in describing $\Delta\omega$ is smaller. I did not do enough careful testing to determine whether this is due to something intrinsic to the devices (*e.g.* different fabrication process, presence of the quasiparticle trap on DS_2B, suppression field on DS_1) or an artifact of the technique (*e.g.* heavier room temperature and cold filtering for DS_2B). The latter seems likely as other spectra of DS_1 showed slightly longer values of T_2^* than those of Fig. 8.5(c).

Also shown in Fig. 8.6, with diamonds, are the resonance statistics for a spectrum of DS_2A. As the qubit critical current was slightly higher for this SQUID, the measurable frequency range is higher. The values of $\Delta\omega$ and T_2^* are in rough agreement with DS_2B. This is potentially interesting because, as mentioned in §4.3.2, the mutual inductance of SQUID A to its own flux line was 71.92 pH, while that of SQUID B to its own flux line was 17.73 pH. Thus the coupling of noise on the flux line to the qubit should be about 16 times as strong in DS_2A as in DS_2B, based on Eq. (4.10). It would seem then that the level of isolation was not limited by the coupling to the flux line, provided that the magnitude of the noise source did not scale with I_f. Biasing the same device with the two different flux lines would have been a more sensitive test, but one we did not do.

In taking the spectrum of DS_2A, we did not reset I_b quickly after a switching event (see §5.2.2), which was done for the spectra of DS_2B. Therefore, there was thermally excited population in $|1\rangle$ and the spectrum did show a clear $1 \rightarrow 2$ branch. In order to see a large signal, the microwave power had to be increased over usual levels, which may explain the increasing Δt seen in Fig. 8.6(a) for this device (dia-

[9]To calculate energy levels, I used $I_0^\omega = 17.754$ μA and $C_J^\omega = 4.44$ pF. To calculate escape rates, I used $I_0^\Gamma = 17.765$ μA and $C_J^\omega = 3.70$ pF.

monds). We did, however, attempt to cancel out the flux in SQUID B due to cross mutual inductances, by applying I_f^A and I_f^B simultaneously. In another spectrum that we took when we did not do this, the peak widths were noticeably larger. As the conditions were not identical (*e.g.* different room temperature filters), it is not possible to draw any firm conclusions about cross-talk between the devices and its connection to T_2^*.

A further test on the description of the peak widths is to examine transitions of the energy levels higher in the potential well. As discussed in §3.4, the relaxation rate from $|n\rangle$ to $|n-1\rangle$ in the harmonic limit is $\Gamma_{n,n-1} = n/R_J C_J$. Assuming dissipation-limited decoherence at $T = 0$, the resonance widths should occur with a $1:3:5$ ratio for the $0 \to 1$, $1 \to 2$, and $2 \to 3$ transitions [see Eq. (3.66)].

Figure 8.7 shows the full width at half maximum of the (a) $0 \to 1$, (b) $1 \to 2$, and (c) $2 \to 3$ transitions of SQUID DS_1. We heated the mixing chamber to 110 mK so that $|1\rangle$ and $|2\rangle$ were sufficiently occupied to make transitions from them visible. The data for the three transitions were taken with roughly the same range of microwave frequencies, but I have plotted the points as a function of ω_{01}; for example, $\omega_{23}/2\pi$ is 7.4 GHz at the bias current where $\omega_{01}/2\pi$ is 8.68 GHz.

At low frequencies, the widths increase substantially, due to escape rate broadening. At high frequencies, the $0 \to 1$ and $1 \to 2$ widths appear to saturate, but at values of 80 and 100 MHz, far from the expected $1:3$ ratio. This suggests that current noise (or perhaps pure dephasing) had a significant effect on the resonance widths. $\Delta\omega_{23}$ was difficult to extract due to poor counting statistics, but it may be saturating near 200 MHz. While $\Delta\omega_{23}/\Delta\omega_{12}$ is consistent with broadening due only to dissipation, the values require $T_1 \approx 5$ ns, which is lower than the measurements of Chapter 7 would suggest.

I attempted to perform a quantitative analysis of the widths using Eq. (3.66), as in Fig. 8.5(b). The dotted lines in Fig. 8.7 indicate the contribution to the

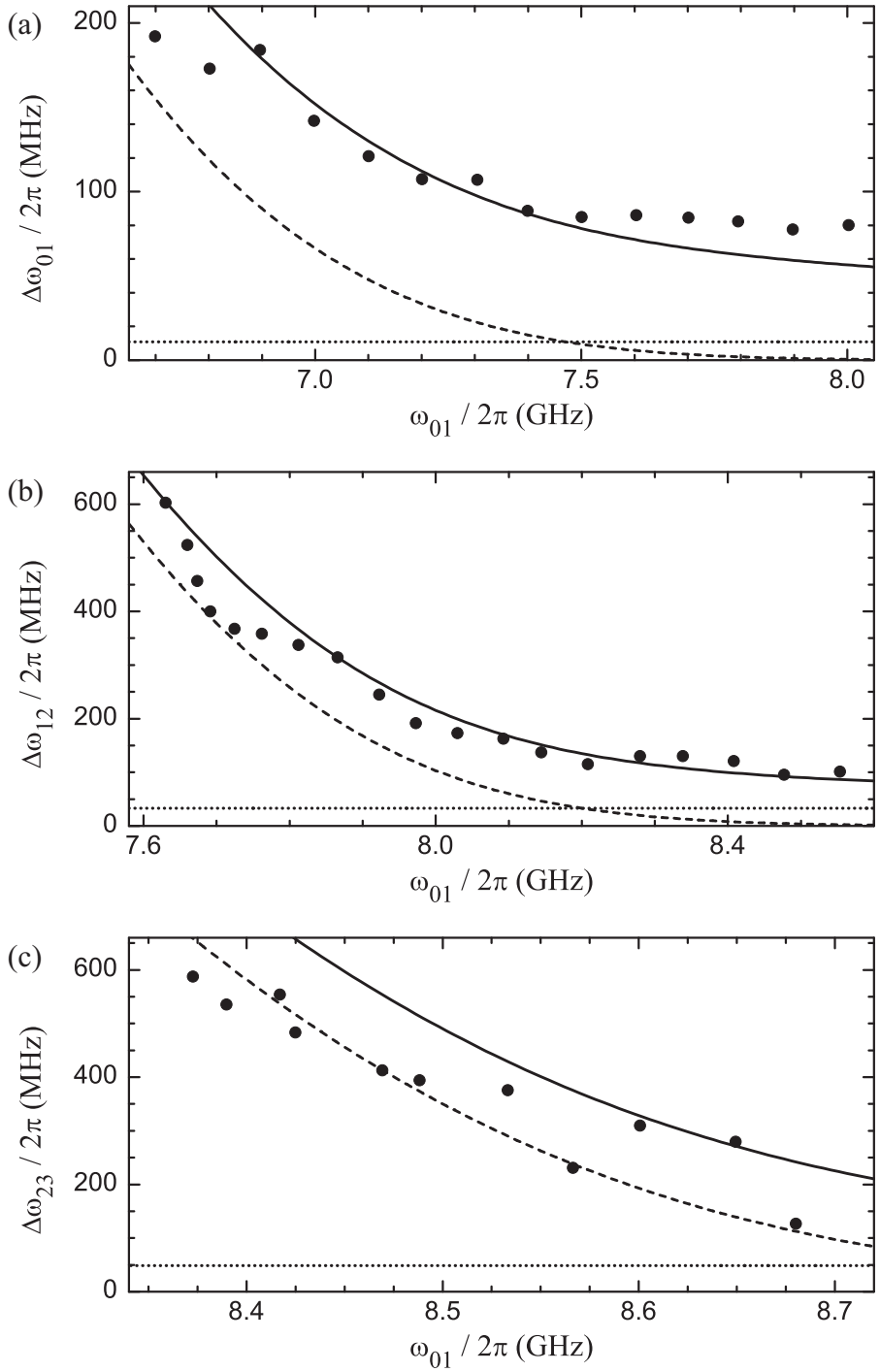

Figure 8.7: Resonance widths of SQUID DS_1 at elevated temperature. The circles show the full width $\Delta\omega$ of the (a) $0 \rightarrow 1$, (b) $1 \rightarrow 2$, and (c) $2 \rightarrow 3$ transitions measured at 110 mK, as a function of ω_{01}. The lines show estimates for dissipation (dotted), tunneling (dashed), and the sum of both and an rms current noise of 2 nA (solid).

widths from inter-level transitions. The thermal rates are given by Eqs. (3.26) and (3.27), which I evaluated (for single level transitions of a four-level system) by using the cubic matrix elements in Eq. (2.38). I assumed that $R_J C_J$ had a frequency-independent value of 15 ns. At 110 mK and the bias current where $\omega_{01}/2\pi =$ 7.5 GHz, the inverse of the sum of the thermal rates is 14.6, 4.84, and 3.27 ns, for the $0 \rightarrow 1$, $1 \rightarrow 2$, and $2 \rightarrow 3$ transitions. The dotted lines are drawn at these values, assuming no frequency dependence.

The dashed lines are estimates for the contribution by tunneling from the higher of the two states in the transition; for example, the dashed line in Fig. 8.7(b) is Γ_2, calculated using Eq. (2.43). Finally, the solid lines in Fig. 8.7 are the sum of the contributions from dissipation, tunneling, and current noise with $\sigma_I = 2$ nA.

As in Fig. 8.5(b), $\Delta\omega_{01}$ is well described by the estimate including current noise [see solid line in Fig. 8.7(a)]. What strengthens the argument for current noise is the fair agreement between data and prediction for $\Delta\omega_{12}$ in Fig. 8.7(b). The agreement is not as good for $\Delta\omega_{23}$ in Fig. 8.7(c). In this case, the widths ΔI_b in current were difficult to extract due to poor counting statistics in the switching histograms. In addition, the conversion to $\Delta\omega$ was inaccurate due to deviations in ω_{23} from the single junction model; this lead to underestimates of $\Delta\omega$ at low frequencies. Nonetheless, it does seem that estimates for Γ_3 based on measurements of Γ_0 are reasonably accurate. It would be useful to examine data at lower bias to determine the saturation value of $\Delta\omega_{23}$.

8.4 Multi-Level and Multi-Photon Transitions

Figure 8.8 shows a spectrum of SQUID DS_2B, taken at 110 mK. As with Fig. 8.4, the excited states were thermally populated, even in the absence of microwaves. As with all of the spectra, data at each frequency were taken at a different microwave power and each horizontal line of the grayscale map has been independently normal-

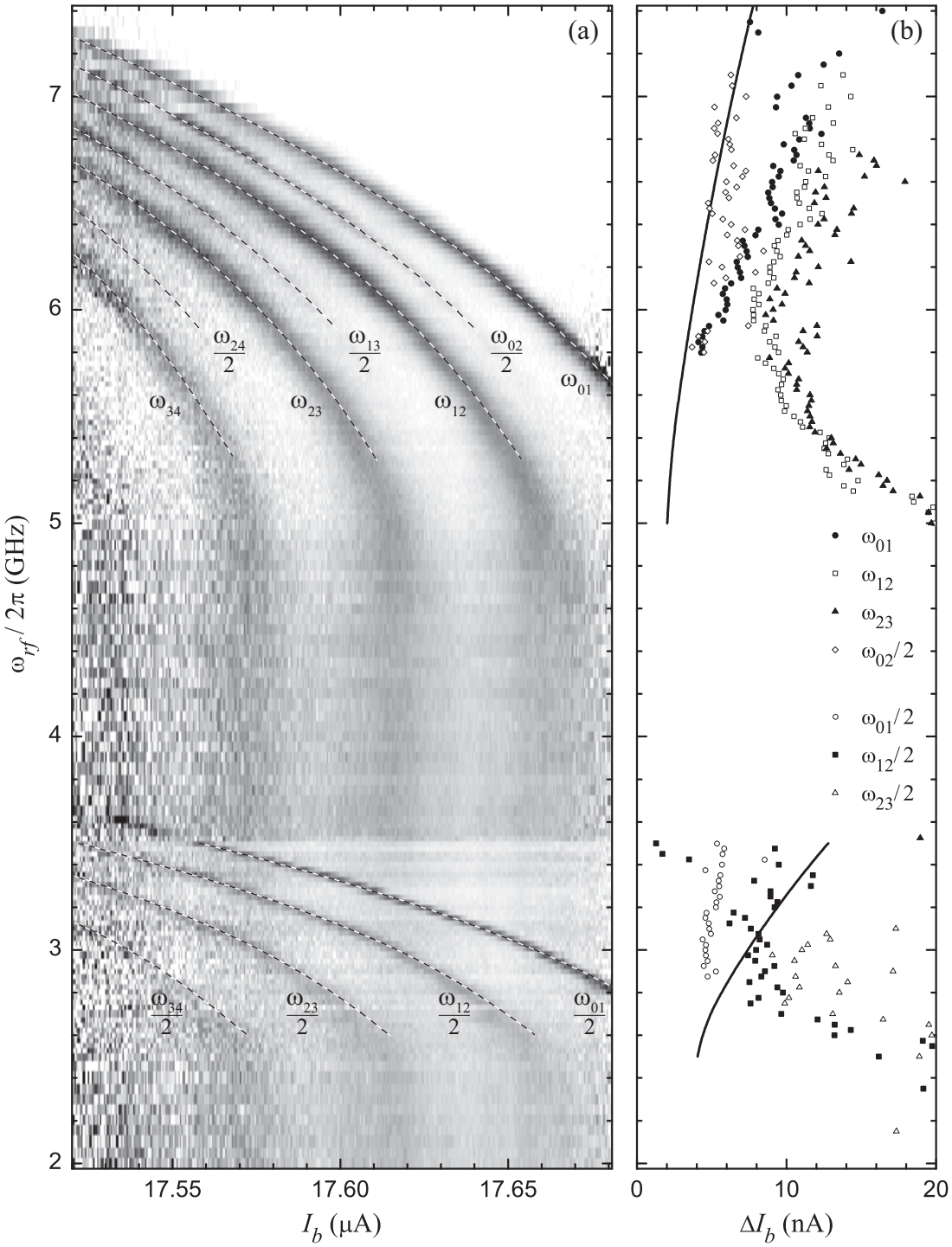

Figure 8.8: Low frequency spectrum of SQUID DS_2B. At 110 mK, the spectrum shows a number of transitions between the lowest five states in the potential well. (a) The grayscale map shows the escape rate enhancement spectrum, while the dashed lines are drawn for a single junction with $I_0 = 17.828$ μA and $C_J = 4.51$ pF. (b) The full width at half maximum of some of the transitions are plotted as a function of frequency. The solid line shows the current width corresponding to a frequency width of 50 MHz for $\omega_{01}/2$ and ω_{01}.

ized. Different features of the spectrum could have been emphasized by the selection of different microwave powers.

Centered about 6 GHz are four branches that correspond to the single photon transitions that I discussed in the previous section. As the tilted washboard potential well is anharmonic, $\omega_{34} < \omega_{23} < \omega_{12} < \omega_{01}$ at any given value of I_b. I fit the $0 \rightarrow 1$ transition to the single junction values given by Eq. (2.44), which yielded $I_0 = 17.828$ μA and $C_J = 4.51$ pF. All of the dashed lines are drawn with these parameters.

Escape rate enhancement is also present at exactly half of these frequencies. The branches labeled $\omega_{01}/2$, $\omega_{12}/2$, $\omega_{23}/2$, and $\omega_{34}/2$ correspond to two-photon transitions between levels. Multi-photon transitions, allowed because the potential is anharmonic, have been previously observed in a number of superconducting systems [42, 43, 121]. They are easy to identify from their quadratic power dependence.

Similarly, in between the single photon branches are three narrows ones that appear at frequencies above 6 GHz. These could have been made more prominent at lower frequencies by increasing the microwave power. As agreement with the dashed lines suggests, these occur at frequencies $\omega_{02}/2$, $\omega_{13}/2$, and $\omega_{24}/2$. They correspond to two-photon transitions between states $|n\rangle$ and $|n+2\rangle$.

Figure 8.9 shows the spectrum of transitions at higher frequencies.[10] Most prominent are the branches labeled ω_{02}, ω_{13}, ω_{24}, and ω_{35}, which are single photon versions of the transitions just described. At higher frequencies still, are transitions that cover the spacing between four levels with a single photon, namely ω_{03}, ω_{14}, and ω_{25}. The microwave power was not set high enough to see these transitions clearly, which explains the noise around 18 GHz. The two-photon version of these transitions ($\omega_{03}/2$ and $\omega_{14}/2$) are barely visible near 9 GHz. I have interrupted the dashed line fit near these branches, so as not to obscure the data. At 13.4 GHz, the

[10]The frequency axis is compressed by over a factor of 3 as compared to Fig. 8.8. Data were also taken at larger intervals.

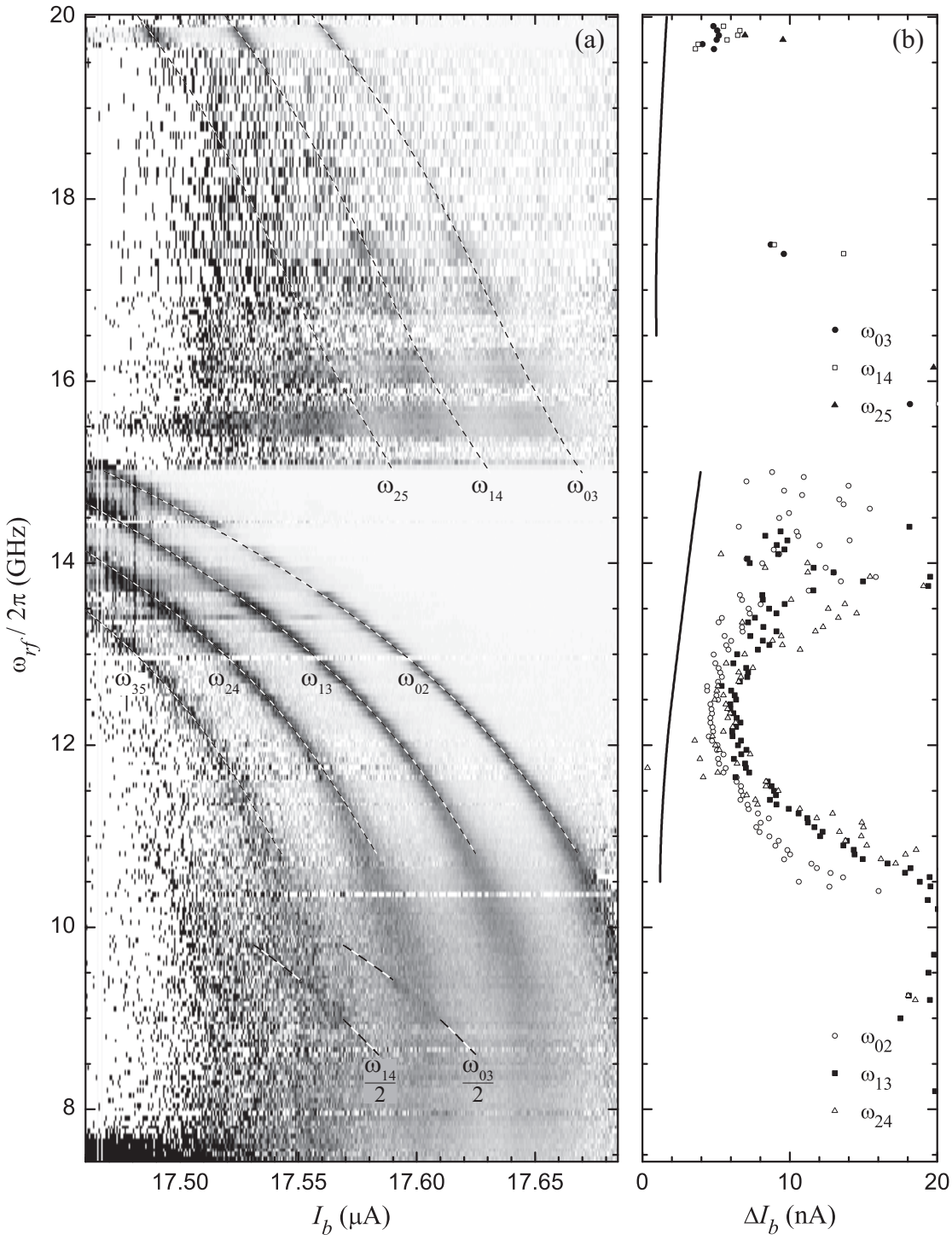

Figure 8.9: High frequency spectrum of SQUID DS_2B. At 110 mK, the spectrum shows a number of transitions between the lowest six states in the potential well. (a) The grayscale map shows the escape rate enhancement spectrum, while the dashed lines are drawn for a single junction with $I_0 = 17.828$ μA and $C_J = 4.51$ pF. (b) The full width at half maximum of some of the transitions are plotted as a function of frequency. The solid line shows the current width corresponding to a frequency width of 50 MHz for ω_{02} and ω_{03}.

power was unintentionally set very high. Three additional peaks appear that seem to correspond to transition frequencies near $2\omega_{01}$, $2\omega_{12}$, and $2\omega_{23}$.

The dashed lines in Figs. 8.8 and 8.9 correspond to twenty transitions (but depend on only five transition frequencies ω_{nm}) and were all plotted with the same values of I_0 and C_J from a fit to ω_{01}. This is encouraging in that it confirms our understanding of the Hamiltonian of the device. However, the presence of all of these transitions does make a liability of this device clear. We would like to control the population in $|0\rangle$, $|1\rangle$, and possibly $|2\rangle$ (if it used as an auxiliary state) for quantum computation. However, in the phase qubit, higher excited are not far separated from the desired states and care must be taken to ensure that they do not become highly populated.

For all of the branches, the dashed-line fits overestimate the observed values at low frequencies. As seen most clearly with the single-level, single-photon transitions between 3.5 and 5 GHz, the branches become nearly vertical. This is at least partly due to the fact that we measured the resonances by sweeping I_b. Thus the escape rates (and their ratios) vary across the resonance. The escape rate out of the higher level of a transition becomes very large as it leaves the potential well, resulting in a distortion of the shape of the resonance of $\Delta\Gamma/\Gamma$. This leads to deviations from the actual energy level spacing.

In Figs. 8.8(b) and 8.9(b), the full width at half maximum ΔI_b of several of the transitions is plotted as a function of frequency. There is a fair bit of scatter in the points, at least partly due to the small number of counts taken at each frequency. At the low frequency end of each branch, the widths increase due to escape rate broadening. As the goal of this data set was to see all available transitions, the microwave power was set fairly high, which probably lead to some power broadening as well. This is particularly true at the high frequency end of each branch, where the background escape rates are small (and the easiest way to get good statistics

on a microwave resonance is to use a high power). Finally, the temperature was high enough to broaden the transition. Nonetheless, several of the transitions (with both one and two photons) have a minimum width of roughly 4 nA, suggesting that there was low frequency current noise that limited the "resolution." As expected, at a given frequency, transitions deeper in the well are sharper and the two-photon transitions are sharper than single photon ones (*e.g.*, the two-photon $0 \rightarrow 2$ is sharper than the single photon $0 \rightarrow 1$).

The solid lines in Figs. 8.8(b) and 8.9(b) show the value of ΔI_b corresponding to a full width of $\Delta\omega/2\pi = 50$ MHz. This is plotted for a transition from the ground state, but all of the transitions in a given frequency range have similar results. A two-photon $0 \rightarrow 1$ transition corresponds to small values of $d\left(\omega_{01}/2\right)/dI_b$. Thus, deep in the well, a 4 nA width corresponds to a sharp resonance of about 25 MHz. For a $0 \rightarrow 3$ transition, $d\omega_{03}/dI_b$ is quite a bit larger, so the same 4 nA corresponds to a frequency width of over 100 MHz at 20 GHz. A detailed comparison of the widths for different transitions could be performed to see if Eq. (3.66) is obeyed.

8.4.1 Power Dependence

So far, most of the spectroscopic data I have shown were taken at relatively low microwave power, so the effects of power broadening could be ignored. One reason to examine the power dependence of the resonance peaks is determine the maximum power that can be used without affecting the width. More importantly, the power dependence can be compared to the expected behavior to verify our understanding of the system dynamics and extract important parameters. I will delay a direct comparison to the expected behavior discussed in §3.7 until §9.1.

The inset of Fig. 8.10(a) shows the measured escape rate of SQUID DS_1 taken without microwaves (solid circles) and with a 7.6 GHz microwave current (open circles). The nominal power of the microwave source was set to $P_S = -26$ dBm.

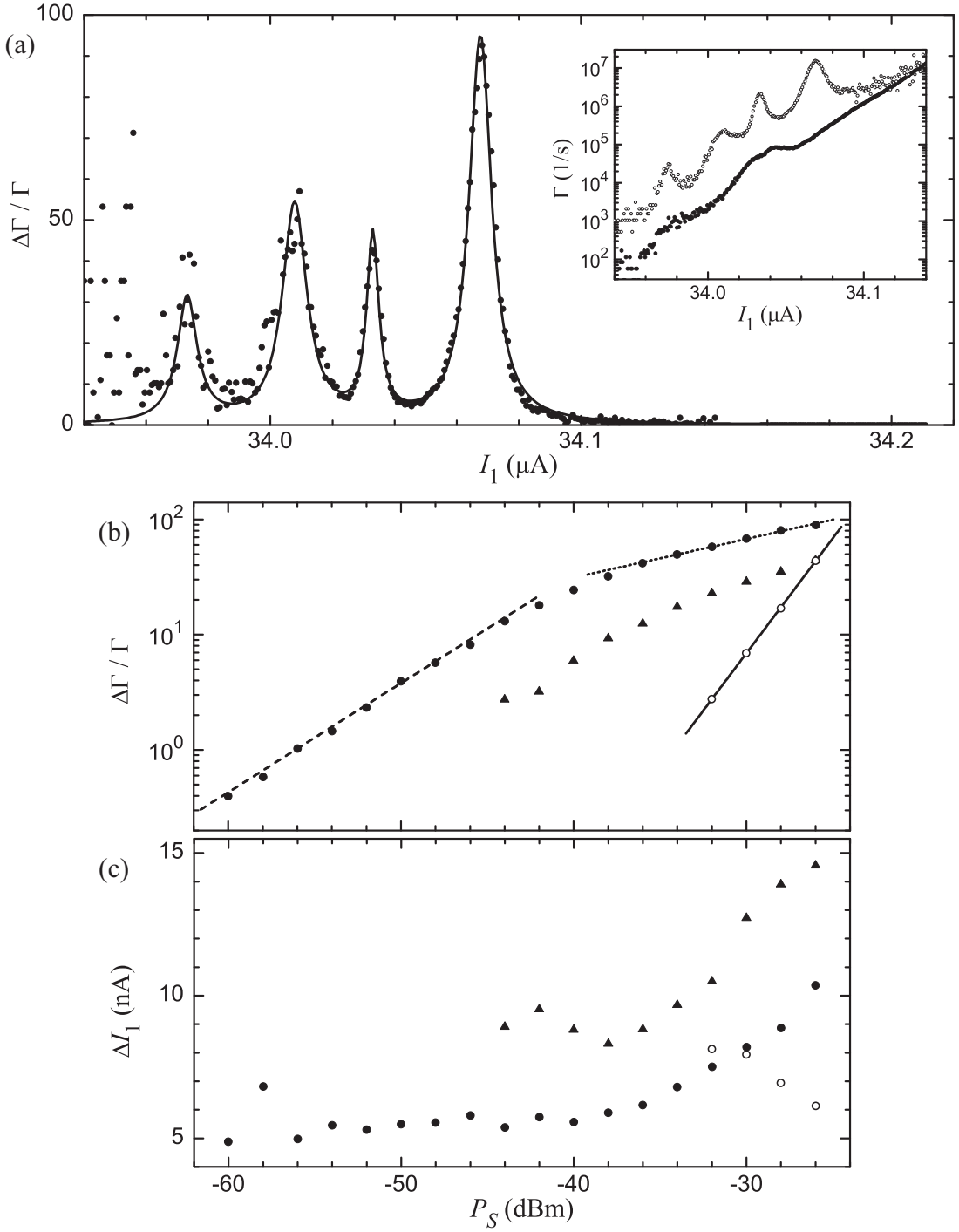

Figure 8.10: Power dependence of spectral peaks in SQUID DS_1. (a) With a microwave current of frequency 7.6 GHz and power $P_S = -26$ dBm, four peaks are seen in the measured escape rate enhancement; the solid line is a fit with a sum of Lorentzians. The inset shows the escape without (solid circles) and with (open circles) microwaves. (b) The maximum enhancement for the single photon $0 \rightarrow 1$ (solid circles), $1 \rightarrow 2$ (solid triangles), and two-photon $0 \rightarrow 2$ (open circles) transitions increase as a function of power. The lines show power law fits. (c) The resonance full widths, in terms of the qubit current I_1, also has a power dependence.

The microwaves excite four transitions: single photon $0 \rightarrow 1$, two-photon $0 \rightarrow 2$, single photon $1 \rightarrow 2$, and two-photon $1 \rightarrow 3$, from right to left. Even though the refrigerator was at base temperature, there was enough population in $|1\rangle$ to make the $1 \rightarrow 2$ and $1 \rightarrow 3$ transitions quite visible at high power.

The escape rate with microwaves is uniformly larger than the background values, making it seem that perhaps the microwave current is heating the device. This hypothesis can be checked by examining the escape rate enhancement, which is plotted with solid circles in the main panel of Fig. 8.10(a). As opposed to the usual enhancement of 1 to 5 (typical for taking a spectrum), $\Delta\Gamma/\Gamma$ reaches nearly 100. The solid line is a fit to the sum of four Lorentzians, which does a good job of reproducing the peaks and also the valleys. This strongly suggests we are mainly seeing resonant phenomena and heating due to the microwaves is making a negligible contribution.

We measured the escape rate for a wide range of source powers P_S and fit the enhancements to extract the height and width of the resonance peaks. The maximum enhancement is plotted in Fig. 8.10(b), for the single photon $0 \rightarrow 1$ (solid circles), $1 \rightarrow 2$ (solid triangles), and two-photon $0 \rightarrow 2$ (open circles) transitions. The values increase with power, with the two-photon process having a stronger dependence.

The straight lines in Fig. 8.10(b) are a fit to a power law, $(P_S)^{\alpha}$, where P_S is expressed in Watts rather than dBm. The single photon $0 \rightarrow 1$ transition begins with a nearly linear dependence, as shown by the dashed line, which is drawn for $\alpha = 0.946$. It eventually slows down to the dotted line, for which $\alpha = 0.336$. This reduction of the slope with power is expected saturation behavior; an incoherent microwave drive cannot populate $|1\rangle$ to more than 50% occupation probability. From Eq. (2.43), I estimate that $\Gamma_0 = 6.3 \times 10^4$ 1/s and $\Gamma_1 = 3.7 \times 10^7$ 1/s, so that $\Delta\Gamma/\Gamma$ should never exceed 290. Even at the highest power, where the enhancement is

100, this suggests dissipation is preventing a complete saturation of the first excited state. The $1 \rightarrow 2$ transition appears to follows the same power laws, but the lack of data at low powers (due to small enhancements) makes it difficult to be sure. The solid line is drawn for $\alpha = 1.99$, showing that the two-photon process does have the expected quadratic power dependence.

Figure 8.10(c) shows the full width ΔI_1 at half maximum of the three resonance peaks. The single photon processes have nearly constant values below $P_S = -40$ dBm, which corresponds to $\Delta\Gamma/\Gamma \approx 25$ in this case. I will return to the dependence of the broadening in §9.1. The two-photon transition (open circles) gets sharper with increasing power. I do not know if this is artifact of the fitting procedure, as the different peaks begin to overlap at high power.

8.5 Spurious Junction Resonances

Recently, much has been made of the importance of materials science for high quality junction qubits.[11] We like to think of our devices as simple "artificial atoms" consisting of a few tunable energy levels. This model works quite well in the variety of experiments I have described so far, but it should come as no surprise that the huge number of real atoms that make up the junctions, wiring, and insulation can have some effect on performance.

It has been long established that Josephson junctions can show behavior associated with coupling to a bath of two-level systems [137, 138]. The standard microscopic picture, now more than 20 years old, is that a group of atoms (or perhaps a single atom) can tunnel between two stable positions inside the tunnel barrier or nearby insulating layers. This may result in a fluctuation of the critical current (which in view of the saturation of ΔI_b in §8.3 is difficult to distinguish

[11] As the material of the junction barrier has received much of the attention, it would be very interesting to see if the NbN/AlN/NbN junctions used in Refs. [37, 136] had intrinsically lower dissipation.

from current noise). Recent experiments have shown that the quantum properties of individual two-level fluctuators can be studied when they come into resonance with a qubit [44, 121].

No consensus has been reached on the impact of these objects on quantum computation, but they have been proposed to be a leading source of decoherence for large junctions [139]. Turning the problem on its head, if these external degrees of freedom show sufficiently long coherence, they may be treated as qubits [140]. The basic idea is that the operations can be performed by bringing the junction and two-level system into resonance, at which point they will coherently evolve.

While we did not come to any hard conclusions on the physical nature of these objects, in this section I will summarize the results that we did obtain. This was important to do, not only to fully characterize the system, but also because the existence of microstates could have a strong influence on other measurements, such as Rabi oscillations. I focused on trying to identify spurious resonators through spectroscopy and confirming that their origins were intrinsic to the junctions.

Figure 8.11(a) shows a spectrum of SQUID DS_2B taken at base temperature. In order to determine the junction parameters, a spectrum with lines taken every 100 MHz is sufficient. This one, though, was taken at 3 MHz intervals and reveals several gaps, with no obvious periodicity. This suggests that the junction is coupled to some extra degrees of freedom. I fit $\Delta\Gamma/\Gamma$ vs. I_b at each frequency to extract the resonance location, height, and full width. The solid circles (in this and subsequent figures in this section), which show the center of the peaks and are offset for clarity, support the idea that some of these features are avoided crossings. However, even the largest of these, for example the one at 6.17 GHz, show a splitting of less than 5 MHz. This very weak coupling makes it difficult to get a clear picture of the origin and impact of these gaps. Given that we generally have linewidths of about 50 MHz, it is a bit surprising that we see anything at all. Incidentally, while there are several

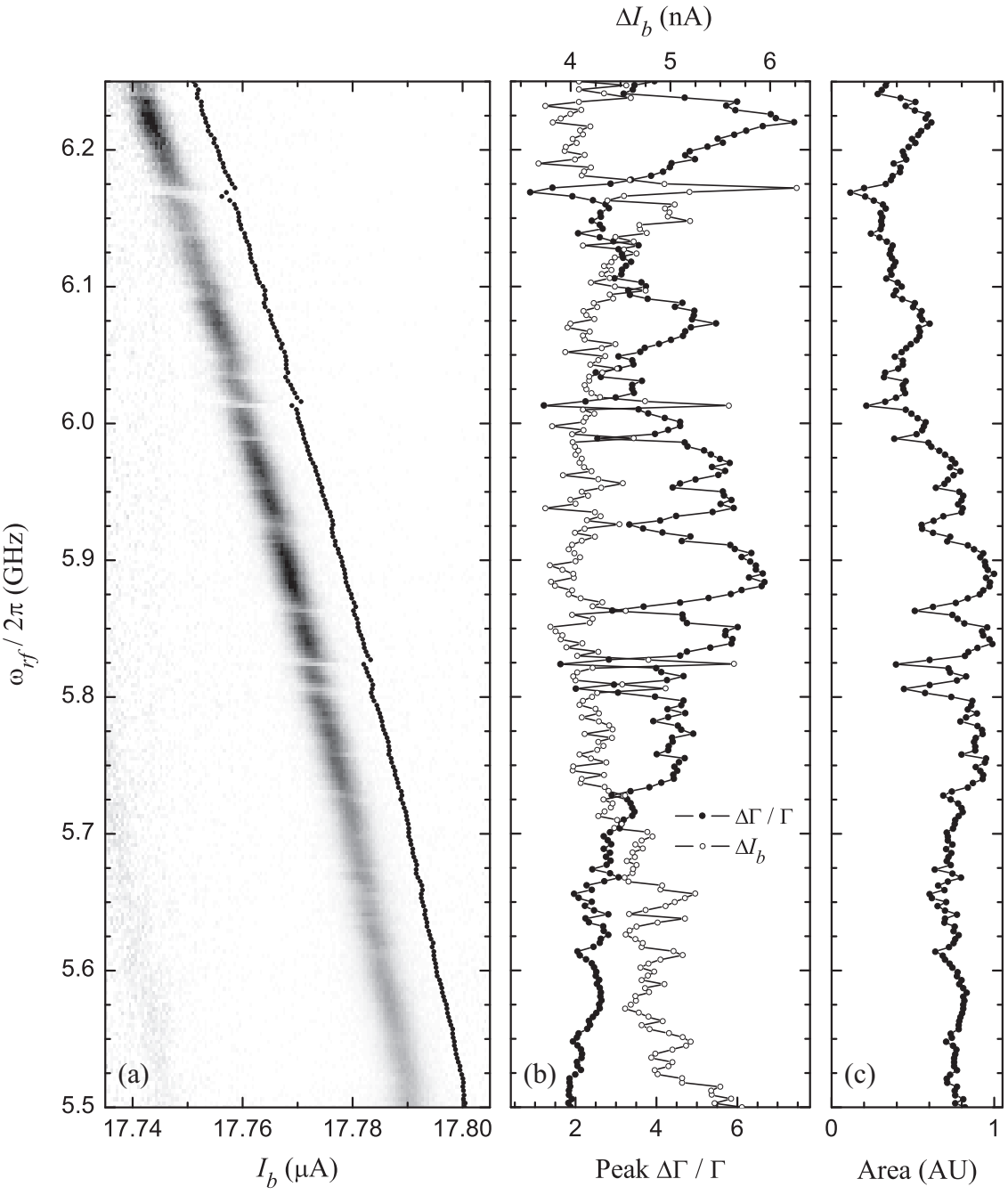

Figure 8.11: Fine spectrum of SQUID DS_2B. (a) A spectrum taken every 3 MHz at a constant power of $P_S = -59$ dBm at 20 mK reveals several small gaps. The centers of the resonances are indicated by the solid points, all of which are horizontally offset for clarity. (b) The maximum enhancement (solid circles, with the bottom axis) and full width ΔI_b (open, top axis) are plotted for each resonance peak, as is the (c) area under each peak.

odd features in the escape rate measured without microwaves (see S7.2.2), there is no obvious correlation between these features and the spectral splittings.

It is entirely possible that the curious features in the spectrum are due to resonances in the microwave lines. We know that transmission varies on large (GHz) frequency scales; the question is whether there are sharp features. We can check this possibility in a few ways. Figure 8.11(b) shows the peak escape rate enhancement $\Delta\Gamma/\Gamma$ and full width ΔI_b for each frequency. The whole spectrum was taken at nominally fixed microwave power, but the width fluctuates quite a bit, never decreasing below 4 nA, just as in Fig. 8.6. Nearly without exception, the enhancement and width are anti-correlated. In theory, when less microwave power reaches the junction, the enhancement should decrease and the full width should either remain constant or get narrower, if there is less power broadening. In the data, the resonances get wider near points where $\Delta\Gamma/\Gamma$ is suppressed, suggesting that the gaps are not due to dips in the drive power. Incidentally, the scatter in the widths could explain some of the variation of T_2^* seen in Figs. 8.5 and 8.6, where we took no steps to avoid these features in the spectrum.

An example of what the escape rate enhancement might look like near an avoided crossing is plotted in Fig. 8.12(a). In generating this plot, I assumed that the resonance has a fixed width in frequency; thus, the full width ΔI_b in terms of current is proportional to $dI_b/d\omega_{01}$, which increases near the splitting. For simplicity, I have also assumed that the area under the Lorentzian resonance (as a function of I_b) is constant. In Fig. 8.12(b), the peak enhancement (solid line) and full width (dashed) are plotted on the horizontal axis, with frequency on the vertical axis. In this model, the signature of an avoided crossing is $\Delta\Gamma/\Gamma$ going to zero, while ΔI_b diverges. There are some similarities between this prediction and the data shown in Fig. 8.11(b), but the relatively large frequency intervals and current noise in the data lead to less pronounced features.

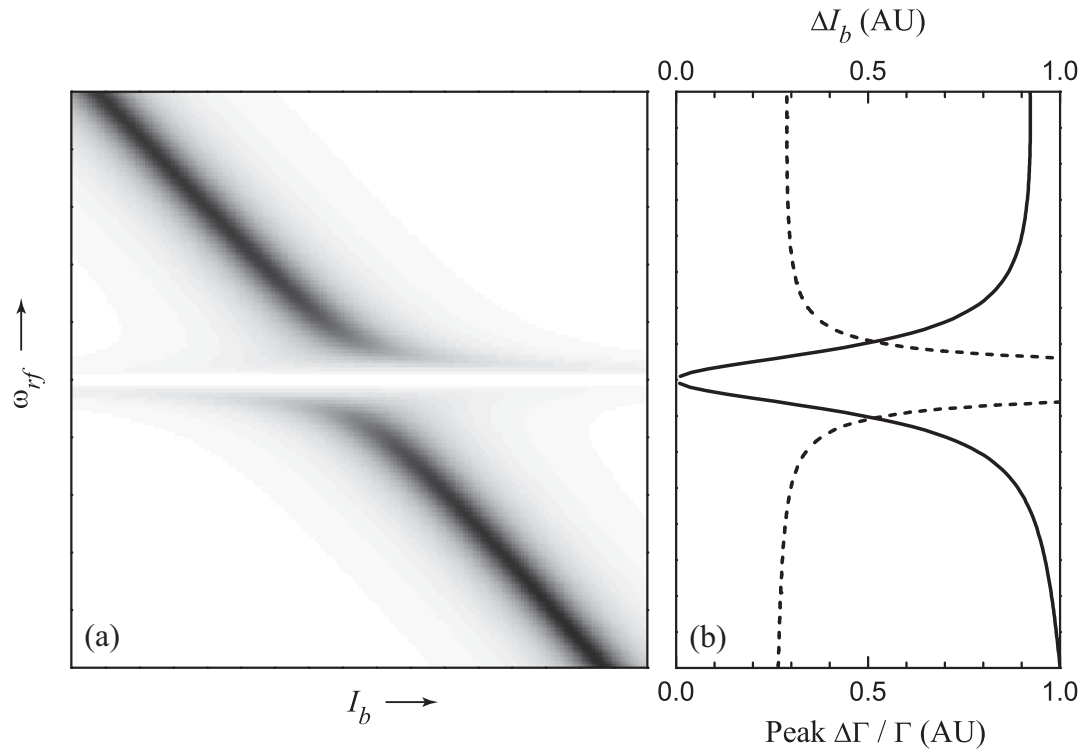

Figure 8.12: Resonance shape near an avoided crossing. (a) The simulated escape rate enhancement shows a splitting in the spectrum at a certain frequency. (b) At this frequency, the maximum enhancement $\Delta\Gamma/\Gamma$ (solid line) reaches a minimum, while the full width ΔI_b (dashed) of the resonance diverges.

In Fig. 8.11(c), the area under each resonance curve is plotted. We initially measured the resonance as escape rate enhancement versus current bias, but it would not necessarily be fair to compare the area at different frequencies in terms of these variables. Instead, I converted the independent and dependent axes to frequency [using the dependence found in Fig. 8.11(a)] and $(\Delta\Gamma/\Gamma)\,(\Gamma_0/\Gamma_1)$ (which, from Eq. (6.9), is an estimate of P_1) before calculating the area. Here, the escape rate ratio comes from Eq. (2.43) for a 1-D tilted washboard with parameters determined from Fig. 8.11(a). Finally, before plotting the results in Fig. 8.11(c), I normalized all of the values to the maximum area, which occurs at $\omega_{rf}/2\pi = 5.89$ GHz. As it turns out, the increased width of the resonance at the spectral gaps does not compensate for the reduced amplitude, as the scatter is still clearly visible in Fig. 8.11(c). We would expect the area to vary if reductions in the transmitted microwave power

were causing the gaps, but this could also be the result of a more subtle effect. The smaller areas for all frequencies above 6 GHz could be suggestive of increased attenuation of the microwave drive there. A better test would be to calculate the area as a function of ω_{rf} for each value of I_b; however in this case, the frequency response of the microwave lines could lead to false features in the extracted areas.

Figure 8.13 shows three spectra of DS_2A taken with different configurations of the microwave drive. Fig. 8.13(a) was taken with a source connected to microwave line A (*i.e.* the one capacitively coupled to the qubit junction of DS_2A).

Figure 8.13(b) was taken under the same conditions, except that an extra 2 m of SMA cables was added to the room temperature lines. That the features remain in the same place in both spectra suggest that they are not due to resonances in the drive lines. As expected, there was an overall decrease in the enhancement in Fig. 8.13(b) due to attenuation in the additional cables (which has been hidden by rescaling the grayscale axis). However, relatively speaking, the enhancement at low frequencies in Fig. 8.13(b) seems to be large. This effect could be due to resonances in the extra cables, but the sharp features clearly are not.

For Fig. 8.13(c), the same microwave source was used to drive microwave line B. Due to the weaker coupling to DS_2A from this line, the enhancement was smaller, which accounts for the noisier signal. Despite this difference, the locations of the splittings are unchanged.

The previous two measurements most likely rule out the microwave lines (both at room temperature and inside the refrigerator) as a source of the spectral resonances. Although the features appear to be intrinsic to the devices, it is possible they are due to resonances in the sample box. Under the same conditions as in Fig. 8.11, we measured the spectrum at lower frequencies and saw a splitting at $\omega_{rf}/2\pi = 3.085$ GHz. This appears to a two-photon transition to the splitting seen at 6.17 GHz in Fig. 8.11(a). Assuming that the box cavity acts as a harmonic res-

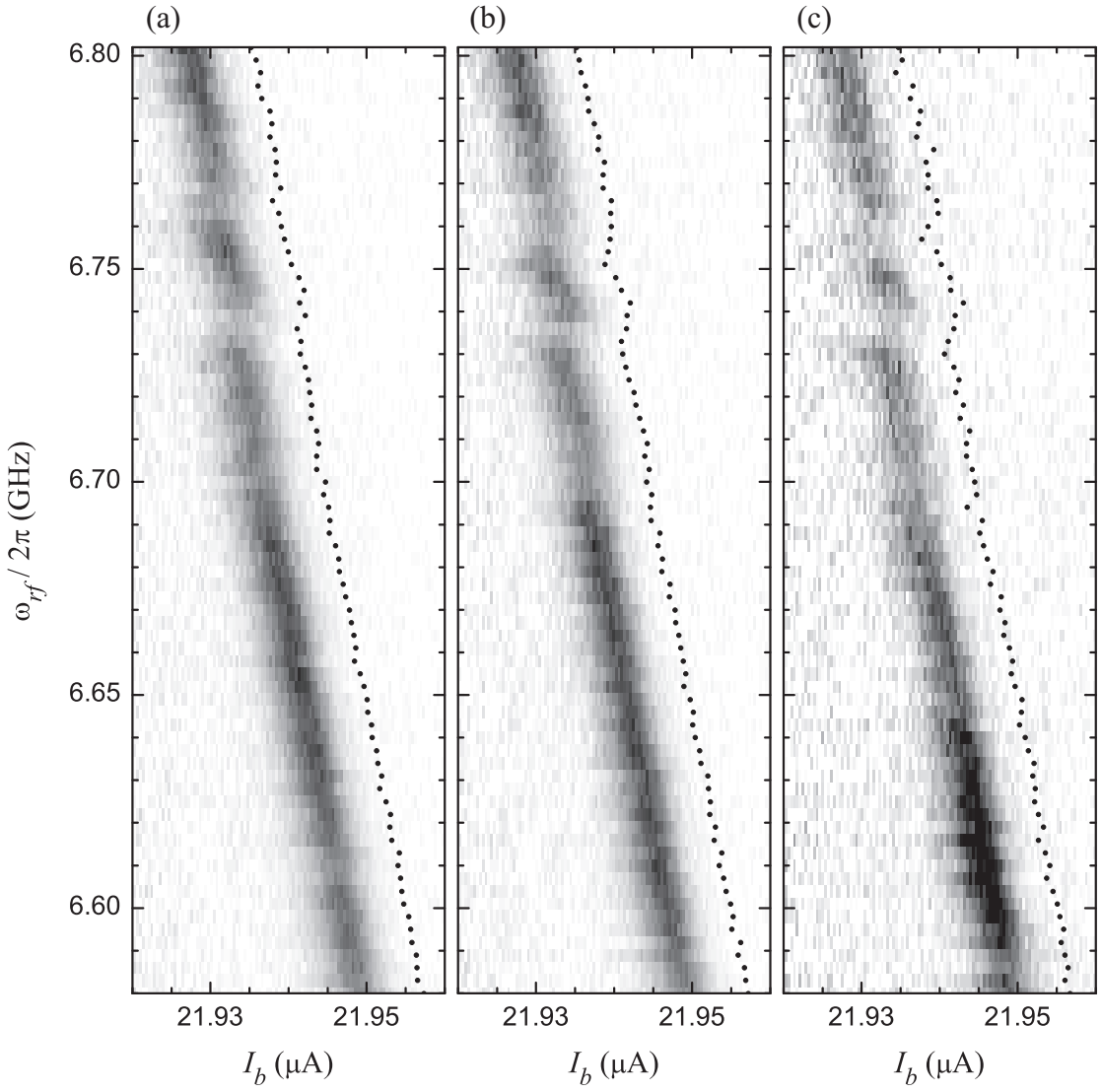

Figure 8.13: Three fine spectra of SQUID DS_2A. The splittings are qualitatively the same when driving (a) microwave line A with a certain length of SMA cable, (b) microwave line A with cable nearly twice as long, and (c) microwave line B. The gray scale for each plot has been normalized to the enhancement near 6.65 GHz. The refrigerator was at 20 mK, but the junctions remained in the voltage state long enough to cause some heating.

onator, it would not have a two-photon response. I would like to think that this rules out the box as a culprit, but it is possible that any non-linear element in bias path could lead to an excitation of a higher order mode. Also if the first excited state of the junction is excited by a two-photon process, it could then couple to a harmonic level of the box. In fact, the resonances at 6 GHz could be higher order modes. More variations of two-photon excitations would have to be performed to check this.

With some evidence pointing towards micro-resonators, we can attempt to develop a model of the interaction. Consider a system consisting of a Josephson junction (JJ) and a two-level system (TLS), whose energy levels are independent of the junction's current bias. In the absence of coupling between the two, I will label the states $|\mathrm{JJ}\,\mathrm{TLS}\rangle$, where TLS can either be 0 or 1. The energies E of the four lowest excited states, measured with respect to the ground state $|0\,0\rangle$, are plotted in Fig. 8.14(a). The junction parameters are $I_0 = 17.736\ \mu$A and $C_J = 4.49$ pF, and the resonator's excited state is at a frequency 6.69 GHz.

Degeneracies of the uncoupled states occur at 13.70 and 6.69 GHz, as shown by the solid lines in Fig. 8.14(b) and (c). If the junction and resonator are coupled, these degeneracies are lifted. Let the states of the coupled system be denoted by the rounded ket $|n)$. The dashed lines in Fig. 8.14(b) and (c) show the four lowest excited coupled states, with a 10 MHz coupling between $|1\,0\rangle$ and $|0\,1\rangle$ and between $|1\,1\rangle$ and $|2\,0\rangle$.

The combination of the solid and dashed lines in Fig. 8.14(d) show all of the transition frequencies near 7 GHz between the coupled states; here, $\hbar\omega^{nm}$ is the difference in energy between $|n)$ and $|m)$. The solid lines roughly indicate where the transition results in an excitation of the junction. With our experimental technique, which relies on an enhancement of the tunneling escape rate, only these transitions can be detected. For example, a transition between $|1\,0\rangle$ and $|1\,1\rangle$ could be allowed

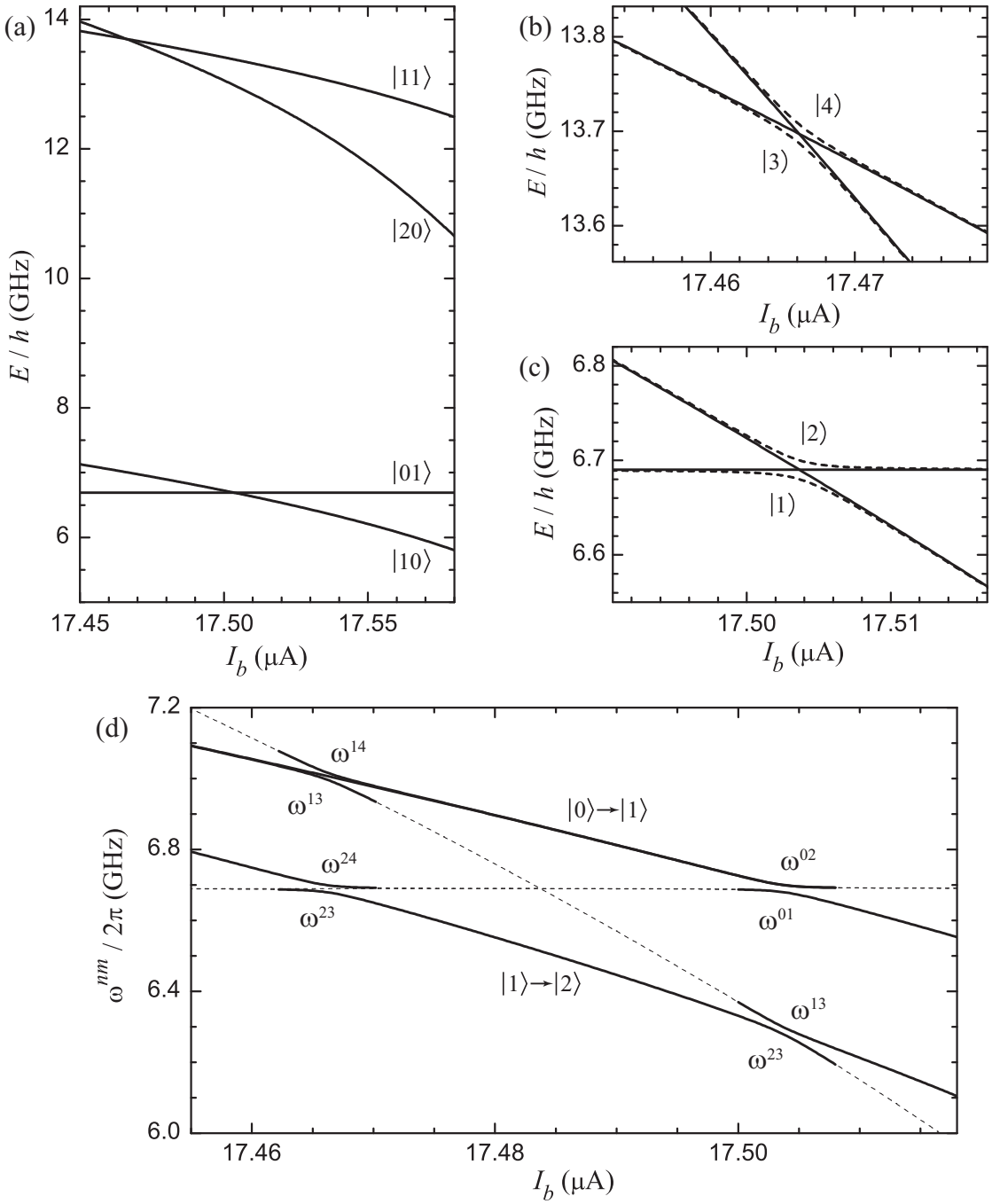

Figure 8.14: Model of a spurious junction resonator. (a) The energy levels E of a junction (JJ) and a two-level system (TLS) (as measured from the ground state $|0\,0\rangle$) in the absence of coupling are plotted as a function of the junction's bias I_b. The labels indicate the state $|\mathrm{JJ\,TLS}\rangle$. (b,c) The energy levels of the uncoupled system (solid) are degenerate at 13.70 and 6.69 GHz. The energy levels, denoted $|n)$, in the presence of a 10 MHz coupling show avoided crossings (dashed). (d) The transition frequencies ω^{nm} between $|n)$ and $|m)$ are drawn as solid and dashed lines; the escape rate of the system is expected to increase along the solid lines. The diagrams are drawn for $I_0 = 17.736$ μA and $C_J = 4.49$ pF, to match Fig. 8.16.

(and result in absorption of the applied microwave power), but it would not cause Γ to increase.[12] Thus, the solid lines correspond to the $0 \rightarrow 1$ and $1 \rightarrow 2$ transitions of the junction.

In this model, the coupling results in avoided crossings for both the $0 \rightarrow 1$ and $1 \rightarrow 2$ transitions at $I_b = 17.504\ \mu$A. What is interesting is that the shape of the anti-crossings are qualitatively different.[13] Two splittings also occur at $I_b = 17.466\ \mu$A, with the one on the $1 \rightarrow 2$ branch occurring at the same frequency as the $0 \rightarrow 1$ splitting at $I_b = 17.504\ \mu$A. In addition, there is a transition unaffected by the coupling at 7.0 GHz. While the transitions between $|0\,0\rangle$ and $|1\,0\rangle$ and between $|0\,1\rangle$ and $|1\,1\rangle$ are degenerate, only the latter of these is affected by the interaction between $|1\,1\rangle$ and $|2\,0\rangle$ at $I_b = 17.466\ \mu$A. It may be that this avoided crossing is difficult to observe experimentally, for weak coupling strengths.

This single resonator results in the four avoided crossings, as well as one for the $0 \rightarrow 2$ transition. The state $|0\,1\rangle$ might also couple to $|2\,0\rangle$ at a higher bias current, causing an avoided crossing of the usual sort on the $1 \rightarrow 2$ branch (and an inverted one on the $2 \rightarrow 3$); unfortunately, we could not take spectra over such a large range of current bias with the escape rate measurement. Additional features will appear if the resonator is a harmonic system, with more than one excited state.

Figure 8.15(a) shows a spectrum of SQUID DS_1 at 20 mK. Although this device was fabricated with a higher critical current density process, the density and appearance of the gaps are roughly the same as for DS_2. The power was adjusted several times during the course of the data taking (indicated by arrows), so the sharp jumps in contrast should be ignored.

In order to test the model of Fig. 8.14, there must be some population in $|1\rangle$.

[12]The resonance areas in Fig. 8.11(c) might vary for a similar reason.

[13]The energy level model also applies (in a qualitative way) to the coupling of the states of the two junctions of the SQUID, where the isolation junction replaces the spurious resonator. In Fig. 8.2(b), where the plasma frequency of the isolation junction is fairly low, it is possible that there is an "inverted" avoided crossing on the $1 \rightarrow 2$ branch of the qubit near 8 GHz.

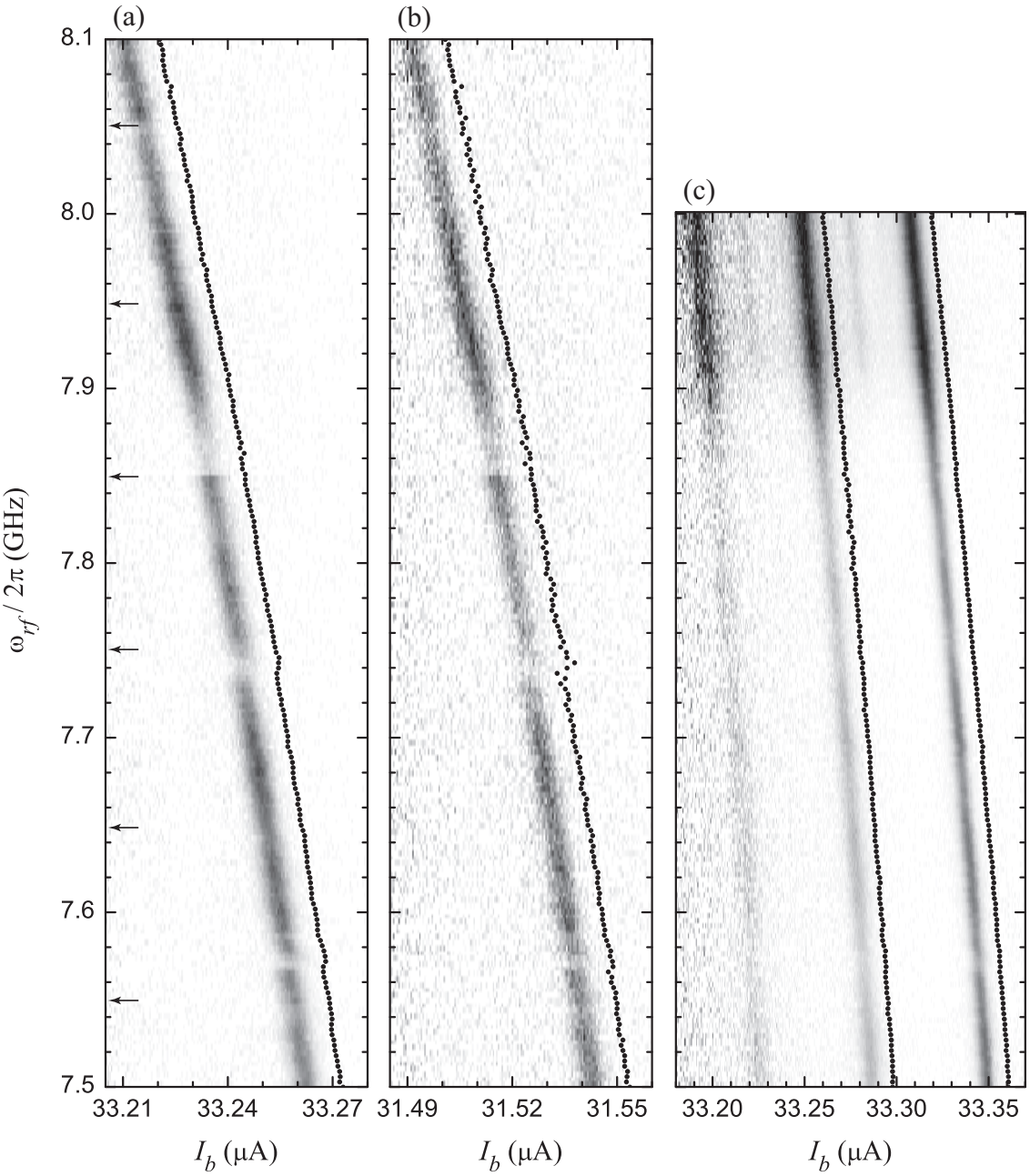

Figure 8.15: Fine spectra of SQUID DS_1 at base and elevated temperatures. Spectra at (a) 20 and (c) 105 mK show gaps at the same frequencies, even on the $1 \rightarrow 2$ branch of (c). The two data sets were taken three weeks apart, which may explain the different current biases. Panel (b) was taken under the same conditions as (a), except that the SQUID was initialized with three fewer flux quanta. For (a) and (b), the power was changed at the frequencies marked by arrows to keep the enhancement roughly constant; panel (c) was taken at constant (albeit higher) power.

Ideally, this would be done by first resonantly driving the $0 \rightarrow 1$ transition and then mapping out the $1 \rightarrow 2$ branch. I found this difficult to do, especially over a wide frequency range. There is also the concern that if the first excitation is not done carefully, it will introduce features of its own in the spectrum.

Instead, $|1\rangle$ can be thermally populated, as in Fig. 8.15(c) [which is plotted on axes with a different aspect ratio than Fig. 8.15(a) and (b)]. Although the same features appear on the $0 \rightarrow 1$ branches, the avoided crossings are much more prominent at low temperatures. In addition, for the data at elevated temperature, the anti-correlation between the height and width of the resonance peaks is not as clear as in, for example, Fig. 8.11(b). The energy level spacing is less than 400 mK, so there is bound to be some thermal smearing at 105 mK. In addition, in order to see any enhancement at higher temperatures, the microwave power had to be set higher, which could have lead to some broadening. The $1 \rightarrow 2$ branch is visible, although the small initial $|1\rangle$ population and the lower current bias (and thus escape rate) result in poor statistics. Nonetheless, it is clear that gaps appear at the same frequencies as for the $0 \rightarrow 1$ branch, as predicted by Fig. 8.14(d). A stronger test of the model would be to identify a $1 \rightarrow 2$ splitting without a $0 \rightarrow 1$ feature at the same frequency.

The spectrum in Fig. 8.16(c) is not over a wide enough range to see transitions on ω_{01} and ω_{12} at the same I_b, a shortcoming that the spectrum in Fig. 8.16 does not have. An avoided $0 \rightarrow 1$ crossing is visible at 6.69 GHz. Figure 8.14 predicts an inverted $1 \rightarrow 2$ anti-crossing at 6.29 GHz, although nothing obvious is visible there. It is possible that our spectroscopy technique of sweeping the bias is not sensitive to this type of feature. For the usual type of anti-crossing, it is possible to sweep "through" the gap, making it easy to see. In the case of the $1 \rightarrow 2$ anti-crossing, two closely spaced peaks would have to be visible over a range of frequencies to identify the feature. In addition, if the system has 4 nA of low frequency noise, it would

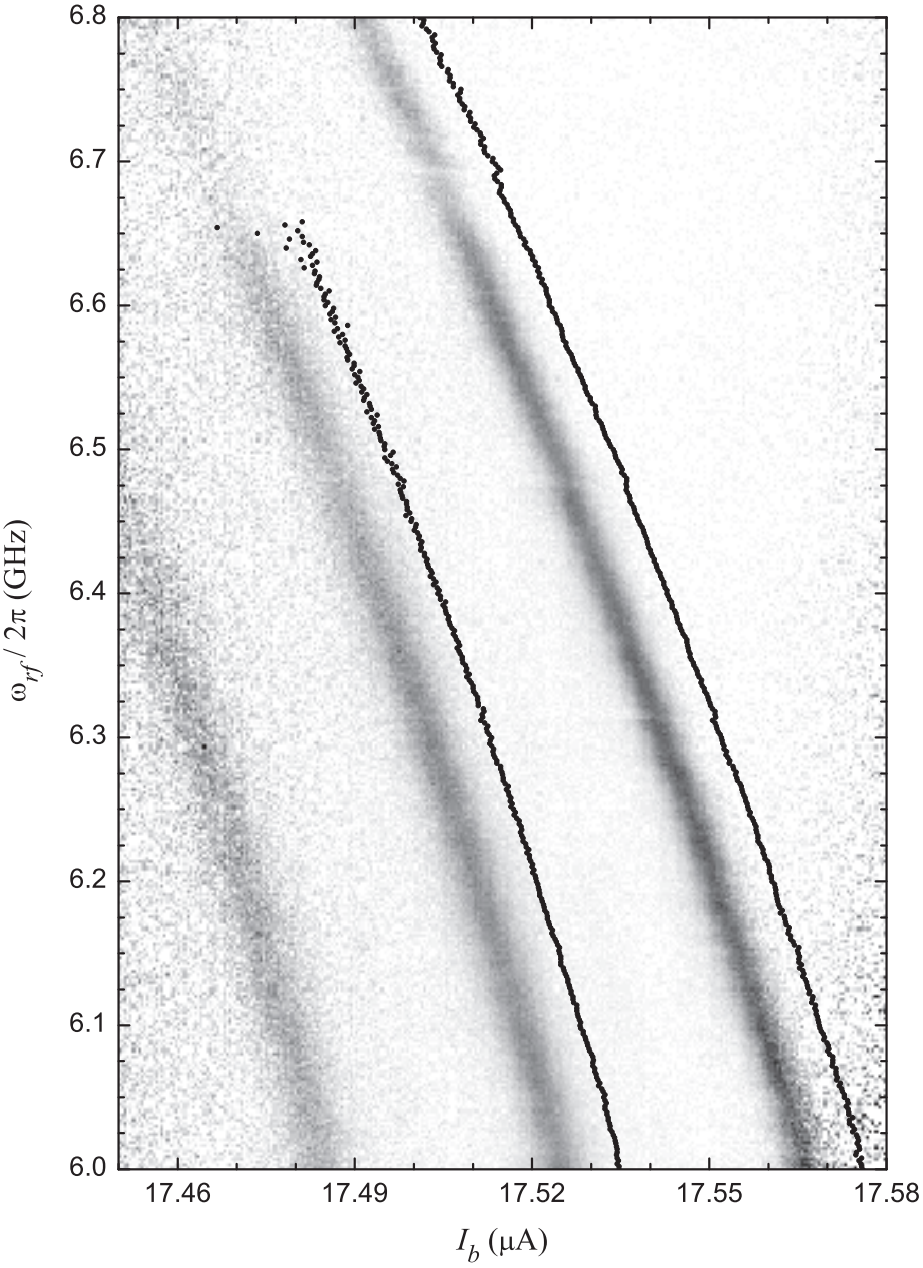

Figure 8.16: Fine spectrum of SQUID DS_2B at elevated temperature. This spectrum, showing ω_{01}, ω_{12}, and (very faintly) ω_{23}, at 105 mK covers a wide enough range of frequencies to be compared to Fig. 8.14.

tend to smear out only the inverted anti-crossing.

The splittings may be difficult to see at high temperature, because they get thermally smeared together. Similarly, it has been suggested that spurious resonators can become saturated at high powers, at which point they no longer are able to interact with the junction. I attempted to reproduce this phenomenon by taking fine spectra at different microwave powers. Two spectra separated by a factor of eight in power showed no qualitative difference in the contrast of the gaps. Perhaps a larger range of microwave powers needs to be investigated.

An intriguing possibility is that these resonances are an intrinsic property of the complicated SQUID potential. One possibility is that we are seeing resonant tunneling between levels of different flux states [131, 132]. However, the well barrier is tiny with respect to the energy difference between wells, so this seems somewhat unlikely. Alternatively, we could be seeing the effects of interaction with the isolation junction (within the well of a single flux state).

To check both of these options, we took spectra when SQUID DS_1 was initialized to different flux states, which should dramatically change the potential that describes the dynamics of the phase particle. Figure 8.15(b) was taken with three fewer flux quanta in the SQUID loop, as compared to (a). This results in a smaller I_b to switch to the voltage state and a larger current through the isolation junction. It also strengthens the coupling of the SQUID to the bias lines, which might also be influencing the spectral gaps. Despite these changes, the features in the spectra occur at the same frequencies. Unfortunately, I never took a detailed spectrum of LC_2 which could have definitively settled this aspect of the problem, as each of its qubits contained only one junction.

So either the junction does contain resonators and we were unable to detect the predicted $1 \rightarrow 2$ feature, the model is incorrect, or the gaps are real spectral splittings due to one or more harmonic systems external to the device, such as the

sample box cavity. In Fig. 8.13, two splittings are seen near 6.75 GHz for DS_2A. However, in Fig. 8.16, no such features are seen for DS_2B even though both devices were on the same chip and measured during the same cool-down, suggesting that the box is not the source. A convincing test would be to thermally cycle a single device and check if the splittings move.

While the spectra can serve to characterize these possible resonators, in the end, we are only concerned with them if they affect the qubit performance. For example they have been reported to affect the amplitude of Rabi oscillations [44] and coherent oscillations between a qubit and resonator (in the absence of a microwave drive) have been observed [114]. These dynamical experiments not only suggest the effect of the resonators on the qubit, but can also exclude several possible origins of the features in the spectra.

For our devices, we saw no clear dependence of a Rabi oscillation on the bias point. There was a slight dependence of the decay behavior (of the sort shown in §8.7.2), but it was difficult to draw any quantitative conclusions. It may be that the defects are very weakly coupled to the junction, leading to small splittings in the spectrum and minimal influence on dynamics. This may also explain the high fidelity seen with a pulsed-bias readout scheme [104]. Further work is needed to determine if the apparent weak coupling is a result of the niobium fabrication process or related to our measurement technique. For example, the junction switches to the disruptive voltage state on each cycle. The resulting large electric field could selectively alter the defects most strongly coupled to the junction, leaving only those corresponding to small splittings in the spectra.

8.6 Spectroscopy of Coupled Qubits

Coupling qubits together in a controlled way is essential to realizing a superconducting quantum computer. Several groups have used spectroscopy to charac-

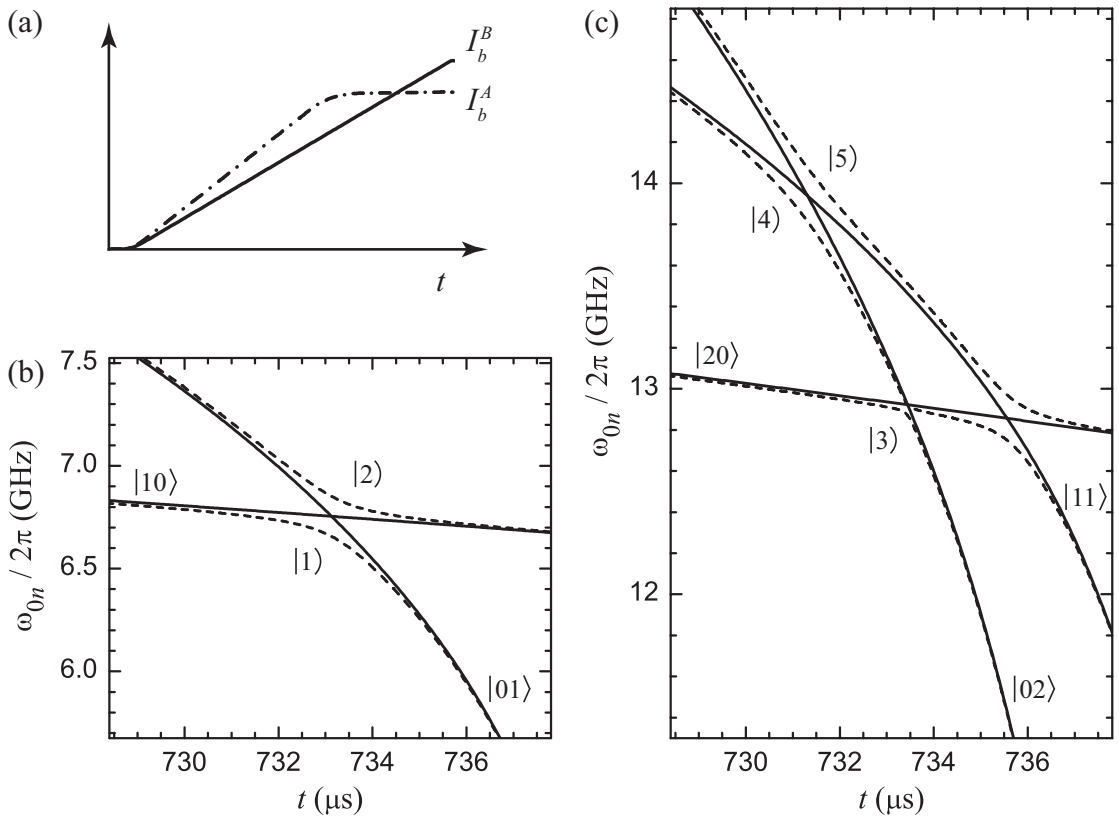

Figure 8.17: Coupled junction spectra. (a) The bias currents I_b^A and I_b^B of two junctions are ramped so that they are degenerate at a particular time. (b), (c) The solid lines show the transition frequencies ω_{0n} (with respect to the ground state) for uncoupled junctions. The labels $|A\,B\rangle$ denote uncoupled states. A coupling capacitor lifts the degeneracy at four points for the states shown, resulting in avoided crossings (dashed lines). States of the coupled system are indicated by a rounded bracket, $|n)$.

terize coupled systems [41, 78, 141, 142]. This simple but powerful technique can aid in the development of gate operations.

In §2.7, I described how a capacitor can be used to couple two current-biased junctions together. Apart from this physical coupling, the effect of the capacitor is strongest when the junctions are dynamically coupled by having their energy levels in resonance.

An experiment to characterize the coupling of junctions is described in Fig. 8.17 [41, 75, 76, 78]. I will first give a qualitative description, before returning to explain how the device parameters were chosen to generate the graphs. The time

dependence of the two bias currents I_b^A and I_b^B are plotted in Fig. 8.17(a), assuming for the moment that the junctions are identical. The solid lines in Fig. 8.17(b) and (c) show the transition frequencies ω_{0n} of the system near the time when the currents are equal, for the case of uncoupled junctions.[14] The labels specify the state $|A\,B\rangle$, which indicates a direct product of the single junction states. For example, the state $|0\,1\rangle$ represents junction A in the ground state and B in the first excited state. As I_b^B increases more quickly with time than I_b^A, $|0\,1\rangle$ decreases more quickly than $|1\,0\rangle$. For the five lowest states shown, there are four times at which two system states are degenerate.

With the addition of the coupling capacitor, the system transitions become those plotted with dashed lines in Fig. 8.17(b) and (c). The states of the coupled system are indicated with rounded brackets; for example, $|1)$ is the first excited state. The degeneracies are lifted, where the magnitude of the splitting depends on the coupling coefficient ζ_0, defined in Eq. (2.72). The coupled state $|1)$, or the "lower branch," in Fig. 8.17(b) is a superposition of the uncoupled states $|0\,1\rangle$ and $|1\,0\rangle$. For small t, this state is roughly $|1\,0\rangle$, while it becomes $|0\,1\rangle$ at large t. At the degeneracy point, it is equal to the maximally entangled Bell state $\left(|0\,1\rangle + |1\,0\rangle\right)/\sqrt{2}$.

I performed this type of spectroscopic experiment with the coupled SQUIDs of device DS_2. Due to the cross mutual inductance of the SQUIDs and their bias lines and some heating effects, simultaneous biasing was configured with the procedure described in §5.2.2. The biasing circuitry of Fig. 5.1 was duplicated to control both qubits. However, the escape rate of the coupled system was measured by only monitoring the voltage across DS_2A. With both qubit junctions near their critical current, when one device switched to the running state, the sudden voltage step generated a current pulse that flowed through the coupling capacitor. This forced the other junction to switch to the running state as well, with a delay of less than

[14] I am using the ambiguous symbol ω_{0n} to indicate the transition frequency between the ground state and an excited state of either uncoupled or coupled system.

200 ps (see Chapter 9 of Ref. [1]). In addition, although the system was excited with a microwave current that coupled only to DS_2B, both junctions were excited. Much of the microwave cross-talk could be due to the coupling capacitor C_C, which is much larger than the microwave coupling capacitor $C_{\mu w}$.

Figure 8.18 shows measured spectra of DS_2, taken with the same biasing, for (a) high and (b) low frequencies. For any given frequency, the enhancement on each branch varied by a large amount, partly because only one microwave line was used. Therefore, I chose to apply a different gray scale to each branch (and as usual, to each frequency). A fine solid line divides regions colored with different scales. Experimentally, the x-axis of Fig. 8.18 is time; the corresponding values are plotted in Fig. 8.17(b) and (c). I converted these times to I_b^A and I_b^B (which apply to *both* plots of Fig. 8.18) using the simple current calibration method of §5.6. The two qubit junctions had quite different critical currents, so different currents had to be applied to bring their energy levels into resonance.

Five branches are clearly visible, with signs of four avoided crossings. There are places on each branch where the escape rate enhancement was negligible for the applied power at that frequency (so rescaling the grayscale axis made no difference). Some of these may be a result of the measurement technique, as the spectrum is assembled by sweeping the bias at fixed frequency. For example, at $\omega_{rf}/2\pi = 6.85$ GHz, the bias trajectory first crosses $|1)$ of Fig. 8.18(b), causing many elements of the ensemble to escape to the voltage state. The remaining members must occupy the upper state before its branch is crossed a few microseconds later. The possibility of a causal relationship between the enhancement on each branch could be verified by turning on the microwave current after crossing the solid line. The gap in $|3)$ of Fig. 8.18(a) at $\omega_{rf}/2/\pi = 12.6$ GHz cannot be explained in this way, as it is the first branch crossed. A power dependence study at this frequency might be interesting. The broad regions of low enhancement below the lowest branches of Fig. 8.18(a)

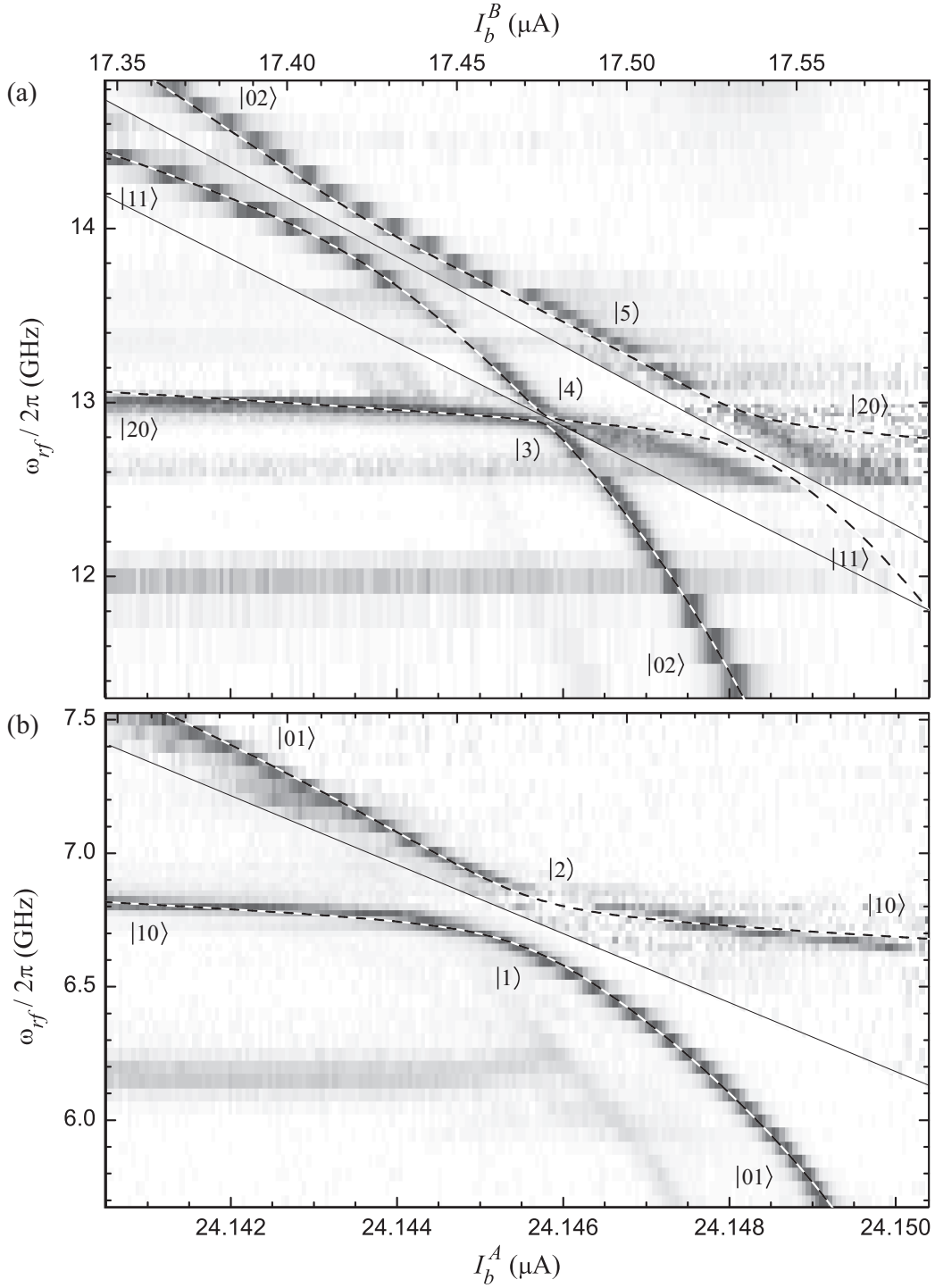

Figure 8.18: Avoided crossing spectra of DS_2. In this experiment, performed at 20 mK, I_b^A was nearly stabilized, while I_b^B was linearly ramped; the x-axis labels apply to *both* (a) and (b). The four degeneracies in Fig. 8.17 are lifted by the coupling capacitor, resulting in anti-crossings. The dashed lines are a fit to the spectrum of two coupled current-biased junctions, where the device fit parameters are different for (a) and (b). The thin solid lines separate regions that are plotted with different gray scales.

and (b) are due to transitions from excited states, suggesting that heating from the junctions being in the voltage state was not entirely eliminated.

To compare the spectra to theory, I first tried to determine the values of the critical current and capacitance for each qubit junction. Ideally, this would be done with independent measurements, with the junctions held out of resonance [41, 78]. With DS_2, that was not easy to do, because of the difficulty of the simultaneous biasing. Errors in the biasing can be (at least partially) compensated for with the choice of I_0 and C_J. The uncoupled energy levels, generated with Eq. (2.44), are shown as solid lines in Fig. 8.17. As there appeared to be some drift between the two data sets (which were taken on different days), I allowed the parameters to vary for the low and high frequency ranges.[15] For the low frequency data [Figs. 8.17(b) and 8.18(b)], the critical currents are $I_{01}^A = 24.332$ μA and $I_{01}^B = 17.709$ μA, while the effective capacitances are $C_{J1}^A\,(1+\zeta_0) = 4.2$ pF and $C_{J1}^B\,(1+\zeta_0) = 4.5$ pF. These parameters for DS_2A do not reproduce the ω_{12} transition frequencies in Fig. 8.18(b) (the light band at 6.2 GHz), which points to an error in the biasing or analysis. For the high frequency data [Figs. 8.17(c) and 8.18(a)], the parameters are $I_{01}^A = 24.367$ μA, $I_{01}^B = 17.707$ μA, $C_{J1}^A\,(1+\zeta_0) = 4.8$ pF, and $C_{J1}^B\,(1+\zeta_0) = 4.5$ pF. The parameters for DS_2B are nearly the same and are consistent with "uncoupled" spectra, but the parameters of DS_2A had to be changed significantly for the two spectra.[16]

From the design parameters given in §4.3.2, the renormalized frequency of the LC mode created by the coupling capacitor and stray inductance is predicted to be $\omega_C/2\pi = 27$ GHz. By biasing the qubit junctions near $\omega_p/2\pi \approx 7$ GHz, the coupling will be largely capacitive. With the simultaneous current and flux bias,

[15] Because the two junctions can drift independently of one another, it is impossible to apply the techniques outlined in §8.1 to remove the drift from a coupled switching histogram. This stresses the importance of stabilizing both the electronics and device conditions when scaling these qubits.

[16] I_0 and C_J are highly correlated. If the same value of C_{J1}^A was used for both data sets, the values of I_{01}^A would also agree, but the "slope" of the energy levels would not quite match the data.

the qubit junction of each SQUID behaves much like a single junction. Thus the capacitively-coupled junction Hamiltonian given in Eq. (2.74) (with two degrees of freedom) should accurately describe the actual system of LC-coupled SQUIDs (which has five degrees of freedom). Solutions of the Hamiltonian can be expressed as a superposition of single junction states $|n\rangle$. I used the MATLAB code in §B.2 to calculate the energy levels for the coupled system.

The dashed lines in Figs. 8.17 and 8.18 show the coupled transition frequencies, calculated with the individual junction parameters given above and a coupling constant $\zeta(\omega) = 0.03$. There is reasonable agreement with the data, although the parameters of DS_2A are different for the two plots. The only major deviations occurs at high bias for the two highest frequency branches, whose origins are unclear.

With $\zeta = 0.03$, C_J is roughly 4.4 pF, which is somewhat larger than the design value of 3.82 pF, given in §4.3.2. The value of ζ is even smaller than the design value of 0.047, suggesting that the LC coupling mode has a frequency above 30 GHz. In this case, the predicted zero-frequency coupling constant is roughly $\zeta_0 = 0.028$, which in turn gives $C_C \approx 130$ fF.

There are two important implications of the coupled spectra. First, the existence of transitions from the ground state to three excited states confirms the presence of a complete basis for two qubits ($|0\,0\rangle$, $|0\,1\rangle$, $|1\,0\rangle$, $|1\,1\rangle$).

In addition, the spectra suggest the possibility of constructing two types of quantum gates. Using the spectra as a guide, the frequency difference between $|1\,0\rangle$ and $|1\,1\rangle$ can be calculated as a function of the bias. By applying a microwave pulse at the appropriate frequency and duration, one half of a period of a coherent Rabi oscillation will lead to the transitions $|1\,0\rangle \leftrightarrow |1\,1\rangle$. If no other transitions are excited, this amounts to a controlled-NOT (CNOT) gate, where $|A\rangle$ is the control bit. However, in an uncoupled system, the energy difference between $|1\,0\rangle$ and $|1\,1\rangle$ is the same as that between $|0\,0\rangle$ and $|0\,1\rangle$, so a microwave pulse will lead to

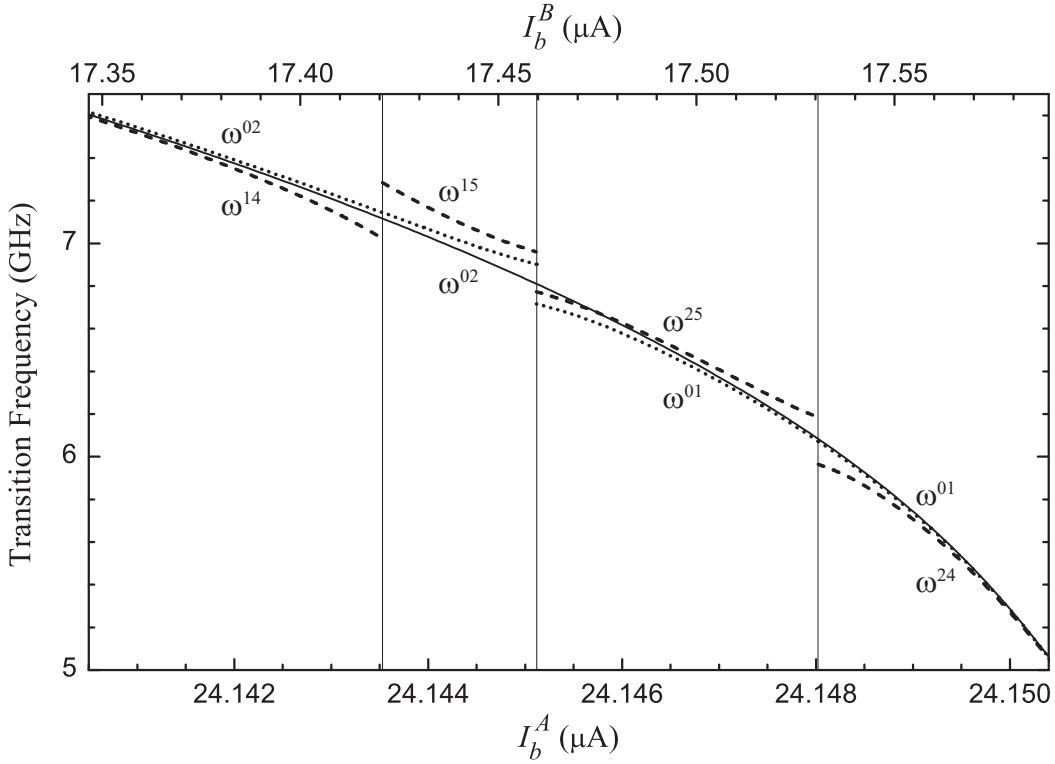

Figure 8.19: Relevant energy levels for a simple controlled-NOT gate. The transition frequency of the coupled system that most resembles $|1\,0\rangle \leftrightarrow |1\,1\rangle$ is plotted as dashed lines, while the one that most resembles $|0\,0\rangle \leftrightarrow |0\,1\rangle$ is plotted as dotted lines. In the absence of coupling, both transition frequencies would be equal to the solid curve. The choice of coupled states changes at the degenerate points, which are indicated by vertical lines.

evolution of all of the states, which is unwanted.

The single junction transition frequency ω_{01} of DS_2B is plotted as a solid curve in Fig. 8.19 [using the same parameters as in Figs. 8.17(c) and 8.18(a)]. The bias currents where degeneracies occur between $|1\,0\rangle$, $|0\,1\rangle$, $|1\,1\rangle$ and any other state are marked with vertical lines. Away from these points, the states of the coupled system are nearly equal to the uncoupled states $|A\,B\rangle$. For example, for small I_b^A and I_b^B, $|4)$ and $|1)$ are roughly $|1\,1\rangle$ and $|1\,0\rangle$, respectively. Therefore the appropriate frequency to apply in this region is ω^{14}, where $\hbar\omega^{nm}$ is the energy difference between $|n)$ and $|m)$. This frequency, required to drive the CNOT gate, is plotted as a dashed line. The unwanted transition, between $|0\,0\rangle$ and $|0\,1\rangle$, is at a frequency ω^{02}, which is

plotted as a dotted line. I have done the same for each of the four regions. The plot shows that it is easiest to address the desired transition at a degeneracy. For example, with $I_b^A \approx 24.1435$ μA and $I_b^B \approx 17.42$ μA, the difference between the two transitions is a relatively large 150 MHz (a value that depends on the coupling strength ζ). However at this point, $|5)$ is an equal superposition of $|1\,1\rangle$ and $|0\,2\rangle$, so additional manipulations are required to realize a true CNOT gate. Also, the microwave drive could cause direct pumping to the states $|0\,2\rangle$ and $|2\,0\rangle$, whose energy levels I have not considered.

Alternatively, gates can be performed by using the coherent evolution of entangled states, without any potentially disruptive microwave current [112]. The phase of $|1\,1\rangle$ can be evolved in a controlled way, by bringing the system to the point where it is degenerate with $|0\,2\rangle$. This is an example of how the auxiliary states $|0\,2\rangle$ and $|2\,0\rangle$ of a multi-level system can be useful. Also $|1\,0\rangle$ and $|0\,1\rangle$ may be evolved into each other by bringing these levels into resonance for a certain amount of time.[17] With the addition of single qubit gates, either of these gates are sufficient for universal quantum computation.

8.7 Time-Domain Measurement of T_1

I have discussed two techniques to experimentally estimate the value of the relaxation time T_1. As described in §7.4, the escape rate of a junction has a T_1-dependent feature at slightly elevated temperature. Secondly, the width of a resonance peak depends on a number of factors, including T_1 [see Eq. (3.66)]. In both cases, T_1 leads to a rate which is balanced against other processes, which may be better understood. Because of this, the experiments may be performed on time scales much longer than T_1. In practice we ramp I_b to make the measurements, but

[17] In the case of DS_2, the two junctions have different critical currents, so $|0\,1\rangle$ and $|1\,0\rangle$ are not degenerate at the same bias that $|0\,2\rangle$ and $|2\,0\rangle$ are. This leads to some complications with accounting for unwanted evolution between $|3)$ and $|4)$.

the sweep is assumed to be stationary, so there is not even an implicit dependence on time.

The use of a microwave drive allows another method of finding T_1. The idea is to promote an excited state population and then measure its decay time back to the ground state. This technique has the advantage of being conceptually simple and a value can be extracted even if the details of the system are not known. However, care must be taken that the decay is really due to relaxation of the qubit and not to, for example, tunneling or the decay of a resonance on the microwave lines.

8.7.1 Microwave Pulse Readout

To measure T_1, we performed microwave pulse readout measurements (see §6.6.2) using the scheme outlined in Fig. 8.20(a). The switching of SQUID DS_1 to the voltage state was continuously monitored while the bias was swept slowly. At a time defined to be $t = 0$, the level spacings of the qubit junction were measured to be $\omega_{01}/2\pi = 8.5$ GHz and $\omega_{12}/2\pi = 7.93$ GHz. This bias was chosen because the ground state escape rate Γ_0 was smaller than 10^3 1/s. Between $t = -2$ μs and $t = 0$, a microwave current with frequency ω_{01} and power P_{01} was applied to the junction to excite population into $|1\rangle$. After an adjustable time delay Δt, a pulse of microwaves of frequency ω_{12} and power P_{12} was applied to junction to serve as a readout.[18] If the system was in $|1\rangle$, this pulse would promote it to $|2\rangle$, whose escape rate was large enough to cause immediate tunneling to the voltage state. Thus the probability to see a tunneling event caused by ω_{12} should be proportional to the occupation of $|1\rangle$ and will decrease exponentially with increasing Δt.

For each setting of Δt and the pulse power, we measured switching histograms for 230000 trials. Figure 8.20(b) shows a typical histogram, which has two unex-

[18]The ω_{01} pulse was applied to the line dedicated to DS_1. For convenience, ω_{12} was applied to another microwave line that was connected to an antenna inside the sample box.

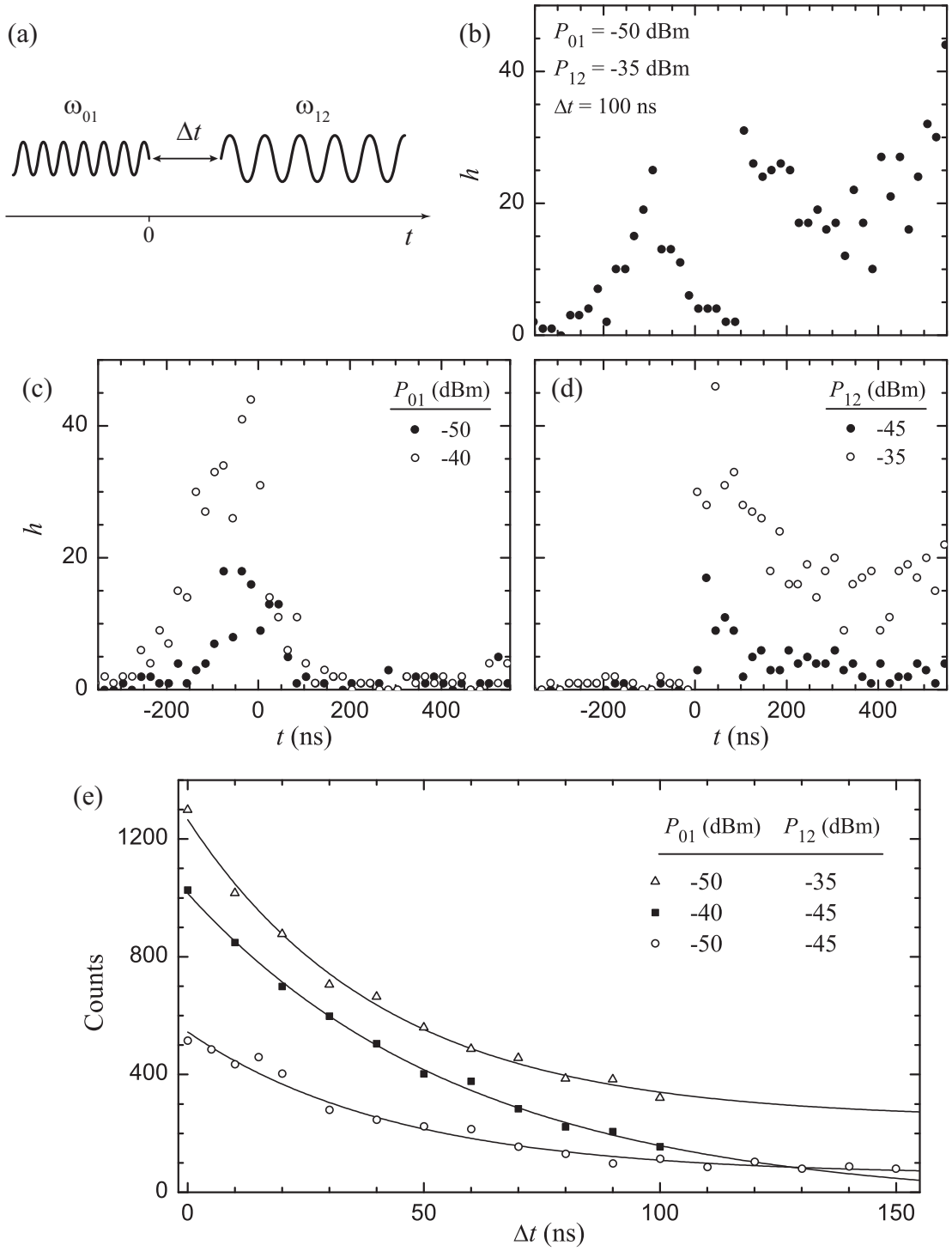

Figure 8.20: T_1 measurement of SQUID DS_1 with pulsed readout. (a) A microwave pulse of frequency ω_{01} (and power P_{01}) creates excited state population which is read out with a pulse of frequency ω_{12} (and power P_{12}) after a delay Δt. The histograms were taken with (b) both excitation and readout, (c) the excitation alone, and (d) the readout alone. (e) The total number of counts, for three sets of pulse powers, due to the readout pulse (symbols) decays exponentially with Δt, as seen by the fits (solid lines). All of the data were taken at 20 mK.

pected features. For $t < 0$, there should be essentially no counts, because ω_{01} only occupies $|1\rangle$, which is assumed to have a small escape rate. Instead, there are quite a few counts, which decay at $t = 0$, when the ω_{01} drive current was turned off. After a delay of $\Delta t = 100$ ns, ω_{12} was turned on which lead to a large number of counts. However, after reaching a minimum at $t \approx 300$ ns, the number of counts begins to increase again.

In Fig. 8.20(c), histograms taken with only the excitation pulse are shown for two values of P_{01}. Although the idea was to work deep in the well where Γ_0 and Γ_1 were small, the selected bias point was not deep enough. This would have been a problem for other measurements, but is not a serious one here.

Figure 8.20(d) shows histograms taken with only a readout pulse (with $\Delta t = 0$), for two values of P_{12}. Even though the refrigerator was at base temperature and no ω_{01} pulse was applied, ω_{12} still caused a substantial number of counts. This is likely to due to relatively large resonance widths. Even off resonance and at low power, the readout pulse promoted the system to a state where it could tunnel. The increasing number of counts at high t are due to a two-photon $0 \rightarrow 2$ transition (whose resonance is at $t \approx 700$ ns).

Ideally, this experiment would be performed at fixed bias and the junction would only escape to the voltage state when both ω_{01} and ω_{12} were applied. Nonetheless, the results can be still be used. I summed the total number of counts between $t = 0$ and 400 ns, for each value of Δt and for three sets of excitation and readout powers. These values, which are proportional to the excited state population, are plotted as symbols in Fig. 8.20(e). Based on predictions using Eq. (2.43), $\Gamma_1 < 10^5$ 1/s, so the decay of the excited state should be dominated by relaxation for $T_1 < 1$ μs.

As Fig. 8.20(e) shows, the number of counts does not decay to zero. This happens because ω_{12} forces counts by itself. To account for this, I fit the data to

Table 8.1: T_1 fit results for SQUID DS_1. The power (at the microwave source) of the excitation and readout pulses are given by P_{01} and P_{12}. The total number of switching events due to both pulses as function of the delay Δt, plotted in Fig. 8.20(e), was fit to the functional form $y_0 + Ae^{-\Delta t/T_1}$, where the best fit parameters and their uncertainties are listed. The last column gives the reduced chi-square.

P_{01} (dBm)	P_{12} (dBm)	y_0	A	T_1 (ns)	χ^2_ν
-50	-45	58.6 ± 8.0	486 ± 13	44.1 ± 3.1	2.0
-40	-45	-36 ± 48	1052 ± 40	59.4 ± 6.4	0.67
-40	-45	70	980 ± 22	45.8 ± 1.3	1.5
-50	-35	249 ± 32	1017 ± 32	41.5 ± 3.9	1.0

$y_0 + Ae^{-\Delta t/T_1}$; results for the parameters are listed in Table 8.1. The first and last rows give $T_1 \approx 40$ ns, with fits of reasonable quality. For $P_{01} = -40$ dBm and $P_{12} = -45$ dBm, an unrestricted fit returns a negative offset y_0, which is unphysical [but which I did plot in Fig. 8.20(e)]. This problem could be solved by taking data to longer values of Δt. By fixing y_0 at 70, which is roughly expected, the best fit value of $T_1 \approx 46$ ns is consistent with the other measurements. Despite the issues of pulse powers and well depth, this technique appears to provide a relatively simple way to measure T_1 in a time resolved way.

8.7.2 Direct Tunneling Readout

In Fig. 8.20(c), the ω_{01} pulse that created excited state population resulted in an unintended enhancement in the measured escape rate. After we turned the pulse off at $t = 0$, the escape rate decays roughly with time constant T_1 for $t > 0$. Thus, the second readout microwave pulse is not needed if the experiment is performed at a bias current where Γ_1 is large. In this case, high powers of the excitation pulse can be studied. There are reasons not to do this for quantum gate operations, but as I am most interested in characterizing the devices in as many ways as possible,

the direct tunneling readout is an easy way to try to measure T_1.

Figure 8.21(a) shows the escape rate of SQUID DS_1 when we applied a 25 ns microwave pulse of frequency 7.6 GHz, which was resonant with the $0 \rightarrow 1$ transition. The three curves, taken at source powers of -26 (circles), -22 (squares), and -16 (triangles) dBm, are vertically offset for clarity. At these high powers, Rabi oscillations (which I will discuss in the next chapter) are visible for $t < 0$. The pulse was shut off at $t = 0$ and the length was chosen long enough for the oscillation amplitude to decrease, so that the decay for $t > 0$ did not show any coherence effects. For much longer drive pulses, it would not be possible to measure the decay, because the junction would always switch to the voltage state during the microwave pulse. This is a drawback of the escape rate measurement that needs to be considered when working with high microwave power.

For $t > 20$ ns, the three curves decay exponentially with roughly the same time constant. Near $t = 30$ ns, the escape rates increase slightly, indicating the presence of more than just simple decay processes. The decay is much faster for earlier times and does not appear to be governed by a single exponential. This is particularly clear for the highest power, where there is a sharp drop for $0 < t < 2$ ns. For $0 < t < 5$ ns, there is a decay with an intermediate time constant, that is again clearest at -16 dBm (triangles).

I fit the escape rate (for $t > 0$) with a sum of four exponentials, where three of them describe the decay. One exponential accounts for Γ increasing with time (with a 475 ns time constant) due to the slow bias ramp used to take the data. Results for the best fits are shown with solid lines in Fig. 8.21(a). For -16 dBm, the time constants of the fit are -1.2, -5.8, and -68 ns, while for -22 dBm, they are -3.7, -4.2, and -59 ns. For -26 dBm, I only used two decaying exponentials, with time constants of -4.4 and -56 ns. The fits are not of particularly good quality, especially around the modulation near 30 ns.

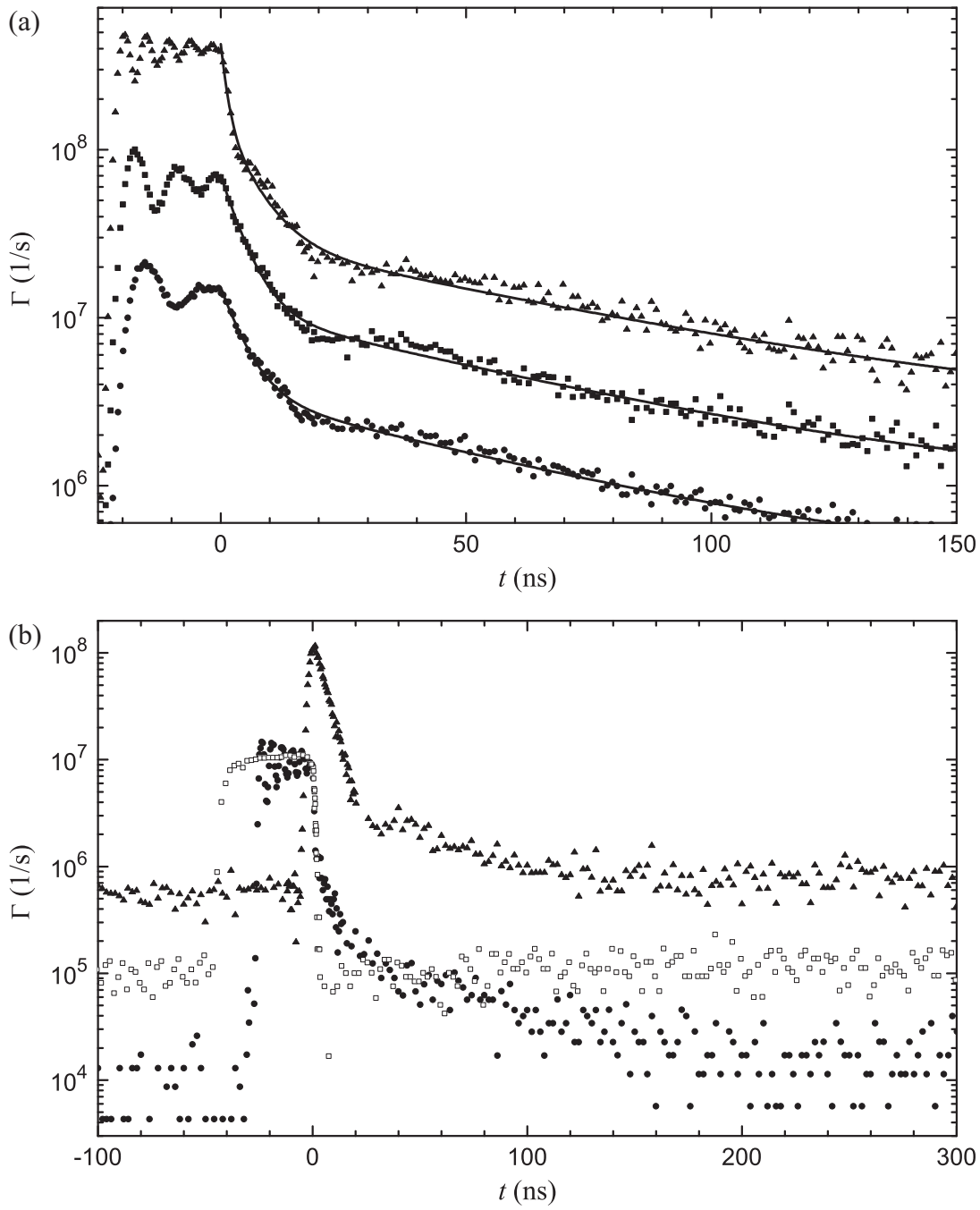

Figure 8.21: T_1 measurement of SQUIDs with a direct tunneling readout. (a) Excited state population was created by a applying a microwave pulse of frequency 7.6 GHz and power -26 (circles), -22 (squares), and -16 (triangles) dBm to DS_1. At $t = 0$, the pulse was shut off, leading to a decay in the measured rates (offset for clarity), which are fit by the solid lines. (b) Similar behavior is seen in DS_2B, for pulses of frequency 6.3 (circles) and 5.6 (triangles) GHz. The decay is much faster for a 1.4 GHz pulse (squares). These curves are not offset. All data were taken at 20 mK.

Decay of the escape rates is indicative of a loss of population of a state, due to a combination of tunneling, dissipation, and perhaps other processes. From measurements using the bias pulse readout described in §6.6.3, it is clear that the fastest decay corresponds to depopulation of $|2\rangle$ by tunneling at rate Γ_2; at high powers, the resonances broaden to the extent that $|2\rangle$ can become populated, even when the microwaves are at a frequency ω_{01}. The time constant is slightly longer than 1 ns, however, which is unexpectedly long. At the bias current where the measurement was performed, Eq. (2.43) gives $\Gamma_2 \approx 3 \times 10^9$ 1/s. Thus, even in the absence of dissipation, the lifetime of $|2\rangle$ should be less than 0.3 ns. The experimentally observed decay is likely due to limited time resolution of the switching experiment (both in detecting a switching event and jitter in triggering the pulse) and the fall time of the microwave pulse. A direct measurement of the microwave pulse shape at the device could be very revealing, but is something I never did.

The other two decays are also quite mystifying. The bias pulse measurement suggests that both of the time constants correspond to a decay of $|1\rangle$, which has previously been reported in niobium phase qubits [39]. The longer constant of ~ 55 ns is consistent with the microwave pulse measurement of §8.7.1. While that measurement was done deep in the well, the data of Fig. 8.21(a) were acquired where $\Gamma_1 \approx 3.5 \times 10^7$ 1/s. Thus, because of tunneling, the naive assumption is that the decay of the population in $|1\rangle$ can be no longer than 30 ns. Perhaps, then, T_1 is given by the intermediate decay, which varied between 5 and 15 ns for different data sets. Only the upper end of this range is consistent with the value of 14 ns obtained from master equation simulations of Fig. 7.13.

A possible explanation for the slow time constant is that the microwave pulse heated the insulators in the device. Then the system would stay in thermal equilibrium, as the chip cooled back down to the mixing chamber temperature. This possibility can be explored by fitting the escape rate to a sum of exponentials. The

magnitude of the slow time constant term should be an indicator of the temperature of the device when the microwave current was shut off at $t = 0$. From other data on DS_1 (not shown), however, I found no correlation between the microwave power and the contribution to the total escape rate from the slow time constant term. In addition, small changes in the duration of the pulse lead to large changes in the magnitude of this term. Therefore the state populations at $t = 0$ affect the decay 50 ns later. Another possibility is that the intermediate decay time could be due to the shape of the microwave pulse (which itself could be a function of frequency), but it seems implausible that the longest time constant could be connected to this.

Yet another possibility is that the SQUID is not behaving as a three-level quantum system. Perhaps it is weakly coupled to another degree of freedom that has a long relaxation time [4]. The tunneling of the qubit junction would just be a gauge of the population of the external system, without affecting its dynamics significantly. Certainly, there are plenty of other systems that could couple to the qubit junction. The isolation junction is coupled to the junction, but it is unlikely to have a 50 ns relaxation time, as it is not isolated from the current bias leads. In addition, the coupling strength between the two junctions can be modulated by varying the current through the isolation junction, but we never saw a change in the slow decay for different levels of isolation. Alternatively, we could be seeing a coupling to the two-level systems discussed in §8.5.

We saw similar effects in SQUID DS_2B. The three curves in Fig. 8.21(b) were taken at different values of I_b. The different background escape rates (at $t = -100$ ns) are due to this fact and not to any offset that I applied in plotting the data. The solid circles show the escape rate for a resonant 6.3 GHz, -22 dBm pulse. The signature of three decay constants is present in this curve, but the small number of counts we took make it difficult to resolve them clearly. The longest time constant appears to be about 30 ns.

The solid triangles were taken with a resonant 5.6 GHz pulse. Because this frequency corresponds to a shallower well and thus higher escape rate, we used a shorter 10 ns pulse and lower source power (-32 dBm), so that the switching histogram would extend beyond the pulse. The fastest time constant is not present in this curve, which could be a consequence of the lower power or of $|2\rangle$ being too broad to be occupied at this high value of the bias. The two decays that do appear have time constants of about 5 and 50 ns. For the bias conditions at 5.6 GHz, Eq. (2.43) predicts $\Gamma_1 \approx 2 \times 10^8$. Naively, one should expect the *longest* time constant to be no more than 5 ns.

As a check, I also measured the escape rate when a low frequency, off-resonant microwave pulse was used to excite the qubit. The data plotted as open squares in Fig. 8.21 were taken with a pulse of 1.4 GHz and -18 dBm. The decay of this curve is very fast and there is no sign of the long time constant. While it is possible that a multi-photon process was very efficient in driving the $0 \rightarrow 2$ transition, it seems unlikely that a lower order process would not populate $|1\rangle$ at all. In addition, the same measurement scheme performed over a range of bias currents yielded similar results. This suggests that the long decay is the result of a resonant process near the plasma frequency of the junction and not due to simple heating effects from the microwave power.

Resolving the origins of the various time constants is an important step in characterizing the SQUID phase qubit, as this information may dictate how the design could be improved to yield longer values of T_1. Unfortunately, as this section has shown, considerably more work needs to be done in this area.

8.8 Summary

To measure the energy level spectrum of a qubit, we swept its bias current (and thus the level spacing) while applying a microwave current of fixed frequency. On

resonance, the escape rate increases as excited states gain occupation probability. In both the LC-isolated (see §8.1) and dc SQUID phase qubits (see §8.2), I found that the spectrum can be fit to simulations of an ideal current-biased junction. This applies not just to the $0 \rightarrow 1$ transition, but to transitions higher in the well and two-photon transitions (see §8.4) confirming that the simple junction Hamiltonian is a good approximation to our more complicated LC-isolated and SQUID phase qubits. Simple spectroscopy also provides clear evidence that our assumed Hamiltonian is incomplete, as small splitting appear in the spectra for the SQUIDs (see §8.5). The microscopic origin of these features and their impact on the system dynamics have yet to be resolved.

The spectrum of two capacitively-coupled SQUIDs provides evidence that the qubits are interacting in the expected way and we see avoided level crossings where there would be degeneracies in the absence of coupling. Such a spectrum gives some of the information needed to design a two-qubit gate.

The shape of the escape rate enhancement is indicative of the linewidth of the resonance. The width is due to energy dissipation (on a time scale T_1), phase coherence (on a scale T_2), tunneling, and inhomogeneous broadening; it is commonly characterized by T_2^* (see §8.3). We measured a maximum $T_2^* \approx 4$ ns for the LC-isolated qubits and 8 ns for the SQUIDs, suggesting that the broadband isolation of the SQUIDs is somewhat more effective, but the times were much shorter than hoped for. The resonance widths may also be used to extract information about dissipation and inhomogeneous broadening.

Finally, T_1 can be measured by creating excited state population and watching it decay back to the ground state. The escape rate is a good way to do this, as it is sensitive to very small population changes. For low excitation powers, the decay time constant is about 45 ns for the SQUIDs. However, at higher powers, we see two time constants, a faster decay of less than 10 ns followed by a slower 50 ns decay.

It is unclear whether, for example, this is an artifact of the measurement or has a connection to splittings in the spectra. Both times are much shorter than can be accounted for from dissipation in the leads.

Chapter 9

Coherent Rabi Oscillations

In the chapter, I will show results from various Rabi oscillation experiments conducted on our qubits. Not only do these manipulations resembles the single qubit gates required for quantum computation (because they involve simple rotations on the Bloch sphere), analysis of the data also reveals information about the coherence time of the devices.

Figure 9.1 shows typical data for SQUID DS_1. Several methods of measuring oscillations have been reported in the literature; we chose to use the simple one described next [136]. As usual, the escape rate Γ of the qubit junction to the voltage state was measured continuously as the bias was slowly swept to the critical current. At time $t = 0$, a microwave pulse of angular frequency ω_{rf} was applied to the junction, which drove any transitions near ω_{rf}. Any changes in the occupation probabilities of the states were reflected in the escape rate. If we were interested in driving a $0 \rightarrow 1$ oscillation, then we set $t = 0$ to occur at the value of the bias for which $\omega_{rf} = \omega_{01}$, where $\hbar\omega_{01}$ is the energy level spacing between the ground and first excited states. We only performed these experiments on the SQUID phase qubits, DS_1 and DS_2. It is possible that oscillations could have been measured in the LC-isolated qubits if they had been measured with fast, low noise electronics, as in the SQUID experiments.

For $t < 0$ in Fig. 9.1, the escape rate is 10^5 1/s, which is roughly Γ_0 (where Γ_n denotes the escape rate from state $|n\rangle$). As $|1\rangle$ becomes occupied, the escape rate increases dramatically. The oscillation that follows has a frequency that depends on the microwave power. The oscillation amplitude decreases with time, due to the loss of phase coherence; we refer to the decay time of the envelope as T', which depends

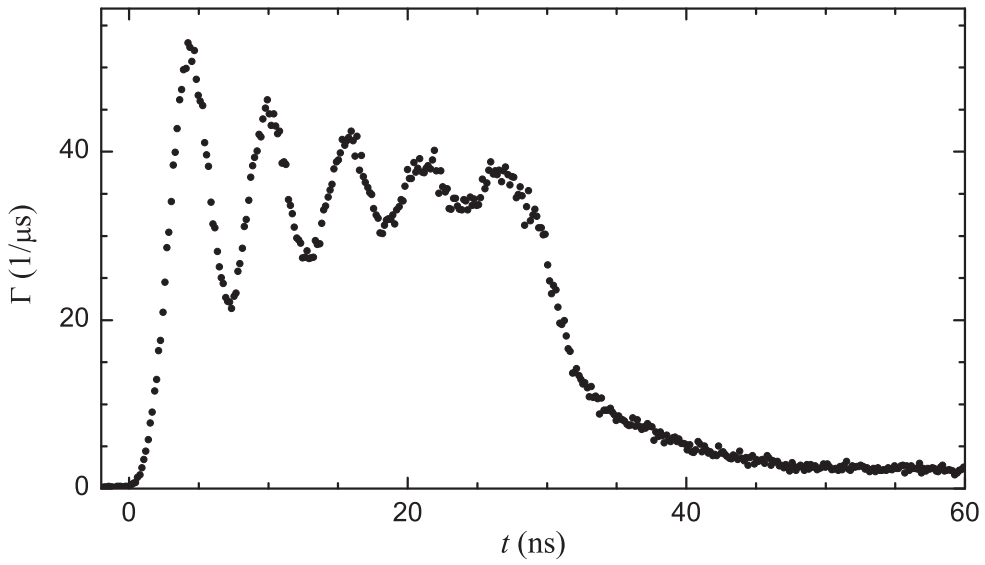

Figure 9.1: Rabi oscillations in SQUID DS_1. A resonant 7.6 GHz microwave pulse causes the escape rate to oscillate with a frequency dependent on the pulse power, -18 dBm at the source in this case. The pulse turns off near 30 ns, resulting in a decay of the excited state population and the escape rate.

on the relaxation time T_1 and coherence time T_2. For times much longer than T', the dynamics can be described by a master equation (see §7.3). The equilibrium value of the escape rate is simply determined by the various transitions rates (microwave pumping, dissipation, tunneling) for each level.

The pulse was nominally set to be 35 ns long, but Γ decreases quickly at $t = 30$ ns, suggesting that the actual pulse was shorter. As discussed in §8.7.2, the form of this decay reveals information about the state occupancy. If we had instead turned off the microwaves at 4.5 ns, this would resemble a simple quantum NOT gate, as $|0\rangle$ would have been taken to $|1\rangle$.

The goal of the experiments described in this chapter is to explain the structure of Fig. 9.1 and to extract key system parameters and the individual level populations. We approached this problem by varying the available parameters (microwave frequency and power, temperature, level spacing) and checking whether the qubit model we have developed could explain the results. I will begin by showing the power

dependence of the oscillations and the resonance widths. Then I will discuss the information that can be obtained by varying the detuning of the microwaves from resonance and finish with density matrix simulations that attempted to reproduce a full oscillation sequence, such as the one shown in Fig. 9.1.

9.1 Power Dependence

Figure 9.2(a) shows five Rabi oscillations in SQUID DS_1 induced by different nominal powers P_S of the microwave source. I have not offset the escape rates; at $t = 0$, $\Gamma = 2{\times}10^5$ 1/s for all of the curves. The escape rate without microwaves resembled the curve shown in Fig. 7.8(b); the resonant pulse began at $I_1 \approx 34.069$ μA, where $\omega_{01}/2\pi = 7.6$ GHz. The pulse was turned off 3 μs later, so the decay is not visible, unlike in Fig. 9.1. As in the previous two chapters, I will assume that the energy levels of the qubit junction of DS_1 are described by $I_0^\omega = 34.300$ μA and $C_J^\omega = 4.43$ pF, while the escape rates are given by $I_0^\Gamma = 34.308$ μA and $C_J^\Gamma = 4.43$ pF.

As expected for Rabi oscillations, the oscillation frequency of the curves in Fig. 9.2(a) increases with the microwave power. For each power, the oscillation amplitude decreases with time, eventually reaching a steady state value. At the highest power, the qubit almost always switched to the voltage state before $t = 20$ ns, which leads to poor statistics at later times. In a two-level system, the steady state value at high power corresponds to both states being equally populated [see Eq. (3.60)]. Thus, we would expect that at high powers, the oscillations would become faster, but that they would be centered about a constant value of Γ. Instead, the equilibrium value increases quite dramatically with power. At the bias where the experiments were performed, I estimate Γ_1 to be 3.7×10^7 1/s using Eq. (2.43). This is the maximum escape rate for a two-level system, which only occurs if $|1\rangle$ is fully occupied. Instead, we see escape rates nearly ten times this value, providing strong evidence for the occupation of $|2\rangle$. As Γ_2 is roughly 3×10^9 1/s, only a 8% population would be

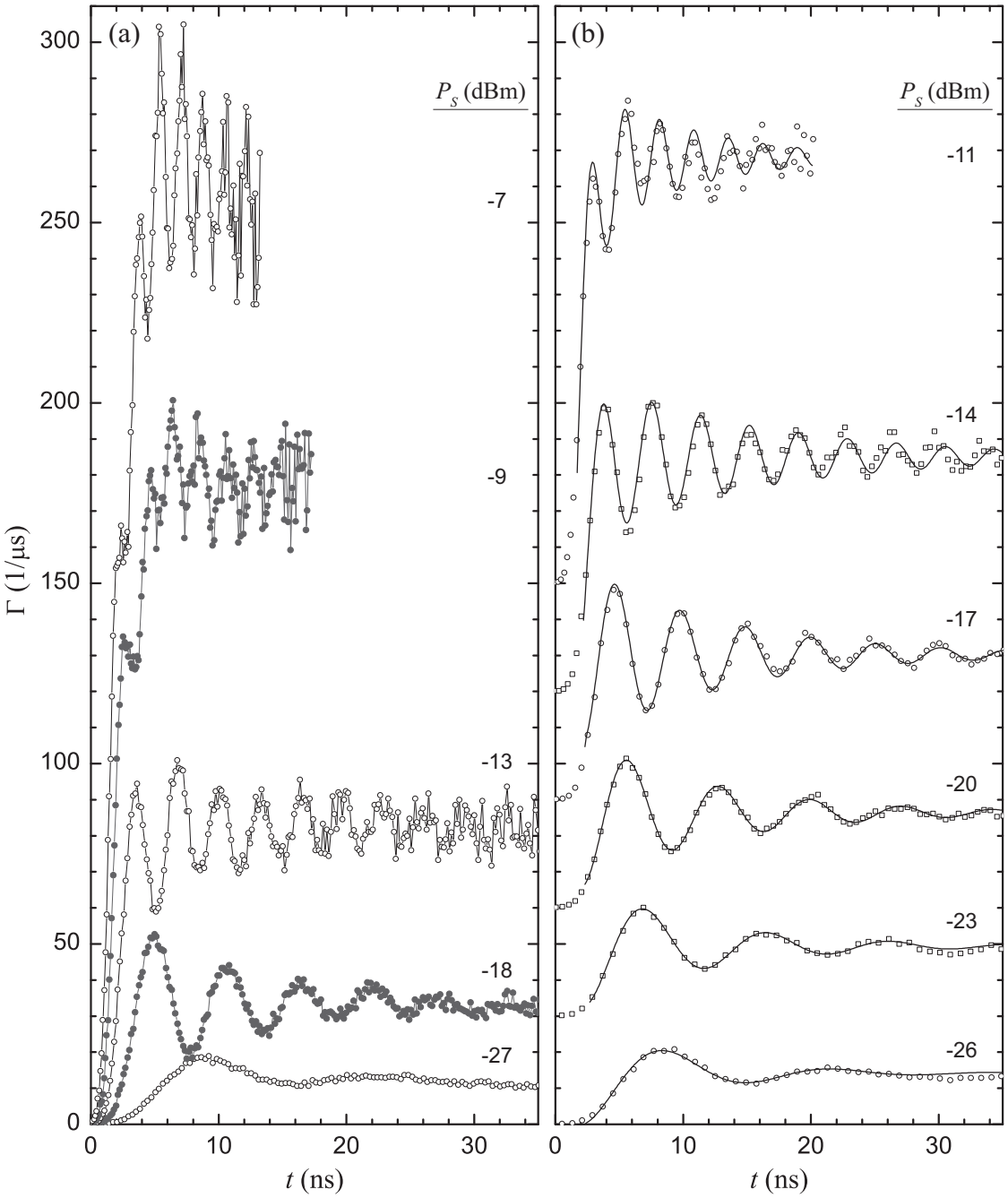

Figure 9.2: Power dependence of Rabi oscillations in SQUID DS_1. (a) The symbols (connected by straight lines to guide the eye) show the escape rate due to a microwave pulse of the indicated source power. As the curves are not offset, it is clear that the escape rate does not saturate with increasing power. (b) Oscillations at a different set of powers, vertically offset for clarity, are fit with the sum of a decaying sinusoid and a saturating exponential background, drawn as solid lines. All of the data were taken at 7.6 GHz and 20 mK.

required to see such large escape rates.

Ideally, we could compare the data to analytical solutions of Rabi oscillations for a three-level system. With the presence of tunneling, dissipation, and decoherence, this is difficult to do accurately. Still, some quantitative information about the system can be obtained by fitting the escape rates curves to a functional form that reproduces their main features. Motivated in part by Eq. (3.62), I chose to use the sum of a decaying sinusoid and an exponentially saturating background [101],

$$\Gamma(t) = g_1 \left(1 - e^{-(t-t_0)/T'}\right) \cos\left[\overline{\Omega}_R (t - t_0)\right] + g_2 \left(1 - e^{-(t-t_0)/T_e}\right), \tag{9.1}$$

where g_1 and T' are the amplitude and time constant of the decay envelope, $\overline{\Omega}_R$ is the observed oscillation angular frequency, g_2 and T_e are the amplitude and time constant of the background, and t_0 is an overall time offset. This form does not reproduce the curvature at small t or the relatively small (but non-zero) value of Γ at $t = 0$, which is acceptable as I was most interested in the main oscillation.

Figure 9.2(b) shows oscillations for six values of P_S, which I have offset for clarity.[1] The solid lines are fits to Eq. (9.1). Most of the features of the data are reproduced, at least qualitatively, including the usual oscillation maxima at high microwave power. The data were taken while I_b and I_f were being ramped; in 35 ns, the energy levels change by a small amount, which could account for the falling Γ at $P_S = -26$ dBm as well the oscillation which appears to increase in frequency with time at $P_S = -14$ dBm.

Some of the parameters of the fits (for more data than are shown in Fig. 9.2) are plotted in Fig. 9.3.[2] The oscillation frequency, plotted with circles in Fig. 9.3(a) and its inset, increases fairly smoothly with power, as expected. The one exception

[1] In calculating the switching histograms, I chose to use large time bins, which accounts for the lower density of points than in Fig. 9.2(a).

[2] For $P_S > -14$ dBm, the fits were done "by eye," so the results are somewhat unreliable.

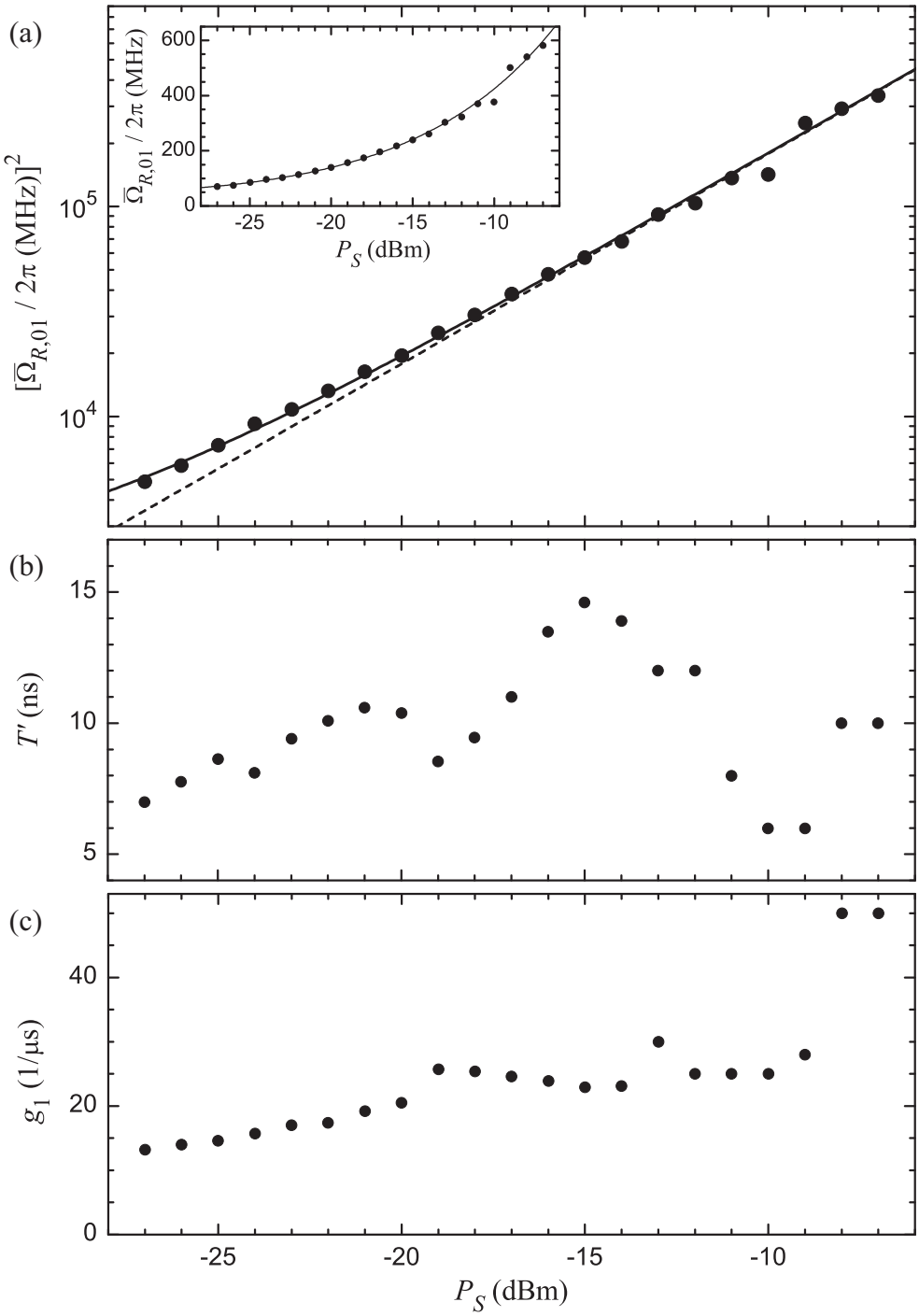

Figure 9.3: Phenomenological fits of Rabi oscillations in SQUID DS_1. A decaying sinusoid with a background was fit to the oscillations in Fig. 9.2 (and others not shown) to yield the (a) square of the oscillation frequency, (b) decay envelope time constant, and (c) oscillation amplitude as a function of the microwave pulse power P_S. The solid line in panel (a) is a fit to the two-level theory; the inset shows the same information for $\overline{\Omega}_{R,01}$. The dashed line is drawn without an offset at $P_S = 0$ W.

is at $P_S = -10$ dBm, where the quality of the oscillation was quite low.

For a two-level system driven resonantly, the Rabi frequency should increase linearly with the microwave current $I_{\mu w}$ or as the square root of the microwave power, in the absence of dissipation. As a check on the expected dependence, the solid line in Fig. 9.3(a) is a linear fit of $\left(\overline{\Omega}_{R,01}/2\pi\right)^2$ as a function of P_S (in Watts, rather than dBm).[3] The best-fit line has a slope 1790 MHz$^2/\mu$W and an offset of 1570 MHz^2. Ideally, the fit would pass through the origin. The dashed line is drawn with the same slope, but with zero offset; I have not included the dashed line on the inset, which shows $\overline{\Omega}_{R,01}$ on a linear scale.

There are several possible causes for the finite offset and what appears to be a slight systematic deviation between the data and fit. In the absence of dissipation, Eq. (3.12) predicts an oscillation frequency of $\left[\left(\omega_{rf} - \omega_{01}\right)/2\pi\right]^2$ at zero power. Thus the offset of the fit could correspond to a detuning of 40 MHz. The full data set did take 37 hours to acquire (during which no adjustments were made to the timing of the microwave pulse), but there appeared to be very little drift during this time.

The detuning, rather than being caused by improper timing, could be the result of inhomogeneous broadening. Low frequency current noise changes the energy level spacing, causing an increase in the oscillation frequency, with the most noticeable effect at low $\overline{\Omega}_{R,01}$.

Neglecting detuning, dissipation also results in a shift of the oscillation frequency at low power. However, as seen in Eq. (3.64), T_1 and T_2 result in a negative offset of $\overline{\Omega}^2_{R,01}$ vs. P_S, whereas the opposite is seen in Fig. 9.3(a).

Finally, from the escape rates of Fig. 9.2, it is clear that we are dealing with a quantum system of at least three levels. The second excited states acts as a perturbation on $0 \rightarrow 1$ Rabi oscillations, as discussed in §3.3. However, this phenomenon

[3] In doing the fit, I made the simple assumption that the uncertainty in $\overline{\Omega}_{R,01}$ was proportional to the value itself. I also did not include the five highest powers, as the oscillations at these powers were not particularly well-defined. Nonetheless, the fit does approximate their values well.

has the largest impact at high power, as I will show in §9.2. Even if the highest powers are ignored in Fig. 9.3(a), a linear fit still gives an offset of roughly 1000 MHz^2. It is likely that all of the effects are playing some role, but it is unclear which one is dominant.

Figure 9.3(b) shows the time constant T' of the decay envelope of the oscillations in Fig. 9.2. The times increase substantially with power until $P_S = -15$ dBm, at which point the fits are unreliable. The maximum value is about 15 ns and the average is roughly 10 ns, which is what we typically saw on-resonance at other drive frequencies.

The amplitudes g_1 of the oscillations, extracted from the phenomenological fits, are plotted in Fig. 9.3(c). Again the values increase weakly with power, saturating at 2.5×10^7 1/s near $P_S = -20$ dBm. Returning to Fig. 9.2(a), the amplitude of the oscillations for $P_S = -18$ and -7 dBm are not that different, even though the background is quite a bit bigger in the latter case. Interestingly, the saturation value is somewhat more than half of the predicted value for Γ_1 of 3.7×10^7 1/s, but this may just be a coincidence.

It is important to understand the mechanism for populating $|2\rangle$, which amounts to leakage out of the desired state space for quantum computation. In the spectrum shown in Fig. 8.8 (taken for a different device), the transitions closest to the $0 \rightarrow 1$ branch are the single photon $1 \rightarrow 2$ and two-photon $0 \rightarrow 2$ transitions, both of which occupy $|2\rangle$. However, all of the transitions appear to be relatively sharp, as compared to their spacing in frequency. Two factors cause the impact of well separated transitions to become significant. The first is that our detection technique of measuring the escape rate is extremely sensitive to population of $|2\rangle$, due to the large values of Γ_2/Γ_1 and Γ_2/Γ_0. More importantly, there would not be any population to detect if the resonances did not broaden to have significant overlap at the high power at which we perform oscillations.

In the rough expression for the resonance width in Eq. (3.66), I did not include a power broadening term, as we usually measure spectra at very low powers. One benefit of analyzing Rabi oscillations is that the fit in Fig. 9.3(a) gives a calibration of the microwave power. With this information, power broadening can be studied, which might not only explain the leakage to $|2\rangle$, but also reveal information about inhomogeneous broadening, T_1, and T_2.

In Fig. 8.10(c), I plotted the resonance full width (in terms of the qubit current I_1) of the $0 \rightarrow 1$ transition of DS_1 at 7.6 GHz as a function of the microwave source power P_S. I converted the power[4] to $\Omega_{R,01}$ and the width to $\Delta\omega$ (using spectroscopic information) and plotted the results in Fig. 9.4 as solid circles.

Equation (3.65), which gives the power dependence of the resonance width $\Delta\omega = (2/T_2') \sqrt{1 + \Omega_{01}^2 T_1' T_2'}$ in terms of the escape rate-dependent parameters $T_1' = (1/T_1 + \Gamma_1)^{-1}$ and $T_2' = [1/T_2 + (\Gamma_0 + \Gamma_1)/2]^{-1}$, should describe the data. I fit the six highest powers, where the broadening is prominent, with the result shown as a solid line in Fig. 9.4. The effective time constants are $T_1' = 3.2$ ns and $T_2' = 4.0$ ns. As the escape rates are predicted to be $\Gamma_0 = 6.3 \times 10^4$ 1/s and $\Gamma_1 = 3.7 \times 10^7$ 1/s at the bias current where the data were taken, T_1 and T_2 are predicted to be 3.7 ns and 4.4 ns. With such short times, the escape rates have a negligible effect. Remarkably, the saturation value at low power is nearly reproduced by the fit, even though the spectroscopic measurements of the previous chapter indicated the presence of significant low frequency noise.

Both T_1 and T_2 are shorter than my previous measurements would suggest. The slow bias sweep method in §7.4.2 gave $T_1 \approx 15$ ns. With a Rabi decay envelope of $T' \approx 10$ ns, Eq. (3.63) predicts $T_2 \approx 7.5$ ns. With the inclusion of tunneling,

[4] I only used the slope of 1790 $\text{MHz}^2/\mu\text{W}$ in Fig. 9.3(a) in the conversion and dropped the 1570 MHz^2 offset. If the offset is due to detuning, then this is legitimate, because the spectroscopic widths were measured by sweeping ω_{01} through resonance. If the offset was a result of an incomplete description of the junction dynamics, then dropping it results in incorrect values of the Rabi frequency.

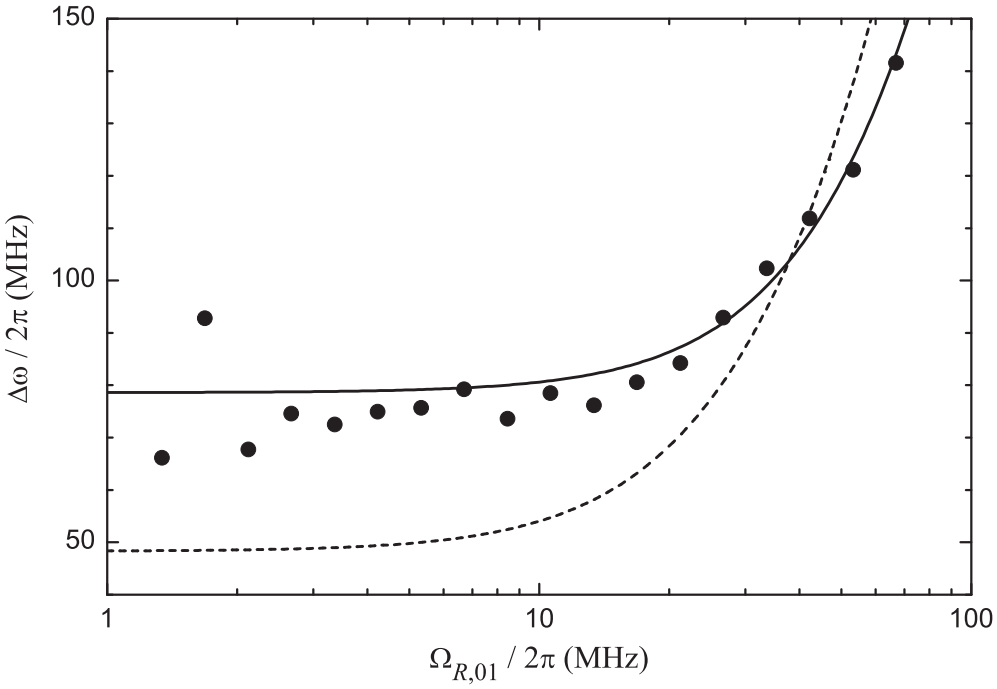

Figure 9.4: Power broadening in SQUID DS_1. The full width $\Delta\omega$ of the $0 \rightarrow 1$ resonance (solid circles) increases above a certain power of the microwave drive, as characterized by the Rabi frequency $\Omega_{R,01}$. The solid line is a fit to data at high power ($T_1' = 3.2$ ns and $T_2' = 4.0$ ns), while the dashed line is drawn with values estimated from other measurements ($T_1' = 9.7$ ns and $T_2' = 6.6$ ns).

the effective time constants become $T_1' = 9.7$ ns and $T_2' = 6.6$ ns. The dashed line in Fig. 9.4 shows the resonance width for these parameters. At low power, the prediction underestimates the data; this can be explained by inhomogeneous broadening, which would uniformly increase the widths, having the most significant impact at low power. However, at high power, the prediction is greater than the data. In our simplified picture of the system, we might have ignored a process that would broaden the widths, but it is hard to imagine how we could overestimate the measured width.

It is unclear how to resolve this critical inconsistency. It is possible that the calibration of $\Omega_{R,01}$ is incorrect. However, it is the most reliable near 100 MHz, where the power broadening discrepancy exists. At lower power, Rabi oscillations are difficult to resolve and susceptible to detuning effects. At higher power, perturbation

by $|2\rangle$ could be causing significant deviations from two-level behavior. It could be that decoherence is having a major impact on the oscillation frequency and thus the calibration of power; comparing the oscillation frequency to theory (without T_1 and T_2) is one of the subjects of the next section.

9.2 Detuning and Strong Field Effects

Before attempting to model the system dynamics in the presence of dissipation and decoherence, I will examine the behavior of the Rabi oscillation frequency. While decoherence has a profound impact on the oscillation amplitude, it should have a negligible impact on the frequency if T_2 is not too short. A careful study of the oscillation frequency is also a strong test of the junction Hamiltonian, because results depend on the matrix elements between states in addition to energy levels [83].

A property of Rabi oscillations that can be easily verified is their frequency as a function of detuning from resonance. Equation (3.12) gives the effective Rabi frequency $\overline{\Omega}_{01} = \sqrt{\Omega_{01}^2 + (\omega_{rf} - \omega_{01})^2}$ for an ideal two-level system. We choose not to increase the detuning by changing ω_{rf}, for the same reason we did not measure spectra by sweeping ω_{rf}; namely, the frequency response of the microwave lines could introduce erroneous features. Instead, just as with spectroscopy, we kept the microwaves at fixed frequency and power and changed the energy levels of the qubit, through its bias current I_b. This approach, however, does not come without complications. If a large range of I_b is covered, then several other properties of the qubit will change along with the energy levels, such as the matrix elements of the phase difference $\hat{\gamma}$ and the escape rates. For this reason, comparing two different transitions (for example, $0 \rightarrow 1$ and $1 \rightarrow 2$) could be problematic, as they will occur at different values of I_b. An alternate approach, which I did not follow, would be to carefully calibrate the frequency response of the microwave lines in terms of, for example, Ω_{01}.

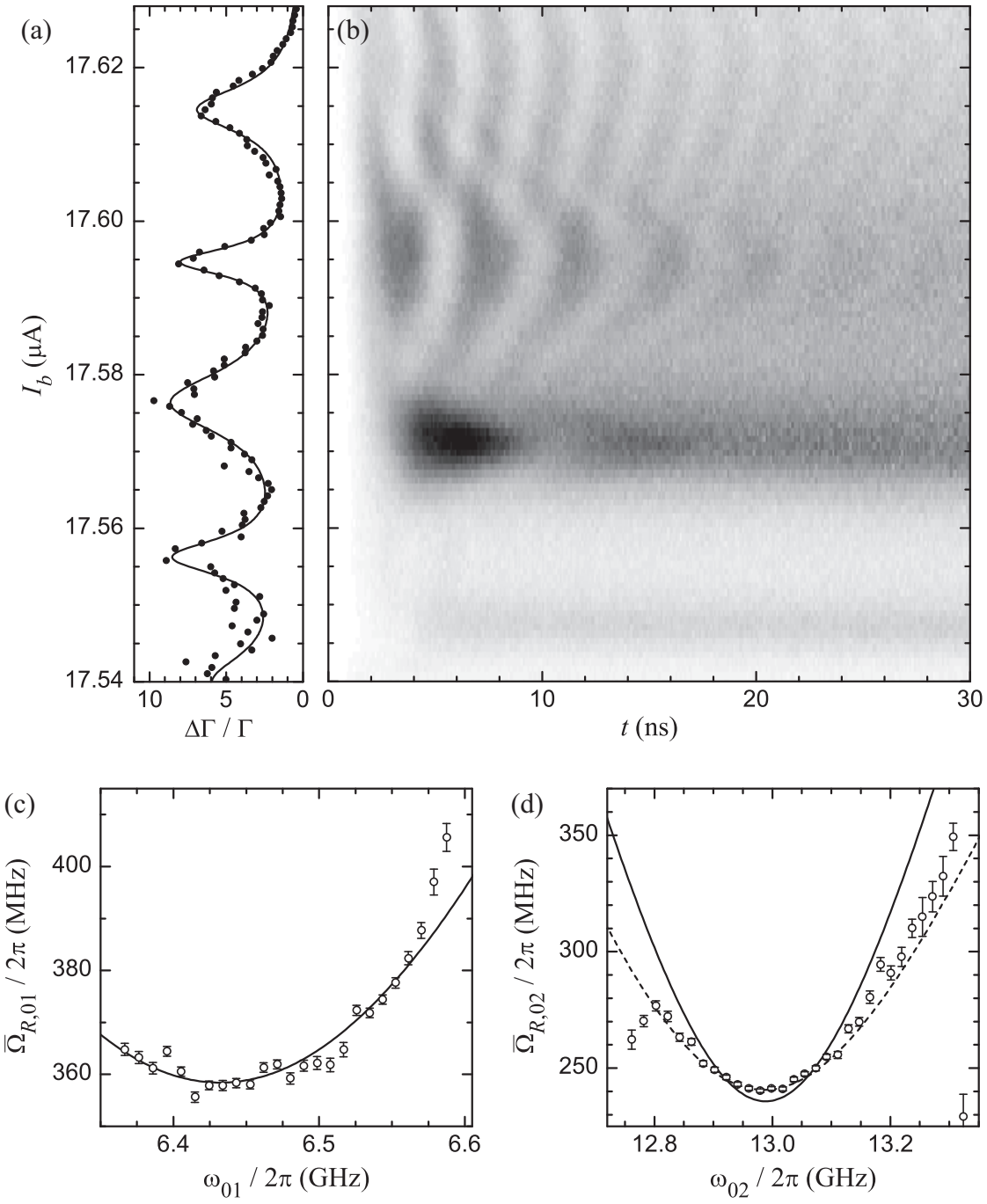

Figure 9.5: Rabi detuning map of SQUID DS_2B at elevated temperature. (a) At 110 mK, the measured escape rate enhancement $\Delta\Gamma/\Gamma$ (circles) at $\omega_{rf}/2\pi = 6.5$ GHz and $P_S = -34$ dBm shows four resonance peaks, which are fit well by a sum of Lorentzians (line). (b) Each horizontal line of the plot is the escape rate due to a microwave pulse, with a source power of $P_S = -15$ dBm. (c) The oscillation frequency is plotted as a function of ω_{01} (circles). The solid line is for a single photon process in a two-level system. (d) The oscillation frequency for the two-photon $0 \rightarrow 2$ transition is reproduced better by a three-level rotating wave solution (dashed line) than by a simple two-level approximation (solid line).

In Fig. 9.5(a), the escape rate enhancement of SQUID DS_2B at $\omega_{rf}/2\pi = 6.5$ GHz is plotted as a function of I_b. As the measurement was performed at 100 mK with a relatively high power of $P_S = -34$ dBm, transitions from $|1\rangle$ are visible, just as in Fig. 8.10(a). From top to bottom, the peaks correspond to single photon $0 \rightarrow 1$, two-photon $0 \rightarrow 2$, single photon $1 \rightarrow 2$, and two-photon $1 \rightarrow 3$ transitions. The solid line is a fit to the sum of four Lorentzians and reproduces the data well, even though they were taken at elevated temperature.

Figure 9.5(a) was obtained by ramping I_b at a relatively slow rate of 0.026 A/s. To investigate the effects of detuning, we measured Rabi oscillations by turning a microwave pulse on at different times during this same ramp. Each of the 98 distinct horizontal lines of Fig. 9.5(b), which I will refer to as a detuning map, is the escape rate due to a microwave pulse (of frequency $\omega_{rf}/2\pi = 6.5$ GHz and power $P_S = -15$ dBm) that started at the value of I_b on the y-axis. I have colored the entire plot with the same scale, where black represents the highest escape rate (1.4×10^8 1/s). The horizontal scale specifies the amount of time from the beginning of the pulse, during which I_b is also changing. In fact, the lines were taken by incrementing the start of the pulse by 35 ns during the bias ramp;[5] thus, a Rabi oscillation was measured at increments in I_b of roughly 0.9 nA. For the 30 ns plotted, the energy level spacing at the end of a particular line is nearly the same as the spacing at the beginning of the next line. This undesired detuning did not appear to have any significant effects.

The $0 \rightarrow 1$ transition is resonant at $I_b = 17.615$ μA, as seen in Fig. 9.5(a). There is a set of "fringes" in Fig. 9.5(b) centered at the same value of I_b. For larger I_b (when $\omega_{rf} > \omega_{01}$) or smaller I_b (when $\omega_{rf} < \omega_{01}$), the detuned Rabi oscillations increase in frequency, resulting in the curvature of the fringes. At $I_b = 17.595$ μA,

[5]There appeared to be a systematic error in the timing of the pulse generator used to gate the microwaves. I measured the generator's output (using a SR620 timer), in order to determine $t = 0$ for each line.

the microwaves are resonant with the two-photon $0 \rightarrow 2$ transition. Another set of fringes (with a longer period) is visible at this current. The curvature is greater, as the effect of detuning is stronger for a two-photon process. Near $I_b \approx 17.61$ μA, there appears to be interference between the two processes.

The single photon $1 \rightarrow 2$ transition is resonant for $\omega_{rf}/2\pi = 6.5$ GHz at $I_b = 17.575$ μA. On this resonance, the Rabi oscillation is quite weak. There are, perhaps, two lobes in the detuning map, but the amplitude variation is small. What is particularly puzzling is that the oscillation frequency is lower than the $0 \rightarrow 1$ transition. For a single photon oscillation between two states, the frequency should be proportional to the matrix element of $\hat{\gamma}$ that links the states. Then from Eq. (2.38), the prediction is that $\Omega_{R,12} \approx \sqrt{2}\Omega_{R,01}$ for a constant microwave power, in contrast to what is seen experimentally. It is possible that the small thermal occupancy of $|1\rangle$ is insufficient to see a clean two-level oscillation between $|1\rangle$ and $|2\rangle$. Better results could be obtained by first resonantly populating $|1\rangle$, and then attempting to perform a Rabi oscillation. This proved to be a rather difficult experiment to carry out and we never obtained good results.

I extracted the oscillation frequency for each horizontal line in Fig. 9.5(b) by fitting the escape rate with the function in Eq. (9.1). While the decay envelope was not always well-defined, particularly at large detuning, the oscillation frequency generally was. The results are plotted as circles in Fig. 9.5(c) and (d), with error bars coming from the uncertainty in the fit parameter.

Figure 9.5(c) shows the effective Rabi frequency for the $0 \rightarrow 1$ transition. In making this plot, I converted the current bias I_b to ω_{01}, using Eq. (2.44) and $I_0 = 17.828$ μA and $C_J = 4.51$ pF, values which came from spectroscopic measurements. Equation (3.12) predicts that for an ideal two-level system, $\overline{\Omega}_{R,01}$ should reach a minimum on resonance, at $\omega_{01}/2\pi = 6.5$ GHz. However, the minimum in the data is clearly at a lower value. While some of the discrepancy could be due to an error in

the calculation of ω_{01}, the presence of $|2\rangle$ perturbs the $0 \rightarrow 1$ oscillation, leading to a shift of resonance at high power (see §3.3). Nonetheless, Eq. (3.12) can be used to check the expected detuning behavior by allowing ω_{rf} to be a fitting parameter, to take into account the resonance shift. The solid line is such a fit to Eq. (3.12), with parameters $\omega_{rf}/2\pi = 6.432$ GHz and $\Omega_{R,01}/2\pi = 358$ MHz. With this adjustment, the oscillation frequency with detuning follows the expected behavior over a wide range.

The detuning of the two-photon $0 \rightarrow 2$ transition is shown in Fig. 9.5(d), where $\overline{\Omega}_{R,02}$ is plotted as a function of ω_{02}. Here, the solid line is given by Eq. (3.23) (which gives the effective Rabi frequency $\overline{\Omega}_{R,02} = \sqrt{\Omega_{R,02}^2 + (\omega_{02} - 2\omega_{rf})^2}$ for a two-photon transition of an ideal system), with fit parameters $\omega_{rf}/2\pi = 6.494$ GHz and $\Omega_{R,02}/2\pi = 239$ MHz. While the resonance occurs near the applied microwave frequency, the agreement between data and theory is quite poor at large detuning. As a more refined test, the three-level rotating wave solution of §3.3 can be used. The dashed line comes from the numerical solution of Eq. (3.14), for $\omega_{rf}/2\pi = 6.429$ GHz and $I_{\mu w} = 15.85$ nA. In this case, the discrepancy between the fit (6.429 GHz) and experimental (6.5 GHz) values of ω_{rf} is unexpected. Either the calibration of ω_{02} has a significant error or the rotating wave solution is not fully capturing the behavior of the two-photon process. Aside from this issue, the dashed line does reproduce the detuning behavior reasonably well.

We further investigated the resonance shift seen in Fig. 9.5(c) by measuring this shift as a function of power. Figure 9.6 shows Rabi detuning maps for SQUID DS_2B, using a 5.9 GHz microwave pulse with a source power P_S of (a) -27, (b) -24, (c) -20, (d) -17, (e) -14, and (f) -11 dBm. The bias ramp rate was reduced to 0.0095 A/s with pulses beginning at 75 ns intervals, to further reduce unwanted detuned during the pulse. I used a different scale to color each map; black represents 2.5×10^7 1/s for -27 dBm and 5.8×10^8 1/s for -11 dBm.

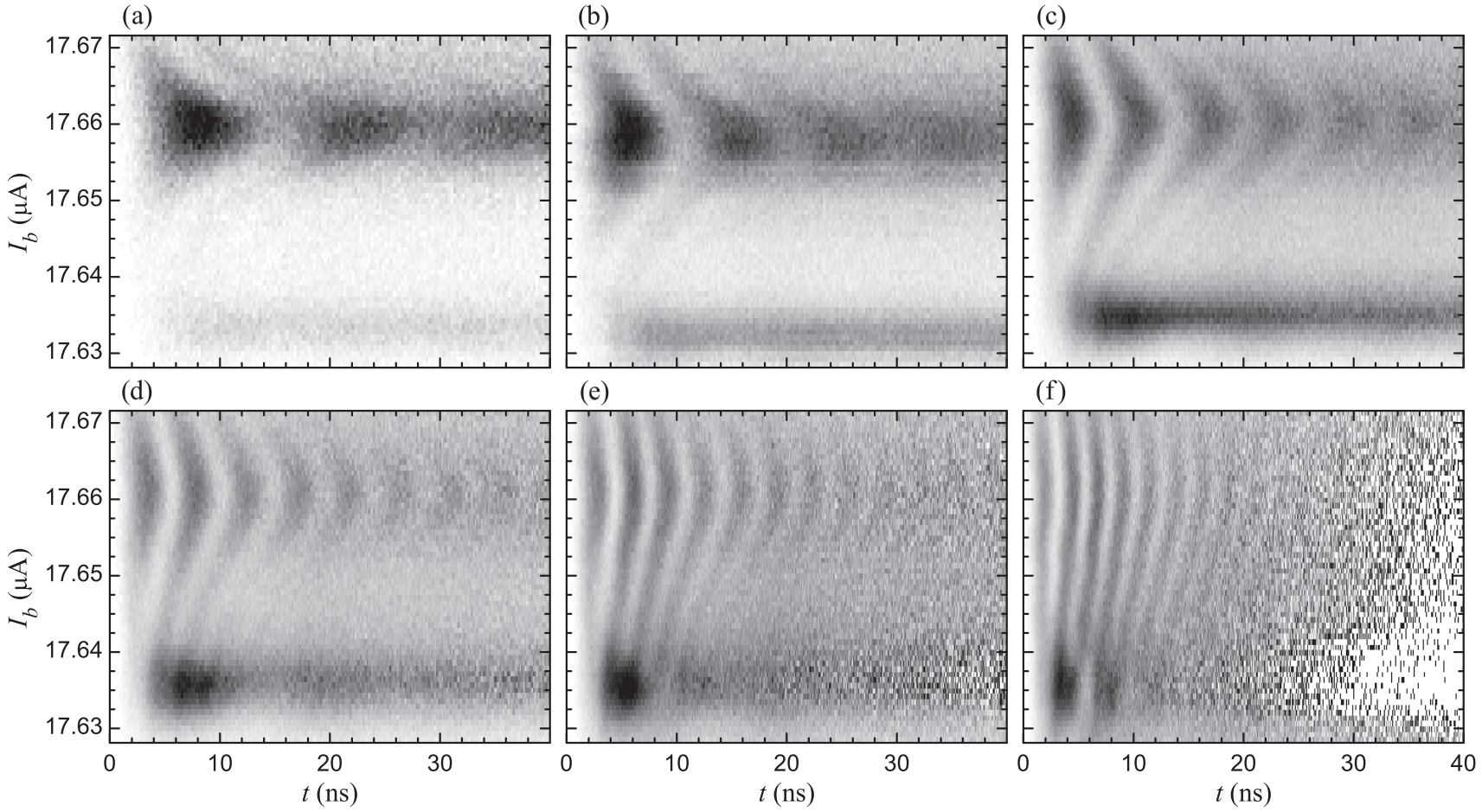

Figure 9.6: Rabi detuning map of SQUID DS_2B at $\omega_{rf}/2\pi = 5.9$ GHz. Each horizontal line is the total escape rate due to a microwave pulse, with a source power of (a) -27, (b) -24, (c) -20, (d) -17, (e) -14, (f) -11 dBm, that starts at $t = 0$. Each map is colored with a different gray scale. When $I_b \approx 17.66$ μA, ω_{rf} is near ω_{01}, while at $I_b \approx 17.635$ μA, it is near $\omega_{02}/2$.

The set of fringes near $I_b = 17.66\ \mu$A corresponds to $0 \rightarrow 1$ Rabi oscillations, while the set near $I_b = 17.635\ \mu$A is for the two-photon $0 \rightarrow 2$ transition. The data were taken at the base temperature of the refrigerator, so the $1 \rightarrow 2$ transition was difficult to resolve. As the power increases, the frequency of the $0 \rightarrow 1$ oscillation increases, as expected. The fringes also flatten out, because a given detuning $\omega_{rf} - \omega_{01}$ will have its largest impact when it is large compared to Ω_{01}. A highly detuned $0 \rightarrow 1$ oscillation is superimposed on the $0 \rightarrow 2$ at $P_S = -17$ dBm.

As discussed earlier in this section and in §3.3, the presence of the second excited state $|2\rangle$ has a two effects on the $0 \rightarrow 1$ Rabi oscillation: the minimum oscillation frequency is suppressed from its two-level value and this resonance occurs for $\omega_{rf} > \omega_{01}$ [83]. The solid line in Fig. 9.7(a) was generated from the three-level rotating wave Hamiltonian of Eq. (3.14), by finding the value of I_b that minimized $\overline{\Omega}_{R,01}$ for a given $I_{\mu w}$. The energy levels and matrix elements for this simulation were calculated for a single junction with $I_0 = 17.821\ \mu$A and $C_J = 4.46$ pF.[6] The dashed line is the ideal two-level solution, where $\Omega_{R,01} \propto I_{\mu w}$, showing the suppression at high power. The resonance shift $\Delta\omega_{R,01} = \omega_{rf} - \omega_{01}$ is plotted as a solid line in Fig. 9.7(b).

To compare these predictions to the data, I fit each horizontal line of Fig. 9.6 to Eq. (9.1) to extract the oscillation frequency and converted I_b to ω_{01} using Eq. (2.44). Then, as in Fig. 9.5(c), fitting the data to Eq. (3.12) gave the resonant oscillation frequency $\Omega_{R,01}$. It was also necessary to convert the source power P_S to microwave current $I_{\mu w}$. As the relationship is expected to be $P_S \propto I_{\mu w}^2$, the proportionality constant may be taken as a free fitting parameter. The circles in Fig. 9.7(a) were plotted using the conversion $I_{\mu w}\,(\text{nA}) = 59.64\sqrt{P_S/\text{mW}}$. The agreement between the solid line and the circles is good, with the two-level solution

[6] These junction parameters are slightly different than the ones I used for Fig. 9.5. Even though the two data sets were separated by less than two weeks, what was probably an offset in the trapped flux resulted in modified values for the effective I_0 and C_J.

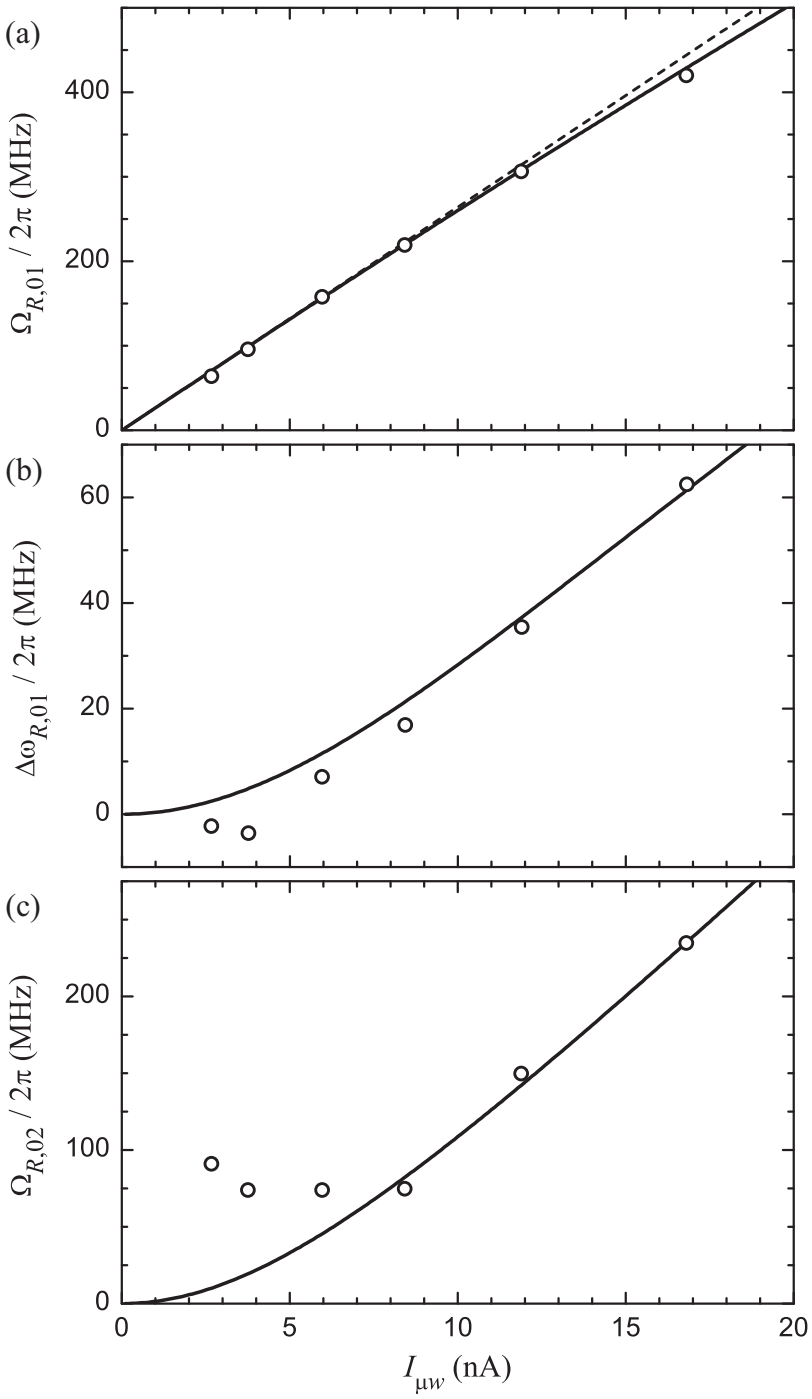

Figure 9.7: Strong field effects in SQUID DS_2B. The points plotted as circles were extracted from the data in Fig. 9.6, after converting the source power P_S to current $I_{\mu w}$ at the junction. The solid lines are calculated from the three-level rotating wave Hamiltonian. (a) The oscillation frequency of the $0 \rightarrow 1$ transition deviates from the two-level solution (dashed) at high current. (b) In addition, the resonance occurs for $\omega_{rf} > \omega_{01}$; the resonance shift is $\Delta\omega_{R,01} = \omega_{rf} - \omega_{01}$. (c) The two-photon $0 \rightarrow 2$ Rabi oscillation frequency has a nearly quadratic dependence on the microwave current.

clearly overestimating the oscillation frequency at high power. As the approximate expression in Eq. (3.21) shows, the suppression of $\Omega_{R,01}$ depends on the difference $\omega_{01} - \omega_{12}$. In fact by fitting the data to that expression, the value of the difference is $(\omega_{01} - \omega_{12})/2\pi = 940$ MHz. The prediction at $I_b = 17.66$ μA for $I_0 = 17.821$ μA and $C_J = 4.46$ pF is 910 MHz.

The resonance shift can be extracted from the same fits of $\overline{\Omega}_{R,01}$ vs. ω_{01}. This effect is barely visible in Fig. 9.6. For $P_S = -27$ dBm, the longest oscillation period appears to occur for $I_b < 17.66$ μA, while for $P_S = -17$ dBm, resonance occurs for $I_b > 17.66$ μA. What complicates the situation is that there was a small amount of drift over the course of taking the different maps. It is unclear whether this was due to, for example, the biasing and detection electronics warming up or the flux offset of the SQUID changing slightly. Aside from -24 dBm, the drift was less than 1.5 nA, which I would ordinarily ignore. However when looking for small resonance shifts, the drift can be significant.

I attempted to correct for the drift in two ways. In one method, I chose a value of I_0 and C_J for each map so that the calculated values of ω_{01} as a function of the background escape rate (no microwaves) would coincide for the six maps. In a second attempt, I simply added an offset in I_b so the background escape rates would match. Fortunately, both techniques agreed within about 2 MHz. Results are plotted as circles in Fig. 9.7(b), using the same calibration of $I_{\mu w}$ as used in (a). At the lowest powers, $\Delta\omega_{R,01}$ is negative, which is likely indicative of the uncertainty in the fits and the junction parameters I_0 and C_J. The agreement at higher powers is much better.

The detuning maps provide a reliable method for finding the resonant oscillation frequency. In contrast, for Fig. 9.2, all of the pulses were started at the same value of I_b. If the resonance shifted at high power, then the measured oscillation frequency would have been greater than $\Omega_{R,01}$.

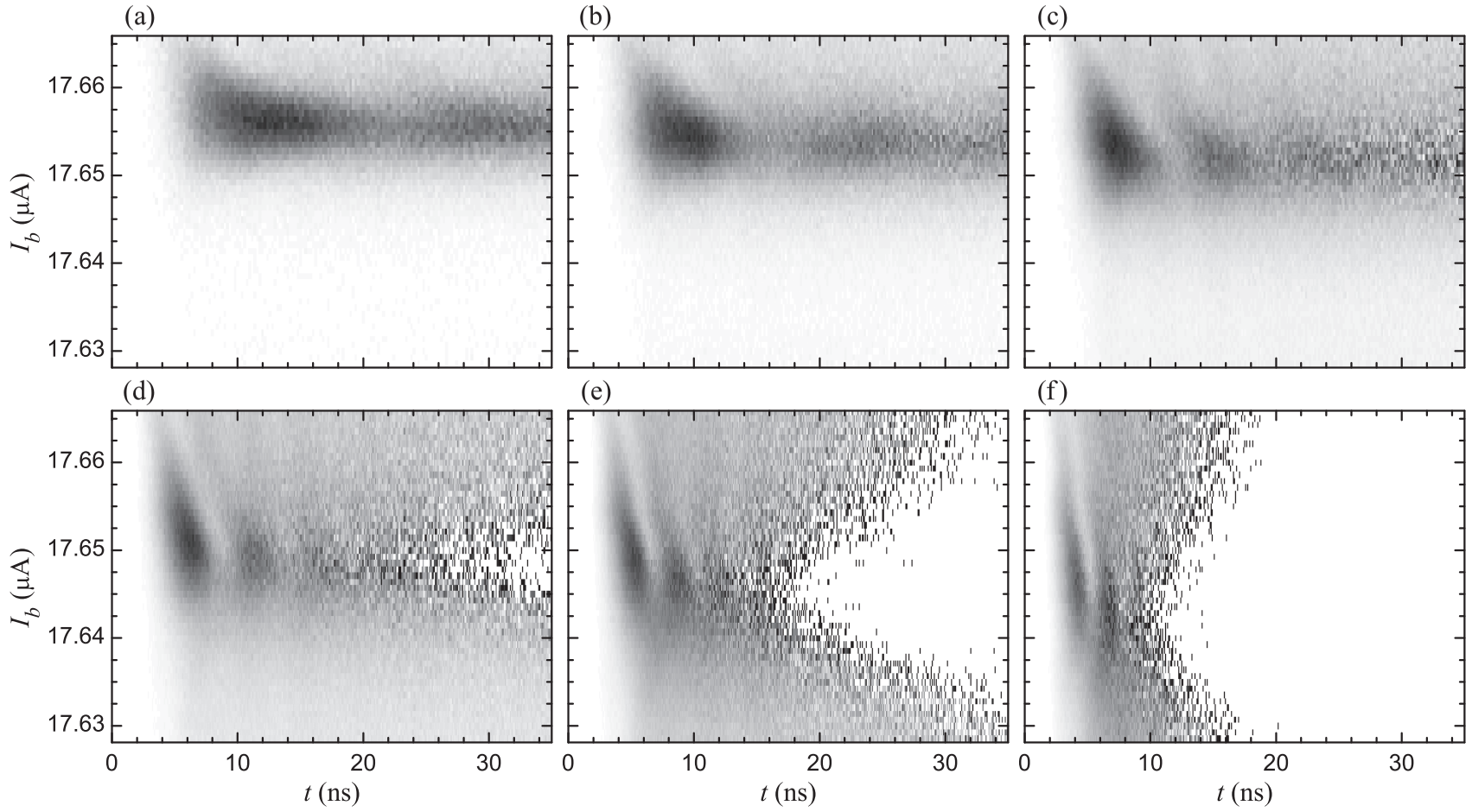

Figure 9.8: Rabi detuning map of SQUID DS_2B at $\omega_{rf}/2\pi = 2.95$ GHz. Each horizontal line is the total escape rate due to a microwave pulse, with a source of power (a) -32, (b) -30, (c) -28, (d) -26, (e) -24, (f) -22 dBm, that starts at $t = 0$. Each map is colored with a different gray scale. The applied microwave frequency is roughly equal to $\omega_{01}/2$ for the values of I_b shown.

Finally, the $0 \rightarrow 2$ oscillation frequency can be examined. As the detuning maps of Fig. 9.6 show, it is quite difficult to see a clean oscillation. In fact for the three lowest source powers, the frequency appears to be constant; the slight modulation could be unrelated to Rabi oscillations. It is possible that $|2\rangle$ is nearing the top of the potential well for $I_b \approx 17.635\ \mu$A, so that the high escape rate would wash out the oscillation. Nonetheless, the rough values I could extract are plotted in Fig. 9.7(c). The line again comes from Eq. (3.14). In spite of the obvious disagreement at low power, the agreement at high power is surprisingly good. It is encouraging that the rotating wave Hamiltonian, derived in the absence of dissipation and evaluated using properties of a simple current-biased junction, reproduces the Rabi oscillation frequency well at a range of powers.

Figure 9.8 shows detuning maps of the same device taken at 20 mK for $\omega_{rf}/2\pi = 2.95$ GHz with source powers of (a) -32, (b) -30, (c) -28, (d) -26, (e) -24, and (f) -22 dBm. As the microwave frequency is half of that used in Fig. 9.6, the oscillations are due to a two-photon $0 \rightarrow 1$ transition. The fringes are not nearly as symmetric as the corresponding single photon ones and there is a noticeably larger resonance shift with power.

In principle, the three-level rotating wave solution could describe these data as well. However, it appears the resonance shift in a two-level system is bigger than the perturbation due to the third level. A accurate model of this transition would confirm the magnitude of the diagonal matrix elements $\gamma_{0,0}$ and $\gamma_{1,1}$.

9.3 Density Matrix Simulations

Having shown that the Rabi oscillation frequency is consistent with theory, I will now turn to describe the full waveform of the oscillations. As discussed in §3.6, it is practically impossible to write down the full Hamiltonian of the system, including all of the degrees of freedom that give rise to dissipation and decoherence.

A common approach to the problem is to use the density matrix formalism to follow the evolution of the system [143,144], with phenomenological time constants T_1 and T_2.

To simulate the junction dynamics, I numerically integrated the Liouville-von Neumann equation to find the time dependence of the elements of the density matrix (see §3.8). The matrix that specifies the evolution of the system, whose structure is given in Appendix D, requires several parameters. For an N level system, there are $N-1$ energy level differences $\hbar\omega_{nm}$, N escape rates Γ_n, $N(N-1)/2$ energy dissipation rates W^t_{nm} (see §3.4), $N(N-1)$ coherence times T_2^{nm} (see §3.7), $N(N+1)$ bare Rabi frequencies Ω_{nm}, and the temperature T.

While this may seem to be a large number of free parameters, most of which depend on the current bias I_b as well, we are most interested in verifying the current-biased junction Hamiltonian, so ideally there are only a few independent choices to be made. For example, the critical current I_0, capacitance C_J, and I_b specify ω_{nm} and Γ_n. A single value for the relaxation time T_1, in addition to T, sets the values of all of the dissipation rates, assuming the matrix elements $\gamma_{n,m}$ of the tilted washboard. The same values of $\gamma_{n,m}$ also give all of the Ω_{nm}, with a single conversion factor between source power P_s and, for example, Ω_{01}. I also chose to set all of the coherence times to the same value T_2. A strong constraint is that the set of parameters should be able to fully explain a wide variety of experiments, including slowly sweeping the bias at elevated temperature, a multi-level Rabi oscillation caused by a microwave pulse, and a T_1 relaxation after the pulse is turned off.

I used the density matrix to simulate the Rabi oscillations in Figs. 9.2 and 9.3. We believe there was significant population in at least three energy level, because the escape rates saturated at ever increasing equilibrium values as the microwave power was increased. The simplest test of the simulation was to see if it could reproduce the equilibrium escape rate values Γ_{eq}. This was a valuable test, because

Γ_{eq} depends strongly on the energy levels, escape rates, and matrix elements, but relatively weakly on T_1 and T_2, given the large range of powers being considered.

The circles in Fig. 9.9 show Γ_{eq} as a function of the measured oscillation frequency $\overline{\Omega}_{R,01}$ for the curves in Fig. 9.2 and several others not shown. I extracted both parameters from fits to Eq. (9.1), where $\Gamma_{eq} = g_1 + g_2$. The lowest point is noticeably higher on the log-log scale because the decaying background at this power lead to a poor fit. At high powers, the large background caused some of the scatter in resulting values of $\overline{\Omega}_{R,01}$.

As I mentioned in §9.1, I was unable to describe the energy levels and escape rates of SQUID DS_1 with single values of I_0 and C_J. Instead, I let the escape rates be described by $I_0^\Gamma = 34.308$ μA and $C_J^\Gamma = 4.43$ pF. Evaluating Eq. (2.43) at $I_1 = 34.069$ μA, where the experiments were performed, gives $\Gamma_0 = 6.31 \times 10^4$, $\Gamma_1 = 3.67 \times 10^7$, $\Gamma_2 = 3.33 \times 10^9$, and $\Gamma_3 = 2.80 \times 10^{10}$ 1/s. The energy levels and escape rates are specified by $I_0^\omega = 34.300$ μA and $C_J^\omega = 4.43$ pF. At $I_1 = 34.069$ μA, $\omega_{01}/2\pi = 7.60$, $\omega_{12}/2\pi = 6.34$, and $\omega_{23}/2\pi = 5.61$ GHz. I used matrix elements in the cubic approximation; several are given in Eqs. (2.38) and (2.39). As the refrigerator was at base temperature and we saw no obvious signs of heating due to the microwave pulse, I usually set $T = 0$. Based on the experiment in §7.4.2, I set $T_1 = 14$ ns. The choice of $T_2 = 7$ ns will be motivated below.

With this set of parameters, I evolved the density matrix with a 5 ps time step to calculate the occupancies ρ_i. From these results, I fit the escape rate [defined in Eq. (3.30)] to Eq. (9.1) in order to extract $\overline{\Omega}_{R,01}$ and Γ_{eq}.[7] The solid line in Fig. 9.9(a) shows the results for a two-level system. Γ_{eq} saturates at roughly $\Gamma_1/2$ as $|0\rangle$ and $|1\rangle$ become equally populated at high power (after the system loses phase coherence).

[7] I ran all of the simulations at $I_b = 34.069$ μA (just as with the experiments), even though this does not correspond to resonance at high power. As a result, $\overline{\Omega}_{R,01} < \Omega_{01}$ because the suppression of $\Omega_{R,01}$ outweighs the effects of detuning. Unlike the data, I held I_b fixed for simulation, on the assumption that the slow ramp did not result in a significant amount of detuning for the short times being considered.

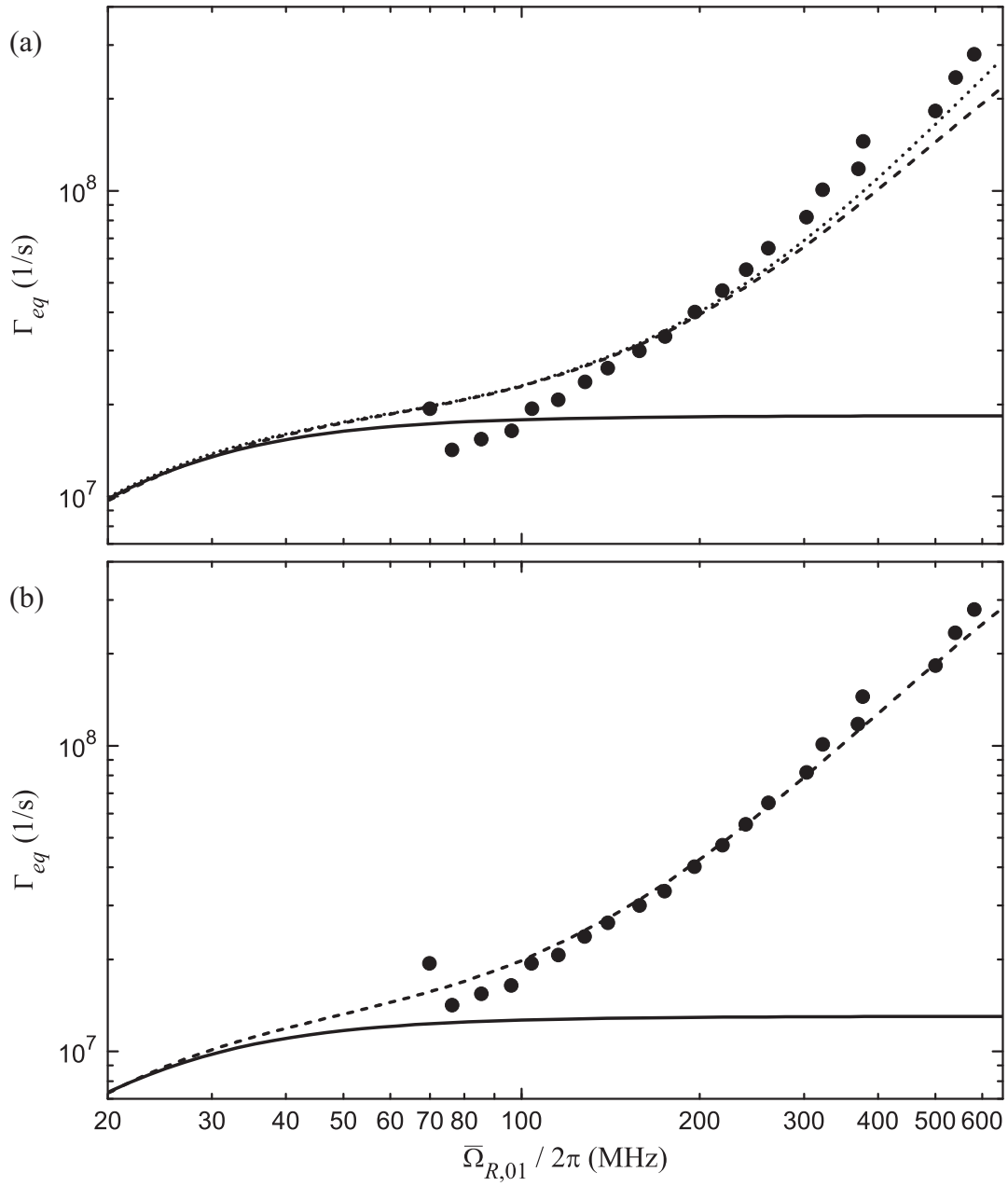

Figure 9.9: Power dependence of Γ_{eq} in SQUID DS_1. The circles show the equilibrium escape rate Γ_{eq} as a function of the measured oscillation frequency $\overline{\Omega}_{R,01}$, for the same data set as in Fig. 9.3. (a) Density matrix simulations with two (solid line), three (dashed), and four (dotted) levels, using junction parameters from independent measurements, underestimate Γ_{eq} at high power. (b) With modified Γ_1, Γ_2, and ω_{12}, the agreement for the three-level system is better.

Equation (3.60) predicts this should happen for $\Omega_{01} \gg 1/\sqrt{T_1 T_2} \approx 2\pi \cdot 16$ MHz, consistent with the simulation.

Since Γ_{eq} clearly exceeded $\Gamma_1/2$ at high power, higher levels are needed to explain the observed escape rates. The second excited state is populate by a two-photon process with a quadratic power dependence, which explains the rapid increase in Γ_{eq} with $\overline{\Omega}_{R,01}$. The dashed line in Fig. 9.9(a) shows simulation results for a three-level system. While the intermediate powers match relatively well, there is significant disagreement at the low and high ends. A fourth level could be necessary at the highest powers. With $I_r \approx 0.993$, the properties of this level will not be well described by Eqs. (2.43) and (2.44); nonetheless, the dotted line comes from a four-level simulation with the parameters listed above. Even the extremely high escape rate of this level cannot account for the observed Γ_{eq} at high power. Despite the nearly 50% disagreement between experiment and theory, the results are still encouraging, because all of the simulation parameters came from low power (or zero power) experiments and predictions from the simple junction Hamiltonian.

To proceed, I decided to change some of the parameters "by hand." It seemed clear that Γ_1 was too large, so I decreased it from 3.67×10^7 to 2.6×10^7 1/s. This is the value that Γ_1 takes at $I_1 = 34.064$ μA, 5 nA smaller than where the experiments were performed. While there is a redistribution of currents with the quantum state [73], the shift is only expected to decrease the qubit current by about 2.5 nA for this device. In addition, the escape rate contribution from $|2\rangle$ was insufficient in Fig. 9.9(a). I decided to increase $\omega_{12}/2\pi$ from 6.34 to 6.45 GHz (to bring the $1 \rightarrow 2$ transition closer to resonance) and increase Γ_2 from 3.33×10^9 to 4×10^9 1/s. The modified ω_{12} and Γ_2 occur at $I_1 = 34.066$ and 34.073 μA, respectively. The quantum simulations suggest that the qubit current decreases for $|2\rangle$ by roughly 6 nA, with respect to the value for $|0\rangle$. This shift would increase ω_{12} (consistent with the modified value I chose), but decrease Γ_2 (inconsistent with my

choice). Although it is difficult to justify the new set of parameters, it is interesting to see how sensitive the results are to such small modifications.

The results of two- and three-level simulations with the three modified parameters are shown with a solid and dashed lines in Fig. 9.9(b). The agreement for the three-level system is good at all but the highest powers, where a fourth level might be necessary. The same results could have been obtained by, for example, increasing Γ_2 to 5×10^9 1/s and leaving ω_{12} untouched. Further work is needed to determine the most realistic junction parameters and obtain the highly accurate values needed for these simulations.

The next thing I used the simulations for was to determine what causes the escape rate in Fig. 9.2 to slowly reach the equilibrium value and why the oscillation amplitude, or "visibility," is small at high power. While insufficient time resolution would decrease the oscillation amplitude, it would not cause the first maximum to occur at a lower Γ than the second. Another possibility is that the shape of the microwave pulse could result in an anomalous Rabi curve. In fact, a pulse that turns on too quickly can excite population to $|2\rangle$ [113]. That the high power curves do not decay with time in Fig. 9.2 suggests that this is not a serious problem for those experiments. A direct measurement of the pulse shape would be very useful in resolving this matter, but it would have to be done near the device, as there could be distortion along the coaxial line in the refrigerator. I estimated the time resolution of the switching measurement in §5.5 to be less than 1 ns. It was difficult to get an accurate number as there are so many places where errors were introduced. Thus, I chose to treat the pulse shape and time resolution as free parameters.

Figure 9.10(a) shows the escape rate generated by a three-level density matrix with the modified system parameters and a $\omega_{rf}/2\pi = 7.6$ GHz microwave pulse, with $\Omega_{01}/2\pi = 260$ MHz. As indicated by the dashed line, I used a square pulse, *i.e.* one that turns on and off instantaneously, that was on between $t = 0$ and 23.5

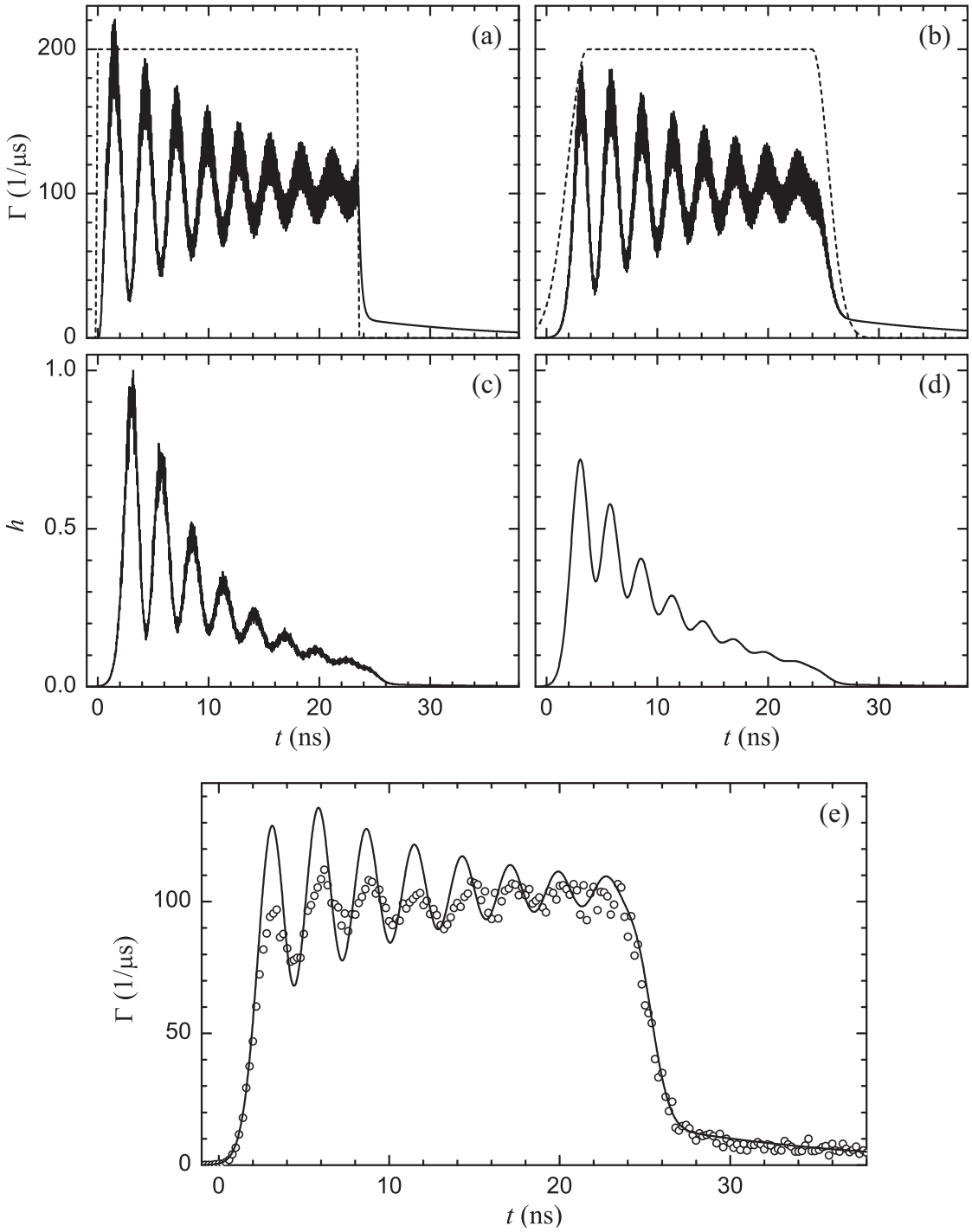

Figure 9.10: Loss of visibility in Rabi oscillations. The density matrix was used to calculate the total escape rate for Rabi oscillations at $\Omega_{01}/2\pi = 360$ MHz with (a) a square microwave pulse of frequency $\omega_{rf}/2\pi = 7.6$ GHz and (b) a pulse that rises and falls with a half-Gaussian profile; the dashed lines show the functions that provided the overall scaling for all of the Rabi frequencies. Histograms for the Gaussian pulse are shown (c) before and (d) after averaging with a time resolution of 1.2 ns. (e) The resulting Γ (solid line) has reduced visibility, but still overestimates the oscillation amplitude of SQUID DS_1 taken at $P_S = -12$ dBm (circles).

ns. During the pulse, the oscillations decay with time constant T', much like in a two-level system. The nearly solid band in Γ during the pulse is due to a highly detuned fast oscillation between $|1\rangle$ and $|2\rangle$. When the pulse turns off, $|2\rangle$ quickly depopulates due to Γ_2. Following this, $|1\rangle$ empties due to Γ_1 and T_1, leading to slow decay for $t > 24$ ns.

In Fig. 9.10(b), I attempted to simulate a realistic pulse by weighting the Ω_{nm} with a time-dependent envelope function, also shown with a dashed line. The pulse turns on with a half-Gaussian line shape, with a 2.5 ns full width. $\Omega_{01}/2\pi$ stays at 260 MHz between 3.7 and 24 ns and then decays to 0 with a half-Gaussian line shape of width 2 ns. Based on the manufacturer's specifications, rise and fall times of this order are to be expected for the microwave source. Of course, reflections in the microwave lines could lead to a completely different rise time. With the modified pulse shape, the escape rate has noticeably slower transition edges. In addition, the second oscillation maximum is slightly higher that the first.

Using the inverse of the process described in §6.2, I converted Γ to a (normalized) switching histogram, as shown in Fig. 9.10(c). Even though the escape nearly reaches equilibrium by the end of the pulse, the number of counts in the histogram decays exponentially.

To mimic the experimental time resolution, I used a Gaussian average of the histogram. That is, if $h(t_i)$ is the number of counts in the bin centered at time t_i, then the number of counts in this bin in the smoothed histogram is

$$h'(t_i) = \frac{\sum_j h(t_j)\, G(t_j - t_i, w)}{\sum_j G(t_j - t_i, w)}, \tag{9.2}$$

where $G(t, w)$ is a Gaussian centered at $t = 0$ with a full width w. Figure 9.10(d) shows the resulting histogram with $w = 1.2$ ns. Although this time is longer than the controlled experiments of §5.5 would suggest, we have never seen an escape rate

feature with a time constant faster than 1 ns, so this value does not seem entirely unrealistic. As a result of the smoothing, the rapid oscillations have been averaged away and the amplitude of the main $0 \rightarrow 1$ oscillation is also smaller.

The solid line in Fig. 9.10(e) is the escape rate calculated from the smoothed histogram. Nearly identical results can be obtained by averaging the escape directly, but that procedure is slightly less justifiable than working with the histogram. The oscillations are centered about 10^8 1/s, just as in Fig. 9.10(a), but their amplitude is much smaller.

The circles in Fig. 9.10(e) show the measured escape rate of SQUID DS_1 due to a 7.6 GHz microwave pulse of source power $P_S = -12$ dBm. The measured Γ has the same frequency and equilibrium level Γ_{eq} as the simulation, which can also be seen in Fig. 9.9(b). In addition, the fast decay starting at $t = 24$ ns matches the prediction, which is a result of the pulse shape and the smoothing; Γ_2 by itself would have lead to a much faster rate. However, the pulse shape has little impact on the subsequent slower decay that begins near $\Gamma = 1.5 \times 10^7$ 1/s. The population in $|1\rangle$ that decays is established during the oscillation, but is hidden by $P_2\Gamma_2$. By turning the pulse off and letting $|2\rangle$ depopulate, the contribution from $|1\rangle$ is visible. The agreement here is a good indicator that T_1 and Γ_1 are faithfully reproducing the junction dynamics. I have not shown that at longer times Γ decays with a time constant of roughly 50 ns, as in Fig. 8.21. The three-level simulation cannot account for both a 10 ns and a 50 ns decay of $|1\rangle$.

The critical feature of the data that is not captured by the simulation is the oscillation amplitude. The first oscillation can be brought to a lower level by further rounding of the pulse shape. However, if Ω_{01} is kept at low levels for a longer time, the oscillation frequency is noticeably slower, which is not seen in the data. The visibility could be reduced by degrading the time resolution. This is inconsistent with the oscillation amplitude we see for very high power. Thus, there appears to

be a key element of simulation that has not been included.

I made further tests of the accuracy of the simulations by examining the variation of the Rabi oscillations with power and time. The symbols in Fig. 9.11 show measured Rabi oscillations, taken under the same bias conditions as Fig. 9.10(e), for (a) a long pulse and (b) a 24 ns wide pulse. The curves are offset vertically and labeled with the microwave source power. The solid lines comes from the density matrix, using the same system parameters and processing shown in Fig. 9.10. I only varied the overall scaling of the Rabi frequencies Ω_{nm}. For source powers of $P_S = -28, -26, -24, -22, -20, -18, -16$ dBm, $\Omega_{01}/2\pi = 65$, 75, 89, 112, 137, 174, 216, 270 MHz.

For the intermediate powers, the agreement between data and simulation is good, both for the main oscillation and the decay. I chose $T_2 = 7$ ns to match the decay envelope of these data. The agreement is good, but not perfect. At high powers, the maximum visibility of the simulated curves is higher than the measurements, as discussed earlier. In addition, at the highest powers we measured, the value of Γ_{eq} is not reproduced by the simulations. At the low powers, the simulation overestimates the measured curves and does not capture the decay correctly, perhaps indicative of an incorrect Γ_1. At the lowest power in Fig. 9.11(a), Γ decays noticeably. This could be due to detuning effects, as the bias was slowly ramped during the oscillation.

Some of the disagreement at low power may be due to low frequency noise in I_b or I_0, which I have not considered. Imagine a simple scenario where during each cycle of the experiment, I_b took a slightly different value. This would mean that the microwaves would not be on resonance and the effective Rabi frequency would increase according to Eq. (3.12). As we extract Γ from a large number of trials, this inhomogeneous broadening could lead to what looks like poor timing resolution. In §8.3, the full width of the resonance peaks of DS_1 were about 4 nA, which places an upper bound on the current noise. For the conditions of Fig. 9.11, a shift in

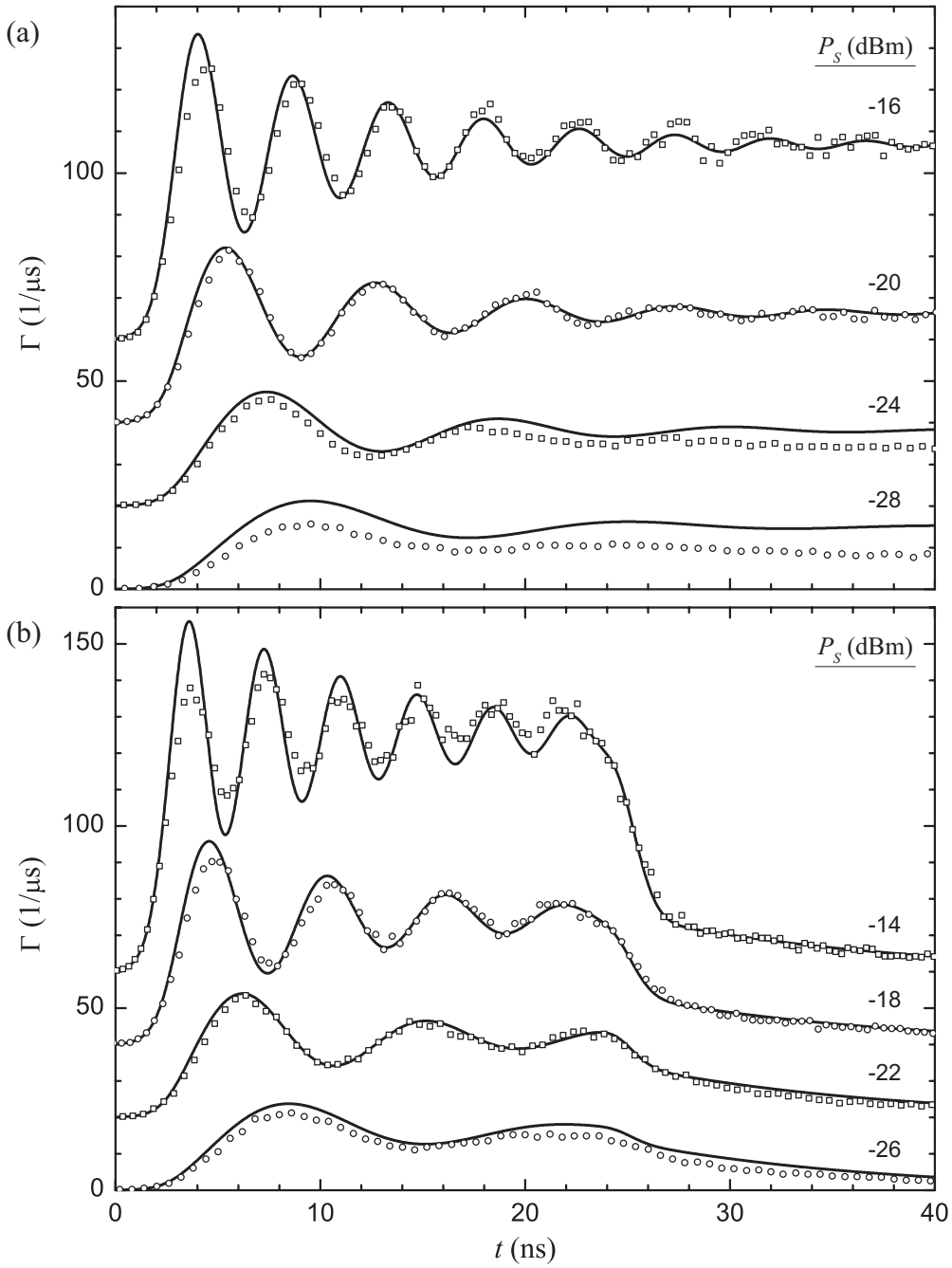

Figure 9.11: Density matrix simulations of Rabi oscillations in SQUID DS_1. The symbols show the total escape rate (vertically offset for clarity) due to a $\omega_{rf}/2\pi =$ 7.6 GHz microwave pulse of the indicated source power and a duration of (a) 3 μs and (b) 24 ns. The solid lines come from a three-level density matrix simulation, where only the overall scaling of the bare Rabi frequencies Ω_{nm} is varied between the different curves.

I_b of 2 nA results in $\omega_{01}/2\pi$ changing by less than 30 MHz. Thus for a 200 MHz Rabi oscillation, this amount of detuning is negligible. However, low frequency noise could explain the lower than expected escape rates at low power. It could also be responsible for the shorter Rabi decay envelope times T' seen in Fig. 9.3(b) at low P_S.

A weakness of the escape rate measurement is that it is only sensitive to the sum of the tunneling contributions from all of the levels, as $\Gamma = \sum_i P_i \Gamma_i$, where P_i is the normalized occupation probability of state $|i\rangle$ (see §3.5). In order to determine P_i, at the very least the individual escape rates Γ_i must be known accurately. Even if the sum is dominated by one term, for example $P_2\Gamma_2$ for high power Rabi oscillations, the difficulty of predicting Γ_2 results in a large uncertainty in P_2. Thus, it is not easy to compare the populations predicted by the density matrix simulation with measurements. Some of these issues are addressed in Fig. 9.12. The measured escape rate of SQUID DS_2B due to a resonant 6.2 GHz microwave pulse (with a power of $P_S = -17$ dBm and width of 26 ns) as a function of time is plotted with circles in Fig. 9.12(a).

Under identical conditions, the bias pulse readout method (see §6.6.3) was used to measure P_1 and P_2, as plotted with circles in Fig. 9.12(b) and (c). Details of this readout technique can be found in Ref. [104]. In the absence of a microwave current, the probability that the junction switched to the voltage state due to a *dc bias pulse* added to I_b was determined for a wide range of pulse amplitudes. Then the same set of dc bias pulses were applied to the junction at a certain time during a Rabi oscillation, which was due to a *microwave pulse*. Finally, the state populations needed to explain the new switching probabilities were extracted. For example, if the system occupied $|1\rangle$ during the oscillation, then a relatively small bias pulse would result in a high probability of switching to the voltage state. Knowledge of the escape rate during a pulse (and not just the resulting switching probability)

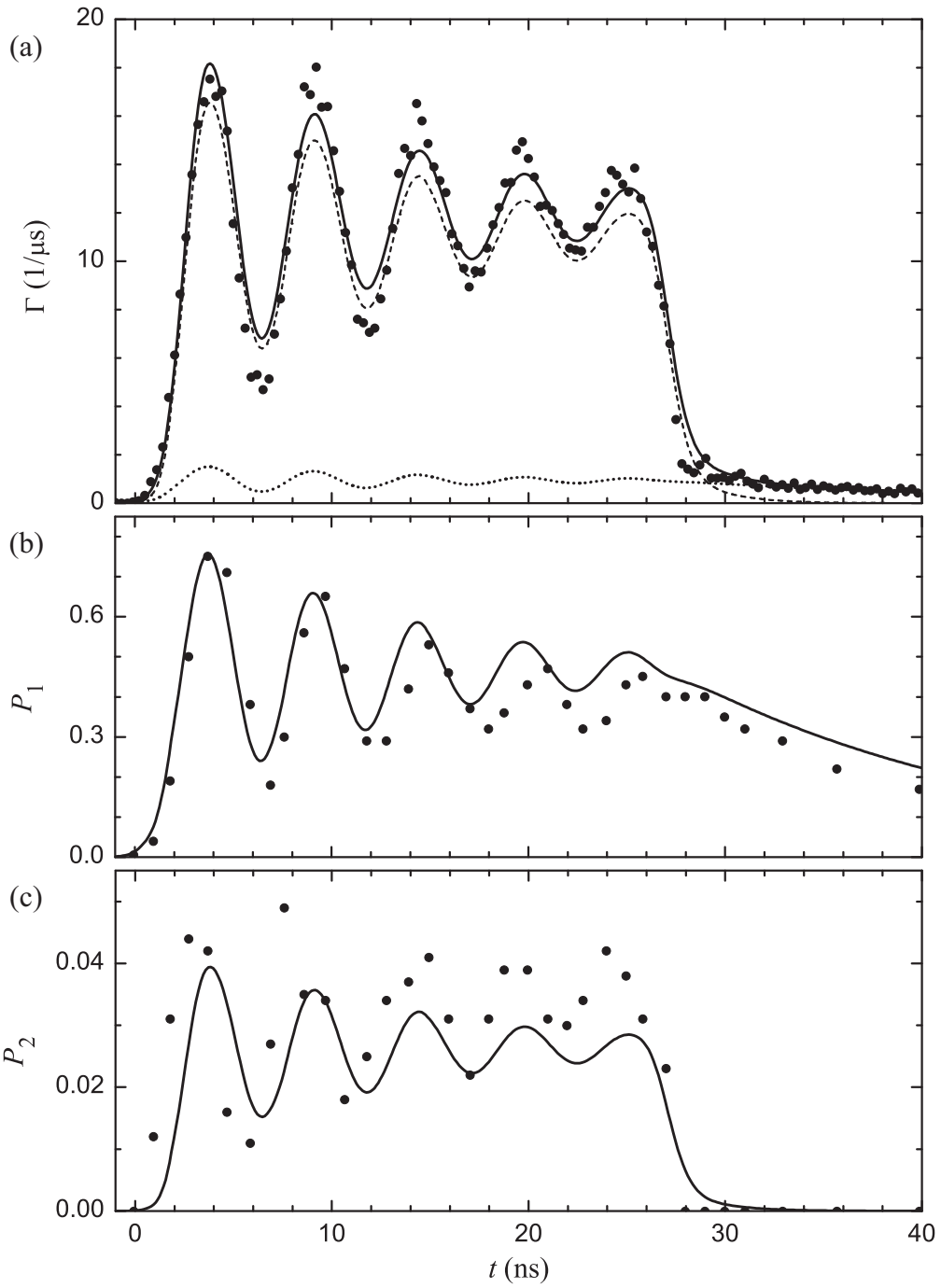

Figure 9.12: Escape rate and current pulse measurements of Rabi oscillations in SQUID DS_2B. Rabi oscillations due to a resonant 6.2 GHz microwave pulse with $P_S = -17$ dBm were readout with two techniques and modeled with a density matrix simulation. (a) The solid circles show the measured escape rate Γ, continuously measured during the oscillation. The simulation gives the total escape rate (solid line), as well the contributions from $|1\rangle$ (dotted) and $|2\rangle$ (dashed). As shown with circles, the bias pulse readout allows direct measurement of (b) P_1 and (c) P_2. The solid lines in (b) and (c) come from the same density matrix simulation that produced the escape rates. The data set was taken at 20 mK by Tauno Palomaki.

made it possible to extract P_2 as well. This procedure was repeated at several points along the Rabi oscillation and decay, to map out the populations as a function of time.

I attempted to reproduce the escape rate and pulsed measurements with a single density matrix simulation; results are shown with solid lines in Fig. 9.12. The qubit junction of DS_2B was roughly described by single junction parameters $I_0 = 18.138$ μA and $C_J = 4.50$ pF. At $I_b = 17.955$ μA, Eq. (2.43) gives $\Gamma_0 = 3.78 \times 10^3$, $\Gamma_1 = 2.88 \times 10^6$, and $\Gamma_2 = 5.28 \times 10^8$ 1/s, while Eq. (2.44) returns $\omega_{01}/2\pi = 6.20$ and $\omega_{12}/2\pi = 5.51$ GHz. As with SQUID DS_1 above, I had to modify some of the parameters to find agreement with the measured escape rate. I chose $\Gamma_1 = 2 \times 10^6$ and $\Gamma_2 = 4.2 \times 10^8$ 1/s, and $\omega_{12}/2\pi = 5.58$ GHz. In addition, T_1 and T_2 were set to 17 and 8 ns, respectively; relaxation rates cames from Eq. (3.26), evaluated with matrix elements in the cubic approximation. For the microwave pulse, I used the same profiles and time averaging given in Fig. 9.10 and a bare Rabi frequency of $\Omega_{01}/2\pi = 190$ MHz.

The agreement between the simulation and the measured escape rate in Fig. 9.12(a) is reasonable, although the decay envelope is not reproduced exactly. In addition, the data decays more quickly than the simulation when the pulse turns off. It is possible that the time resolution was slightly better than 1.2 ns for this data set. The simulation also gives P_1, which agrees well with the data [see Fig. 9.12(b)], aside from a slight difference in the decay rate for $t > 30$ ns. The population P_2 in the second excited state [see Fig. 9.12(c)] is roughly reproduced by the simulation, confirming that a reasonable value of Γ_2 was used. However, for $t > 10$ ns, the simulation predicts a noticeable decay in P_2 that is not seen in the data. Oddly, fairly good agreement is found for $T_1 = 50$ ns, which is the slower time constant we see in the decay following a high power Rabi oscillation.

The two measurement techniques complement each other well. The escape

rate is particularly sensitive to a small population in $|2\rangle$, while it is relatively easy to measure the large population in $|1\rangle$ with the pulsed readout. Even though the density matrix simulation is far from perfect (it only works for a small range of powers, for example), it is encouraging that it can reproduce the results from both readouts.

With some confidence that the simulation is generating accurate values, the total escape rate in Fig. 9.12(a) can be broken into its components; the dashed line is $P_2\Gamma_2$ and the dotted is $P_1\Gamma_1$. This shows that the majority of the measured Γ actually comes from $|2\rangle$, even when we wanted to drive the $0 \rightarrow 1$ transition. However, the plot shows that P_2 essentially follows P_1, because the $1 \rightarrow 2$ transition is being driven well off resonance. Thus the effect of the tunneling from $|2\rangle$ is to amplify P_1. Even though we are measuring P_2 with the escape rate, we can get an idea of Ω_{01}. This is why the oscillation frequency in Fig. 9.3(a) followed the expected dependence of a two-level system, even when there was such clear evidence for a third level.

The density matrix can be used to further examine the effect of $|2\rangle$. The solid lines in Fig. 9.12 show the populations for the simulation in Fig. 9.13. P_1 and P_0 oscillate out of phase about 48%. The dashed lines were generated with the same simulation parameters, except Ω_{02}, Ω_{12}, and Ω_{22} were set to zero, which removed $|2\rangle$ from the dynamics. Now the oscillation is centered about 50%, but there are no significant qualitative changes.

It is possible that tunneling to the voltage state is responsible for some of the observed decoherence; this effect can be studied with the simulations as well. With $\Gamma_0 = \Gamma_1 = 0$ and the second excited state removed, P_1 changes by a maximum of only 0.001 during the oscillation as compared to the case with finite tunneling. As $1/\Gamma_1$ is long compared to T_1 and T_2, tunneling has a negligible impact on the populations during a Rabi oscillation, but it does make a slightly larger contribution

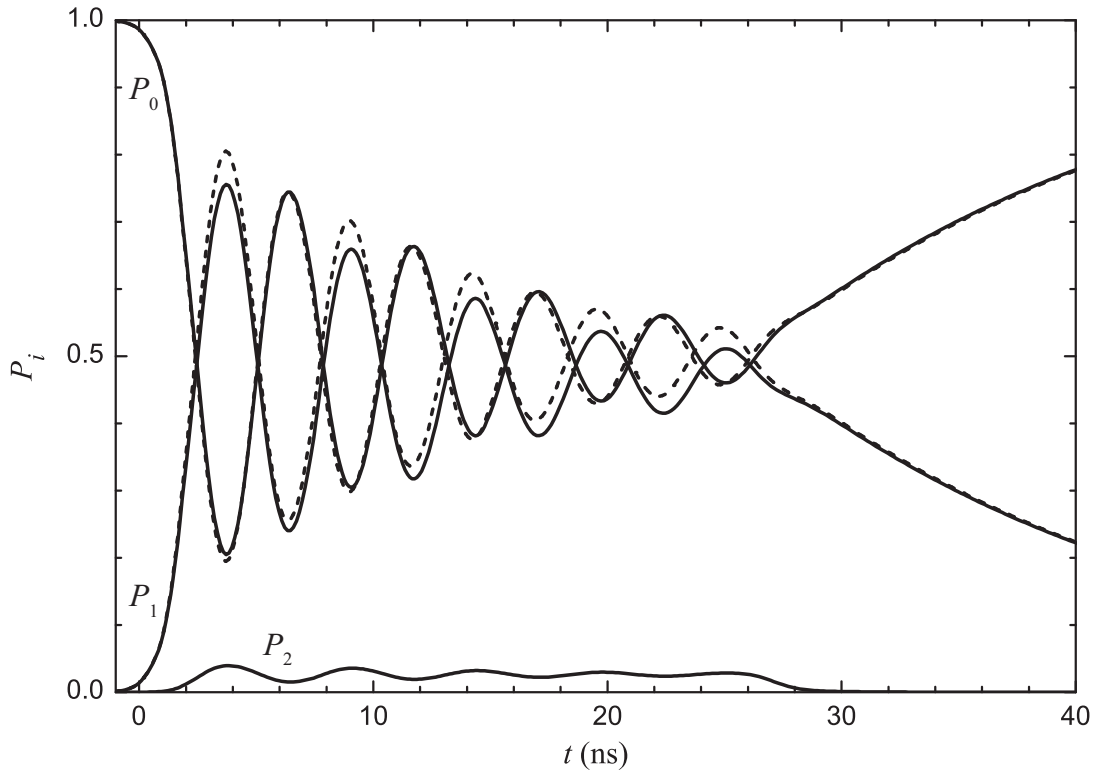

Figure 9.13: Effect of $|2\rangle$ on $0 \rightarrow 1$ Rabi oscillations. The three-level simulation used in Fig. 9.12 gives the occupation probabilities P_0, P_1, and P_2 (solid lines). The probabilities calculated for a two-level system oscillate about 50% (dashed lines).

to the decay once the microwaves are turned off. For the simulations in Fig. 9.11, the maximum change in P_1 due to tunneling is 0.01. Even though Γ_1 is an order of magnitude larger for the conditions of that figure, tunneling has a small effect on the Rabi decay envelope.

9.4 Summary

For quantum computation, Rabi oscillations represent a coherent manipulation of the state of the qubit. In practice, our junction devices are not two-level systems and it is important to understand the dynamics of the actual system. For example, we see clear evidence of leakage to the second excited state at the high powers that are needed to realize fast quantum gates (§9.1). This appears to be due to a

two-photon process, involving off-resonant $0 \rightarrow 1$ and $1 \rightarrow 2$ transitions.

The oscillations offer a way to confirm our understanding of the Hamiltonian. The measured oscillation frequency is consistent with a three-level rotating wave model, which requires the matrix elements and energy levels of the single junction Hamiltonian (§9.2). The shift of resonance at high power is a particularly sensitive test of the system parameters.

These measurements also provide estimates for the time constants that determine the quality of the qubit. The observed power broadening of the $0 \rightarrow 1$ transition corresponds to $T_1 \approx T_2 \approx 4$ ns. Such short values are inconsistent with T_1 measurements of the previous chapters and with the average Rabi decay time $T' = 10$ ns. I used a density matrix simulation to model the dynamics during a microwave pulse. This was a useful test, because in a single Γ curve, the escape rate during the pulse depends strongly on Γ_2, energy levels, and the matrix elements, while the decay after the pulse reveals T_1 and Γ_1. I had to make certain assumptions about the shape of the microwave pulse and the timing resolution in the experiment, but the data of SQUID DS_1 are consistent with $T_1 \approx 14$ ns and $T_2 \approx 7$ ns. Further work is needed to explain the observed loss of visibility at high power.

Chapter 10
Conclusions

10.1 The DiVincenzo Criteria Revisited

In this thesis, I have discussed the implementation of Nb/AlOx/Nb Josephson junction devices as phase qubits for quantum computation. I would first like to summarize the status of the work in view of the DiVincenzo criteria [19–21], given in §1.1.

Hilbert space control: The dynamics of a current-biased junction are analogous to a particle (with a mass proportional to the junction capacitance) in the tilted washboard potential. The two lowest energy levels of this anharmonic potential can serve as qubit states (§2.3). Care must be taken so as not to occupy the higher excited states. Microwave spectroscopy provides clear evidence for quantized energy levels (§8.1 and §8.2) that can be tuned with an external current bias during the course of an experiment. Additional qubits can be added to the full state space by capacitively coupling junctions (§8.6). In the future, a variable coupling scheme may be required [145].

State preparation: Initialization of our qubits is most easily accomplished by cooling the devices below 50 mK, so that the system occupies the energetic ground state. Active methods may also work at higher temperatures (§7.5), but we have not implemented any such technique. For a SQUID phase qubit, the flux state can be initialized with flux shaking (§6.5), a procedure which appears to work for a wide range of device parameters and for coupled qubits.

Low decoherence: The trade-off that comes with the ease of controlling the energy levels of the qubit is that the bias lines originate at room temperature, leading to an unacceptable level of dissipation. I have studied two types of isolation: an

LC filter that is particularly effective at high frequencies (§4.2) and a broadband inductive current divider that results in a dc SQUID (§4.3). In addition, it may be that junction quality plays an important role in decoherence, as we see evidence for coupling to microstates that may be due to defects in the barrier (§8.5). For the SQUID phase qubits I examined, I estimate the coherence time T_2 to be under 10 ns. The time scale for a gate operation is set by the plasma frequency $\omega_p/2\pi \approx 5$ GHz of the junction, with a typical two-qubit gate taking roughly 10 ns [112]. Thus, far better coherence times are required for quantum computation, but studies of error correction can perhaps begin soon.

Controlled unitary transformations: A microwave current can be used to induce transitions between $|0\rangle$ and $|1\rangle$, with Rabi oscillations representing a simple single qubit gate (§9.1). Two-qubit gates may be performed by bringing the junctions in resonance with each other [112]. While I did map out the energy level structure of two coupled qubits (§8.6), I did not do any experiments where the state of the coupled system was coherently controlled.

State-specific quantum measurements: Measuring the tunneling escape rate of a junction from the supercurrent to the finite voltage state is a simple way to perform state measurement (§6.2). This technique is extremely sensitive to population in the excited state, but some modeling is required to accurately extract the individual state occupation probabilities (§9.3). The use of a microwave (§8.7.1) or current (§6.6.3) pulse will be more suitable for state readout. However, all three of these techniques are very destructive; not only is there significant heat generated, but the system leaves the computational space and takes substantial time to reset.

Quantum communication: I did not do any work on the conversion of stationary to flying qubits and this criterion is not of much relevance to solid state qubits that are coupled by wires.

10.2 Summary of Experiments

Many of the experiments I performed tested the validity of the Hamiltonian of the current-biased junction, given in Eq. (2.23). The hope is that a detailed understanding of the systems will aid in the design of better qubits in the future. The single-junction Hamiltonian describes a circuit with three main components: a current source, an ideal junction, and its shunting capacitance. In contrast, our phase qubits are made from a multi-layer fabrication process involving different materials and are controlled by a potentially noisy current source through a series of on- and off-chip filters that allow some coupling to the environment. An additional complication for the dc SQUID phase qubits is that each of the two junctions represent a quantum degree of freedom. We attempted to reproduce single junction behavior by holding the designated isolation junction well out of resonance with the qubit junction (§6.4).

A strong test of our description of the circuits was reproducing the escape rate during Rabi oscillations using a density matrix simulation (§9.3). This generic three-level simulation required many input parameters that were checked independently through a series of experiments. The escape rate of the ground state was measured directly (§7.2), while theoretical predictions for the excited states were tested at elevated temperatures with master equation simulations (§7.4). The $0 \rightarrow 1$ transition frequency was mapped out with spectroscopy, which also showed the existence of levels above the two qubit states and of multi-photon transitions that are the leading cause of leakage out of the $|0\rangle$ and $|1\rangle$ qubit basis (§8.4). Finally the matrix elements of the phase operator $\hat{\gamma}$ that characterize transitions were verified by comparing the Rabi oscillation frequency at high powers to a three-level rotating wave Hamiltonian §9.2.

Another objective of the work was to characterize the quality of the qubits for

Table 10.1: Summary of characteristic times. The relaxation time T_1, coherence time T_2, spectroscopic coherence time T_2^*, and Rabi decay time T' were estimated several ways for the three devices. The first line is a purely theoretical prediction; the rest of the values were extracted from experiments. The measurements were performed for qubit plasma frequencies 5 GHz $< \omega_p/2\pi <$ 10 GHz. For the coupled devices, the measurements were performed on one qubit, while the other was held well out of resonance.

Time	Method	LC_2	DS_1	DS_2
T_1	Design prediction	5 μs	200 ns	200 ns
	IV curve	$>$ 400 ns		
	Thermal activation	8 ns	10 - 30 ns	10 - 30 ns
	Master equation	4 ns	14 ns	
	Fast ramp	$<$ 50 ns		$<$ 50 ns
	Time domain; μwave pulse		45 ns	
	Time domain; tunneling		10 / 50 ns	10 / 50 ns
	Power broadening		4 ns	
T_2	Power broadening		4 ns	
	Density matrix		7 ns	8 ns
T_2^*	Spectroscopy	3 ns	4 ns	8 ns
T'	Rabi oscillations		5 - 15 ns	5 - 20 ns

quantum computation. Results are summarized in Table 10.1 for the capacitively-coupled LC-isolated junctions (device LC_2), the single dc SQUID phase qubit (DS_1), and the capacitively-coupled dc SQUID phase qubits (DS_2). For the coupled devices, most of the measurements happened to be on LC_2B and DS_2B, but we never saw any dramatic differences with LC_2A and DS_2A, which they were coupled to. I will mostly focus on the dc SQUID phase qubits below, as our measurements were incomplete for the LC-isolated junctions and their performance was not as good.

Although the coherence time T_2 is the most relevant parameter for characterizing a qubit's utility for quantum computation, the dissipation time T_1 serves as an upper bound on T_2 (actually, $2T_2 < T_1$, using the common definitions) and is an

important measure of the isolation of the qubit. In addition, one of the biggest mysteries in the superconducting quantum computing community has been the short T_1 values, regardless of the qubit type, so it is useful to measure dissipation with a variety of techniques.

Measurement of the IV curve of a junction gives an estimate for the intrinsic dissipation at low frequency, through the sub-gap resistance and retrapping current. For our Hypres junctions, the shunting resistance R_J appears to be greater than 100 kΩ. With a typical junction capacitance of $C_J = 4$ pF, this would correspond to $T_1 = R_J C_J > 400$ ns. However, this represents a "high power" measurement and there may be less dissipation at high powers if saturation of two-level systems occurs.

We performed two types of measurements of T_1 at the plasma frequency of the junction. T_1 leads to a dissipation rate that is balanced by other processes in the junction, such as tunneling and microwave activation. Measurement of the populations after equilibrium has been established can give estimates for T_1; these experiments can be done on long time scales. Analysis of the escape rate with classical thermal activation was inconclusive, yielding a possible range between $T_1 =$ 10 and 30 ns (§7.1.2). I used a quantum master equation simulation to analyze the same data, which gave 14 ns (§7.4.2). A related technique is to increase the bias ramp rate until it moves the system away from dynamic equilibrium (§7.5). As we never obtained positive results, I can only say $T_1 < 50$ ns. The dependence of the $0 \rightarrow 1$ resonance width on the applied power depends on T_1; the extracted value was roughly 4 ns (§9.1).

Alternatively, energy relaxation can be measured in the time domain, by creating an excited state population resonantly, and monitoring the system as it returns to dynamic equilibrium. This method showed the presence of two time constants (of roughly 10 and 50 ns) for the decay of population in $|1\rangle$ (§8.7.2). A low power

measurement only detected the slower of the two (§8.7.1).

The coherence time T_2 can also be measured. We measured a maximum spectroscopic coherence time $T_2^* \approx 8$ ns and this parameter is susceptible to dissipation, decoherence, and low frequency noise (§8.3). The same power broadening measurement mentioned earlier suggested $T_2 \approx 4$ ns. Finally, the Rabi decay time T' was about 10 ns at intermediate powers (§9.1), which corresponds to $T_2 = 7.5$ ns for $T_1 = 15$ ns. Density matrix simulations with $T_2 \approx 7$ ns accurately reproduced the observed decay envelope of Rabi oscillations for a range of powers.

There is a significant uncertainty in the determination of T_1, but the values are far below the value of 200 ns predicted if the noise on the bias lines is characterized by a 50 Ω resistance (§4.3). While it is clear that T_1 is not limited by intrinsic dissipation of the junction at low frequency, high frequency materials properties may be causing serious problems. It will be crucial to uncover whether the two decay time constants, splittings in the spectra, and short T_1 and T_2 are related.

Although there clearly are a great number of important questions to answer and inconsistencies to resolve at this early stage in the research, superconducting circuits hold a great deal of potential for realizing a quantum computer.

Appendix A
Circuit Hamiltonians

This appendix gives the general procedure for deriving the Hamiltonian of an electrical circuit. I applied this method to several devices in Chapter 2. The procedure begins by identifying the equations of motion that describe the circuit, generally obtained from Kirchhoff's law and other constraints, such as flux quantization for superconducting circuits. A generalized coordinate q_i in these equations could be the phase difference across a junction, the charge on a capacitor, or the flux in a loop.

A valid Lagrangian $\mathcal{L}$ for the system will generate the equations of motion from the Euler-Lagrange equations

$$\frac{d}{dt}\left(\frac{d\mathcal{L}}{d\dot{q}_i}\right) = \frac{\partial \mathcal{L}}{\partial q_i}. \tag{A.1}$$

With the Lagrangian in hand, the conjugate momenta p_i and Hamiltonian $\mathcal{H}$ can be found as

$$p_i = \frac{\partial \mathcal{L}}{\partial \dot{q}_i} \tag{A.2}$$

$$\mathcal{H} = \sum p_i \dot{q}_i - \mathcal{L}. \tag{A.3}$$

Here, $\mathcal{H} = \mathcal{H}(p_i, q_i)$ and the generalized velocities $\dot{q}_i$ may be eliminated using Eq. (A.2). In addition, $\mathcal{H}$ obeys Hamilton's equations:

$$\dot{p}_i = -\frac{\partial \mathcal{H}}{\partial q_i} \tag{A.4}$$

$$\dot{q}_i = +\frac{\partial \mathcal{H}}{\partial p_i}. \tag{A.5}$$

Proceeding in this formal way will guarantee that the Hamiltonian is expressed

in terms of operators that are conjugate pairs ($[\hat{q}_i, \hat{p}_i] = i\hbar$), which is required for a quantum mechanical treatment. To obtain Schrödinger's equation in coordinate space, one just makes the substitutions

$$\hat{p}_i = \frac{\hbar}{i}\frac{\partial}{\partial \hat{q}_i}. \tag{A.6}$$

It is often the case that the Lagrangian for a system can be written as a simple sum:

$$\mathcal{L} = \mathcal{L}_1\left(q_i, \dot{q}_i\right) + \mathcal{L}_2\left(q_j, \dot{q}_j\right) + \mathcal{L}_C\left(q_i, \dot{q}_i, q_j, \dot{q}_j\right), \tag{A.7}$$

where $\mathcal{L}_1$ and $\mathcal{L}_2$ are the Lagrangians for two sub-systems and $\mathcal{L}_C$ characterizes the coupling between them (and introduces no additional degrees of freedom). Equation (A.2) gives the momenta

$$p_i = \frac{\partial \mathcal{L}_1}{\partial \dot{q}_i} + \frac{\partial \mathcal{L}_2}{\partial \dot{q}_i} + \frac{\partial \mathcal{L}_C}{\partial \dot{q}_i} \tag{A.8}$$

and Eq. (A.3) gives the Hamiltonian of the full system

$$\begin{aligned} \mathcal{H} &= \sum_i \left(\frac{\partial \mathcal{L}_1}{\partial \dot{q}_i}\dot{q}_i + \frac{\partial \mathcal{L}_C}{\partial \dot{q}_i}\dot{q}_i\right) + \sum_j \left(\frac{\partial \mathcal{L}_2}{\partial \dot{q}_j}\dot{q}_j + \frac{\partial \mathcal{L}_C}{\partial \dot{q}_j}\dot{q}_j\right) - \mathcal{L}_1 - \mathcal{L}_2 - \mathcal{L}_C & \text{(A.9)} \\ &= \mathcal{H}_1\left(q_i, \dot{q}_i\right) + \mathcal{H}_2\left(q_j, \dot{q}_j\right) + \mathcal{H}_C\left(q_i, \dot{q}_i, q_j, \dot{q}_j\right), & \text{(A.10)} \end{aligned}$$

where the contribution from the coupling is

$$\mathcal{H}_C = \sum_i \frac{\partial \mathcal{L}_C}{\partial \dot{q}_i}\dot{q}_i + \sum_j \frac{\partial \mathcal{L}_C}{\partial \dot{q}_j}\dot{q}_j - \mathcal{L}_C. \tag{A.11}$$

This expression shows that the system Hamiltonian is the sum of the sub-system Hamiltonians and coupling contribution, expressed in terms of the generalized coordinates and velocities. Equations (A.8) may be inverted to give $\mathcal{H} = \mathcal{H}\left(q_i, p_i, q_j, p_j\right)$.

Appendix B

MATLAB Code

The following programs calculate the eigenfunctions, energy levels, and tunneling rates of a single current-biased junction and two capacitively coupled junctions. The heart of the algorithms was written by Huizhong Xu; see §2.4 and §3.3.2 of Ref. [1].

B.1 Solutions of the Junction Hamiltonian

The programs in this section solve the Hamiltonian for a current-biased junction in the absence of dissipation, given in Eq. (2.23). The nature of these solutions is discussed in §2.3.3. `jjspectrum` is the main driver that just collects the solutions returned by `jjeigentbc`, given below. The `diary` command creates a file of everything that is dumped to the screen, which I found useful for debugging.

```
function [stuff,wavefn] = ...
  jjspectrum(Io, Cj, Iri, Irf, dIr, levelmaxIr, E0, psi0)

% [stuff, wavefn] =
%   jjspectrum(Io, Cj, Iri, Irf, dIr, levelmaxIr, E0, psi0)
% This calculates all the energies and wavefunctions for a single
% junction with critical current 'Io' (Amps), junction capacitance
% 'Cj' (Farads), from reduced bias current 'Iri' to 'Irf', in 'dIr'
% steps.  'levelmaxIr' sets the number of levels to calculate; it's
% defined in 'keeplevels'.  'E0' and 'psi0' are optional -- they
% specify the initial guesses for all the levels.  Everything sent
% back in a big structure.
% calls: hbar, keeplevels, jjeigentbc, wp, plotlevels, xaxis

more off
diary on
global hbar;
```

```
stuff.params.Io = Io;
stuff.params.Cj = Cj;
stuff.params.Iri = Iri;
stuff.params.Ifr = Irf;
stuff.params.dIr = dIr;
stuff.params.levelmaxIr = levelmaxIr;
stuff.params.start = clock;

NIr = floor( (Irf - Iri) / dIr ) + 1;

for Ircount = 1 : NIr
  Ir = Iri + (Ircount-1) * dIr;
  stuff.Ir(Ircount) = Ir;
  disp(['Reduced current ' num2str(Ir)]);

% After the first current, use the previous wavefunction as the
% initial guess.  Use the same n, which (at a higher current) will
% give a lower initial guess for the energy.

  for levelcount = keeplevels(levelmaxIr, Ir)
    disp(['Level ' num2str(levelcount)]);

    if Ircount == 1
      if nargin == 8
        % User supplied energy and wavefunction
        solution = jjeigentbc(Ir*Io, Io, Cj, length(levelmaxIr)-1,...
          E0(levelcount+1)/hbar/wp(Ir*Io, Io, Cj) - 0.5, ...
          psi0(levelcount+1,:));

      elseif nargin == 7
        % User supplied energy -- use a random initial wavefunction
        solution = jjeigentbc(Ir*Io, Io, Cj, length(levelmaxIr)-1,...
          E0(levelcount+1)/hbar/wp(Ir*Io, Io, Cj) - 0.5);

      else
        % User didn't give you anything.  Guess the energy and use a
        % random psi.
        corr = 0.15 - 5 * (1 - Ir - 0.005);
        solution = jjeigentbc(Ir*Io, Io, Cj, length(levelmaxIr)-1,...
                              levelcount*(1-corr));
      end

      stuff.params.xleft = solution.x(1);
```

```
      stuff.params.dx = solution.dx;
      stuff.params.Ngrid = length(solution.x);

    else
      solution = jjeigentbc(Ir*Io, Io, Cj, length(levelmaxIr)-1, ...
                            n0(levelcount+1), psi(levelcount+1,:));
    end

    energy = real(solution.E);
    gamma = -imag(solution.E) / (hbar/2);

    psi(levelcount+1,:) = solution.wavefn;
    n0(levelcount+1) = energy / hbar / wp(Ir*Io, Io, Cj) - 0.5;

    levstr = num2str(levelcount);
    Irstr = num2str(Ircount);
    eval(['stuff.energy' levstr '(' Irstr ') = energy;']);
    eval(['stuff.gamma' levstr '(' Irstr ') = gamma;']);
    eval(['wavefn.level' levstr '(' Irstr ',:) = solution.wavefn;']);
  end

  if Ircount == 1
    Eplot = figure;
  end

  figure(Eplot);
  plotlevels(stuff);
  xaxis([stuff.Ir(1) 1]);
  shg;
end

stuff.params.stop = clock;
more on
diary off
```

This is the primary routine that calculates the solutions for a single value of the bias current, using transmission boundary conditions.

```
function solution = jjeigentbc(Ib, Io, Cj, nmax, n0, psi0)

% solution = jjeigentbc(Ib, Io, Cj, nmax, n0, psi0)
% Calculates the energy, potential, and wavefunction (on a grid x,
```

```
% with steps dx) for bias current 'Ib', critical current 'Io',
% capacitance 'Cj', maximum number of levels 'nmax', and current
% level 'n0' (or the best guess of what it is).  'psi0' is the
% (optional) inital guess for the wavefunction.  Uses transmission
% boundary conditions.  Results sent back in a structure.
% calls: mj, wp, hbar, jjeigengrid

% Some constants
global hbar;

% Set up a grid to solve Schrodinger's eq.
[xleft, dx, Ngrid] = jjeigengrid(0.97, 0.999, Io, Cj, nmax);

disp(['xleft = ' num2str(xleft) '  dx = ' num2str(dx) '  ...
      Ngrid = ' num2str(Ngrid)]);

% This constant is in front of d2(psi)/dx2.  Multiply it over to
% V and E and call them Vp and Ep (p for prime)

m = mj(Cj);
a = 2 * m * (dx / hbar)^2;

Umin = twb(Ib, Io, asin(Ib/Io));

for i = 1 : Ngrid
  x(i) = xleft + dx * (i-1);
  Utwb(i) = twb(Ib, Io, x(i)) - Umin;
end

Uleft = Utwb(1);
Uright = Utwb(Ngrid);

% The matrix is N-2 x N-2, because the boundary conditions are
% evaluated in the 2 and N-1 equations.  Set up H*psi = E*psi.

A(1 : Ngrid-2) = -1;
C(1 : Ngrid-2) = -1;

for i = 1 : Ngrid-2
  B(i) = 2 + Utwb(i+1) * a;
end

% Here's the first guess at the eigenvalue.  Start with a random
% wavefunction (if one isn't provided) and use inverse iteration
```

```
% (Numerical Recipes 11.7) to improve it.

Ep = (n0 + 0.5) * hbar * wp(Ib, Io, Cj) * a;

if nargin == 6
  newpsi = psi0(2:end-1);
else
% This is the MATLAB R12 command
%  newpsi = random('unif', 0, 1, 1, Ngrid-2);

% This is the MATLAB R14 command
  newpsi = rand(1, Ngrid-2);
end

newpsi = newpsi / sqrt(sum(newpsi.^2));

% Boundary conditions for first go round.

Btbc = B;
Kleft = sqrt(2 * m * (Uleft - Ep/a)) / hbar;
Btbc(1) = B(1) - exp(-1 * Kleft * dx);
Kright = sqrt(2 * m * (Ep/a - Uright)) / hbar;
Btbc(Ngrid-2) = B(Ngrid-2) - exp(sqrt(-1) * Kright * dx);

% First iterate a couple times, without updating the eigenvalue.
diff = 2; err = 0;

count1 = 0;
while (diff > 1e-6) & (err == 0)
  oldpsi = newpsi;
  [temppsi, err] = tridiag(A, Btbc - Ep, C, oldpsi);
  newpsi = temppsi / sqrt( sum(abs(temppsi).^2) );
  diff = max(abs( (abs(newpsi)./abs(oldpsi)).^2 - 1 ));

  count1 = count1 + 1;
end

% Now update the energy too
oldEp = Ep;
newEp = oldEp + sum( conj(temppsi) .* oldpsi ) ...
          / sum(abs(temppsi).^2);
diff = 1;

count2 = 0;
```

```
while((diff > 1e-7) ...
    | max(abs( imag(newEp)/imag(oldEp) - 1 )) > 1e-7) & err==0
  oldpsi = newpsi;
  oldEp = newEp;

  Kleft = sqrt(2 * m * (Uleft - oldEp/a)) / hbar;
  Btbc(1) = B(1) - exp(-1 * Kleft * dx);
  Kright = sqrt(2 * m * (oldEp/a - Uright)) / hbar;
  Btbc(Ngrid-2) = B(Ngrid-2) - exp(sqrt(-1) * Kright * dx);

  [temppsi, err] = tridiag(A, Btbc - oldEp, C, oldpsi);
  newpsi = temppsi / sqrt( sum(abs(temppsi).^2) );
  diff = max(abs( (abs(newpsi)./abs(oldpsi)).^2 - 1 ));
  newEp = oldEp + sum( conj(temppsi) .* oldpsi ) ...
            / sum(abs(temppsi).^2);

  count2 = count2 + 1;
end

% So far, have been normalizing the vector psi.  But to make it
% a 'continuous' function on x, do a Riemann sum.

newpsi = -sqrt(-1) * newpsi / sqrt(dx);
wavefn = [newpsi(1)*exp(-1 * Kleft * dx) newpsi ...
          newpsi(Ngrid-2)*exp(sqrt(-1) * Kright * dx)];
wavefn = wavefn / sqrt( sum(abs(wavefn).^2) ) / sqrt(dx);

solution.E = newEp/a;
solution.x = x;
solution.Utwb = Utwb;
solution.wavefn = wavefn;
solution.dx = dx;

disp([num2str(count1) ' iterations of first loop; ' ...
      num2str(count2) ' iterations of second']);
```

This sets up the grid on which the solution is calculated.

```
function [xleft, dx, Ngrid] = jjeigengrid(Irmin, Irmax, Io, Cj, nmax)

% [xleft, dx, Ngrid] = jjeigengrid(Irmin, Irmax, Io, Cj, nmax)
% This calculates a grid for jjeigentbc.  It should select the
% smallest grid compatible for currents between 'Irmin' and 'Irmax',
```

```
% critical current 'Io', capacitance 'Cj', and maximum quantum level
% 'nmax'.  If everything is done on the same grid, then you can take
% inner products and stuff with the wavefunctions later.
% calls: mj, wp, hbar, twb

% Some constants
global hbar;
m = mj(Cj);

% Ideally, you would use the smallest range for a given Irmin/max and
% Cj.  However, this is complicated.

% First, you need to find the values of the phase, where the
% washboard hits (again) the local max (to the left) and min (to the
% right) of the first well.  The widest range of phase occurs for the
% smallest bias current.  Just pick a fixed [0.8, 2.3], which should
% cover down to Ir = 0.95.

% Then, you want enough phase outside of this to capture some
% oscillations (to the right of the well) and the decay (to the
% left).  This is set by the constant alpha below.  The longest
% spatial scale occurs at the highest current, opposite of the
% previous paragraph -- ignore this.  Don't really know how many of
% these spatial constants to keep.  This should be optimized.

wpmin = wp(Irmax*Io, Io, Cj);
alphamin = sqrt(m*wpmin/hbar);
wpmax = wp(Irmin*Io, Io, Cj);
alphamax = sqrt(m*wpmax/hbar);

xleft = 0.8 - 4/alphamin;
xright = 2.3 + 4/alphamin;

% Next get the step size, which is based on the oscillations of the
% highest energy you plan to calculate.  These should be evaluated at
% the highest current, where the potential is steep and the energy
% differences are large.

xmin = asin(Irmax);
Umin = twb(Irmax*Io, Io, xmin);
Uleft = twb(Irmax*Io, Io, xleft) - Umin;
Uright = twb(Irmax*Io, Io, xright) - Umin;

Emax = (nmax + 0.5) * hbar * wpmax;
```

```
lambdal = sqrt(2*m * (Uleft - Emax)) / hbar;
lambdar = sqrt(2*m * (Emax - Uright)) / hbar;
dx = 1 / max([alphamax lambdal lambdar]) / 10;

Ngrid = floor((xright - xleft) / dx) + 1;
```

Finally, the main M-files above call several simple routines, given below. In addition, global variables called `hbar` and `Phio` (which, not surprisingly, are equal to $\hbar$ and Φ_0) should be defined in the workspace.

```
function levels = keeplevels(levelmaxIr, Ir)

% levels = keeplevels(levelmaxIr, Ir)
% This returns a vector of the levels to keep at a given reduced bias
% current, 'Ir'.  'levelmaxIr'(i) gives the reduced current where the
% (i-1)th state leaves the well (or least where you don't want it
% anymore).  If you should keep it, i-1 is included in 'levels'.
% 0 is the ground state.  The number of elements in 'levelmaxIr' sets
% the maximum number of levels to keep.

levels = [];
for i = 1 : length(levelmaxIr)
  if Ir <= levelmaxIr(i)
    levels = [levels i-1];
  end
end
```

```
function omegap = wp(Ib, Io, C);

% wp(Ib, Io, C) gives the plasma frequency of a junction

global Phio;
omegap = sqrt(2*pi*Io/C/Phio) .* (1-(Ib./Io).^2).^(1/4);
```

`plotlevels` plots the energy levels as the solutions are calculated. Running the program for a large number of bias currents can be time-taking, so this is a useful way of spotting trouble early.

```
function plotlevels(eigenstuff)

% plotlevels(eigenstuff)
% This assumes 'eigenstuff' has fields named Ir and energy0, energy1.

colors = 'bgrcmy';
plotcnt = 0;

fields = fieldnames(eigenstuff);

for i = 1 : length(fields)
  if strncmp(fields(i), 'energy', 6) == 1
    data = getfield(eigenstuff, char(fields(i)));
    plot(eigenstuff.Ir(1:length(data)), data, ...
      colors(mod(plotcnt, 6) + 1));
    hold on
    plotcnt = plotcnt + 1;
  end
end



function xaxis(xbounds)

% xaxis([xmin xmax])
% This replots the current graph, using new x bounds.

graphaxes = axis;
graphaxes(1) = xbounds(1);
graphaxes(2) = xbounds(2);
axis(graphaxes);



function mass = mj(Cj);

% mass = mj(Cj) returns the phase particle mass, given the junction
% capacitance.
% calls: Phio

global Phio;
mass = Cj * (Phio/2/pi)^2;
```

```
function U = twb(Ib, Io, gamma);

% U = twb(Ib, Io, gamma) returns the tilted washboard potential.
% calls: Phio

global Phio;
U = -Phio/2/pi * (Io * cos(gamma) + Ib * gamma);
```

B.2 Solutions of the Coupled-Junction Hamiltonian

Equation (2.74) gives the Hamiltonian for two capacitively-coupled current-biased junctions. Solutions of it can be expressed in terms of the uncoupled junction basis (which can be calculated with the programs of the previous section). The Hamiltonian was derived under the assumption that the two junction had the same capacitance. In the program, the uncoupled states are calculated with potentially different capacitances, while the strength of the coupling depends on the average of the two capacitances.

```
function [Nlevel1, EVs, WFs, EVs1, WFs1, EVs2, WFs2] = ...
  coupledjj(Io1, Cj1, Io2, Cj2, Cc, Ir1, Ir2, EVs1, EVs2, WFs1, WFs2)

% [Nlevel1, EVs, WFs, EVs1, WFs1, EVs2, WFs2] = ...
% coupledjj(Io1, Cj1, Io2, Cj2, Cc, Ir1, Ir2, EVs1, EVs2, WFs1, WFs2)
% This gives the solutions for two capacitively coupled junctions,
% with critical currents 'Io1' and 'Io2' (in Amps), capacitances
% 'Cj1' and 'Cj2' (in Farads), coupling capacitor 'Cc', at reduced
% bias currents 'Ir1' and 'Ir2'.  All the input parameters are single
% numbers.
%
% 'EVs1', 'WFs1', 'EVs2', and 'WFs2' are optional arguments that give
% the initial guess for the energies and wavefunctions for
% jjeigentbc.m.  Pass in both energies or all four.
%
% 'Nlevel1' is the number of levels kept for JJ1.  'EVs' and 'WFs'
% are the complex eigenvalues and wavefunctions (in terms of the
% coupled state basis), both sorted in order of increasing energy.
% The first row is for the ground state.  The last four outputs are
```

```
% for the uncoupled junctions.
%
% calls: hbar, Phio, momentumH, wp

global hbar Phio;

% Get the effective capacitances, from the coupled Hamiltonian.

Ceff1 = Cj1 * (1 + Cc/(Cc+Cj1));
Ceff2 = Cj2 * (1 + Cc/(Cc+Cj2));

% Get the coupling parameter for equivalent junctions; pull out the
% hbars from the momentum terms.

Cavg = (Cj1 + Cj2)/2;
zavg = Cc/(Cc + Cavg);
coupling = -1*hbar^2 * zavg / Cavg / (1+zavg) / (Phio/2/pi)^2;

if nargin == 7
  [momH1, EVs1, WFs1] = momentumH(Ir1, Io1, Ceff1);
  Nlevel1 = length(EVs1);

  [momH2, EVs2, WFs2] = momentumH(Ir2, Io2, Ceff2);
  Nlevel2 = length(EVs2);
else
% jjeigentbc wants the level number n, not energy

  n0s1 = real(EVs1) / hbar / wp(Ir1*Io1, Io1, Cj1) - 0.5;
  n0s2 = real(EVs2) / hbar / wp(Ir2*Io2, Io2, Cj2) - 0.5;

  if nargin == 9
    [momH1, EVs1, WFs1] = momentumH(Ir1, Io1, Ceff1, n0s1);
    [momH2, EVs2, WFs2] = momentumH(Ir2, Io2, Ceff2, n0s2);
  else
    [momH1, EVs1, WFs1] = momentumH(Ir1, Io1, Ceff1, n0s1, WFs1);
    [momH2, EVs2, WFs2] = momentumH(Ir2, Io2, Ceff2, n0s2, WFs2);
  end

  Nlevel1 = length(EVs1);
  Nlevel2 = length(EVs2);
end

% Form the coupled Hamiltonian.  The order of the basis vectors
% |jj#1 jj#2>: |0 0>, |0 1>, |0 2>, ..., |0 N2>, |1 0>, |1 1>, ...,
```

```
% |1 N2>, ..., |N1 N2>.  i labels rows; j labels columns.

for i1 = 1 : Nlevel1
  for i2 = 1 : Nlevel2
    row = (i1-1)*Nlevel2 + i2;
    for j1 = 1 : Nlevel1
      for j2 = 1 : Nlevel2
        col = (j1-1)*Nlevel2 + j2;
        coupledH(row,col) = coupling * momH1(i1,j1) * momH2(i2,j2);
        if row == col
          coupledH(row,row) = coupledH(row,row) + EVs1(i1)+EVs2(i2);
        end
      end
    end
  end
end

[WFs, eigenvalm] = eig(coupledH);

for i = 1 : Nlevel1*Nlevel2
  EVs(i) = eigenvalm(i,i);
end

energy = real(EVs);
[energy, order] = sort(energy);
EVs = EVs(order);
WFs = WFs(:, order);
WFs = WFs';
```

`coupledjj` calls `momentumH`, which forms the momentum coupling term in the Hamiltonian. It calls a function `DU`, which just returns the tilted washboard barrier.

```
function [momH, EVs, WFs] = momentumH(Ir, Io, Cj, n0s, WF0s)

% [momH, EVs, WFs] = momentumH(Ir, Io, Cj, n0s, WF0s)
% This calculates the matrix representation 'momH' of the momentum
% operator for a single junction, (apart from h/i) at a reduced
% current 'Ir'.  It also returns the complex eigenvalues 'EVs' and
% wavefunctions 'WFs' for all the levels in the well (where the first
% row is the ground state).  The junction critical current 'Io' is in
% Amps and its capacitance 'Cj' is in Farads.
%
```

```
% 'n0s' and 'WF0s' are optional arguments that specify initial
% guesses for the energy level number and wavefunction (for
% jjeigentbc).  'n0s' should be a vector, where the first entry is
% for the ground state.  If you want to pass in 'WF0s', then both
% parameters must be passed in.  'WF0s' should be 2D, where the first
% row is the ground state.  They both must be long enough, so this
% only works if you are doing a positive sweep and the number of
% levels can only decrease.
%
% calls: hbar, Phio, DU, wp, jjeigentbc

global hbar Phio;

m = Cj * (Phio/2/pi)^2;

% Overestimate the number of levels in the well, to give a good basis

Nlevel = floor( DU(Ir*Io, Io) / hbar / wp(Ir*Io, Io, Cj) ) + 2;

% Get the energy and wavefunction for each level, with an initial
% energy guess slightly smaller than harmonic states.

corr = 0.10 - 10*(1-Ir-0.007);

for i = 1 : Nlevel
  disp(['Level ' num2str(i) ' of ' num2str(Nlevel)]);

  if nargin == 3
    jjsoln = jjeigentbc(Ir*Io, Io, Cj, Nlevel, (i-1)*(1-corr));

  elseif nargin == 4
    jjsoln = jjeigentbc(Ir*Io, Io, Cj, Nlevel, n0s(i));

  elseif nargin == 5
    jjsoln = jjeigentbc(Ir*Io, Io, Cj, Nlevel, n0s(i), WF0s(i, :));
  end

  U = jjsoln.Utwb;
  EVs(i) = jjsoln.E;
  Ngrid = length(jjsoln.wavefn);
  WFs(i, 1:Ngrid) = jjsoln.wavefn;
  dx = jjsoln.dx;
end
```

```
% Calculate dpsi/dx.  The left BC is exponential decay; the right is
% plane wave -- jjeigentbc calculates the wavefunction past the right
% side of the well.

dWFs = WFs;

for i = 1 : Nlevel
  dWFs(i, 2:Ngrid-1) = (WFs(i, 3:Ngrid) - WFs(i, 1:Ngrid-2)) / 2/dx;

  E = real(EVs(i));
  lambdal = sqrt(2*m * (U(1) - E)) / hbar;
  dWFs(i,1) = dWFs(i,2) * exp(lambdal*dx);

  lambdar = sqrt(2*m * (E - U(Ngrid))) / hbar;
  dWFs(i, Ngrid) = dWFs(i,Ngrid-1) * ...
    ( cos(lambdar*dx) + sqrt(-1)*sin(lambdar*dx) );
end

% Integrate psistar * dpsi

for i = 1 : Nlevel
  for j = 1 : i
    momH(i,j) = sum( conj(WFs(i,1:Ngrid)) .* dWFs(j,1:Ngrid) ) * dx;
    if i ~= j
      momH(j,i) = conj(momH(i,j));
    end
  end
end
```

Appendix C

Three-Level Rotating Wave Approximation

This appendix gives the Hamiltonian of a generic three-level system in the rotating wave approximation. Details of the derivation are due to Fred Strauch [2, 83].

In matrix form, the Hamiltonian for a three-level system (with orthonormal basis $|0\rangle$, $|1\rangle$, $|2\rangle$) under an oscillatory perturbation of angular frequency ω_{rf} can be written as

$$\mathcal{H} = \begin{pmatrix} E_0 & 0 & 0 \\ 0 & E_1 & 0 \\ 0 & 0 & E_2 \end{pmatrix} + A\cos\omega_{rf}t \begin{pmatrix} y_{0,0} & y_{0,1} & y_{0,2} \\ y_{0,1}^* & y_{1,1} & y_{1,2} \\ y_{0,2}^* & y_{1,2}^* & y_{2,2} \end{pmatrix}, \tag{C.1}$$

where the position matrix elements $y_{n,m} = \langle n \,|\, \hat{y} \,|\, m \rangle$ of the perturbation are dimensionless. Let $\psi = c_0\,|0\rangle + c_1\,|1\rangle + c_2\,|2\rangle$ be a solution of Schrödinger's equation, $\mathcal{H}\psi = i\hbar\dot{\psi}$. Thus for example, $i\hbar\dot{c}_0 = \mathcal{H}_{0,0}c_0 + \mathcal{H}_{0,1}c_1 + \mathcal{H}_{0,2}c_2$. Here, $\mathcal{H}_{n,m} = \langle n \,|\, \mathcal{H} \,|\, m \rangle$; for example, $\mathcal{H}_{0,0} = E_0 + Ay_{0,0}\cos\omega_{rf}t$.

Consider the time-dependent transformation $\widetilde{c}_i = e^{i\phi_i(t)}c_i$, where $i = 1, 2, 3$. Then the state vector $\widetilde{\psi} = \widetilde{c}_0\,|0\rangle + \widetilde{c}_1\,|1\rangle + \widetilde{c}_2\,|2\rangle$ will be a solution of $\widetilde{\mathcal{H}}\widetilde{\psi} = i\hbar\dot{\widetilde{\psi}}$. The coefficients of $|0\rangle$ in the modified Schrödinger's equation satisfy

$$\begin{aligned} i\hbar\frac{d\widetilde{c}_0}{dt} &= -\hbar\frac{d\phi_0}{dt}\,e^{i\phi_0}\,c_0 + i\hbar e^{i\phi_0}\frac{dc_0}{dt} && \text{(C.2)} \\ &= \left(\mathcal{H}_{0,0} - \hbar\frac{d\phi_0}{dt}\right)\widetilde{c}_0 + \mathcal{H}_{0,1}\,\widetilde{c}_1\,e^{i(\phi_0-\phi_1)} + \mathcal{H}_{0,2}\,\widetilde{c}_2\,e^{i(\phi_0-\phi_2)}, && \text{(C.3)} \end{aligned}$$

from which the identifications $\widetilde{\mathcal{H}}_{0,0} = \mathcal{H}_{0,0} - \hbar\dot{\phi}_0$, $\widetilde{\mathcal{H}}_{0,1} = \mathcal{H}_{0,1}\,e^{i(\phi_0-\phi_1)}$, $\widetilde{\mathcal{H}}_{0,2} = \mathcal{H}_{0,2}\,e^{i(\phi_0-\phi_2)}$ can be made. The remaining elements of $\widetilde{\mathcal{H}}$ can be found by examining

the coefficients of $|1\rangle$ and $|2\rangle$: $\widetilde{\mathcal{H}}_{1,1} = \mathcal{H}_{1,1} - \hbar\dot{\phi}_1$, $\widetilde{\mathcal{H}}_{1,2} = \mathcal{H}_{1,2}\, e^{i(\phi_1-\phi_2)}$, $\widetilde{\mathcal{H}}_{2,2} = \mathcal{H}_{2,2} - \hbar\dot{\phi}_2$.

The values of $\phi_i(t)$ are chosen to give the rotating frame of interest. For a single photon transition between $|0\rangle$ and $|1\rangle$, the appropriate choices are

$$\phi_0 = \frac{E_0}{\hbar}t + \frac{Ay_{0,0}}{\hbar\omega_{rf}}\sin\omega_{rf}t \tag{C.4}$$

$$\phi_1 = \left(\frac{E_0}{\hbar} + \omega_{rf}\right)t + \frac{Ay_{1,1}}{\hbar\omega_{rf}}\sin\omega_{rf}t \tag{C.5}$$

$$\phi_2 = \left(\frac{E_0}{\hbar} + 2\omega_{rf}\right)t + \frac{Ay_{2,2}}{\hbar\omega_{rf}}\sin\omega_{rf}t. \tag{C.6}$$

Then, the time dependence of the diagonal elements of $\widetilde{\mathcal{H}}$ vanishes. Each off-diagonal matrix element will contain the exponential of a sine, which can be expanded as sum of Bessel functions of the first kind using the identity

$$e^{ix\sin\theta} = \sum_{n=-\infty}^{+\infty} J_n(x)\, e^{in\theta}. \tag{C.7}$$

So the matrix element responsible for the $0 \rightarrow 1$ transition becomes

$$\widetilde{\mathcal{H}}_{0,1} = Ay_{0,1}\cos\omega_{rf}t\; e^{-i\omega_{rf}t}\exp\left[i\frac{A(y_{0,0}-y_{1,1})}{\hbar\omega_{rf}}\sin\omega_{rf}t\right] \tag{C.8}$$

$$= Ay_{0,1}\cos\omega_{rf}t\; e^{-i\omega_{rf}t}\sum_{n=-\infty}^{+\infty} J_n\left(\frac{A(y_{0,0}-y_{1,1})}{\hbar\omega_{rf}}\right)e^{in\omega_{rf}t} \tag{C.9}$$

$$\approx \frac{Ay_{0,1}}{2}\left[J_0\left(\frac{A(y_{0,0}-y_{1,1})}{\hbar\omega_{rf}}\right) + J_2\left(\frac{A(y_{0,0}-y_{1,1})}{\hbar\omega_{rf}}\right)\right], \tag{C.10}$$

where in the last expression, only terms in the infinite sum with no time dependence have been kept. This amounts to making the rotating wave approximation. The remaining elements of $\widetilde{\mathcal{H}}$ can be found in a similar way, resulting in the Hamiltonian given in Eq. (3.14) through Eq. (3.17).

Appendix D

Dynamical Evolution Matrices

D.1 Density Matrix

The evolution matrix for the Liouville-von Neumann equation in Eq. (3.68), for the transitions that we are interested in, can be expressed as

$$\underline{P} = -i\underline{E} - \underline{G} + \underline{D} - i\underline{M}\cos\left(\omega_{rf}t\right), \tag{D.1}$$

where the structure of each of the matrices is described next.

The convention I will follow is that the elements ρ_{ij} of the density matrix are ordered in a vector, such that i is fixed while cycling through j. For example, $\boldsymbol{\rho} = [\rho_{00}, \rho_{01}, \rho_{02}, \rho_{10}, \rho_{11}, \rho_{12}, \rho_{20}, \rho_{21}, \rho_{22}]$ for $N = 3$. Then, ρ_{ij} will be element number $\alpha \equiv (ij)_N + 1$ in this vector, where the number in parentheses is expressed in base N and N is the number of levels in the system.[1] For $N = 3$, ρ_{21} is element number $(2 \times 3 + 1 \times 1 + 1) = 8$.

An element of the energy matrix $\underline{E}$ depends on the static Hamiltonian and can be found directly from Eq. (3.35) as $i\hbar\dot{\rho}_{ij} = \sum_m \left(\mathcal{H}^0_{im}\rho_{mj} - \rho_{im}\mathcal{H}^0_{mj}\right)$. $\mathcal{H}^0$ is diagonal, so each sum has only one element: $i\hbar\dot{\rho}_{ij} = E_i\rho_{ij} - \rho_{ij}E_j = \left(E_i - E_j\right)\rho_{ij}$. Therefore, $\underline{E}$ is diagonal, with $E_{\alpha\alpha} = (\omega_i - \omega_j)$.

In the simple way that we have decided to include tunneling, the matrix $\underline{G}$ is also diagonal; $G_{\alpha\alpha} = \left(\Gamma_i + \Gamma_j\right)/2$.

The matrix $\underline{D}$ accounts for dissipation and decoherence. Each is described by $N\left(N-1\right)/2$ time constants, which represent transitions between pairs of states. As in the previous section, decoherence is assumed to make a diagonal contribution

[1] In this appendix, Roman letters are quantum state indices and run from 0 to $N-1$, while Greek letters index the vectors and matrices in Eq. (3.68) and run between 1 and N^2.

$D_{\alpha\alpha} = -1/T_2^{ij}$, for $i \neq j$. Typically, I set all of the times T_2^{ij} to the same value T_2, as I had no physical reason not to.

On the assumption that dissipation affects only state populations ρ_{ii}, only the elements $D_{\beta\delta}$ are non-zero, where $\beta = (ii)_N + 1$ and $\delta = (jj)_N + 1$. For $\beta < \delta$, $D_{\beta\delta} = W_{ij}^t = \Gamma_{ij} / \left(1 - e^{-\hbar\omega_{ij}/k_B T}\right)$, to account for gains in $|i\rangle$ due to dissipation from all higher states $|j\rangle$. The spontaneous emission rate Γ_{ij} and total thermal rate W_{ij}^t are defined in §3.4. For $\beta > \delta$, $D_{\beta\delta} = W_{ij}^t = \Gamma_{ji} / \left(e^{\hbar\omega_{ji}/k_B T} - 1\right)$ to account for gains in $|i\rangle$ due to thermal excitations from all lower states $|j\rangle$. The diagonal term $D_{\beta\beta} = -\sum_{\delta \neq \beta} D_{\delta\beta}$ to account for losses in $|i\rangle$ due to both up and down transitions.

The microwave drive is characterized by $(N+1)\,N/2$ matrix elements between each pair of quantum states of the form $\Omega_{ij} \equiv \langle i \,|\, \gamma I_{\mu w} \,|\, j \rangle / \hbar$, with $\Omega_{ij} = \Omega_{ji}^*$. The evolution matrix $\underline{M}$ is largely banded, but I found no obvious pattern to simply describe it. There are N^2 equations of the form $\dot{\rho}_{ij} = -i\left(\Omega_{im}\rho_{mj} - \Omega_{mj}\rho_{im}\right)$, which can be used to fill out $\underline{M}$.

For $N = 3$, the matrices are

$$\underline{E} = \begin{pmatrix} 0 & 0 & 0 & 0 & 0 & 0 & 0 & 0 & 0 \\ 0 & -\omega_{01} & 0 & 0 & 0 & 0 & 0 & 0 & 0 \\ 0 & 0 & -\omega_{02} & 0 & 0 & 0 & 0 & 0 & 0 \\ 0 & 0 & 0 & \omega_{01} & 0 & 0 & 0 & 0 & 0 \\ 0 & 0 & 0 & 0 & 0 & 0 & 0 & 0 & 0 \\ 0 & 0 & 0 & 0 & 0 & -\omega_{12} & 0 & 0 & 0 \\ 0 & 0 & 0 & 0 & 0 & 0 & \omega_{02} & 0 & 0 \\ 0 & 0 & 0 & 0 & 0 & 0 & 0 & \omega_{12} & 0 \\ 0 & 0 & 0 & 0 & 0 & 0 & 0 & 0 & 0 \end{pmatrix}, \qquad \text{(D.2)}$$

$$\underline{G} = \begin{pmatrix} \Gamma_0 & 0 & 0 & 0 & 0 & 0 & 0 & 0 & 0 \\ 0 & \frac{\Gamma_0+\Gamma_1}{2} & 0 & 0 & 0 & 0 & 0 & 0 & 0 \\ 0 & 0 & \frac{\Gamma_0+\Gamma_2}{2} & 0 & 0 & 0 & 0 & 0 & 0 \\ 0 & 0 & 0 & \frac{\Gamma_0+\Gamma_1}{2} & 0 & 0 & 0 & 0 & 0 \\ 0 & 0 & 0 & 0 & \Gamma_1 & 0 & 0 & 0 & 0 \\ 0 & 0 & 0 & 0 & 0 & \frac{\Gamma_1+\Gamma_2}{2} & 0 & 0 & 0 \\ 0 & 0 & 0 & 0 & 0 & 0 & \frac{\Gamma_0+\Gamma_2}{2} & 0 & 0 \\ 0 & 0 & 0 & 0 & 0 & 0 & 0 & \frac{\Gamma_1+\Gamma_2}{2} & 0 \\ 0 & 0 & 0 & 0 & 0 & 0 & 0 & 0 & \Gamma_2 \end{pmatrix}, \quad \text{(D.3)}$$

$$\underline{D} = \begin{pmatrix} -W_{k0}^t & 0 & 0 & 0 & W_{01}^t & 0 & 0 & 0 & W_{02}^t \\ 0 & -\frac{1}{T_2^{01}} & 0 & 0 & 0 & 0 & 0 & 0 & 0 \\ 0 & 0 & -\frac{1}{T_2^{02}} & 0 & 0 & 0 & 0 & 0 & 0 \\ 0 & 0 & 0 & -\frac{1}{T_2^{01}} & 0 & 0 & 0 & 0 & 0 \\ W_{10}^t & 0 & 0 & 0 & -W_{k1}^t & 0 & 0 & 0 & W_{12}^t \\ 0 & 0 & 0 & 0 & 0 & -\frac{1}{T_2^{12}} & 0 & 0 & 0 \\ 0 & 0 & 0 & 0 & 0 & 0 & -\frac{1}{T_2^{02}} & 0 & 0 \\ 0 & 0 & 0 & 0 & 0 & 0 & 0 & -\frac{1}{T_2^{12}} & 0 \\ W_{20}^t & 0 & 0 & 0 & W_{21}^t & 0 & 0 & 0 & -W_{k2}^t \end{pmatrix}, \quad \text{(D.4)}$$

where $W_{k0}^t \equiv W_{10}^t + W_{20}^t$, $W_{k1}^t \equiv W_{01}^t + W_{21}^t$, $W_{k2}^t \equiv W_{02}^t + W_{12}^t$, and

$$\underline{M} = \begin{pmatrix} 0 & -\Omega_{01}^* & -\Omega_{02}^* & \Omega_{01} & 0 & 0 & \Omega_{02} & 0 & 0 \\ -\Omega_{01} & 0 & -\Omega_{12}^* & 0 & \Omega_{01} & 0 & 0 & \Omega_{02} & 0 \\ -\Omega_{02} & -\Omega_{12} & 0 & 0 & 0 & \Omega_{01} & 0 & 0 & \Omega_{02} \\ \Omega_{01}^* & 0 & 0 & 0 & \Omega_{01}^* & -\Omega_{02}^* & \Omega_{12} & 0 & 0 \\ 0 & \Omega_{01}^* & 0 & -\Omega_{01} & 0 & -\Omega_{12}^* & 0 & \Omega_{12} & 0 \\ 0 & 0 & \Omega_{01}^* & -\Omega_{02} & -\Omega_{12} & 0 & 0 & 0 & \Omega_{12} \\ \Omega_{02}^* & 0 & 0 & \Omega_{12}^* & 0 & 0 & 0 & -\Omega_{01}^* & -\Omega_{02}^* \\ 0 & \Omega_{02}^* & 0 & 0 & \Omega_{12}^* & 0 & -\Omega_{01} & 0 & -\Omega_{12}^* \\ 0 & 0 & \Omega_{02}^* & 0 & 0 & \Omega_{12}^* & -\Omega_{02} & -\Omega_{12} & 0 \end{pmatrix} . \quad \text{(D.5)}$$

D.2 Master Equations

The evolution matrix $\underline{p}$ in Eq. (7.9) for solving the master equations is quite similar to $\underline{P}$ for the density matrix, except there are no coherence terms. As I only considered dissipation and tunneling with the master equations,

$$\underline{p} = -\underline{g} + \underline{d}. \tag{D.6}$$

The tunneling matrix $\underline{g}$ is purely diagonal with $g_{ii} = \Gamma_i$. The off-diagonal elements of the dissipation matrix $\underline{d}$ are $d_{ij} = W^t_{ij}$, where these thermal rates are given by Eqs. (3.26) and (3.27), and the diagonal elements are $d_{ii} = -\sum_{j\neq i} d_{ji}$.

For $N = 3$, the matrices are

$$\underline{g} = \begin{pmatrix} \Gamma_0 & 0 & 0 \\ 0 & \Gamma_1 & 0 \\ 0 & 0 & \Gamma_2 \end{pmatrix} \tag{D.7}$$

and

$$\underline{d} = \begin{pmatrix} -W^t_{10} - W^t_{20} & W^t_{01} & W^t_{02} \\ W^t_{10} & -W^t_{01} - W^t_{21} & W^t_{12} \\ W^t_{20} & W^t_{21} & -W^t_{02} - W^t_{12} \end{pmatrix}. \tag{D.8}$$

Bibliography

[1] H. Xu, *Quantum Computing with Josephson Junction Circuits*, Ph.D. thesis, University of Maryland, College Park (2004).

[2] F. W. Strauch, *Theory of Superconducting Phase Qubits*, Ph.D. thesis, University of Maryland, College Park (2004).

[3] A. J. Berkley, *A Josephson Junction Qubit*, Ph.D. thesis, University of Maryland, College Park (2003).

[4] F. C. Wellstood, *unpublished*.

[5] W. D. Phillips and J. V. Porto, "PHYS 721 Lecture Notes," (2005). Available at http://www.physics.umd.edu/courses/Phys721/Fall2005/.

[6] R. P. Feynman, "Simulating Physics with Computers," Int. J. Theor. Phys. **21**(6/7), 467 (1982).

[7] P. W. Shor, "Scheme for reducing decoherence in quantum computer memory," Phys. Rev. A **52**(4), R2493 (1995).

[8] A. M. Steane, "Error Correcting Codes in Quantum Theory," Phys. Rev. Lett. **77**(5), 793 (1996).

[9] J. Preskill, "Battling Decoherence: The Fault-Tolerant Quantum Computer," Phys. Today **52**(6), 24 (1999).

[10] P. W. Shor, "Polynomial-Time Algorithms for Prime Factorization and Discrete Logarithms on a Quantum Computer," SIAM J. Comput. **26**(5), 1484 (1997).

[11] L. K. Grover, "From Schrödinger's equation to the quantum search algorithm," Am. J. Phys. **69**(7), 769 (2001).

[12] A. Aspuru-Guzik, A. D. Dutoi, P. J. Love, and M. Head-Gordon, "Simulated Quantum Computation of Molecular Energies," Science **309**(5741), 1704 (2005).

[13] E. Farhi, J. Goldstone, S. Gutmann, J. Lapan, A. Lundgren, and D. Preda, "A Quantum Adiabatic Evolution Algorithm Applied to Random Instances of an NP-Complete Problem," Science **292**(5516), 472 (2001).

[14] G. Stix, "Best-Kept Secrets," Sci. Am. **292**(1), 79 (2005).

[15] J. I. Cirac and P. Zoller, "Quantum Computations with Cold Trapped Ions," Phys. Rev. Lett. **74**(20), 4091 (1995).

[16] D. Loss and D. P. DiVincenzo, "Quantum computation with quantum dots," Phys. Rev. A **57**(1), 120 (1998).

[17] B. E. Kane, "A silicon-based nuclear spin quantum computer," Nature **393**(6681), 133 (1998).

[18] N. A. Gershenfeld and I. L. Chuang, "Bulk Spin-Resonance Quantum Computation," Science **275**(5298), 350 (1997).

[19] D. P. DiVincenzo, "Topics in Quantum Computers," in *Mesoscopic Electron Transport*, edited by G. Schoen (Kluwer, 1997). Available as cond-mat/9612126.

[20] D. P. DiVincenzo and D. Loss, "Quantum information is physical," Superlattices and Microstructures **23**(3/4), 419 (1998).

[21] D. P. DiVincenzo, "The Physical Implementation of Quantum Computation," Fortschr. Phys. **48**(9-11), 771 (2000).

[22] A. O. Caldeira and A. J. Leggett, "Quantum Tunnelling in a Dissipative System," Ann. Phys. **149**(2), 374 (1983).

[23] R. F. Voss and R. A. Webb, "Macroscopic Quantum Tunneling in 1-μm Nb Josephson Junctions," Phys. Rev. Lett. **47**(4), 265 (1981).

[24] J. M. Martinis, M. H. Devoret, and J. Clarke, "Energy-Level Quantization in the Zero-Voltage State of a Current-Biased Josephson Junction," Phys. Rev. Lett. **55**(15), 1543 (1985).

[25] R. H. Koch, G. A. Keefe, F. P. Milliken, J. R. Rozen, C. C. Tsuei, J. R. Kirtley, and D. P. DiVincenzo, "Experimental Demonstration of an Oscillator Stabilized Josephson Flux Qubit," Phys. Rev. Lett. **96**(12), 127001 (2006).

[26] M. H. Devoret, A. Wallraff, and J. M. Martinis, "Superconducting Qubits: A Short Review," (2004). cond-mat/0411174.

[27] J. Q. You and F. Nori, "Superconducting Circuits and Quantum Information," Phys. Today **58**(11), 42 (2005).

[28] G. Johansson, L. Tornberg, V. S. Shumeiko, and G. Wendin, "Readout methods and devices for Josephson-junction-based solid-state qubits," J. Phys.: Condens. Matter **18**(21), S901 (2006).

[29] A. Shnirman, G. Schön, and Z. Hermon, "Quantum Manipulations of Small Josephson Junctions," Phys. Rev. Lett. **79**(12), 2371 (1997).

[30] Y. Nakamura, Yu. A. Pashkin, and J. S. Tsai, "Coherent control of macroscopic quantum states in a single-Cooper-pair box," Nature **398**(6730), 786 (1998).

[31] A. Cottet, D. Vion, A. Aassime, P. Joyez, D. Esteve, and M. H. Devoret, "Implementation of a combined charge-phase quantum bit in a superconducting circuit," Physica C **367**(1-4), 197 (2002).

[32] D. Vion, A. Aassime, A. Cottet, P. Joyez, H. Pothier, C. Urbina, D. Esteve, and M. H. Devoret, "Manipulating the Quantum State of an Electrical Circuit," Science **296**(5569), 886 (2002).

[33] J. R. Friedman, V. Patel, W. Chen, S. K. Tolpygo, and J. E. Lukens, "Quantum superposition of distinct macroscopic states," Nature **406**(6791), 43 (2000).

[34] T. P. Orlando, J. E. Mooij, L. Tian, C. H. van der Wal, L. S. Levitov, S. Lloyd, and J. J. Mazo, "Superconducting persistent-current qubit," Phys. Rev. B **60**(22), 15398 (1999).

[35] C. H. van der Wal, A. C. J. ter Haar, F. K. Wilhelm, R. N. Schouten, C. J. P. M. Harmans, T. P. Orlando, S. Lloyd, and J. E. Mooij, "Quantum Superposition of Macroscopic Persistent-Current States," **290**(5492), 773 (2000).

[36] R. C. Ramos, M. A. Gubrud, A. J. Berkley, J. R. Anderson, C. J. Lobb, and F. C. Wellstood, "Design for Effective Thermalization of Junctions for Quantum Coherence," IEEE Trans. Appl. Supercond. **11**(1), 998 (2001).

[37] S. Han, Y. Yu, X. Chu, S. Chu, and Z. Wang, "Time-Resolved Measurement of Dissipation-Induced Decoherence in a Josephson Junction," Science **293**(5534), 1457 (2001).

[38] A. J. Berkley, H. Xu, M. A. Gubrud, R. C. Ramos, J. R. Anderson, C. J. Lobb, and F. C. Wellstood, "Decoherence in a Josephson-junction qubit," Phys. Rev. B **68**(6), 060502(R) (2003).

[39] J. M. Martinis, S. Nam, J. Aumentado, and C. Urbina, "Rabi Oscillations in a Large Josephson-Junction Qubit," Phys. Rev. Lett. **89**(11), 117901 (2002).

[40] M. Steffen, M. Ansmann, R. C. Bialczak, N. Katz, E. Lucero, R. McDermott, M. Neeley, E. M. Weig, A. N. Cleland, and J. M. Martinis, "Measurement of the Entanglement of Two Superconducting Qubits via State Tomography," Science **313**(5792), 1423 (2006).

[41] A. J. Berkley, H. Xu, R. C. Ramos, M. A. Gubrud, F. W. Strauch, P. R. Johnson, J. R. Anderson, A. J. Dragt, C. J. Lobb, and F. C. Wellstood, "Entangled Macroscopic Quantum States in Two Superconducting Qubits," Science **300**(5625), 1548 (2003).

[42] A. Wallraff, T. Duty, A. Lukashenko, and A. V. Ustinov, "Multiphoton transitions between energy levels in a current-biased Josephson tunnel junction," Phys. Rev. Lett. **90**(3), 037003 (2003).

[43] J. Claudon, F. Balestro, F. W. J. Hekking, and O. Buisson, "Coherent Oscillations in a Superconducting Multilevel Quantum System," Phys. Rev. Lett. **93**(18), 187003 (2004).

[44] R. W. Simmonds, K. M. Lang, D. A. Hite, S. Nam, D. P. Pappas, and J. M. Martinis, "Decoherence in Josephson Phase Qubits from Junction Resonators," Phys. Rev. Lett. **93**(7), 077003 (2004).

[45] S. Oh, K. Cicak, J. S. Kline, M. A. Sillanpää, K. D. Osborn, J. D. Whittaker, R. W. Simmonds, and D. P. Pappas, "Elimination of two level fluctuators in superconducting quantum bits by an epitaxial tunnel barrier," Phys. Rev. B **74**(10), 100502 (2006).

[46] T. Bauch, T. Lindström, F. Tafuri, G. Rotoli, P. Delsing, T. Claeson, and F. Lombardi, "Quantum Dynamics of a d-Wave Josephson Junction," Science **311**(5757), 57 (2006).

[47] X. Y. Jin, J. Lisenfeld, Y. Koval, A. Lukashenko, A. V. Ustinov, and P. Müller, "Enhanced Macroscopic Quantum Tunneling in $Bi_2Sr_2CaCu_2O_{8+\delta}$ Intrinsic Josephson-Junction Stacks," Phys. Rev. Lett. **96**(17), 177003 (2006).

[48] B. D. Josephson, "Possible new effects in superconductive tunnelling," Phys. Lett. **1**(7), 251 (1962).

[49] P. W. Anderson, "How Josephson discovered his effect," Phys. Today **23**(11), 23 (1970).

[50] P. W. Anderson and J. M. Rowell, "Probable Observation of the Josephson Superconducting Tunneling Effect," Phys. Rev. Lett. **10**(6), 230 (1963).

[51] S. Shapiro, "Josephson Currents in Superconducting Tunneling: The Effect of Microwaves and Other Observations," Phys. Rev. Lett. **11**(2), 80 (1963).

[52] R. P. Feynman, R. B. Leighton, and M. Sands, *The Feynman Lectures of Physics*, vol. 3 (Addison-Wesley, Reading, MA, 1965).

[53] A. Barone and G. Paternò, *Physics and Applications of the Josephson Effect* (Wiley, New York, 1982).

[54] R. S. Newrock, C. J. Lobb, U. Geigenmüller, and M. Octavio, *Solid State Physics*, vol. 54 (Academic Press, San Diego, 2000).

[55] M. Tinkham, *Introduction to Superconductivity*, 2nd ed. (McGraw-Hill, New York, 1996).

[56] W. C. Stewart, "Current-Voltage Characteristics of Josephson Junctions," Appl. Phys. Lett. **12**(8), 277 (1968).

[57] D. E. McCumber, "Effect of ac Impedance on dc Voltage-Current Characteristics of Superconductor Weak-Link Junctions," J. Appl. Phys. **39**(7), 3113 (1968).

[58] L. Solymar, *Superconductive Tunnelling and Applications* (Wiley, New York, 1972).

[59] D. R. Tilley and J. Tilley, *Superfluidity and Superconductivity*, 3rd ed. (IOP, Bristol, 1990).

[60] T. A. Fulton and L. N. Dunkleberger, "Lifetime of the zero-voltage state in Josephson tunnel junctions," Phys. Rev. B **9**(11), 4760 (1974).

[61] M. Büttiker, E. P. Harris, and R. Landauer, "Thermal activation in extremely underdamped Josephson-junction circuits," Phys. Rev. B **28**(3), 1268 (1983).

[62] I. Giaever and K. Megerle, "Study of Superconductors by Electron Tunneling," Phys. Rev. **122**(4), 1101 (1961).

[63] V. Ambegaokar and A. Baratoff, "Tunneling between superconductors," Phys. Rev. Lett. **10**(11), 486 (1963). Erratum, **11**(2), 104 (1963).

[64] M. A. Gubrud, M. Ejrnaes, A. J. Berkley, R. C. Ramos, I. Jin, J. R. Anderson, A. J. Dragt, C. J. Lobb, and F. C. Wellstood, "Sub-Gap Leakage in $Nb/AlO_x/Nb$ and $Al/AlO_x/Al$ Josephson Junctions," IEEE Trans. Appl. Supercond. **11**(1), 1002 (2001).

[65] P. Silvestrini, O. Liengme, and K. E. Gray, "Current distrbutions of thermal switching in extremely underdamped Josephson junctions," Phys. Rev. B **37**(4), 1525 (1988).

[66] B. Ruggiero, C. Granata, V. G. Palmieri, A. Esposito, M. Russo, and P. Silvestrini, "Supercurrent decay in extremely underdamped Josephson junctions," Phys. Rev. B **57**(1), 134 (1998).

[67] A. J. Leggett, "Macroscopic Quantum Systems and the Quantum Theory of Measurement," Prog. Theor. Phys. (Suppl.) **69**, 80 (1980).

[68] J. M. Martinis, *Macroscopic Quantum Tunneling and Energy-Level Quantization in the Zero Voltage State of the Current-Biased Josephson Junction*, Ph.D. thesis, University of California (1985).

[69] W. H. Press, S. A. Teukolsky, W. T. Vetterling, and B. P. Flannery, *Numerical Recipes in C++*, 2nd ed. (Cambridge University Press, Cambridge, 2002).

[70] C. D. Tesche and J. Clarke, "dc SQUID: Noise and Optimization," J. Low Temp. Phys. **29**(3/4), 301 (1977).

[71] C. D. Tesche, *Noise and Optimization of the dc SQUID*, Ph.D. thesis, University of California (1978).

[72] T. A. Palomaki, S. K. Dutta, H. Paik, H. Xu, J. Matthews, R. M. Lewis, R. C. Ramos, K. Mitra, P. R. Johnson, F. W. Strauch, A. J. Dragt, C. J. Lobb, J. R. Anderson, and F. C. Wellstood, "Initializing the flux state of multiwell inductively isolated Josephson junction qubits," Phys. Rev. B **73**(1), 014520 (2006).

[73] K. Mitra, F. W. Strauch, H. Paik, S. K. Dutta, R. M. Lewis, T. A. Palomaki, A. J. Przybysz, B. K. C. A. J. Dragt, J. R. Anderson, C. J. Lobb, and F. C. Wellstood, "Quantum behavior of the dc SQUID phase qubit," *manuscript in preparation* .

[74] W.-T. Tsang and T. Van Duzer, "dc analysis of parallel arrays of two and three Josephson junctions," J. Appl. Phys. **46**(10), 4573 (1975).

[75] R. C. Ramos, F. W. Strauch, P. R. Johnson, A. J. Berkley, H. Xu, M. A. Gubrud, J. R. Anderson, C. J. Lobb, A. J. Dragt, and F. C. Wellstood, "Capacitively Coupled Josephson Junctions: A Two-Qubit System," IEEE Trans. Appl. Supercond. **13**(2), 994 (2003).

[76] P. R. Johnson, F. W. Strauch, A. J. Dragt, R. C. Ramos, C. J. Lobb, J. R. Anderson, and F. C. Wellstood, "Spectroscopy of capacitively coupled Josephson-junction qubits," Phys. Rev. B **67**(2), 020509(R) (2003).

[77] A. J. Berkley, H. Xu, R. C. Ramos, M. A. Gubrud, F. W. Strauch, P. R. Johnson, J. R. Anderson, A. J. Dragt, C. J. Lobb, and F. C. Wellstood, "Defining Entaglement," Science **301**(5637), 1183 (2003).

[78] H. Xu, F. W. Strauch, S. K. Dutta, P. R. Johnson, R. C. Ramos, A. J. Berkley, H. Paik, J. R. Anderson, A. J. Dragt, C. J. Lobb, and F. C. Wellstood, "Spectroscopy of Three-Particle Entanglement in a Macroscopic Superconducting Circuit," Phys. Rev. Lett. **94**(2), 027003 (2005).

[79] A. Abragam, *The Principles of Nuclear Magnetism* (Oxford, London, 1961).

[80] M. A. Nielsen and I. L. Chuang, *Quantum Computation and Quantum Information* (Cambridge University Press, Cambridge, 2000).

[81] D. J. Griffiths, *Introduction to Quantum Mechanics* (Prentice Hall, Upper Saddle River, NJ, 1995).

[82] L. Allen and J. H. Eberly, *Optical Resonance and Two-Level Atoms* (Dover, New York, 1987).

[83] F. W. Strauch, S. K. Dutta, H. Paik, T. A. Palomaki, K. Mitra, B. K. Cooper, R. M. Lewis, J. R. Anderson, A. J. Dragt, C. J. Lobb, and F. C. Wellstood, "Strong-field effects in the Rabi oscillations of the superconducting phase qubit," *submitted* .

[84] W. D. Oliver, Y. Yu, J. C. Lee, K. K. Berggren, L. S. Levitov, and T. P. Orlando, "Mach-Zehnder Interferometry in a Strongly Driven Superconducting Qubit," Science **310**(5754), 1653 (2005).

[85] G. S. Paraoanu, "Running-phase state in a Josephson washboard potential," Phys. Rev. B **72**(13), 134528 (2005).

[86] R. P. Feynman, *Statistical Mechanics: A Set of Lectures* (W. A. Benjamin, Reading, MA, 1972).

[87] J. J. Sakurai, *Modern Quantum Mechanics*, rev. ed. (Addison-Wesley, Reading, MA, 1994).

[88] J. Weiner and P.-T. Ho, *Light-Matter Interaction*, vol. 1 (John Wiley & Sons, Hoboken, NJ, 2003).

[89] R. A. Smith, "Excitation of transitions between atomic or molecular energy levels by monochromatic laser radiation," Proc. R. Soc. Lond. A **362**(1708), 1 (1978).

[90] H. Xu, A. J. Berkley, M. A. Gubrud, R. C. Ramos, J. R. Anderson, C. J. Lobb, and F. C. Wellstood, "Analysis of Energy Level Quantization and Tunneling From the Zero-Voltage State of a Current-Biased Josephson Junction," IEEE Trans. Appl. Supercond. **13**(2), 956 (2003).

[91] A. I. Larkin and Yu. N. Ovchinnikov, "Effect of level quantization on the lifetime of metastable states," Zh. Eksp. Teor. Fiz. **91**(1), 318 (1986). [Sov. Phys. JETP **64**(1), 185 (1986)].

[92] K. S. Chow, D. A. Browne, and V. Ambegaokar, "Quantum kinetics of a superconducting tunnel junction: Theory and comparison with experiment," Phys. Rev. B **37**(4), 1624 (1988).

[93] H. Xu, A. J. Berkley, R. C. Ramos, M. A. Gubrud, P. R. Johnson, F. W. Strauch, A. J. Dragt, J. R. Anderson, C. J. Lobb, and F. C. Wellstood, "Spectroscopic resonance broadening in a Josephson junction qubit due to current noise," Phys. Rev. B **71**(6), 064512 (2005).

[94] C. Moler and C. Van Loan, "Nineteen Dubious Ways to Compute the Exponential of a Matrix," SIAM Rev. **20**(4), 801 (1978).

[95] Hypres, Inc. 175 Clearbrook Road, Elmsford, NY 10523. www.hypres.com.

[96] K. M. Lang, S. Nam, J. Aumentado, C. Urbina, and J. M. Martinis, "Banishing Quasiparticles From Josephson-Junction Qubits: Why and How to do it," IEEE Trans. Appl. Supercond. **13**(2), 989 (2003).

[97] A. J. Berkley, H. Xu, M. A. Gubrud, R. C. Ramos, J. R. Anderson, C. J. Lobb, and F. C. Wellstood, "Characterization of an LC-Isolated Josephson Junction Qubit," IEEE Trans. Appl. Supercond. **13**(2), 952 (2003).

[98] M. Steffen, M. Ansmann, R. McDermott, N. Katz, R. C. Bialczak, E. Lucero, M. Neeley, E. M. Weig, A. N. Cleland, and J. M. Martinis, "State Tomography of Capactively Shunted Phase Qubits with High Fidelity," Phys. Rev. Lett. **97**(5), 050502 (2006).

[99] S. K. Dutta, H. Xu, A. J. Berkley, R. C. Ramos, M. A. Gubrud, J. R. Anderson, C. J. Lobb, and F. C. Wellstood, "Determination of relaxation time of a Josephson junction qubit," Phys. Rev. B **70**(14), 140502(R) (2004).

[100] S. S. Mohan, M. Hershenson, S. P. Boyd, and T. H. Lee, "Simple Accurate Expressions for Planar Spiral Inductances," IEEE J. Solid-State Circuits **34**(10), 1419 (1999). On-line calculator available at http://smirc.stanford.edu/spiralCalc.html.

[101] H. Paik, S. K. Dutta, R. M. Lewis, R. C. Ramos, T. A. Palomaki, H. Xu, A. J. Dragt, J. R. Anderson, C. J. Lobb, and F. C. Wellstood, "Dephasing and noise in dc SQUID phase qubits with variable isolation from the bias leads," *in preparation* .

[102] H. Paik, S. K. Dutta, R. M. Lewis, R. C. Ramos, H. Xu, T. A. Palomaki, K. Mitra, A. J. Przybysz, B. K. Cooper, A. J. Dragt, J. R. Anderson, C. J. Lobb, and F. C. Wellstood, "Varying high-frequency noise-induced transitions

in the inductively isolated current biased Josephson junction qubit," *in preparation* .

[103] J. R. Reitz, F. J. Milford, and R. W. Christy, *Foundations of Electromagnetic Theory*, 4th ed. (Addison-Wesley, Reading, MA, 1993).

[104] T. A. Palomaki, S. K. Dutta, R. M. Lewis, H. Paik, , K. Mitra, B. K. Cooper, A. J. Przybysz, A. J. Dragt, J. R. Anderson, C. J. Lobb, and F. C. Wellstood, "Fast High-Fidelity Measurements of the Ground and Excited States of a dc SQUID Phase Qubit," *submitted to* Phys. Rev. B .

[105] F. Pobell, *Matter and Methods at Low Temperatures*, 2nd ed. (Springer, Berlin, 1996).

[106] A. B. Zorin, "The thermocoax cable as the microwave frequency filter for single electron circuits," Rev. Sci. Instrum. **66**(8), 4296 (1995).

[107] P. C. Magnusson, G. C. Alexander, and V. K. Tripathi, *Transmission Lines and Wave Propagation*, 3rd ed. (CRC Press, Boca Raton, FL, 1992).

[108] J. M. Martinis, M. H. Devoret, and J. Clarke, "Experimental tests for the quantum behavior of a macroscopic degree of freedom: The phase difference across a Josephson junction," Phys. Rev. B **35**(10), 4682 (1987).

[109] A. Fukushima, A. Sato, A. Iwasa, Y. Nakamura, T. Komatsuzaki, and Y. Sakamoto, "Attenuation of Microwave Filters for Single-Electron Tunneling Experiments," IEEE Trans. Instrum. Meas. **46**(2), 289 (1997).

[110] K. Bladh, D. Gunnarsson, E. Hürfeld, S. Devi, C. Kristoffersson, B. Smålander, S. Pehrson, T. Claeson, and P. Delsing, "Comparison of cryogenic filters for use in single electronics experiments," Rev. Sci. Instrum. **74**(3), 1323 (2003).

[111] A. Wallraff, A. Lukashenko, C. Coqui, A. Kemp, T. Duty, and A. V. Ustinov, "Switching current measurements of large area Josephson tunnel junctions," Rev. Sci. Instrum. **74**(8), 3740 (2003).

[112] F. W. Strauch, P. R. Johnson, A. J. Dragt, C. J. Lobb, J. R. Anderson, and F. C. Wellstood, "Quantum Logic Gates for Coupled Superconducting Phase Qubits," Phys. Rev. Lett. **91**(16), 167005 (2003).

[113] M. Steffen, J. M. Martinis, and I. L. Chuang, "Accurate control of Josephson phase qubits," Phys. Rev. B **68**(22), 224518 (2003).

[114] K. B. Cooper, M. Steffen, R. McDermott, R. W. Simmonds, S. Oh, D. A. Hite, D. P. Pappas, and J. M. Martinis, "Observation of Quantum Oscillations between a Josephson Phase Qubit and a Microscopic Resonator Using Fast Readout," Phys. Rev. Lett. **93**(18), 180401 (2004).

[115] R. A. Ferrell and R. E. Prange, "Self-Field Limiting of Josephson Tunneling of Superconducting Electron Pairs," Phys. Rev. Lett. **10**(11), 479 (1963).

[116] S. Oh, K. Cicak, R. McDermott, K. B. Cooper, K. D. Osborn, R. W. Simmonds, M. Steffen, J. M. Martinis, and D. P. Pappas, "Low-leakage superconducting tunnel junctions with a single-crystal Al_2O_3 barrier," Supercond. Sci. Technol. **18**(10), 1396 (2005).

[117] J. M. Rowell, "Magnetic Field Dependence of the Josephson Tunnel Current," Phys. Rev. Lett. **11**(5), 200 (1963).

[118] D. N. Langenberg, D. J. Scalapino, and B. N. Taylor, "Josephson-Type Superconducting Tunnel Junctions as Generators of Microwave and Submillimeter Wave Radiation," Proc. IEEE **54**(4), 560 (1966).

[119] V. Lefevre-Seguin, E. Turlot, C. Urbina, D. Esteve, and M. H. Devoret, "Thermal activation of a hysteretic dc superconducting quantum interference device from its different zero-voltage states," Phys. Rev. B **46**(9), 5507 (1992).

[120] M. G. Castellano, F. Chiarello, G. Torrioli, and P. Carelli, "Static flux bias of a flux qubit using persistent current trapping," (2006). cond-mat/0608115.

[121] B. L. T. Plourde, T. L. Robertson, P. A. Reichardt, T. Hime, S. Linzen, C.-E. Wu, and J. Clarke, "Flux qubits and readout device with two independent flux lines," Phys. Rev. B **72**(6), 060506 (2005).

[122] S. Washburn, R. A. Webb, R. F. Voss, and S. M. Faris, "Effects of Dissipation and Temperature on Macroscopic Quantum Tunneling," Phys. Rev. Lett. **54**(25), 2712 (1985).

[123] M. H. Devoret, J. M. Martinis, and J. Clarke, "Measurements of Macroscopic Quantum Tunneling out of the Zero-Voltage State of a Current-Biased Josephson Junction," Phys. Rev. Lett. **55**(18), 1908 (1985).

[124] M. G. Castellano, R. Leoni, G. Torrioli, F. Chiarello, C. Cosmelli, A. Costantini, G. Diambrini-Palazzi, P. Carelli, R. Christiano, and L. Frunzio, "Switching dynamics of Nb/AlOx/Nb Josephson junctions: Measurements for an experiment of macroscopic quantum coherence," J. Appl. Phys. **80**(5), 2922 (1996).

[125] H. A. Kramers, "Brownian Motion in a Field of Force and the Diffusion Model of Chemical Reactions," Physica **7**(4), 284 (1940).

[126] I. Affleck, "Quantum-Statistical Metastability," Phys. Rev. Lett. **46**(6), 388 (1981).

[127] H. Grabert and U. Weiss, "Crossover from Thermal Hopping to Quantum Tunneling," **53**(19), 1787 (1984).

[128] F. Balestro, J. Claudon, J. P. Pekola, and O. Buisson, "Evidence of Two-Dimensional Macroscopic Quantum Tunneling of a Current-Biased dc SQUID," Phys. Rev. Lett. **91**(15), 158301 (2003).

[129] Y. C. Chen, M. P. A. Fisher, and A. J. Leggett, "The return of a hysteretic Josephson junction to the zero-voltage state: I-V characteristic and quantum retrapping," J. Appl. Phys. **64**(6), 3119 (1998).

[130] M. G. Castellano, G. Torrioli, F. Chiarello, C. Cosmelli, and P. Carelli, "Return current in hysteretic Josephson junctions: Experimental distribution in the thermal activation regime," J. Appl. Phys. **86**(11), 6405 (1999).

[131] P. R. Johnson, W. T. Parsons, F. W. Strauch, J. R. Anderson, A. J. Dragt, C. J. Lobb, and F. C. Wellstood, "Macroscopic Tunnel Splittings in Superconducting Phase Qubits," Phys. Rev. Lett. **94**(18), 187004 (2005).

[132] P. R. Johnson, W. T. Parsons, F. W. Strauch, J. R. Anderson, A. J. Dragt, C. J. Lobb, and F. C. Wellstood, "Erratum: Macroscopic Tunnel Splittings in Superconducting Phase Qubits," Phys. Rev. Lett. **95**(4), 049901 (2005).

[133] T. A. Palomaki, *unpublished*.

[134] B. Ruggiero, M. G. Castellano, G. Torrioli, C. Cosmelli, F. Chiarello, V. G. Palmieri, C. Granata, and P. Silvestrini, "Effects of energy-level quantization on the supercurrent decay of Josephson junctions," Phys. Rev. B **59**(1), 177 (1999).

[135] C. Cosmelli, P. Carelli, M. G. Castellano, F. Chiarello, G. Diambrini Palazzi, R. Leoni, and G. Torrioli, "Measurement of the Intrinsic Dissipation of a Macroscopic System in the Quantum Regime," Phys. Rev. Lett. **82**(26), 5357 (1999). S. Han and R. Rouse, Phys. Rev. Lett. **86**(18), 4191 (2001).

[136] Y. Yu, S. Han, X. Chu, S. Chu, and Z. Wang, "Coherent Temporal Oscillations of Macroscopic Quantum States in a Josephson Junction," Science **296**(5569), 889 (2002).

[137] D. J. Van Harlingen, T. L. Robertson, B. L. T. Plourde, P. A. Reichardt, T. A. Crane, and J. Clarke, "Decoherence in Josephson-junction qubits due to critical-current fluctuations," Phys. Rev. B **70**(6), 064517 (2004).

[138] F. C. Wellstood, C. Urbina, and J. Clarke, "Flicker $(1/f)$ noise in the critical current of Josephson junctions at 0.09-4.2 K," Appl. Phys. Lett. **85**(22), 5296 (2004).

[139] L. Faoro and L. B. Ioffe, "Quantum Two Level Systems and Kondo-Like Traps as Possible Sources of Decoherence in Superconducting Qubits," Phys. Rev. Lett. **96**(4), 047001 (2006).

[140] A. M. Zagoskin, S. Ashhab, J. R. Johansson, and F. Nori, "Quantum Two-Level Systems in Josephson Junctions as Naturally Formed Qubits," Phys. Rev. Lett. **97**(7), 077001 (2006).

[141] J. B. Majer, F. G. Paauw, A. C. J. ter Haar, C. J. P. M. Harmans, and J. E. Mooij, "Spectroscopy on Two Coupled Superconducting Flux Qubits," Phys. Rev. Lett. **94**(9), 090501 (2005).

[142] A. O. Niskanen, K. Harrabi, F. Yoshihara, Y. Nakamura, and J. S. Tsai, "Spectroscopy of three strongly coupled flux qubits," (2006). cond-mat/0609627.

[143] N. Kosugi, S. Matsuo, K. Konno, and N. Hatakenaka, "Theory of damped Rabi oscillations," Phys. Rev. B **72**(17), 172509 (2005).

[144] M. H. S. Amin, "Rabi oscillations in systems with small anharmonicity," Low Temp. Phys. **32**(3), 198 (2006).

[145] H. Paik, F. W. Strauch, R. C. Ramos, A. J. Berkley, H. Xu, S. K. Dutta, P. R. Johnson, A. J. Dragt, J. R. Anderson, C. J. Lobb, and F. C. Wellstood,

"Cooper-Pair Box as a Variable Capacitor," IEEE Trans. Appl. Supercond. **15**(2), 884.